NORTH ATLANTIC TREATY ORGANISATION

RESEARCH AND TECHNOLOGY ORGANISATION

AC/323(SET-080)TP/50

www.rta.nato.int

RTO MEETING PROCEEDINGS **MP-SET-080**

Target Identification and Recognition using RF Systems

(Reconnaissance et identification de cibles à l'aide des systèmes RF)

Papers presented at the RTO Sensors and Electronics Technology Panel (SET) Symposium held in the Banner Hall at the Defence Museum, Akershus Fortress in Oslo, Norway on 11-13 October 2004.

Published October 2004

NORTH ATLANTIC TREATY ORGANISATION

RESEARCH AND TECHNOLOGY ORGANISATION

AC/323(SET-080)TP/50

www.rta.nato.int

RTO MEETING PROCEEDINGS **MP-SET-080**

Target Identification and Recognition using RF Systems

(Reconnaissance et identification de cibles à l'aide des systèmes RF)

Papers presented at the RTO Sensors and Electronics Technology Panel (SET) Symposium held in the Banner Hall at the Defence Museum, Akershus Fortress in Oslo, Norway on 11-13 October 2004.

The Research and Technology Organisation (RTO) of NATO

RTO is the single focus in NATO for Defence Research and Technology activities. Its mission is to conduct and promote co-operative research and information exchange. The objective is to support the development and effective use of national defence research and technology and to meet the military needs of the Alliance, to maintain a technological lead, and to provide advice to NATO and national decision makers. The RTO performs its mission with the support of an extensive network of national experts. It also ensures effective co-ordination with other NATO bodies involved in R&T activities.

RTO reports both to the Military Committee of NATO and to the Conference of National Armament Directors. It comprises a Research and Technology Board (RTB) as the highest level of national representation and the Research and Technology Agency (RTA), a dedicated staff with its headquarters in Neuilly, near Paris, France. In order to facilitate contacts with the military users and other NATO activities, a small part of the RTA staff is located in NATO Headquarters in Brussels. The Brussels staff also co-ordinates RTO's co-operation with nations in Middle and Eastern Europe, to which RTO attaches particular importance especially as working together in the field of research is one of the more promising areas of co-operation.

The total spectrum of R&T activities is covered by the following 7 bodies:

- AVT Applied Vehicle Technology Panel
- HFM Human Factors and Medicine Panel
- IST Information Systems Technology Panel
- NMSG NATO Modelling and Simulation Group
- SAS Studies, Analysis and Simulation Panel
- SCI Systems Concepts and Integration Panel
- SET Sensors and Electronics Technology Panel

These bodies are made up of national representatives as well as generally recognised 'world class' scientists. They also provide a communication link to military users and other NATO bodies. RTO's scientific and technological work is carried out by Technical Teams, created for specific activities and with a specific duration. Such Technical Teams can organise workshops, symposia, field trials, lecture series and training courses. An important function of these Technical Teams is to ensure the continuity of the expert networks.

RTO builds upon earlier co-operation in defence research and technology as set-up under the Advisory Group for Aerospace Research and Development (AGARD) and the Defence Research Group (DRG). AGARD and the DRG share common roots in that they were both established at the initiative of Dr Theodore von Kármán, a leading aerospace scientist, who early on recognised the importance of scientific support for the Allied Armed Forces. RTO is capitalising on these common roots in order to provide the Alliance and the NATO nations with a strong scientific and technological basis that will guarantee a solid base for the future.

Published October 2004

ISBN 92-837-1145-9

Target Identification and Recognition using RF Systems

(RTO-MP-SET-080)

Executive Summary

The goal of this symposium was to describe the current and projected capability of RF systems for Non-Cooperative Target Identification/Recognition (NCTI/NCTR) at long range and in all weather conditions. Specific objectives were to review NCTI/NCTR R&D efforts available to NATO nations, suggest how and when this technology may contribute to an operational Combat Identification (CID) capability, and address coalition interoperability issues. The symposium was organized along the following themes: NCTI/NCTR of air targets, surface targets, passive RF systems & technology, and countermeasures against NCTI/NCTR.

The first half of this three-day symposium was classified NATO (S) and consisted of twenty-three oral presentations; these papers are available in a classified supplement to Symposium Proceedings. The second-half consisted of eighteen unclassified oral presentations and sixteen unclassified posters that were open to Partnership-for-Peace (PfP) nations.

The symposium started with overview presentations of three active SET TGs: SET-053 “Ground Target Recognition by Radar”, SET-068 “Modeling, Analysis and Recognition of Radar Signatures for Non-Cooperative Aircraft Identification”, and SET-069 “Advanced mmW Techniques for Ground Target Acquisition”. Chairmen of these TGs described their Programmes of Work and presented major results; much of the work discussed was later elaborated by other oral and poster presentations.

Most of the contributed papers discussed the state-of-the-art and problems associated with non-cooperative aircraft and ground vehicle recognition. Target classifiers were based mostly on analysis of high range resolution (HRR) profiles and synthetic aperture radar (SAR) or inverse synthetic aperture radar (ISAR) image analysis. A recurrent theme was the comparison of classification results based on real data with results obtained from synthetic (model) data. Numerous presentations described and compared the relative merits of various computational electromagnetic codes for predicting synthetic target signatures and imagery. Various target classification algorithms and/or systems were described and compared. One general observation is that each classifier described performs about as well as another; there is no compelling reason to chose a particular classifier. This conclusion seems to be independent of target type. A few fielded systems consisting of sensor and classifier were described.

Other topics included the contribution of RF polarimetry to target ID, the application of joint time-frequency analysis for improving radar imagery, and passive bi/multi-static sensor systems for covertly obtaining target data. The capability of NCTI/NCTR using HF radar was described in a contribution from Australia.

Reconnaissance et identification de cibles à l'aide des systèmes RF

(RTO-MP-SET-080)

Synthèse

Ce symposium avait pour objectif de présenter la capacité actuelle et projetée en systèmes RF pour l'identification/reconnaissance de cibles non coopératives (NCTI/NCTR) à grande distance et tous temps. Les organisateurs ont voulu entre autres faire le point sur les activités de R&D en cours au sein de l'OTAN dans ce domaine, prévoir à quelle échéance et de quelle manière ces technologies pourraient être mises à contribution dans la réalisation d'une capacité d'identification de cibles non coopératives (CID), et examiner la question de l'interopérabilité des coalitions. Il était organisé autour des thèmes suivants : le NCTI/NCTR de cibles aériennes et de cibles de surface, les technologies et les systèmes RF passifs, ainsi que les contre-mesures contre le NCIT/NCTR.

La première partie de ce symposium de trois jours était classifiée NATO (S) et consistait en vingt-trois présentations orales. Ces communications sont disponibles sous forme d'un supplément classifié au compte rendu du symposium. La deuxième partie était composée de dix-huit communications orales non classifiées, ainsi que de seize présentations données lors des séances d'affiches, ouvertes aux membres des pays du Partenariat pour la paix (PPP).

Le symposium a débuté par des présentations résumant l'état d'avancement des trois TG actifs, à savoir : SET-053 « La reconnaissance radar des cibles au sol », SET-068 « La modélisation, l'analyse et la reconnaissance des signatures radar pour la reconnaissance de signatures radar aux fins d'identification d'aéronefs non coopératifs », et SET-069 « Les techniques mmW avancées de reconnaissance de cibles au sol ». Le président des TG a décrit leurs programmes de travail et a présenté les principales conclusions ; bon nombre des sujets évoqués ont été développés plus avant lors d'autres présentations orales et de séances d'affiches ultérieures.

La plupart des communications reçues ont porté sur l'état actuel des connaissances dans le domaine ainsi que sur les problèmes associés aux aéronefs non coopératifs et la reconnaissance des véhicules au sol. Les classificateurs de cibles étaient basés sur l'analyse de profils de haute résolution en distance (HRR), ainsi que sur l'analyse d'imagerie obtenue par des systèmes radar à ouverture synthétique (SAR) et à ouverture synthétique inverse (ISAR). La comparaison des résultats de classification basés sur des données réelles avec des résultats obtenus à partir de données synthétiques (modèles) est revenue souvent dans les discussions. De nombreuses communications présentaient et comparaient les avantages relatifs de différents codes de calcul électromagnétiques pour la prévision de signatures et de l'imagerie de cible synthétiques. Différents algorithmes et/ou systèmes de classification de cibles ont été présentés et comparés. Il est apparu de façon générale que les performances des différents classificateurs étaient plus ou moins égales et que, par conséquent, il n'y avait pas de raison impérieuse de choisir tel classificateur plutôt que tel autre. Cette conclusion semble être indépendante du type de cible. Un certain nombre de systèmes mis en service, composés de capteurs et de classificateurs, ont été présentés.

Les autres questions examinées comprenaient la contribution de la polarimétrie RF à l'identification des cibles, la mise en application de l'analyse temps-fréquence pour l'amélioration de l'imagerie radar et les systèmes bi/multistatiques passifs pour la recherche furtive de données de cible. Enfin, l'Australie a présenté les possibilités de NCTI/NCTR à l'aide de radars HF.

Table of Contents

‡ No papers were submitted for the Overview presentations.

* Paper published in Classified Supplement RTO-MP-SET-080(S).

\+ Associated presentation is NATO Restricted, therefore is published in Classified Supplement RTO-MP-SET-080(S).

* Paper published in Classified Supplement RTO-MP-SET-080(S).

* Paper published in Classified Supplement RTO-MP-SET-080(S).

† Paper not presented.

Sensors and Electronics Technology Panel

CHAIRMAN

Prof. M. TACKE
FGAN-FOM
Gutleuthausstr. 1
76275 Ettlingen
GERMANY

DEPUTY CHAIRMAN

Dr. Y. JONES KING
US Air Force
AFRL/VSS
Kirtland AFB, NM 87117-5776
UNITED STATES

TECHNICAL PROGRAMME COMMITTEE

CHAIRMAN

Dr. William MICELI (US)
Dr. René VAN DER HEIDEN (NE)

MEMBERS

Dr. Svein-Erik HAMRAN (NO)
Dr. Udo USCHKERAT (GE)
Dr. Roger CRANOS (US)
Dr. Luc VIGNAUD (FR)
Dr. Trygve SPARR (NO)
Dr. Sjoerd GELSEMA (NE)
Dr. David BLACKNELL (UK)
Dr. Hartmut SCHIMPF (GE)
Dr. Adrian BRITTON (UK)
Dr. Bert VAN DEN BROEK (NE)

HOST NATION LOCAL COORDINATOR

Dr. Trygve SPARR

PANEL EXECUTIVE

Lt. Col. G. FIAMINGO (ITAF)

From Europe:
RTA-NATO
Attn: SET Executive
BP 25
F-92201 Neuilly-sur-Seine Cedex
FRANCE

From the USA or Canada:
RTA-NATO
Attn: SET Executive
PSC 116
APO AE 09777

Aspects of NCTR for Near-Future Radar

Robert Miller, David Shephard, Mark Newman
BAE SYSTEMS Advanced Technology Centre
West Hanningfield Road
Great Baddow, Chelmsford
Essex CM2 8HN
United Kingdom

robert.j.miller@baesystems.com

SUMMARY

This paper considers a number of aspects related to the achievement of non-cooperative target recognition capabilities in current and near-future radar systems. The scope of the paper is restricted to consideration of the use of high range-resolution profiles. Three particular aspects are discussed. Firstly, the problem of achieving a high range-resolution capability on radars which typically have only narrow instantaneous bandwidths is considered; an approach is described in which the usual shortcomings associated with step-frequency waveforms are avoided. Secondly, the consequences of having less than ideal performance from the radar system are considered. The loss in classification performance which occurs when returns are degraded in terms of resolution and signal-to-noise ratio are described. The results given apply to civil aircraft and compare performance from a feature-matching and a profile-correlation algorithm. The third aspect considered relates to the nature of the classifier itself. There are numerous choices to be made; we discuss what data should be used for classification, sources of reference data for classifiers and different types of classification algorithm. A focus is placed on the representation of reference data as a scattering centre model of each aircraft of interest; such a model attempts to give an abstract representation of key features in a form which may incorporate both radar and non-radar data, and which is not particular to any one radar system.

1.0 INTRODUCTION

The desirability of the inclusion of some degree of non-co-operative target recognition (NCTR) capability in current and future radar systems is widely recognised. Discussions of NCTR techniques frequently assume the use of a purpose-built radar; however, in view of the long life-times of contemporary radar systems, this is not realistic. It is highly desirable to utilise if at all possible the untapped potential of current radar systems to perform NCTR. The paper starts from this view-point, and discusses a number of issues associated with introducing NCTR capability to contemporary or near-future radar systems.

Two different approaches for using radar to provide NCTR capability are commonly discussed, i.e. (i) analysis of frequency modulation of returns (jet engine modulation, helicopter rotor modulation) and (ii) comparison of high-resolution range profiles (HRRP) with reference data on signatures of targets of interest. This paper considers only the latter approach. The scope of the paper is also limited to a consideration of air targets.

The use of existing or modestly upgraded radar systems often implies that there are limitations on the waveforms that can be used for NCTR, and these will impact on NCTR performance. The first part of this paper discusses a novel technique for generating HRRP waveforms from a sequence of narrow-band pulses. This technique avoids the shortcomings of a conventional step-frequency approach, which may lead to aliasing, high range sidelobes and wrap-round of long targets. The new technique combines pulses

Paper presented at the RTO SET Symposium on "Target Identification and Recognition Using RF Systems", held in Oslo, Norway, 11-13 October 2004, and published in RTO-MP-SET-080.

using motion compensation which is accurate to within a fraction of a wavelength to achieve a high bandwidth synthetic waveform which is free of phase discontinuities.

The second part of the paper considers results obtained from degrading high-resolution profiles to show how classifier performance changes with variation in resolution and signal-to-noise ratio. Two different kinds of classifier are considered, the first based on feature matching, and the second based on direct comparison of profiles with reference data.

The third part of the paper considers in greater depth the performance of different types of classifier, and the nature of the reference data used to perform the classification and its impact on performance. This consideration also overlaps with fundamental concerns regarding the source of reference data on many targets of interest – while it may sometimes be possible to obtain detailed radar measurements of friendly aircraft, different sources of data will need to be used for other aircraft. Particular consideration is given to the use of a reference model which describes the principal scattering centres on each aircraft of interest. The validity of such a model is considered, as is the inclusion of both radar and non-radar data in such a model.

2.0 GENERATION OF HRRP WAVEFORMS

The ability of a radar system to identify a target from its radar range profile is directly dependent on the achieved range resolution, which is in turn dependent on the transmitted bandwidth of the signal. Early work indicated that a bandwidth of about 400 MHz is required to identify air targets. Ideally this would be achieved using a wideband instantaneous waveform. Most radars currently in service have a very limited instantaneous bandwidth. This makes it impossible without a major redesign to achieve the required bandwidth using an instantaneous waveform. The overall RF bandwidth of the system is generally wide enough that an alternative is to synthesise the required bandwidth by frequency stepping.

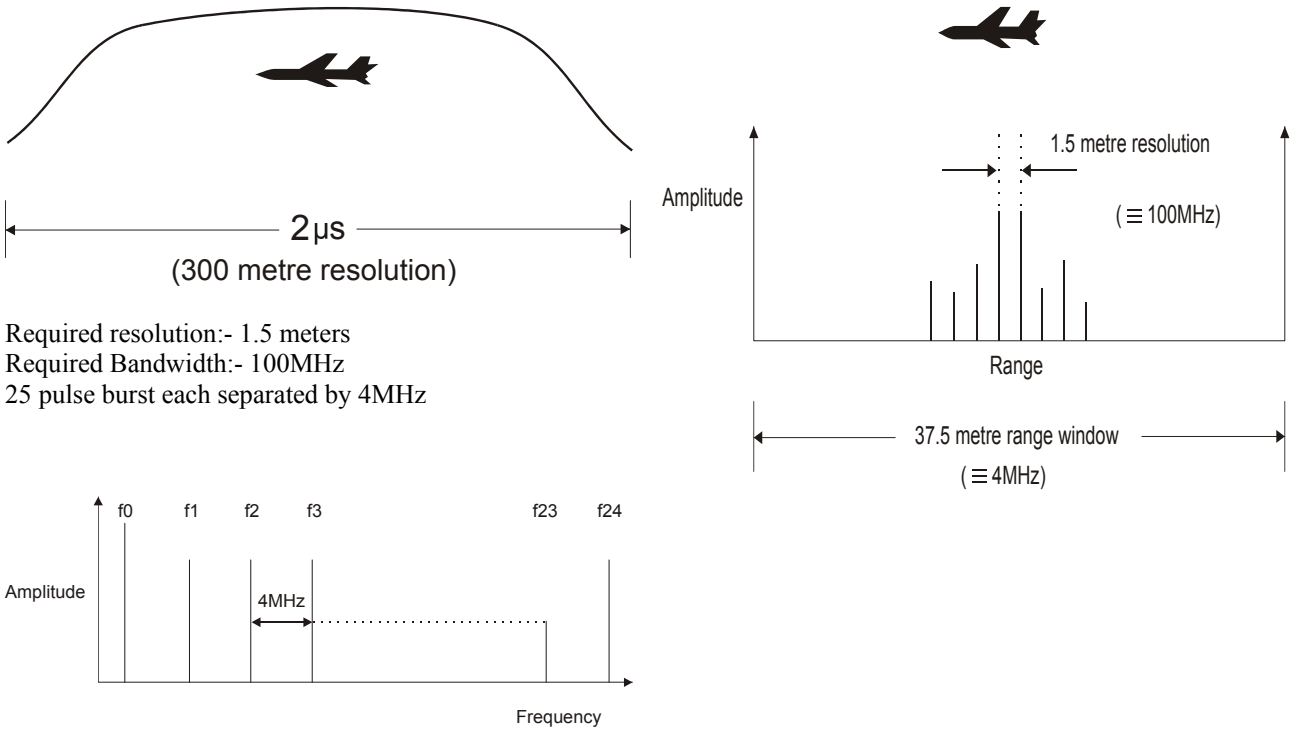

Figure 1: Traditional Step Frequency Technique

This frequency-stepping technique has been shown to work successfully and is described in detail in standard reference books such as that by Wehner [1]. This type of technique is shown schematically in Figure 1. In this example, a 25-pulse burst with a 4 MHz separation between pulses is used to generate a synthetic bandwidth of 100 MHz. It is important to note that the size of the resulting time-domain window is proportional to the reciprocal of the frequency step; in the example given the 4 MHz frequency step results in a synthesised range window 37.5 metres long. Aircraft longer than this window will be incorrectly profiled due to wraparound effects. This will restrict the length of targets that can be profiled using the traditional step frequency technique. To address this issue, an alternative technique known as Hybrid Stepped Frequency Range Profiling has been developed by BAE SYSTEMS ATC.

The hybrid stepped-frequency method involves the transmission of a series of narrow-band FM chirps, transmitted at stepped carrier frequencies. The returned signals are combined to form a wide bandwidth result spanning a continuous range of frequency – there are no gaps or phase discontinuities. The FM chirps can be compressed against a reference either individually before summation, or all together after summation. This technique has been successfully demonstrated at our radar test site in Great Baddow, UK.

The technique has been used to produce range profiles of both stationary calibration targets and aircraft in flight. Figure 2 shows a range profile of a stationary test target. The range swath is in excess of one kilometre and shows that the hybrid step-frequency technique is not limited by the 1/frequency-step range ambiguity of the traditional method.

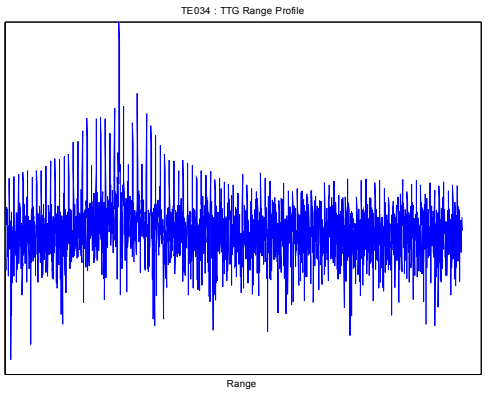

Figure 2: Range profile of test target

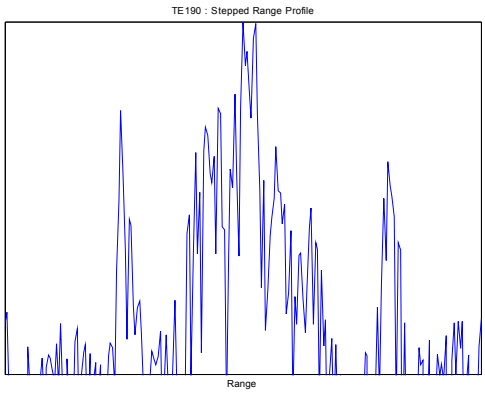

Figure 3: Profile of airborne target

Figure 3 shows a range profile of a target of opportunity identified as a Boeing 747 measured at a range of 21 km and having a radial speed of 351 knots. The 747 has a length of over 70 m; it is evident that no fold-over is occurring in the profile.

The detailed sidelobe structure of the motion-compensated waveform obtained from airborne targets has been compared with that obtained from calibration targets; they are found to be virtually identical. This demonstrates that the motion-compensation techniques employed are sufficiently accurate and robust to generate high-quality profiles. The range profiles obtained using the hybrid technique are generally found to be of very high fidelity and compare favourably with data measured using an instantaneous wideband waveform.

The processing can be taken a stage further by applying the technique to each Doppler channel in a burst. The resulting range-Doppler map is shown in Figure 4(a). The distribution of the Jet Engine Modulation, either side of the skin return, is within the anticipated range window and does not show any range-Doppler coupling. Figure 4(b) shows a second result measured from a Boeing 737. This target was at 13.5 km and a radial speed of 272 knots. In this example, each of two engines give rise to two distinct Doppler sidebands.

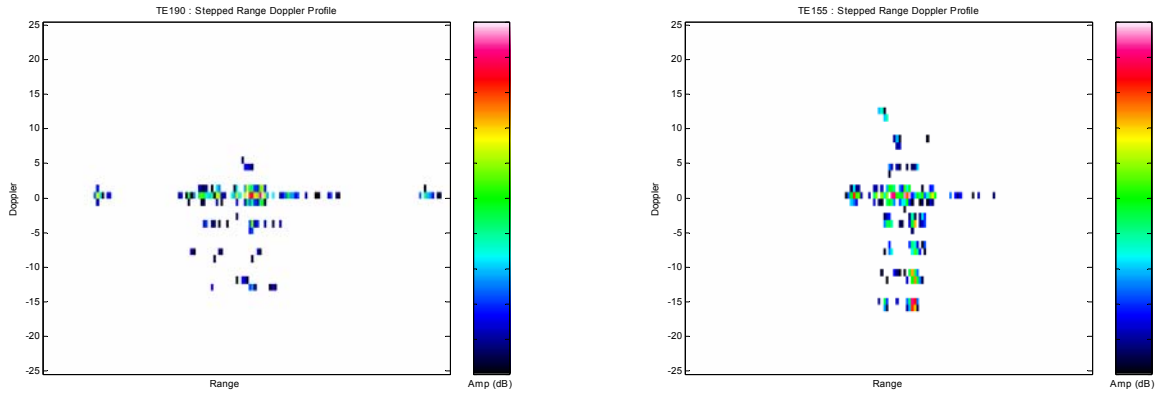

(a) range-Doppler map for Boeing 747 **(b) range-Doppler map for Boeing 737**

Figure 4: Range-Doppler maps

This technique for producing high range resolution profiles of air targets is robust. It can be applied to targets of opportunity with sufficient information available from the measured data to enable motion compensation to be undertaken to high accuracy.

3.0 VARIATION OF RESOLUTION AND SNR

This section considers the effects of variation of range-resolution and signal-to-noise ratio on classifier performance. Two forms of classifier are considered.

3.1 Data

High-resolution data was collected consisting of a sequence of 50 1 μS pulses, each modulated with a 270 MHz linear FM chirp. 1000 samples of each pulse were taken at a rate of 400 MHz. Pulses are compressed using a reference profile from a point target and the results are motion-compensated to produce a stack of aligned range profiles. Doppler processing is then applied to produce a range-Doppler map. This separates the skin echo from engine returns. A sample set of 58 aircraft datasets, consisting of six different types, was selected from a database of trial data. Table 1 lists the aircraft selected. The identity of these aircraft has been confirmed by National Air Traffic Services (NATS).

Aircraft Type	Class	No. of Datasets
Boeing 747	large civil	11
Lockheed Tristar	large civil	8
Boeing 707	large civil	8
Boeing 737	medium civil	10
Boeing 757	medium civil	11
McDonald Douglas MD80	medium civil	10
Total		*58*

Table 1: Aircraft types in trial data

3.2 Classification Algorithms

Two types of algorithm have been considered, a *feature-matching* algorithm and a *profile-correlation* algorithm.

The feature-matching algorithm attempts to match features of the observed aircraft to a list of features stored in a database. These features include length, distance of engines from the nose and number of engines. A range-Doppler map (see Figure 4) is used to distinguish the skin return from engine returns. The algorithm is designed to recognise aircraft over aspect angles between 0° and ±40° from the nose since the JEM required to distinguish the engines is typically visible only over this range. The reference database used contains 71 aircraft types and variants. These aircraft have been separated into 4 generic classes: large civil, medium civil, small civil and large military. The information about each aircraft in the database has been gathered from technical data available in the public domain. The aircraft type is determined according to the greatest number of satisfactory matches; the class is determined from the type classification. An aircraft may be unclassified if no satisfactory matches occur.

The profile-correlation algorithm uses only the range profile of the skin echo from the data, i.e. the contents of the zero-Doppler bin in the range-Doppler map. Profiles are correlated with profiles in a reference database which consists of 612 sampled range profiles. The identity of most aircraft has been confirmed by NATS. The profiles in this database have been separated into the same four generic types as before: large civil, medium civil, small civil and large military. The trial dataset used is a subset of the reference profiles, but the algorithm excludes correlation of a profile with itself. A k nearest-neighbour algorithm is used with classification being based on the majority type or class from the 10 best matches.

In normal use, any NCTR algorithm would be used in conjunction with tracking data to estimate the aspect angle of the target aircraft; such data was not available for the profiles considered here, so classifier performance is generally not as good as it could be.

3.3 Reduction of Resolution and SNR

To assess the effect of variation of range resolution and SNR on the performance of the classifiers, the trial data was degraded in one of two ways, either (i) by reducing the sampling rate to approximately emulate the effect of reducing range resolution or (ii) by decreasing the signal-to-noise ratio by injecting additional noise into the original data.

3.3.1 Range Resolution

To estimate the effects of degradation in range resolution, the data in each of the trial datasets was methodically reduced by re-sampling. The effect of an increase in sampling interval (SI) from 0.375 m to 1.875 m on the range-Doppler map and the range profile is illustrated in Figure 5.

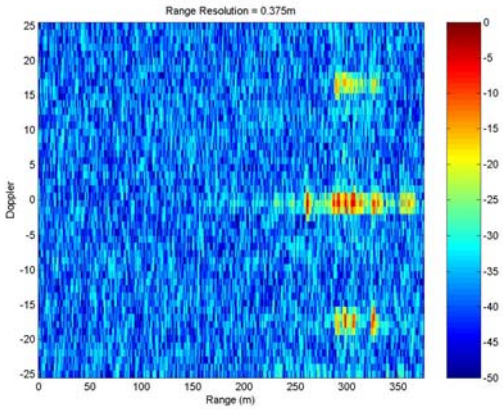

(a) range-Doppler map SI = 0.375 m

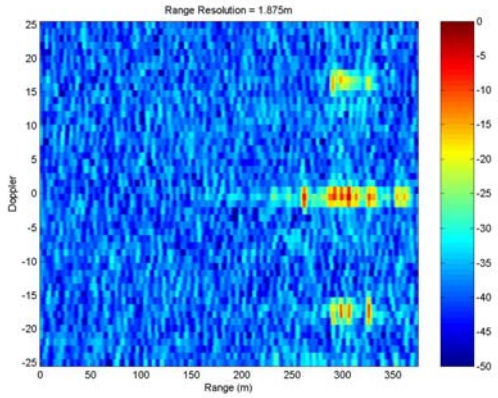

(b) range-Doppler map SI = 1.875 m

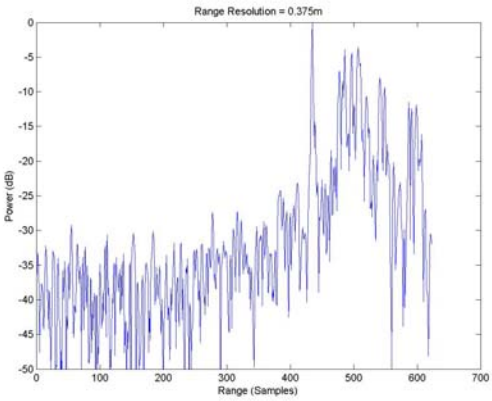

(c) range-profile SI = 0.375 m

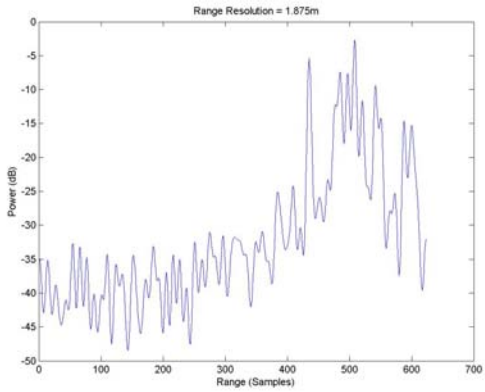

(d) range profile SI = 1.875 m

Figure 5: Effects of reduced range resolution on range-Doppler map and range profile

3.3.1.1 Feature-Matching Algorithm

Figure 6(a) shows that the feature-matching algorithm initially classifies around 50% of the trial datasets correctly to type, and that this performance falls away approximately linearly as resolution is decreased. Figure 6(b) shows that the algorithm is able to correctly identify the generic class of all classified datasets. The number of unclassified datasets rises as the sampling interval is increased. Datasets are unclassified when the algorithm is unable to match the aircraft length and the position of its engines to any reference set in the database.

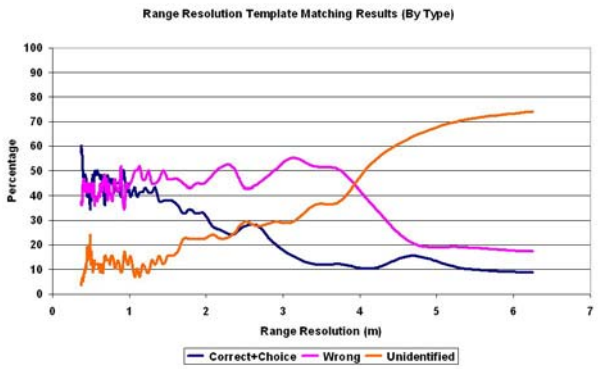

(a) classification to type

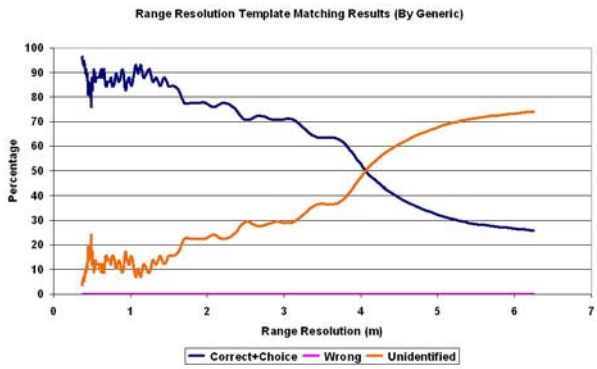

(b) classification to class

Figure 6: Effects of reduction in range resolution for feature-matching classifier

More detailed analysis of the results indicates that smaller aircraft are mis-identified, but that they are always identified with an aircraft of the same class. This is why the class results are much better than the type-specific results.

3.3.1.2 Profile-Correlation Algorithm

Figure 7(a) shows that the profile-correlation algorithm displays an approximately linear drop in performance as the sampling interval is increased. This algorithm is capable of correctly identifying over 80% of aircraft measured with a range resolution of 2.5 meters or less. Figure 7(b) shows that performance for identification of target class is similar to that for identification of target type. Datasets are never unclassified under the profile-correlation algorithm, but performance to class may be worse than performance to type. For example, suppose that 4 of the 10 matches are of a Boeing 747, 3 matches are a Boeing 767 and the remaining 3 are a Boeing 757. The type chosen would be a Boeing 747 (correct) but the generic class would be a medium civil aircraft (incorrect).

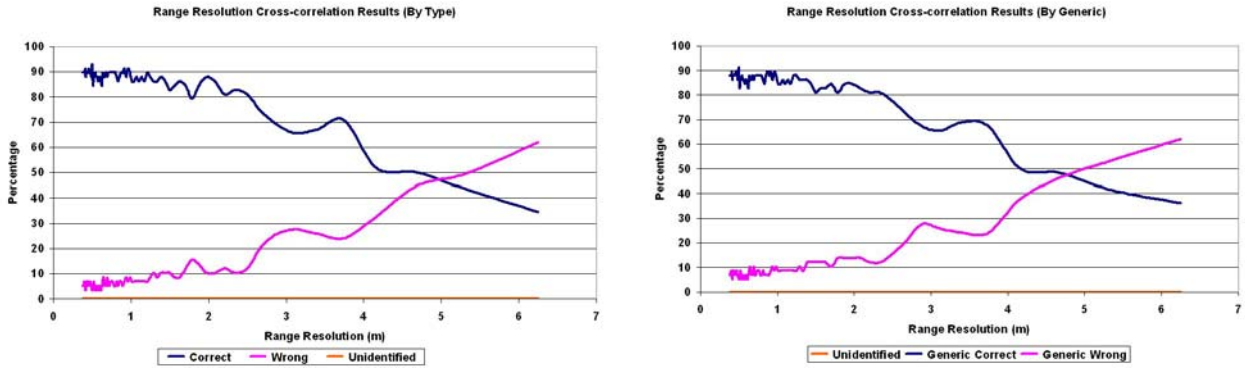

(a) classification to type **(b) classification to class**

Figure 7: Effects of reduction in range resolution for profile correlation classifier

Again, smaller aircraft tend to be more frequently mis-identified. The large Boeing 747 is correctly identified for 10 of the 11 Boeing 747 datasets, even with a sampling interval of 6.5 meters.

3.3.2 Signal to Noise Ratio

To simulate a reduced signal to noise ratio, the original datasets were combined with sampled noise data taken from the radar system with the transmitter turned off. Repeatable results were produced by using a single noise dataset injected at varying intensities.

3.3.2.1 Feature-Matching Algorithm

Figure 8(a) shows that there is a linear drop in the number of correct identifications as the SNR decreases. Figure 8(b) shows that the algorithm's ability to identify the generic class of the aircraft is not significantly affected until the signal to noise ratio is decreased by around 15 dB. Up to this point, over 90% of the target aircraft are correctly identified to class.

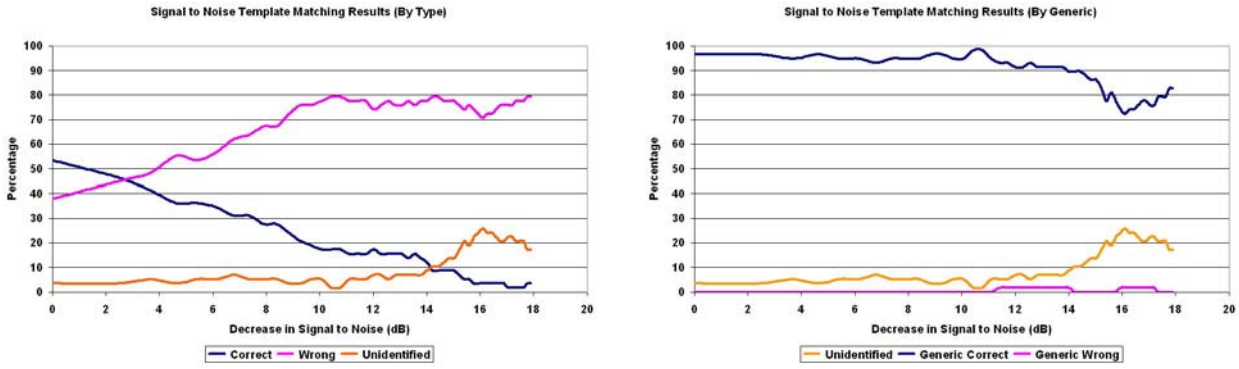

(a) classification to type **(b) classification to class**

Figure 8: Effects of reduction in SNR for feature-matching classifier

As the signal to noise ratio was reduced the smaller aircraft begin to be mis-identified. Since the larger aircraft like the Boeing 747 produce a larger return, and therefore have a higher signal to noise ratio to start with, the degradation of the signal is less than that of the smaller aircraft. The signal to noise change has a more significant effect on the signature of smaller aircraft than on larger aircraft.

3.3.2.2 Profile-Correlation Algorithm

Figure 9(a) and Figure 9(b) show that initially there is very little drop in the performance of the algorithm as the signal to noise ratio is decreased. However, once the signal to noise level has been decreased by around 8 dB, the performance begins to drop linearly. As previously, the performance of this classifier when identifying targets to class is slightly worse than when identifying the type of the aircraft.

As with the feature-matching algorithm, smaller targets are mis-identified first.

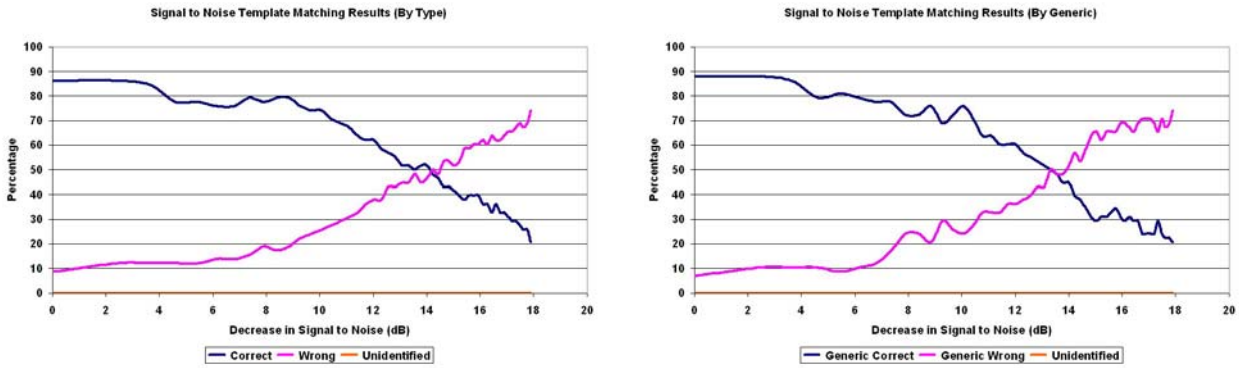

(a) classification to type **(b) classification to class**

Figure 9: Effects of reduction in SNR for profile-correlation classifier

3.4 Conclusions

Even with the relatively large aircraft considered here, it is apparent that decrease in range resolution leads to quite a rapid fall-off in classifier performance for both algorithms. It therefore seems desirable to use sub-metre range resolution if at all possible. Profile-correlation seems to be more robust to decrease in SNR for classification to type, whereas template-matching seems to be more robust for classification to class. It would be of interest to determine which features of the algorithms are responsible for these different performance characteristics. Finally, the performance of the profile-correlation algorithm is

generally substantially better than the feature-matching algorithm, which indicates that it may be possible to identify a richer feature set to improve the performance of the latter algorithm.

4.0 CLASSIFICATION ISSUES

In the present context, a classifier is a mechanism which makes an association between radar measurements of an aircraft and a particular class or type of aircraft. In order to make this association, it makes reference to some form of prior knowledge about each type of aircraft which may be of interest. Statistical classification algorithms work on the basis that the measurements, possibly after some processing, may be regarded as a point in a high-dimensional 'decision space'. The prior knowledge serves to divide up the decision space into non-overlapping regions, each of which is associated with a particular target type. The algorithm notes which of these regions the measurement point falls into, and makes its decision accordingly. Provision may also be made for measurement points to be unclassified – the measurements may, for example, be too noisy.

There are many different types of classification algorithm - nearest neighbour, neural nets, tree pruning and so on. These vary in the complexity of the decision surfaces they may represent. However, they all depend critically on the quality of the information they are supplied with to form the decision surfaces. The information that is available and its quality is the focus of our emphasis here; the classification algorithm used is in all cases a simple, classical k-nearest neighbour algorithm [2].

4.1 Target Measurements

Classification is generally performed on the basis of several measured profiles of the target aircraft, not just one. In the extreme case, hundreds of profiles may be used in order to form an ISAR image of the aircraft. Rihaczek and Hershkowitz [3] use this approach in order to filter out off-fuselage returns; this has a distinct advantage, in that returns from the wings of an aircraft can often be confusing since many different stores configurations may be employed with a single type of aircraft. The use of ISAR has, however, at least two distinct disadvantages. Firstly, in order to obtain the large number of profiles required, the dwell time must be long, and this is often operationally unattractive. Secondly, ISAR relies on the use of cross-track motion relative to the radar, and it is therefore not at all clear that ISAR may be used for the important case of aircraft flying more or less directly towards the radar. For these reasons, ISAR has not been considered further in the present work.

Radar returns from aircraft vary rapidly with aspect angle, principally due to multiple scatterers occurring in the same range gate and interfering with each other. This variability is unhelpful to classifiers and it is therefore desirable to reduce it where possible. Some degree of reduction in variability may be achieved by averaging over a small number of profiles; this technique has therefore been adopted in the current work. Separation of engine returns from fuselage returns may also be achieved by applying Doppler processing to a small number of profiles.

4.2 Prior Knowledge

Prior knowledge of the backscatter characteristics of an aircraft may be obtained from many sources. The best classification results have been obtained using detailed radar measurements of target aircraft of interest. Such measurements must be made over all aspect angles from which the aircraft is likely to be observed, and are therefore time-consuming and expensive to obtain. Exemplars of likely hostile aircraft may also be difficult to obtain. Consequently, alternative sources of prior knowledge have been sought.

Good results have also been obtained using scale measurements of detailed aircraft models. Such models are again expensive, and the quality of classification achieved depends on the level of detail which goes

into the models. It is not sufficient to represent backscatter from the just the skin of the aircraft, since returns may be obtained from components hidden under the skin by radar-transparent materials; perhaps the most obvious case is radar equipment covered by a radome in the front of many fighter aircraft.

A third source of prior knowledge is the use of detailed computer models of aircraft used in conjunction with computational electromagnetics (CEM) codes to infer backscatter characteristics. Errors may occur from two principal sources. Firstly, the model may be insufficiently accurate or lack critical components such as antennas or small air inlets. Secondly, CEM codes used are often based on approximations such as physical optics and GTD (geometric theory of diffraction). Rigorous 'full-wave' codes such as method of moments and FDTD (finite difference time domain) also exist, but they are computationally expensive, and it is not yet feasible to apply such codes to, say, fighter-sized aircraft illuminated with X-band frequencies. However, there is continual progress in this area [4].

Prior knowledge from any of the sources noted above can be used to provide templates to which measured profiles are matched, or may be used as training data to set up decision surfaces. Rather than use reference profiles directly in this manner, we have chosen to identify prominent returns in each profile and to incorporate these into a model from which reference profiles may be regenerated. The notion is that, for each aircraft of interest, we generate a model of the prominent scattering centres on the aircraft. Each scattering centre is described in terms of its position and how the amplitude and phase of its return varies with aspect angle – note that this is quite different from describing the returns in terms of those from a number of isotropic point scatterers. For the scattering centre model to be of value in classification, there should be only a small number of scattering centres for each aircraft (say less than 10), and the returns from each scattering centre should persist over an appreciable range of aspect angle (say greater than 10°).

An advantage of this approach is that other forms of prior knowledge than those mentioned above may be easily incorporated into the model. In particular, the approximate location of at least some scattering centres may be inferred from material such as engineering drawings, CAD models and photographs of aircraft.

The scattering centre model is only a model – it is at best an approximate representation of radar backscatter from an aircraft. This model may be directly validated by forming a map of reflectivity over the whole aircraft constructed from profiles taken over a range of accurately known aspect angles using tomographic principles. Scattering centres should be evident as 'hot-spots' on tomograms generated in this manner.

Figure 10 shows a set of range profiles obtained at different aspect angles (a) and the tomogram derived from them (b). The range profiles are aligned in such a way that the aircraft appears to rotate about some fixed point. Prominent scattering centres in the range profiles will describe sinusoidal arcs – several of these are evident in Figure 10(a). The tomographic reconstruction maps these arcs into single points in the tomogram.

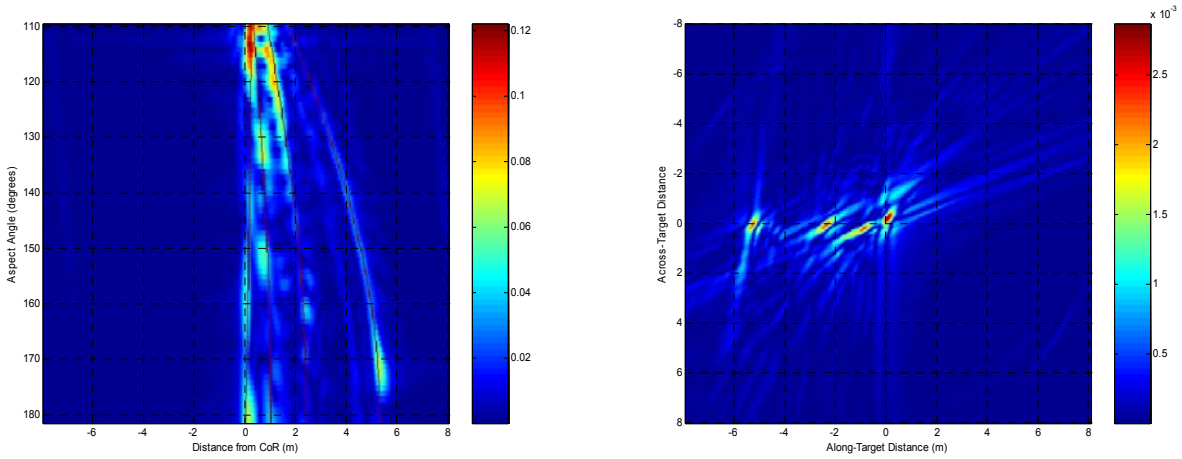

(a) aligned range profiles **(b) tomogram constructed from profiles**

Figure 10: Range profiles and tomogram

The range profiles shown in Figure 10 were obtained by applying a CEM code to a computer model of an aircraft. The fact that the tomogram exhibits only a small number of discrete points supports the validity of representing backscatter from an aircraft as a scattering centre model. A similar analysis may be applied to actual radar measurements of an aircraft to determine to what extent a scattering centre model is appropriate.

4.3 Classification

The nearest neighbour method of classification relies on a comparison of measured data, or features derived from it, with reference data. For aircraft targets, comparison is complicated by the following two factors.

Firstly, aircraft signatures depend on aspect angle, but the aspect angle at which an aircraft is measured is seldom known at all accurately. The course of the aircraft may be estimated from tracking data, but this does not accurately indicate its aspect, since aircraft commonly do not point in the direction they are heading due to cross-winds – they 'crab' with respect to their course. The crab angle may be several degrees. For this reason, it is necessary to compare measurements with reference data applicable to a range of aspect angles – we use ±5° about the estimated course.

Secondly, the range at which features occur in range profile measurements is potentially a powerful discriminant amongst aircraft, so that, before reference data can be used, it must be aligned with the measured profiles. Such alignment is a significant part of the overall classification algorithm.

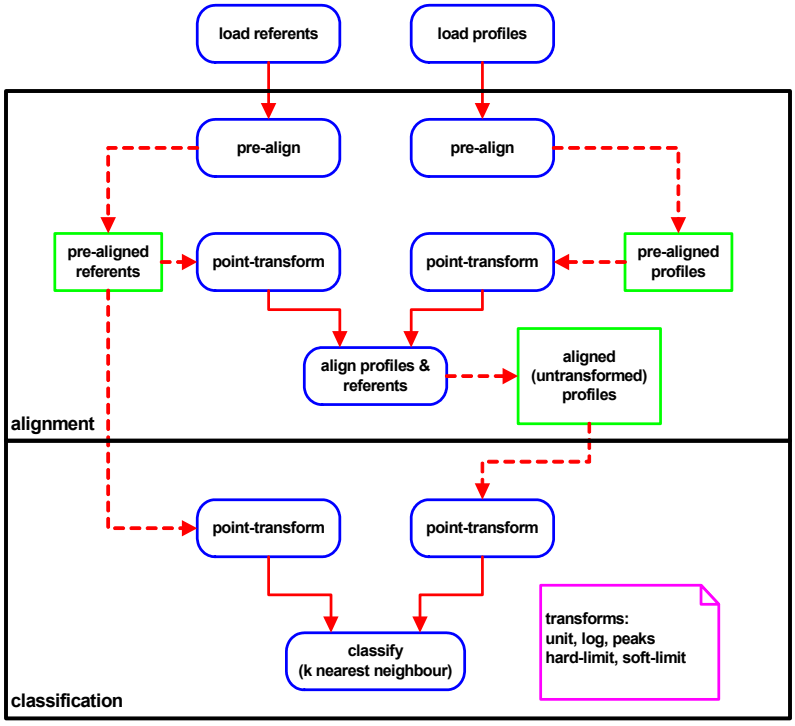

Figure 11: Classification scheme overview

An overview of the classification scheme used in the current work is given in Figure 11. First, relevant (measured) profiles and referents are loaded. These are then roughly aligned by centring them within the range swath. Next, the pre-aligned profiles and referents are subject to a *point transformation*; the use of these point transformations is a key feature of the scheme described here. Point transformations may be as simple as taking the logarithm of each point on the referent or profile, or may be more complicated such as detecting the positions of peaks then taking a hard limit, i.e. applying a threshold to reduce the value to one or zero. The point transformations allow particular features in the profiles to be emphasised or de-emphasised. A soft threshold, i.e. reducing all values below a specified threshold to zero, is useful in screening out noise in measurements. Alignment is achieved by one of a variety of methods, such as minimising the correlation between profile and referent with respect to shift in range.

Following alignment, the referents and profiles are subjected to another point transform, which is generally different to that used for alignment. An identity transform leaves data unchanged, giving a comparison between the full profile and referent; the referent acts as a template, so the algorithm amounts to template-matching. Comparisons of this form tend to give undue emphasis to noise. A combination of soft-limiting and peak detection allows just the positions and amplitudes of peaks to be compared. With this point transform, features are essentially extracted from the profile so that the classification scheme is feature-based rather than template-based. A slightly different transform may be used to hard-limit the peak amplitudes; this variation of the algorithm thus compares just the positions of high returns in the profile. This is valuable, given that use of non-radar data to form referents may give reasonably accurate indications of peak positions, but will seldom give accurate information on the amplitudes of these returns. Using the scheme above, it is possible to directly gauge the effect of discarding or ignoring parts of the original data.

5.0 CONCLUSION

A number of aspects of NCTR for near-future radar have been discussed. It has been shown that it is feasible to provide such radars with high-resolution capability, and the need for such capability, even for

classifying large aircraft, has been demonstrated. The use of a codified form of reference data in the form of a scattering centre model has been discussed – a model of this kind allows both radar data and non-radar data to be utilised as reference material. A classification scheme has also been described which allows a range of options to be explored in exploiting reference data of this kind. What remains is to establish the performance of such algorithms both in classifying the type and the generic class of aircraft of interest.

6.0 ACKNOWLEDGEMENTS

The work reported here on high-resolution waveforms was sponsored by BAE SYSTEMS Avionics; the work on the effect of decreased range resolution and signal-to-noise ratio was sponsored by AMS (UK). Work on classification issues has been performed under the joint industry/MoD sponsored Electromagnetic Remote Sensing Defence Technology Centre (EMRS DTC). The authors wish to thank all of these sponsors for their encouragement in this work and for their permission to publish it.

7.0 REFERENCES

[1] D. R. Wehner, “High Resolution Radar”, Artech House, 1987.

[2] P. A. Devijver, J. Kittler, “Pattern Recognition - A Statistical Approach”, Prentice/Hall International, 1982.

[3] A. W. Rihaczek, S. J. Hershkowitz, “Theory and Practice of Radar Target Identification”, Artech House, 2000.

[4] J. A. Lord, J. D. S. Langley, “Finite-difference time-domain (FDTD) analysis of antennas on a supercomputer”, GEC-Marconi RF Technology Conference Digest, pp.115-119, April 1998.

Time-Frequency Analysis of Radar Signals

G. Boultadakis, K. Skrapas and P. Frangos
Division of Information Transmission Systems and Materials Technology
School of Electrical and Computer Engineering
National Technical University of Athens
9 Iroon Polytechniou Street, Zografou
GR-15773, Athens
Greece

1. INTRODUCTION

It has been well understood that a given signal can be represented in an infinite number of different ways. Of course, different signal representations can be used for different applications. Despite the fact that the number of ways describing a given signal are countless, the most "popular", important and fundamental variables are: time and frequency. The time domain indicates how a signal's amplitude changes over time and the frequency domain indicates how often these changes take place.

The key for the description of a signal was to find a form which would unite the variables above. The tool that matched time and frequency was the "Fourier Transform". Since its introduction in the nineteenth century, the Fourier Transform has become one of the most widely used signal-analysis tools across many disciplines of science and engineering. The fundamental idea behind Fourier Transform is the decomposition of a signal as the sum of weighted sinusoidal functions of different frequencies. The projection of the values of these sinusoidal functions (each of which is a function with a unique frequency) form the Fourier Transform of the original signal.

Despite their simple interpretation of pure frequencies, the Fourier transform is not always the best tool to analyze "real life signals". These are usually of finite, perhaps even relatively short duration, and they have frequency contents that change over time. The most common examples of such signals are biomedical, musical and seismic signals. Especially seismic signals are not like sinusoidal functions, extending from negative infinity to positive infinity in time. For such kind of applications, the sinusoidal functions are not good models.

Joint Time Frequency Transforms were developed for the purpose of characterizing the time-varying frequency content of a signal. Many transforms were developed and used at different applications. The developed transforms are divided into two classes:

- Linear Time Frequency Transforms, and
- Quadratic (Bilinear) Transforms.

At the first class belong a lot of transforms. The most-known are Short Time Fourier Transform (STFT), Continuous Wavelet Transform (CWT) and Adaptive Time-Frequency Representation. At the second class belongs the Wigner-Ville Distribution (WVD). Scientific research, in the last decade, has focused on Short Time Fourier Transform modifications and especially on Wigner-Ville Distribution. [1]

Paper presented at the RTO SET Symposium on "Target Identification and Recognition Using RF Systems", held in Oslo, Norway, 11-13 October 2004, and published in RTO-MP-SET-080.

2. FOURIER TRANSFORM

The oldest method for signal processing is Fourier Transform. The Fourier Transform of a signal s(t) is defined as:

$$S(\omega)=\int_{-\infty}^{+\infty} s(t)\exp(-j\omega t)dt$$

where $\omega=2\pi f$ is the angular frequency. The original function can be constructed from the processing values by the process of:

$$s(t)=\frac{1}{2\pi}\int_{-\infty}^{+\infty} S(\omega)\exp(j\omega t)d\omega$$

The above function is known as Inverse Fourier Transform.

Uncertainty Principle

A well-known principle of the Fourier Transform is the uncertainty principle, or Heisenberg inequality. According to this property, the time duration Δ_t of a signal s(t) and the frequency bandwidth Δ_ω of the Fourier Transform S(ω) are related by:

$$\Delta_t \Delta_\omega \geq \frac{1}{2}$$

The definitions of the above functions are:

Time Duration	$\Delta_t = \left[\frac{\int_{-\infty}^{\infty}(t-\mu_t)^2\lvert s(t)\rvert^2 dt}{\int_{-\infty}^{\infty}\lvert s(t)\rvert^2 dt}\right]^{\frac{1}{2}}$
Frequency Duration	$\Delta_\omega = \left[\frac{\int_{-\infty}^{\infty}(\omega-\mu_\omega)^2\lvert S(\omega)\rvert^2 d\omega}{\int_{-\infty}^{\infty}\lvert S(\omega)\rvert^2 d\omega}\right]^{\frac{1}{2}}$
Mean Time	$\Delta_t = \frac{\int_{-\infty}^{\infty} t\lvert s(t)\rvert^2 dt}{\int_{-\infty}^{\infty}\lvert S(t)\rvert^2 dt}$

Mean Frequency	$\Delta_\omega = \frac{\int_{-\infty}^{\infty} \omega \lvert S(\omega)\rvert^2 d\omega}{\int_{-\infty}^{\infty} \lvert S(\omega)\rvert^2 d\omega}$

As can be assumed from above, time resolution and frequency resolution cannot be arbitrarily small. Specifically, smaller time duration of s(t) means greater frequency bandwidth of S(ω) and vice versa [2]. The equality of the uncertainty principle is valid in case of Gaussian signals.

3. SHORT-TIME FOURIER TRANSFORM

One of the best-known time-frequency representations of a time signal dates back to Gabor and is known as "Short Time Fourier Transform - STFT". STFT is based on the Fourier Transform and its basic idea is a moving window Fourier Transform [3]. The window is moving over the time domain and the examination of the frequency content of the signal generates a 2-D time-frequency distribution called "spectrogram". The STFT of a signal s(t) is defined as:

$$STFT(t,\omega)=\int s(t')w(t'-t)\exp(-j\omega t')dt'$$

where w(t'-t) is the moving window. The only difference from Fourier Transform is the presence of the window function. The definition of STFT can be also expressed in the frequency domain as:

$$STFT(t,\omega)=\frac{1}{2\pi}\exp(-j\omega t)\int S(\omega')W(\omega'-\omega)\exp(-j\omega' t)d\omega'$$

where W(ω'-ω) is the Fourier Transform of the moving window. At the first definition the window is moving at the time domain while at the second definition is moving at the frequency domain. Many window functions are used, each of them at different application. Some of them are known as: Hamming, Hanning, Kaiser-Bessel and Gaussian windows.

STFT has two major advantages. First of all, according to its definition, STFT is simple enough, as it is equal with the computation of multiple Fourier Transforms. The second advantage is the absence of cross terms. As the width of the time window is getting smaller, the cross terms are limited, in contrast to bilinear transforms (i.e. Wigner-Ville distribution).

The major disadvantage of STFT is that during processing, the results are not good in both time and frequency domain. The processed signal can be either analyzed with good time resolution or frequency resolution [2]. This disadvantage is a characteristic of the Fourier Transform which is transferred to the STFT. According to the uncertainty principle, the functions Δ_t and Δ_ω are proporately inverse and their value is equal to the width of the moving window and the frequency bandwidth. In addition, any component of the signal, whose time duration is smaller than the time duration of the window is "disappeared" after the transform of the signal.

To overcome these limitations of the STFT, in order to obtain a multi-resolution analysis, wavelet transforms are used.

CONTINUOUS WAVELET TRANSFORM

General

The spectrogram generated by STFT is limited in resolution by the extent of the sliding window function. Contrary to the fixed resolution of the STFT, the Continuous Wavelet Transform – CWT is a time-frequency representation capable of achieving variable resolution in one domain (time or frequency) and multiresolution in the other domain [3].

The CWT was generated by a scientific group consisted of P. Goupillaud, A. Grossman and J. Morlet at 1984 [4]. The basic idea of the CWT is the "wavelet theory" which is the reason of the generation of many categories of signal processing. The most-known applications are the multi-resolution signal processing, the sub band coding and the wavelet series expansion.

The research of I. Daubechies was a great assistance at the exponential prevalence of wavelet transforms at the telecommunication and the signal-processing domain, as he generated its mathematical theory [5].

As the Wavelet Transform is an advancement of the Fourier Transform, it is also divided in two classes:

- Continuous Wavelet Transform, and
- Discrete Wavelet Transform

A main characteristic of the wavelet transforms is a new term called "scale" which displays the frequency, the basic variable of Fourier Transforms. According to that, in wavelet transforms is introduced the "time-scale representation".

Wavelet Theory

The "scale" is the basic variable of wavelet transform for non-stationary signals. Small values of scaling are proporal to high values of frequency and vice-versa. At wavelet theory, instead of the variable of time is used the variable of "shift".

A wavelet is just a waveform of finite time duration. The basic difference of the sinusoidal function is that wavelet functions are asymmetrical and irregular.

The basic idea behind wavelet analysis is the decomposition of the signal into varying wavelet function, called "mother wavelet". A fundamental condition of a mother wavelet is the "admissibility condition" [6]. The satisfaction of the above condition is necessary for the existence of inverse transform. The mother wavelet has to satisfy the next function:

$$\int_{-\infty}^{\infty} \frac{|\Psi(\omega)|^2}{|\omega|} d\omega < \infty$$

where $\Psi(\omega)$ is the Fourier transform of the mother wavelet. In addition to that, it is known that the admissibility condition is equivalent to the nullity of the mother wavelet's DC component.

Many mother-wavelets are used for different applications. The most known are Morlet, Daubechies and Haar wavelets. Of great importance are also the coiflet, symlet, Mexican Hat and biorthogonal wavelets.

Haar

Any discussion concerning wavelets starts with Haar wavelet, the first and simplest. Haar wavelet is discontinuous, and resembles to a step function. It represents the same wavelet as Daubechies db1.

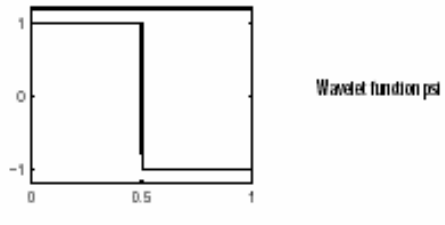

Daubechies

Ingrid Daubechies, one of the most significant scientists in the world of wavelet research, invented what are called compactly supported orthonormal wavelets — thus making discrete wavelet analysis practicable. The names of the Daubechies family wavelets are written dbN, where N is the order, and db the "surname" of the wavelet. The db1 wavelet, as mentioned above, is the same as Haar wavelet. Here are the wavelet functions psi of the next nine members of the family:

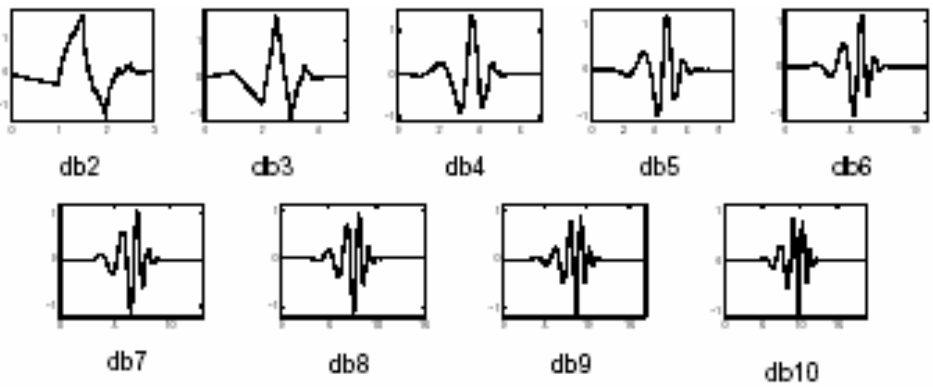

Coiflets

Built by I. Daubechies at the request of R. Coifman. The wavelet function has 2*N* moments equal to 0 and the scaling function has 2*N*-1 moments equal to 0. The two functions have a support of length 6*N*-1.

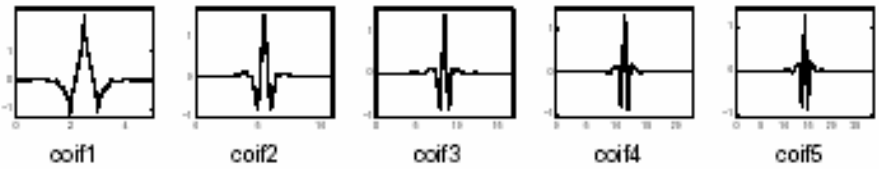

Symlets

The symlets are nearly symmetrical wavelets proposed by Daubechies as modifications to the db family. The properties of the two wavelet families are similar. Here are the wavelet functions psi.

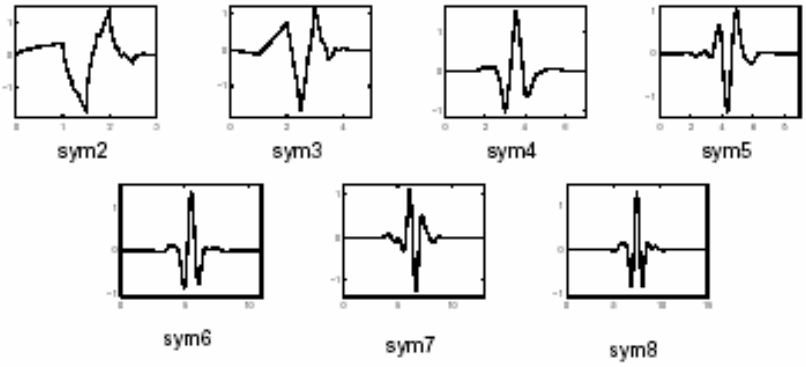

Mexican Hat

This wavelet has no scaling function and is derived from a function that is proportional to the second derivative function of the Gaussian probability density function.

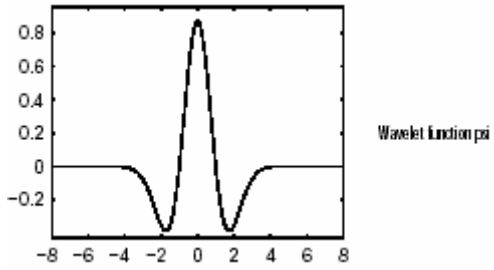

Mathematical Definition

The CWT of a signal s(t) can be defined as:

$$\mathrm{CWT}(t,\omega)=\left(\frac{\omega}{\omega_0}\right)^{1/2}\int s(t')\psi^*\left(\frac{\omega}{\omega_0}(t'-t)\right)dt'$$

where ψ(*) is the mother wavelet [3]. The scale parameter is expressed as the ratio $\frac{\omega}{\omega_0}$. The 2-D result is the scalogram of the transform. If the mother wavelet is centered at time zero and oscillates at frequency ω_0 , the definition of the Continuous Wavelet Transform is the decomposition of the signal s(t') into shifted and dilated wavelets $\psi[(\omega/\omega_0)(t'-t)]$.

The basic advantage of the CWT over the STFT is the multi-resolution property. According to the above mathematical definition, the wavelet ψ(*) has two variables: time and frequency. By shifting or dilating the wavelet ψ(*) at a fixed parameter t or ω, signal processing is accomplished according to time or scale parameter.

The wavelet transform can also be expressed as:

$$\mathrm{CWT}(t,\omega)=\frac{\left(\omega_0/\omega\right)^{1/2}}{2\pi}\int S(\omega')\Psi^*\left(\frac{\omega_0}{\omega}\omega'\right)\exp(j\omega' t)d\omega'$$

where Ψ(ω') is the Fourier transform of ψ(t'). The above equation is also defined as the Fourier transform of $S(\omega')\Psi^*\left(\frac{\omega_0}{\omega}\omega'\right)$.

A comparison between STFT and CWT shows that Ψ*(ω) is similar to the frequency window W(ω). Of course, the admissibility condition has to be satisfied, which means Ψ(0)=0.

In CWT the uncertainty condition is satisfied but in a different way than the STFT. At CWT the time analysis is better at high frequencies and the scale analysis is better at lower frequencies.

The basic difference between the Fourier Transform and the STFT and CWT is that, in the second case, functions based at finite extent are used, and that is the reason they are used in many applications.

5. COMPARISON BETWEEN STFT AND CWT USING MATLAB

As it has already been mentioned, Time-Frequency Transforms are ideal for a great variety of signal processing applications. In our research, the goal is to use Space Time Frequency and Continuous Wavelet Transforms, in order to extract the features of a moving target (i.e. aircraft) using the information provided by radar systems. In particular, we focus on the process of reconstructing images of radar targets from recorded data, using time-frequency transformation.

The first step of the research, described in this section, is the thorough examination of all these different categories of window functions, in STFT, and mother wavelets, in CWT. In order to examine and find out the similarities and differences between window functions or between mother wavelets, as well as between STFT and CWT, we used simple functions as examples.

In the following example a simple sine function, consisted of four sins of different frequency, is presented. The first diagram shows our function, whereas the next diagrams give a detailed comparison between all the parameters concerning window functions and mother wavelets.

$$s(t) = \begin{cases} \sin(2\pi f_1 t), & 0 < t \le 250\text{sec} \\ \sin(2\pi f_2 t), & 250 < t \le 500\text{sec} \\ \sin(2\pi f_3 t), & 500 < t \le 750\text{sec} \\ \sin(2\pi f_4 t), & 750 < t \le 1000\text{sec} \end{cases}$$

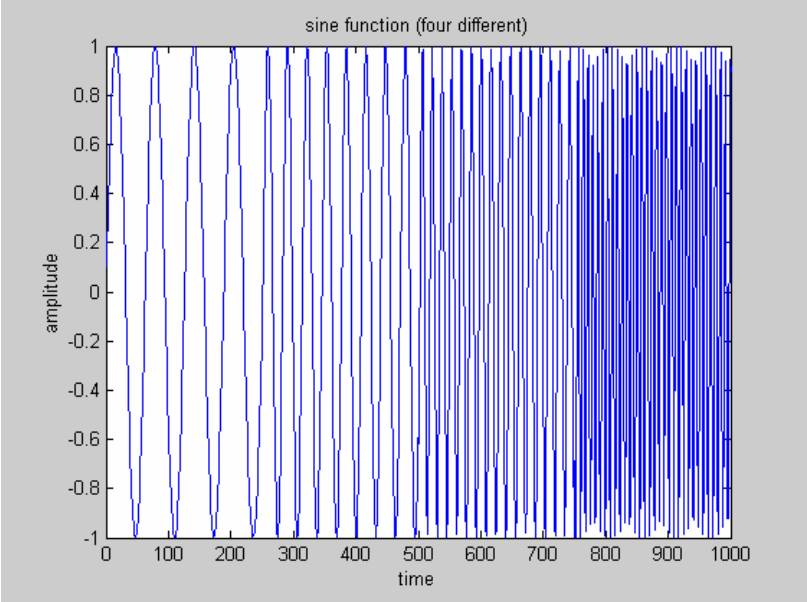

Fig.1. Signal under processing

In the following step, we calculated the STFT (spectrogram) of our signal using the Gaussian pulse as window function. The Gaussian wavelet is described as:

$$w(t) = \frac{1}{\pi^{1/4}\sqrt{\sigma}} e^{-\frac{t^2}{2\sigma^2}}$$

The parameter σ is the one of great importance, as it affects the distinctive ability of the transform. When σ is used to give a narrow window in time, then information is getting lost in frequency domain. In the opposite situation, information for our signal reconstruction is being lost in the time domain. In the following figures is explained exactly the above conclusion using the Gaussian window of length 128 and 1024. These values determine the frequencies in which the Fourier Transform is computed. The computation took place in Matlab® environment.

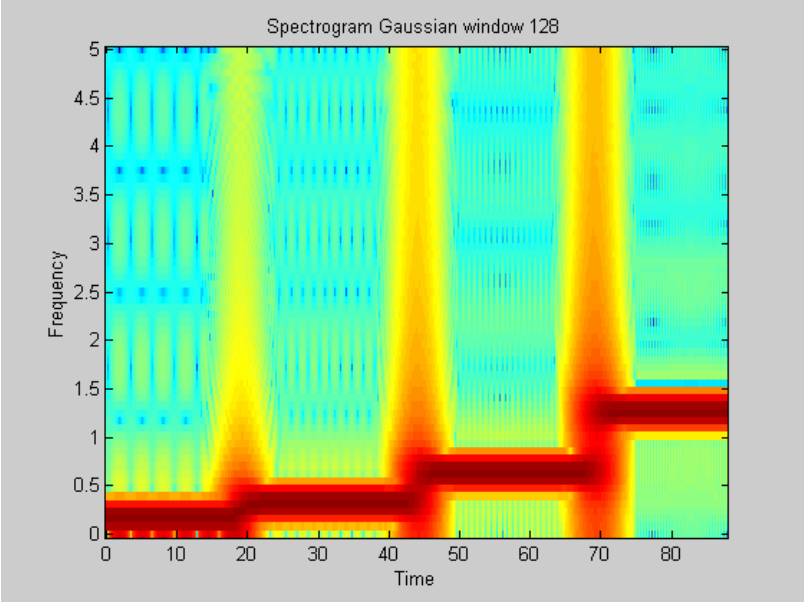

Fig.2. STFT using window parameter 128

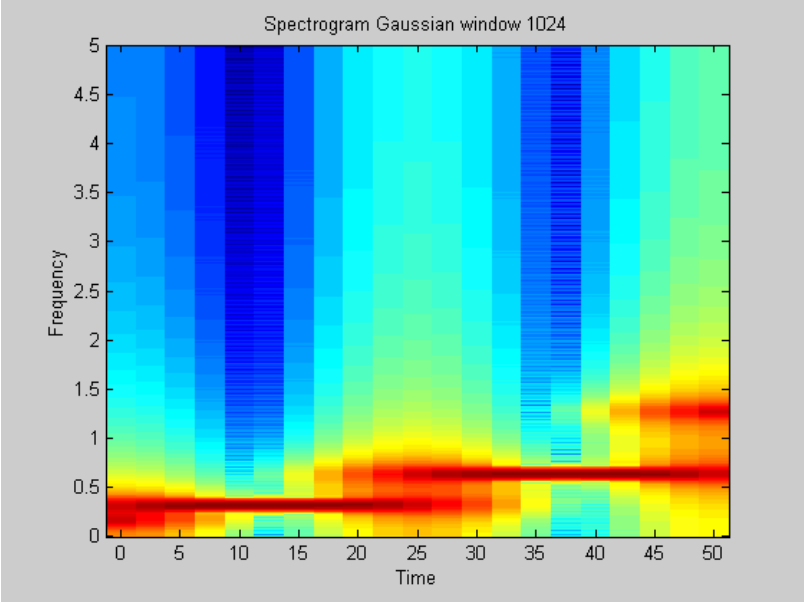

Fig.3. STFT using window parameter 1024

Furthermore, we had the same sine function's computation using other windows that prove to be quite effective in Space Time Frequency Transform. The next three figures show the resulting spectrograms with Hamming, Hanning and Kaiser window, for a window length value of 512. As can be noticed, the Hamming window has a low distinctive ability in the frequency domain. This leads to an image blurring, without letting us take much informaton about our signal in the frequency domain.

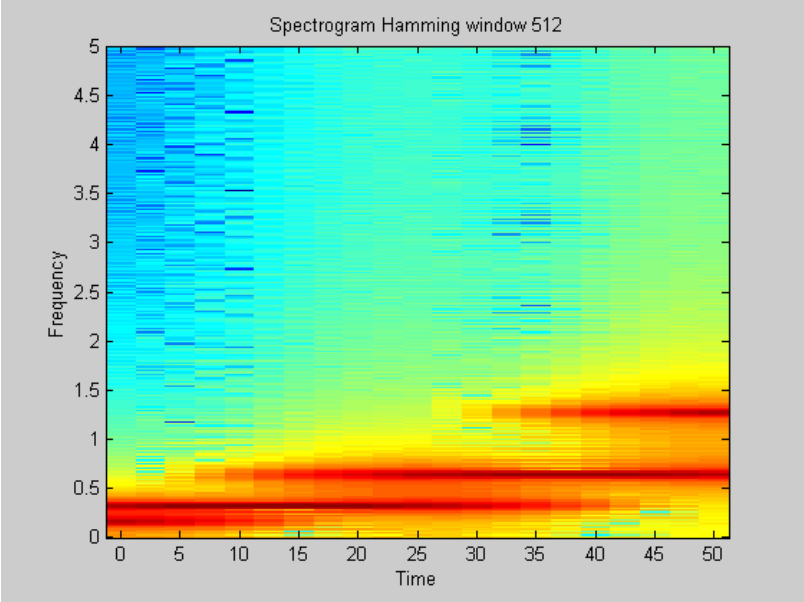

Fig.4. STFT using Hamming window

On the other hand, Hanning window is much more informative than the Hamming one. It gives great information in the frequency domain, using exactly the same parameters we used for the previous computation (window length 512). The following figure presents the image of our signal and, as can be easily seen, it provides the frequency values with great precision. The last spectrogram has been computed using Kaiser pulse, and is assumed to be of quite high distinctive ability.

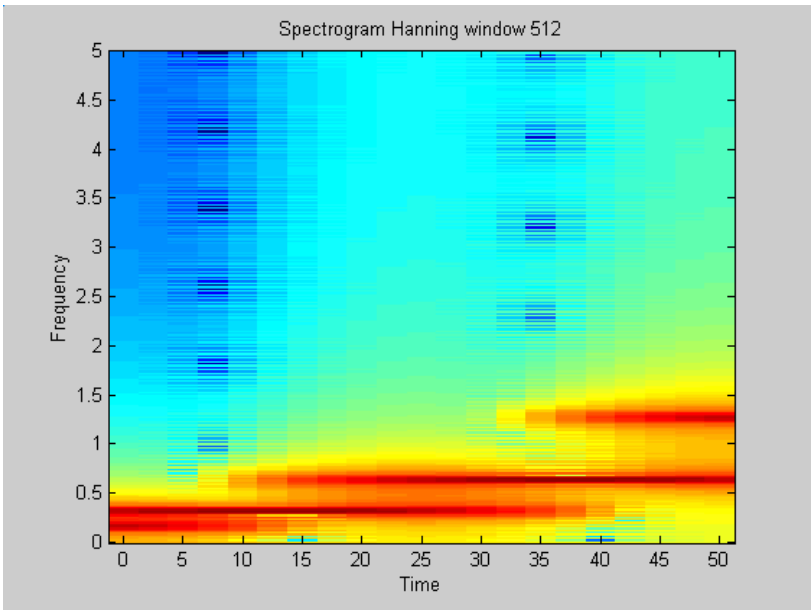

Fig.5. STFT using Hanning window

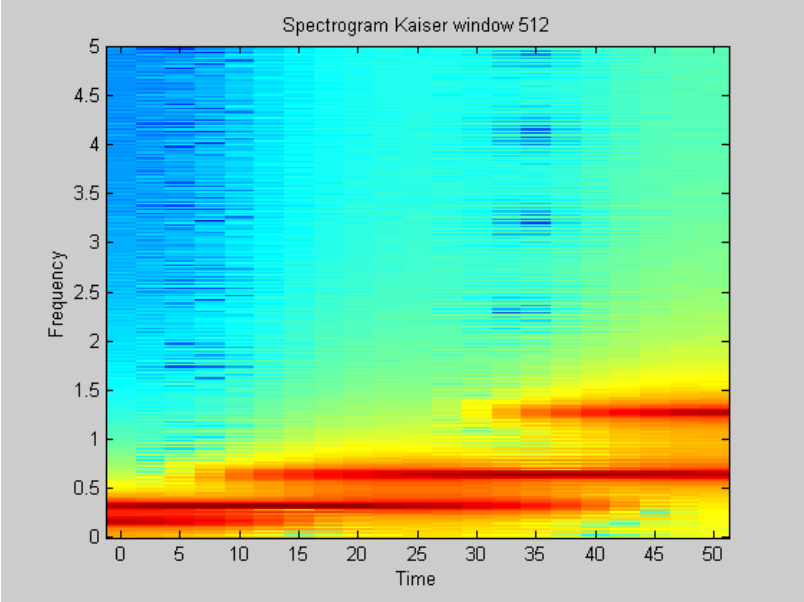

Fig.6. STFT using Kaiser window

To sum up, as far as STFT is concerned, we found out with the figures' help, that the four different sins of our signal are presented consequently in time, but whether we can have or not high distinctive ability, in time or frequency domain, depends on the window length and other parameters of the window functions, as well as the type of the window function we use.

We went on using the same signal in order to find out the differences between the mother wavelets in Continuous Wavelet Transform. We also tried to compare the two transforms, their attitude in time and frequency (or scale) domain. The following figures are the results of CWT computation (scalograms) using two different Gaussian wavelets (Gaussian1 and Gaussian8), Mexican Hat wavelet, Morlet wavelet (a complex sinusoid windowed with a Gaussian envelope) and Symlet wavelet. In the plots the x-axis represents position along the signal (time), the y-axis represents scale, and the color at each x-y point represents the magnitude of the wavelet coefficient C. The darker one point is, the smaller coefficient it represents. Recall that the higher scales correspond to the most "stretched" wavelets. The more stretched the wavelet, the longer the portion of the signal with which it is being compared, and thus the coarser the signal features being measured by the wavelet coefficients. What we tried to work out with the following figures was to build an image with the less scale computation, which means an informative result without comparing our signal with infinite shifted and dilated versions of the mother wavelet we used. This will lessen the computation time, and taking under consideration that our research has the goal to image radar targets, one can understand that computation time is priceless.

The process took place in Matlab® environment using 256 or 512 different scaled (stretched) versions of the wavelet. Gaussian1 wavelet, compared with Gaussian8, seems to be quite clear from the very first scales, whereas Gaussian8 gives information in greater scales. Of course, such a conclusion cannot be stable for every signal under processing. It depends on the signal form that is used each time.

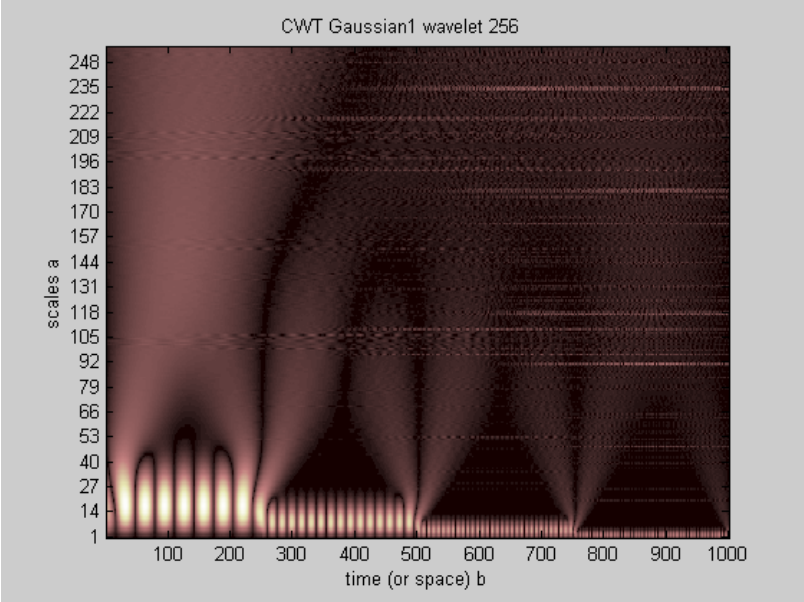

Fig.7. CWT using Gaussian1 wavelet

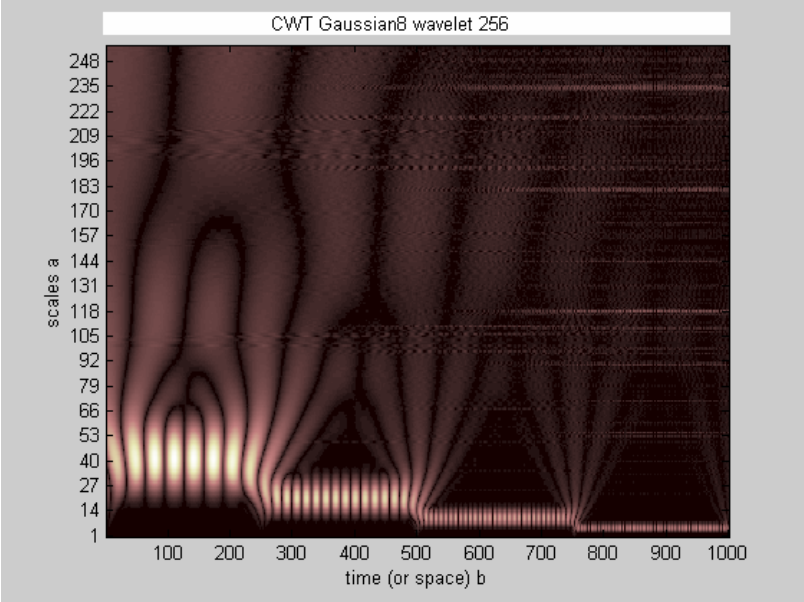

Fig.8. CWT using Gaussian8 wavelet

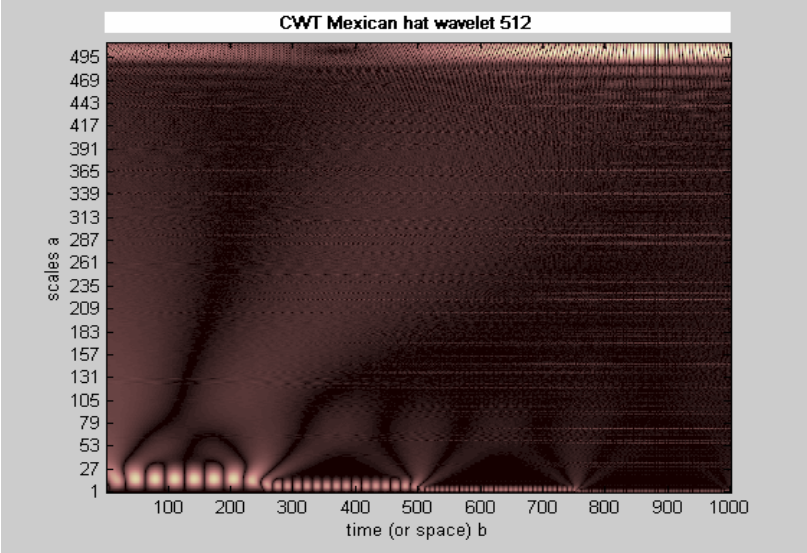

Fig.9. CWT using Mexican Hat wavelet

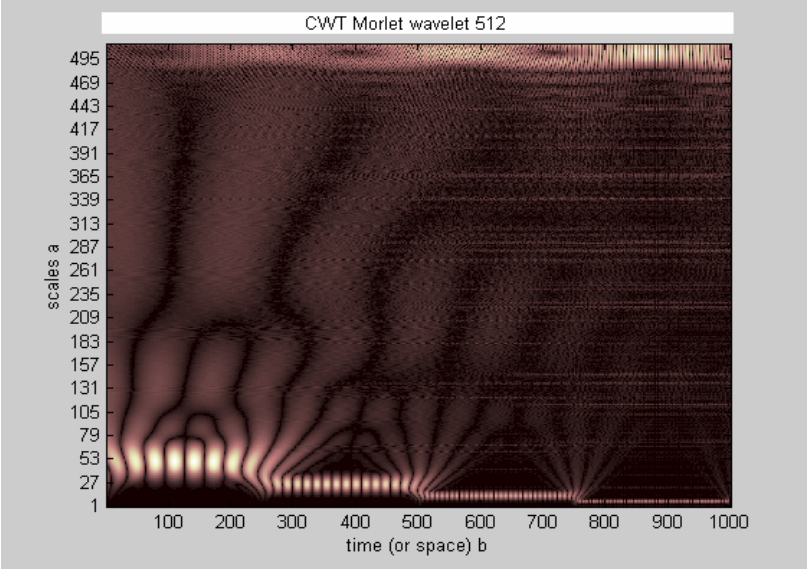

Fig.10. CWT using Morlet wavelet

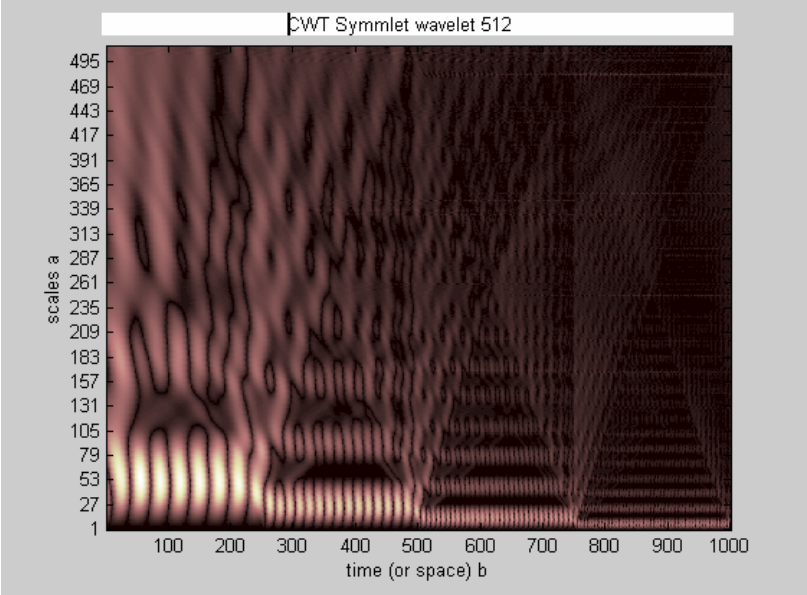

Fig.11. CWT using Symlet wavelet

In CWT, in low frequencies (large scales), the distinct ability in the time domain is low. Nevertheless, it does not appear to be a problem. While frequency is getting greater, which means smaller scales, we get better results in time domain. On the contrary, in scale domain the processing proves to be more effective.

As can be seen from the figures, wavelet analysis is capable of revealing aspects of data that other signal analysis techniques (like STFT) miss, aspects like breakdown points, discontinuities in higher derivatives, and self-similarity. Furthermore, because it affords a different view of data than those presented by traditional techniques, wavelet analysis can often compress or de-noise a signal without appreciable degradation.

Our research continued with the same processing but with the use of a more complex signal, a chirp pulse with quadratic instantaneous frequency deviation (1 KHz sample rate), that is presented below:

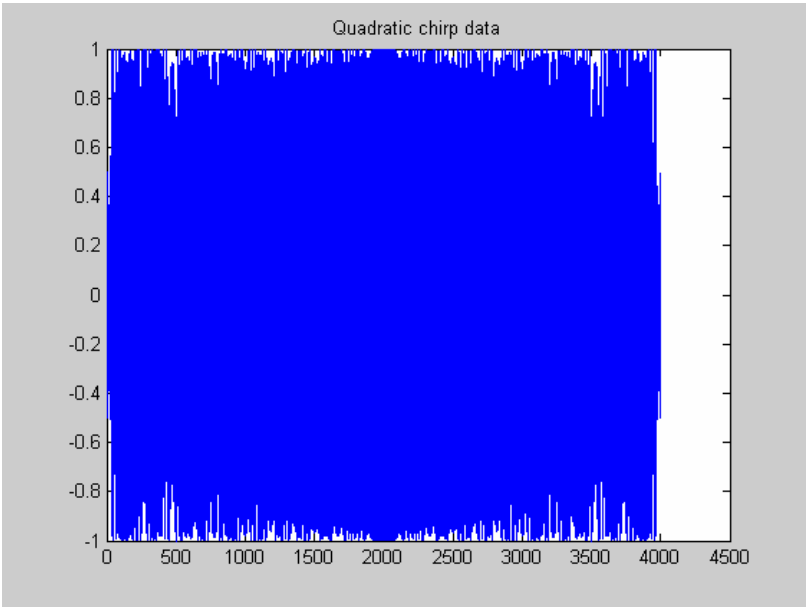

Fig.12. Quadratic chirp data

We used the same window functions to compute the spectrograms, as well as the same mother wavelets.

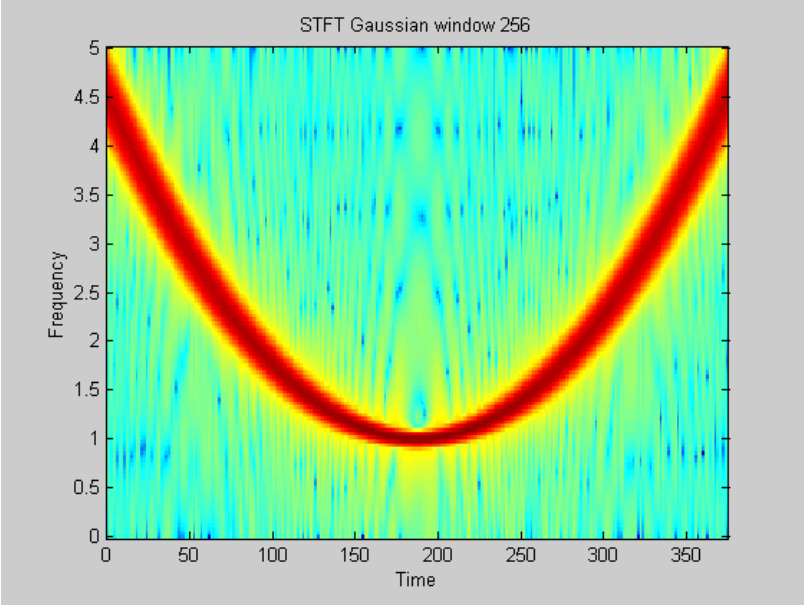

Fig.13. STFT using Gaussian window

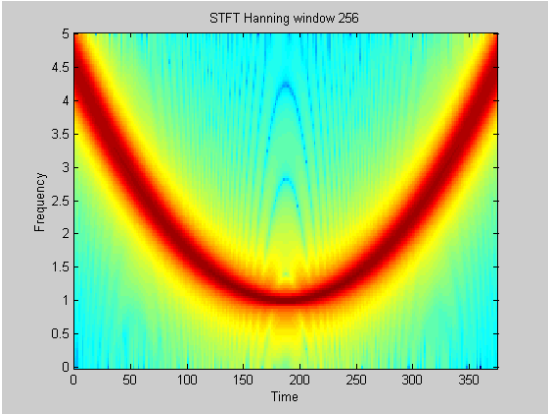

Fig.14. STFT using Hanning window

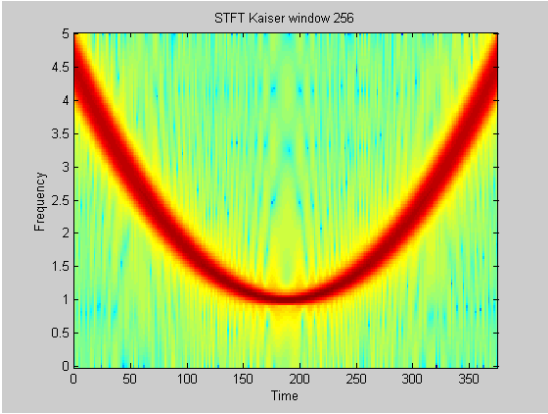

Fig.15. STFT using Kaiser window

The results and the conclusions of the second example were almost identical to the first example, which ensured that what we noticed in the previous figures was correct.

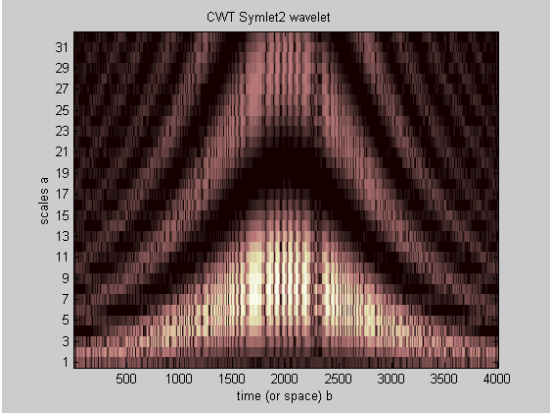

Fig.16. CWT using Symlet2 wavelet

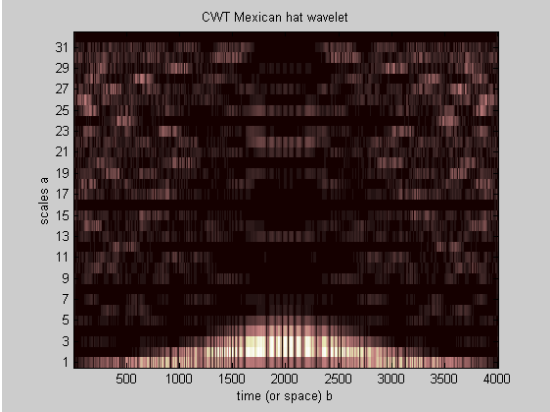

Fig.17. CWT using Mexican Hat wavelet

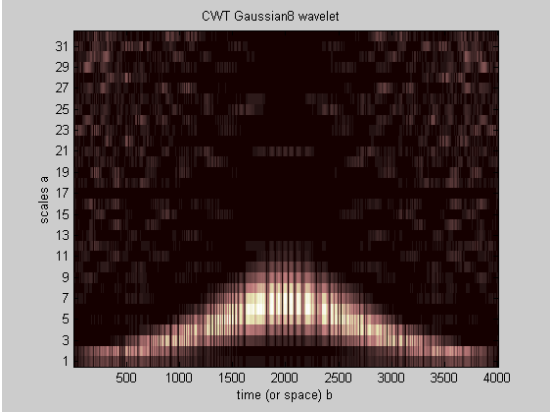

Fig.18. CWT using Gaussian8 wavelet

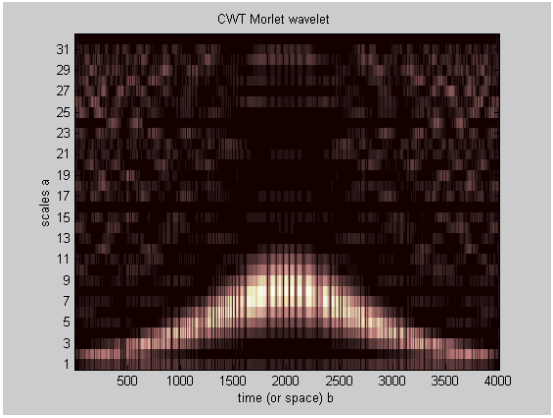

Fig.19. CWT using Morlet wavelet

6. IMAGE GENERATION FOR A SIMULATED TARGET

In this section, we formulated a model for the received scattered radar signal of a synthetic (operative) aircraft target. According to [7], a radar target can be considered as a collection of finite number of scatteri sum of scattered signals from each center. Based on this concept, and using the procedure described in [7], we worked on Matlab® environment and generated an aircraft target. We used nine (9) scattering centers that are presented in Figure 20, as well as 31 different look angles. The rotation center for our model is on coordinates [4530,0]. The radar is located on [0,0] and each of its bursts is consisted of 16 pulses (frequencies). Furthermore, we defined the scattering intensity for all scatterers and the Cartesian coordinates for all scatterers relative to the center of rotation. To improve even more our scattered signal before imaging the target, we interpolated the frequency-angular domain data to Cartesian coordinates. The image of the target acquired, after all the described procedure and the final Continuous Wavelet Transform, using a Symlet wavelet, is shown in Figure 21. The image is quite clear and the plot is intense on the scatterers' position, forming in that way our target.

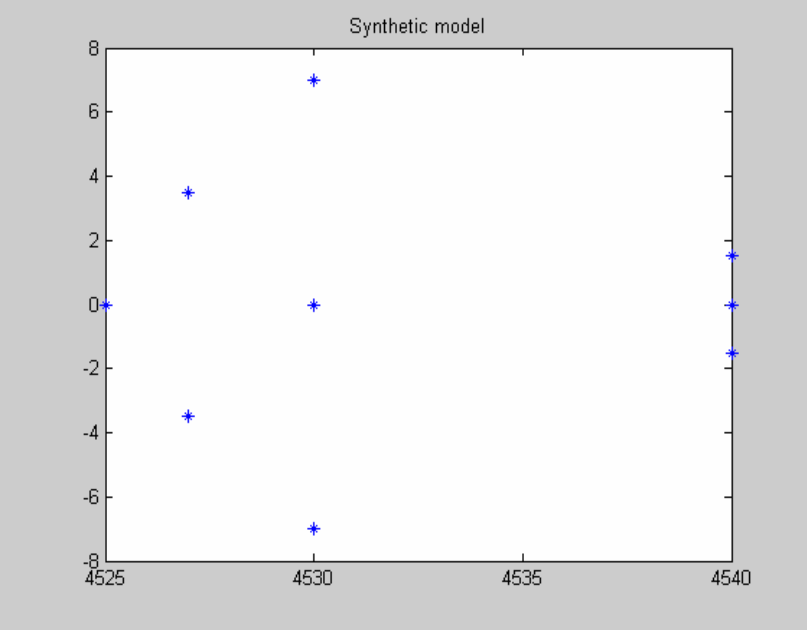

Fig.20. Scatterers of the Synthetic model

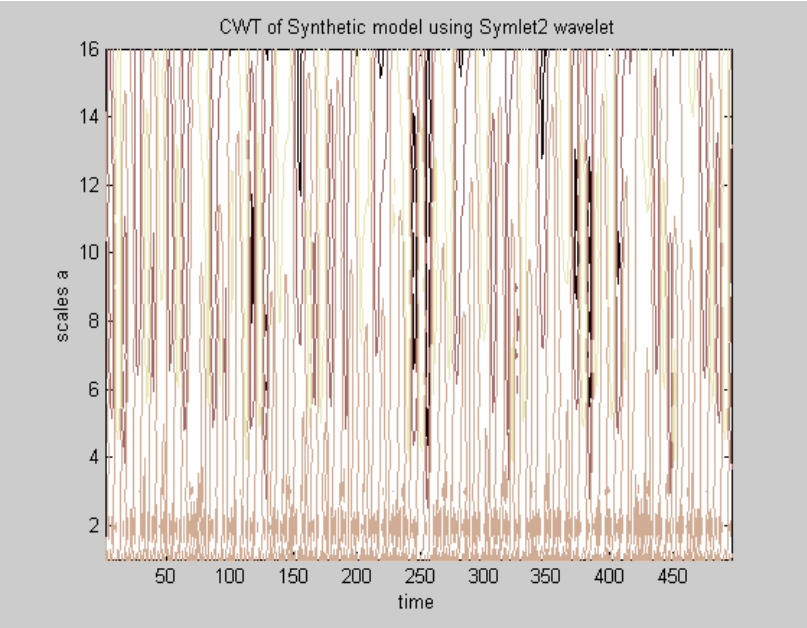

Fig.21. CWT of the Synthetic model

7. CONCLUSION

We have seen that both the Short Time Fourier Tranform and the Continuous Wavelet Transform represent ways to divide and examine more thoroughly the time-frequency (or time-scale) plane. We used some simple functions to show the differences, the benefits and drawbacks, of each method. Our research even concluded comparison between different window functions or mother wavelets. The two methods were demonstrated in detail, whereas CWT was also used to form the image of a simulated target.

The results, as far as the recognition accuracy of the target is concerned, were satisfying, showing that the proposed technique – Continous Wavelet Transform – has significant advantages in signal processing, and especially in radar target recognition, that is the goal of our research.

This means that the echoes of radar signals can be collected and processed to generate a two-dimensional representation of a target. Nevertheless, a simple time-frequency transform is not enough, when a non-cooperative target is being studied, due to its radial and rotational motion that leads to a blurred image [8]. This issue is extremely important and is an area of future research.

REFERENCES

[1] L.Durak, O.Arikan, "Short-Time Fourier Transform : Two Fundamental Properties and an Optimal Implementation", IEEE Trans. SP, Vol.51(5), May 2003, pp. 1231-1242

[2] O.Rioul, M.Vetterli, "Wavelets and Signal Processing", IEEE SP Magazine, Vol.8, Oct. 1991, pp.14-38

[3] V.Chen, H.Ling, "Time-Frequency Transforms for Radar Imaging and Signal Analysis", Artech House, Boston-London, 2002

[4] P.Goupillaud, A.Grossmann, J.Morlet, "Cycle-Octave and Related Transforms in Seismic Signal Analysis", Geoexploration, Vol.23, 1984, pp.85-102

[5] I.Daubechies, "The Wavelet Transform, Time-Frequency Localization and Signal Analysis", IEEE Trans. IT, Vol.36(5), Sept.1990, pp.961-1005

[6] J.Sadowsky, "Investigation of Signal Characteristics Using the Continuous Wavelet Transform", Johns Hopkins APL Technical Digest, Vol.17(3), 1996, pp.258-269

[7] J.Odendaal, E.Barnard, C.W.Pistorius, "Two-Dimensional Superresolution Radar Imaging Using the MUSIC Algorithm", IEEE Trans. Ant. and Propagation, Vol.42(10), Oct.1994, pp.1386-1391

[8] J.Son, G.Thomas, B. Flores, "Range-Doppler Radar Imaging and Motion Compensation", Artech House, Boston-London, 2001

Comparison of Several Spectral Estimation Methods for Application to ISAR Imaging

A. Karakasiliotis and P. Frangos
Division of Information Transmission Systems and Materials Technology
School of Electrical and Computer Engineering
National Technical University of Athens
9 Iroon Polytechniou Street, Zografou
GR-15773, Athens
GREECE

SUMMARY

During the last decade, several spectral estimation techniques have been proposed for application to SAR/ISAR imaging. The present study attempts to shed light to a number of parametric spectral estimation methods, employed for ISAR imaging of aircraft targets. We focus on performance comparison with respect to 1-D and 2-D image resolution. Auto-regressive methods and MUSIC algorithm are examined and simulated, based on synthetic radar data, for both 1-D (range profiles) and 2-D (ISAR images) cases.

1 INTRODUCTION

In view of radar target recognition and classification, ISAR (inverse synthetic aperture radar) images shall be highly resolved (high-resolution imaging), so as to allow for decision making with respect to the target category and type. An important step in ISAR imaging is the implementation of high-resolution spectral estimation algorithms. Indeed, it is well-known that, under most circumstances, conventional Fourier transform processing of the two-dimensional raw radar data (2-D FFT) is not adequate to yield high-resolution radar aircraft images. Therefore, several spectral estimation techniques, both nonparametric and parametric, are applied in order to improve the resolution of both 1-D (i.e. range profiles) and 2-D (i.e. ISAR images) radar target images.

One-dimensional radar signatures of a target can be generated by applying spectral estimation techniques to the frequency domain data of the target, and it has been demonstrated that the resulting images are enhanced over those obtained via a Fourier transform-based technique. In bibliography, we come along extensions from 1-D spectral estimation-based radar signatures to two dimensions, where a Fourier transform of the angular domain data to the Doppler domain (cross-range) takes place. Hybrid methods for 2-D radar imaging employ an inverse Fourier transform on the frequency domain data, and then, a super-resolution technique is used to transform the angular domain data to the cross-range. Additionally, 1-D super-resolution spectral estimation methods can be applied to the frequency domain data and a superposition of the resulting 1-D signatures at different angles forms the desired 2-D radar image (known as backprojection technique). All these statements of bibliographic nature are more or less the history of 2-D spectral estimation-based radar imaging before the introduction of direct 2-D extensions of 1-D super-resolution spectral estimation methods [1]. Over the last decade, a great deal of research efforts has been devoted to this particular field and several ISAR imaging methodologies have been proposed [2] - [3].

In this paper, we compare and evaluate the performance of a number of parametric spectral estimation methods [4]. We firstly refer to the covariance and modified covariance methods, and the classical Burg method. Although these autoregressive (AR) model-based methods are more suitable for spectral estimation of signals with rational spectra, their computational simplicity makes them appealing for radar

Paper presented at the RTO SET Symposium on "Target Identification and Recognition Using RF Systems", held in Oslo, Norway, 11-13 October 2004, and published in RTO-MP-SET-080.

applications. Next, we elaborate on an eigenanalysis-based method, namely MUSIC (MUltiple SIgnal Classification), belonging to the very interesting class of super-resolution subspace methods. All the spectral estimation techniques mentioned in this paragraph are compared in the framework of simulated 1-D radar data, generated in accordance to the analysis of [5]. The resulting range profiles serve as valuable metrics of the achievable range resolution of each technique.

Spectral estimation methods for 2-D radar imaging are also examined in this work. Following the simulation setup described in [1], we generate 2-D simulated radar data in the frequency-angular domain, and then, we transform them to the spatial (2-D) frequency domain. Two-dimensional extensions of the classical AR [6] and MUSIC [1] methods are simulated, in order to perform 2-D spectral estimation and overcome the resolution limitations of the 2-D FFT. ISAR images are displayed via contour plots, indicating the advantages of each technique.

This paper is organized as follows. Section 2 refers to the format of the simulated 1-D and 2-D radar data on which the 1-D and 2-D spectral estimation techniques, described in Section 3, are applied. Section 3 is mainly focused on the 2-D methods, since 1-D spectral estimation methods are extensively described in [4]. Range profiles and ISAR images are the simulation results presented in Section 4, so as to compare the performance of the employed spectral estimation techniques. Conclusions and comments on the simulation results are derived and stated in Section 5, also including comments for future work.

2 SIMULATED RADAR DATA FORMAT

It is common knowledge that, in the high-frequency limit, a radar target can be considered as a collection of a finite number of scattering centers and scattering center interactions. The coherent scattered signal from such a radar target can be represented as the sum of complex scattered signals from each scattering center. As it is strongly stressed in [1], the assumption of a non-dispersive nature of the discrete scattering centers holds for most radar targets in the high-frequency limit, if the measurement bandwidth is narrow and the angular sector is small.

2.1 One-Dimensional Radar Data

Following the analysis of [5], we have simulated 1-D radar data (i.e. meaning that there is dependence on one coordinate), so as to compare the 1-D spectral estimation methods with respect to their range resolution. According to [5], the measured high-frequency radar cross-section (RCS) at frequency f_i can be represented by a sum of undamped exponentials as

$$y_i = \sum_{k=1}^{L} a_k \exp\left(-j\frac{4\pi}{c} f_i r_k\right) + n_i \,, \quad i = 1,2,...,N \qquad (1)$$

where r_k is the location of the kth scattering center, a_k is the corresponding amplitude, L is the number of scattering centers on the target, N is the number of frequency measurements (f_i), n_i is the measurement noise, and c denotes the speed of light.

2.2 Two-Dimensional Radar Data

In order to generate 2-D radar data in our simulations, we have followed the problem formulation of [1]. According to [1], the measured radar scattering signal from d scattering centers at frequency f_m ($m = 0,1,...,M-1$) and look angle θ_n ($n = 0,1,...,N-1$) is given as

$$x'(m,n)=\sum_{k=1}^{d} s_k \exp\left(j\frac{4\pi}{c} f_m \left[x_k \cos\theta_n - y_k \sin\theta_n \right] \right) + u(m,n) \qquad (2)$$

where s_k is the complex scattering intensity of the *k*th scattering center, x_k and y_k are the coordinates of the *k*th scattering center[1] on the rotation plane (*xy*-plane), $u(m,n)$ symbolizes the additive noise, usually assumed (as is the case in our simulations) to be white Gaussian with zero mean and variance σ^2.

In 2-D ISAR imaging, the frequency domain is transformed to the down-range and the angular domain to the cross-range. One can notice that the above 2-D data format contains two Fourier transform pairs not separable in terms of f and θ. Adopting the small angle approximation ($\cos\theta \approx 1$ and $\sin\theta \approx \theta$) is a way to obtain data consisting of two separable Fourier transform pairs, but the radar image generated using this approximation is unfocused. Interpolation of the frequency-angular domain data to Cartesian coordinates (rectangular grid of *M* x *N* points) with separable variables ($f^x = f\cos\theta$ and $f^y = f\sin\theta$) is the way to obtain a focused radar image. Rewriting the previous radar data equation we obtain

$$x(m,n)=\sum_{k=1}^{d} s_k \exp\left(j\frac{4\pi}{c} \left[f_m^x x_k - f_n^y y_k \right] \right) + u(m,n) \qquad (3)$$

In our simulations, we have performed this particular interpolation process described in [1], which is based on the following explanatory figure. Note that the "interpolated" data are available on a rectangular grid with equal increments in both the directions f^x and f^y, so that the fast Fourier transform (FFT) can be applied for the conventional radar image generation.

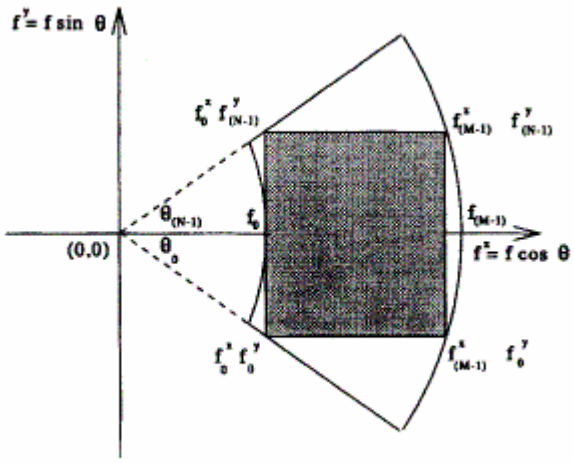

Figure 1. Frequency-angular domain of scattered radar data and the rectangular grid for the interpolation process (reproduced by [1])

It worths mentioning that the majority of high-resolution spectral estimation methods requires the computation of a correlation matrix, based on averaging over a number of snapshots of 1-D and 2-D radar data. Since only one snapshot is in most of the times available in radar applications (real-time processing),

[1] The *xy*-coordinates are relative to the center of rotation on the target.

there is need for decorrelating signals from various scattering centers. A special technique, known as spatial smoothing preprocessing (SSP) [7], and its modified version (MSSP – modified SSP) [8] have been proved sufficient to perform the required decorrelation of radar data. However, such preprocessing decreases the effective bandwidth and, consequently, results in reduced resolution. Because of this disadvantage, we have chosen not to simulate this preprocessing technique and allow some degree of correlation between the signals from different scattering centers. This is the reason for the presence of some redundant peaks in the resulting range profiles, not causing significant blurring in the final ISAR image.

3 SPECTRAL ESTIMATION METHODS FOR 1-D AND 2-D RADAR IMAGING

3.1 One-Dimensional Spectral Estimation Methods

3.1.1 AR Methods

For the generation of 1-D radar images (i.e. range profiles), we firstly employ three methods belonging to the class of autoregressive (AR) spectral estimation methods. These methods are called parametric, since they are based on the assumption of an autoregressive model structure for the signal being spectrally analyzed. Namely, the covariance, modified covariance and Burg methods are examined. We choose not to duplicate the details of each method, since they are widely covered in [4]. In general, all AR methods estimate the AR filter coefficients (or AR parameters) a_i $(i=1,...,N)$ and the average power σ^2 of the white noise, filtered by the autoregressive filter to produce a model of the examined signal. The resulting power spectral density (PSD) estimate is

$$P_{AR}(\omega)=\frac{\sigma^2}{|A(\omega)|^2} \text{ where } A(\omega)=1+a_1 e^{-j\omega}+\ldots+a_N e^{-jN\omega} \qquad (4)$$

A common concept behind all three AR methods is the unified estimation of the correlation matrix and their main difference lies in the definition of the data matrix.

3.1.2 MUSIC Method

Another spectral estimation technique, also member of the wide class of parametric methods, simulated to obtain 1-D radar images is the MUSIC algorithm [4]. This method has been used for radar target recognition applications, providing super-resolved range profiles compared to those of the conventional IFFT for the same frequency bandwidth [5].
In the next two paragraphs, we shortly present the mathematical background of MUSIC for range profile generation. Rewriting equation (1) in vector notation we have

$$\mathbf{y}=\mathbf{E}\mathbf{a}+\mathbf{n} \qquad (5)$$

where $\mathbf{y}=[y_1,...,y_N]^T$ is the data vector, $\mathbf{E}=[e(r_1),...,e(r_L)]$ is a matrix with columns the N direction vectors of the form $e(r_k)=\left[\exp\left(-j\frac{4\pi}{c}f_1 r_k\right),...,\exp\left(-j\frac{4\pi}{c}f_N r_k\right)\right]^T$, $\mathbf{a}=[a_1,...,a_L]^T$ is the amplitude vector**,** and $\mathbf{n}=[n_1,...,n_N]^T$ is the noise vector.

The first step of the MUSIC algorithm involves the computation of the correlation matrix of the radar scattering signal **y**. The data correlation matrix is defined as

$$R_{yy} = \mathrm{E}[\mathbf{y}\,\mathbf{y}^{\mathrm{H}}] \qquad (6)$$

where we shall not forget that usually one data snapshot is available in radar applications, thus the ensemble average can be discarded from (6). Eigenanalysis of the correlation matrix is the second step of MUSIC, resulting in N eigenvectors, L of which correspond to the L maximum eigenvalues and constitute the signal subspace. The $(N–L)$ eigenvectors, corresponding to the $(N–L)$ minimum eigenvalues of the correlation matrix, form the noise subspace. The MUSIC algorithm takes advantage of the fact that the direction vector $e(r)$ is orthogonal to the noise eigenvectors u_i ($i = L+1, ..., N$), at each scattering center location $r = r_k$. The generation of the MUSIC pseudo-spectrum is the final step of the algorithm (estimated range profile) and is given by

$$P_{MUSIC}(r) = \frac{1}{\sum_{i=L+1}^{N} \left| u_i^H\, e(r) \right|^2} \qquad (7)$$

3.2 Two-Dimensional Spectral Estimation Methods

Two-dimensional ISAR images are obtained by applying 2-D spectral estimation techniques. In our simulations, we have developed 2-D MUSIC algorithm [1] and 2-D autoregressive spectral estimation (similar to the autocorrelation method in one dimension) [6].

3.2.1 MUSIC Method

Starting from the 2-D radar data format specified through equation (3), we present the basic theory of the 2-D MUSIC in the next paragraphs. Rewriting equation (3) in vector notation we have

$$\mathbf{x} = \mathbf{A}\mathbf{s} + \mathbf{u} \qquad (8)$$

where $\mathbf{x} = [x(0,0), x(1,0), ..., x(M-1,0), x(0,1), ..., x(M-1,N-1)]^T$ is the column-ordered data vector, $\mathbf{u} = [u(0,0), u(1,0), ..., u(M-1,0), u(0,1), ..., u(M-1,N-1)]^T$ is the column-ordered noise vector, $\mathbf{s} = [s_1, ..., s_d]^T$ is the scattering intensity vector, $\mathbf{A} = [a(x_1, y_1), ..., a(x_d, y_d)]$ is a matrix with columns the d direction vectors of the form

$$a(x_k, y_k) = \left[\exp\left(j\frac{4\pi}{c}\left[f_0^x\, x_k - f_0^y\, y_k\right]\right), ..., \exp\left(j\frac{4\pi}{c}\left[f_{M-1}^x\, x_k - f_0^y\, y_k\right]\right), ... \right.$$

$$\left. ...\exp\left(j\frac{4\pi}{c}\left[f_0^x\, x_k - f_1^y\, y_k\right]\right), ..., \exp\left(j\frac{4\pi}{c}\left[f_{M-1}^x\, x_k - f_{N-1}^y\, y_k\right]\right)\right]^T$$

Similarly to the 1-D case, the first step of the 2-D MUSIC algorithm is the computation of the correlation matrix, based on one snapshot of 2-D radar data. The data correlation matrix is defined as

$$R_{xx} = \mathrm{E}[\mathbf{x}\,\mathbf{x}^{\mathrm{H}}] \qquad (9)$$

Following the 1-D analysis, the next step of 2-D MUSIC involves the eigendecomposition of the correlation matrix. At this point, one should notice that the data vector $\mathbf{x}$ has length $M{\cdot}N$. As a result, the correlation matrix is square with dimension $M{\cdot}N$ and its eigendecomposition produces $(M{\cdot}N - d)$ noise

eigenvectors and d signal eigenvectors. All eigenvectors have the same length as the data vector. The eigenvectors of the noise subspace (corresponding to the ($M \cdot N - d$) minimum eigenvalues) form a matrix $\mathbf{E}_n$. The final step of the algorithm is the formation of the 2-D MUSIC pseudo-spectrum

$$P_{MUSIC}(x,y) = \frac{a(x,y)^H \, a(x,y)}{a(x,y)^H \, E_n \, E_n^H \, a(x,y)} \qquad (10)$$

which indicates the positions of the scattering centers, identified as peaks of the pseudo-spectrum. Note that the scattering intensity information embodied in the 2-D MUSIC pseudo-spectrum (estimated ISAR image) is not very accurate. Therefore, amplitude estimation methods (such as least squares or weighted least squares) have to be applied separately from the 2-D MUSIC, if one desires more accurate estimation of the intensity of each scattering center.

3.2.2 AR Method

Two-dimensional AR spectral estimation can be implemented in a number of ways, starting from simple inversion of the data correlation matrix (direct method) and ending to iterative techniques, proposed to reduce the computational cost[2]. In the following paragraph, we briefly describe the direct method that is simpler than recursive solutions. In our simulations, we employ a small dataset and the computational burden of the direct method is not deterrent.

Typically, for the application of AR methods in two dimensions the data must be broken up into separate regions (i.e. sub-matrices of the original data matrix), each with distinct prediction error filter coefficients. The direct 2-D AR method for each region is summarized in the next lines. Firstly, the examined radar signal $x(n_1,n_2)$ is modeled as the output of a two-dimensional AR filter driven by white noise $e(n_1,n_2)$

$$x(n_1,n_2) = -\sum_{k=0}^{N_1-1}\sum_{l=0}^{N_2-1} a(k,l)\,x(n_1-k,n_2-l) + e(n_1,n_2) \qquad (11)$$

To determine the AR filter coefficients from the available data, we define the prediction error filter (PEF), which is formed by stacking columns of the array of coefficients $a(i,j)$, as $\alpha = [1, a(0,1), ..., a(0,N_2-1), a(1,0), ..., a(1,N_2-1), a(2,0), ..., a(N_1-1,N_2-1)]^T$. The coefficients are chosen so as to minimize the mean square value of the prediction error, defined as

$$MSE = E\left[e^*(n_1,n_2)\,e(n_1,n_2)\right] = \alpha^H \, R_{xx} \, \alpha \qquad (12)$$

where the data correlation matrix is R_{xx} = E[$\mathbf{x}^*$ $\mathbf{x}^T$], with the column-ordered data vector given by $\mathbf{x} = [x(n_1,n_2), ..., x(n_1,n_2-N_2+1), x(n_1-1,n_2), ..., x(n_1-N_1+1,n_2-N_2+1)]^T$. With $\varepsilon_k(i)$ being a vector of length k whose ith element is unity, with all the other elements equal to zero, $\omega = [\omega_1,\omega_2]^T$ denoting the vector of angular frequencies (one for each dimension of the resultant spectral estimate), and the matrix E defined as

$$E = \left[\exp\left(-j\,\omega^T\begin{bmatrix}0\\0\end{bmatrix}\right), ..., \exp\left(-j\,\omega^T\begin{bmatrix}0\\N_2-1\end{bmatrix}\right), \exp\left(-j\,\omega^T\begin{bmatrix}1\\0\end{bmatrix}\right), ..., \exp\left(-j\,\omega^T\begin{bmatrix}N_1-1\\N_2-1\end{bmatrix}\right)\right]^T$$

[2] There is always a trade-off between computational cost and algorithmic complexity.

the 2-D AR estimate of the PSD of the 2-D radar signal is given by

$$P_{AR}(\omega_1,\omega_2)=\frac{\sigma^2}{\left|E^T\,\alpha\right|^2}=\frac{\varepsilon_{N_1N_2}(0)^T\,R_{xx}^{-1}\,\varepsilon_{N_1N_2}(0)}{\left|E^T\,R_{xx}^{-1}\,\varepsilon_{N_1N_2}(0)\right|^2} \qquad (13)$$

4 SIMULATION RESULTS

The simulated radar target is a simple wire model of an aircraft with nine scattering centers, drawn in the following figure. The maximum target extent is 15 m and it is initially nose-on to the radar. The position of the radar on the *xy*-plane is (0,0) and the center of rotation is set on the position (4530,0) on the target. The positions of the nine scattering centers are (4525,0), (4527,3.5), (4527,-3.5), (4530,0), (4530,7), (4530,-7), (4540,0), (4540,1.5), (4540,-1.5). The *xy*-coordinates in the next figure are with respect to the center of rotation.

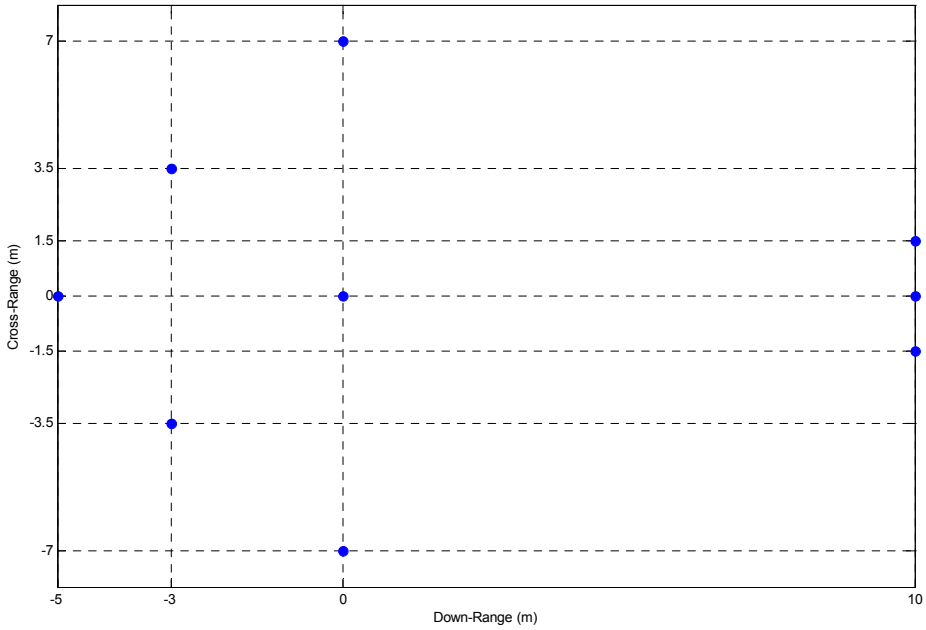

Figure 2. Simple aircraft model simulated as radar target

Taking into account the chosen parameters of the stepped frequency radar waveform (frequency step = 5 MHz, pulse repetition frequency = 10 KHz), the unambiguous down-range window is 30 m and the unambiguous maximum detection range is 15 km. Consequently, when plotting range profiles of the above target, we expect to identify scattering centers at down-range positions of 0 m (for down-range 4530 m), 10 m (for down-range 4540 m), 25 m (for down-range 4525 m) and 27 m (for down-range 4527 m). In our simulations, we have set the initial carrier frequency equal to 16.7 GHz, so as to imitate the frequency band of the imaging radar of the TIRA system[3].

As far as the Fourier processing for radar imaging is concerned, it is well-known that the corresponding down-range and cross-range resolution depend on the radar signal bandwidth and the aperture angle (i.e.

[3] TIRA stands for Tracking & Imaging RAdar. TIRA system (FGAN-FHR) is a radar system used to track and image air-borne targets in space and in atmosphere.

total look angle variation) respectively. Stepped frequency radar waveform is chosen in order to efficiently increase the signal bandwidth and improve the range resolution of FFT-based radar images. In our simulations, we do not employ windowed versions of the FFT, since there is always a trade-off between resolution and sidelobes' level (i.e. lower sidelobes are achieved at the cost of wider spectral peaks). Hanning and Hamming windows, for either one dimension or two dimensions, can satisfactorily reduce sidelobes.

The following two figures show range profiles generated by applying IFFT, covariance, modified covariance, Burg and MUSIC methods, for signal-to-noise ratio (SNR) of 25 dB and 10 dB. The stepped frequency waveform consists of 128 pulses (i.e. 128 frequencies), scanning a total signal bandwidth of 640 MHz. Note that the amplitude estimates for MUSIC-based range profile shall not be compared with those of the other four spectral estimates, since they are obtained by the MUSIC pseudo-spectrum.

The next three figures picture ISAR images generated by 2-D FFT, 2-D MUSIC and 2-D AR methods. The FFT-based image is obtained by simulating 512 frequencies and 200 look angles, so that its resolution is comparable to the one of the spectral estimation-based images. Note the dependence of resolution capabilities on the number of simulated frequency or angle steps. The other two images, based on 2-D spectral estimation, are obtained by simulating 16 frequencies and 31 look angles. Furthermore, considerable amount of white noise is added to the 2-D radar data (SNR = 25 dB). It worths noticing that the achievable resolution is sufficient for radar target recognition applications, even though very small datasets are simulated. The amplitude estimates are normalized to their maximum value (recall that the MUSIC-based amplitude estimates are derived from the 2-D pseudo-spectrum) and are quite similar. The extraneous peaks observed in MUSIC-based ISAR image are because of the correlation between data from different scattering centers. MSSP shall be employed in cases where the correlation causes severe image blurring.

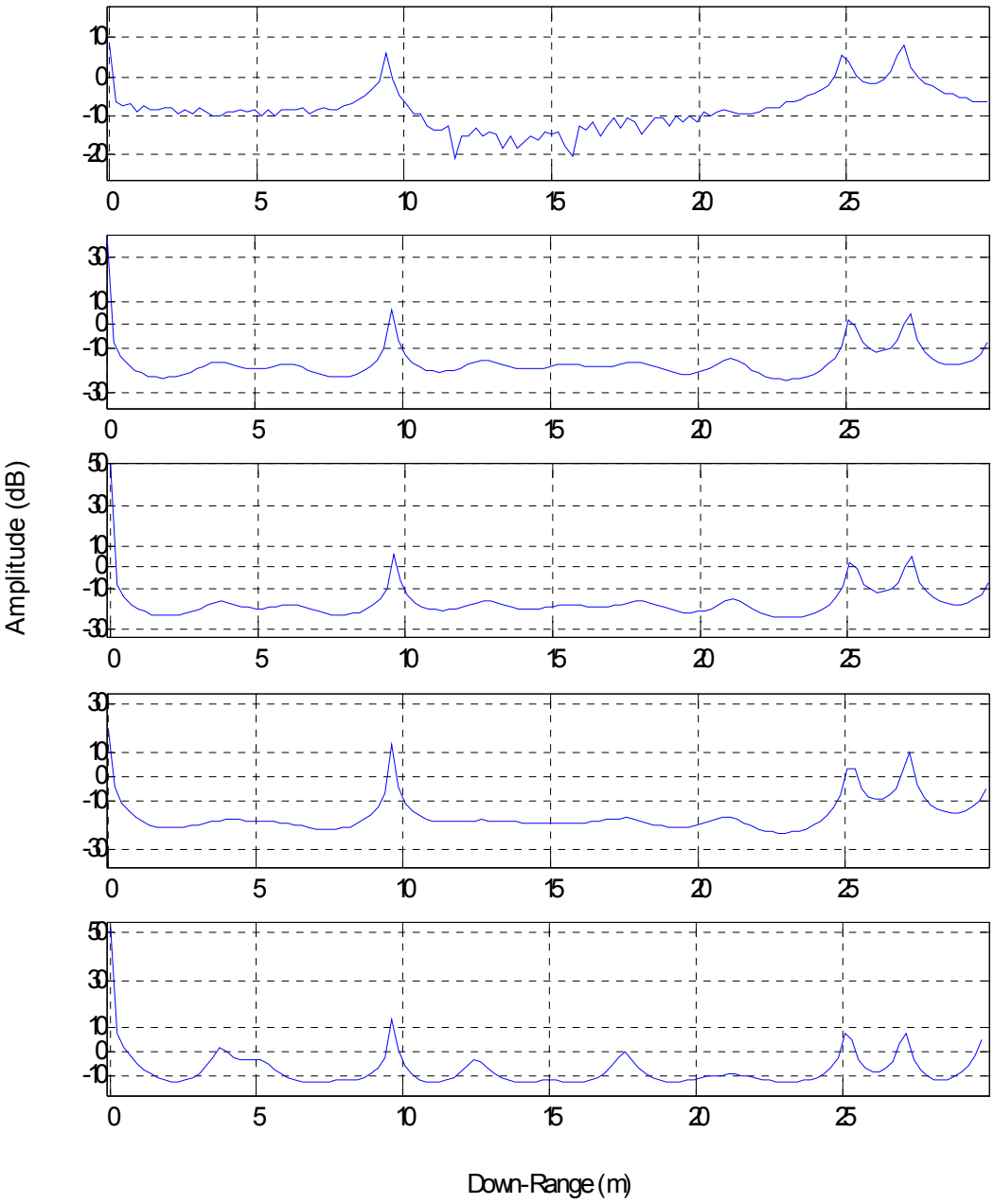

Figure 3. Range profiles generated respectively by applying IFFT, covariance, modified covariance, Burg and MUSIC methods, for SNR = 25 dB

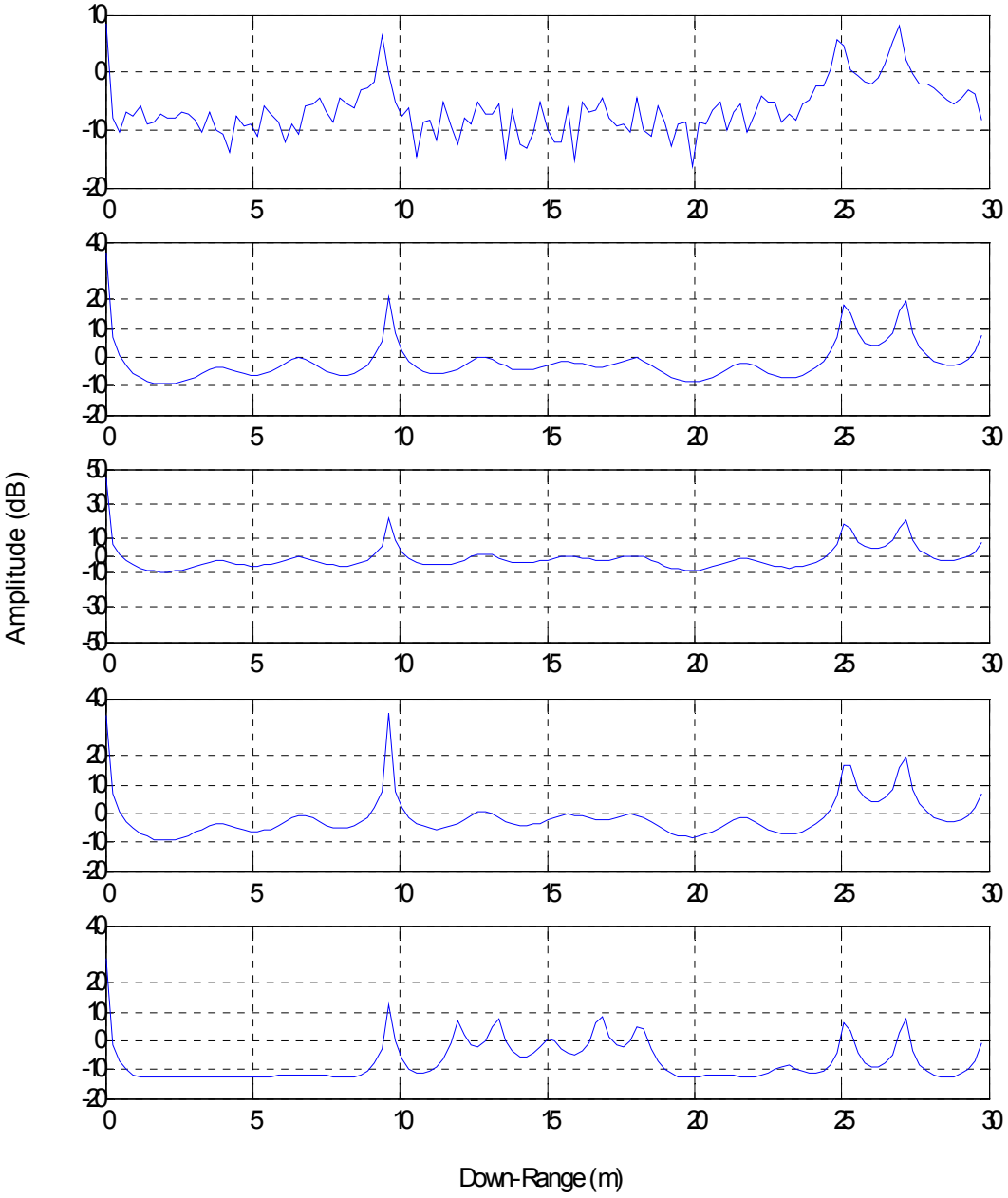

Figure 4. Range profiles generated respectively by applying IFFT, covariance, modified covariance, Burg and MUSIC methods, for SNR = 10 dB

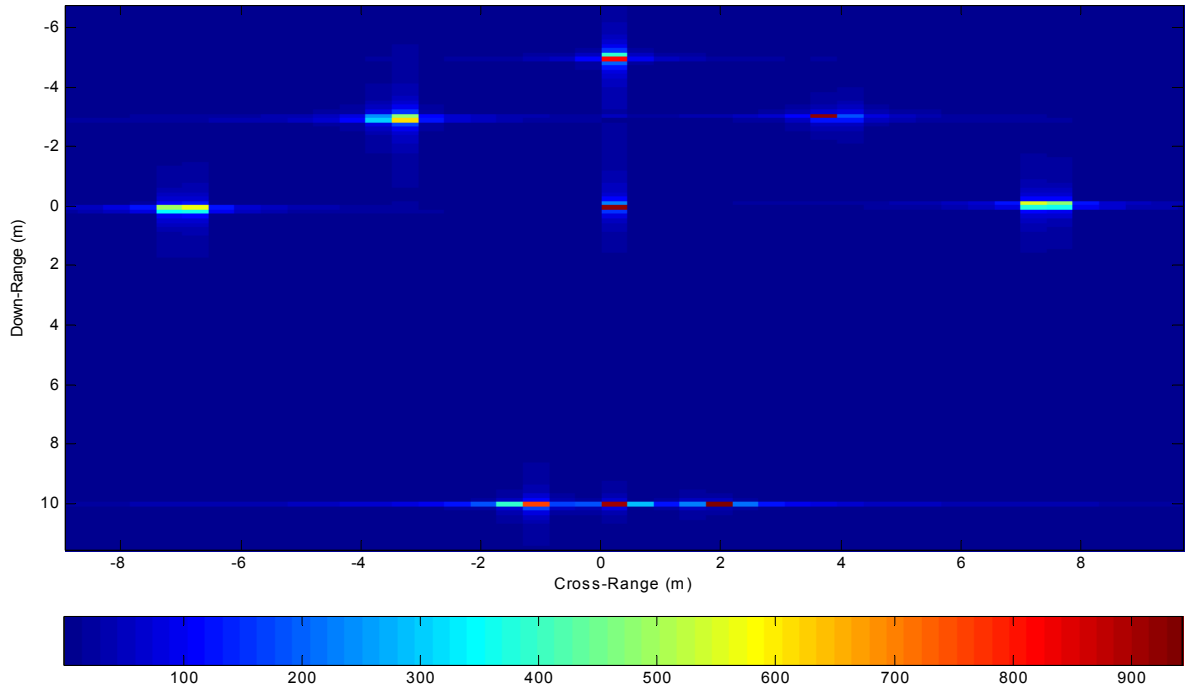

Figure 5. ISAR image generated by 2-D FFT (SNR = 40 dB)

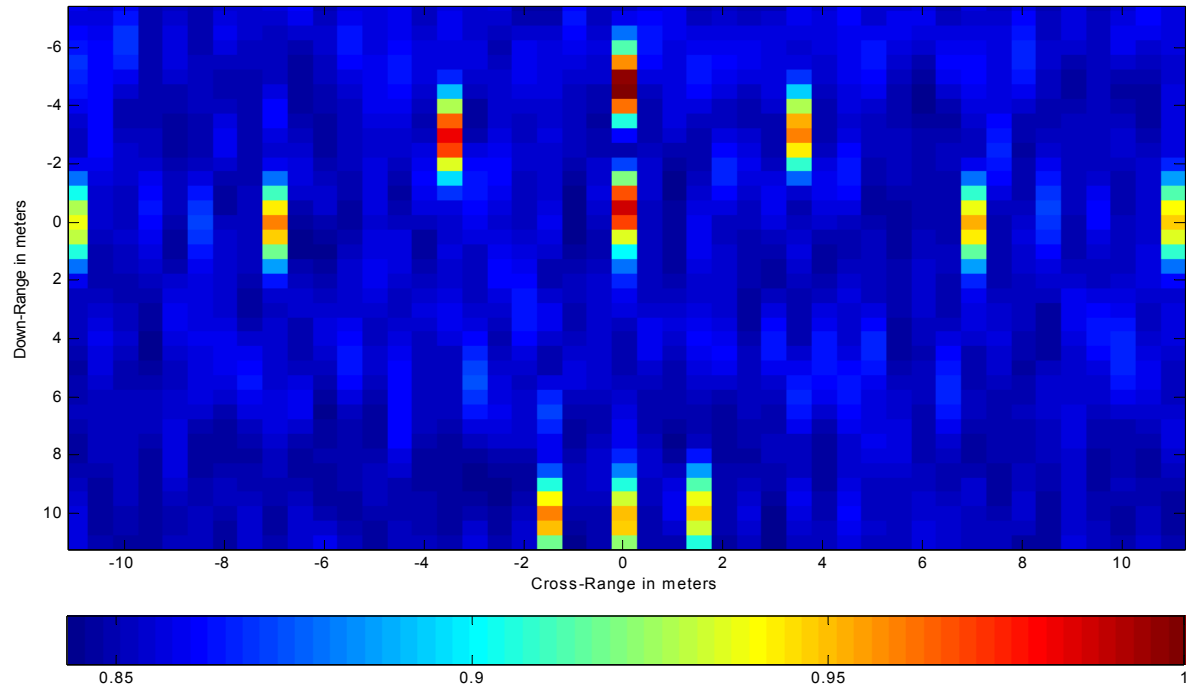

Figure 6. ISAR image generated by 2-D MUSIC (SNR = 25 dB)

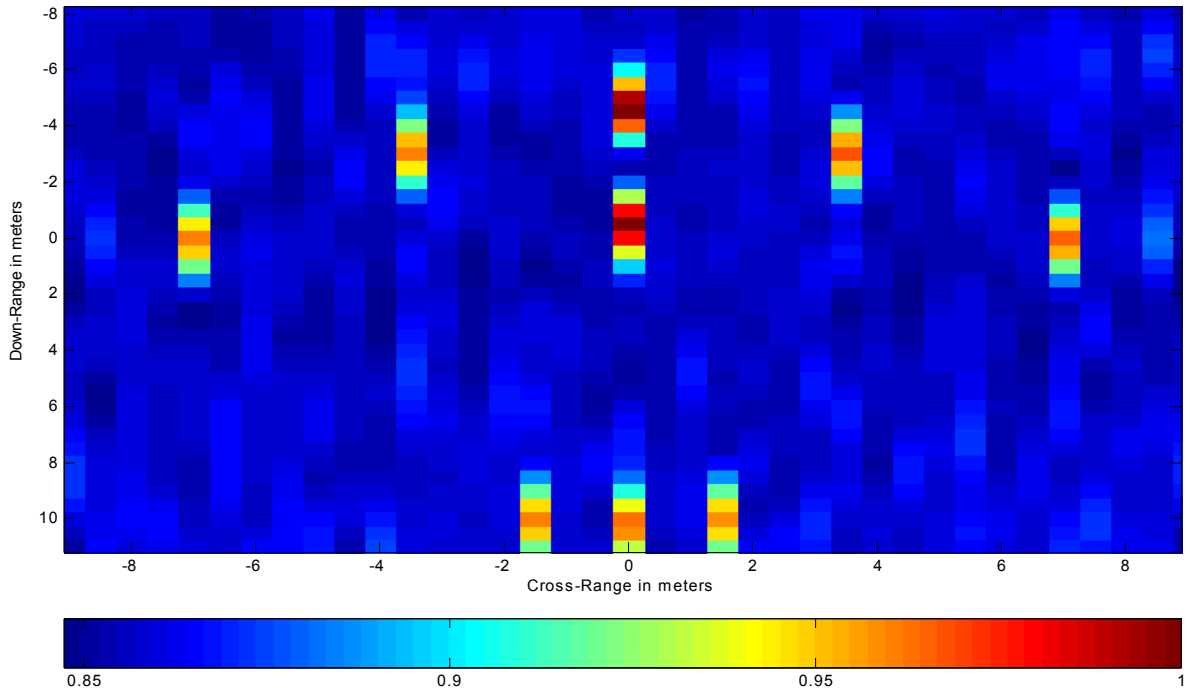

Figure 7. ISAR image generated by 2-D AR method (SNR = 25 dB)

5 CONCLUSIONS AND FUTURE WORK

Judging from the simulation results presented in Section 4 and those obtained through various simulation cases, we have reached the following conclusions with respect to the performance of spectral estimation-based radar imaging techniques:

(i) The spectral peaks of the IFFT-based range profiles are not as accurate (with respect to scatterers' ranges) as those of the spectral estimation-based range profiles. Moreover, higher sidelobes are evident in case of IFFT, compared to the smoother spectral estimates of AR methods (see Figure 3).

(ii) MUSIC-based range profiles, in case of moderate or high SNR, are more highly resolved than those of AR methods. Nonetheless, the problem of redundant spectral peaks shall be overcome by applying the MSSP technique, especially in case of low SNR values where the resulting range profile is severely worsened.

(iii) Burg method exhibits high-resolution capability for low SNR, whereas the sidelobes' level of IFFT-based range profiles increases as SNR decreases.

(iv) Spectral estimation-based ISAR images are characterized by satisfactorily high resolution, even for quite small datasets. On the other hand, the resolution of 2-D FFT-based images strongly depends on the number of frequencies (i.e. signal bandwidth) or look angles (i.e. aperture angle) simulated.

(v) Extraneous scattering centers, with low amplitude estimates, are identified by 2-D MUSIC pseudo-spectrum. In radar target recognition applications, MSSP may be necessary.

(vi) Two-dimensional AR spectral estimation and MUSIC result in quite similar ISAR image resolution. More complex target models would probably indicate the superiority of 2-D MUSIC.

The present study has motivated future research into three important topics:

(i) The computational cost of super-resolution spectral estimation techniques, especially for two-dimensional radar imaging, is the basic reason for choosing datasets as small as possible. The main advantage of FFT-based imaging is the computational speed. In order to lessen the computational burden, efficient techniques for computing the data correlation matrix shall be examined in future studies. The advantage of saving valuable memory space is of crucial importance for real-time radar signal processors.

(ii) Possible combinations between parametric (AR, MUSIC) and nonparametric high-resolution spectral estimation methods (Capon, APES) are under careful evaluation for two-dimensional radar imaging.

(iii) Above all, we are currently involved in processing real TIRA data provided by FGAN-FHR. Conventional FFT and super-resolution spectral estimation methods are to be applied on these measured data.

6 REFERENCES

[1] J. Odendaal, E. Barnard and C. Pistorius, "Two-Dimensional Superresolution Radar Imaging Using the MUSIC Algorithm," *IEEE Trans. Ant. & Propag.*, Vol. 42, No. 10, Oct. 1994.

[2] A. Quinquis, E. Radoi and F. Totir, "Some Radar Imagery Results Using Superresolution Techniques," *IEEE Trans. Ant. & Propag.*, Vol. 52, No. 5, May 2004.

[3] K. Kim, S. Kim and H. Kim, "Two-Dimensional ISAR Imaging Using Full Polarisation and Super-Resolution Processing Techniques," *IEE Proc. Radar, Sonar & Navig.*, Vol. 145, No. 4, Aug. 1998.

[4] P. Stoica and R. Moses, *Introduction to Spectral Analysis*, Prentice Hall, Upper Saddle River, NJ, 1997.

[5] K. Kim, D. Seo and H. Kim, "Efficient Radar Target Recognition Using the MUSIC Algorithm and Invariant Features," *IEEE Trans. Ant. & Propag.*, Vol. 50, No. 3, March 2002.

[6] B. McGuffin and B. Liu, "An Efficient Algorithm for Two-Dimensional Autoregressive Spectrum Estimation," *IEEE Trans. ASSP*, Vol. 37, No. 1, Jan. 1989.

[7] T. Shan, M. Wax and T. Kailath, "On Spatial Smoothing for Direction-of-Arrival Estimation of Coherent Signals," *IEEE Trans. ASSP*, Vol. 33, No. 4, Aug. 1985.

[8] R. Williams, S. Prasad, A. Mahalanabis and L. Sibul, "An Improved Spatial Smoothing Technique for Bearing Estimation in a Multipath Environment," *IEEE Trans. ASSP*, Vol. 36, No. 4, Apr. 1988.

The Desirability of a NATO-central Database for Non-Cooperative Target Recognition of Aircraft

S.J. Gelsema
Oude Waalsdorperweg 63
2597 AK, Den Haag
THE NETHERLANDS

Sjoerd.Gelsema@ tno.nl

ABSTRACT

For a decade, NATO nations, both on their own and within NATO groups have performed studies in the field of Twodimensional Inverse Synthetic Aperture Radar (2D-ISAR) and High Resolution Radar (HRR) Range Profiles. During that work high-quality radar imagery data of aircraft has become available through measurement campaigns. It was shown that the acquisition of a sufficiently large and representative reference database is a difficult and laborious process. Other database properties, such as its contents, size, upgradability, retrieval speed, operational use, etcetera have not received sufficient attention within these studies. In the future, NATO may be playing a major role in maintaining a NATO central database of radar signatures. This paper provides an initial understanding of the operational implications for performing such a task. It argues that, instead of providing a central database to NATO nations, NATO should stimulate the use of decentralized classifiers and databases and ensure that coalition partners can access them via a data network in operational situations.

1. INTRODUCTION

Target identification is essential for any combat command and control and weapon system. Effective response to threats can be generated only if the ability exists to rapidly detect, track and identify targets present. Cooperative identification techniques play an important role. These techniques include IFF and the use of airspace control procedures.

A serious drawback of these methods is that they require the cooperation of the targets. This can lead to serious consequences if friendly or neutral targets fail to cooperate. In the extreme case, the target will be marked hostile and will be engaged by own fire. Furthermore, enemy units can exploit cooperative identification to mask their identity. Nevertheless, cooperative identification methods remain crucial for the positive identification of own troops.

Positive identification of neutral or enemy troops under all operational circumstances, however, remains a deficiency in NATO's air defence capability. In fact, it is acknowledged that it is the most serious deficiency and one that impacts almost every aspect of air command and control and weapon system employment. The lack of timely and reliable means to identify all air vehicles at all aspect ranges necessitates the use of very restrictive airspace and weapon control orders. This limits the effective use of advanced weapon systems, specifically of beyond visual range systems.

To improve identification capabilities and to ensure high confidence in positive air target identification, more advanced techniques and additional information sources have been proposed (see for example STANAG 4162 on the "*Technical Characteristics of the NATO Identification System (NIS)"*). These include Non-Cooperative Target Identification (NCTI) by radar.

Paper presented at the RTO SET Symposium on "Target Identification and Recognition Using RF Systems", held in Oslo, Norway, 11-13 October 2004, and published in RTO-MP-SET-080.

Radar based NCTI techniques include modulation techniques (like Jet Engine Modulation (JEM), Helicopter Rotor Modulation (HERM) and Propeller Rotor Modulation (PRRM)) and imaging techniques, either one-dimensional (High Range Resolution (HRR) profiles) or two-dimensional Inverse Synthetic Aperture Radar (2D-ISAR)). Under the Sensors and Electronics Technology (SET) Panel of the Research and Technology Organization (RTO) of NATO, extensive research has been conducted over the past two decades to establish and enhance the benefits of these techniques.

At the end of the eighties, JEM was regarded as most promising but limited only to nose-on aspects. Nowadays, modern tracking radars generally have JEM capabilities. HRR was also looked upon as promising but required further development. The past decade, research within NATO focused on classifying HRR profiles and on the generation of synthetic databases for HRR classifiers. It is foreseen that next-generation radars generally will possess means of generating HRR profiles. HRR classification means are expected on a longer term though.

While considerable attention has been paid to the development of NCTI classifiers, only limited attention has been paid to issues concerning their operational use. These issues include the desirability and the definition of requirements for a possible future NATO database for NCTI.

This paper discusses some of the issues related to the operational deployment of NCTI classifiers. It attempts to develop a coherent view on the future operational use of NCTI classifiers, specifically HRR based ones. Therefore, the second and third section current trends in concepts of operations and technological trends, respectively, to the foreseeable future. The fourth section then formulates general requirements for NCTI databases. Finally, the fifth section combines the results from the previous chapters and formulates a coherent view on the future use of NCTI classifier and databases within NATO.

2. OPERATIONAL CONSIDERATIONS

It is imperative to understand that the next military operation where NATO is involved in differs from the last one and that making statements about any future conflict therefore is quite hazardous. However, it is safe to say that the probability of NATO having to respond to large-scale aggression against one or more of the members is low. Instead, potential threats to Alliance security are more likely to result from regional conflicts, ethnic strife or other crises beyond Alliance territory, as well as the proliferation of weapons of mass destruction and their means of delivery.

Future NATO operations are therefore likely to be smaller in scale, they may be longer in duration, extend multinational co-operation to lower levels and take place concurrently with other NATO operations. The operations possibly will include contributions from Partnership for Peace (PfP) nations or even from other non-allied nations.

These developments will make their demands on the combined NCTI capability. The next few sections will develop some of the interoperability issues a little bit more. The final section exemplifies the foreseen use of NCTI capabilities.

2.1 Types of Conflict and Anti Fratricide

The types of conflict NATO nations have been and will continue to be involved in, can be divided into non-combat and combat operations. Non-combat operations typically have the aim to promote or to keep peace. They may include contributions from many nations, not necessarily allied with NATO. The level of force applied is relatively low and one might argue that these operations don't have the need for extremely accurate non-cooperative identification means. Combat type operations typically have the aim to resolve conflicts, to deter war or even to fight and win war. The level of force applied is higher than in non-

combat operations, and consequently the need for accurate and complete NCTI means may be more urgent.

Operational analysis has demonstrated that when the Blue Force has an overwhelming superiority over the Red Force, with all other factors being equal, the ratio of fratricide to the total number of Blue casualties can be greater than the fratricide rate in situations where Blue and Red are more evenly matched. The ratio indeed approaches 100 percent, even if the Blue losses are much lower [1, 2]. The accelerated operational tempo, the increased accuracy, lethality and speed/range of modern weapons, the lack of common tactics, techniques and procedures, and the absence of combined training of the coalition partners can explain the apparently increasing fratricide rates [2].

These factors contribute to augment both the likelihood and adverse consequences of human error, particularly in a coalition that consists of forces with varying degrees of interoperability, i.e. a coalition that is more likely to be found with no-combat, peace keeping operations. If we start from the idea that better means of identification can significantly decrease the number of friendly fire casualties, it is inevitable that both in non-combat operations as well as in combat operations, non-cooperative identification means have to be as accurate as possible, even though the level of force differs. In all situations, an NCTI database should therefore at least contain signatures of every allied platform in theatre and preferably a vast number of enemy platforms.

2.2 A Networked Force

Information technology is undergoing a fundamental shift from platform-centric computing to network-centric computing. This shift is most obvious in the explosive growth of the internet, intranets and extranets. Information can now be distributed, and exploited across the extremely heterogeneous global computing environment.

Evidently, the technology that enables network-centric computing is also available in military environments. The use of networks of (weapon)platforms in military operations stirred the imagination of military thinkers. In fact, they have embraced the new technology and developed theories like Network-Centric Warfare (NCW), Network Centric Operations (NCO) and Network Enabled Capabilities (NEC). In theory, NCW, or NCO and NEC for that matter, will result in a revolutionary change in the way we think about and conduct warfare [3]. In reality, it is more likely to result in incremental, evolutionary changes in military capabilities and doctrines.

Whatever the outcome of these developments will be, it is safe to assume that platform operators have access to relevant information via, or contained by the network, and that they have knowledge, or have access to knowledge, about the location and capabilities of other platforms in the network.

2.3 Identification within a Networked Force

As an example of how platforms could behave in a networked force, consider the air superiority mission.

In a conventional force, each fighter pilot is able to develop situational awareness by three means: firstly, by direct visual observation, secondly by indirect observation using on-board sensors and thirdly, via voice or Link-16 communications with other fighter pilots. If a pilot is to establish ID on a threat, he relies solely on his own sensors, classifiers and databases.

In a networked force, the pilot has a fourth means to develop situational awareness, namely digital information that is exchanged with external sources, such as other fighter aircraft or airborne surveillance and C2 aircraft, over a network. At the time of the information request, the information can already be contained by the network, or can be generated by other platforms. Specifically, the pilot can ask the

airborne surveillance aircraft to establish ID on the threat he is currently facing. Alternatively, he can use his own sensors to measure a HRR profile of the threat and ask a central classifier to classify the profile using a central database.

In these examples, the platform operator (the pilot) only uses the network to communicate with other platforms. However, he still needs to know where the information that he needs can be obtained. Although the platforms can communicate via a data network, the environment can still be characterized as Platform-Centric.

In Network-Centric environments, the pilot approaches the network as a separate entity. If he needs ID on a threat he queries the network rather than the individual platforms. The network then takes care of the selection and deployment of resources (platforms, sensors, classifiers, and databases) to answer the query.

Although the distinction between a networked Platform-Centric environment and a Network-Centric environment is small to the platform operator, it is a large one to the network technology. We shall see, however, that the distinction has only fractional impact on the requirements on NCTI databases.

3. TECHNICAL CONSIDERATIONS

3.1 Radar Technology

Implementations of HRR and 2D-ISAR techniques in radar systems require that those radars be wideband and coherent. The most important requirements for NCTI relate to the geometrical resolutions (range resolutions in HRR, range and cross-range resolution in 2D-ISAR). Resolution requirements impose radar system bandwidth requirements, and bandwidth is a key parameter which is usually limited by the transmitter or antenna technology for a given radar design.

The Final Report of the Task Group (TG) 09 of the Sensors and Electronics Technology Panel (SET) lists a comprehensive set of requirements for radar imaging techniques [4]. These requirements are not very stringent, apart maybe from the motion compensation requirements for ISAR. The latter is, however, more a processing/algorithmic requirement than a system requirement. A number of existing radars already have the required bandwidth and some of these even could support NCTI modes.

It is the expectation that many future radar systems will have a HRR and/or ISAR mode if such a mode fits into their operational scope. Motion compensation for ISAR will remain a different task that requires a lot of processing power. Meeting this requirement, however, will be a matter of availability of motion compensation algorithms, rather than processing power.

The required bandwidth can be achieved relatively easily by the transmitter technology, even within a single pulse. X-band will be the preferred choice for the operational frequency. The growing use of phased array antennas might limit the HRR capabilities to stepped frequency waveforms (SFWs) if phase shifters are applied. Since these waveforms require longer dwell times, the use of an HRR classification dwell must be seriously considered in an operational situation as to not consume too much time budget. Furthermore, HRR classifiers should be able to handle HRR profiles obtained with SFWs and be robust for subtle differences. Phased array antennas using time-delay steering can handle larger bandwidths though.

3.2 Classifiers

The process of identifying aircraft based upon its JEM, HRR or ISAR signature can be separated in a number of stages. These include motion compensation, other pre-processing (like range alignment,

dynamic range compression and dimension reduction), feature extraction and finally classification. Apart from the motion compensation, these stages can be considered an integral part of the classifiers.

Classifiers for radar NCTI can be divided into three groups. The first group comprises of classifiers based on *correlation techniques*. The nearest neighbour (NN) classifier is perhaps the most widely known. Since an NN-classifier does not incorporate statistical distributions, its use in the (Bayesian) IDCP framework (see section 3.3) is not straightforward. Another type of classifier based on correlation techniques is the Template Matching (TM) classifier. Its theoretical basis is well-established and the algorithm can be made as robust as in the NN case. Moreover, the template allows for information about the statistical distribution of the feature vectors and the incorporation in an IDCP framework much easier.

A second group of classifiers uses *neural networks*. The most elementary classifier that uses a neural net is the Radial Basis Functions (RBF) classifier. Radial Basis Functions provide a way to construct a smooth, non-linear mapping from a high dimensional feature vector space to a lower dimensional space, in which the class labels are defined. The important advantage, as opposed to many neural network types, is that the fitting is done in a well-defined linear way. There is no need for tuning the learning rate nor the size of the network, and there is no danger of slipping into a local optimum instead of a global one. As in the nearest neighbour case, the only quantities that enter the classifier are, as in the NN case, profile to profile distances. Incorporation into an IDCP framework is possible but not straightforward.

A final group of classifiers consist of *model* or *feature based classifiers*. While the actual classification step might very well consist of Radial Basis Functions, Nearest Neighbour, Template Matching or other previously mentioned classifier, they distinguish themselves by the presence of a feature extraction step. JEM classification algorithms all make use of simple features, such as the number of blades on a compressor stage and the blade chopping frequency. For HHR, recent investigation showed that positions of peaks in an HRR profile can be used as class discriminating features.

From this overview, it is clear that the databases belonging to these very divergent types of classifier are also very different in their nature. It is safe to say that the type of classifier defines the database and vice-versa. Therefore, classifiers and databases cannot be viewed separately.

3.3 IDCP

No single identification sensor or source is capable of providing positive identification of all friend, foe and neutral platforms under all conditions (e.g. countermeasures). The combination, however, of more than one identification sensor or source can increase the probability of correct identification. The Identification Data Combining Process (IDCP) is a component of the NATO Identification System (NIS) and it provides a standardized process for using, combining and exchanging identification data, in order to improve identification accuracy and timelines.

As of November 1996 there are (completed) parts of STANAG 4162 Annex D which cover the processing of the following identification sensor and source types: IFF, ESM, Flight Plans, Procedural Routing, Track Behaviour, Identification by point of Origin, Link 16 PPLI Messages, Nationally Sensitive Sources, and Discrete Events (e.g. target is jamming a friendly radar). A first draft of the NCTI part just covers the JEM NCTI technique, as imaging radar was considered insufficiently mature to be included at that time. Nevertheless, the general principles covering the addition of radar imaging sensors to the IDCP framework are clear, even if the details remain to be defined.

The IDCP specifies Bayes' theorem to fuse the information from different types of sensors. Fusion can be carried out in the Platform Object Class (e.g. F-14, F-15, Tornado, etc.) and/or the Basic Identity Object Class (i.e. Own Forces, Enemy Forces, Non-Aligned), depending on the sensor type. It is appropriate to convert the declaration from a radar JEM, or imaging sensor into a Likelihood Vector of the Platform Object Class.

Given the operational trend from platform-centric towards network-centric, the IDCP concept will only gain in importance. To be able to fuse ID information from different radar NCTI sensors (e.g. classifiers) it is essential that they provide a measure of reliability with their declarations. The databases coupled to these classifiers should allow for this (extra) information.

3.4 Information and Communication Technology

Information and communication technology and the networks they enable play a fundamental role in future military operations. Consequently, understanding the underlying trends that govern technology and influence the value-creation potential of networks is important to understanding the potential power of network-centric operations.

Military operations employ commercial information technologies, as well as military specific information technologies. In general, the primary difference between the networks used by deployed warfighters and the networks used by non-mobile entities, is the characteristics of the links. The primary transmission path for the deployed warfighter is radio frequency communications enabled by radio, data link, or satellite. Furthermore, military operations typically require special link features, such as anti-jam properties, which to date have not been priorities for commercial users.

There are a number of fundamental business and technology trends that shape the future of networks and the future of network-centric operations [5].

- *Moore's law*: *Computer chip performance doubles every eighteen months*. The same technology trends which have enabled the performance-cost ratio for personal computers to double approximately every 18 months have also enabled relatively small, powerful chips to be deployed in a wide variety of devices, such as personal digital assistants (PDAs). Analogous trends are being played out in warfare as we make the shift to network-centric operations.
- *Data storage capacity doubles every twelve months.* Like silicon integrated circuits, data storage devices has put on a spurt of their own, first matching the pace of chip developments but over the few years surpassing it. Since the giant magnetoresistive head (GMR) reached the market in 1997, density has been doubling each year. At the same time, costs of data storage device has fallen from approximately 1 dollar per megabyte to only a few tenths of a cent per megabyte and is now well below the cost of paper [6].
- *Transmission Capacity doubles every twelve months.* Currently, the primary backbone of advanced networks (both voice and data) is fiber optic cable. Recent and ongoing developments in the field of optical communications have resulted in the doubling of the transmission capacity of fiber optic cable every 12 months. This performance trend in fiber optical communications is key to enabling the significant capacity increase of the Internet. The last ten years has seen a rapid evolution of radio communication systems, GSM systems in particular. To maintain competitive advantage, equipment manufacturers are being driven to develop low cost and high volume products with increasing levels of functionality and miniaturization. In addition, companies are pursuing efforts to launch large constellations of satellites to provide high capacity bandwidth worldwide over radio frequency. In February 2002, regulatory approval for the development of Ultra Wideband (UWB) Communications was granted. As a result, the IEEE is expected to announce the use of UWB in their new communications standard. UWB technology allows systems to operate across a range of frequency bands, without interfering with existing systems. UWB signals appear as very low background noise to an unauthorized receiver. This radically reduces the probability of interception or detection and provides high physical security benefits compared with more conventional technologies. The operating range of current systems is, however, still limited to tens of metres.

- *Confluence of Trends—Network-Centric computing.* The consequences of these mutually reinforcing trends have been profound. The combination of increasing performance and cost suppression has resulted in the widespread adoption of computers in business and in the home which, when combined with trends in communications, has set the stage for network-centric computing and network-centric operations. The combination of digital communications capabilities and breakthroughs in software technology has enabled information interactions among entities of virtually any size that can be connected to the network.

Military information and communication technology generally follows commercial technology with a delay of several years and thus the same evolution rate can be assumed. This implies that future military platforms will possess networking capabilities comparable to today's commercially available capabilities.

4. DATABASE REQUIREMENTS

Basic requirements for NCTI databases include requirements for the following properties: type of information, size, retrieval speed, maintenance, data sources, aircraft types and configurations, etc. Requirements for these properties are not universal but depend heavily on technical possibilities, on their operational use, i.e. on the type of conflict in which they are deployed and, most importantly, on the classifier they are used with.

Furthermore, practical issues may restrict their contents. It will be impossible to build an NCTI database based upon measurements of all possible aircraft that can be encountered in theatre. While measurements of every friendly aircraft may be available, this is certainly not the case for neutral, let alone for hostile aircraft. Databases based upon synthetic data might relief this problem partly.

However, even the availability of friendly signatures (either measured or synthetic) might be limited, especially in multinational operations. It is not unthinkable that NATO members are reluctant to share signatures of some of their national aircraft with other members, let alone with possible non-NATO members within a certain coalition.

While technical requirements, like speed and size, can (eventually) be met by the ever-increasing technological possibilities, the issues related to classifier dependence and to database contents (i.e. signature availability and proliferation) need to be solved explicitly.

4.1 Dependence on NCTI Technique and NCTI Classifier

The precise information required in an operational database clearly depends on the imaging technique and the classification algorithm. The database for a JEM classifier will typically comprise JEM features like the blade-chopping frequency, the number of blades per compressor and the number of compressor stages of individual jet engines.

The database for an HRR profile classifier will typically comprise either individual range profiles, averaged range profiles, templates that are similar to averaged range profiles, or of features that are extracted from range profiles. If the classification algorithm is preceded by a pre-processing stage, for example a power law transformation, the same pre-processing of the reference profiles in the database will be required. Furthermore, depending on the classification algorithm, it may be computationally more efficient to store the Fourier Transformed range profiles, instead of the profiles themselves.

The contents of an operational ISAR database will also depend on the feature extraction and classification algorithms employed. Database for ISAR may comprise of 3D peak locations of carefully selected scatterers that are visible at each aspect angle of interest. Other recognition algorithms proposed for ISAR require databases consisting of sets of moments of the ISAR image intensity.

It is clear that NCTI databases depend heavily on the classifier they belong to. Indeed, it is impossible to view them separately. The type of classifier defines the database and vice-versa. This means that if there are to be NATO databases for NCTI, then there have to be corresponding NATO classifiers as well. This would require a lot of extra research and development efforts to co-ordinate the development and maintenance of such a classifier/database combination.

4.2 Nationally Sensitive Contents

The concept of a NATO NCTI central database, or rather NATO-central NCTI classifiers including databases, suffers from the problem of data availability. Since the database of signatures depends on the classifier, dedicated measurement campaigns have to be organized, or dedicated synthetic signatures have to be generated. Clearly, operational aircraft from non-NATO nations will never participate in such a measurement campaign. NATO intelligence sources, however will be able to provide detailed CAD models of hostile aircraft, and therefore the generation of synthetic signatures is feasible in principle.

While using synthetic signatures might relieve the need for signatures of neutral and hostile aircraft, the real challenge might be the availability of signatures of aircraft of individual member nations, to other NATO nations. It is not unthinkable that nations will be very reluctant to share such sensitive information as HRR or ISAR signature to every other NATO nation.

A possible way to diminish this reluctance is to ensure confidentiality by encrypting the information in the database and to offer the NATO classifier/database combination on a operation-by-operation basis as a black box to nations that participate in the operation. However, next to the research and development overhead caused by the classifier/database generation, this would require additional administrative overhead. Even if confidentiality within a NATO central office is guaranteed, it is still questionable if every nation can be convinced to release signature data of their most modern aircraft.

4.3 The Network Enabled Approach

The two previous sections roughly sketched the difficulties related to a NATO NCTI database with the aim to provide it to nations if circumstances call for it. Firstly, it is useless to provide databases to member nations without a corresponding classifier and secondly, it may be very hard to obtain relevant signature data. Solving these difficulties seems to implicate such a lot of effort that it may be sensible to look for alternatives for a centralized database.

A possible solution to solve the main difficulties would be to stimulate the use of decentralized classifier/database combinations. Each nation that participates in a multi-national operation is responsible for providing means to classify their own aircraft using their own classifier / database combinations. This way, signatures of their own aircraft do not have to be distributed to other nations. Of course, other nations would need access to the classifier/database combinations. This can be achieved by using a network.

Consider for instance the individual fighter aircraft that operates in a multi-national war-like operation. In the previous chapters we have established that future fighter aircraft will possess the following resources:

- Sensors that allow for the measurement of NCTI signatures, being JEM spectra, HRR profiles and/or ISAR imagery.
- A classifier that accepts these measurements as input and classifies them against a database, which, at the least, contains their own national aircraft and possibly other friendly, neutral or hostile aircraft in theatre.
- A communication link, which connects to a network. This communication channel allows for the distribution of NCTI signatures to other linked platforms.

Now suppose the platform operator (the pilot) needs ID on a threat he is facing. His first action will be to query the network for an ID on the threat. If this is not available or if it is unreliable, he uses his own sensors to obtain a JEM, HRR or ISAR signature of the threat. He then offers this signature to his classifier and at the same time sends out a request to other platforms to classify the signature using their classifiers. All classifiers in the network will prioritize and schedule this request and possibly come up with an answer that gets sent back to the requesting platform. Finally, the requesting platform combines the ID information, preferably using the IDCP protocol, and stores the ID for immediate and future use.

5. DISCUSSION AND CONCLUSIONS

Accurate identification has always been a requirement on the battlefield and has nowadays become even more stringent when military operations involve multi-national coalitions. Better means of identification significantly reduces the risk of fratricide and –partly therefore– enhances the effectiveness of advanced weapon systems, especially of those that can be employed beyond visual range.

In the past few decades, considerable attention has been paid to the development of non-cooperative identification systems and algorithms. As a result, the majority of future radar systems will possess a HRR and/or ISAR mode if such a mode fits into their operational scope. Contrarily, only limited attention has been paid to the operational use of NCTI classifiers, including the desirability and the requirements for a possible NATO central database for use with NCTI systems.

To assess if a NATO-central NCTI database is desirable, the previous chapters highlighted some operational and technological trends and projected them into the foreseeable future. The analysis of these trends seems to indicate that the answer to the question whether a NATO-central database is desirable is a negative.

There are a two serious impediments to the idea of a NATO-central NCTI database, that cannot be circumvented in practice. Firstly, we have established that NCTI classifiers and NCTI databases cannot be separated (see section 3.2 and 4.1). The availability of a NATO-central database implies the availability of a NATO-central NCTI classifier, which would require a lot of research and development in NATO panels. Efforts that are much more effective when conducted within the NATO nations themselves.

Secondly, Section 2 argued that both in non-combat and in combat operations, non-cooperative identification means have to be as accurate as possible, even though the level of force differs from the one type to the other. An NCTI database should therefore at least contain signatures of every allied platform in theatre and preferably a vast number of enemy platforms. While using synthetic signatures might relieve the need for signatures of hostile and neutral aircraft, security considerations might restrain NATO nations from sharing signatures of their own aircraft with other NATO nations. Confidentially guaranteed via NATO encryption and procedures might not convince every nation to release signature data of their most modern aircraft.

The alternative to enhance identification within multi-national coalitions is to stimulate the use of decentralized classifiers and to use a network to offer access within the coalition. Each nation that participates in a multi-national operation is responsible for providing means to classify their own aircraft using their own classifier / database combinations. This way, signatures of their own aircraft do not have to be distributed to other nations. This concept is further specified in section 0. In concreto, next to the non-trivial issues related to a networked force (which lie beyond the scope of this report), this approach would require NATO to:

- Stimulate nations to develop and maintain classifiers that report a measure of reliability with their declarations.

- Stimulate nations to develop and maintain classifier/database combinations that allow for the identification of at least their own national aircraft.
- Stimulate nations to include foreseeable neutral and hostile aircraft as well, by organizing measurement campaigns that include neutral / civil aircraft and by providing CAD models of non allied fighter aircraft.
- Specify a data format for the exchange of HRR and ISAR signatures, as well as for the exchange of ID classification results.

6. REFERENCES

[1] James D. Sinclair, *A Methodology for Assessing Air-to-Air Combat ID Requirements*, Combat Identification Systems Conference 2000, 12-14 September 2000.

[2] C. Carrier, J. Dubois, D.R. Elliot, D.H. Saint, *Achieving Interoperability: Technologies for Combat Identification in Combined Air/Land Operations*, Defence R&D Canada, June 2002.

[3] Arthur K. Cebrowski, John J. Gartska, *Network-centric warfare: Its origin and future*, Naval Institute Proceedings, **124(1)**, p28-35, January 1998.

[4] *Radar Imaging Techniques and the Problem of Data Base Generation for the Non-Cooperative Target Identification (NCTI) of Aircraft*, RTO Technical Memorandum 12, April 2001.

[5] David S. Alberts, John J. Garstka, Frederick P. Stein, *Network Centric Warfare, Developing and Leveraging Information Superiority*, ISBN 1-57906-0196, 2nd Edition (Revised), February 2000.

[6] Brian Hayes, *Terrabyte Territory*, American Scientist, **Vol 90, Nr. 3**, p. 212-216, May-June 2002.

Passive Radar Imaging and Target Recognition using Illuminators of Opportunity

Aaron D. Lanterman
Georgia Institute of Technology
School of Electrical and Computer Engineering
Mail Code 0250
Atlanta, GA 30332

E-mail: lanterma@ece.gatech.edu

SUMMARY

Passive radar systems that exploit illuminators of opportunity, such as FM radio and television broadcasts, to detect and track airborne targets have been under development for over a decade. This paper reviews efforts to add radar imaging and target recognition capabilities to such systems. We discuss recent developments along two parallel threads:

1) Target recognition via radar cross section (RCS) profiles: In this approach, databases of the RCS of targets at different incident and observed angles are created using method-of-moments computational electromagnetics codes. The extracted RCS profiles for different targets, scaled to account for antenna patterns and atmospheric propagation, are compared to the collected data. A coordinated flight model is used to estimate the aircraft's orientation along its flight path. The low frequencies used in passive radar naturally give stable features well suited for automatic target recognition.

2) Radar imaging: A traditional inverse synthetic aperture approach to forming images with passive radar data results in severe artefacts due to the sparse and irregular Fourier sampling patterns resulting from realistic data collection scenarios. We review the application of a recent optimization-based, region-enhancing imaging algorithm to passive radar imaging that effectively suppresses these artefacts, and illustrate the difficulties posed by the underlying multidimensional autofocus problem.

1.0 INTRODUCTION

Traditional active radar systems transmit waveforms and deduce information about targets by measuring and analyzing the reflected signals. A radically different approach to radar arises when we consider that modern civilization is already drenched in transmissions such as FM radio, television, and cell phone signals. Passive radar systems that "hitchhike" off of such existing "illuminators of opportunity" remain covert compared to their active brethren. Other covert sensors, like as ESM sensors employing multilateration,[1] are available, but *they rely on the assumption that the objects of interest are broadcasting and don't mind announcing their presence*. PCL sensors require no such assumption. We save on the cost of building a transmitter, since another party has already gone through the trouble. However, communication signals were not designed with radar applications in mind. The cost of the radar system then shifts from traditional radar hardware to the digital signal processing know-how and horsepower required to make sense of the received signals. The price of radar hardware remains relatively fixed, while the cost of computational power continues to plummet.

[1] For example, see http://www.roke.co.uk/download/datasheets/multilateration.pdf.

Paper presented at the RTO SET Symposium on "Target Identification and Recognition Using RF Systems", held in Oslo, Norway, 11-13 October 2004, and published in RTO-MP-SET-080.

Passive radar can thus boast something active radar cannot: its further development is primarily driven by Moore's law. The passive radar approach has often been referred to as PCL (Passive Coherent Location.) To our knowledge, the term PCL was first coined by Dick Lodwig and colleagues at what was then IBM, later Loral, and currently Lockheed Martin. The term PCL is closely tied with Lockheed Martin's Silent Sentry series, of which Silent Sentry 3 is the latest incarnation, although the acronym PCL has evolved to refer to passive radar systems in general. The term PCR (either "Passive Coherent Radar" or "Passive Covert Radar") has also become popular. Interest in PCR has skyrocketed in the past five years. International conferences on PCR were hosted by Roke Manor in the United Kingdom in June 2002, and by the University of Washington in Seattle in the United States in October 2003. At the time of writing, the IEE Proceedings Radar, Sonar, and Navigation is preparing a special issue devoted to PCR guest edited by Paul Howland (NATO C3 Agency) and Paul Gilgallon (U.S. Air Force Research Lab).

A three-year DARPA-sponsored program at the Univ. of Illinois at Urbana-Champaign on the "Design and Optimization of Passive and Active Imaging Radar" began in the Fall of 1998. A prime thrust of this effort was the development of ways to add automatic target recognition (ATR) and radar imaging components to passive radar systems. Follow-up efforts (some in collaboration with colleagues at MIT and Univ. of Michigan Ann Arbor) have continued at Georgia Tech, sponsored by NATO NC3A, AFOSR, startup funds from Georgia Tech's School of Electrical and Computer Engineering, and the Demetrius T. Paris Professorship. This paper briefly reviews some of this work, and points out some avenues for further research.

2.0 AUTOMATIC TARGET RECOGNITION

One approach to target identification compares the collected data to target libraries synthesized using electromagnetic codes. To ensure robust classification in the presence of noise and errors in estimates of position and orientation, it is helpful if the Radar Cross Section (RCS) of the targets vary "slowly" with small changes in these components of the state vector. The variation in RCS, as characterized by the number of nulls encountered as a target's aspect changes, is proportional to the electrical length of the target. At FM-band frequencies (100 MHz), a fighter-sized aircraft is approximately five wavelengths long. In contrast, at the X-band frequencies used by many active radars (10 GHz), the same aircraft would be 500 wavelengths long.

In the late 70's and early 80's, a series of papers [1-3] illustrated that low frequencies are quite natural for target classification. Those papers had active radars in mind, but low-frequency radar did not catch on in the West since most of the desired spectrum has been allocated to communications. PCR systems, on the other hand, which directly exploit existing long wavelength emissions that are convenient for target recognition, circumvent the frequency allocation problem faced by active radars.

2.1 Joint Tracking/Recognition with Particle Filters

Target tracking and target recognition are generally considered to be separate tasks. In particular, target tracking algorithms generally track two-dimensional or three-dimensional target positions in Cartesian coordinates via simple constant velocity or constant acceleration models; target orientation is generally not directly accounted for. The notion that tracking and recognition algorithms could help one another dates back to work by Sworder and colleagues [4-6]; in particular, the authors suggest using imaging information to detect manoeuvre changes. Sensors detailed enough to provide target recognition data generally can also provide orientation; in fact, orientation must often be estimated as a nuisance parameter. The orientation and position of aircraft paths are clearly coupled. Miller, Srivastava, and Grenander [7] suggest fusing the recognition and tracking tasks into a single joint estimation problem.

Picking up this thread, Herman [8-9] followed up on an earlier suggestion [10] to conduct joint recognition and tracking from passive radar data using particle filters. Instead of trying to form two-dimensional Inverse Synthetic Aperture Radar (ISAR) or one-dimensional range profiles to provide the "imaging data," Herman used the raw RCS. This avoided issues relating to calibrating phase information. Since high-frequency codes such as XPATCH are not accurate at the long wavelengths of interest in passive radar, the RCS of different targets was simulated from CAD models using the method-of-moments code FISC (Fast Illinois Solver Code) [11-12].

2.2 ATR with a Coordinated Flight Model

Herman's joint tracking/recognition approach described in the previous section is quite complicated to implement, and computationally intensive because of the particle filter. This prompted the search for a simpler method that could perhaps be implemented in real-time in the immediate future. Drawing from traditional aerodynamics texts, Ehrman created a simple algorithm for finding the likely orientation sequence of an aircraft given a flight path [13], and considered ATR from passive radar RCS data using the orientation sequence estimated by that algorithm [14-16], assuming the track estimated by the tracker to be correct. This is a simpler feed-forward strategy than Herman's approach, in that the results of the RCS data are not fed back into the tracker. Ehrman also considered atmospheric propagation and antenna pattern effects not considered by Herman (although they could easily be adapted and included in Herman's procedure).

Ehrman's initial studies considered vertically polarized data, and gave quite encouraging results on a four-class problem consisting of a Falcon-20, a Falcon-100, a T-38, and a VFY-218.[2] When horizontal polarization was considered [17-18], an interesting phenomenon was observed: for a complex path derived from an instrumented F-15 flight, the Falcon-20 was never correctly identified, even at low noise levels. This pointed out the limitation of the simple coordinated flight model. In essence, the Falcon-20 at the estimated orientation looked more like the Falcon-100 at the correct orientation than the Falcon-20 at the correct orientation! Thus, Ehrman's PhD work is currently moving in the direction of jointly estimating the orientations and target type from the data (although still not as complex as jointly estimating the orientations, target type, and positions from the data as in Herman's approach.) The coordinated flight model can provide a mean, and the algorithm can search in an "error ball" of orientations around that mean.

2.3 Performance Analysis

In some scenarios, we might expect aircraft to be flying around certain common flight paths (for instance, routes between airports). In these situations, it may be reasonable to ask: how long do we need to collect data for a particular aircraft before we can make a decision about its type with a certain degree of accuracy? Ehrman [19] has been considering information-theoretic measures [20], such as relative entropies (i.e. Kullback-Leibler distances [21]) and Chernoff distances, as means of approximating probabilities of error without having to conduct extensive Monte Carlo simulations. As part of her ongoing PhD work, Ehrman has computed approximations for these information-theoretic distances between Rician distributions, which are appropriate for slowly fluctuating targets.

[2] The VFY-218 is not a real aircraft; it is a CAD model commonly used by the computational electromagnetics community.

2.4 The Difficulty of Computing Scattering Databases

The scattering databases needed for ATR consist of complex reflectances sampled over the five-dimensional space of incident azimuth, incident elevation, observed azimuth, observed elevation, and frequency. A full viewing sphere of bistatic angles is needed to accommodate manoeuvring aircraft. To reduce the time complexity of creating such databases, especially using computationally intensive codes such as FISC, it is helpful to sample the space as sparsely as possible while maintaining accuracy. Sampling densely enough to satisfy the Nyquist criteria requires a tremendous amount of computing time.

There is a need for the development of informative scattering models that will permit sampling at a rate below the Nyquist limit. In the high-frequency regime, the electric current induced on a metallic scatter by an incident electromagnetic wave tends to clump at the corners of that object; hence, scattering center models are quite powerful [22-25]. At low frequencies, the current tends to spread out over the aircraft; radar images take on a distributed appearance, instead of the point-like appearance often seen at high frequencies. Thus, to make this approach to ATR practical for a large number of targets, novel techniques and models will need to be developed.

2.5 Helicopter Blade Modulation

For helicopters, the Doppler modulation lines arising from blade motion form a strong target type discriminant. The ability to identify different helicopter types using active low-frequency radar has been demonstrated by Kuschel (see Section 2 of [26]). We do not know of any PCR-specific studies along these lines, although it is clearly a ripe area for exploration.

3.0 IMAGING

In the previous section on ATR, most of the discussion focused on using raw RCS data. One could also conduct ATR using, for instance, ISAR images or range profiles. Considering the difficulty of forming ISAR and related images from passive radar data, we have found it easier to use raw RCS for ATR, since phase errors are not an issue in using RCS. However, radar images may be useful in their own right. There may always be targets present that are not in the ATR system's library, and in such cases it would be useful to have some sort of image to present to a human analyst.

3.1 Nonlinear vs. Linear Imaging Models

The "nonlinear vs. linear" question may have two different meanings in this context. In one meaning, it refers to the *underlying data model*, i.e. whether the quantities of interest map linearly to the data space. In the other meaning, it refers to the *processing of the algorithm*, i.e. whether the algorithm is a linear transformation of the received data.

At the beginning of the DARPA project mentioned in the introduction, much effort was focused on nonlinear data models, including forays into the distorted Born iterative method [27] and the so-called "linear sampling" methods [BLW] (which are not really linear) of Colton, Kirsch, and colleagues. While these efforts are interesting in their own right, they may be overkill for the passive radar problem, and nonlinear imaging models may be a red herring in this context. Indeed, if extensive data are available, simple inversion methods based on linear models produce surprisingly superb images, as discussed in the next section.

Ye, Bresler, and Moulin [29-31] developed several interesting two-dimensional contour estimation techniques, along with associated performance bounds, for both linear and nonlinear data models. To be practical, these should be extended to the three-dimensional case.

3.2 Nonlinear Algorithms for Linear Models

In traditional radar imaging using linear data models, the received complex radar data can be thought of as samples of the Fourier transform of the image of interest. If a sufficient amount of data is available in a sufficiently concentrated region, one can simply zero-pad the parts of Fourier space where data is unavailable and take a two-dimensional inverse Fourier transform. Using this technique on low-frequency data sets derived from FISC yields images that, remarkably, resemble optical images of the aircraft, far more than at microwave frequencies, where the images have a point-like appearance. The trouble is that to form such an image, unrealistically rich data sets are needed. In a realistic collection scenario, the available data is strongly limited by the collection geometry, and straightforward zero-padding usually leads to unrecognizable images [32-33].

The sampling patterns arising in passive radar bear a passing resemblance to those found in radio astronomy; hence, it became natural to try algorithms from radio astronomy such as CLEAN. Unfortunately, the complex-valued and distributed nature of passive radar images lead to disappointing results from CLEAN [34]. CLEAN works best on images that are point-like in nature, such as microwave radar images, whereas low-frequency radar images are more evenly distributed throughout regions. This led to a search for a more sophisticated technique, such as Çetin's [35-36] region-enhanced nonquadratic optimization techniques. In this approach, an objective function is formulated that combines a term indicating fidelity to the data with a term incorporating prior knowledge about likely images. The term chosen encourages smoothness within regions while allowing sharp edges between regions. When applied to the same passive radar examples used in [31], the region-enhanced technique was found to provide remarkable improvements [37]. Along another path, Ye, Bresler, and Moulin [38] developed a level-set based method for reconstruction from sparse Fourier samples, which should be revisited in this context.

Another issue that may arise is the angular dependence of radar reflection. At high frequencies, reasonable cross-range resolution may be obtained using data from a small angular extent. At low frequencies, data may need to be collected over a wide range of angles to obtain good cross-range resolution. Some wide-angle imaging algorithms, based on Wigner-Ville distributions, are proposed in [39].

3.3 The Autofocus Problem

In an ISAR imaging scenario, the distance from the radar platform to an airborne target must be known to demodulate the received radar signal and retrieve the imaging data. When this distance is not known exactly, a phase error term results that corrupts the imaging data. The effect is a phase error function, varying with each received echo, which acts as a blurring filter, defocusing the radar image. All of the studies described in the previous section assumed there was no such phase error. Autofocus algorithms create an estimate of this phase error function to correct the defocused image. Such a capability will be a vital component of any working imaging system.

Existing autofocus algorithms developed for ISAR imaging assume a monostatic scenario. This assumption implies a single transmitter is colocated with a single receiver, and large bandwidth pulses are available to illuminate targets. The sampled Fourier imaging data collected under these conditions form a two dimensional polar ribbon in frequency space. The angular extent of this ribbon corresponds to the received echos, and the

radial extent to the samples from each echo. Here the phase error varies only with echo, or with the angular dimension.

In a passive radar-imaging scenario, multiple transmitters, such as different FM radio and/or television signals operating at different frequencies, are used to illuminate the airborne targets. The advantage of this scheme is stealthiness; targets are unaware that they are being watched. However, several drawbacks make forming images challenging. First, the tracking data produced by a passive system is not as accurate as that of a conventional active system. Secondly, unlike active systems, which employ specially crafted high bandwidth pulses, passive systems must rely upon narrowband FM or TV signals, which are essentially an impulse in the frequency domain when thought of from an imaging standpoint. Consequently, only a thin arc of Fourier data is collected from each station, in contrast to a two dimensional polar ribbon associated with a single active wideband transmitter. In the passive scenario, the range from transmitter to target to receiver must be known to demodulate the received radar signal. Inaccurate target position estimates result in inaccurate calculated two-way ranges, and thus phase errors appear. Because the transmitters are located at different positions, and operate at different frequencies, the phase error function corresponding to each station, or each arc in frequency space, will be different (though related by the geometry). Thus, we cannot think of the autofocus problem as compensating for a phase error function that varies in only one dimension. We effectively have a two-dimensional autofocus problem.

We might conjecture that a passive radar autofocus algorithm should be built around correcting the trajectory of the aircraft itself rather than directly estimating phase errors. Although the phase error functions corrupting multiple arcs of Fourier imaging data are different, they are related by the underlying geometry. We seek the trajectory that most closely resembles the actual trajectory, and consequently results in the best image. The autofocus perspective turns this on its head, and seeks the best image, which consequently may give a better track. A measure of image sharpness may be utilized as a cost function in determining the best trajectory. Several such measures, such as the entropy of the image, are available [40]. Morrison [41-42] has conducted further work in this direction.

4.0 CONCLUSIONS

This paper has reviewed recent efforts to develop ATR and radar imaging technologies appropriate for passive radar systems. Radar imaging is particularly difficult, as problems of sparse Fourier samples, angle-dependant scattering, and phase errors need to be overcome. The first two problems have been considered extensively, but they have been considered *separately*. Bringing solutions to all of these challenges together into a single algorithm will be extremely challenging.

5.0 REFERENCES

[1] A.A. Ksienski, Y.T. Lin, L.J. White, “Low-Frequency Approach to Target Identification,” Proc. of the IEEE, Vol. 63, Dec. 1975, pp. 1651-1660.

[2] Y.T. Lin, A.A. Ksienski, “Identification of Complex Geometrical Shapes by Means of Low-Frequency Radar Returns,” The Radio and Electronic Engineer, Vol. 46, No. 10, Oct. 1976, pp. 472-486.

[3] Y.T. Lin, A.A. Ksienski, “Optimum Frequencies for Aircraft Classification,” IEEE Trans. on Aerospace and Electronic Systems, Vol. 17, No. 5, Sept. 1981, pp. 656-665.

[4] D.D. Sworder, R.G. Hutchins, "Image-Enhanced Tracking," IEEE Trans. on Aerospace and Electronic Systems, Vol. 25, No. 5, Sept. 1989, pp. 701-710.

[5] D.D. Sworder, R.G. Hutchins, "Maneuver Estimation Using Measurements of Orientation," IEEE Trans. on Aerospace and Electronic Systems, Vol. 26, No. 4, July 1990, pp. 625-638

[6] D.D. Sworder, P.F. Singer, D. Doria, "R.G. Hutchens, Image-Enhanced Estimation Methods," Proceedings of the IEEE, Vol. 81, No. 6, June 1993, pp. 797-811.

[7] M.I. Miller, A. Srivastava, U. Grenander, "Conditional-Mean Estimation via Jump-Diffusion Processes in Multiple Target Tracking/Recognition," IEEE Trans. on Signal Processing, Vol. 43, No. 11, Nov. 1995, pp. 2678-2690.

[8] S.M. Herman, P. Moulin "A Particle Filtering Approach to Joint Radar Tracking and Automatic Target Recognition," Proc. IEEE Aerospace Conference, Big Sky, Montana, March 10-15, 2002.

[9] S.M. Herman, "A Particle Filtering Approach to Joint Passive Radar Tracking and Target Classification," Ph.D. Dissertation, Univ. of Illinois at Urbana-Champaign, Department of Electrical and Computer Engineering, 2002.

[10] A.D. Lanterman, "Tracking and Recognition of Airborne Targets via Commercial Television and FM Radio Signals," Acquisition, Tracking, and Pointing XIII, SPIE Proc. 3692, Eds: M.K. Masten and L.A. Stockum, Orlando, FL, April 1999, pp. 189-198.

[11] J.M. Song, W.C. Chew, "The Fast Illinois Solver Code: Requirements and Scaling Properties," IEEE Computational Science and Engineering, Vol. 5, No. 3, July-Sept. 1998, pp. 19-23.

[12] J.M. Song, W.C. Chew, "Fast Illinois Solver Code (FISC)," IEEE Antennas and Propagation Magazine, Vol. 40, No. 3, June 1998, pp. 27-34.

[13] L.M. Ehrman and A.D. Lanterman, Estimation of Aircraft Orientation from Flight Paths Using a Coordinated Flight Model, submitted to IEEE Trans. on Aerospace and Electronic Systems, Nov. 2002; currently undergoing revision.

[14] L.M. Ehrman, A.D. Lanterman, "Automated Target Recognition using Passive Radar and Coordinated Flight Models," Automatic Target Recognition XIII, Proc. SPIE 5094, Ed: F.A. Sadjadi, April 2003.

[15] L.M. Ehrman, A.D. Lanterman, "Target Identification Using Precomputed Radar Cross Sections and a Coordinated Flight Model," Third Multinational Conference on Passive and Covert Radar, Ed: P. Kurzenhauser, B. Spickler, Univ. of Washington Applied Physics Laboratory, Oct. 21-23, 2003.

[16] L.M. Ehrman, A.D. Lanterman, "A Robust Algorithm for Automatic Target Recognition using Passive Radar," 36th IEEE Southeastern Symposium on System Theory, Atlanta, GA, March 14-16, 2004.

[17] L.M. Ehrman, A.D. Lanterman, "Automatic Target Recognition via Passive Radar, Using Precomputed Radar Cross Sections and a Coordinated Flight Model," submitted to IEEE Trans. on Aerospace and Electronic Systems, Nov. 2003.

[18] L.M. Ehrman, Automatic Target Recognition Using Passive Radar Data and a Coordinated Flight Model, M.S. Thesis, Georgia Institute of Technology, Fall 2003.

[19] L.M. Ehrman, A.D. Lanterman, "Robust Algorithm for Automated Target Recognition using Precomputed Radar Cross Sections," Automatic Target Recognition XIV, Proc. SPIE 5426, Ed: F.A. Sadjadi, April 12-16, 2004.

[20] T. Cover, J. Thomas, "Elements of Information Theory," John Wiley and Sons, 1991.

[21] A.D. Lanterman, J.A. O'Sullivan, M.I. Miller, "Kullback-Leibler Distances for Quantifying Clutter and Models," Optical Engineering, Vol. 38, No. 2, Dec. 1999, pp. 2134-2146.

[22] R. Bhalla, H. Ling, "Three-dimensional scattering center extraction using the shooting and bouncing ray technique," IEEE Trans. on Antennas and Propagation, Vol. 44, No. 11, Nov. 1996, pp. 1445-1453.

[23] L.C. Trintinalia, R. Bhalla, H. Ling, "Scattering Center Parameterization of Wide-Angle Backscattered Data Using Adaptive Gaussian Representation," IEEE Trans. on Antennas and Propagation, Vol. 45, No. 11, Nov. 1997, pp. 1664-1668.

[24] R. Bhalla, J. Moore, H. Ling, "A Global Scattering Center Representation of Complex Targets Using the Shooting and Bouncing Ray Technique," IEEE Trans. on Antennas and Propagation, Vol. 45, No. 12, Dec. 1997, pp. 1850-1856.

[25] B. Bhalla, H. Ling, S.W. Lee, J. Hughes, "Bistatic Scattering Center Extraction Using the Shooting and Bouncing Ray Technique," Algorithms for Synthetic Aperture Radar Imagery, SPIE Proc. 3721, Ed: E.G. Zelnio, Orlando, FL, April 1999, pp. 612-619.

[26] H. Kuschel, "VHF Radar Part 2: Operational Aspects and Applications," Electronics and Communications Engineering Journal, Vol. 14, No. 3, June 2002, pp. 101-1111.

[27] M. Brandfass, W.C. Chew, "A Multilevel Fast Multipole Based Approach for Efficient Reconstruction of Perfectly Conducting Scatterers," Journal of Electromagnetic Waves and Applications, Vol. 55, No. 1, Jan. 2001, pp. 81-106.

[28] M. Brandfass, A.D. Lanterman, K.F. Warnick, "A Comparison of the Colton-Kirsch Inverse Scattering Methods with Linearized Tomographic Inverse Scattering," Inverse Problems, Vol. 17, No. 6, Dec. 2001, pp. 1797-1816.

[29] J.C. Ye, Y. Bresler, P. Moulin, "Asymptotic Global Confidence Regions in Parametric Shape Estimation Problems," IEEE Trans. on Information Theory, Vol. 46, No. 5, August 2000, pp 1881-1895.

[30] J.C. Ye, Y. Bresler, and P. Moulin, "Cramér-Rao Bounds for Estimation of Target Boundaries in Nonlinear Inverse Scattering Problems," IEEE Trans. on Image Antennas and Propagation., Vol. 49, No. 5, May 2001, pp. 771-783.

[31] J.C. Ye, Y. Bresler, and P. Moulin, "Cramér-Rao Bounds for Parametric Shape Estimation in Inverse Problems," IEEE Trans. on Image Processing, Vol. 12, No. 1, Jan. 2003, pp. 71-84.

[32] Y. Wu, D.C. Munson, Jr., "Multistatic Synthetic Aperture Imaging of Aircraft using Reflected Television Signals," Algorithms for Synthetic Aperture Radar Imagery VIII, Proc. SPIE 4382, Ed: E.G. Zelnio, Orlando, FL, April 2001.

[33] Y. Wu, D.C. Munson, Jr., "Multistatic Passive Radar Imaging Using the Smoothed Pseudo Wigner-Ville Distribution," Proc. of the IEEE International Conf. on Image Proc., Thesaloniki, Greece, Oct. 2001.

[34] A.D. Lanterman, D.C. Munson, Jr., "Deconvolution Techniques for Passive Radar Imaging," Algorithms for Synthetic Aperture Radar Imagery IX, Proc. SPIE 4727, Ed: E.G. Zelnio, Orlando, FL, April 2002.

[35] M. Çetin, W.C. Karl, "Feature-Enhanced Synthetic Aperture Radar Image Formation Based on Nonquadratic Regularization," IEEE Trans. on Image Processing, Vol. 10, No. 4 , April 2001, pp. 623-631.

[36] M. Çetin, W.C. Karl, D.A. Castanon, "Feature Enhancement and ATR Performance Using Nonquadratic Optimization-Based SAR Imaging," IEEE Trans. on Aerospace and Electronic Systems, Vol. 39, No. 4, Oct. 2003, pp. 1375 - 1395.

[37] M. Çetin, A.D. Lanterman, "Region-Enhanced Imaging for Sparse-Aperture Passive Radar," Algorithms for Synthetic Aperture Radar Imagery XI, SPIE Proc. 5427, Ed: E.G. Zelnio and F.D. Garber, Orlando, FL, April 2004.

[38] J.C. Ye, Y. Bresler, P. Moulin, "A Self-Referencing Level-Set Method for Image Reconstruction from Sparse Fourier Samples," International Journal of Computer Vision, Vol. 50, No. 3, Dec. 2002.

[39] A.D. Lanterman, D.C. Munson, Jr., and Y. Wu, "Wide-Angle Radar Imaging Using Time-Frequency Distributions," IEE Proc. Radar, Sonar, and Navigation, Vol. 150, No. 4, Aug. 2003, pp. 203-211.

[40] L. Xi, "Autofocusing of ISAR Images Based on Entropy Minimization," IEEE Trans. on Aerospace and Electronic Systems, Vol. 35, No. 4, Oct. 1999, pp. 1240-1252.

[41] R.L. Morrison, Jr., "Entropy-Based Autofocus for Synthetic Aperture Radar," M.S. Thesis, Univ. of Illinois at Urbana-Champaign, 2002.

[42] R.L. Morrison, Jr., D.C. Munson, Jr., "An Experimental Study of a New Entropy-Based SAR Autofocus Technique," Proc. of the IEEE International Conf. on Image Processing, Rochester, NY, Sept. 22-25, 2002.

Target Classification, Recognition and Identification with HF Radar

Stuart J. Anderson
Intelligence, Surveillance and Reconnaissance Division
Defence Science and Technology Organisation
PO Box 1500 Edinburgh SA 5111
AUSTRALIA

stuart.anderson@dsto.defence.gov.au

SUMMARY

Radars operating in the HF band achieve extremely long range detection by exploiting propagation modes which preclude many of the standard target classification techniques, at least in their conventional form. Yet, in order to take full advantage of an over-the-horizon detection capability, reliable target classification, recognition and identification is essential. This paper explores the options for target classification at HF, reviews some of the results which have been achieved, mainly but not exclusively with reference to skywave radars, and assesses the prospects for operational target classification, recognition and identification.

1.0 INTRODUCTION

Radars operating in the HF band are well known for their 'over-the-horizon' detection capabilities, whether via skywave propagation as with Jindalee [1] and ROTHR [2], for instance, or via surface wave propagation, as with SECAR [3], SWR503 [4], the AMS HFSWR [5] and others. These radars achieve extremely long range detection by exploiting propagation modes which preclude many of the established target classification techniques, at least in their conventional form. Indeed, given the vicissitudes of the ionosphere and the losses encountered with any form of over-the-horizon propagation, it is remarkable that even the detection mission can be achieved with adequate reliability. When one also takes into account the dramatic constraints on spatial resolution imposed by aperture and bandwidth limitations, and the fact that the radar wavelength is of the same order as the target dimensions, the prospect of determining target class, type, or possibly even identity, would appear remote.

From the operational perspective, this prognosis has long been a major concern. In order to take full advantage of an over-the-horizon detection capability, reliable target classification, recognition and identification is regarded as essential. This applies not only to the need to satisfy rules of engagement in the event of hostilities but, more routinely, to situational awareness, to the assignment of other assets on the basis of HF radar cueing, and to potential intelligence collection and analysis. Indeed, from the operational perspective, the value of virtually all wide area surveillance products generated by HF radar is substantially reduced in the absence of a moderately capable target classification functionality.

In spite of this motivation, with few exceptions the technical challenges posed by target classification at HF have not succumbed to the efforts of the radar researchers. Nevertheless, considerable progress has been made in a number of areas. On the basis of many experiments, much of the relevant physics is now understood, a variety of approaches to differentiating between targets of interest have been conceived and explored by experiment or modelling, concepts for integrating these schemes within the radar tasking and control architecture have been proposed, and many mathematical and computational tools have been devised to model and interpret radar observations. Moreover, the realisation that the ability to classify targets depends on the degree of control over radar resources, and radar design, is now taken into consideration when proposing enhancements to existing radar systems.

Paper presented at the RTO SET Symposium on "Target Identification and Recognition Using RF Systems", held in Oslo, Norway, 11-13 October 2004, and published in RTO-MP-SET-080.

Techniques which have been explored in the quest for an NCTR capability in existing HF radar systems include :

(i) statistics of target echo magnitude
   a. shape of the distribution
   b. absolute RCS via calibration using co-located scatterers
   c. ratios of RCS for different targets
(ii) multi-frequency interrogation
   a. discrete spanning set
   b. target-matched illumination
   c. wide sweep waveforms
(iii) bistatic and multi-static scattering geometries (all of the above)
(iv) modulation signatures
(v) micro-Doppler information
(vi) distributed scattering signature analysis
(vii) nonlinear scattering
(viii) accurate determination of target kinematics

This paper explores the options for target classification at HF, reviews some of the results which have been achieved, mainly but not exclusively with reference to skywave radars, and assesses the prospects for operational target classification, recognition and identification.

2.0 THE SEMANTICS OF CLASSIFICATION, RECOGNITION AND IDENTIFICATION

At the outset, it is essential to clarify the terminology used to describe the various levels of specificity with which a sensor might distinguish between different targets. According to NATO definitions (Source: AAP-6 NATO Glossary of Terms and Definitions) :

IDENTIFICATION *is the indication by any act or means of one's own friendly character or individuality. The determination by any act or means of the friendly or hostile nature of a detected person, object or phenomenon.*

RECOGNITION *is the determination of the nature of a detected person, object or phenomenon, and possibly its class or type. This may include the determination of an individual within a particular class or type. There are consequently various degrees of recognition :*

- ***General recognition****: recognise an object by class e.g. recognise a vehicle as tank, infantry fighting vehicle, or truck, or recognise an aircraft as either a bomber or a fighter. A lower level of general recognition might be to recognise a vehicle as tracked or wheeled, or recognise an aircraft as swept winged or straight winged*
- ***Detailed recognition****: recognise an object by type e.g. recognise a vehicle as either a T-80 tank or an M-1 Abrams tank, or recognise an aircraft as an Su-27 or a Tornado. It may entail the recognition of an individual person or object e.g. "finger printing."*

These definitions were no doubt adopted to serve important operational purposes, but they are not entirely consistent with their etymology, nor do they span the range of possible scenarios. In particular, the use of *identification* as the signifier of *intent* is unfortunate. One might suggest, only half in jest, a new term – ***intentification*** – to fill this need. Accordingly, the following alternatives and additions, based on usage in the domain of statistical pattern recognition, are adopted in this paper. For clarity they are formulated as *verbs* rather than as *nouns*.

Proceeding from the most general level,

Classify *– associate with, or assign to, one of a number of sets (classes) which are distinguished by one or more criteria, irrespective of whether there is any prior knowledge of the class membership or class boundaries.*

Recognise *- establish membership of one of a number of disjoint* ***known*** *sets (classes)*

Identify *– establish the absolute sameness with one of a number of possible individual members of a class of known elements*

For example, suppose we were to take a number of aircraft and, for each, measure (i) its weight, and (ii) its median RCS (over some range of parameter values). If we were then to plot the results as points on the plane, we might find that they tend to cluster in two groups, with larger weights generally associated with larger RCS values. Without even labelling the axes, or knowing anything about what the points represent, a given point could be associated with one cluster or the other by means of purely statistical measures. To ***classify*** objects in the most general sense is to perform this kind of assignment. Now if we are told that there are only two types of aircraft involved – fighters and bombers – we might label the two classes appropriately, even if we don't have confirmation that any particular point is in the correct class. If some points are labelled – the case of ***supervised training*** – we can use these points first to design our classifier, allowing for subsequent *unsupervised training* if desired. Then, confident in our labelling of the classes, we have the possibility of ***recognition***, that is, assignment to a *known* class. Finally, if that class is feature-rich, and there is adequate prior information, the prospect of ***identifying*** the individual members of the class can be entertained.
With this hierarchy, a typical sensor mission has the structure shown in Figure 1, where the additional term *discrimination* is used to denote the acceptance of some input patterns and the rejection of others, as with situations where strong clutter is present. This, of course, is equivalent to increasing the number of pattern classes.

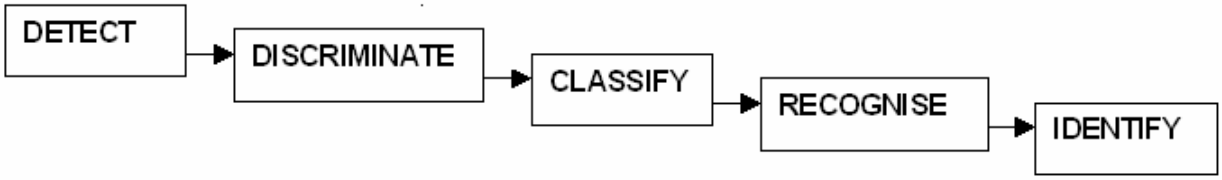

Figure 1: The sequence of progressively more intimate assignment as implemented in many sensor systems

2.0 HF RADAR SYSTEMS

Radars operating in the HF band can be classified according to the propagation mechanisms they exploit, noting that the mode of propagation from transmitter to target may differ from that occurring between target and receiver. A taxonomy based on this classification is presented in Figure 2. The key to understanding this diagram is to note the use of the columns to refer to transmitter-to-target aspects and rows for the receiver-to-target aspects. Common sense suggests that it would be unreasonable to expect any single classification technique to be effective for such a diverse group of radar configurations, and this turns out to be indeed the case. Further, quite striking differences exist between alternative implementations of radars from each of the principal categories shown in Figure 2, so that what may be possible with the Australian Jindalee radar, for example, may not possible with the US Navy's ROTHR,

or vice versa., though both these radars are bistatic land-based skywave-out, skywave-back radars. For this reason, the discussion which follows will attempt to avoid system-specific judgments. Further, the emphasis will be placed on skywave radars, with surface wave radars treated in lesser detail, noting that though there are numerous commonalities.

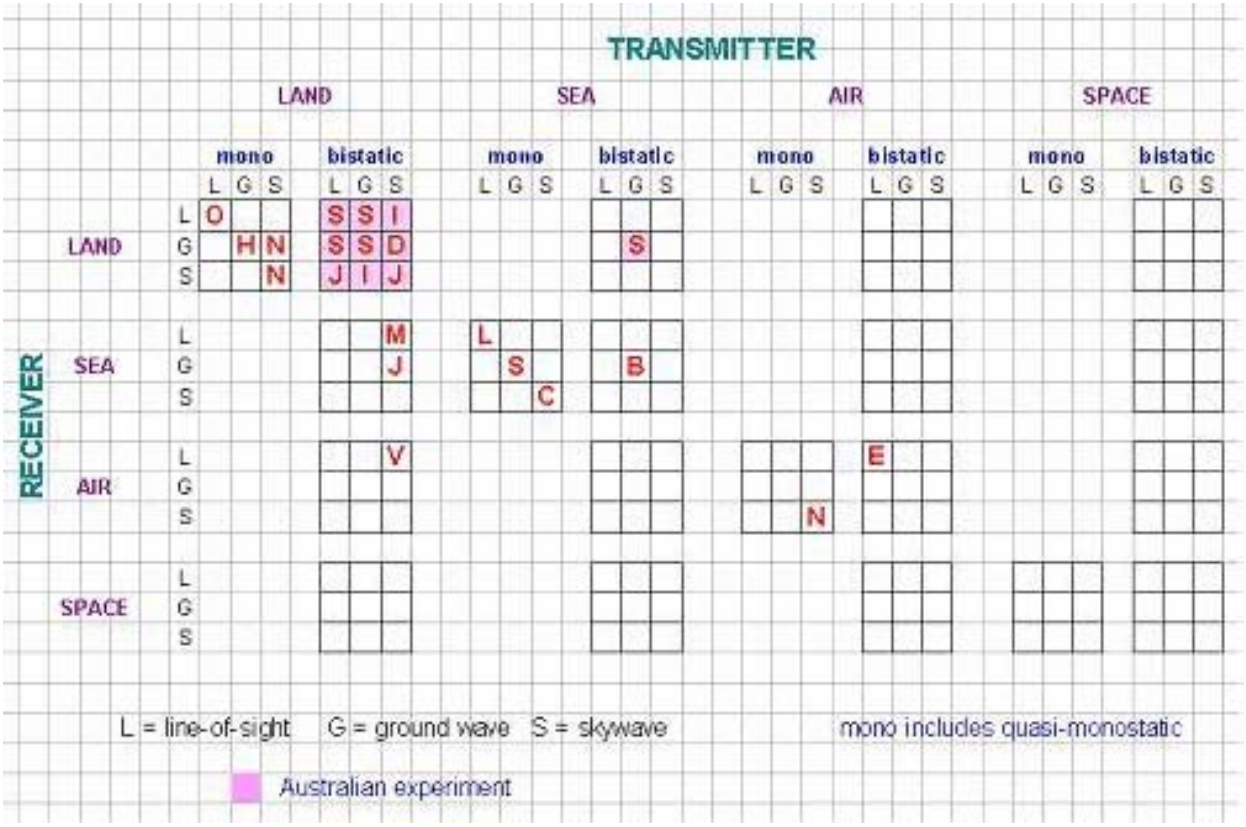

Figure 2: Taxonomy of HF radar configurations, with selected radars indicated

2.1 Radar Process Models

The starting point for an analysis of target classification at HF is a model of the radar process, that is, a formal representation of the relationship between the *measurements* and *the system being measured*. Such a model has been developed and used extensively for HF skywave radar applications [6-8]. Following [7], the radar process model allowing for multihop propagation can be written

$$s = \widetilde{P} \sum_{n_B=1}^{N} \widetilde{R} \left[\prod_{j=1}^{n_B} \widetilde{M}_{S(j)}^{S(j+1)} \widetilde{S}(j) \right] \widetilde{M}_{T}^{S(1)} \widetilde{T} w$$

$$+ \widetilde{P} \sum_{l=1}^{N_J} \sum_{m_B=1}^{M} \widetilde{R} \left[\prod_{k=1}^{m_B} \widetilde{M}_{S(k)}^{S(k+1)} \widetilde{S}(k) \right] \widetilde{M}_{N}^{S(1)} n_l + m$$

where

w represents the selected waveform

$\widetilde{T}$ represents the transmitting complex, including transmitters and antennas

$\widetilde{M}_T^{S(1)}$ represents propagation from transmitter to the first ground scattering region

$\widetilde{S}$ represents all scattering processes in the current region

$\widetilde{M}_{S(j)}^{S(j+1)}$ represents propagation from j-th scattering region to the (j+1)-th region

$S(n_B)$ and $S(m_B)$ represent the receiver location

n_l represent external noise sources, interferers or jammers

$\widetilde{M}_N^{S(1)}$ represents propagation from a noise source to its first ground scattering region

m represents internal noise

$\widetilde{R}$ represents the receiving complex, including antennas and receivers

P represents the signal processing

s represents the signal decomposition after processing

When appropriate substitutions are made, and the squared modulus of this 'voltage' formulation taken, equation (1) reduces to the familiar scalar radar equation,

$$\sigma = \frac{(4\pi)^3 R^4 kTB.SNR}{P_T G_T G_R \lambda^2}$$

This conventional form is of little use for HF radar applications, even when various system and propagation losses are incorporated in the form of multiplicative loss factors With HF skywave radar, the range dependence of signal intensity is governed by the electron density profile of the ionosphere and the modal structure of the earth-ionosphere waveguide, not by a simple power law. For HF surface wave radar, the range dependence of signal intensity is dominated by diffraction processes, modified by the prevailing surface roughness.

2.2 Observables, signatures and the classification domain

The raw materials on which the target classification process operates are the sensor responses to the universe around it – the ***observables***. In the main, these are related to the intrinsic physical attributes of the target which govern its interaction with the electromagnetic field of the radar signal, but the electromagnetic field in the vicinity of the target is not *observed* by the radar, nor even is the field arriving at the receiving antenna. In most cases, though, the observables can be represented mathematically by an integral operator which maps the set of target 'states' into the space of radar output signal parameters. One other category of observable needs to be mentioned – perturbations to the target's environment which might be independently observable, such as ship wakes. Of course, the interaction with the environment also reacts on the target's intrinsic observables, such as the airframe oscillations causing micro-Doppler modulation.

Clearly, the first issue to be decided in any target classification task is to establish which observables will be available for consideration. The second step is to explore their information content, as embodied in their statistical properties, so that the classification scheme can make most effective use of the 'evidence'. Subsequent development deals with the design of the classifier and the prediction of its performance; these later stages will not be addressed in this paper.

Target classification may thus be viewed as a statistical decision theoretic problem based on observations of the radar output *s,* subject to specified constraints on the degrees of freedom of the radar measurements. For example, the observations may take the form of :

- a single look, by which is meant (for HF radar) almost invariably the spectral decomposition of time series corresponding to a single coherent integration period, from a number of simultaneous spatial cells
- a sequence of looks, with the advantage of multiple sampling of any stochastic behaviour, as well as the prospect of establishing a track on each target
- a sequence of measurements carried out with different radar parameters (eg carrier frequency, scattering geometry), possibly as an adaptive decision-making process

The process of classifying (recognising, identifying) a target echo may exploit any information thus obtained, and make use of any ancillary information, such as anticipated target behaviour, in conjunction with the direct information which has been imprinted on the received radar signal by the physics of scattering from the target and retrieved by the radar reception and signal processing.

#	ACCESSIBLE FUNCTIONALITY	OBSERVATION METHODOLOGY	CLASSIFICATION DOMAIN
5	network control	stereoscopic operation multistatic operation cooperative waveforms	multi-aspect RCS bistatic RCS nonlinear scattering
4	individual radar control	multi-frequency operation spatial mapping optimised clutter calibration spatio-polarisation agility	multi-frequency RCS ratios distributed echo analysis absolute RCS polarisation scattering matrix
3	signal processing (beyond basic range-azimuth-Doppler decomposition)	high-resolution Doppler time-frequency analysis higher-order spectrum analysis harmonic extraction	micro-Doppler time-varying parameters nonlinear scattering periodic internal motions
2	processed data - multiple dwells	target dynamics statistical echo analysis targets in company multimode analysis track history inter-track correlation track future	performance data monostatic RCS RCS ratios differential RCS point-of-origin mission analysis response to stimuli
1	processed data - single dwell	peak amplitude peak coordinates peak phase modulation	monostatic RCS performance data environmental coupling

Table 1: Levels of system control and corresponding domains for target classification

This latter quantity – the information imprinted on the radar signal by the target – is usually termed the target's ***radar signature***. Unfortunately such a definition is lacking in two respects. First, it appears to confine attention to the electromagnetic phenomena occurring at the target, and fails to mention the role of the observing radar – 'the paper on which the signature is written and the pen which writes it'. Second, it ignores certain target-related perturbations to the received signal, such as shadow effects and some multiple scattering processes. While this is true for all radars, it acquires special significance in the case of HF radars, where propagation is often hard to separate from scattering. For this reason there is merit in adopting a more pragmatic definition.
Following [9], the ***generalised radar signature (GRS)*** of an object ***x*** is defined as :

GRS (x) = response of radar when x is present - response of radar when x is absent

This immediately raises the question as to how radar resources should be allocated and scheduled in order to provide the best outcome because the radar timeline is generally heavily committed, so opening up possibilities for extracting more detailed information is generally possible only at the expense of coverage or revisit rate. The situation is complicated by the variability of the HF propagation environment, which impacts on tasking through the need to balance mission priority against the ability of the prevailing conditions to support that mission. Thus it is highly probable that a radar attempting to classify targets will be obliged to operate in modes which are sub-optimum insofar as they do not allocate the maximum of potentially useful resources to this task. Table 1 presents a plausible hierarchy of accessible functionality, together with the corresponding options for radar signature measurements relevant to target classification.

2.3 Complications arising with HF systems, propagation and scattering

With most conventional radars, operating at microwave frequencies, the various terms in the radar equation can be assumed known or calculable to reasonable precision. Propagation losses are dominated by the inverse square law dependence, noise by internal thermal noise, antenna gains are accurately known, the transmitted polarisation is the same as the polarisation incident on the target, range resolution cell size can be orders of magnitude smaller than overall target dimensions, and so on. Correction terms for additional losses due to polarisation mismatch, antenna insertion loss, etc, are often introduced, but these effects are relatively modest and, in any event, generally known with considerable accuracy. Thus, it is normally possible to interpret the received echo power directly in terms of the effective RCS of the scattering object. Under these circumstances, target classification has a very favourable prognosis.
In the case of HF radars, virtually all these convenient idealisations must be discarded, as departures from the idealised models mentioned above are typically measured in tens of dB. The reasons for this are evident from a consideration of the properties of the individual operators in the radar process model and the environmental phenomena which impact on them; some of these are summarised in Table 2.

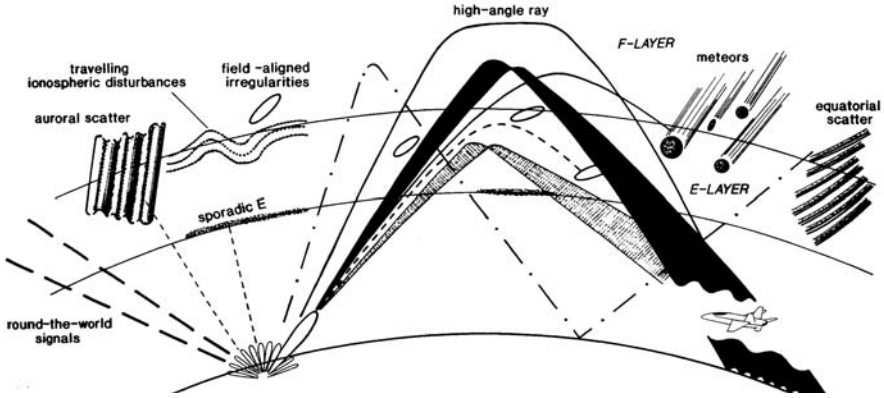

Figure 3: Some features of ionospheric radiowave propagation

OPERATOR	ATTRIBUTE or ENVIRONMENTAL PHENOMENON
T	- limited to fixed linear (V or H) polarisation - antenna array gain is imprecisely known
M_{SKY}	- path losses are frequency dependent, with deviative and non-deviative absorption - wave-like disturbances in the ionosphere tilt, focus and defocus the radiowaves - various large-scale processes in the ionosphere modulate the phase of traversing radiowaves, causing Doppler shifts and Doppler broadening - generalised Faraday rotation causes unknown random, time-varying, frequency-dependent transformation of the polarisation state of the radiowave on each transit - only a limited band of frequencies will propagate to a given region at one time - the available frequency band can change on time-scales of 10 minutes - phase and group paths are strongly frequency-dependent, limiting signal bandwidth and hence range resolution - wavefronts after ionospheric reflection are no longer planar/cylindrical but corrugated, so scattering geometry is not strictly determinstic - the ionospheric plasma supports nonlinear coupling mechanisms by which different transitting signals can cross-modulate
$M_{SURFACE}$	- multiple scattering of surface waves modulates them in phase/Doppler, direction of travel, time delay, and azimuthal angle of arrival
S	- the radar wavelength is comparable with target size, denying access to target detail - ship targets are immersed in a field of scattering water waves with comparable speeds and RCS, with no prospect of spatial domain separation - uncertainty in the propagation path means that the scattering geometry is not accurately known, especially in elevation
R	- only a single polarisation component of the received field is measured (V or H) - array calibration is difficult and may depend on direction of arrival, etc - imperfections in receivers cause severe significant distortion
n	- under almost all conditions, HF radars are externally noise-limited - the external noise is strongly non-Gaussian

Table 2 : Phenomena impacting on the process model operators at HF

3.0 MODELLING AND MEASUREMENT OF TARGET SIGNATURES

As mentioned in Section 2.2, the first stage in NCTR development is to identify the observables which will be used for the analysis. A list of possible candidates is provided in the Introduction and, in a slightly different form, in column 3 of Figure 1. The stochastic nature of almost signature component measurements means that classifier design and the achievable performance will be governed by the underlying probability distributions of these observables. These distributions are not always accessible to direct measurement, but a deep understanding of the physical origins of stochastic behaviour can be used instead to infer statistical behaviour, construct models, and generally facilitate a Bayesian estimation approach. In this section, some of the more obvious observables used for target classification, recognition and identification are considered and illustrated with data from various Australian HF radar programs.

3.1 Classification based on target RCS estimates

The scattering of radar signals from a deterministic target is usually described by the target polarisation scattering matrix which relates the scattered field to the incident field,

$$\vec{E}_{scat} = \tilde{S}\,\vec{E}_{inc}$$

from which the conventional RCS for the scattering process where the incident field is α-polarised and the scattered field β-polarised is defined by

$$\sigma_{\beta\alpha} = S_{\beta\alpha}^{*}.\, S_{\beta\alpha}$$

At HF the linear V-H polarisation basis is normally appropriate because of antenna designs. This representation applies for bistatic and monostatic scattering. A key advantage of the scattering matrix formulation at HF is that the most important subspaces – those spanning the azimuthal bistatic geometry combinations – are conveniently represented graphically, as illustrated in Figure 4. In almost all practical situations, the variations with elevation are less sensitive and occur operationally on much slower timescales. Classification based on RCS attempts to establish a mapping between scalar RCS estimates and the set of candidate targets. Unfortunately, as discussed in Section 2.3, ionospheric polarisation transformations and propagation losses intervene to complicate this process, forcing a statistical treatment.

3.1.1 RCS Modelling

In order to develop a target recognition capability, some library of signature data must be accumulated. Opportunities to collect real-world measurements are obviously limited, and scale model measurements are expensive and time-consuming, so the training sets for RCS-based classification are most conveniently derived by numerical modelling.

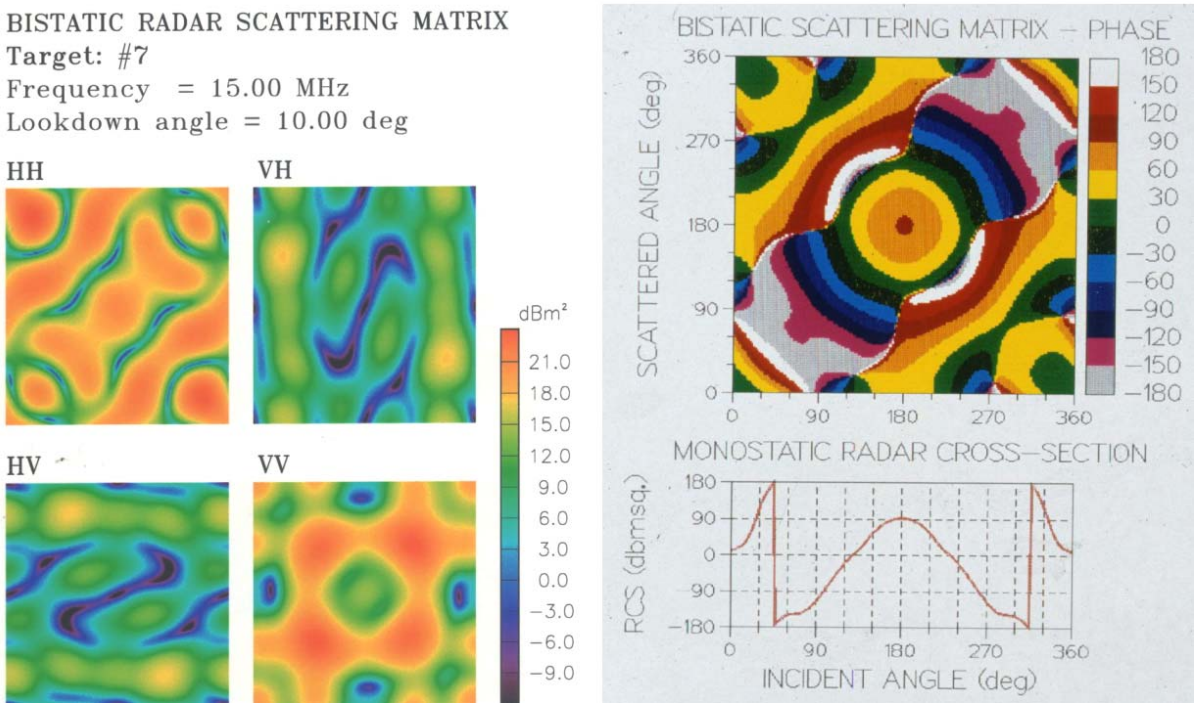

Figure 4: (a) Magnitudes of the elements of the bistatic polarisation scattering matrix of an aircraft, and (b) phase plot of the HH component

Figure 4 shows typical outputs of the Jindalee radar signature modelling facility. In these examples, the magnitude of the elements of the polarisation scattering matrix are plotted for all bistatic Tx – Rx azimuth combinations, at a common fixed elevation angle (left picture). In each coloured square, the abscissa corresponds to incident azimuth, ranging from 0° to 360°, with the ordinate representing scattered azimuth from 0° to 360°. The trailing diagonal is the monostatic solution. On the right, in this example, the phase of the HH element of the polarisation scattering matrix is plotted against the same coordinates.

3.1.2 Model validation

Experimental validation of computer model predictions can be performed in two ways – by scale model measurements in an anechoic chamber, and in field trials with real targets collocated with suitable reference scatterers to provide absolute RCS calibration. Figure 5 shows examples of each of these

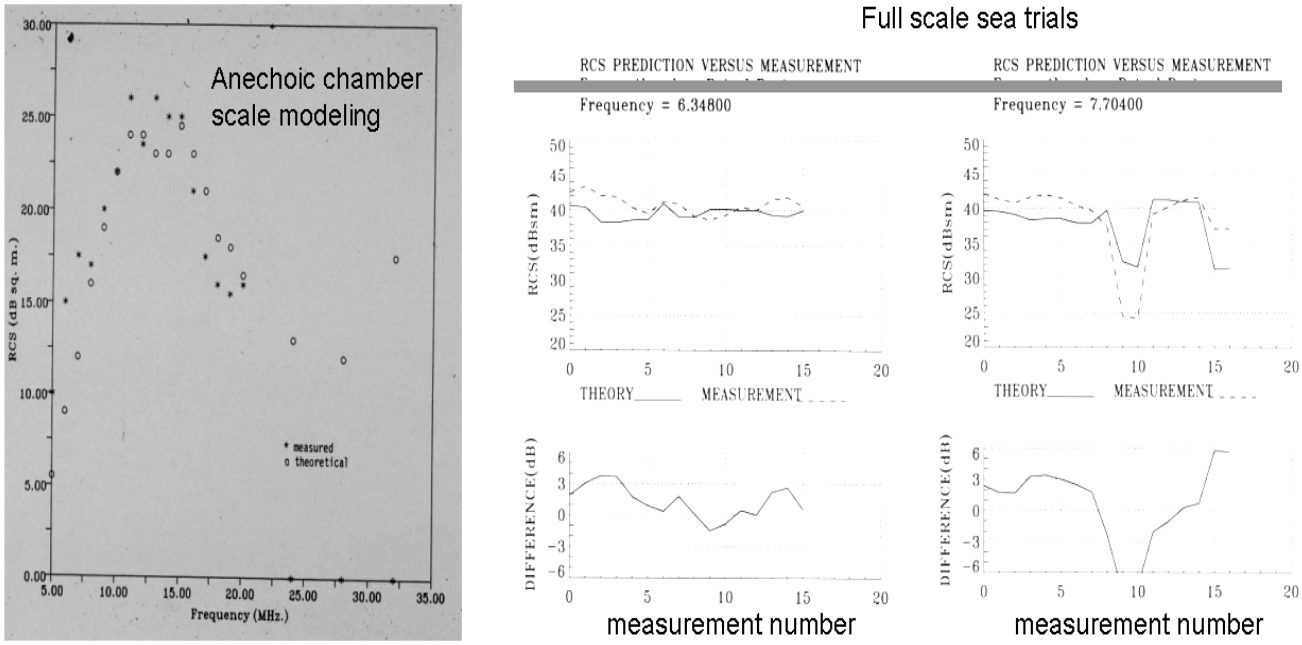

Figure 5: (a) Comparison of theoretical predictions with scale model measurements of the H-H RCS of an aircraft, carried out in the DSTO anechoic chamber, and (b) comparison of theoretical predictions with calibrated at-sea measurements of a ship (V-V component).

approaches. In Figure 5(a), anechoic measurements of a 1:144 scale model aircraft are compared with the predictions of NEC2 – the well-known numerical code based on the method of moments technique. In this example, there is agreement to within 2 – 3 dB over most of the (scaled) frequency range 8 – 20 MHz, degrading at lower frequencies. More significantly, a consistent trend is apparent, with the model under-estimating at low frequencies and over-estimating at high frequencies. This is a consequence of the inadequate fidelity of the numerical grid model used for the calculations which was matched to 10 MHz. Adapting the model as a function of frequency yields results to better than 2 dB across the band. Figure 5(b) shows the results of field trials with an HF surface wave radar and a cooperating vessel, which carried out manoeuvres around a calibration buoy at a range of about 50 km from the radar. Despite the complexity of the target and the complications introduced by the rough sea in the vicinity of the target, the discrepancy between theory and measurement (lower panel) is within 3 dB, generally 1 – 2 dB, except near the null which occurred at one aspect. The conclusion to be drawn from these examples is that modelling to within 2 – 3 dB is achievable, even for reasonably complex targets.

3.1.3 Precision requirements

In many practical situations the inter-class distances are small, imposing stringent requirements on modelling fidelity. This is illustrated in Figure 6 which shows the close similarity of the bistatic RCS of two aircraft of similar overall dimensions as a function of bistatic angle for illumination at an incidence angle of 30°. The aircraft concerned have very similar dimensions, as shown in Table 3 (this example is taken from a study undertaken in 1986). This type of study establishes minimum requirements for model precision.

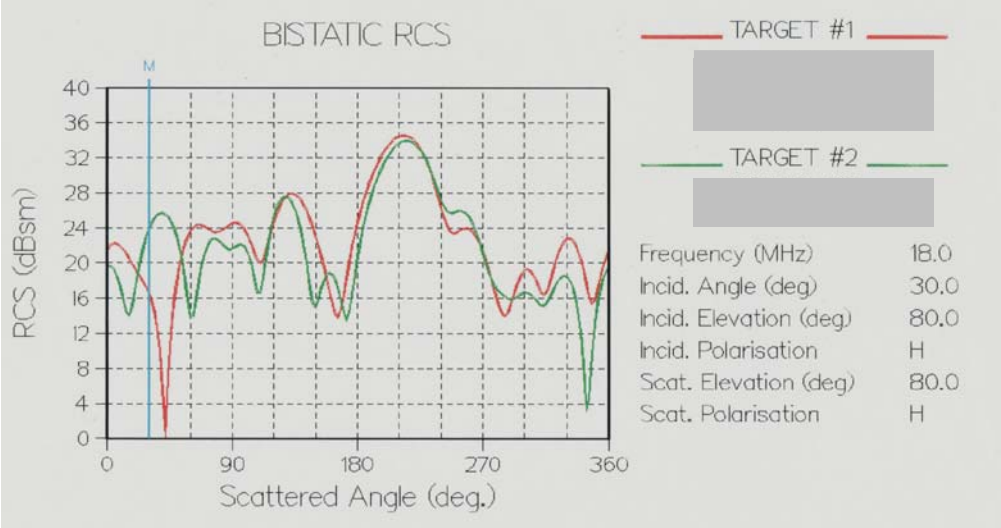

Figure 6: Bistatic RCS comparison for one illumination geometry

AIRCRAFT	LENGTH (m)	WINGSPAN (m)	HEIGHT (m)	CRUISING SPEED (km/hr)
Aircraft #1	42.4	34.3	10.8	900
Aircraft #2	40.6	32.9	10.4	917

Table 3: Major dimensions of Tu-22M-3 and Boeing 727-100

3.1.4 RCS calibration using sea clutter

Sea clutter at HF has a characteristic Doppler spectrum which embodies detailed information about the distribution of waves on the sea surface, that is to say, the directional wave spectrum. Knowledge of this spectrum at one radar frequency suffices to calculate the absolute RCS per unit area of the sea (scattering coefficient) at ***any*** HF frequency. Combined with the resolution cell area, this immediately yields a reference RCS enabling absolute calibration. Techniques for estimating the ocean directional wave spectrum from the radar Doppler spectrum, have been developed by several researchers (eg.[10-12]); an example of this process is shown in Figure 7. On the left is a measured Doppler spectrum, superimposed on which is the 'best fit' Doppler spectrum obtained by optimising a 7-parameter model of the directional wave spectrum. On the right is an example of a measured Doppler spectrum together with the discretised directional wave spectrum computed by an iterative non-parametric technique ([13]).

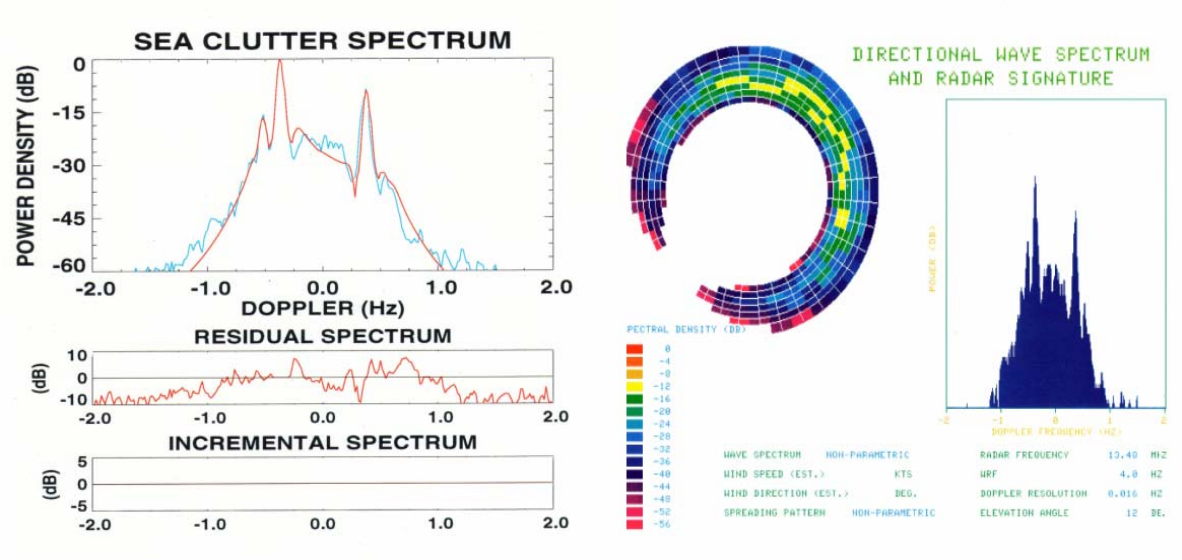

Figure 7: (a) Best-fit 7-parameter sea clutter Doppler spectrum model matched to measured data (b) measured Doppler spectrum (right) with the inferred directional wave spectrum (centre).

3.1.5 Bistatic RCS and stereoscopic observations

Inspection of figures 4 and 8 confirms that target classification information is distributed across the full bistatic domain [14]. The opportunity to collect bistatic RCS only arises when spatially-separated transmit and receive facilities view the same region, which might seem to be a rare (and extravagant) arrangement. One consideration which makes it worthy of serious study is the prospect of exploiting transmitters of opportunity to collect data which supplements that provided by dedicated radar facilities [15].

3.2 Classification based on target RCS ratios

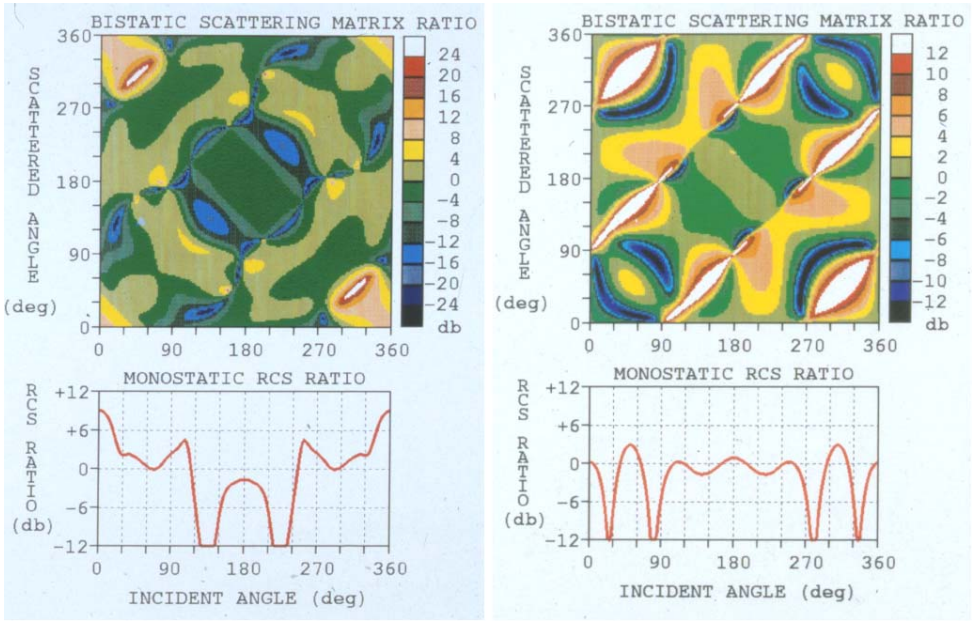

Figure 8: (a) Magnitude of the ratio of the HH bistatic RCS of fighter aircraft #1 at two frequencies, and (b) for fighter aircraft #2 at the same two frequencies.

Given the difficulty and often impossibility of calibrating the target echo by means of sea clutter or other reference scatters in the vicinity of the target, classification based on absolute RCS must often be abandoned in favour of techniques based on target RCS ratios. Figure 8 shows how the ratios of the bistatic RCS (HH component) at two frequencies differ between two fighter aircraft. This kind of information can be used for target discrimination / classification when the propagation losses cannot be inferred. By selecting two frequencies which yield very different RCS values for target #1, say, and such that the differential propagation loss is not likely to exceed some threshold $T < \left|RCS(f_1) - RCS(f_2)\right|$ a simple binary classification rule can be formulated. Repeated application of the rule, with a suitable set of frequencies, provides, in principle, a multi-class recognition capability [16].

3.3 Classification based on target RCS distributions

As noted in Section 2.3, ionospheric propagation subjects the signal to a host of phenomena which modulate the signal's amplitude, phase, frequency, polarisation state, harmonic content, and so on. It is therefore desirable, if not essential, when utilising echo amplitude information, to employ statistics which are commensurate with the required discrimination. The design of suitable statistics is nontrivial, keeping in mind the operational constraints, but modelling and experiment have established some guidelines [17].

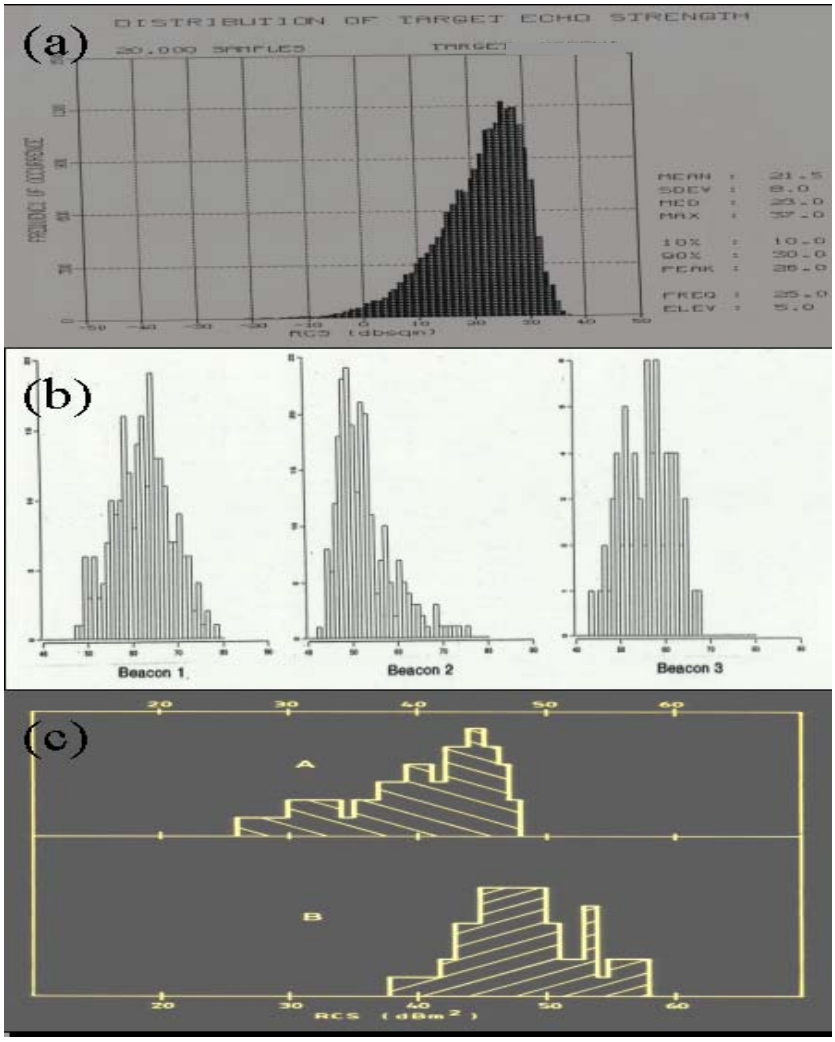

Figure 9: (a) Predicted and measured histograms of inferred scalar RCS.

Figure 9a shows the predicted distribution of inferred RCS for an aircraft target at a prescribed altitude, taking into account the ground reflections and the major ionospheric processes, and employing correct bistatic RCS values, averaging with respect to a designated probability distribution for the generalised Faraday rotation. Figure 9b presents histograms of skywave radar measurements of three specially constructed targets, with different scattering matrices, designed to test the adopted models for the ionospheric propagation phenomena. Finally, Figure 9c compares the measured distributions of inferred RCS from two different ships – one merchant, one naval.

3.4 Classification based on target modulation signatures

At HF the radar wavelength is comparable with the target dimension, so it is not meaningful to attempt to isolate the contributions to the scattered field from individual parts of the target, some of which may be moving relative to others. Instead, for non-relativistic targets, the scattering may be approximated quite accurately by the temporal evolution of the field scattered from a target whose spatial configuration may be taken as instantaneously at rest in the coordinate frame of its centre of mass (the quasi-stationary approximation [18]). The frequency spectrum ('Doppler') of the field scattered from such a time dependent target can then be written

$$\vec{E}_{scat}(\omega) = \int \vec{E}_{scat}(t)\, e^{-i\omega t} dt = \int \tilde{S}(t) \vec{E}_{inc}(t)\, e^{-i\omega t} dt$$

so, for a time-harmonic incident field, $\vec{E}_{inc}(t) = \vec{E}_0\, e^{i\omega_0 t}$,

$$\vec{E}_{scat}(\omega) = \int \tilde{S}(t)\, \vec{E}_0\, e^{-i(\omega-\omega_0)t} dt$$

In the case of periodic modulation of the target geometry (or electrical properties), with some period T and corresponding fundamental frequency $\Omega \equiv T^{-1}$,

$$\tilde{S}(t) = \sum_{k=-\infty}^{\infty} \tilde{S}_k\, e^{ik\Omega t}$$

Substituting,

$$\vec{E}_{scat}(\omega) = \int \sum_{k=-\infty}^{\infty} S_k \vec{E}_0\, e^{-i(\omega-\omega_0-\Omega)} dt$$

$$= \sum_{k=-\infty}^{\infty} \tilde{S}_k \vec{E}_0 \int e^{-i(\omega-\omega_0-k\Omega)} dt$$

$$= \sum_{k=-\infty}^{\infty} \tilde{S}_k \vec{E}_0\, \delta(\omega-\omega_0-k\Omega)$$

so, after demodulation, the signature takes the form of a line spectrum at harmonics of the fundamental frequency of modulation Ω [19] (shifted by the Doppler associated with the forward movement of the helicopter). In the case of a helicopter rotor or aircraft propeller,

$$\Omega = (\textit{shaft rate}) \times (\textit{number of blades})$$

so the line spacing alone provides a characteristic signature, unique in almost all cases, and independent of the line intensities or the transmitting and receiving antenna polarisations. Figure 10 shows the modulation signatures of two helicopters measured in 1983 with the Jindalee radar. The discrimination power of these

signatures is obvious, so helicopter classification / recognition is a viable mission for HF skywave radar. In contrast, Figure 11(a), which shows a Lockheed P-3C Orion, one of the most common propeller-driven military aircraft, with its 4.11 m diameter 4-bladed propeller. Figure 11(b) is the theoretical spectrum computed for a comparable propeller-driven aircraft. The strongest modulation sideband is almost 50 dB below the 'DC' term (often erroneously referred to as the 'skin' echo), so only if the target SNR were to exceed ~ 60 dB would there be any prospect of recognition.

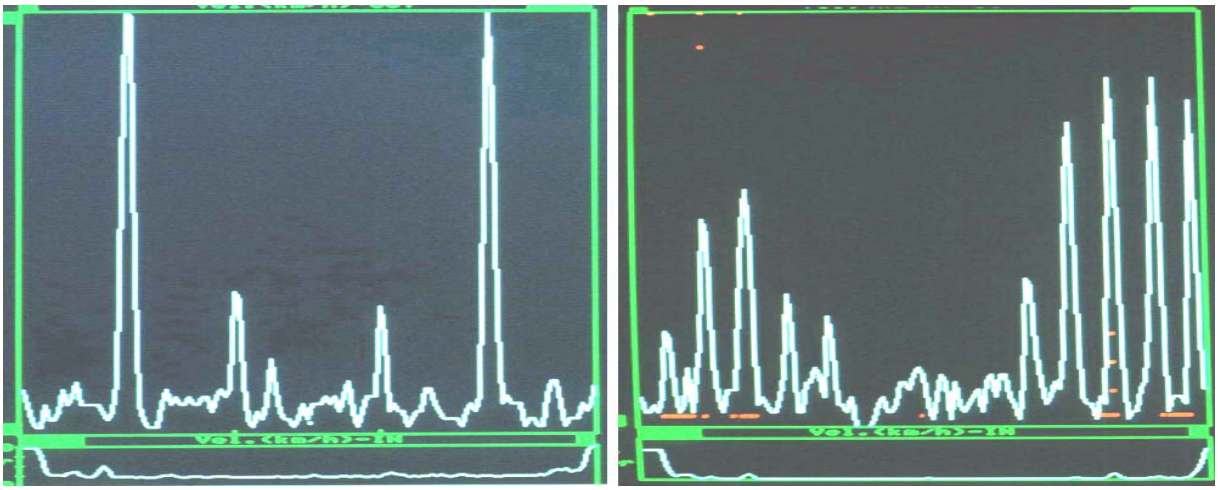

Figure 10: Measured Doppler signatures of two helicopters (Jindalee, 1983)

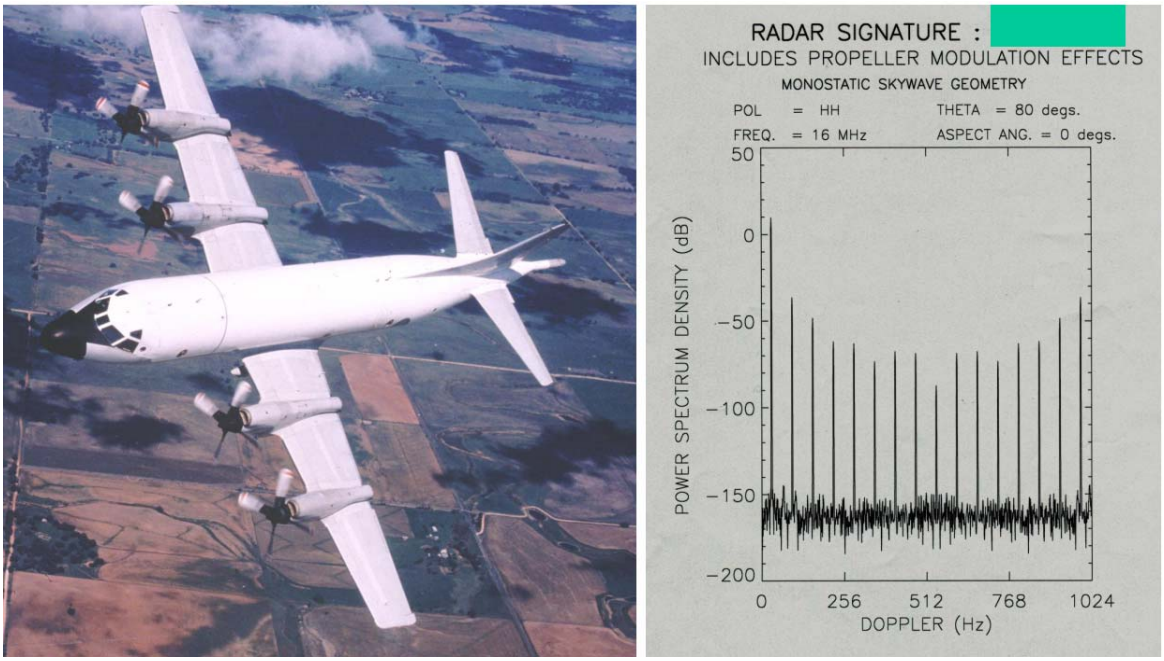

Figure 11: (a) Lockheed P-3C LRMP aircraft showing its 4.11 m diameter propellers, and (b) the computed line spectrum signature for a different propeller-driven aircraft

3.5 Classification based on the target polarisation scattering matrix

The methods discussed so far rely on estimates of target RCS derived from scaled projections of unitary transformations of the scattering matrix, or on statistical distributions or ratios of such projections. Clearly

it would be much more informative of the target if the entire complex scattering matrix could be determined [20], rather than samples of the squared modulus of some unknown linear combinations of its elements.
This would seem to be an impossibility – the signal leaving the transmitter undergoes a 'random' polarisation transformation en route to the target, samples the scattering matrix, the undergoes another random transformation en route back to the receiver, so how could the consequences of these unknown transformations be removed ? Figure 12 shows this hypothetical polarisation transformation sequence and the resultant mismatch at the receiving antenna. Surprisingly, as reported in [21], under certain constraints the scattering matrix might be determinable, though development of a practical classification scheme based on this is in its infancy.
Assuming for the moment that the scattering matrix were observable, the question of how to perform classification / recognition arises. One approach, which has been explored in some depth [22], is to compute the characteristic eigenvectors associated with the optimal polarisation states, that is, the states which correspond to solutions of a family of extremal problems, as formulated by Kennaugh (see Huynen [23]) and others in the context of microwave polarimetry. These solutions have varying sensitivities to illumination geometry, radar frequency and so on, but numerical experiments using computed scattering matrices for two fighter aircraft found well-behaved differences which could be used in a target classification scheme based on the geodesic metric on the Poincare sphere. An example from this study is presented in Figure 13, which shows elevation and plan views of the Poincare sphere with the loci of the characteristic eigenvectors traced out as the target azimuth is varied.

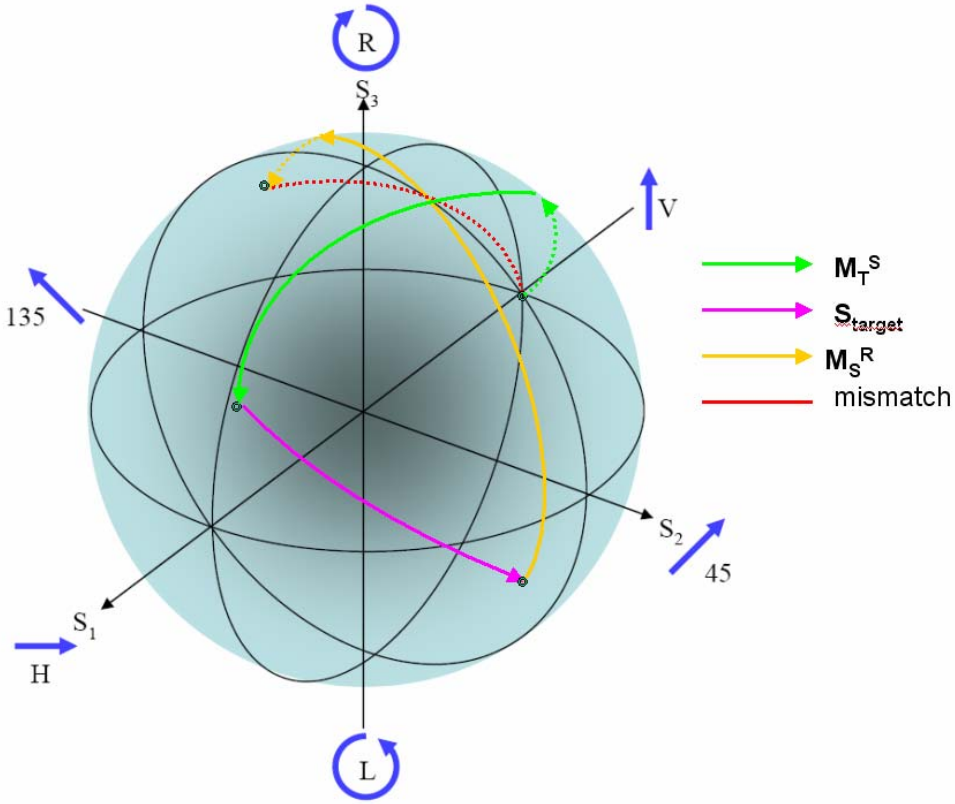

Figure 12: The sequence of polarisation transformations in HF skywave radar

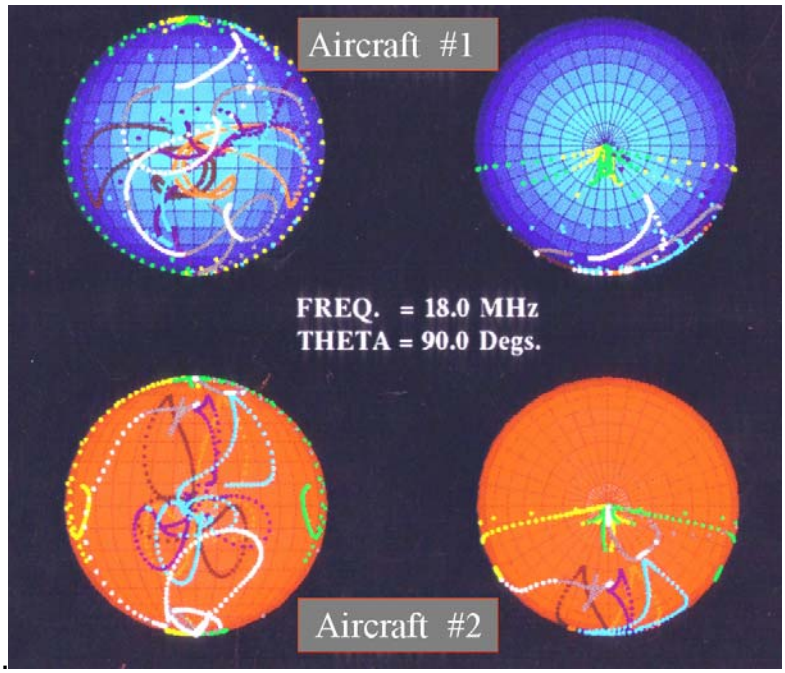

Figure 13: Trajectories of optimum polarisation states under target aspect changes

Of course, in the case of HF surface wave radar, this technique is of no use as the propagation of surface waves over seawater is overwhelmingly confined to vertically polarised fields.

3.6 Classification based on other scattering mechanisms

3.6.1 Nonlinear scattering

Most targets of interest can be modelled as linear media, so the scattering matrix representation is valid. On occasion, though, targets can manifest nonlinear electromagnetic properties – the so called 'rusty bolt' phenomenon associated with ships is an example. Under these conditions, the conventional notion of RCS must be generalised, as described in [24].

3.6.2 Distributed scattering

Multiple and diffuse scattering processes are potentially active in the resolution cell, so energy arriving at the receiver via these mechanisms will be distributed across time delay, azimuth and elevation angle, and Doppler. Detailed modelling (see eg. [15]) has shown that, under some circumstances, these contributions can contribute to target classification for both skywave and surface wave radars.

3.7 Classification based on target kinematics

It is a consequence of aerodynamics and fluid dynamics that aircraft and ships achieve their optimum performance in terms of economy, or speed, or manoeuverability, over a relatively narrow range of kinematic parameters – speed, altitude, climb rate, velocity relative to prevailing seas, and so on. While one cannot presume that classification / recognition based on this kind of target information will be robust under all circumstances, it is surprisingly effective and adds to the dimensionality of the classification space, thereby enhancing classifier performance.

3.8 Classification based on target IFF transponders

So far the discussion has focussed on non-cooperative target classification and recognition. Yet there are situations where IFF is a useful facility, even at over-the-horizon distances. Various beacons able to serve in this capacity have been developed and tested on ships, aircraft and, of course, on land. The example shown in Figure 14 was measured in 1977; the IFF was mounted on a small (30 m) patrol boat.

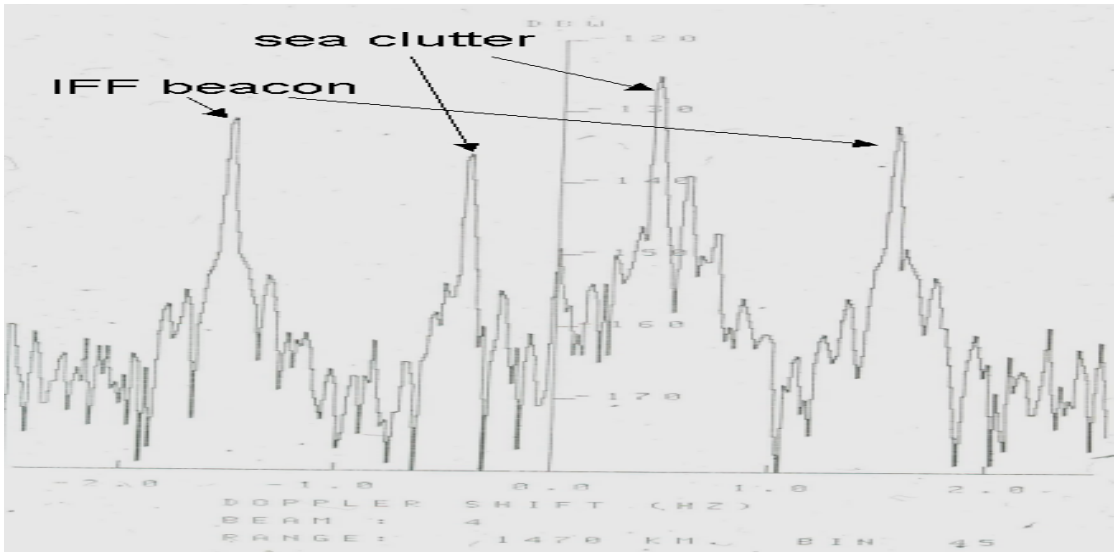

Figure 14: Cooperative target recognition – IFF modulation signature at a range of 1470 km

4.0 CONCLUSIONS

In spite of some daunting challenges posed by the propagation mechanisms involved and the vagaries of the environment, a modest target classification capability is slowly emerging as a potentially viable option for both skywave and surface wave radars. Given a deep understanding of the physics involved, and access to sophisticated computer modelling codes, it would seem possible, in principle, to exploit the technical features of advanced HF radar systems to achieve a limited but still operationally significant target classification capability.

The prospects for the future emergence of a universal target classification and recognition system are not nearly so bright. The fundamental information limits imposed by under-sampling, and the ill-posedness of the corresponding inverse problems, make it unlikely that HF radar will deliver all the classification and recognition capabilities desired by the operational community, while identification in the intimate sense defined in this paper is not likely to emerge except as an outcome of data fusion with other sources.

While it is gratifying that some success has been achieved with these approaches, it is an unfortunate reality that almost all existing HF radar designs have largely ignored the issues related to target classification, and hence fail to incorporate some features which could enhance their ability to extract target information leading to reliable classification, recognition and identification.

5.0 REFERENCES

[1] Anderson, S.J., Remote sensing with the JINDALEE skywave radar, IEEE Journal of Oceanic Engineering, Vol. OE-11, No. 4, pp. 158-163, April 1986

[2] www.raytheon.com/businesses/rids/docs/ROTHR.pdf

[3] Anderson, S.J., Edwards, P.J., Marrone, P. and Abramovich, Y.I., ' Investigations with SECAR - a bistatic HF surface wave radar', Proceedings of RADAR 2003, Adelaide, September 2003[4] www.raytheon.com/products/swr503/ref_docs/swr_503.pdf

[5] Emery, D.J.,Money, D.G., and Mainwaring, H.W., 'Some aspects of design and environmental management in HF surface wave radar', Proceedings of RADAR 2002, Edinburgh, pp.51-55, October 2002

[6] Anderson, S.J., `The Challenge of Signal Processing for HF Over-the-Horizon Radar', Proceedings of the Workshop on Signal Processing and Applications, WOSPA'93, Brisbane, Australia, December 1993

[7] Anderson, S.J., 'Limitations to the extraction of information from multi-hop skywave radar signals', Proceedings of RADAR 2003, Adelaide, September 2003

[8] Anderson, S.J., 'The Doppler structure of diffusely-scattered skywave radar echoes', Paper to be presented at RADAR 2004, Toulouse, October 2004

[9] Anderson, S.J., 'Multi-parameter radar – how not to get lost in parameter space', Proceedings of the Workshop on Multi-Parameter Radar, Adelaide University, May 2004

[10] Anderson, S.J., `The Extraction of Wind and Sea State Parameters from HF Skywave Radar Echoes', IREECON International Digest, IREECON-83, Sydney, Australia, pp.654-656, September 1983

[11] Wyatt, L.R., 'A relaxation method for integral inversion applied to HF radar measurement of the ocean directional wave spectrum', International Journal of Remote Sensing, Vol. 11, pp. 1481-1894, 1990

[12] Hisaki ,Y., "Nonlinear inversion of the integral equation to estimate ocean wave spectra from HF radar", Radio Science, Vol. 31, pp. 25-39 , 1996

[13] Anderson, S.J., `HF Skywave Radar Measurements of Cyclone-Generated Ocean Waves', Proceedings of Radarcon-90, Adelaide, Australia, pp.315-323, April 1990

[14] Anderson, S.J., `Stereoscopic and Bistatic Skywave Radars : Assessment of Capabilities and Limitations', Proceedings of Radarcon-90, Adelaide, Australia, pp.305-313, April 1990

[15] Anderson, S.J., 'Identifiability and compensation of propagation distortion in passive radar systems at HF', Proceedings of the Conference on Passive and Covert Radar, PCR2002, Roke Manor Research, UK, June 2002

[16] Bennett, C.L. and Toomey, J.P., 'Target classification with multiple frequency illumination', IEEE Transactions on Antennas and Propagation, Vol. AP-29, No.2, pp.352-358, March 1981

[17] Strausberger, D.J., Garber, F.D., Chamberlain, N.E., and Walton, E.K., 'Modeling and performance of HF/OTH radar target classification systems', IEEE Transactions on Aerospace and Electronic Systems, Vol. 28, No. 2, pp.396-403, April 1992

[18] Van Bladel, J., '*Electromagnetic Fields*', McGraw Hill, 1964

[19] Green, H.E., 'Electromagnetic backscattering from a helicopter rotor in the decametric wave band regime', IEEE Transactions on Antennas and Propagation, Vol. 42, No.4, pp.501-509, April 1994

[20] Chamberlain, N.F., Walton, E.K., and Garber, F.D., 'Radar target identification of aircraft using polarisation-diverse features', IEEE Transactions on Aerospace and Electronic Systems, Vol. 27, No. 1, pp.58-67, January 1991

[21] Anderson, S.J., Abramovich, Yu.I., and Boerner, W-M., 'On the solvability of some inverse problems in radar polarimetry', Proceedings of the SPIE Conference on Wideband Interferometric Sensing and Imaging Polarimetry, San Diego, USA, July 1997

[22] Anderson, S.J., `S-Matrix Eigenvector Dynamics on the Poincare Sphere', Proceedings of the Workshop on Wideband Imaging and Sensing Polarimetry, S.J.Anderson and W-M. Boerner (Ed.), Adelaide, Australia, August 1992

[23] Huynen, J.R., 'Phenomenological Theory of Radar Targets', PhD. Dissertation, Drukkerij Bronder-Offset, NV Rotterdam, 1970

[24] Anderson, S.J., Mahoney, A.R., and Zollo, A.O., `Applications of Higher-Order Statistical Signal Processing to Radar', pp.405 – 446 (Chapter 13) in `*Higher-Order Statistical Signal Processing'*, B. Boashash, E.J.Powers and A.M.Zoubir, (Ed.), Longman Australia and Halstead Press, 1995

A Doppler-Based Target Classifier Using Linear Discriminants and Principal Components

A. G. Stove
Thales Airborne Systems
Manor Royal
Crawley RH10 9PZ
United Kingdom

andy.stove@uk.thalesgroup.com

SUMMARY

This paper describes the design of the automatic target classifier which has been introduced into the AMSTAR Battlefield Surveillance Radar. It discusses the requirements which have driven the design of the classifier, the data which is used to make the classification, the choice of Linear Discriminant Analysis as one of the classification techniques used and the use of Principal Components Analysis to simplify the training of the discriminator. It also discusses the addition of other classes by the use of other data about the targets. It includes a discussion of the testing of the classifier and the performance achieved.

1.0 INTRODUCTION

The classifier described in this paper has been designed and implemented for the AMSTAR (Advanced Man Portable Surveillance and Tracking Radar) radar. This is a man-portable battlefield surveillance radar, derived from the earlier MSTAR radar [1]. Fig. 1 shows a picture of the radar. The principal features of the radar are:

- small size and light weight
- low power consumption enabling operation from long periods from rechargeable batteries and
- very good Doppler performance.

The small size, light weight and low power consumption allow the radar to be man-portable. The Doppler processing allows it to perform its battlefield surveillance task, detecting slow-moving personnel and other targets, but rejecting clutter. The original MSTAR radar had been in service with the UK and other armed forces since 1989. It was designed primarily as a artillery spotting aid, for locating targets of interest and observing fall of shot. The advanced MSTAR (AMSTAR) variant originated as a Mid-Life Improvement (MLI) of the original design which was undertaken during the year 2000. In common with most, if not all, radars of its general class, MSTAR is a coherent radar and has from the outset possessed a so called 'audio' output which can be used by the operator to classify targets. This audio mode uses a sample-and-hold to 'stretch' the train of pulses returned from a target so that they form a continuous signal. The frequency spectrum of the resulting signal is the Doppler spectrum which would be obtained from CW illumination of the same target. The radar operates in the upper J-band and for this carrier frequency the Doppler frequencies lie within the audio band, being of the order of a kilohertz, and so can be presented as an audio tone to the radar operator, via headphones. After listening to the target for a few seconds a trained operator can classify it with a high degree of accuracy.

Paper presented at the RTO SET Symposium on "Target Identification and Recognition Using RF Systems", held in Oslo, Norway, 11-13 October 2004, and published in RTO-MP-SET-080.

The Doppler audio frequently sounds surprisingly like the actual sound of the object, perhaps because the same underlying mechanisms modulate both the sound which the target makes and its Doppler spectrum.

The audio-based classifier has three deficiencies, however. The first deficiency is that it must stop scanning and stare at the target which is to be classified, interrupting the execution of its other tasks. The second deficiency is that classification imposes a high workload on operator. He must use the cursor to set the radar to the desired bearing to 'stare' at the target of interest, and must frequently search in range to find the range cell which contains the target of interest. He must then listen intently to the audio to decide the target class. The third deficiency with such a classifier is that the operator must be trained to discriminate the different sounds made by different targets, which require a considerable investment in time and resources.

An automatic classification aid which operates whilst the radar continues to perform its surveillance is thus a significant aid in reducing the operators' workload. The classifier is thus required to operate 'on the fly' during the normal surveillance dwell of the radar so the operator does not have to interrupt normal surveillance operations to obtain a classification - classifications must be generated automatically for all plots and made available on demand.

For the surveillance application, the classifier has to be sufficiently accurate that after observing a target for a few scans the operator can be reasonably confident of its class. It is important to realise that this application does not need the same level of reliability as some other non-cooperative target classification applications (see, for example, reference 2), since the operator can make use of other information, such as target speed and, if desired, the audio mode, to supplement the information provided by the automatic classifier. It should be emphasised again that the purpose of the automatic classifier is to relieve the operators of the workload required to listen to the Doppler signals of each target one at a time. In an environment with few targets, the operators still generally prefer the confidence they obtain by listening to the Doppler from a target, but when there are many targets present, that is not always possible and then the automatic classifier can be used as an aid to help to decide which targets should be examined individually.

2.0 CLASSIFICATION DURING THE SCAN

Since the radar must classify the target as it scans past during its normal surveillance operations, the sample of the Doppler which it can use is limited in length. The dwell during which the classification must be performed is typically less than 100ms. This time is much shorter than that used for audio classification, where the operator can in principle listen to the Doppler for as long as he likes and will typically listen for several seconds. This difference between the 'audio' case and the 'scanning' case means that the techniques which are appropriate for audio recognition are not necessarily appropriate for the automatic classifier. Indeed, the fact that audio-based classification is possible does not in itself prove that classification with a scanning radar is possible.

Jahangir et al. [3] describe a Doppler classifier which uses speech-recognition principles, but they concentrate more on longer audio samples and show that the performance degrades with shorter samples. They point out that a classifier, such as ours, which treats the spectrum as stationary and performs a single transform over all of the data is likely to be sub-optimal for longer data sets, where the spectrum generally changes with time. In our case, however, the shortness of the samples means that the spectrum can reasonably be considered to be stationary. To continue the analogy with speech: conventional speech recognition looks at the chain of successive phonemes, whereas this 'scanning mode' classifier is trying to perform a task which is closer to trying to recognize a single phoneme.

3.0 CLASSIFIER ARCHITECTURE

For the MSTAR MLI, the set of possible target classes between which discrimination was required was:

- Personnel
- Wheeled Vehicle
- Tracked Vehicle

Internally the classifier also generated the classes of

- Unknown
- Reject.

The later versions also includes the classes of

- Helicopter
- Small ship
- Large ship

The original MSTAR MLI variant, which distinguished between Personnel, Wheeled Vehicles and Tracked Vehicles, used a linear discriminant[4] for the classification, with separate templates for each of a number of velocity bands, and used principal component analysis[5] to simplify the training process. This was preceded by pre-processing to organize the data into a form which was suitable for the linear discrimination process. The set of velocity bands ensured that the class of 'Personnel' could not be returned from a target which was moving faster than a running man.

3.1 Rejected and Unknown

It is important to be able to recognize the cases where the classification breaks down. A class of 'Unknown' is returned if the Doppler sideband information is likely to have been corrupted by noise sidebands returned from a much larger clutter return in the same range/azimuth cell. This process is also refined to allow the target itself to be rejected if it may be purely a detection of the transmitter noise sidebands. The stability of the radar is such that this almost never happens, but it is a theoretical possibility in the presence of extremely large clutter returns at relatively short range, and is an easy condition for which to check within the classifier, since all of the preliminary work the has already been done in order to check the validity of the Doppler sideband information.

3.2 Helicopters

As shown in figure 12 of reference 6, the signature of the helicopter blade 'flash' is very distinctive. The approach which has been taken is to look for significant energy in the part of the spectrum which is moving in the opposite sense from the body of the object. Since the blade flash is a fleeting phenomenon, it is not appropriate to process it using the relatively long sampling windows used by the linear discriminant system. The actual detection process is therefore performed in the time domain, where the energy from the blade flash is concentrated, rather than in the frequency domain, where it is diffuse, so the detection process can then be more efficient. The ability to detect the blades, together with the basic radar's ability to detect a crawling man, i.e. a target which is moving extremely slowly, means that the radar now has an effective capability to detect as well as recognise hovering helicopters.

The process of detecting the blade-flashes was found to be significantly more reliable than attempting to use the rotor hub motion as a classification 'feature' in a linear discriminant system.

3.3 Ships

Ships are in effect defined as targets which are not helicopters but which are over the sea. Preliminary studies were made to look at the effectiveness of a Doppler-based classifier for ships. Although under some circumstances the audio obtained from the Doppler from ships can be quite distinctive, it was found to be difficult reliably to incorporate ships into the scheme of the linear discriminant, because of the variability of their signatures.

It may be possible in some cases to determine whether the clutter background is land or sea from its statistical variations and Doppler spectrum, but it was reckoned that, again, it would be very difficult to do this reliably, particularly with a radar like MSTAR which was designed to reject the clutter, so in the end this decision was made using maps and this determines whether a target is assumed to be a land target or a ship. The details of this process are discussed in section 8.

3.4 Architecture

When the classifier was extended to include the additional classes, the decision was taken to move away from the almost pure 'linear discriminant-based' approach originally used. The positive reason for doing this was to take account of additional information, such as radar cross section, which although not a reliable discriminant in itself, does contain useful information. The negative reason was to avoid the possibility of the classification being degraded as more classes are added. For example, if there are N classes then N-1 binary comparisons might be made to determine the target class. If each classification has a probability of p of being correct, then the overall probability of correct classification is only

$$p_0 = p^{N-1}$$

For example, if p = 90% and N =3, typical of the original classifier, then p_0 = 81%. Extending the number of classes to 5 would therefore be expected to reduce the probability of correct classification to only about 66%.

Another desire is to be able, where the resultant update rate is acceptable to the user, to correlate the classification obtained on the same object on different scans, again to improve the performance.

The overall algorithm of the classifier is thus:

if *target is below the clutter sidebands* **then** *Class* **:=** '*Reject*'
else **if** *Doppler sidebands are masked by clutter sidebands* **then** *Class* **:=** '*Unknown*'
else **if** *target is small and slow-moving* **then** *Class* **:=** '*Personnel*'
else **if** *'blade flash' detected* **then** Class **:=** '*Helicopter*'
else *perform linear discrimination to distinguish between*
'*Wheeled*,' '*Tracked*' *and* '*Personnel*'**;**
if *the target is over the sea* **and** ***C****lass* **in [**'*Personnel*,' '*Wheeled*,' '*Tracked*'**]** **then**
if *radar cross section > threshold* **then** *Class* := '*Small Ship*'
else *Class* **:=** '*Large Ship*'**;**
*compare class with other classifications of the same object***;**
if *there is a clear winner* **then** *return weighted majority class*
else *return 'Unknown.'*

4.0 PRE-PROCESSING THE SIGNAL SPECTRA

The sequence of samples obtained during the radar's dwell is first Fourier transformed to form a spectrum, representing the Doppler shifts of the body of the target and of any parts of the target which are moving independently of the main body at that moment. Figs. 2 to 4 show typical spectra of a wheeled vehicle, a tracked vehicle and a man walking. The clean spectrum of the wheeled vehicle can be contrasted with the much more complex, but asymmetrical, spectrum of the tracked vehicle, and this can again be distinguished from the more symmetrical spectrum of the walking man.

This spectrum is also used to assess whether the target should be 'Rejected' or classified as 'Unknown' on account of the level of clutter present.

4.1. Pre-Processing for the Linear Discriminant Algorithm

Before the spectrum is presented to the linear discriminant classifier it is edited in the frequency domain to remove Doppler cells which it is calculated can only contain noise. Typically 100 Doppler bins are kept to ensure that all significant features of the signal are retained. The spectrum is also regularized by moving its peak, which is assumed to represent the Doppler shift of the bulk of the target, to the centre of the spectrum.

To avoid too great a degree of reliance on the normalization of the spectra with respect to different target velocities, six separate classifiers are used, covering differing velocity bands. The body velocity is estimated from the peak of the spectrum and the signal is presented to the appropriate classifier.

The spectrum is also normalized in amplitude. This normalization presents some theoretical problems which can be solved only by experimentation to provide an acceptable ad-hoc solution: if the spectrum is not normalized then changes in signal level can affect the signature, confusing the classification process. If it is normalized, however, potentially useful information about signal levels is lost. Normalization also assumes implicitly that the amplitudes of all the Doppler components change together, but this has in practice been found to be the more successful approach.

The normalized spectrum is then treated as a vector of features which is passed to the classifier.

5.0 ROBUSTNESS TO SIGNAL TO NOISE RATIO

The Doppler-based classification approach is relatively robust to the signal to noise ratio of the targets. Provided that the signal to noise ratio is sufficiently high for the Doppler sidebands to be distinguished from the noise, the classification performance is substantially independent of that ratio.

Although the power level in any one Doppler sideband is relatively low compared with the body return, the total power in all the sidebands is quite high. The 'classic' radar range equation also means that reduction in classification range compared with the detection range is proportional only to the fourth root of the ratio of 'body' to 'sideband' power, so good classification performance is maintained over most of the radar's detection range against a given target.

The detection process, and likewise the classification process, of the AMSTAR radar is substantially immune to the effects of clutter because:

- low power radars such as this have relatively low dynamic ranges, making good clutter suppression easier,
- the all-solid state design makes the radar very stable

- the fine Doppler resolution makes it easy to distinguish even slow-moving targets (and their Doppler sidebands) from the Doppler sidebands of the nominally-stationary clutter.

6.0 CLASSIFICATION APPROACH

Since the radar must have low power consumption any algorithms used in the real-time classification process must be simple, although complex, time-consuming processes can be used, if required, for off line, training.

6.1. Fisher Linear Discriminant

A statistical classification technique, Fisher's Linear Discriminant Analysis (LDA), was chosen [4]. This provides an optimum discrimination solution for a linearly separable problem. A possible alternative approach would be to use a neural network [6], of which a multi-layer perceptron, trained by back-propagation would perhaps have been the most appropriate form. The principal theoretical advantage of the neural network is that it can cope with problems in which the two classes are not linearly separable. The potential difficulties of training the network mean, however, that it is generally best to try a linear technique first and stick to that if it can give adequate results.

It is sometimes very hard to understand the inner workings of a neural network, although the behaviour of the LDA can also sometimes be hard to understand in a multi-dimensional problem. Understanding how the algorithm is working is of considerable practical benefit when it is to be used in a radar system. It can help to show whether the performance which has been achieved is as good as it should be, whether the pre-processing and the choice of classification parameters have been appropriate and, on a more mundane level, even whether the algorithm has been coded properly.

6.1.1. Choice of Decision Point

As mentioned above, the basic LDA treats the normalized Doppler spectrum as a feature vector, treating each frequency bin as a separate dimension. As is well-known, the algorithm determines the hyperplane which best separates the points in one class from another.

The position of this hyperplane is determined from the statistical distributions of the positions of the returns from the two classes. One 'tunable' parameter is the criterion for the position of this line. Alternative definitions allow it to be, for example, at the point where the probability distributions overlap, so that the most probable answer is given for any particular point in the hyperspace. If the distributions have different covariances, however, this is not necessarily the same as the position which gives equal probabilities of error for the two classes. This point is illustrated in Fig. 5. In practice, a hybrid approach was used in the AMSTAR classifier, which was chosen to give the best balance of performance overall.

6.1.2. Run-Time Complexity

The actual output of the training stage is the vector representing a normal to the discriminant line, or, more generally, a normal to the discriminant hyperplane. The test of a particular spectrum is performed by calculating the scalar product of the feature vector and this reference normal, which projects the point in the hyperspace onto that normal. The choice of class is made by determining to which side of the discrimination hyperplane the point falls. The run-time complexity is thus one multiplication and one addition per element of the spectrum plus one comparison, which is all very simple compared, for example, with the Fourier transformation required to generate the spectrum in the first place.

6.2 Principal Component Analysis

The amount of training data required increases with the number of elements in the vector. As mentioned above, typically 100 elements are used in the vector, but it is clear that the number of independent 'features' in the data is far fewer than that. If the dimensionality of the test vector can be reduced to reflect the number of degrees of freedom in the underlying data then the amount of training data can be reduced. A well-known way of doing this is to use the Principal Components Analysis (PCA) technique [5], also known as the Karhunen-Loeve transform..

As is well known, the principal directions found by the PCA are the eigenvectors of the autocorrelation matrix of the data, and the significance of each dimension is indicated by the relative value of the associated eigenvalue, so the simplification of the problem is achieved by retaining only a relatively small number of the most significant components.

In general the PCA complements rather than replaces the LDA, because the PCA is not looking for directions which optimize the between-class discrimination, but rather for directions which explain as much as possible of the variance within the union of both classes.

It is not commonly recognized that it is theoretically possible that the most significant directions chosen by the PCA could *only* explain components of the covariance which are common to both classes, in which case if the other 'less significant' dimensions are discarded, it would no longer be possible to discriminate between the classes. Figure 8 illustrates how this can occur by taking a hypothetical example where the data contains two dimensions. The ellipses represent the distributions of the two classes in these dimensions. It can be seen that most of the variance in this case is in dimension 1, whereas all the discrimination information is in dimension 2. A 'degenerate' PCA which, took only the first principal component, would therefore in this case discard all the discrimination information. Although this is clearly an extreme, simplified, case it will be appreciated that similar effects can in theory happen in more complex, practical, cases.

In practice, however the principal dimensions do usually contain most of the classification information. This has been specifically checked for this classifier by showing that if the principal components are *excluded* from the classification vector, very poor discrimination is achieved between the classes.

Removal of only a few dimensions, with the lowest eigenvalues, on the other hand, can sometimes significantly help the discrimination process by eliminating dimensions which explain virtually none of the variance, but which serve only to compromise the stability of the algorithm. It is sometimes difficult to relate some of these phenomena directly back to the original data set, but dimensions which explain nothing of the variance are probably due to artefacts in the pre-processing.

Although the directions chosen by the PCA contain most of the discrimination information, the principal direction is in general not aligned exactly with the normal to the original discrimination plane. In order to obtain good discrimination the PCA is thus followed by an LDA process as described previously. The PCA is thus used during the training process as a 'pre-processor', to reduce the dimensionality of the problem. About ten principal components are typically retained, leading to a ten-fold reduction in the amount of training which must be obtained.

It is important to emphasize that the PCA does not affect the complexity of the real-time classification, since the dimensionality of the reference vector can be increased again after training to match the size of the data vector, so that no additional real-time processing of the data is required.

7.0 TESTING AND PERFORMANCE

7.1 Tests during Development

During the training phase, 10% of the available data, chosen at random, was set aside for testing, i.e. 90% was used to train the discriminator but the other 10% was only used to test it. The individual types of the vehicles used to gather the training data, their registration numbers and the identities of the personnel who acted as the 'targets' were all recorded to allow checks to be made that the classifier was not accidentally discriminating between the identities of individual targets when it should generalize for broad classes.

Tests were made of the correlation of false alarms between adjacent data samples to assess what time delay was needed before samples of training data could be considered to be independent. It was concluded that, very approximately, samples of personnel which were separated by 50ms could be considered independent whereas the delay had to be 100ms for wheeled vehicles and 150ms for tracked. Since each sample was about 50ms along, all the 'personnel' data could be used to provide independent training samples, but only alternate samples of the wheeled vehicle data and one in every three of the tracked vehicle data. This 'thinning out' of the data meant that we avoided the possibility that some of the 'test' data could have been highly correlated with particular adjacent examples of the training data.

During the training phase, tests were carried out to assess the sensitivity of the classifier to the aspect of the targets, by training a discriminator using only data gathered at one nominal aspect angle and testing it with data gathered at another. As expected, it was found that the Doppler signature is relatively insensitive to changes in aspect angle. The signatures remained correlated over about 30 degrees, although large changes in aspect can causes significant changes in the signatures, probably due to obscuration of parts of targets.

The sensitivity to variations in range was tested by adding noise to the test data to simulate a reduction in the signal to noise ratio. The sensitivity to changes in velocity was tested by varying the number of velocity bands and checking that this did not significantly change the performance.

7.2. Acceptance Tests

Proposing a test plan for the classifier can present a significant theoretical problem if one does do not know *a priori* what factors, such as target range or speed or direction, might affect its performance. In that case field tests would have to cover all possible target conditions and would be prohibitively expensive. The problem of testing the classifier can, however, be made manageable by making use of the tests which have been performed during the development to assess the sensitivity to aspect angle, range, velocity etc. This allows a suitable range of tests to be devised, but there may still be a relatively large number of combinations to be tested.

For AMSTAR most of the testing was performed using the 'test set' extracted from the training data, as described above, which had been used for the tests performed during the training. This contained enough data to obtain statistically significant results in different scenarios to ensure that the classifier's performance was satisfactory in all combinations of scenarios. Since the whole training and testing system operated in software, the process of obtaining the results in these laboratory based tests was also many times faster than reading each result individually from the radar display and recording it by hand. Although this procedure is efficient, it suffers from the fact that it is still dependent on the correctness of the sensitivity analysis carried out during the training phase and can only test the classifier against data gathered in the same scenarios as the training data. A relatively small number of completely independent 'field' tests were therefore performed to give confidence that the results of the 'laboratory' testing were reliable. Whilst these could confirm that the classifier worked in the scenarios tested, it could not give statistically significant information on a large number of the scenarios individually.

The overall classification performance obtained for the three-class case used in the MLI variant has already been reported before [8]. The comparable results with four classes plus 'Unknown' are:

Table 1: Overall Classification Accuracy for the AMSTAR Classifier

True Class	Reported As				
	Personnel	Wheeled	Tracked	Helicopter	Unknown
Personnel	83%	14%	3%	1%	0%
Wheeled	0%	82%	10%	5%	4%
Tracked	0%	15%	77%	8%	0%
Helicopter	3%	6%	4%	82%	6%

The totals are not exactly 100% due to rounding errors. It will be appreciated that these results are for a single observation of the target and the results seen by the operator will be better, once successive looks have been compared as discussed below.

It will be noted that, compared with the three-class case, the performance on tracked vehicles has dropped slightly below 80% for this 'single look' case reported above, although the change in the numbers is probably not significant. It is noteworthy that these results are still generally better than those reported in [3] for short dwells, although better results were obtained with the hidden Markov models when longer dwells were available.

The corresponding field trials of this 'four class' classifier showed correct classifications of between 73% and 80% on a single 'look', which, is in equivalent to a value of the order of 90% after the scan-to-scan comparisons, and is thus comparable with the results reported in reference 8. The field trials also showed that, as predicted, correct classification was achieved at ranges of the same order as the detection range.

8.0 POST PROCESSING

8.1. Scan to Scan Processing

The classifier follows the radar's plot extractor. The output of the classifier is used to tag the plot when it is sent to the radar's Control and Display Assembly. The operator accesses the classification by putting the cursor near the plot. This placement does not have to be as precise as is needed for audio classification. If the nominated plot is part of a trail, the display processing can be arranged to look at the classification of adjacent plots to reject occasional false classifications or to report 'unknown' if the classifications are inconsistent. This process ensures that the accuracy after a few scans is at least as 80% for any combination of target type and velocity band, i.e. it gives good results not only in 'average' scenarios but in the worst case. In other variants, an automatic tracker can be used to associate the plots together, and the individual classifications within the track can be compared to eliminate the occasional erroneous classifications.

If the classification is inconsistent, this is used in some variants as an additional 'trap' which also allows the class to be reported as 'Unknown.' User feedback suggests that operators are much happier with a relatively high proportion of returns being classed as 'Unknown' than they are with firm classifications which are in fact erroneous.

8.2. Sea Target Classifications

It is also at this stage that the classification of sea targets is incorporated. The map in the MMI is used to ascertain whether the target is on the land or on the sea. If it on the sea and not a helicopter or an

'unknown,' it is classified as a ship. Ships are distinguished between 'large' and 'small' on the basis of their radar cross sections. The ratio of radar cross section between 'small' and 'large' targets is 50:1 (17dB) and by placing the threshold 5dB above the limit for a 'small' target there is a 94% chance that a target with a Swerling 2 fluctuation and an RCS at the limit of the values to be classified will be classified correctly.

9.0 CONCLUSION

An automatic classifier has been successfully incorporated into the AMSTAR Battlefield Surveillance Radar. It uses Linear Discriminant Analysis to exploit the Doppler signatures of the targets to provide classification between the classes of Personnel, Wheeled vehicle and Tracked vehicle on land, Small and Large Ships on the sea and Helicopters in both domains. This provides classification aids which can significantly reduce the operator's workload without compromising the radar's surveillance mode performance. A performance equivalent to better than 90% average and better than 80% worst-case after scan-to-scan comparisons, equal to that reported in reference 8 for the three-class case has now been achieved for the four-class case. The technique of Principal Components Analysis has also been used to minimize the amount of training data required.

10.0 ACKNOWLEDGEMENTS

The Mid Life Improvement of the MSTAR radar, which led to the evolution to AMSTAR, was funded by the UK Ministry of Defence. The initial design of the algorithms was performed by Mr Rick Rickman and Mr Stephen Sykes of Racal Research Laboratories (now Thales Research and Technology). The incorporation of the Helicopter and Ship classes was designed and executed by Mr Graeme Evans and Mr Alastair McIver of Thales Airborne Systems. Much of the exploration of the behaviour of the PCA with this data set was carried out by Mr. Simon Gibbs.

11.0 REFERENCES

[1] C. J. Baker and B. D. Trimmer, "Short-Range Surveillance Radar Systems," *Electronic Commun. and Engineering J.*, August 2000, pp.181-192

[2] R. van der Heiden, L. J. van Ewijk and F. C. A. Groen, "A Comparison of Radar Range Profiles Between In-Flight Measurement and RCS Prediction," *Proc. NATO RTO Meeting on "Non-Cooperative Air Target Identification Using Radar 22-24 April 1998,* RTO Meeting Proceedings 6, published November 1998.

[3] M. Jahangir, M., K. M. Pointing and J. W. O'Loghlen, "A Robust Doppler Classification Technique Based on Hidden Markov Models," *Proc. Radar 2002*, IEE Conf. Publ. 490, October 2002, pp.162-6.

[4] P. A. Devijver and J. Kittler, "Pattern Recognition: A Statistical Approach," London, Prentice-Hall, 1982.

[5] D. F. Morrison, "Multivariate Statistical Methods," New York, McGraw-Hill, 1978.

[6] P. M. Grant, "Artificial Neural Network and Conventional Approaches to Filtering and Pattern Recognition," *Electronic Commun. and Engineering J.*, September/October1989, pp.225-232

[7] M. Moruzzis and N. Colin, "Automatic Recognition of Air targets for Future SHORAD Radars," *Proc. NATO RTO Meeting on "Non-Cooperative Air Target Identification Using Radar 22-24 April 1998,"* RTO Meeting Proceedings 6, published November 1998. pp.30-1 to 30-10.

[8] A. G. Stove and S. R. Sykes, "A Doppler-Based Automatic Target Classifier For A Battlefield Surveillance Radar," *Proc. Radar 2002*, IEE Conf. Publ. 490, October 2002, pp.419-423.

Figure 1: The AMSTAR Radar

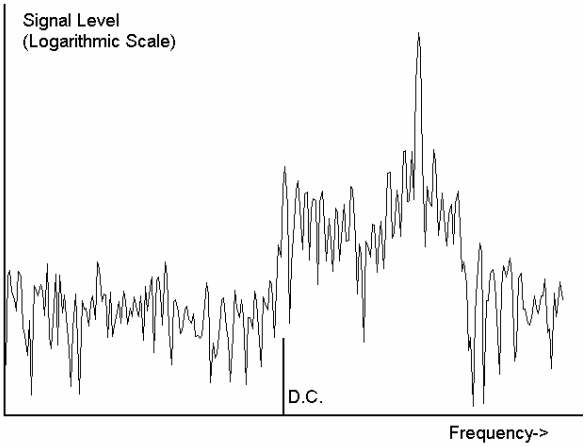

Figure 2: Spectrum of a Tracked Vehicle

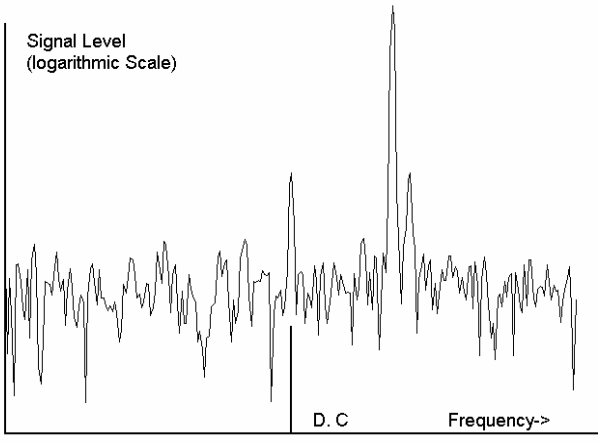

Figure 3: Spectrum of a Wheeled Vehicle

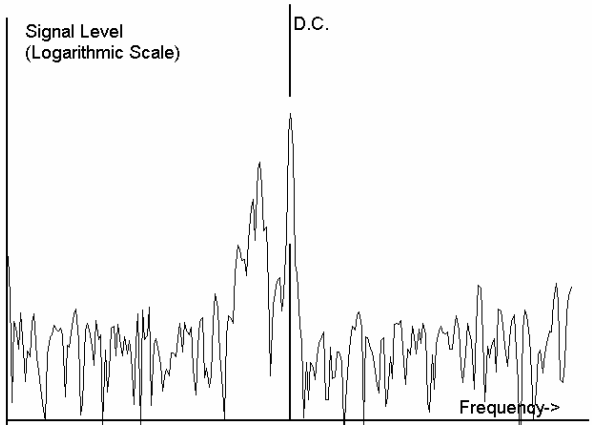

Figure 4: Spectrum of a Walking Man

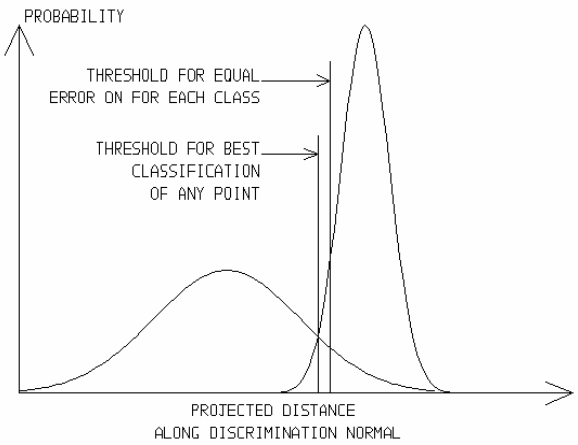

Figure 5: Different Discrimination Choices for the Linear Discriminant Classifier

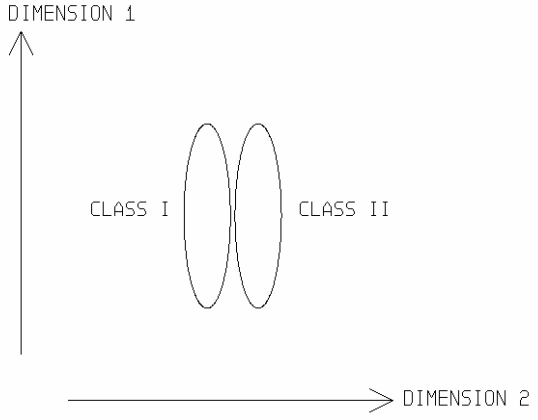

Figure 6: Hypothetical a Case when PCA would not work with LDA

Recognition of Targets by Linear and Non-Linear (Delta K) Processing of Multi Frequency Data

D.T. Gjessing, J. Saebboe, OE. Helleren
Triad AS, Storgata 6, 2000 Lillestroem
Norway

triad@triad.no

ABSTRACT

Multi frequency data from continuous wave radar is used to recognize air, sea and land targets. Target range profile data is extracted both from the linear combination of the frequencies and the non-linear Delta K processing. The results are discussed in light of the motion pattern and the vibration of the target. Continuous wave data offers long integration time for Doppler processing, which can be used to get high-resolution Doppler signatures of the targets. These features are discussed as target classifiers. The paper describes the technology and presents some experimental results. The application and limitations of the technology is discussed with focus on integration in a pulsed system.

1.0 INTRODUCTION

Using a multi frequency continuous wave or range gated radar system we can sample the targets Doppler shifts at several frequencies in parallel.

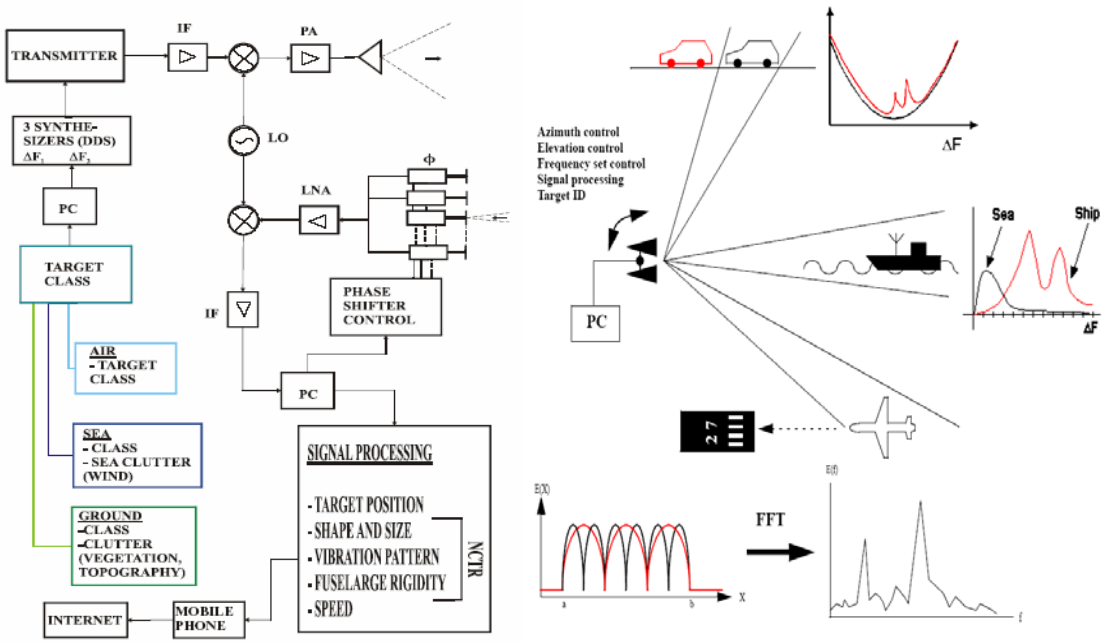

Figure 1: To the left in the figure is an overview of the system under developing. To the right the fundamental idea of operation of the system is presented.

Paper presented at the RTO SET Symposium on "Target Identification and Recognition Using RF Systems", held in Oslo, Norway, 11-13 October 2004, and published in RTO-MP-SET-080.

The multi frequency return can be processed linear or by non-linear ΔK. The author's organisation is developing a range gated radar system for multi frequency experiments for targets at air, sea and land. An overview of this system is given in figure 1. In our stepwise development of this system we execute experiments and simulations as to understand the fundamental theory and the possibilities for our system.

Office of Naval Research (ONR) is sponsoring parts of the work presented in this paper.

2.0 BASIC THEORY

2.1 Electromagnetic theory

When solving the basic scattering equations the following very simple relationship results after several approximations:

$$E(K) \sim \int \sigma(r) e^{-jK \cdot r} dr$$

Here $\mathbf{r}$ is the position vector, $\mathbf{K}$ the scattering wave number, σ the scattering cross section on voltage basis.

If the scatterers are distributed in space along the direction as a delay function $\sigma(\mathbf{r})$, the field strength as a function of wave number of the backscattered wave is the Fourier transform of this delay function. Hence, if we measure $E(K)$ (the received fields as function of wave number), we can find the spatial distribution of the target by an inverse Fourier transformation process:

$$\sigma(r) \sim \int E(K) e^{jK \cdot r} dK$$

The target can also be described in the $\Delta\mathbf{K}$ domain using an autocorrelation function

$$R(\Delta K) \sim e^{-j(\Delta K)z} \int R_{\sigma}(r) e^{jKr} e^{j(\Delta K)r} dr$$

Here z is the distance to the target. Different type of targets will have different autocorrelation function as seen in figure 2.

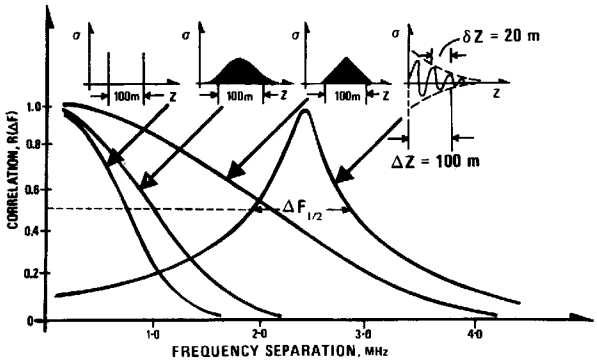

Figure 2: Different type of targets has different correlation functions.

2.2 DK processing

Linear processing of multi frequency data combines the different frequency components that are obtained in parallel or stepwise and gives range resolution through a Fourier transform of this.

In ΔK processing each frequency component is selected through narrowband filters. These frequency components are then multiplied with each other to form a set of ΔK timeseries. Using unequal spacing between the frequencies it is possible to obtain a higher number of unique frequency spacing than the number of frequencies used. For valid Coulomb rulers we obtain $N = \left[n(n-1)\right]/2$ frequency spacing by using *n* frequencies.

As a basic example of the ΔK processing we use a target that consist of two corner reflectors of unit amplitude spaced *z* meters apart in radial distance. The target moves at a given speed in outward radial distance. A timeseries for a single frequency component is given by

$$V_i = \exp\left(jK_i r_0\right) + \exp\left(jK_i r_1\right).$$

Here K_i is the scattering wave number for frequency component *i.* r_0 and r_1 the radial distance to the two scattereres, which is a function of time when the target moves.

A ΔK time series is found by multiplying two frequency components as

$$V_k conj(V_l) = \exp(j\Delta Kr)\left[1 + \exp(-jK\Delta r) + \exp(jK\Delta r)\exp(j\Delta K\Delta r) + \exp(j\Delta K\Delta r)\right].$$

Here *K* is the scattering wave number of the carrier, Δr the distance between the scattering elements, *r* the distance to the first scattering element and ΔK the difference wave number.

We see that the first term in the above equation, $\exp(j\Delta Kr)$, is recognized as the ΔK channel Doppler shift. This can be removed by mixing. The second term, $\exp(jK\Delta r)$, is dependant on the 'carrier frequency' and Δr. Since Δr is supposed be to unknown, we cannot predict this term. If Δr is vibrating sufficiently with time/range it is averaged to zero. The desired signature $\exp(j\Delta K\Delta r)$ lies in term 3 and 4. If the term $\exp(jK\Delta r)$ is not averaged the overall result is a signature that is a summation of the desired signature and a phase shifted version of it. Note that for non-vibrating objects it is possible to modulate the transmitted signal with a random phase shift or a frequency sweep to average out the unwanted interferences.

A simple simulation illustrates the dependence on the targets motion pattern. Our target consists of two identical reflectors spaced 10 meters apart in radial direction. The simulated carrier frequency is 3.4 GHz. The simulated target is at 8000 m range and moving 100 meter in one second. The separation between the scatterers is varying randomly within 4 centimeters in radial direction during motion. In figure 3 results form the simulation is presented in 9 subfigures. The subfigures are numbered from 1 in the upper left to 9 in the lower right. 1-6 are intensity plots with the y-axis as range/time and the x-axis as ΔF 0-25 MHz (left to right). The contents of the subfigures are:

1. Term 1, $\exp(j\Delta Kr)$, from the ΔK function. This is the ΔK Doppler signal. We clearly se that as the target moves the Doppler signal from the higher ΔK channels is of higher frequency.

2. Term 2, $\exp(jK\Delta r)$, from the ΔK function. As this term is dependant on the carrier wave number K and not the separation ΔK, there is no variation along the frequency axis. The randomness of the target element vibration, Δr, is seen along the y-axis.

3. Term 3, $\exp(j\Delta K\Delta r)\exp(jK\Delta r)$, from the ΔK function. We can se that the wanted signature is randomly shifted along the frequency axis.

4. Term 4, $\exp(j\Delta K\Delta r)$, from the ΔK function. This is the desired signature of the target.

5. The whole ΔK function. Through its randomness it is possible to view the contours of the ΔK signature.

6. The direct multi frequency function. Here the x-axis is frequency from carrier (left) up to carrier + 25 MHz (right). No particular signature is visible.

7. A time sample of one of the received channels.

8. The average in time/range of the signals the DK function (sub image 5, solid line) and the multi frequency function (sub image 6, dashed line). We can see that there is more coherent contribution to the signature when averaging over ΔK than over plain multi frequency.

9. The averages in sub image 8 have been normalized. The solid line is the desired signature of the target. The dashed line is the simulated ΔK signature and the dotted line is the multi frequency signature. We can se that the simulated ΔK signature nearly overlaps the expected signature whereas the plain multi frequency signature contains errors.

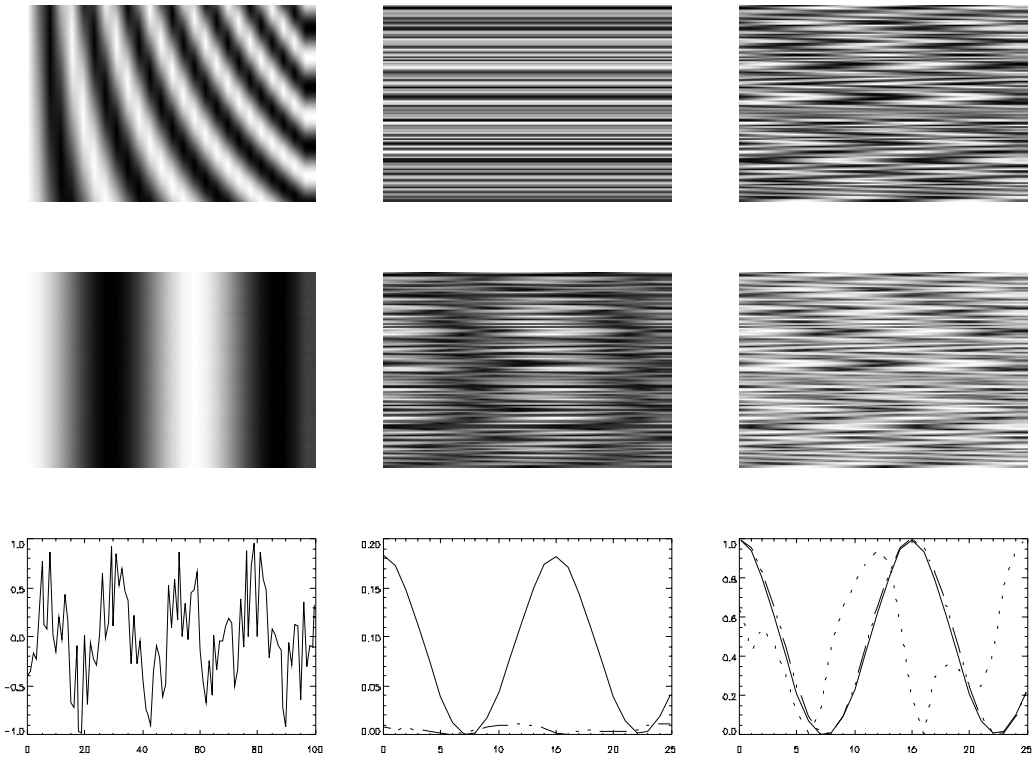

Figure 3: The subfigures are numbered [1,2,3] from left to right in the upper row, [4,5,6] in the middle row and [7,8,9] in the lower row. Each subfigure is commented in the text.

2.3 Delta K estimation error function

Setting the starting range to zero we can simplify the a single DK channel response to

$$V_k conj(V_l) = 2\exp(j(k_k - k_l)\Delta r)\left[\cos(j(k_k - k_l)\Delta r) + \cos(j(k_k + k_l)\Delta r)\right].$$

Here the target consists of two corner reflectors one placed at zero meters and one placed Δr in radial direction. k_k and k_l are the wave numbers of which the difference wave number in this example arises from. Investigating this equation we see that the first cosinus term represent the desired difference wave number amplitude, while the second term represents the rapidly fluctuating estimate error. We see that the latter expression depends on the sum of the wave numbers and the distance between the scattering elements.

In figure 4 this latter function is evaluated for two different carrier frequencies, increasing separation between the scattering elements and a carrier sweep.

Evaluating the subfigures in figure 4 we find

1. Error function evaluated for a carrier frequency of 5 GHz. As the distance between the scattering elements increases the error function rotates at a constant ratio defined by the sum of the wave numbers. As we sweep the carrier towards higher frequency, thus increasing the sum of the wave numbers the rotation ratio as a function of target element separation increases.

2. The same as subfigure 1 with 10 GHz carrier. We can se that the ratio of rotation as a function of range between the scattering elements has increased. This means that a vibration of less displacement than can average out the estimation error for using higher carriers.

3. We can se that using a carrier sweep to average out the estimation error the sweep length necessary depends on the distance between the target elements and not the carrier frequency.

4. The same as 3.

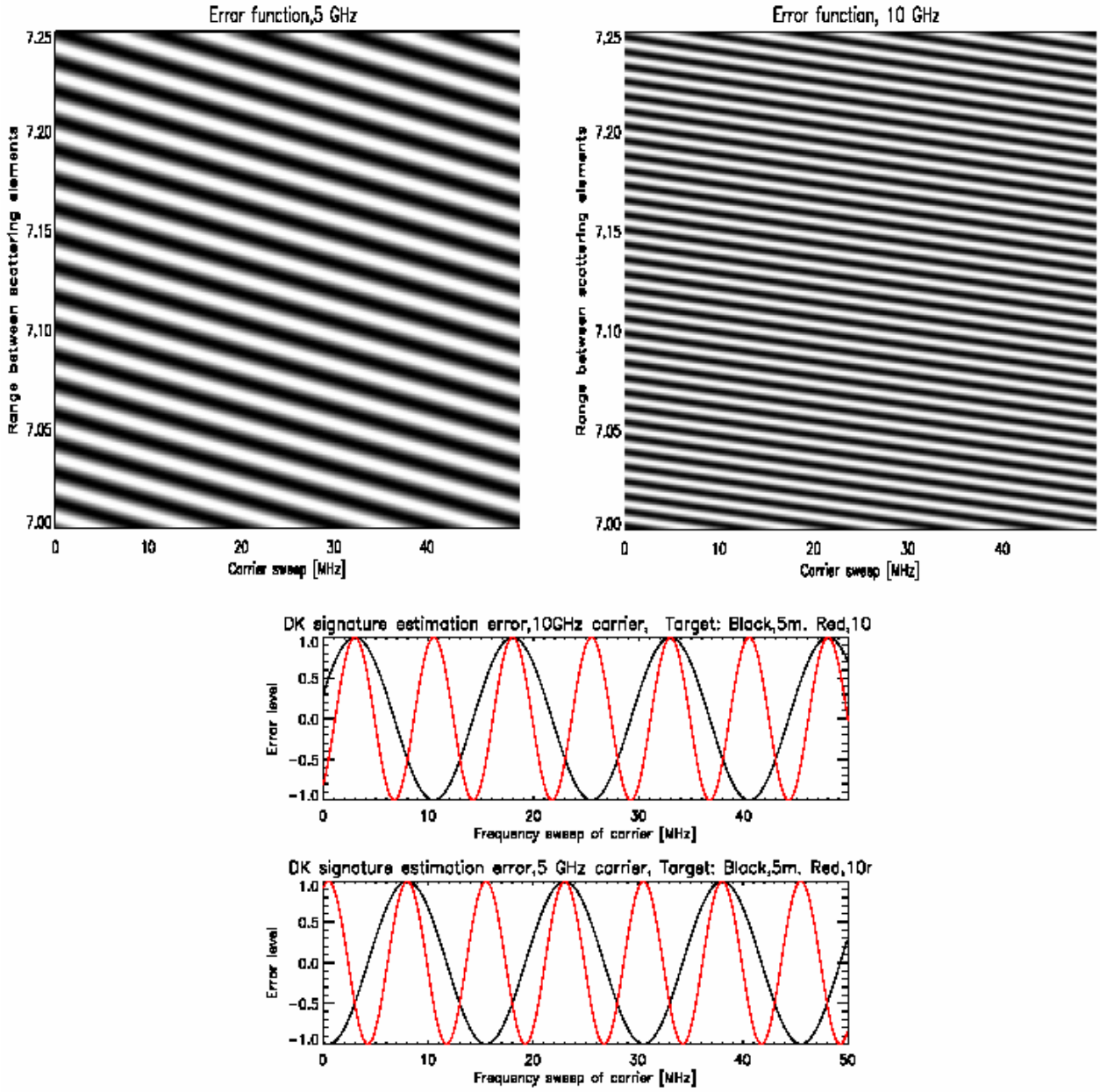

Figure 4: The subfigures 1 upper left 2 upper right, 3 middle and 4 lower are commented in the text.

3.0 CLUTTER VIEWED IN THE FREQUENCY DOMAIN

3.1 Sea surface clutter

The dominating sea surface gravity capillary wave is described by the basic wave equation

$$\omega = \sqrt{gK}$$

The phase velocity of this wave is then given by

$$v = \frac{\omega}{K} = \sqrt{\frac{g}{K}}$$

The dispersivity of this equation is seen in figure 5.

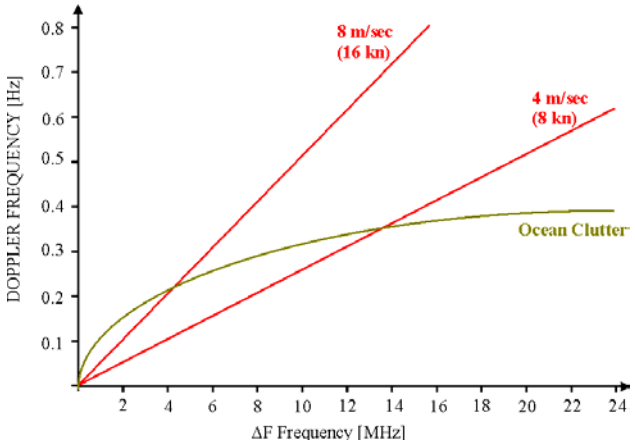

Figure 5: The dispersivity of the sea surface waves gives rise to a characteristic Doppler signature in the frequency domain.

Using the wind as the driving force this velocity cannot exceed that of the wind. Setting the phase velocity of the wave equal to the wind speed we can construct the minimum coupling wave number as

$$K_{\min} = \frac{g}{V_{vind}^2}$$

If EM waves have the same wave number they will couple to these ocean waves.

$$K_{EM} = K_{Ocean} = \frac{4\pi \sin(\theta/2)}{\lambda} = \frac{4\pi F \sin(\theta/2)}{c}$$

This equation leads us to a frequency (or difference frequency) that for maximum coupling to the wind driven waves as

$$F = \frac{cg}{4\pi V^2 \sin(\theta/2)}.$$

For backscattering the sinusoidal term equals unity. The same expression is valid for matching the ocean waves by ΔF by substituting F with ΔF in the equation.

Defining a 10dB width of this spectrum we can form a function that tells where the interaction between the EM waves and the sea surface waves is dominating. Avoiding these regions, as seen in figure 6, is essential for suppression of the sea surface clutter.

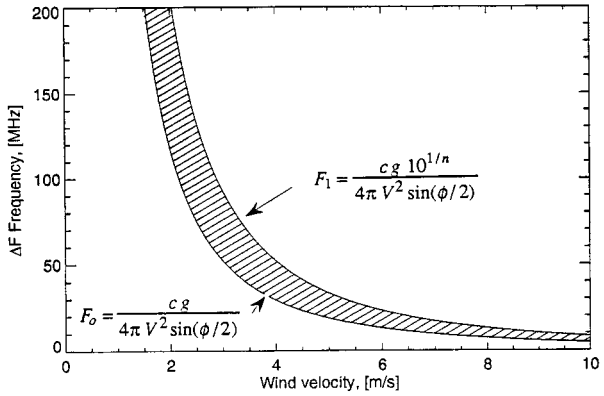

Figure 6 : Region of Interaction between EM waves and sea surface waves

3.2 LAND clutter

For many stochastic processes is popular to use the Komolgorov spectral function. Kolomgorov characterize randomly orientated scatterers in wave number space as $\Phi(K,\omega) = K^{-n}$ where n in most cases is -11/3. Applying this theory to a forest background we can use the dominating distance between the trees as the dominant scale. This is illustrated in figure 7, left. Dealing now with targets of rectangular shape that corresponds to a ΔK frequency signature of the form $\sin(x)/x$. This gives a signal to clutter structure as illustrated in the figure 7, right.

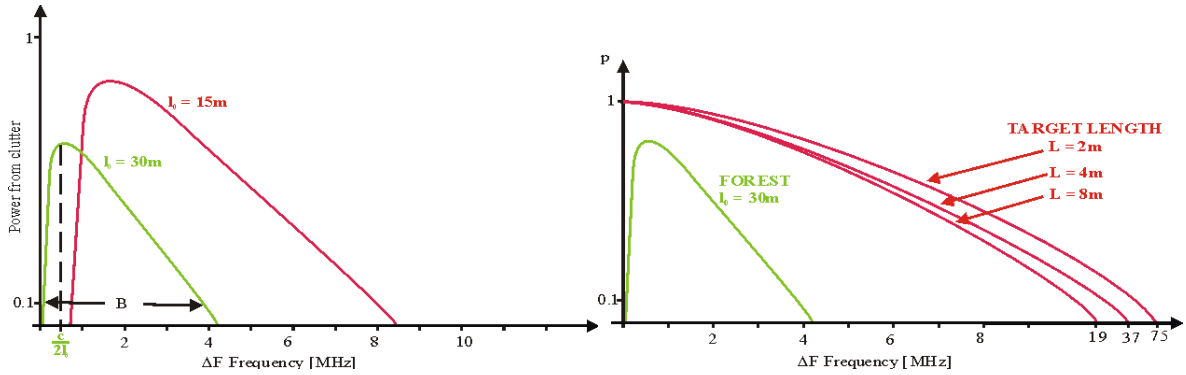

Figure 7: Left, two forests with different dominating spacing between the trees have different ΔK frequency signature. Right, a typical target of less length than the dominating clutter scale will have a larger bandwidth in the ΔK frequency domain.

4.0 EXPERIMENTAL VERIFICATION

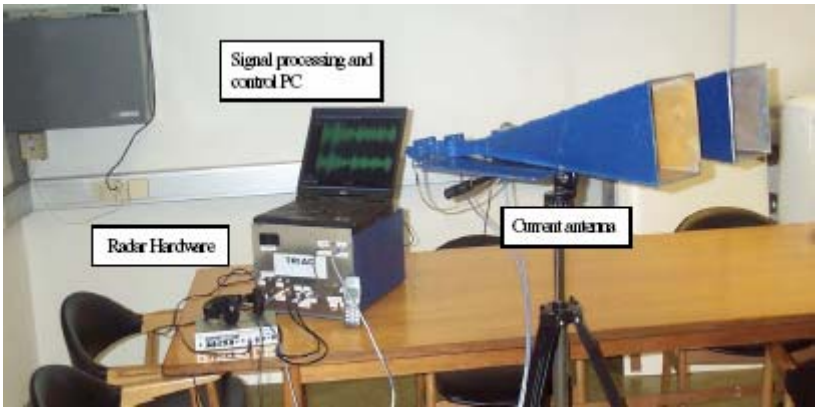

Figure 8: Experimental hardware.

Our experimental radar, which performs a subset of the system presented in figure 1, is seen in figure 8 and can be summarized by the following statements:

- Size of radar 20x30x40 cm
- Size of antennas 20x20cm aperture, 60 cm length
- Weight of radar with antennas appx 12 kilo
- Detection range for a target of $\sigma = 20m^2$ is 80 km
- Receiver noise factor 1 dB
- Transmitted power up to 10W cw

This experimental radar system was used in the experiments presented in the following subchapters.

4.1 Small boat

A boat with a length 5 meters was the target for a measurement campaign in the Oslo Fjord in Norway. One small corner reflector was mounted in the front of the boat and one in the stern. To frequencies were on the air simultaneously giving data to form one ΔK channel. The measurements were done in backscatter mode with the boat travelling in radial inwards direction. The experiment was repeated several times with different frequency settings to construct a ΔK signature.

The ΔK frequency signature of the target and the ΔK Doppler signature of the target can be seen in figure 9. We can see that the measured points fit well with the theoretical curves.

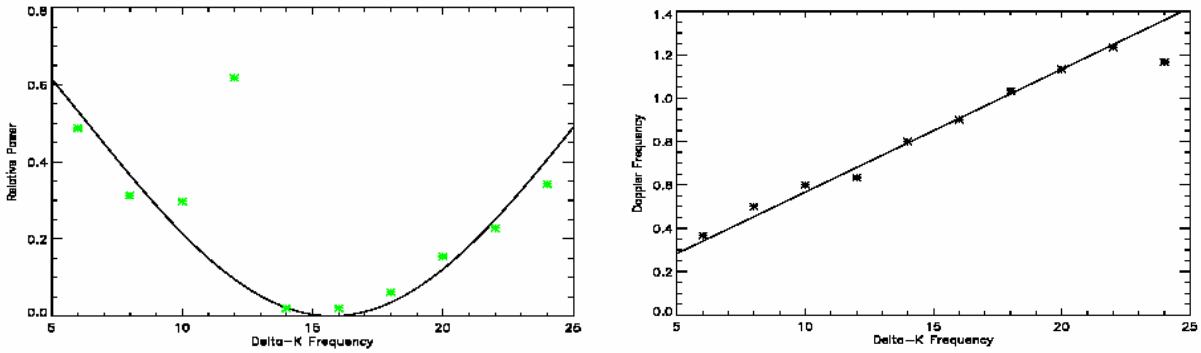

Figure 9: Left: Measured points of the ΔK signature of the target upon the theoretical curve for 5 m spacing. Right: Measured points of ΔK Doppler signature of the target upon the theoretical curve based on GPS measured speed

4.2 Detection and ID of land targets

4.2.1 Calibration

This experiment was conducted by the shore side of the lake Mjøsa in Norway. Two targets of corner reflectors with different spacing were towed on a rope in near radial direction. Transmitting 4 frequencies in parallel we towed each target several times with different frequency sets. Figure 10 presents the measured points from two runs for each target. We can see that the measured points fit well with the theoretical curve.

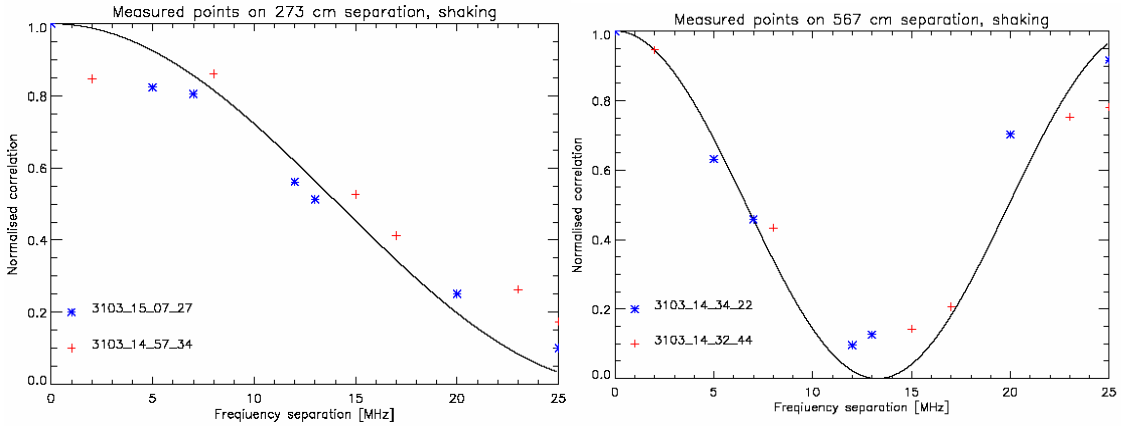

Figure 10: To the left is the signature of a target consisting of two reflectors spaced 275 cm in radial direction. To the right the spacing is 565 cm. Both targets were towed in near radial direction. The reflectors was vibration during motion

4.2.2 Cars with a forest background

This experiment took place at a road with a forest background. The distance to the target was 500 meters. Two cars of same length but of different shape were driving in near radial direction. In figure 11 we can se the difference in their signature.

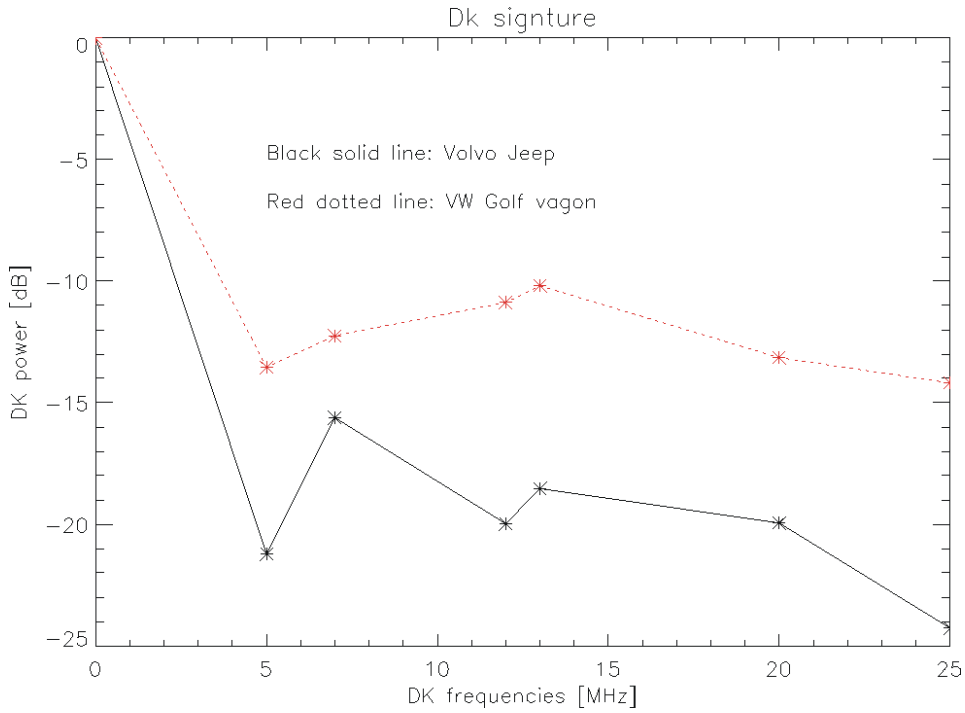

Figure 11: Measured signatures of a military jeep and a VW golf wagon.

4.2.3 ISAR

At the same site as for the calibration experiment two targets of corner reflectors where used in ISAR measurements. A single continuous wave frequency illuminated the corner reflectors that were sliding along a fixed rope.

We present here measurements of a two elements target. The first with a length of 565 cm and the second with a length of 275 cm. The measurements were done in backscatter mode with an aspect angle of 45 degrees. The different targets moved with the same speed and along the same path. Figure 12 displays the smoothed time series for a single channel for the 275 cm target and the same for the 565 cm target.

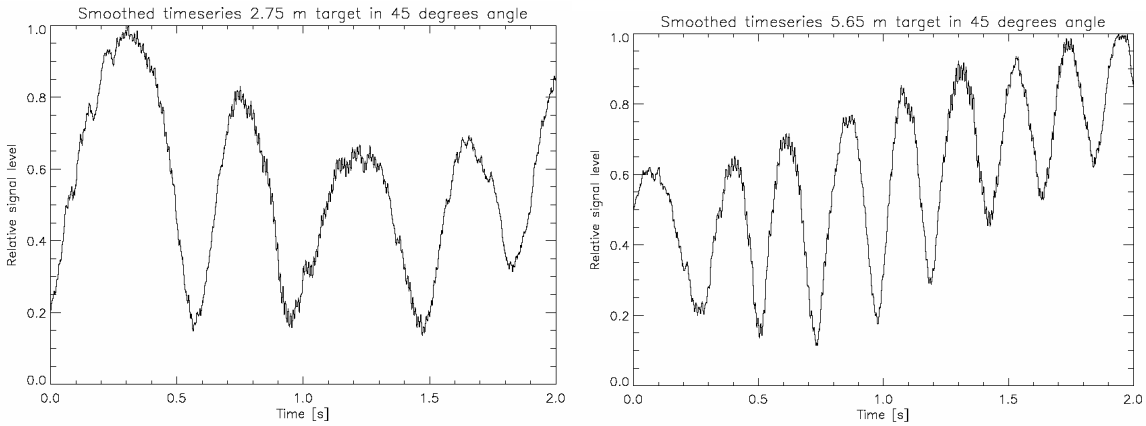

Figure 12: Smoothed time series of a cross range moving target of two corner reflectors spaced 2.75 m Left and spaced 5.65 m right

In figure 12 we can see that the different target lengths modulate the received signal with a different 'frequency'. Using a FFT we can find the frequency. This is presented in figure 13.

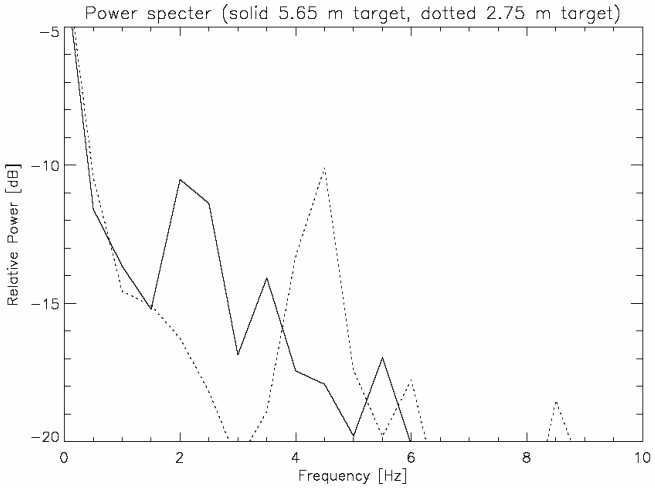

Figure 13: FFT of the ISAR time series. The solid line represents the target of 275 cm. The dotted line represents the 575 cm target. We see that as expected the dominating frequency of the 575 cm target is close to double that of the 275 cm target.

5.0 CONCLUSION

We have presented the fundamental theory around our experimental multi frequency system. From simulations we find the dependency on the target motion pattern to obtain valid results. The simple experiments presented reflect the theoretical values and is a good basis for more advanced measurements.

6.0 BIBLIOGRAPHY

[1] GJESSING, D.T.: 'Remote surveillance by Electromagnetic Waves for Air-Water-Land' (Ann Arbor: Science Publishers, 1978)

[2] GJESSING, D.T.: 'Adaptive Radar in remote Sensing' (Ann Arbor: Science Publishers, 1981)

[3] GJESSING, D.T.: 'Target adaptive matched illumination, principles and applications' (Peter Peregrinus IEE, 1986)

[4] HAYKIN, S.: 'Communication Systems' (WILEY, New York, 1983)

[5] ISHIMARU, A.: 'Electromagnetic Wave Propagation, Radiation, and Scattering' (PRENTICE HALL, New Jersey, 1991)

[6] ISHIMARU, A.: 'Wave Propagation and Scattering in Random Media, volume 2' (ACADEMIC PRESS, New york, 1978)

[7] STRATTON, J.A.:, 'ELECTROMAGNETIC THEORY' (McGraw-Hill, New York, 1941)

Robust Acquisition of Relocatable Targets

Hartmut Schimpf
FGAN Forschungsinstitut für Hochfrequenzphysik und Radartechnik (FHR)
D-53343 Wachtberg – Werthhoven, Neuenahrer Straße 20
GERMANY

ABSTRACT

Three target types, namely T72, ZSU 23-4 and BMP-2 were measured in a tower/turntable configuration in several articulations each. A set of geometric, statistical, structural and polarimetric features is used to study the robustness of classification. Based on the Kolmogoroff-Smirnov distance between histograms a metric is defined that at the same time allows to quantify intra-class robustness and inter-class separability for an individual feature. For sets of several features, a simple classification approach in connection with a reference confusion matrix allows to assess the robustness of classification. It is demonstrated, that averaging the feature reference over all available target articulations improves the classification performance as compared to a reference that is based on one articulation only. Also, it is shown that in most cases, the classification is the better the more precisely the target aspect angle can be estimated independently. -- The paper reports work that is done in the framework of the NATO RTO/SET-069 working group.

1 INTRODUCTION

Features are a means of statistical pattern recognition that ATR algorithms use to discriminate ground targets from the surrounding clutter background and, subsequently, to sort potential targets into one of several target classes (including the non-target case). Problems for ATR arise from the specular nature of radar imagery because small changes to the configuration of targets can result in significant changes to the resulting target signature [3][4]. This adds to the challenge of constructing a classifier that is both robust to changes in target configuration and target aspect, and which is capable of generalizing to previously unseen targets.

ATR features have to provide at the same time good inter-class separability and good intra-class stability. The reference vectors usually are obtained from former measurements of the respective target either on a turntable or by means of SAR and are stored in look-up tables. The test vectors are obtained on-line while the seeker is passing over the target area. In order for the ATR to provide reliable results both the test vectors and the reference vectors have to show **robustness** against target modifications, preferably including camouflage, different target realizations or articulations, slight changes in depression angle, aspect angle changes that occur during the time-on-target, and many more. Robustness has to be understood in the sense that the statistics of the test and reference vectors either remain unchanged, or that their changes are taken into account appropriately, and that the estimates that are obtained of these vectors are representative for this statistics. As a consequence, the classification performance should not be degraded. In order to obtain the desired robustness it is of great importance to eliminate those target variations that can be handled beforehand, the most crucial one being the aspect angle dependence. The analysis of tower/turntable measurements on typical targets shows that feature values as a function of aspect angle do not only fluctuate around a stable mean, but that their statistics themselves, i.e. mean and standard deviation, are a function of aspect angle. It has been demonstrated before [1][2] how important an independent determination of the target aspect angle is. Among the methods most commonly used are the Hough transform or a process of pattern matching [1] [5].

Paper presented at the RTO SET Symposium on "Target Identification and Recognition Using RF Systems", held in Oslo, Norway, 11-13 October 2004, and published in RTO-MP-SET-080.

Three different military vehicles were measured in a tower/turntable configuration at 35GHz with 800MHz bandwidth using the fully polarimetric MEMPHIS radar. Each vehicle was measured in several different articulations (hatches open or closed, turret turned to different positions) while its positioning on the turntable remained unchanged. All data underwent an identical polarimetric calibration to warrant optimal comparability.

As a means to assess feature robustness several metrics were developed to quantify the results. Two approaches are compared:

- the separability between feature histograms (using the Kolmogoroff-Smirnow distance as a distance measure)
- analysis of confusion matrices based on a generic classification scheme

Typical features of various types (geometric, statistical, polarimetric, scatterer power, structural etc.) are used, each one depending on one or two parameters that allow optimization.

The paper is organised in five sections. The first one gives a short description of the measurement setup. In the second, the features used for classification are described in some detail. Next, the relationship between robustness and inter-class separability is analysed. Section four shows how confusion matrices can be used to characterize robustness. Finally, some thoughts on the aspect angle behaviour of the features are presented.

2 MEASUREMENT SETUP

For the measurements that are analysed here, the FGAN operated fully polarimetric MEMPHIS radar [8] was located on top of a tower at a height of 47 meters. The three targets (T72, ZSU 23-4 and BMP) were positioned on a turntable at a distance of about 154m, giving rise to a slant range of 161m and a depression angle of 17°.

The MEMPHIS 35 GHz radar transmitted linear V polarisation, and received H and V simultaneously thus providing orthogonal VV and VH channels. The basic waveform is a linear chirp with 200 MHz bandwidth. In order to achieve higher range resolution, this chirp is combined with a stepped frequency mode with 8 steps of 100 MHz increment [9]. The resulting maximum processing bandwidth thus is 800 MHz. However, as this requires a 320-point DFT (2.5 MHz frequency sampling step), here only a reduced bandwidth of 640 MHz was processed allowing the use of a 256-point FFT. The resulting range resolution is about 0.24m which is sufficient for this kind of ATR analysis [10].

A full revolution of the turntable took place in 130 seconds, the effective PRF was $2300s^{-1}/8$ such that a 128-point Doppler FFT results in a cross-range resolution of 0.2m, sufficiently close to the desired square-pixel case. The targets were measured in the following configurations: the turret of the T-72 was positioned 20° to the left, and in 30° intervals from 0° (forward) to 180° (backward). In the case of the ZSU 4 different and of the BMP 5 different combinations of shut/closed driver's, commander's and turret hatches were realized, cf.[6].

3 CALCULATION OF THE CLASSIFICATION FEATURES

All feature values were computed on the basis of 2-D ISAR images with 0.24m (range) by 0.2m (cross-range) pixels. They were taken from a list prepared by the NATO SET-TG14 working group [7]. For geometrical, statistical, and structural features, the total power map ($|VV|^2 + |VH|^2$) was used, for the polarimetric features the VV and VH power map were used in parallel.

- ft1 = range extent of 20 strongest scatterers
- ft2 = cross-range extent of 20 strongest scatterers
- ft3 = ft1*ft2 (= area of the "minimum bounding rectangle" (MBR))
- ft4 = mean/std.dev.(total power|MBR)
- ft5 = (powersum 10 strongest scatterers) /powersum(MBR)
- ft6 = log10(pmax(1)/pmax(5)) (ratio between strongest and 5th strongest scatterer within the MBR)
- ft7 = log10(pmax(1)/pmin)|MBR (ratio between strongest and weakest scatterer within the MBR)
- ft8 = max(pvv/pvh)$|_{dB}$ - min(pvv/pvh)$|_{dB}$ (span of parallel/cross channel separation)
- ft9 = slope(pmax vs.dif)$|_{dB}$
- ft10 = shift(pmax vs.dif)$|_{dB}$

(in ft9 and ft10 "pmax" stands for the 10 strongest scatters within the MBR, sorted in descending order, "dif" contains the related channel differences pvv/pvh, shift and slope refer to a least squares line fit that is applied to these 10 pairs of values).

The rationale for the selection of this set of features is not that they constitute a "best" set. Rather they are considered to be a "generic" set with representatives from several feature types, namely geometric, statistical, scatterer power related or structural, and polarimetric. Of course, some of these features are more or less correlated with one another. This can be assessed either by determining all the mutual cross correlation coefficients, or by a principal component analysis (PCA, [11]). Therefore, only certain subsets out of these 10 features will form meaningful sets of ATR features.

4 INTRA-CLASS ROBUSTNESS VS. INTER-CLASS SEPARABILTY

The basic test of robustness is to analyse how strongly the feature statistics is changed when the respective target is modified. It is clear that each feature as a function of aspect angle will reflect any target modifications under those angles where they become effective. But in the ideal case, the overall statistics as measured over a certain aspect angle interval, should only slightly be affected, i.e. the probability density function (pdf) should be more or less the same.

There is a duality between intra-class robustness and inter-class separabilty. The more tolerant a feature or set of features or a classification scheme is towards different articulations of a certain target type, the less likely it is to precisely discriminate between a large number of different target types.

A convenient way to compare two probability density functions (pdf's) or histograms is by determining the Kolmogoroff-Smirnov distance (KSD) which is defined as the maximum difference between the two pertinent cumulative distributions:

Let $p_1(f)$ and $p_2(f)$ be two probability density functions (pdf's) of a certain feature "f" obtained from two different vehicles. The pertinent distribution functions then are

$$P_i(f) = \int_{-\infty}^{f} p_i(f')df' \quad (i=1,2)$$

and hence

$$KS(p_1, p_2) = \max_f |P_1(f) - P_2(f)|.$$

By definition, the KSD can vary between 0 and 1, where "0" means identity, and "1" means complete separation without any overlap.

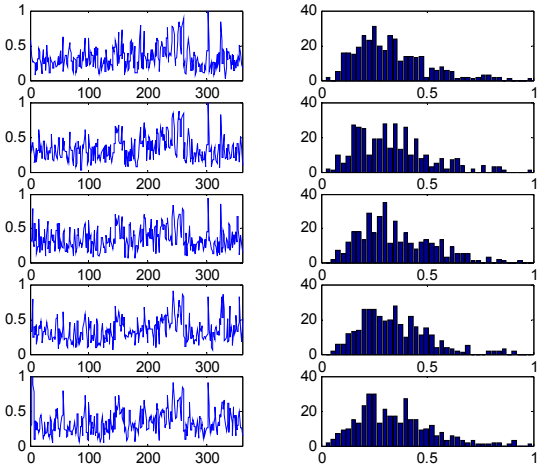

Figure1 plot of feature #6 vs. aspect angle, and related histograms for5 articulations of the BMP

Fig. 1 shows as an example the power feature #6 for the five different articulations of the BMP. As one sees, the polar curves in some cases may differ considerably e.g. in the interval 80° to 120° or near 330°. However, the histograms look rather similar. Thus, at first sight this seems to be a candidate for a robust feature.

On the other hand, robustness is only one criterion that an ATR feature has to fulfill. Good discrimination w.r.t. other targets is another important one, and both properties have to be examined and eventually a trade-off has to be made.

Let us now quantify the similarity between the pdfs of different target articulations by means of the KSD. This is best done using a table that lists all possible combinations of pairs of targets for a selected feature. Let us again look at feature #6 (Table 1). The KSD between pairs of different T72 are fairly low, mostly less than 0.1 with some outliers up to 0.144, which suggests a few major differences.

For pairs of ZSU or BMP, values are below 0.086 and hence close to zero as required. In the areas that are dark grey-shaded we have pairs of different target types. Here, in the ideal case we would expect values close to 1, i.e. complete separation. Of course, this is not the case, rather the values are around 0.2, hardly above 0.23. This is certainly not satisfactory, but one has to keep in mind that the classification will not be done with only one feature but that one will go to higher dimensions of the feature space where less overlap is expected.

The dark shaded areas of the triangular matrix K is where KSD values close to "1" are expected, all others should be close to zero. If we define a reference matrix R which contains only the desired values 0 or 1 in the appropriate positions, then the quality of a feature can be judged by computing the distance between the actual matrix and the reference matrix.

	T72b	T72c	T72d	T72e	T72f	T72g	T72h	ZSUa	ZSUb	ZSUc	ZSUd	BMPa	BMPb	BMPc	BMPd	BMPe
T72a	0.052	0.108	0.041	0.069	0.061	0.044	0.061	0.136	0.088	0.111	0.113	0.180	0.144	0.138	0.136	0.127
T72b	0	0.091	0.047	0.066	0.047	0.077	0.069	0.119	0.075	0.091	0.116	0.227	0.180	0.161	0.169	0.161
T72c	0	0	0.113	0.122	0.108	0.122	0.144	0.097	0.116	0.1	0.072	0.247	0.208	0.186	0.211	0.205
T72d	0	0	0	0.055	0.052	0.075	0.072	0.136	0.1	0.108	0.113	0.2	0.175	0.158	0.144	0.144
T72e	0	0	0	0	0.077	0.083	0.083	0.15	0.102	0.125	0.144	0.216	0.175	0.169	0.163	0.172
T72f	0	0	0	0	0	0.077	0.077	0.108	0.069	0.094	0.097	0.205	0.186	0.147	0.166	0.166
T72g	0	0	0	0	0	0	0.05	0.15	0.113	0.119	0.136	0.177	0.133	0.116	0.122	0.102
T72h	0	0	0	0	0	0	0	0.166	0.127	0.144	0.147	0.194	0.161	0.136	0.141	0.133
ZSUa	0	0	0	0	0	0	0	0	0.072	0.041	0.036	0.227	0.225	0.202	0.233	0.211
ZSUb	0	0	0	0	0	0	0	0	0	0.05	0.063	0.222	0.202	0.172	0.197	0.175
ZSUc	0	0	0	0	0	0	0	0	0	0	0.069	0.222	0.213	0.177	0.205	0.186
ZSUd	0	0	0	0	0	0	0	0	0	0	0	0.222	0.216	0.172	0.211	0.188
BMPa	0	0	0	0	0	0	0	0	0	0	0	0	0.061	0.086	0.080	0.080
BMPb	0	0	0	0	0	0	0	0	0	0	0	0	0	0.086	0.077	0.063
BMPc	0	0	0	0	0	0	0	0	0	0	0	0	0	0	0.055	0.063
BMPd	0	0	0	0	0	0	0	0	0	0	0	0	0	0	0	0.038

Table 1 KSD between pdf's of all 17 targets for feature #6

$$d = \sqrt{\frac{2}{17 \cdot 16} \sum_{i<j} \| K - R \|^2} \qquad (1$$

Table 2 shows an example. The smaller this value is, the closer the measured matrix is to the reference. Taking this metric, the range extent (feature 1) performs best.

However, this single value does no longer allow to differentiate between robustness and separability. Robustness is the better the closer the intraclass KSD are to zero, and separability is the better the closer the interclass KSD are to 1. One can therefore average all intraclass KSD (resulting in K_0) and all interclass KSD (resulting in K_1) and plot the results in K_0-K_1-coordinates (fig.3). The closer a feature is located to the point (0,1) the better its performance will be [6].

Feature #	d
1	.55
2	.68
3	.583
4	.647
5	.635
6	.695
7	.638
8	.758
9	.68
10	.68

Table 2 mean difference "d" between matrices K and R

As one sees from the definitions of the classification features, they all depend at least on one free parameter. First of all this is the number of scatterers (N_{sc}) that is is used to create the MBR on which all subsequent computations are performed. N_{sc}=20 was used for most of the analyses presented here. In addition, feature #5 uses a subset of scatterers within the MBR (here 10 out of 20), and feature #6 is the power ratio between the strongest and 5th-strongest scatterer within the MBR, thus introducing a second parameter for each of them. One can think of using these free parameters in connection with either the reference matrix described above, or the point (0,1) in the K_0-K_1-plane to somehow optimize the features. The values that were used in the original definitions may seem somewhat arbitrary and need a justification. Let us begin with the reference matrix and the related distance measure (1). If we vary the common parameter N_{sc}, we can consider d=d(N_{sc}) and try to find a minimum in a certain reasonable interval. Fig.2 shows d(N_{sc}) for all 10 features where N_{sc} was varied between 10 and 30. As one sees, there is almost no dependence on N_{sc}, features 1,3,4,5,7,9,10 show a very small decrease of d(N_{sc}) with increasing N_{sc}, features 2 and 8 show an increase of d(N_{sc}), and #6 is not influenced at all. From this one cannot get a clear recommendation towards a certain value of N_{sc}.

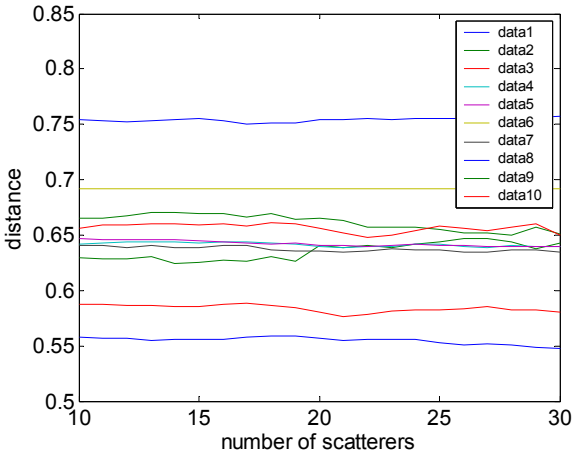

Figure 2 distance between K and R for varying N_{sc}

Because d(N_{sc}) cannot distinguish between robustness and separability, we now want to look to K_0 and K_1 which describe these two properties individually. Fig.3 shows how each feature moves in the K_0-K_1-plane when N_{sc} is varied between 10 and 30. The starting point (N_{sc}=10) is marked by 'o' while the final point is marked by '*'.

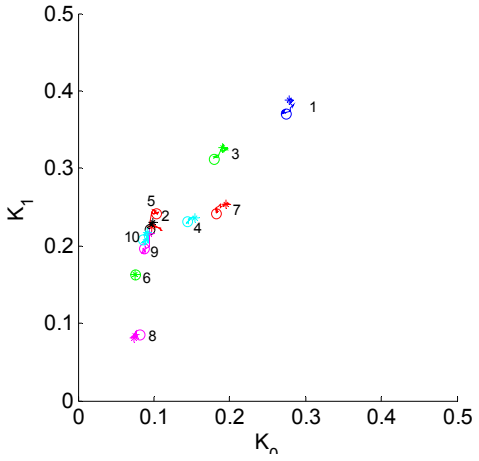

Figure 3 K_1 vs. K_0 for varying N_{sc}, features 1 - 10

What we hope to find is a tendency to approach K_0=0 and K_1=1. However, none of the 10 features follows this pattern. Rather, K_0 and K_1 both tend to increase with increasing N_{sc} (features 1,3,4,7,9) or are almost constant (features 6 and 8). Obviously, it is not possible to push K_0 beneath a value of ≈0.08. As one recognizes, none of the 10 features comes close to the desired locus (0,1) in the K_0-K_1-plane for values of N_{sc} between 10 and 30. One must conclude that N_{sc} offers only a very limited optimization potential for the 10 features under consideration. It seems as if the 10 features as defined above do not reflect sufficiently the geometrical and scatterer structure of the targets and therefore are too insensitive w.r.t. N_{sc}.

5 CONFUSION MATRICES

Another means to assess feature robustness is to apply a generic classification scheme to the available data and determine the probabilities of classification (P_c) which can either be probabilities of correct classification (P_{cc}) in the case of the like target class, or probabilities of false alarm (P_{fa}), for the other target classes. This classification is performed for certain sets of features. For this purpose one has to create reference feature vectors (or training data) for all available targets or target types. Then a target under test is chosen, a test feature vector determined, and the Euclidian distance

$$d_{eukl}(\alpha) = \sqrt{\sum_{i=1}^{N} \frac{(f_i(\alpha) - F_i^{ref}(\alpha))^2}{\sigma_i^2}}$$

in feature space computed between this test vector and all reference vectors. The target under test for this special feature vector then gets the label of the reference target to which its distance is minimum. This is repeated for a large number of test vectors of the respective target under test (either from a limited aspect angle interval or - as in our examples - from all aspect angles between 0° and 360°), the scores being summed up for all reference categories. The P_c values finally are determined as the ratio between the individual scores and the total number of test vectors. In this simple implementaion, we can talk of a "forced decision classifier" because the non-target case is not taken into account.

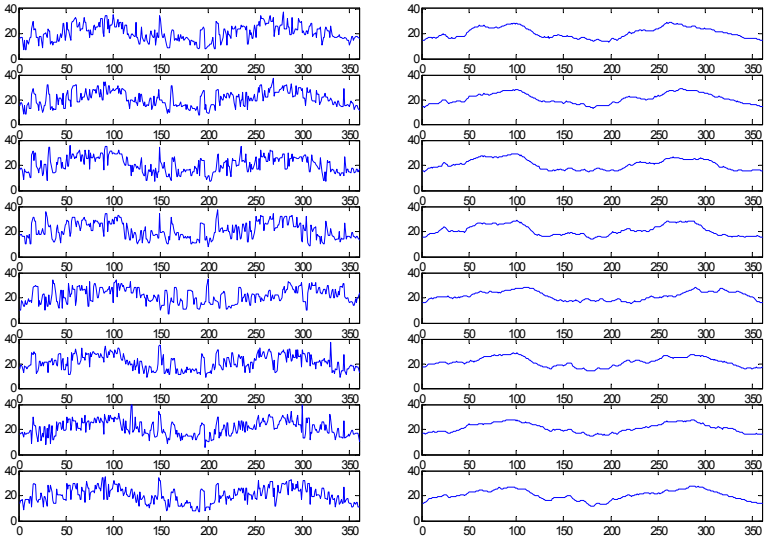

Figure 4: Feature 2 (cross-range extent for 8 T72, test values (left) and reference values (right)

Out of the 10 features analysed here, subsets of only a few of them were formed for classification purposes. The main requirement for feature selection is that they carry independent information, i.e. are statistically independent. There are several ways to achieve this goal. A common one is the principal component analysis (PCA, [11]) where, dependent on the eigenvalues of the covariance matrix, only the most "meaningful" features or linear combinations of features are retained. Another, simpler way is to determine the cross-correlation coefficients for all possible pairs of features, and then select only those sets that are essentially uncorrelated. The feature sets analysed in the following are the result of this latter procedure.

How can one create reference feature vectors? For this purpose we refer to results from former analyses [1][12] that demonstrated the importance of an independent determination of the orientation of the target under test. Thus, comparison has only to be done to reference feature vectors out of a limited aspect angle interval instead of [0°, 360°] which considerably increases the classification performance. An achievable value for the precision of pose estimation is 10° to 20° or even better. Therefore, for the present analysis, a sliding window averaging was applied to the original features over a ±10° interval with respect to each aspect angle thus creating the pertinent reference value. Fig.4 shows the effect of this averaging. The

dependence of the classification result on the width of this interval, i.e. the precision with which the aspect angle can be determined, is analysed in [13].

Feature #1	Reference target class		
Test target ↓	T72	ZSU 23-4	BMP2
T72	39.7±12.6	35.8±14.0	24.4±10.2
ZSU 23-4	27.4±13.6	55.5±16.9	17.2±9.5
BMP2	26.0±15.0	20.1±11.3	53.8±19.6

Feature #2	Reference target class		
Test target ↓	T72	ZSU 23-4	BMP2
T72	47.3±5.3	26.9±5.0	25.8±4.4
ZSU 23-4	31.7±5.0	39.8±7.2	28.6±3.5
BMP2	31.2±3.7	24.3±4.4	44.6±4.1

Table 3 Means and standard deviations of P_c values (%) for range extent (#1) and cross-range extent (#2)

We have now at our disposition a total of 17 test targets (8 T72, 4 ZSU, 5 BMP) and 17 references, accordingly. If we want to construct a confusion matrix, we have to choose a triplet of test targets out of the three target classes, as well as a triplet of references. For each triplet we have 8·4·5=160 ways to choose from the given data, hence 160·160 ways to obtain a confusion matrix. It is not reasonable to perform all possible combinations, though. Instead, for a total of 500 randomly generated combinations, the confusion matrices were computed and the means and standard deviations of all matrix elements determined. By definition, the main diagonale of the confusion matrix contains the P_{cc} values whereas the off-diagonale values represent P_{fa}. All lines sum up to 100%. The P_c standard deviations can be used as another measure of robustness. The smaller they are the less sensitive the classification process is to different articulations of a target, and to the influence of selecting test and reference targets.

As an example (table 3) let us consider the geometrical features #1 (range extent) and #2 (cross-range extent). Ft.1 performs quite well in the case of the ZSU and the BMP, but almost fails for the T72. Ft.2, on the other hand, performs well for the T72 and the BMP, but less well for the ZSU. What is striking, however, are the standard deviations, which are in the range of 4%-7% for ft.2, but between 11% and almost 20% for ft.1! Obviously, the range extent is less stable and reliable and consequently less robust than the cross-range extent. This is due to self-masking (shadowing) effects that cause scatterers at the rear parts of the target to be invisible under many aspect angles. This confirms results from former analysis [14].

Ft. set #1	Reference target class		
Test target ↓	T72	ZSU 23-4	BMP2
T72	50.0±8.0	25.5±6.0	24.5±5.2
ZSU 23-4	28.9±9.4	49.8±14.7	21.3±6.2
BMP2	22.1±4.2	20.1±3.9	57.8±5.0

Ft. set #2	Reference target class		
Test target ↓	T72	ZSU 23-4	BMP2
T72	48.3±12.5	28.5±12.2	23.2±8.4
ZSU 23-4	24.3±14.9	59.3±20.4	16.4±8.4
BMP2	26.9±15.0	15.4±9.6	57.6±19.4

Table 4 Means and standard deviations of P_c values (%) for feature set #1 (fts.2,6,8,9) and set #2 (fts.1,5,7,8,9)

The second example (table 4) deals with sets of features instead of individual features. Set #1 consists of features 2,6,8,9, set #2 consists of features 1,5,7,8,9. Both show comparable performance for the T72 and the BMP, set #2 yields 10% higher P_c for the ZSU. However, set #2 has much higher standard deviations, especially for the P_{cc}(ZSU) the value is 20% which reflects a lack of reliability of the result. It may be excellent, but it may as well be insufficient, depending on the random choice of the test and reference sets. This striking difference may be due to the use of feature 1 in set #2, and of feature 2 in set #1.

Another approach to assess classification robustness is suggested by a former result [6] which states that the most stable reference (which is not necessarily the one with the best performance) is obtained by averaging the references from all available articulations of a certain target class. We will analyse this result a little more in-depth. Averaging the 8 references of T72, 4 of ZSU and 5 of BMP results in one overall reference triplet (designated by ORT). Without averaging, we can define a total of 8·4·5=160 different reference triplets as pointed out earlier. Thus we can obtain a total of 161 confusion matrices of

size 17 x 3 if we test all 17 targets against all possible reference triplets. We then want to compare the 160 cases of individual reference triplets (IRT) with the ORT case.

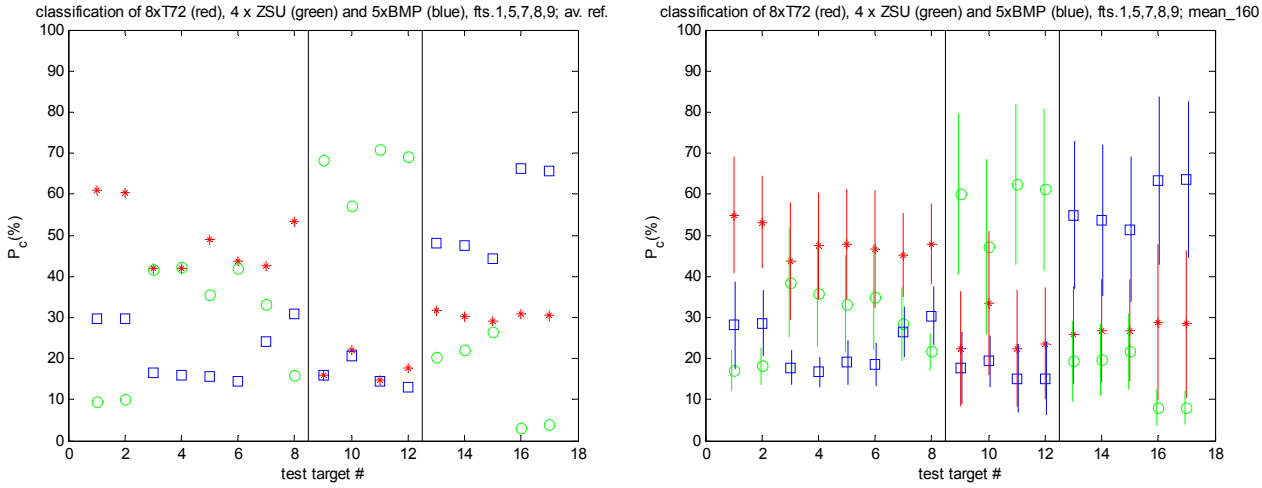

Figure 5 ORT (left) vs. <IRT> case for set of features 1,5,7,8,9

As an example we show the case of a feature set consisting of features 1,5,7,8,9. Fig.5 shows on the left side the ORT case, on the right side the <IRT> case, i.e. mean±std.dev. from all 160 combinations. On the abscissa we have the 17 test targets, subdivided by vertical lines into three classes. The ordinate represents P_c(%). We see that all 17 test targets get the highest score in their respective class, although in two cases (ORT, T72 #3 and #4) the results are very tight w.r.t a possible misclassification as ZSU. For the ZSU, the ORT results are better than the IRT average, but the large std.dev. indicates that there are IRT combinations that outperform the ORT case. For the BMP there is no clear tendency: the "weak" cases (#13,14,15) get weaker with ORT, the "strong" cases (#16,17) get stronger. For the T72, only #1,2 and 8 show an advantage for ORT, for the remaining articulations, the IRT shows a larger P_c-difference to a possible ZSZ misclassification.

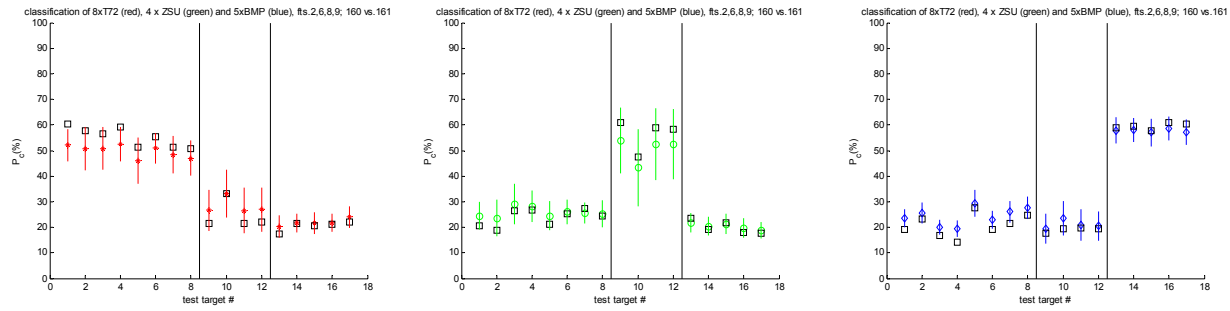

Figure 6 <IRT> results for T72 (left), ZSU(center) and BMP(right), set of features 2,6,8,9

An easier comparison is shown in fig.6, this time for a feature set consisting of fts.2,6,8,9. The diagrams show the results of testing against the T72 reference (left), the ZSU reference (center) and the BMP reference (right). The <IRT> results are indicated by their respective symbols and color, including ±1σ-error bars. The pertinent ORT results are marked by black squares. In all 17 cases, the ORT results are better than the <IRT> results, although only slightly for the BMP. – After looking in many more examples of individual features and sets of several features one may summarize that in the "robust" cases (characterized by small standard deviations) the ORT is to be preferred to the IRT, whereas in less robust cases IRT may be better, although a clear tendency is often missing. Also, one can state that the classification results in the ORT case become more homogeneous, i.e. each articulation is recognized with essentially the same probability, as was already found in [6].

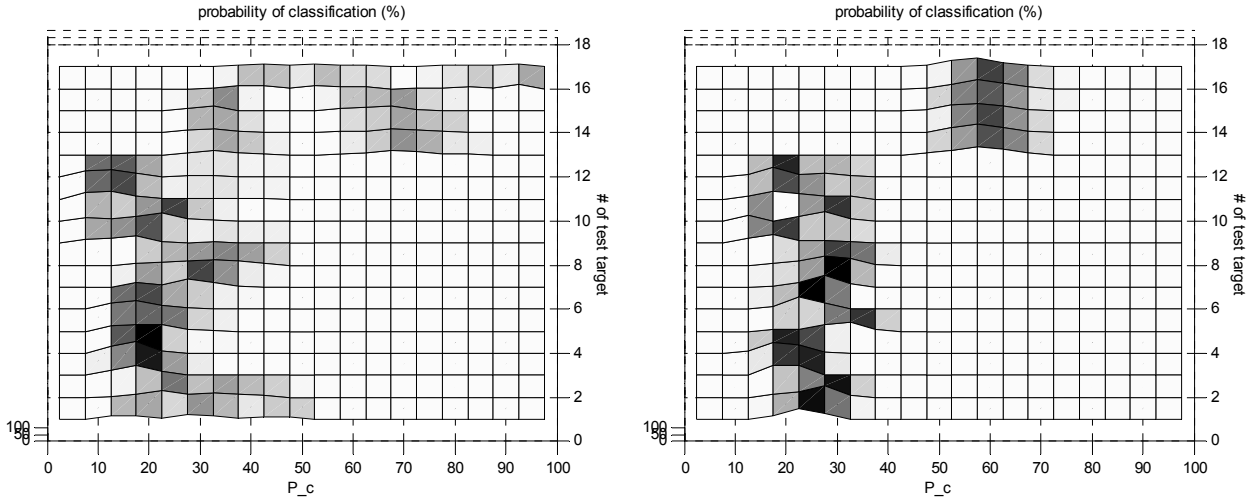

Figure 7 greyshade histograms of classification probabilities for two feature sets

It is interesting to look not only at the mean and standard deviation of the 160 IRT cases but also to study their complete histograms (fig.7). These are represented by grey-shading where 'black' means highest frequency of occurrence. We compare the two feature sets 1,5,7,8,9 (left) and 2,6,8,9 (right) where the reference in both cases is the BMP. The abscissa represents the P_c(%) values, the ordinate shows all 17 test targets. Set #1 shows some strange phenomena: first, the histograms for test targets #13-16 are bimodal, i.e.there is one group of cases with P_c up to 60-80%, another group, where P_c is only around 30% which means no classification at all. Second, the histogram in the case of test target #17 is smeared almost uniformly between 40% and more than 90%. Clearly, this set of features is not robust because it does not provide reliable and reproduceable results. Picking a random set of references can mean anything from success to failure. On the other hand, set #2 shows narrow and well defined histograms which indicate reproduceability and robustness.

6 CONSIDERATIONS OF ASPECT ANGLE DEPENDENCE

We want to conclude with some thoughts on the aspect angle dependence of classification features. For certain features, especially geometric ones like range and cross-range extent, it is clear that they will vary as a function of aspect angle. For others, like statistical or polarimetric features, it is not clear what behaviour to expect, although an aspect angle dependence should be anticipated in every case.

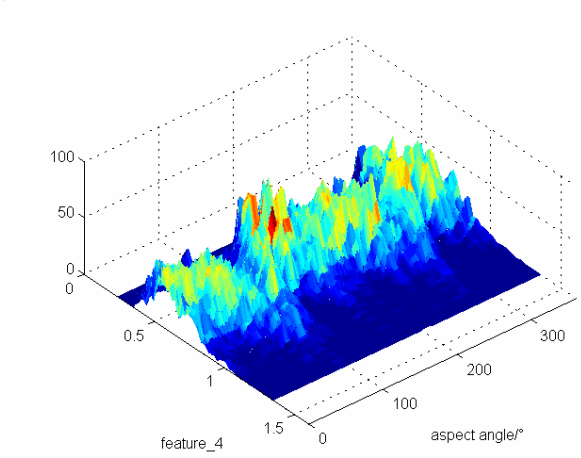

Fig.8 feature #4 histograms for sliding windows

An example is shown in fig.8 where a typical statistical feature (f4) is represented. F4 is defined as the ratio between mean and standard deviation of the 20 strongest scatterers belonging to the target, its area being declared to be the "minimum bounding rectangle" (MBR) within each 2-d ISAR image. These ISAR images are processed with angular increments of about 1/40 of a degree (as a cross-range resolution of 0.2m at 35GHz requires an angular increment of 1.2°, this means overlapping ISAR processing). Thus, an aspect angle interval of 12° which may be assumed to be a typical value for the precision with which the target orintation can be determined, gives rise to about 500 templates. The resulting feature values are transformed into a histogram which represents the f4 statistics at the respective aspect angle. Fig.8 shows the full series of histograms between 0° and 360°. As one sees, the statistics of f4 is by no means constant.

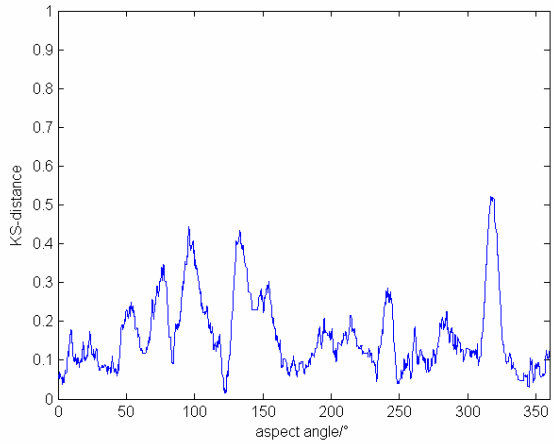

Fig.9 KS distance between global and local f4 pdf's

Fig.9 shows this KS distance between the overall pdf of f4 (out of 360°) and the "local" pdf's as a function of aspect angle. The deviation in this example can be as high as 0.5!

How does this aspect angle dependence influence the target recognition process? For each potential target, a reference vector has to be established in a multi-dimensional feature space. These reference vectors normally are derived from tower/turntable or spot SAR measurements if available. The target that has to be classified provides a test vector (or a series of test vectors during the time-on-target) that now is compared to the available reference vectors. A certain distance measure in feature space is defined, and the reference which is closest to the test vector determines the target class.

Now, if no information is available on the target orientation and the variability of the respective feature statistics, the reference vector has to be determined from the [0°, 360°] interval with no preferred aspect angle. Consequently, this reference can be unnecessarily far away from the true reference that would apply for the present target aspect. This could result in a misclassification and hence a degradation in performance.

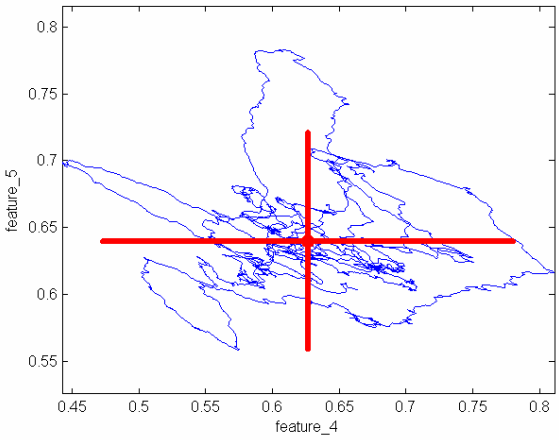

Fig.10 behaviour of features 4&5 references between 0° and 360°

This effect is demonstrated in fig.10. As a simple example, a 2-dimensional feature space is shown defined by f4 as above, and f5, where f5 is the fraction of backscatter energy that is contained in the 20 sttrongest scatterers as compared to the total energy within the MBR. The red cross marks the overall (i.e. averaged over 360°) reference vector with the pertinent standard deviations "σ" of features f4 and f5. The irregular line shows the behaviour of the "local" reference as a function of aspect angle, where each local reference is averaged over a sliding 12° interval. As one sees, the aspect angle dependent reference vectors can lie far outside the 1σ-ellipse around the overall reference vector so that using the latter clearly may lead to erroneous classification. All this underlines the importance of an independent determination of the target orientation to initialize the ATR process, as was already found in former analyses [1][2][5]. More details can be found in [13].

7 SUMMARY AND CONCLUSIONS

Three target types, namely T72, ZSU 23-4 and BMP-2 were measured in a tower/turntable configuration in 8, 4 and 5 articulations, respectively. Based on 2-D ISAR images in the VV and VH channel, a set of 10 geometric, statistical, structural and polarimetric features was calculated which was used to study the robustness of classification. The Kolmogoroff-Smirnov distance measure between histograms (pdf's) was used to define a metric that at the same time allows to quantify intra-class robustness and inter-class separability for an individual feature. For sets of several features, a simple classification approach in connection with a reference confusion matrix allows to assess the robustness of classification. At the same time this reference matrix can be used to maximize robustness by varying the free parameters of the feature definitions such that the difference of the measured confusion matrix with respect to the reference matrix is minimized. It was found that the number of scatterers N_{sc} does not offer a good potential for optimization.

As former analysis has shown the importance of an independent pose estimation of the target under test, reference feature vectors were computed as sliding window averages over +/-10° aspect intervals. It could be demonstrated further, that averaging this reference over all available target articulations improves the classification performance as compared to a reference that is based on one articulation only.

The set of 17 measurements was used to establish a statistics of the confusion matrices. The standard deviations of the P_c values vary widely depending on the type of feature or feature set. They lend themselves to be used as another metric to characterize robustness.

Finally, it was demonstrated that the feature statistics may be strongly dependent on the aspect angle of the target. As a consequence, the ATR performance has to be improved by independently determining the target orientation, e.g. by means of a Hough transform or pattern matching.

8 REFERENCES

[1] **A.C.van den Broek, R.J.Dekker, W.L.van Rossum, A.J.E.Smith, L.J.van Ewijk,** Feature Extraction for Automatic Target Recognition in High Resolution and Polarimetric SAR Imagery, TNO Report FEL-00-A236, Den Haag, Feb.2001

[2] **H.Schimpf**, Automatic Recognition of Military Targets using High Resolution Signatures at mmw frequencies, NATO RTO Symposium "High Resolution Radar Techniques", Granada, Proceedings MP-40, Nov.1999

[3] **Guy T.Maskall, Andrew R.Webb**, Nonlinear feature extraction for MMW image classification: an unsupervised approach, SPIE 2002

[4] **Adrian Britton, Keith D. Copsey, Guy T. Maskall, Andrew R. Webb and Karl West,** Nonlinear feature extraction and Bayesian mixture model approaches to target classification using MMW ISAR imagery: a preliminary study, SPIE Proc.**4033** #14, Orlando, April 2000

[5] **Albertus van den Broek, Rob Dekker, and Philippe Steeghs,** Robustness of Features for Automatic Target Discrimination in High Resolution Polarimetric SAR Data, SPIE Proc.**5094** #34, Orlando, April 2003

[6] **Hartmut Schimpf**, Millimeter Wave ATR - A Study on Feature Robustness, SPIE Proc.**5426** #28, Orlando, April 2004

[7] **NATO-RTO/SET/TG.14 and SET-069 Research and Study Groups**, List of features for Automatic Target Recognition, unpublished

[8] **H.Schimpf, H.Essen, S.Boehmsdorff, T.Brehm,** MEMPHIS – a Fully Polarimetric Experimental Radar, Proc.IGARSS 2002, Toronto, Canada, June 2002

[9] **H.Schimpf; A.Wahlen, H.Essen,** High range resolution by means of synthetic bandwidth generated by frequency-stepped chirps, El.Letters, **39**,18, pp.1346-48, Sept.2003

[10] **L.Novak,** Automatic Target Recognition using enhanced resolution SAR data, IEEE AES-35, pp.157-175 (1999)

[11] **R.O.Duda et.al.,**Pattern Classification, 2nd ed., , chapter 3, Wiley 2001

[12] **H.Schimpf,** Polarimetry and High Resolution as Key Features for Millimeter Wave Automatic Target Recognition, Proc.GRS 2000, p.283ff., Berlin, 11-12 Oct.2000

[13] **H.Schimpf, M.Hägelen,** The Influence of Target Aspect Angle Estimation on Robust Target Acquisition, Proc. "Radar 2004", Toulouse, Oct.2004

[14] **H.Schimpf,** The Estimation of Target Length from Radar High Range Resolution Profiles, Proc. Int'l Radar Symposium "IRS 2003", pp.663-668, Dresden, Sept.2003

Acknowledgement My thanks are due to my colleagues from FGAN for performing the measurements and creating an outstanding data set, and to my colleagues from NATO SET-069 Research and Study Group on "Robust Acquisition of Relocatable Targets using Millimeterwave Sensors" for numerous fruitful discussions and inspiring comments.

Kernel Machines for Object Classification in High-Resolution SAR Data

Dr. W. Middelmann / U. Thoennessen
FGAN-FOM – Research Institute for Optronics and Pattern Recognition
Gutleuthausstrasse 1, D-76275 Ettlingen
GERMANY

Middelmann@fom.fgan.de / thoe@fom.fgan.de

ABSTRACT

The focus of this paper is the classification of military vehicles in high-resolution SAR images in an ATR framework. The usage of kernel machine classifiers is discussed. A new kernel machine, the relevance vector machine with integrated generator (RVMG) is introduced. Here, a single parameter controls the trade-off between speed and classification quality. Moreover classification heuristics and an adaptive feature extraction are used. These methods enable an improvement of the classification quality as well as a reduction of the computational effort. A parametrized reject criterion is presented to handle the classification of confusion objects. Therefore receiver operator characteristic (ROC) curves have been calculated. Tests have been performed using the MSTAR public target dataset and a fully polarimetric dataset from QinetiQ. An assessment of several polarimetric features has been performed.

1.0 INTRODUCTION

This paper focuses on the classification module of an ATR system of military vehicles in high-resolution SAR images. Modern digitally controlled radar systems have the ability to operate quasi simultaneously in two or more different modes. After detection of moving targets by MTI or other sensors the region of interest with the target cue can be recorded by a high-resolution spotlight SAR. Template based matching is a common approach for classification, i.e. the taken signature is matched with image catalogs of the interesting vehicles. The drawback is the high computational effort for the cross-classification. On the other hand during the last years a series of novel classification techniques – the kernel machine classifiers – have been introduced, see [1,2,3,4].

These kernel machines enable an improvement of the classification quality as well as a reduction of the computational effort. An enhanced new kernel machine, the Relevance Vector Machine with integrated Generator (RVMG) has been developed [9]. The basic idea is combining the high classification quality of the Support Vector Machine (SVM) by margin maximization and the low effort of the Relevance Vector Machine (RVM) caused by the special statistical approach. A single parameter controls the trade-off between its speed and classification quality.

Kernel machines are limited to two-class problems. Therefore, additional classification heuristics are required to solve multi-class problems. A simple but effective heuristic is proposed to handle operational classification problems of ten or more classes.

Obtaining real time capability of a classification module is possible by automatic feature extraction. We follow the common approach using adaptive Fourier-coefficients. The normalized 2D-SAR image is transformed via discrete Fourier transformation. Each single Fourier coefficient defines a weak classifier for the training dataset (two-class problem), i.e. a linear discrimination is defined. Then the best of these

Paper presented at the RTO SET Symposium on "Target Identification and Recognition Using RF Systems", held in Oslo, Norway, 11-13 October 2004, and published in RTO-MP-SET-080.

weak classifiers are chosen as feature extractors. Because of by the significantly lower dimension of the samples involved, the computational effort is now noticeably less time consuming.

Our investigations have been carried out with different datasets. Using the MSTAR public target dataset [10] ten classes were taken into consideration. The tests have shown that an RVMG with 500 Fourier coefficients yields a better classification quality (93.23%) for the ten class MSTAR problem than the nearest neighbor classifier (88.17%). Additionally the classifier (test phase) is 116 times faster than the nearest neighbor classifier that works on the original data set.

Current investigations with a nine class data set from QinetiQ deal with full polarimetric SAR data. The objective is to assess polarimetric feature extraction in combination with kernel machines to yield an even more robust ATR processing chain. The tests have shown that polarimetric features can slightly improve the classification quality. Among these the simple energy based features have proven more robust than complex ones.

Moreover, ROC curves have been calculated for the QinetiQ data set with four training classes and five classes with confusion objects. Therefore a parametrized reject criterion is proposed in this paper. It is possible to optimize the classification result with respect to the reject threshold and the kernel parameter. The ROC curves related to different polarimetric features enable an assessment relative to the False Alarm Rate (FAR).

The paper ends with the conclusion that reviews our work. Furthermore we will give attention to generalizability of SAR image catalogs for future investigations.

2.0 KEY PROPERTIES OF THE CLASSIFICATION MODULE

The proposed classification module is a part of the ATR processing chain shown in Figure 1. It is responsible for the classification of high resolution target signatures in SAR (and other) image data.

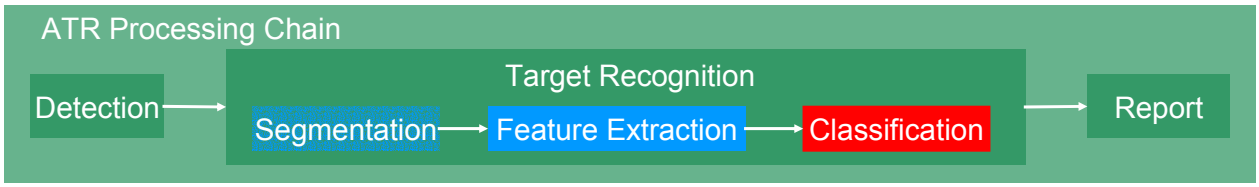

Figure 1: ATR processing chain with main modules

It has the following key properties that are dependent on several methods:

- Robust classification – kernel classifiers
- Improved applicability for multi-class problems – decision heuristic
- Real time ability – Fourier-coefficient-based feature extraction and RVMG
- Tunable trade-off between quality and FAR – RVMG
- Possible adaptation to requirements concerning classification quality, computational effort, FAR – parametrized reject criterion

The feature extraction has a very close connection to the classifier. Especially the Fourier-coefficient-based feature extraction works as a pre-classifier because of its adaptivity. Therefore the classification module may be understood as combination of the feature extraction, the kernel classifier, and the decision heuristic.

3.0 IMPLEMENTED METHODS

In this paragraph we introduce the methods implemented in the classifiers processing chain.

3.1 Kernel Machines

Our investigations are focused on kernel machines as classifiers. In many applications these have shown a high potential for robust classification [3,4,5,7]. Therefore the SVM (Support Vector Machine) and the RVM (Relevance Vector Machine) have been implemented.

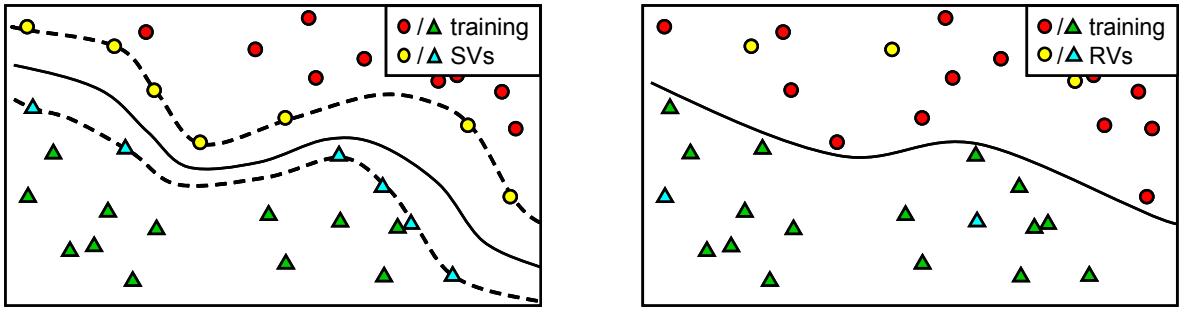

Figure 2 left: SVM – robustness and high quality by margin maximization
right: RVM – low effort by low number of RVs

The main characteristics of SVM and RVM are sketched in Figure 2. The SVM calculates Support Vectors (SVs) with non zero weights by margin maximization. This results in robustness and high generalization ability. In contrast, the RVM uses a special statistical approach to maximize the auto-classification quality and reduce the number of Relevance Vectors (RVs) – these are the vectors with non zero weights.

All investigated kernel machines use the RBF (Radial Basis Function) kernel, see Figure 3. As mentioned in [7] it has been shown that the RBF kernel is usually better than linear or polynomial kernels.

$$f(x) = \sum_{i=1}^{l} w_i K(x, x_i) + w_0 \qquad K(x, x_i) = \exp\left(-\frac{\| x - x_i \|^2}{\sigma} \right)$$

Figure 3: Test function of SVM and RVM, K is chosen as RBF kernel

SVM and RVM have the same test function (Figure 3). But the training – i.e. the determination of the weights – is based on different concepts. Therefore they have a very different behavior.

3.2 RVMG – Relevance Vector Machine with Integrated Generator

Customizing kernel machines results in the RVMG (RVM with integrated Generator), see [9]. A single parameter controls the trade-off between speed and classification quality of the RVMG. The basic idea is to combine the advantages of the SVM – high classification quality by margin maximization – and the RVM – low effort caused by the special statistical approach. Therefore additional points are generated in dependence on a single parameter λ controlling the relative distance of the new points to the margin, see Figure 4.

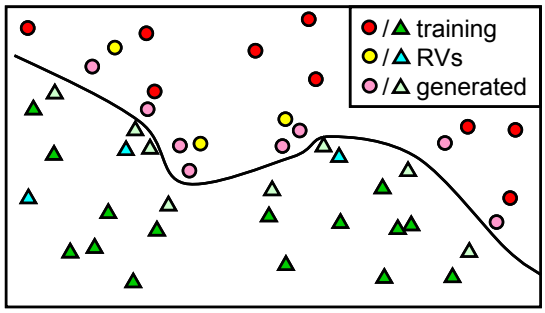

Figure 4: RVMG - Generated points establish a margin between the points of the two training classes

Using such additional points it is possible to define the RVMG as a modified RVM. The training algorithm of the RVM only uses a system matrix Φ with kernel elements K, e.g. K is the RBF kernel. It also uses class labels, so called hyper-parameters, and weights w_i, that have to be determined, see [5,6]. The rows of Φ correspond to the training vectors. The columns correspond to the basis functions. Basis functions and the RVM training dataset are independent of each other. It follows: The training dataset can be extended by generated data without any effect on the basis functions, see Figure 5.

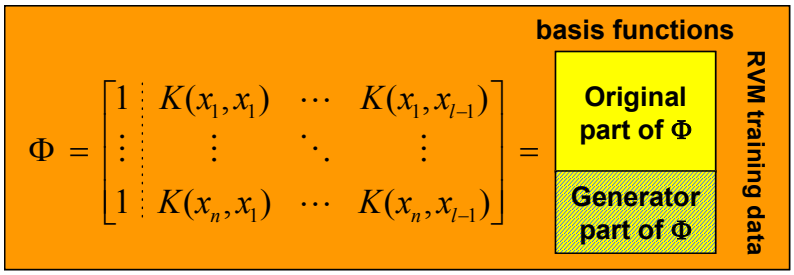

$$\Phi = \begin{bmatrix} 1 & K(x_1,x_1) & \cdots & K(x_1,x_{l-1}) \\ \vdots & \vdots & \ddots & \vdots \\ 1 & K(x_n,x_1) & \cdots & K(x_n,x_{l-1}) \end{bmatrix} =$$

Figure 5: Extended system matrix by generated points, basis functions are not affected

This is in contrast to the original RVM where the basis functions have been set up corresponding to the training dataset. For more details refer to [9].

The RVMG has the following characteristics:

- Fortification of class boundaries
- No blur of class boundaries, no increase of class overlap
- No density increase of inner class regions
- Manageable number of additional training points
- Variable distance (controlled by the scalar parameter λ) between original and generated training points

First tests were conducted in [9] using a three-class problem with MSTAR data that present a wide spectrum of RVMGs (dependent on λ). They vary from a machine (original RVM) 15 times faster and 10% lower quality than the SVM to a machine a little faster than the SVM and even better. In this paper we present experimental set-ups with up to ten classes.

3.3 Heuristics for Multi-Class Problems

Decision heuristics qualify the two-class kernel machines for multi-class problems. The approaches used have been assessed for suitability concerning problems with many classes. Different approaches were feasible.

The first one is the 1-to-rest-heuristic. It discriminates each class against the union of all other classes. Each machine gives +1 or –1 relative to the decision surface. A class is determined if an unambiguous decision exists. The test sample is rejected if any conflict occurs.

A slight modification of the 1-to-rest heuristic is possible if each machine gives the distance to the decision boundary. Then the class with maximum distance is chosen. A reject is not possible.

The third heuristic is the 1-to-1-heuristic. It uses classifiers for each pair of classes. A two stage majority decision follows: The test sample is rejected if all classes get 70% or lower of the possible votes. The winner class is determined by direct comparison of the three best classes.

All three heuristics were tested using ten classes of vehicles provided by the MSTAR public target dataset. Hereby we found that for all tested kernel machines the classification results obtained using the 1-to-1-heuristic are the most favorable. The 1-to-restMx (with maximum decision) is sometimes better but it contradicts the idea of a necessary reject class.

3.4 Preprocessing & Feature Extraction

Kernel machines map input data into a high dimensional feature space. This is sometimes taken to mean that feature extraction is not necessary for such classifiers. But nevertheless preprocessing and feature extraction are able to enhance the generalization and to speed-up the whole classification.

It is well known, e.g. see [3], that in many cases a simple data-independent low pass filter not only reduces the computational effort but also generally improves the quality of the classification. This behavior is confirmed by our tests presented below.

Other investigations on Fourier-coefficient-based feature extraction have been done. This is an adaptive method for pre-classifying. The 2D-SAR data normalized with respect to energy is transformed via 2D discrete Fourier transformation. Each single Fourier coefficient defines a weak classifier for the training dataset (two-class problem), i.e. a linear discrimination is defined. Then the best of these weak classifiers are chosen as feature extractors.

3.5 Reject Criterion and ROC Curves

If the classifier is only tested against trained classes the tests only deliver a proposition concerning a closed world performance. More reliable and robust results can be achieved by tests against a set of unknown signatures, so-called confusers. For this, a reject criterion parametrized by a scalar d_{min} is introduced. Therefore ROC (Receiver Operator Characteristics) curves can be computed, presenting the interrelationship of FAR (False Alarm Rate) and classification quality.

The reject criterion is sketched in Figure 6. It is given in the high dimensional feature space of the kernel machine that is defined implicitly by the kernel – here we use the RBF kernel only. Classification in this feature space is done by simple linear discrimination. Therefore using the 1-to-1 decision heuristic each class has been trained against each other, i.e. hyperplanes c_{ij} define the classes' boundaries. An acceptance region is defined by the minimal distance d_{min} to all related hyperplanes, i.e. we use the 1-norm.

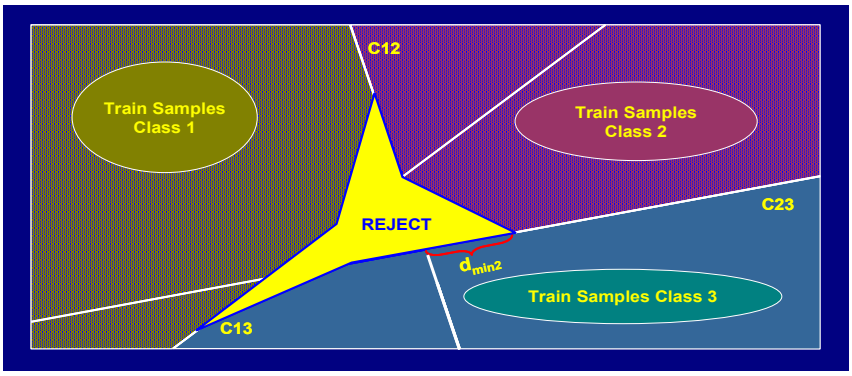

Figure 6: Parametrized reject criterion – An acceptance region is defined for each class.

The already used 1-to-1 decision heuristic is extended by the reject criterion. Thus there are two reasons to reject samples: The sample is rejected by the parametrized reject criterion or due to a class conflict inclusive ambiguous class voting.

4.0 MSTAR DATA TESTS

The first investigations in classifying high resolution SAR data have been done with the MSTAR public dataset. The chosen MSTAR data consists of 3671 training and 3203 test chips organized in ten classes: BMP2, BTR70, T72, BTR60, 2S1, BRDM_2, D7, T62, ZIL131, and ZSU_23_4. The data has been taken under a depression angle of 17° for the training samples and of 15° for the test samples. Only the magnitude data have been used for the tests.

4.1 Heuristics and Kernel Machines for Robust Classification

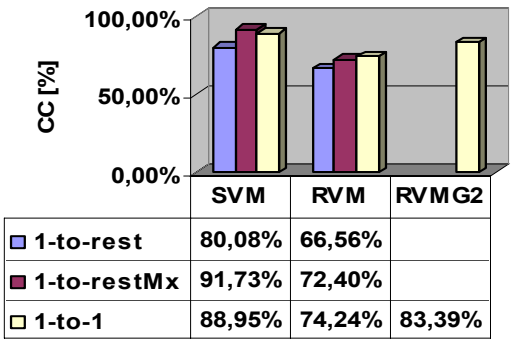

	SVM	RVM	RVMG2
1-to-rest	80,08%	66,56%	
1-to-restMx	91,73%	72,40%	
1-to-1	88,95%	74,24%	83,39%

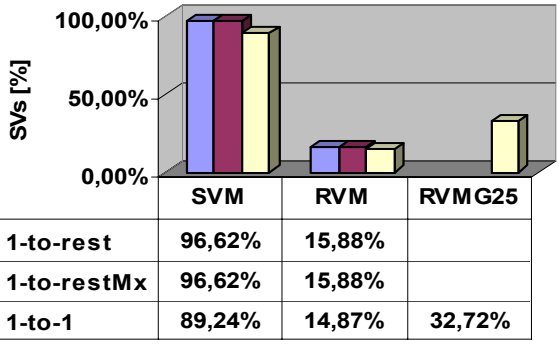

	SVM	RVM	RVMG25
1-to-rest	96,62%	15,88%	
1-to-restMx	96,62%	15,88%	
1-to-1	89,24%	14,87%	32,72%

Figure 7: Results of different combinations of heuristics and machines applied to the MSTAR ten classes problem. Left: Correct classified samples, Right: Percentage of used SVs or RVs

The decision heuristics and kernel classifiers introduced above are tested with the ten-class MSTAR problem. The results given in Figure 7 demonstrate the different behavior of the kernel machines.

For the SVM and RVM machines the results of the 1-to-1 heuristic are even better than these of 1-to-rest heuristic due to the stability of voting strategy. The 1-to-restMx with maximum decision yields good results but is off the discussion because of the necessity of a reject class. The RVMG ($\lambda = 0.25$) has been tested for the 1-to-1 heuristic only, because of the higher stability of the 1-to-1 heuristic – take a look at the number of SVs / RVs – and the huge computational effort for the training. The better generalization

(low number of RVs) of the RVMG with respect to the SVM (factor 2.7) results in a 5.56% lower classification quality.

The nearest neighbor classifier produces a similar result with 88.17% (and 100% SVs). Here it should be remarked that we count the overall used number of SVs (RVs) and do not sum up the SVs used in all two-class sub-problems.

4.2 Real-Time-Capability by Fourier-Coefficient-Based Feature Extraction

Fourier-coefficient-based feature extraction is an adaptive method for pre-classifying and was tested for different kernel machines. The results are given in Figure 8. For each the best 500 or 1000 coefficients are chosen.

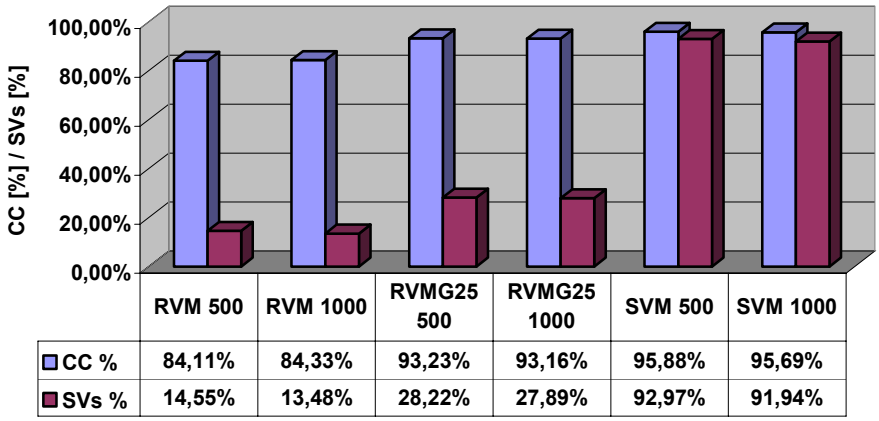

	RVM 500	RVM 1000	RVMG25 500	RVMG25 1000	SVM 500	SVM 1000
CC %	84,11%	84,33%	93,23%	93,16%	95,88%	95,69%
SVs %	14,55%	13,48%	28,22%	27,89%	92,97%	91,94%

Figure 8: Real time ability by Fourier coefficients (500 or 1000 coefficients have been selected) Classification quality (CC) and percentage of SVs or RVs for MSTAR ten classes are given.

RVMG25 with 500 coefficients is real-time-capable because it is 116 times faster (more than 100 samples per second without I/O) than the nearest neighbor classifier (CC_{NN}=88.17%) without feature extraction. This speed increase is due to the reduction in dimensions from 16384 (original data) to 500 (Fourier coefficients).

5.0 FULLY POLARIMETRIC QINETIQ DATA TESTS

It is a very interesting question how the classifier performance can be improved by fully polarimetric data. We investigated this problem using the QinetiQ dataset. The QinetiQ dataset contains 4006 images subdivided into 9 target classes A to I. Each of these classes is further subdivided into a training set consisting of 335 different target aspects and into a test set consisting of 110 test samples. Each of the complex-valued images of size 150x100 is depicting one single target. However, the target positions are varying from image to image. As a fixed target position is a prerequisite for achieving good results using SVM, 64x64 image sub-windows were selected in a pre-processing step. In the new images the centre of gravity of the binary object mask of the target coincides with the centre of the image window. Because the investigations were carried out with magnitude based features, only the magnitudes are stored (QinetiQ64). In order to be able to assess the influence of the image resolution, a further dataset (QinetiQ32) was generated degrading the 64x64 images to 32x32 using a 2x2 window.

5.1 Polarimetric Feature Selection

For both QinetiQ32 and QinetiQ64 different polarimetric features were investigated using the SVM. The classification results obtained using complex-valued features, especially the Pauli decomposition, were lower than 50%. Therefore in the following only magnitude based features were considered.

The tested polarimetric features based on the magnitudes are:

- a single coplanar channel (VV, HH)
- the average of the two coplanar channels (MAGVVHH)
- the concatenation of the two coplanar channels (VVHH)
- the average of all four channels (MAG)
- the concatenation of all four channels (ALL)

The investigations were done using QinetiQ64 as well as QinetiQ32 applying the SVM with Gaussian filtering ($\sigma = 0.75$ for QinetiQ32 , $\sigma = 1.5$ for QinetiQ64). A survey of the results is shown in Figure 9. The classification quality is represented in blue whereas the computational effort is depicted in purple.

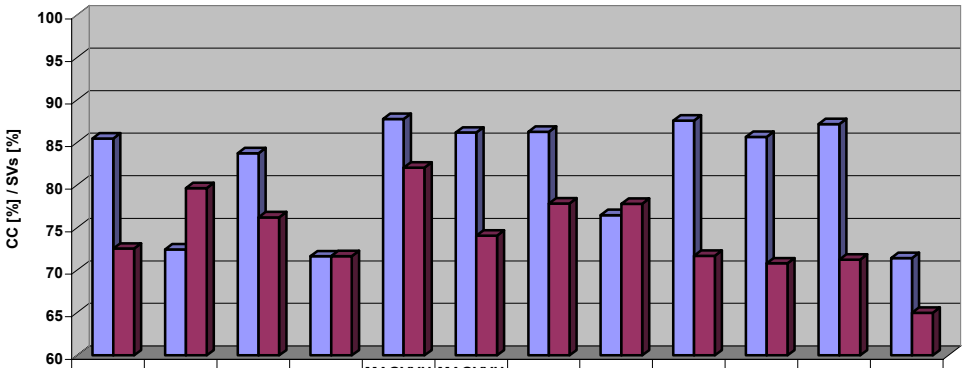

	HH32	HH64	VV32	VV64	MAGVVHH32	MAGVVHH64	VVHH32	VVHH64	MAG32	MAG64	ALL32	ALL64
CC[%]	85,47	72,45	83,75	71,64	87,79	86,18	86,28	76,49	87,59	85,67	87,18	71,44
SV [%]	72,54	79,64	76,22	71,67	82,06	74,06	77,84	77,81	71,71	70,81	71,24	64,98

Figure 9: Efficiency and quality achieved using SVM

The results pointed out that it is more favorable to use QinetiQ32 with the reduced geometrical but improved signal-to-noise-ratio than to use QinetiQ64 possessing the fully geometrical information. However, there is a clear distinction between the features based on averaging and those based on concatenation. In case of averaging the increase of the classification rate is small, less than 2%. In case of concatenation the increase is essentially larger, more than 10%.

Using the fully polarimetric information is also of value. For QinetiQ32 an increase, concerning the classification rate, of about 2% was noticeable. For the QinetiQ64 an increase of about 5% was detected. In both cases the best classification results were obtained using both coplanar channels. The main advantage of using all four channels is the reduction of the number of support vectors. Assessing the computational effort it is necessary to consider that concatenation enlarges the dimension of the support vectors by two or even four times. Therefore a reduction of the computational effort can be achieved only for averaging based features. Thus the most promising feature is MAG32 because of its good classification results and its low computational effort. Considering only the classification rate MAGVVHH32 and ALL32 are also well suited features. Finally HH32 is also a good choice as the classification performance is diminished only by 2% and the support vector quota is similar to the one of MAG32.

5.2 Real-Time-Capability by Advanced Methods

For usage in an operational ATR system the classification task must be solved in real time. In the case of high-resolution SAR data this is actually not state of the art. To achieve this objective we use the RVM and RVMG which minimize the number of support vectors, as well as adaptive Fourier coefficients and the combination of these using the most promising features MAG32, MAGVVHH32 and ALL32.

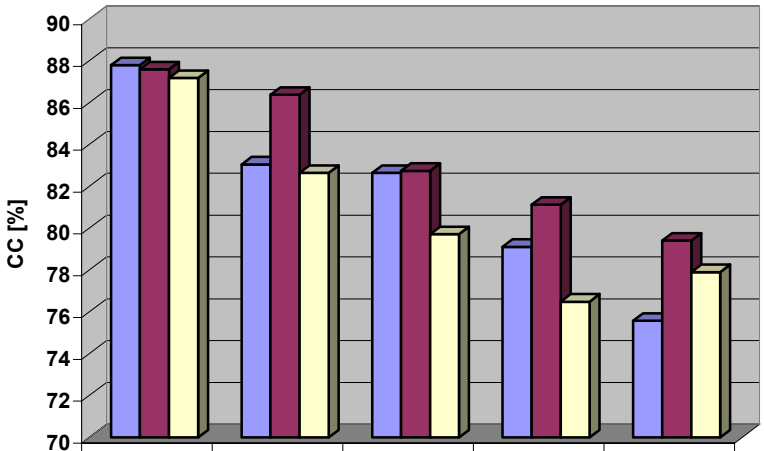

	SVM	SVMF	RVMG25	RVMG10	RVMG10F
MAGVVHH32	87,79	83,05	82,64	79,11	75,58
MAG32	87,59	86,38	82,74	81,13	79,41
ALL32	87,18	82,64	79,72	76,49	77,90

Figure 10: Classification quality of the most favorable features

The classification results obtained using these new methods with Gaussian filtering are depicted in Figure 10. The results for the SVM are given in the first column. Results of the SVM with image data transformed into 100 Fourier coefficients (SVMF) are indicated in the second column. The third and fourth column present the results of the new RVMG when using the control value $\lambda = 0.1$ (RVMG10) respectively $\lambda = 0.25$ (RVMG25). Finally, the fifth column indicates the results of the RVMG with image data transformed to 100 Fourier coefficients (RVMG10F).

As expected the best results were obtained applying the SVM achieving a classification rate of more than 87%. The poorest results were obtained using RVMG10F with a classification rate varying for the different features between slightly more then 75% and slightly less than 80%. The best results were obtained using MAG32 with a loss of about 1% in case of SVMF and about 8% in case of RVMG10. With the exception of RVMG10F with the MAGVVHH32 feature, all classification rates decrease by less than 10%.

An important assessment criterion for the tested methods was the computational effort. Comparing the different methods we have to consider that in case of SVMGF and RVMGF the image data consisting of 1024 pixels was reduced to a vector of 100 Fourier coefficients which causes a nearly 90% reduction of the computational effort.

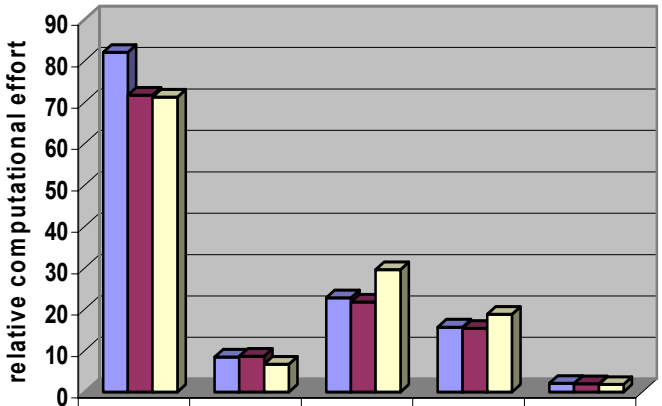

	SVM	SVMF	RVMG25	RVMG10	RVMG10F
MAGVVHH32	82,06	8,49	22,75	15,72	2,08
MAG32	71,71	8,65	21,79	15,36	2,01
ALL32	71,24	6,77	29,59	18,81	1,87

Figure 11: Computational effort of the most favorable features in percent of that of an SVM with 100% SVs without Fourier coefficients

In Figure 11 a survey of the corresponding adapted computational efforts is given. All new methods have an essentially lower effort. For the RVMG25 test the speed up factor is considerably higher than 2. The RVMG10F yields a speed up factor of nearly 40, with respect to the SVM.

5.3 Optimization of FAR against Quality

In the preceding sections the performance concerning the discrimination between trained classes was investigated. In case of ATR however not only objects of the trained classes but also objects of non-trained classes or even artifacts will occur. Therefore an important property of a classifier would be the capability to reject objects not belonging to one of the trained classes.

In order to test whether the implemented reject criterion fulfills this demand, the following experiment was carried out. Only the four classes A, B, D and G of the QinetiQ dataset were trained. Then the test samples of all nine classes were classified. The results obtained are depicted in Figure 12 in case of MAG32, in Figure 13 in case of MAGVVHH32 and in Figure 14 in case of ALL32. The results are controlled by two parameters. The curves family is parametrized by the reject criterion, i.e. the minimal distance (1-norm) d_{min} to all related hyperplanes. The curves were determined by varying the kernel factor σ of the RBF.

The results demonstrate that for distinct FAR intervals related optimal d_{min} values and optimal features exist. Generally using a larger d_{min} i.e. a stronger reject criterion will result in a poorer classifier performance. However, as MAG32 is indicating, this global trend may no longer be valid for small FARs – usually the most interesting part of the curves. In this specific example the reject criterion $d_{min} = 0.5$ is the most favorable one. This may be the reason that generally only small values of the normalization factor σ can guarantee small FARs. But these settings also cause the rejection of a large number of real targets. Reducing the false alarms by increasing the strength of the reject criterion permits the rise of the factor σ normalizing the RBF kernel. By this, the efficiency of the classifier will increase, too.

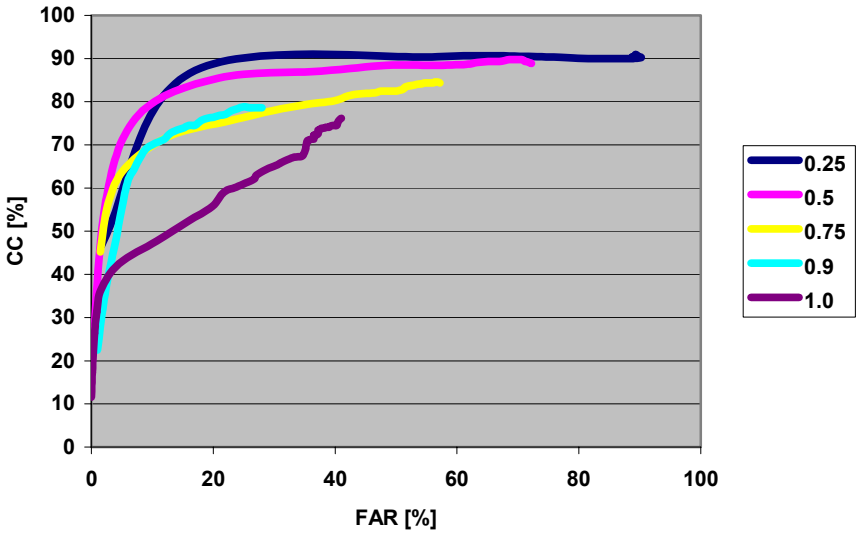

Figure 12: Result of the reject criterion for MAG32

Evaluating the tested features shows that no feature is always better than the two other ones. For a demand of a FAR below 15% using MAGVVHH32 is more favorable than using MAG32 or ALL32. However in case of a FAR above this level MAG32 is the best choice.

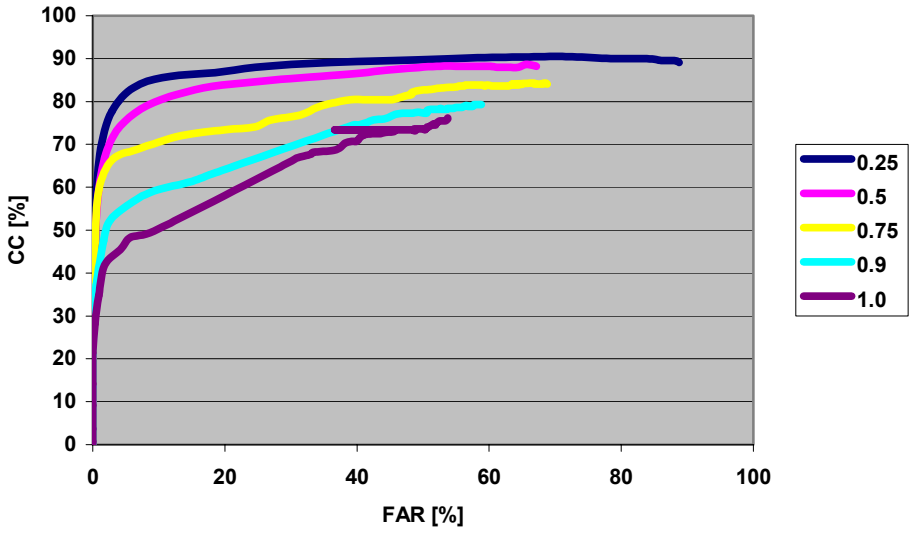

Figure 13: Result of the reject criterion for MAGVVHH32

The ROC curve of ALL32 is always positioned below the ROC curves of either MAG32 or MAGVVHH32 indicating a poorer performance of this feature. By this, the ranking of the features presented in the preceding section is confirmed.

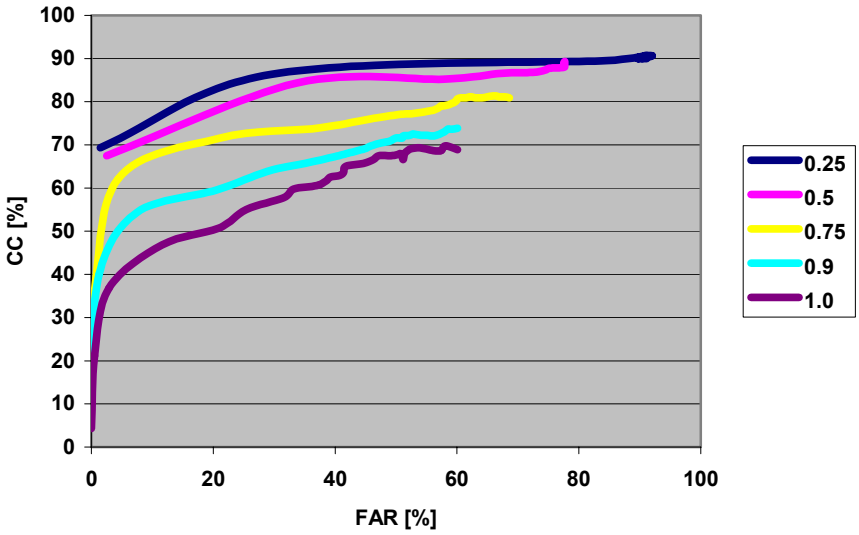

Figure 14: Result of the reject criterion for ALL32

6.0 CONCLUSION

In this paper we introduced classification methods for the processing chain of ATR in high-resolution SAR images. Kernel machines as robust classification methods are the basis of our approach. A novel kernel machine was presented that controls the trade-off between classification quality and computational effort, i.e. number of relevance vectors. The multi class classification capability is given by an efficient 1-to-1 decision heuristic. An adaptive feature extraction based on Fourier coefficients enables the module for real time execution.

The investigations have taken place for the MSTAR public database. Tests with a ten-class problem have been analyzed. For example the RVMG25 machine with a pre-classifier using 500 Fourier coefficients is 116 times faster than the original nearest neighbor. The classification quality has been improved from CC_{NN}=88.17% to CC_{RVMG25_500}=93.23%.

Further investigations have used the fully polarimetric QinetiQ dataset with nine classes. The tests carried out indicate that the most favorable polarimetric features for the depicted hard targets are the magnitude based ones. Especially the two coplanar polarizations embody the essential information for the class distinction, e.g. the SVM result of MAGVVHH32 with CC=87.79% is similar to MAG32 with CC=87.59%. But the crossplanar channels cause a better generalizability, e.g. the SVM gives SV=82.06% for MAGVVHH32 and SV=71.71% for MAG32. On the other side complex features like those based on the Pauli decomposition are off the discussion because of their weak performance.

An important property of a classifier used in the ATR framework is the capability to reject objects not belonging to one of the trained classes. Therefore the QinetiQ data have been divided into two class systems: the training and test classes and the confusion objects. The classification module with reject criterion is controlled by the reject parameter and the kernel parameter of the RBF. To determine ROC curves we have varied both parameters. For example the SVM with MAGVVHH32, reject parameter r=0.25, and RBF parameter σ=0.1 yields a very low FAR=2.9% and a classification quality of CC=77.73%.

By the way classification quality of CC_{NN}=91.83% was achieved for the nine class QinetiQ data by the nearest neighbor classifier with MAGVVHH32 and a simple pre-filtering. This single result also approves the well selected polarimetric feature for hard targets.

This paper has shown that polarimetric data is also useful for ATR tasks in high-resolution SAR data. Future work should deal with a more physically founded analysis of polarimetric features. Especially the whole complex information should be made available in a proper way for the classifiers. This could lead to a better generalizability of SAR image catalogs.

ACKNOWLEDGEMENTS

The authors wish to thank D. Blacknell at QinetiQ for the polarimetric data set. Moreover many thanks to A. Ebert at FGAN-FOM for his technical assistance in implementing the software system and testing.

REFERENCES

[1] V. Vapnik, A. Chervonenkis, “Theory of Pattern Recognition“ [in Russian], Nauka, Moscow, 1974, (German Translation: W. Wapnik, A. Tscherwonenkis, Theorie der Zeichenerkennung, Akademie-Verlag, Berlin, 1979)

[2] V. Vapnik, Statistical Learning Theory, Wiley, New York, 1998

[3] B. Schölkopf, “Support Vector Learning”, PhD Thesis, R. Oldenbourg Verlag, Munich, 1997

[4] N. Cristianini, J. Shawe-Taylor, “An Introduction to Support Vector Machines and other kernel-based learning methods”, Cambridge University Press, 2000

[5] M. E. Tipping, “The Relevance Vector Machine”, Advances in Neural Information Processing Systems, 12, S. A. Solla, T. K. Leen, K.-R. Muller (eds), MIT Press, Cambridge, MA, 2000.

[6] M. E. Tipping, “Sparse Bayesian Learning and the Relevance Vector Machine”, Journal of Machine Learning Research, 1, 211-244, 2001.

[7] H. Byun, S.-W. Lee, “A Survey on Pattern Recognition Applications of Support Vector Machines”, International Journal of Pattern Recognition and Artificial Intelligence, Vol. 17, No. 3, 459-486, 2003

[8] W. Middelmann, U. Thoennessen, “Classification in High-Resolution SAR Data”, Proceedings of SPIE - Algorithms for Synthetic Aperture Radar Imagery X, E. G. Zelnio, F. D. Garber (eds.), 5095, pp. 325-335, 2003

[9] W. Middelmann, “Classification with Controlled Robustness in High-Resolution SAR Data”, Proceedings 25th DAGM Symposium, Magdeburg, Germany, September 2003, B. Michaelis, G. Krell (eds.), LNCS 2781, pp. 92-99, Springer, 2003.

[10] MSTAR, Air Force Research Lab., Model Based Vision Lab., Sensor Data Management System, http://www.mbvlab.wpafb.af.mil/public/sdms/datasets/mstar/overview.htm

ATR of Battlefield Targets by SAR – Classification Results Using the Public MSTAR Dataset Compared with a Dataset by QinetiQ, UK

Rolf Schumacher and Kh. Rosenbach
FGAN – Forschungsgesellschaft für Angewandte Naturwissenschaften e. V.
FHR – Forschungsinstitut für Hochfrequenzphysik und Radartechnik
Neuenahrer Str. 20
D-53343 Wachtberg
GERMANY
Phone / Fax (+49) 228 9435 487 /-212

rolf.schumacher@fgan.de

SUMMARY

The development of ATR algorithms and the comparison of different classification schemes is one of the main goals of the SET-053 group. The group mainly focuses on SAR images of stationary ground targets, in which the targets are detected. These single image chips form a databank for ATR evaluation and identification to which the classification schemes can be applied. Because of the inhomogeneous measured and modelled datasets of the different nations we start our evaluation with the public MSTAR dataset, which is used since many years for ATR evaluation and identification.

In most of the publications dealing with the MSTAR dataset [1,2,3] classification rates between 97% and 100% could be reached due to the good quality of the chip images (good adjustment, centered, good signal/noise ratio, nearly exact scaling).But these results should not be overestimated because the image quality can decrease having real applications with targets in battlefield situations.

We investigate the performance of simple classification approaches when the quality of the MSTAR dataset was degraded by adding noise, decentering the targets and introducing errors in the crossrange scaling. In addition we used a dataset from real field measurements which was made available to the SET-053 group by QinetiQ,UK. As anticipated, the classification rates dropped considerable in all mentioned cases. Consequently changes in the feature extraction schemes were investigated which were able to improve the classification rates again.

Additionally we analyze the influence of clutter and target shadow on the classification rate. In both datasets the classification rate decreases when we separate the target from clutter and shadow. This is a hint, that a strict separation and segmentation of target and clutter is necessary to classify the real target. Therefore the targets should be measured independently and, if possible, at different locations, so that the clutter doesn't correlate between the test and training data. The target shadow can be used for additional information dependent on the depression angle.

By comparing different classifiers (Nearest neighbour, different types of SVMs, HNet…) we can conclude that the main work is not choosing and applying the classifier, but concentrate more on the data collection, preprocessing and feature extraction process.

Therefore in this paper the results of the different investigations concerning the preprocessing of the datasets will be presented. Main topics are the target centering, segmentation, clustering and the influence of the image resolution on the classification rate.

Paper presented at the RTO SET Symposium on "Target Identification and Recognition Using RF Systems", held in Oslo, Norway, 11-13 October 2004, and published in RTO-MP-SET-080.

1.0 INTRODUCTION

Because ATR has become more important during the last years it is essential to develop robust classification schemes, which can be applied reliably in military operations. Especially the identification of ground targets in battlefield situations is one of the most difficult tasks, because in relation to the identification of air targets [5, 6] the general conditions are much more unfavorable. The major problems are the clutter (which is not present in air), the unknown target orientation (aspect and elevation angle), high variability of the target scatterers and the possible multiple variants of the target.

2.0 DATASETS

For our investigations we use two different datasets: the public release of the MSTAR dataset and a dataset which was provided from QinetiQ (UK) to the NATO-SET-053 group. Both datasets consist of single target SAR image chips and are divided into test and training data. The following section gives a more detailed description of both databases.

2.1 MSTAR ("Public release")

The Moving and Stationary Target Acquisition and Recognition (MSTAR) was a joint Defense Advanced Research Projects Agency (DARPA) and Air Force Research Laboratory (AFRL) effort to develop and evaluate anadvanced ATR system. The program began in June of 1995 and ended in 1999. The public release of the MSTAR dataset provides approx. 20.000 SAR image chips covering 10 target types from the former Soviet Union. MSTAR has conducted three data collections in September 95, November '96 and May '97. The target images were collected near Huntsville, Alabama by the Sandia National Laboratory (SNL) using the STARLOS sensor. The imagery used here was collected as part of the MSTAR data collection #1, Scene 1 and as part of the Data Collection #2, Scenes 1,2 and 3. The targets contain three T72 Main Battle Tanks (MBT) three BMP2 Armoured Personnel Carriers (APC), a BTR70, 2S1, BDRM2, D7, T62, ZIL131, ZSU23/4 (see table 3).

The data consist of X-band SAR images with 1 foot by 1 foot resolution measured in spotlight mode. The targets have been measured over the full 360° azimuth angles with 1°-5° increments and over multiple depression angles (15°, 17°, 30° and 45°). The target data is presented as subimage chips centered on the target with a standard chip size per target type, usually 128px x 128px. Table 1 gives an overview of the dataset used in our experiments. Data collected at 15° depression angle were used for testing (3423 images) and 17° for training (3451 images).

2.2 QinetiQ SAR data

The imagery, which was kindly provided from QinetiQ (UK) to the NATO-SET-053 group, was collected from a measurement campaign in November 2001. The fully polarimetric X-band data of nine targets was recorded with the Enhanced Surveillance Radar (ESR) from QinetiQ in spotlight mode. The resolution of the images is 0.4m x 0.4m, the pixel spacing 0.3m x 0.3m, respectively. Two different circles around the target area were flown to collect training and test data separately and independently. The low depression angle of 6° caused long shadows in the images in range direction behind the targets. The squinted processing allows obtaining 360° coverage in the azimuth direction for the image dataset. Table 1 and 2 show the aspect coverage of all targets in the test and training data. Here the number of measured images is shown for an aspect interval of 10° (Asp. 1 means the interval from 0 to 9°, Asp. 2 stands for the aspect interval 10-19° and so on). The underlying colour is a measure for data density (black: no data, red: some data and white: data every 1°). We see that the training data was measured nearly completely over the whole azimuth, but the test dataset shows some gaps in the aspect angle distribution because it was measured only in some segments of the flown circle. The total ratio of train and test data is nearly 3 to 1 (330:110 for each class). In our studies we used only the HH-channel representative.

Table 1: number of images separated in 10° aspect interval (Asp. Int.) for QinetiQ training data (black: no data, red: some data, white: 1° data); Cl=target class

Asp Int. / Cl	1	2	3	4	5	6	7	8	9	10	11	12	13	14	15	16	17	18	19	20	21	22	23	24	25	26	27	28	29	30	31	32	33	34	35	36
1	9	10	10	10	9	3	10	10	10	10	10	10	10	10	10	10	10	10	10	10	10	8	5	10	10	10	10	10	10	10	10	8	2	10	10	10
2	9	10	3	10	10	10	10	10	10	10	10	10	3	7	10	10	10	10	10	10	10	4	8	10	10	10	10	10	10	10	10	10	10	10	10	10
3	1	10	10	10	10	10	10	10	10	2	10	10	10	10	10	10	10	10	10	10	10	10	10	10	10	9	4	10	10	10	10	10	10	10	10	9
4	9	10	10	10	10	8	2	10	10	10	10	10	10	10	9	3	10	10	10	10	10	10	10	10	10	10	10	10	10	10	10	8	5	10	10	10
5	9	10	10	10	10	10	10	10	10	10	10	10	8	5	10	10	10	10	10	10	10	10	8	2	10	10	10	10	10	10	10	9	3	10	10	10
6	9	10	10	10	10	10	10	10		10	10	10	10	10	10	10	10	2	10	10	10	10	10	10	10	10	10	10	10	10	10	10	10	10	3	10
7	3	9	10	10	10	10	10	10	10	10	4	6	10	10	10	10	10	10	10	5	7	10	10	10	10	10	10	10	10	10	10	10	10	10	10	10
8	4	10	10	10	10	10	10	10	10	9	1	10	10	10	10	10	10	10	10	2	10	10	10	10	10	10	10	10	10	10	10	10	10	10	10	9
9	9	10	10	10	10	10	10	10	10	10	10	6	7	10	10	10	10	10	10	10	10	6	4	10	10	10	10	10	10	10	7	5	10	10	10	10

Table 2: number of images separated in 10° aspect interval for QinetiQ test data

Asp Int. / Cl	1	2	3	4	5	6	7	8	9	10	11	12	13	14	15	16	17	18	19	20	21	22	23	24	25	26	27	28	29	30	31	32	33	34	35	36
1			1	10	5		6	10	10		3	10	8		4	5										10	6							5	10	7
2						5	10	1							10	10	2			6	10		1	10	10	5			8	10	3		9			
3		4	10	8			10	6		5	10	10	1		2	10	9		3	6										9	7					
4	5						5	10	7				1	10	5		6	10	10			3	10	8		4	5									10
5			3	10	8		4	5									10	6							5	10	7			1	10	5		6	10	10
6		8	8							3	10	9				9	7		4	10	10	2		1	10	10		2	7							
7				4	10	2							9	10	3			5	10	1		10	10	6			7	10	4		8	1				
8				9	7							4	10	8				10	6		5	10	10	1		2	10	9		3	6					
9		5	10	6		6	3								2	10	4							7	10	5			3	10	3		8	10	8	

2.3 Comparison of the MSTAR and QinetiQ dataset

Comparing the 10-class-MSTAR with the 9-class-QinetiQ dataset (Fig. 1 and 2, Table 3), the total number of images in the MSTAR train and test case are nearly the same (3671 training and 3203 test images). Each target class has approximately 300 training and 200-280 test images, which are distributed over the complete 360 azimuth homogenously. Only class 1 (BMP2) and 3 (T72) consist of trice more images because here three different serials are integrated. The training QinetiQ dataset (table 1) consists of slightly more images (330 images with nearly 1° aspect increment), but in contrast to MSTAR the test dataset (tab.2) comprises only one third of the training data (110 images per class). The aspect angle distribution of this test data is very inhomogeneous compared to the training data.

As an example for the quality of the images we see in fig. 2 a sample image from the MSTAR dataset (left) and one from the QinetiQ dataset (right). The differences between these datasets are: The MSTAR image is centered a priori and has a good signal to clutter ratio. Furthermore the clutter is distributed very homogeneously. The QinetiQ data are not centered a priori, and the S/C ratio is lower than in the MSTAR data. The target shadows in the MSTAR dataset are pronounced in contrast than the longer target shadows in the QinetiQ data.

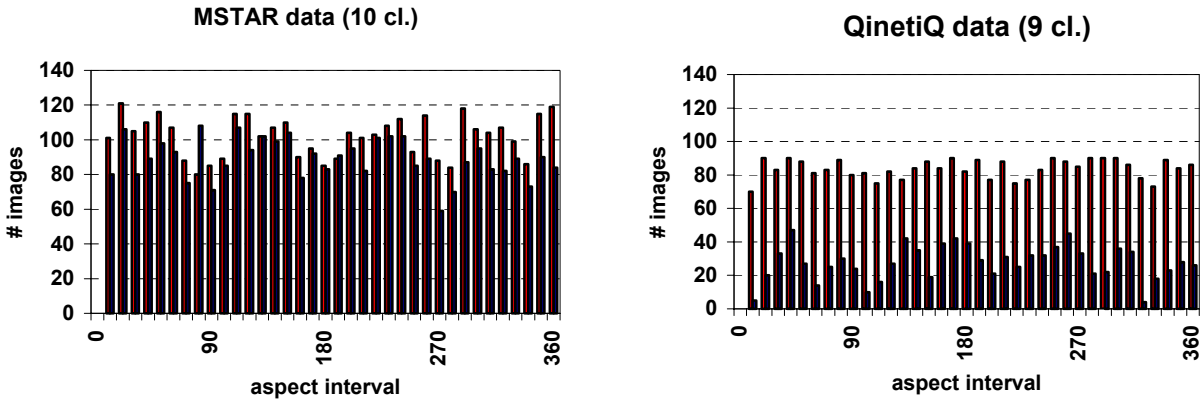

Figure 1: total number of training (red) and test (blue) images in 10° aspect interval for the MSTAR 10-class data (l.) and the 9- class QinetiQ data (r.)

Table 3: number of images per class for the MSTAR and QINETIQ dataset

	Class Type	*1 BMP2*	*2 BTR70*	*3 T72*	*4 BTR60*	*5 2S1*	*6 BRDM2*	*7 D7*	*8 T62*	*9 ZIL131*	*10 ZSU23/4*	**Sum**
MSTAR	**Train 17° dep**	698	233	691	256	299	298	299	299	299	299	3671
	Test 15° dep	587	196	582	195	274	274	274	273	274	274	3203
QinetiQ	***Class***	***1***	***2***	***3***	***4***	***5***	***6***	***7***	***8***	***9***		**Sum**
		-	-	-	-	-	-	-	-	-		
	Train Circ 1	330	335	335	335	335	335	335	335	335		3015
	Test Circ 2	110	110	110	110	110	111	110	110	110		991

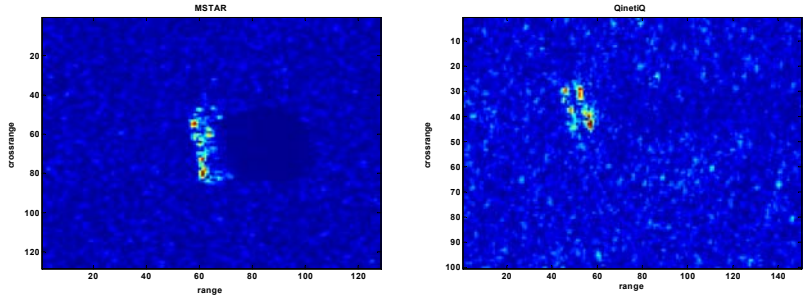

Figure 2: Sample images from datasets MSTAR (l.) and QinetiQ (r.)

3.0 DATA PREPROCESSING SCHEMES

Because we want to classify the target (and not the clutter) it is not much meaningful to take the complete original images as input for the classifier. The main work before doing classification is the preprocessing and feature extraction of the data. In order to standardize the information of each image to be classified some degree of preprocessing is required, so that the images are adjusted for the used classifier. For our further investigations we used the following processing scheme:

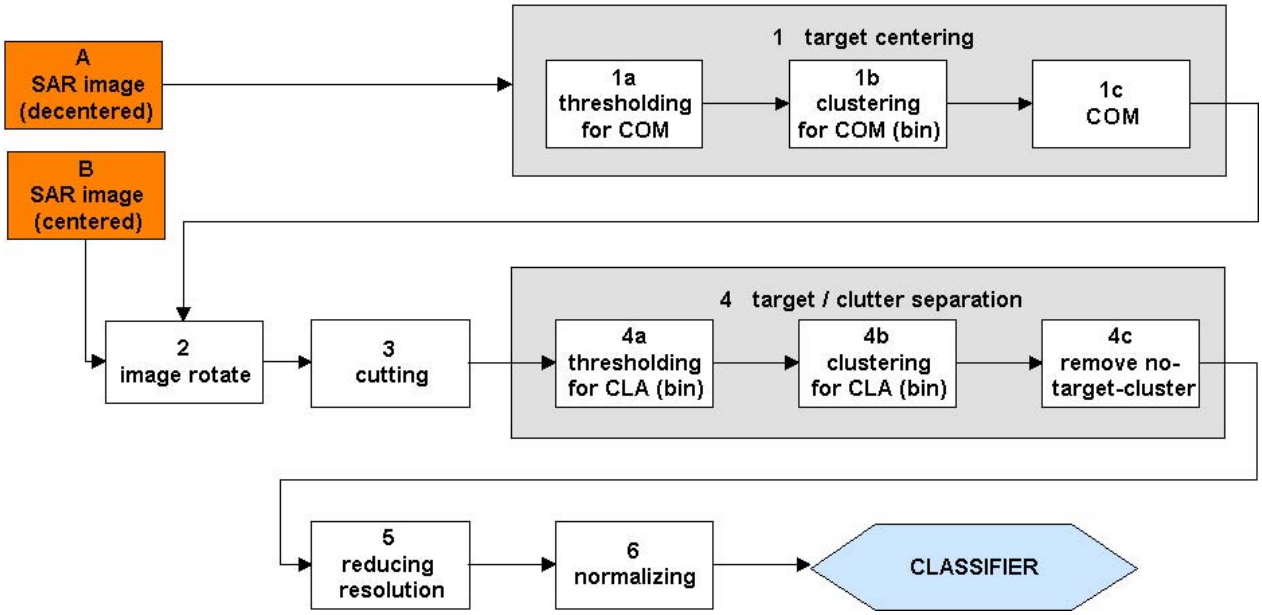

Figure 3: Data Preprocessing scheme (COM=Center of MASS; CLA=Classifcation)

Starting from the original datasets we have on the one side the centered MSTAR images (B) and the uncentered QinetiQ images (A). The image sizes are 128px x 128px for the MSTAR and 150px x 100px for the QinetiQ data. Because we use for our classification a pixelbased minimum distance Nearest Neighbour classifier (section 5.1) we have to center the data as accurately as possible.

To illustrate the preprocessing steps (fig. 4) we take an uncentered image of the QinetiQ data (fig. 2). The first step is to center the image. This can be done in three steps: first we determine a threshold to detect the target (step 1a). This threshold is adjusted on the image dimensions and the estimated ratio of target to background area. In our calculations we have used a 95%-median on the amplitude data, so that the 5% highest amplitudes are selected for further processing. In a second step we remove single pixels and clusters, which have less than 8 connected pixels. From the remaining large clusters we choose the largest one and replace the amplitudes with ones (step 1b, clipping) to eliminate the amplitude variations on the target. On this binary image we calculate the Center of mass "COM" (step 1c) with the indices i_m and j_m, where i and j are the pixel indices in range (R) and crossrange (CR) respectively and x are the amplitudes of the image data.

$$COM = (i_m, j_m) \,|\, i_m = \frac{\sum_{j=1}^{CR}\sum_{i=1}^{R} i \cdot x_{ij}}{\sum_{j=1}^{CR}\sum_{i=1}^{R} x_{ij}}; j_m = \frac{\sum_{i=1}^{R}\sum_{j=1}^{CR} j \cdot x_{ij}}{\sum_{j=1}^{CR}\sum_{i=1}^{R} x_{ij}}$$

At last the image with the original amplitudes is shifted according to the COM and the centering process is finished.

Step 2 is optional. If the azimuth orientations of the targets with respect to the sensor are known (ground truth or tracking information), they can be used to rotate the images so that all targets point in the same direction. Because of the different direction of rotation in both datasets the MSTAR images have to be rotated clockwise and the QinetiQ images counter clockwise. If no information about the aspect angle is

available, we ignore this step and proceed with step 3. Here a "cutting" step is introduced with a resulting concentration on the (centered) target. In our processing the clipped image has the dimension of 64px x 64px in both datasets.

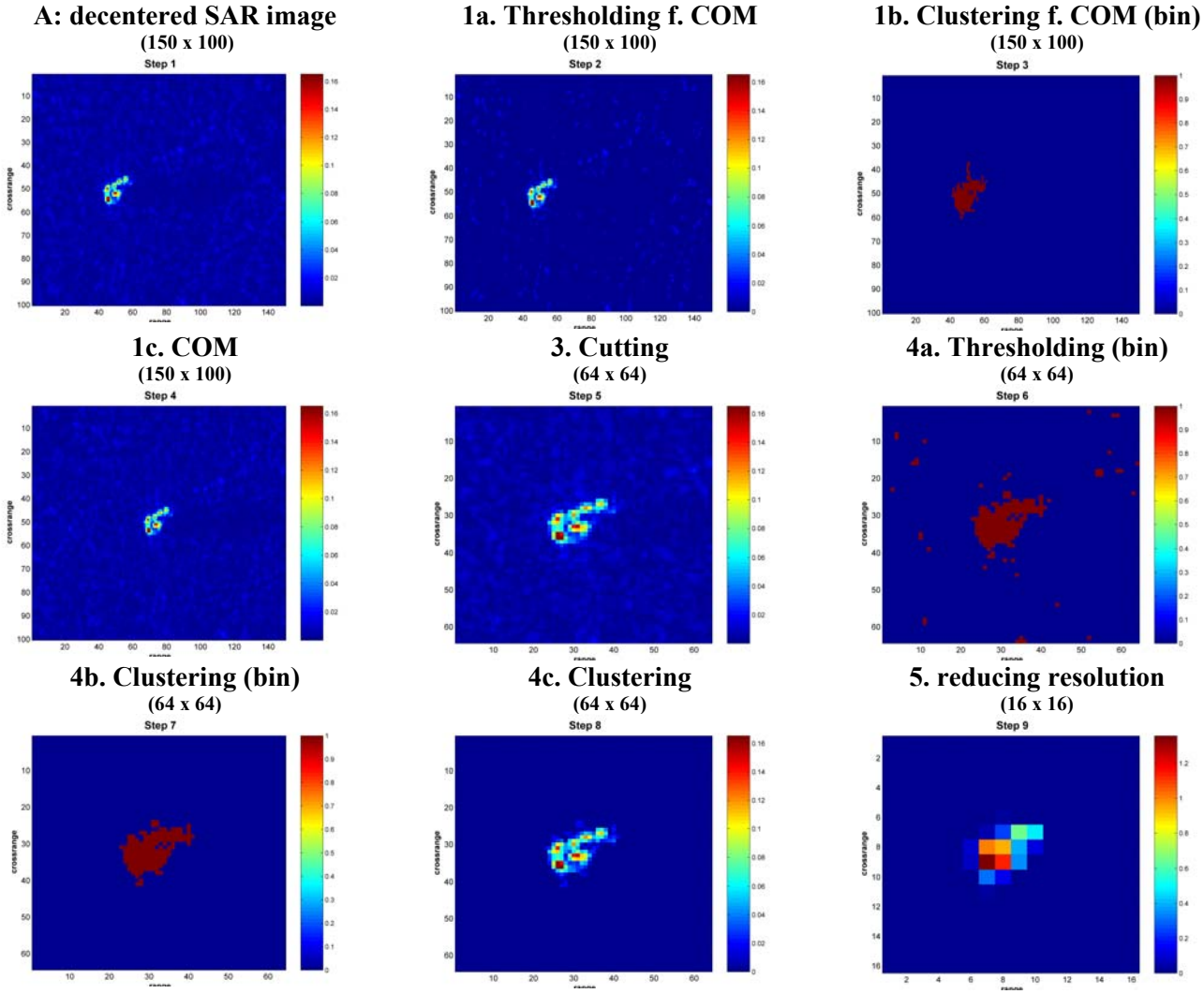

Figure 4: example for image processing before classification

In the fourth step we have the option doing image segmentation. This can be done in different ways: the normal way is to separate the target from the background clutter. Beside this we investigate cases of separating target shadow from image and clutter separately so that we can determine the influences of these parts of the image on the classification rate. In Fig. 4 the usual target segmentation is shown. Comparable to the COM calculation the thresholding (step 4a) and clustering (step 4b) of the image is done. The threshold T is adapted from a clutter level defined by a box around the target with $T=C_{mean}+3*C_{std}$ from the mean C_{mean} and standard deviation C_{std} of the clutter. After that connected pixels above this threshold are clustered, whereas little clusters and single pixels are removed. Additional clusters which are far away from the largest target cluster are eliminated (step 4c).

Step 5 of the preprocessing allows data reduction by reducing the image resolution. The clipped 64px x 64px image can be smoothed by a factor 2 or 4 so that the input image for the classifier has a size of 32px x 32px or 16px x 16px respectively.

To achieve a comparable set of preprocessed images the image is normalized to the image power of the preprocessed image finally (Step 6).

4.0 CLASSIFIER

For our investigations we used a simple pixel based Nearest Neighbor Classifier, which calculates the minimum distance between the amplitudes x of the test and the training images.

$$C(TE) = C(TR,\Delta) \mid \Delta(TE,TR) = \min\left\{\sum_{i=1}^{R}\sum_{j=1}^{CR}\left(x_{ij}^{TE} - x_{ij}^{TR}\right)^2\right\}$$

This means that all test images TE are compared with all replica images TR and the class of the test image C(TE) with the minimal distance Δ(TE,TR) to the replica TR is assigned. This minimum distance is equivalent to the correlation coefficient between the two images. The advantage of using a Nearest Neighbor classifier is on the one hand the simplicity of such a classifier (no parameters) on the other hand the missing training phase combined with its versatility of changing combinations of exspected targets. So this kind of classifiers is very simple and easy to use. Its drawback can be found in the bigger database and a somewhat longer decision time.

In the following section we applied this classifier on three different identification problems: a 5-class MSTAR, 10-class MSTAR and 9-class QinetiQ problem. Usually all test data are tested against all reference data (replica). A rejection class was not installed. The complexity of the three identification problems (number of test images and replicas, target classes) can be extracted from table 3.

To evaluate our results we compare the classification rates achieved with the NN-Classifier with other classifiers (linear and polynomial SVM, RBF).

5.0 CLASSIFICATION RESULTS

For our investigations we used three kinds of problems: 5-class MSTAR (M5), 10-class MSTAR (M10) and a 9-class QinetiQ (Q9) problem. We used forced decision classifiers with no rejection class. The test data is tested against all replicas.In our investigations we quantify the influence of the following key aspects on the classification rate:

- Target centering (using COM algorithms)
- Image segmentation (target, clutter, shadow)
- NN compared to different types of SVM classifiers
- Image resolution
- Target orientation (knowledge of the aspect angle)

Depending on computer power restrictions we sometimes worked with a reduced dataset. Especially for extensive calculations (decentering and shifting) we used the M5 instead of M10 dataset.

5.1 Target centering

Because we applied in our studies a pixel based classifier it is very important to adjust the image by target centering. This is indispensable when using the uncentered QinetiQ dataset, in contrast to this the original MSTAR dataset is centered already. Generally it cannot be assumed that the target images are centered in

a consistent format. To demonstrate the effect of classifying decentered and centered data we use the 5-class MSTAR (M5) dataset. First we make a random decentering of the target by ±10 pixel (V001), after that we decrease the misalignment to ±5 pixel (V002) and then we use our COM-algorithm to center the target (V003). When we finally allow additional shifts of ±1 pixel around the COM (V004), we get classification rates (97.9%) comparable to those of the original MSTAR centered data (V005, 98.1%). The results for these different centering studies are shown in table 4. Additional to our NN classifier the results of other classifier are demontrated (linear, polynominal, and RBF SVMs). The confusion matrices of the M5 (V004) and additionally of M10 and Q9 are given in fig. 5.

Table 4: Classification rates CLR [%] for centering studies V001-V005 with M5, 32px x 32px images with NN classifier (left table) and different types of SVM classifiers (right)

No	Case	CLR [%]
V001	±10 pix	**62.5**
V002	±5 pix	**80.2**
V003	±10 / COM	**96.1**
V004	±10 / COM / shift 1	**97.9**
V005	Original MSTAR	**98.1**

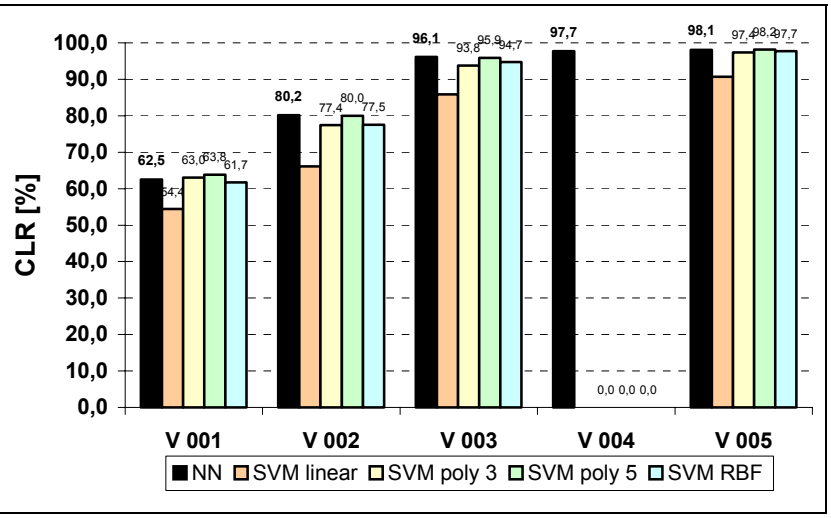

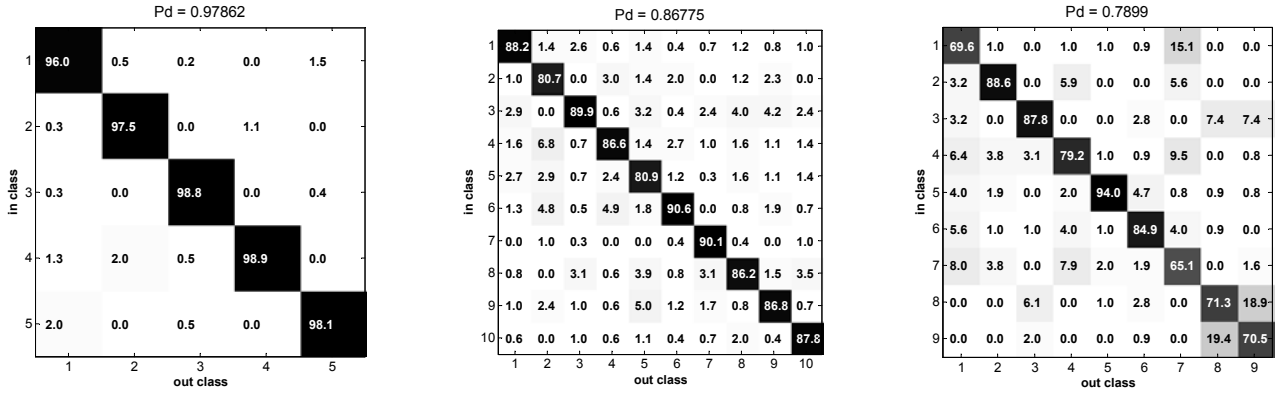

Figure 5: confusion matrices for SAR images of M5 (V004), M10 and Q9, 32px x 32 px

By applying this COM-centering algorithm on the 10-class MSTAR (M10) and 9-class QinetiQ (Q9) dataset (± 0 shifts) we get classification rates from 86.8% and 79.0% respectively (fig. 5).

5.2 Image segmentation

In section 5.1 we have calculated the classification rate of the *complete* SAR images by neglecting the influence of the clutter and the target shadow on the classification rate. In a next step we quantify this effect by separating and segmenting different parts of the image. So we are able to compute the real target

classification rate and analyze the influence of the surrounding clutter and target shadow. Fig. 6 shows different analyzed cases of segmented images, which were used as inputs for the NN-classifier. While the original image has a classification arte CLR of 97.9% the separated target classification rate drops down to 93.6%. Thus the target shadow and the clutter contribute to the classification of the SAR image. Quantifying this we get the CLR of the separated target shadow of 58.8% and a classification rate of the clutter of 99.4%. The evidence is that the clutter of the test and training images is highly correlated. To analyze this effect in detail, we put a defined zerobox over all targets and calculate the dependence of the clutter classification rate on the dimension of the box (which is a measure for the image clutter content ICC, fig. 7).

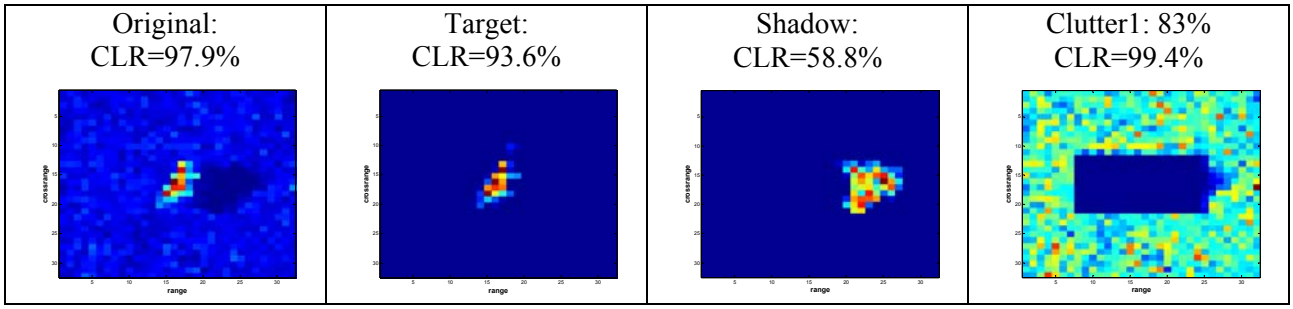

Figure 6: Segmentation of images for the M5 case; original, only target, only shadow, only clutter (from left to right)

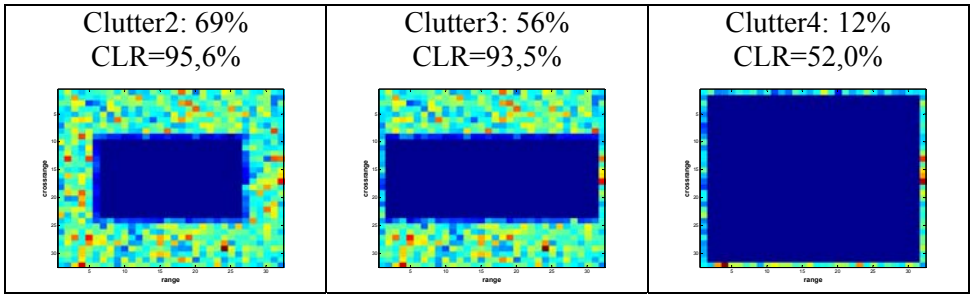

Figure 7: Clutter Classification rates CLR [%] for different image clutter content (ICC) for M5

The results are shown in fig. 8. Here we see the dependence of the clutter classification rate on the image clutter content for the two datasets M5 and Q9 classified with the NN-classifier and with a SVM-RBF classifier. In general the course of each case (M5 and Q9) is typical for the dataset, so the M5 lines are slightly convex curved, whereas the Q9 lines are more linear. The classification rate calculated with the NN classifier is much higher compared to the SVM-RBF classifier for the M5 case (up to 40%) and less high for Q9 case (4-10%). In all cases we get a significant classification rate only due to the clutter and the pixelbased minimum distance NN classifier seems to be more sensitive than the SVM classifier. This fact underlies a requirement on the used test and training dataset: To become independent from the clutter the targets in the test dataset have to be measured in different clutter environments than the training data.

To avoid this difficulty we separate the target from the clutter (step 4 in fig.3) resulting in a target classification rate of 82.7% for the M10 and 70.9% for Q9. The confusion matrices are shown in fig. 9.

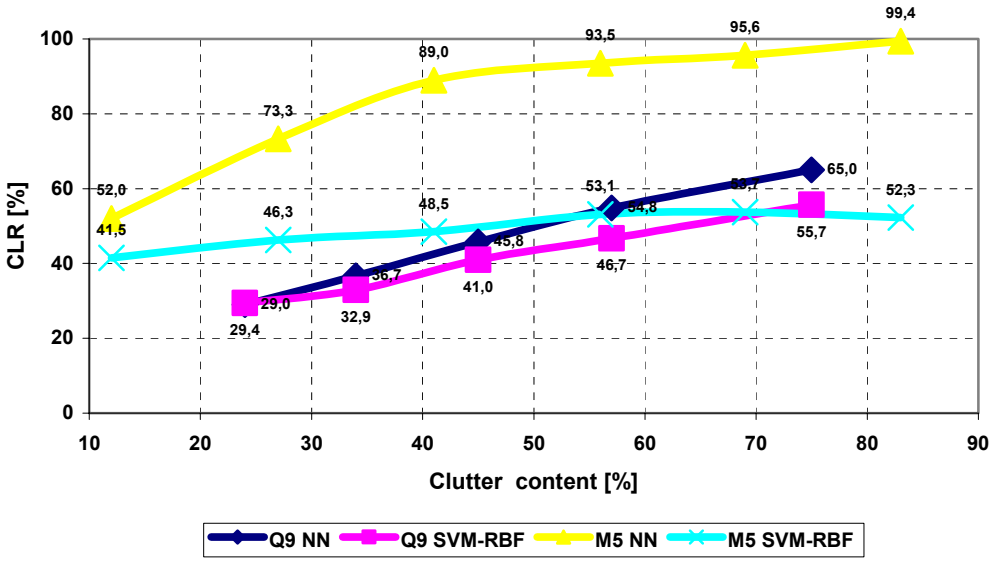

Figure 8: Classification rate CLR [%] of clutter for M5 and Q9 dataset dependent on the image clutter content

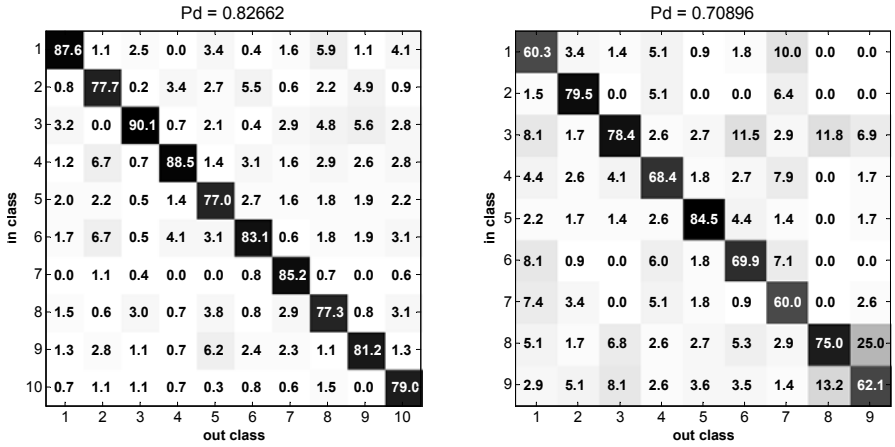

Figure 9: Confusion Matrix for M10 (l.) and Q9 (r.) for centered targets (without clutter)

This result can be optimized by shifting the COM-centered image by some pixels to compensate possible variations in the COM-calculations. A maximal target classification rate of 77.5% can be reached with an additional shift of ±4 pixels for the Q9 case (fig. 10). This fact points to the problem of the uncertainty in calculating the COM. The COM centering is only a coarse method, the fine adjustment has to be done in an additional step, for example with possible little shifts as applied here.

5.3 Classifier, image resolution and azimuth angle

Finally we compared exemplarily the identification results from the NN-classifier with different types of SVM-classifiers (linear, polynomial and RBF kernels). For these investigations (see fig. 11) we used the Matlab OSU Support Vector Machine Toolbox V.3 [4]. Because we know in both datasets the azimuth orientation of the target it is useful to rotate the images, so that all targets point in the same direction (step 2 in fig.3).

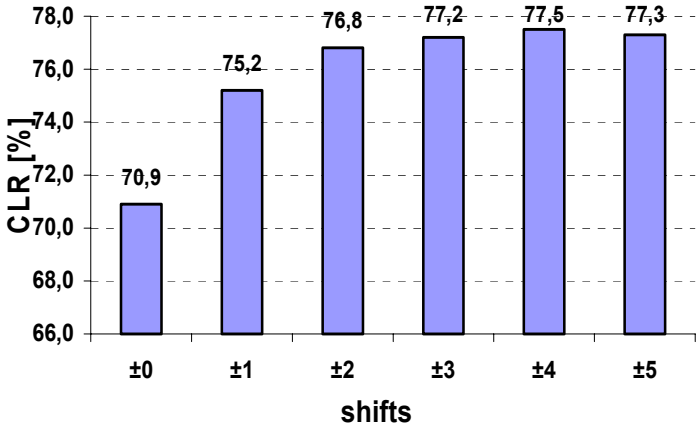

Figure 10: Classification rate for Q9 (NN, 32x32) with additional shifts on COM-centered targets

With this option the classification rates can be increased in all cases (4%-10%). The differences in the classification rate between the classifiers are marginal except the SVM with linear kernel, which produces 15-20% lower classification rates. In the M10 case we get maximal classification rates of 85-90%, in the Q9 case approximately 75%-82%. Additionally in fig. 11 the dependence of the image resolution (16, 32 and 64 pixel) is shown. In nearly all cases the best rates can be achieved using the 32 pixel (corresponding to 2ft (MSTAR) and 60cm (QinetiQ) resolution). So we cannot support the (often heard) statement that the highest resolution gets the best identification results.

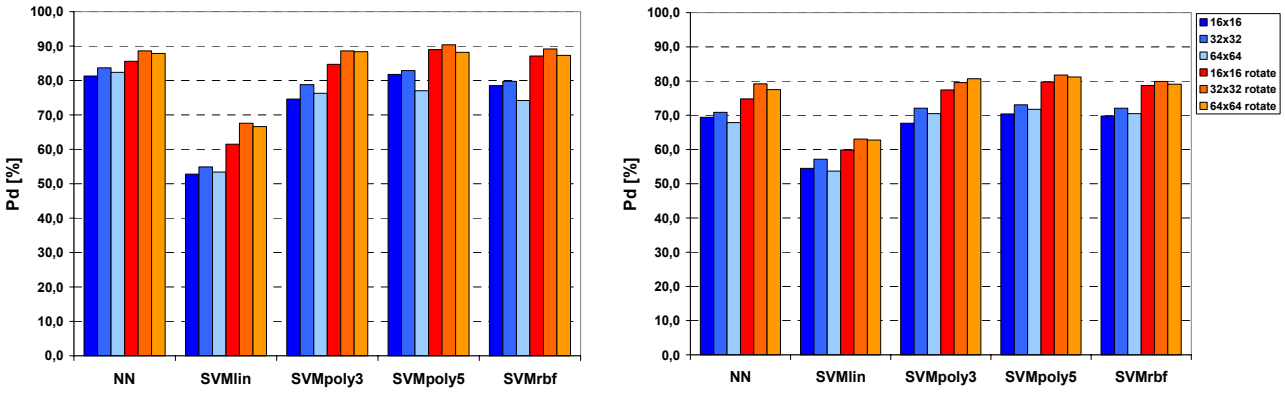

Figure 11: Classification rate [%] for different classifiers and different image resolutions (blue: without azimuth rotation, red: same azimuth orientation) for the M10 (l.) and Q9 (r.) case

6.0 CONCLUSION

Recapitulating we can conclude with the following results:

- Because of reasons of simplicity and the variety of parameters in other classifiers we used in our investigations in general a simple NN-classifier. Because our "features" are the image pixels target centering is essential. With a Center of Mass algorithm this can be done in a coarse way. Here we get target classification rates of 96.1% for the M5 case. Allowing additional shifts for a fine adjustment the classification rate can be increased to 97.9%.

- The clutter around the target and the target shadow has non negligible influence on the target classification rate. Of course the target must be separated from the clutter. This statement is true in general to reduce the S/C ratio as far as possilble. Doing this with the data under consideration in this report the classification rates drop from 87.3% to 82.7 (M10) and from 78.2% to 70.9% (Q9). With allowing shifts for fine adjustment classification rates of 77.5% can be reached for Q9. This surprising result can be explained by the "non-independence" between the test and replica images and underlies again the requirement for statistical independence of test and training data.
- For the M5 case the separated target shadow alone leads to a classification rate of 58.8%. Using only the clutter area of the images after removal of the target and shadow still classification rates varying from 52% to 99% (depending on the image clutter content ICC) were achieved, again highlightning the pronounced clutter correlation between test and training data. For clarification the dependence of the image clutter area on the classification rate was analyzed. For the Q9 case the clutter classifies the targets with 29%-65% depending on the ICC.
- By comparing the NN classifier with other classifiers (SVMs with different kernels) we get comparable results in the target classification rate.
- Dependent on the dataset best results can be reached with an image resolution of 32 pixels which correspond to 2ft (MSTAR) and 60cm (QinetiQ) pixel resolution.
- The classification rate can be tuned knowing the aspect angle of the target. Then the images can be oriented in the same direction, which increases the classification rate.

All these investigations show that the preprocessing of the data has extreme significance in the identification process. The applied classifier is then the last step with less importance. The requirements on the datasets are the strict independence of the measured test and training data.

ACKNOWLEDGEMENTS

We thank QinetiQ (UK) for providing the 9-class-dataset to the SET-053 group.

REFERENCES

[1] Moving and Stationary Target Acquisition Recognition (MSTAR), Program Review, Denver, CO, Nov. 1996

[2] Keydel, E.R., S.W. Lee and J.T. Moore: MSTAR Extended Operating Conditions. A Tutorial, In Proc. Of SPIE, Vol. 2757, Algorithms for Synthetic Aperture Radar Imagery III, p.228-242, 1996

[3] Ross, T.D. and J. Mossing: MSTAR Evaluation Methodology. In Proc. of SPIE, Vol. 3721, Algorithms for SAR Imagery VI, p.705, Orlando, USA, 1999

[4] Junshui Ma, Yi Zao: OSU Support Vector Machines Toolbox V3.00 for Matlab, Feb. 2002

[5] Gelf, S., J. Schiller and J. Chadwick: Non-Cooperative Air Target Identification using radar range profiles, 5th International Military Sensing Symposium, Gaithersburg, MD, 2002

[6] Rosenbach, K. and J. Schiller: Non-Cooperative Air Target Identification using radar imagery, IEEE International Radar Conference – RADAR 2000, Alexandria, VA, 2000

Use of Non-Ideal Training Data in SAR ATR for Targeting

S. J. Lycett, J. Denton and D. Blacknell
QinetiQ
R105
Malvern Technology Centre
St. Andrews Road
Great Malvern, Worcs, WR14 3PS
United Kingdom

ABSTRACT

This paper investigates a template-matching approach to automatic target recognition (ATR) for SAR for the case in which positive identification of a single known target type is required. ATR schemes are necessarily supported by databases of training imagery and of particular interest in this study was the impact on performance of using a database of simulated imagery to match against real in situ SAR imagery. Assessments have been made using 30cm resolution, X-band, spotlight imagery to provide the in situ test data and training databases firstly based on different examples from the same in situ data to provide an idealised baseline and secondly using simulated imagery. The impact on performance for both single channel and polarimetric data is reported and discussed.

1. INTRODUCTION

A particularly important automatic target recognition (ATR) task for synthetic aperture radar (SAR) targeting applications is that of single target identification which requires the positive identification of a single known target type within a relatively confined area. A database of previously generated training images will be available which may contain previously collected *in-situ* data, images of the target on a turntable in a controlled environment (ISAR) or images generated through the use of signature prediction tools. In this paper, a template-matching approach to the single target identification problem has been considered rather than a feature-based approach as discussed in Section 2. The robustness of template-matching to variations in aspect angle, measurement day and use of different vehicles of the same type has been studied using 30cm resolution, X-band, ISAR data of a military vehicle as discussed in Section 3. This natural within-class variation has been used to quantify confidence bounds in the matching process. The performance of the resulting ATR scheme has then been assessed in the ideal case in which independent training and test sets derived from the same 30cm resolution, X-band, spotlight imagery data source are used. However, in an operational system, the training database will be non-ideal in that it will have been obtained under different circumstances to the operational imagery against which the ATR is to be used. Performance assessments using a training database of simulated target signatures and a test set of spotlight SAR imagery have thus been performed to investigate the impact on performance of using such non-ideal training data. The results are presented in Section 4 and conclusions are drawn in Section 5.

Several data-sets have been used to support this study consisting of in situ images of targets in spotlight SAR imagery, turntable ISAR imagery of a target and simulated target images. These are described in more detail in the Appendix.

Paper presented at the RTO SET Symposium on "Target Identification and Recognition Using RF Systems", held in Oslo, Norway, 11-13 October 2004, and published in RTO-MP-SET-080.

2. TARGET CLASSIFICATION SCHEMES

Target classification is achieved using a database containing previously generated imagery of targets from a variety of different classes of interest. This is called the training set. The target image under test is compared to the images in the database and the closest match is established in some manner. If a sufficiently close match is found, then the target is declared to belong to the same class as the closest match. However, if the match is insufficiently close, then the target is declared as being unrecognised. The fundamental characteristic of different classification algorithms is how they establish the closeness of the test image to the target classes represented in the training set. There are many possible ways in which this can be achieved but they basically divide into two different types of approach, namely template-matching and feature-based classification.

In template-matching, the test image is compared with every image in the training database on a pixel-by-pixel basis to find the closest match. This comparison will normally be achieved by some form of correlation operation with the classification being declared on the basis of the highest correlation value found. One of the main drawbacks with template matching is that searching through each image in the training database can be extremely computationally expensive since the training database must contain representative images of every target in every possible configuration. This can require a very large number of images given that SAR images of the same vehicle at different aspect angles can look very different, together with the fact that a particular vehicle can assume many different configurations depending on the articulation of moving parts, such as the turret of a main battle tank, and the attachment of objects such as oil drums. Nevertheless, the template-matching concept provides a basic, robust approach to classification.

The alternative feature-based approach to classification alleviates the problem of searching through every image in the training database by characterising the targets of a particular class in terms of particular properties termed ‘features’. Features can be based on obvious physical characteristics of the target such as length and width or may be more abstract such as statistical measures of the variation in pixel brightness across the target. The idea is that a single set of features can be used to characterise many of the target images from a particular class. This means that, rather than comparing a particular test image with a large number of training images, the feature values measured for the test image can be compared with the single set of feature values which characterise a whole set of training examples. Feature-based approaches are thus potentially much more efficient than temple-matching approaches. However, the problem comes in defining an appropriate set of features and defining the method of comparison with features measured for the training examples.

For the targeting application considered in this study, the classification problem is to detect and recognise one particular target type within a SAR scene. For example, the mission may be to find a missile launcher based on collateral information that one or more are likely to be present in a particular area. In this case, the training database will require examples of only one target type and so the use of a template-matching approach may be appropriate. For this reason, the classification scheme developed in this study has taken the template-matching approach.

3. WITHIN-CLASS SIMILARITY

3.1 Introduction

SAR imagery can be presented in a number of forms. The initial SAR image produced from the raw data consists of complex-valued pixels which constitute the complex SAR image. The complex image can then be used to form the amplitude image, by taking the modulus of the complex values, or the intensity image, by taking the square of the modulus of the complex values. Either of these can be displayed as greyscale images to the operator although, because of the large dynamic range of SAR imagery, it is found that the

amplitude image is the more suitable of the two for display. For template-matching, it is necessary to establish which form of SAR image it is most appropriate to use. The determining factors on which this decision should be made are the degree to which targets from the same class are assessed as being similar, i.e. the similarity within class, and the degree to which targets from different classes are assessed as being different, i.e. the classification performance. An additional consideration is that a different form of SAR image may be even more appropriate for classification based on template matching. For example, if an appropriate threshold is applied to the target images to give a binary output such that pixels on the target are assigned a value 1 and pixels in the background are assigned a value 0 then a true template of the target results. Whether this form of image provides better template-matching performance needs also to be considered.

3.2 Correlation measures

The standard measure of correlation is given by the correlation coefficient

$$\rho = \frac{\frac{1}{N}\sum_i x_i y_i - \left(\frac{1}{N}\sum_i x_i\right)\left(\frac{1}{N}\sum_i y_i\right)}{\sqrt{\left(\frac{1}{N}\sum_i x_i^2\right) - \left(\frac{1}{N}\sum_i x_i\right)^2}\sqrt{\left(\frac{1}{N}\sum_i y_i^2\right) - \left(\frac{1}{N}\sum_i y_i\right)^2}} \tag{3.1}$$

where x and y are pixel values in the images to be correlated, N is the number of pixels and i enumerates the pixels in the image. The correlation coefficient can take values between –1 and 1 where a value of 1 indicates perfect correlation, a value of 0 indicates that the variables (i.e. images in this case) are uncorrelated and a value of –1 indicates perfect anti-correlation (e.g. one image will be the negative of the other image). This measure is the best estimate of the correlation assuming that both variables are subject to additive, Gaussian noise. For SAR images, the noise process is multiplicative speckle [1] and so the correlation coefficient given above will not provide the most accurate estimate. However, the calculation of this measure can be implemented extremely efficiently using Fourier transforms and this advantage far outweighs the disadvantage of some loss of accuracy. In this section, the variation of the correlation coefficient over example images for a particular target class is investigated. The objective is to establish that the correlation coefficient can be used to determine that the images are of the same target.

3.3 Self-correlation

The ISAR turntable imagery used for this investigation provides images of the target at every degree over 360° of aspect angle. Each of these images can be correlated with the same full set of 360 images to produce 360×360 values of the correlation coefficient. In the following results, the HH polarimetric channel was used.

The self-correlation properties using SAR images in the complex, intensity, amplitude and binary forms have been investigated. Figure 3.1 shows the averaged correlation coefficient variation is shown as a function of angular difference. In these graphs, the fitting procedure has smoothed the spike at 0° angular difference and the fact that all the graphs rise to a value of 1.0 at this point is not clear. However, the important point is that the value of the correlation coefficient drops off at different rates for different image forms. This drop-off rate is most for the complex image and least for the amplitude image. In terms of classification, it is desirable that the procedure should be robust to small changes in aspect angle otherwise the training database would need to be populated using images at a very fine sampling of the aspect angle. From this point of view, it is thus clear that the amplitude image is to be preferred. The “de-correlation” length for the amplitude image, measured in this case by a drop in the correlation coefficient to 0.8, is about 5° for the amplitude image which is an important consideration when forming the training database.

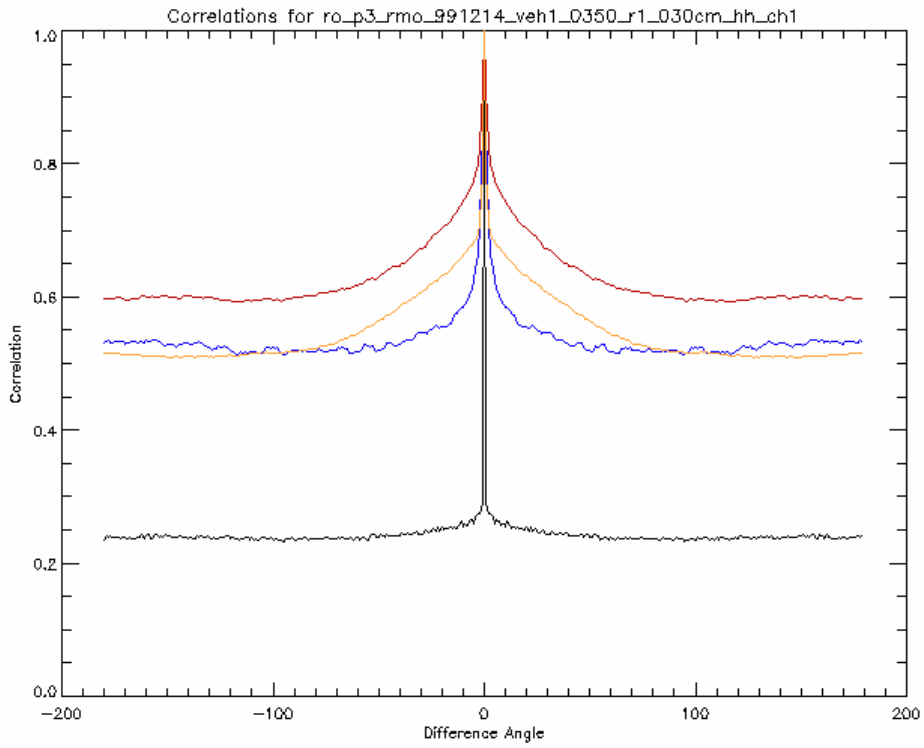

Figure 3.1: Plots of average correlation coefficient as a function of angular difference for the complex image (black), the intensity image (blue), the amplitude image (red) and the binary image (yellow).

3.4 Cross-correlation between different days

It is now necessary to investigate the robustness of the correlation coefficient to variations in the imaging circumstances. Firstly, if the same target is imaged on two different days, a robust classification scheme should still recognise it as the same target.

It is to be expected that, due to noise variations in imaging between the two days, the maximum correlation for an image at a particular aspect angle on one day will not necessarily be obtained using the image at exactly the same aspect angle on the other day. However, it should be the case that the angular difference between the best matching images will be small. Given the de-correlation length of 5° observed earlier, it is thus reasonable to search for the maximum correlation value within ± 5° of the matching angle.

Figure 3.2 shows graphs of the maximum correlation values found within this interval as a function of aspect angle. In other words, for images at each aspect angle on the first day, the maximum correlation with images on the second day within an angular difference of ± 5° was found and plotted on the graph. It can be see that the amplitude image produces the highest maximum values whilst the complex image produces the lowest maximum values.

The mean and standard deviation of these maximum values as they vary over aspect angle have been calculated and are presented in Table 3.1. This quantifies the observation that correlation applied to the amplitude image provides the greatest robustness to image variations between different days.

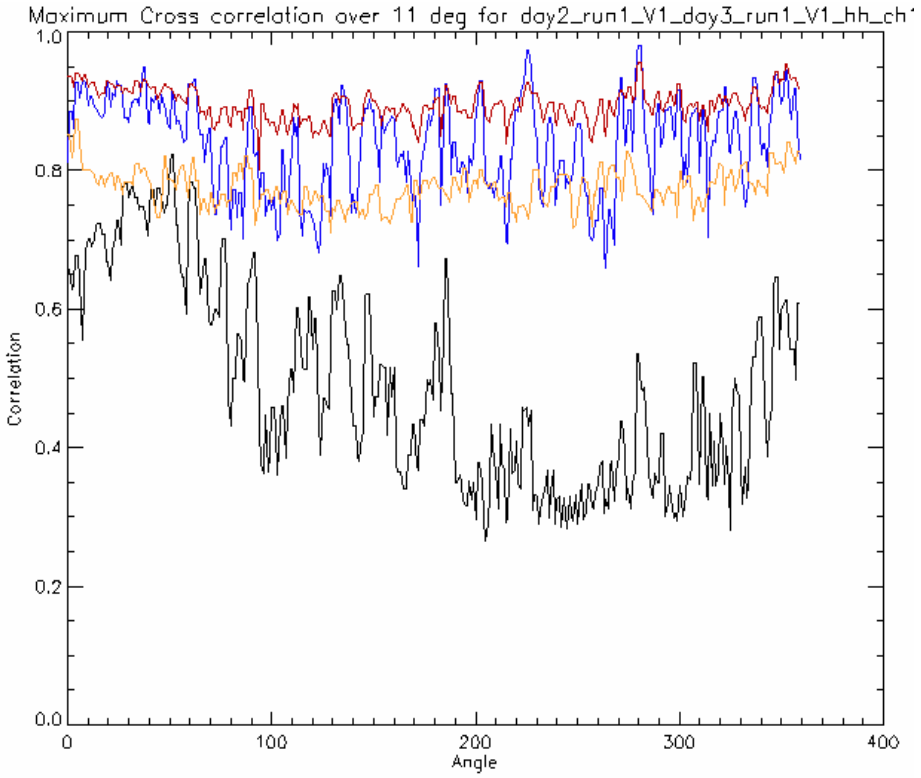

Figure 3.2: Plots of the maximum correlation within an angular difference of ± 5° from the corresponding aspect angle for target images obtained on different days for the complex image (black), the intensity image (blue), the amplitude image (red) and the binary image (yellow).

Image form	Mean	Standard deviation
Complex	0.49	0.15
Intensity	0.84	0.07
Amplitude	0.90	0.02
Binary	0.78	0.03

Table 3.1: Mean and standard deviation of maximum correlation values over aspect angle for plots shown in Figure 3.2.

3.5 Cross-correlation between different examples of same vehicle

A similar exercise can now be undertaken to investigate robustness to image variations which result when the correlation measure is applied to images of two different vehicles of the same type, i.e. it is only the registration numbers that are different.

Figure 3.3 shows graphs of the maximum correlation values found within the angular difference interval of ± 5°. Once again it can be seen that amplitude image correlation provides the highest maximum values whilst complex image correlation provides the lowest maximum values.

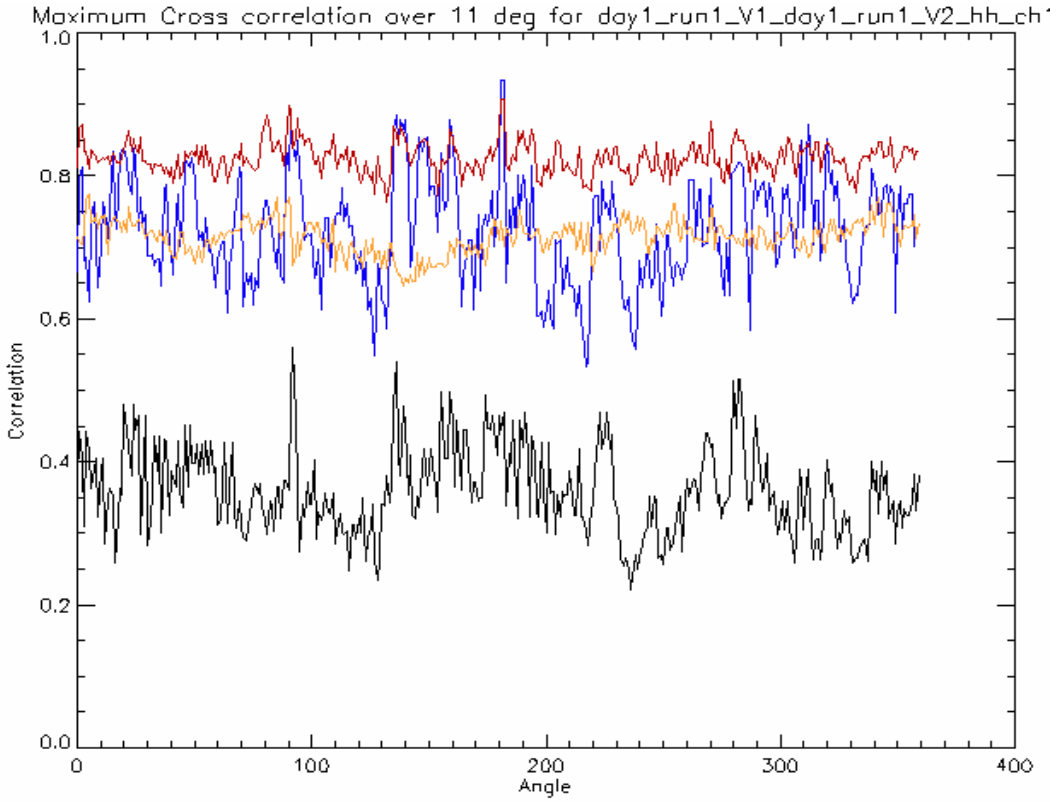

Figure 3.3: Plots of the maximum correlation within an angular difference of ± 5° from the corresponding aspect angle for target images obtained using a different vehicle of the same type for the complex image (black), the intensity image (blue), the amplitude image (red) and the binary image (yellow).

These observations are quantified in Table 3.2 using the mean and standard deviation of the maximum correlation value as before. It is clear that amplitude image correlation provides the greatest robustness to variations between different examples of the same target type. It should be noted that the mean maximum correlation coefficient in this case is significantly lower than the value obtained for variation between different days. Essentially the experiment for variation between different days involves taking a single example of the vehicle type, driving it onto the turntable, imaging it, driving it off, driving it on again and imaging it a second time. However, the experiment for different examples of the same vehicle type involves exactly this process together with the replacement of the vehicle with another of the same type between imaging runs. Thus it is to be expected that the loss in correlation observed for different days will be incurred together with an additional loss associated with use of different examples of the vehicle. These results are thus consistent with expectation.

Image form	Mean	Standard deviation
Complex	0.36	0.06
Intensity	0.72	0.07
Amplitude	0.83	0.02
Binary	0.71	0.02

Table 3.2: Mean and standard deviation of maximum correlation values over aspect angle for plots shown in Figure 3.3.

4. PERFORMANCE RESULTS

4.1 Introduction

The aim of this section is to assess the performance of the template-matching approach to target recognition. On the basis of the discussions in section 3, the amplitude image has been used in the experiments. Furthermore, since the trials data which has been used to support these experiments is fully polarimetric, the amplitude of the polarimetric span image has been used.

Whilst it has been argued earlier that template-matching is not appropriate for many-class problems due to the computational effort required, it is valid to explore the performance experimentally when computation time is not a critical issue. In particular, it is important to introduce the concept of an unrecognised class and also to investigate the impact on performance of the presence of targets not represented in the training database (termed "confusers"). These issues will be addressed in this section under the discussion of classification results.

The main problem to be addressed by this study was identified as that of single target identification which is of particular relevance for targeting applications. This can be viewed as an extreme example of the classification problem with confusers when everything other than the single target of interest can be considered to be a confuser. The results for the single target identification performance assessment are also presented in this section and follow naturally from the discussion of more general classification.

4.2 Classification results

For a classifier to be effective, it must not only be able to classify targets of interest, but it must also be able to declare targets as being unrecognised if there is insufficient confidence that the target belongs to one of the known classes. The correlation coefficient provides an effective means of assessing confidence since it provides a normalised measure lying between 0 and 1 which quantifies the goodness of the match between a test image and a training image. Thus it is simply necessary to define a threshold on the correlation coefficient values such that positive classification declarations are only made when the coefficient exceeds this threshold and otherwise the target is declared to be unrecognised.

Previous discussions regarding similarity within class in section 3 have shown that the maximum correlation coefficient generally exceeds 0.8 for targets from the same class which have been imaged under different circumstances. This value thus provides a suitable threshold value to be considered. In the following results, a threshold values of 0.8 will be used together with 0.0 to illustrate the performance when there is no unrecognised class.

	A	B	C	D	E	F	G	H	I	U
A	79	1	0	5	1	1	14	0	0	0
B	0	96	0	2	2	0	0	0	0	0
C	4	8	74	3	5	2	5	0	1	0
D	8	1	0	85	0	4	3	0	0	0
E	5	1	0	5	86	0	3	0	1	0
F	6	10	0	5	8	65	5	0	0	0
G	0	0	0	2	3	1	95	0	0	0
H	3	16	0	7	2	0	5	59	8	0
I	1	13	0	1	5	0	3	0	78	0

Table 4.1: Confusion matrix for 9 class problem with correlation threshold defining unrecognised class set to 0.0.

	A	B	C	D	E	F	G	H	I	U
A	68	1	0	0	1	1	12	0	0	17
B	0	94	0	1	2	0	0	0	0	4
C	0	0	0	0	0	0	0	0	0	100
D	8	0	0	77	0	4	2	0	0	9
E	4	0	0	0	58	0	1	0	0	38
F	0	0	0	4	2	14	0	0	0	81
G	0	0	0	2	3	1	93	0	0	2
H	0	0	0	0	0	0	0	5	0	95
I	0	0	0	0	0	0	0	0	0	100

Table 4.2: Confusion matrix for 9 class problem with correlation threshold defining unrecognised class set to 0.8.

Tables 4.1 and 4.2 show confusion matrices including an unrecognised class using the correlation coefficient thresholds of 0.0 and 0.8 respectively. The entries show the percentage of test examples classified as a particular target class. When there is no unrecognised class, the average correct classification rate is close to 80%. However, it is interesting to note that., when the unrecognised class is introduced, a number of images fail to produce correlation values exceeding 0.8 despite being represented in the training data. Indeed, almost all test examples of target types C, H and I are declared as being unrecognised as well as significant numbers of target types E and F. It should be noted that target types C, H and I are the decoy targets in the scene whilst E is a tractor with trailer and F is a water tower, i.e. none are true military vehicles. In fact, the only vehicles for which the classifier is confident , i.e. A, B, D and G, are precisely the military vehicles in the scene. This appears to suggest that the characteristics of military vehicles appear to make them more easily distinguishable than non-military objects.

	A	B	C	D	E	F	G	H	I	U
A	70	1	0	0	0	0	12	0	0	17
B	0	95	0	1	0	0	0	0	0	4
C	0	0	0	0	0	0	0	0	0	100
D	9	1	0	79	0	0	2	0	0	9
E	4	1	0	0	0	0	3	0	0	93
F	4	0	0	7	0	0	4	0	0	85
G	1	1	0	2	0	0	95	0	0	2
H	0	0	0	0	0	0	0	0	0	100
I	0	0	0	0	0	0	0	0	0	100

Table 4.3: Confusion matrix for 4 class problem with 5 confusers and correlation threshold defining unrecognised class set to 0.8.

In an operational ATR system, it is likely that the training database will contain comprehensive examples of military vehicles but that other objects will not necessarily be represented. Thus it is important to understand the performance of a classifier when the training set is restricted to military vehicles but confusers are present in the test set. Table 4.3 shows the classification results when only target types A, B, D and G are represented in the training database but an unrecognised class is included with a threshold of 0.8. It can be seen that the classifier rejects all the decoys (C, H and I) as being unrecognised as well as most of the tractor with trailer images (E) and water tower images (F). Confusers which are classified as military targets are false alarms and these represent 4.4% of the total in this experiment. For the military vehicles, 8% are declared as being unrecognised so that 92% can be considered to have been detected as being military vehicles. These concepts of detection and false alarm rates within a classifier will be seen to be of great relevance in the single target identification case. Finally, the correct classification rate for the four military vehicles is 85% in this case.

4.3 Single target identification results

Single target identification is essentially a classification problem in which the training database contains only one class of military target. A suitable confidence threshold must be set, i.e. a threshold on the correlation coefficient value in this case, and then a test target image is declared as either being the target of interest or unrecognised. The concepts of detection and false alarm rates are then entirely appropriate to this classification problem. Detections occur when an example of the target class is correctly recognised whilst false alarms occur when a confuser is incorrectly declared to be a member of the target class. It is thus possible to plot the probability of detection against the probability of false alarm as the correlation threshold is varied to produce the so-called receiver operating characteristic (ROC) curves most usually associated with target detection assessments.

ROC curves have been produced for each of the nine targets in the *in situ* trial set. In each case, the training database contains only images of the particular class of interest. All the images in the test set are classified as either belonging to this class or as being unrecognised. The correlation threshold is varied from 0 to 1 and the resulting variation of probability of detection against probability of false alarm is plotted. Figure 4.1 shows the resulting curves for Targets A to I excluding Target G whilst the first graph in Figure 4.2 shows the ROC curve for Target G. It is interesting to first consider the decoy targets C, H and I. The curves for these essentially follow the line of equal probabilities for detection and false alarm. This indicates that no useful performance is being achieved since, for any given threshold, the same proportions of detections and false alarms are being obtained. In other words, the classification is essentially random. At the other end of the scale, the military vehicles (A, B, D and G) are showing a level of classification performance in that relatively high probabilities of detection can be achieved for relatively low probabilities of false alarm. The ROC curves for the tractor with trailer (E) water tower (F) lie between these extremes. These results are consistent with the observation made in section 4.2 that the military vehicles appear to be more easily distinguishable than the non-military objects.

	Probability of detection	Probability of false alarm
Target A	0.80	0.11
Target B	0.95	0.09
Target D	0.89	0.10
Target G	0.98	0.14

Table 4.5: Summary of probabilities of detection and false alarm for military vehicles using a correlation threshold of 0.8.

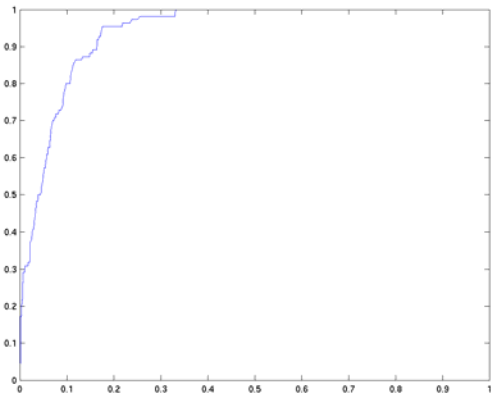	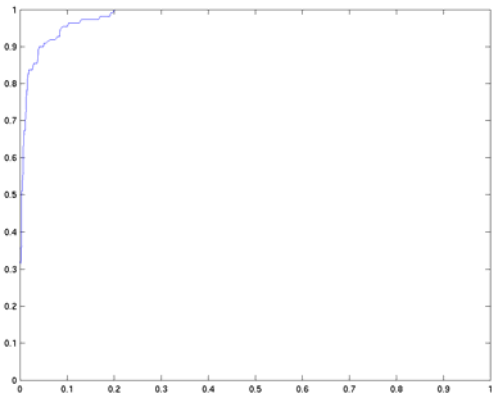
Target A	Target B
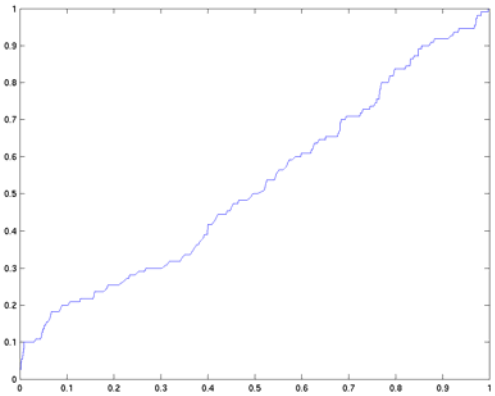	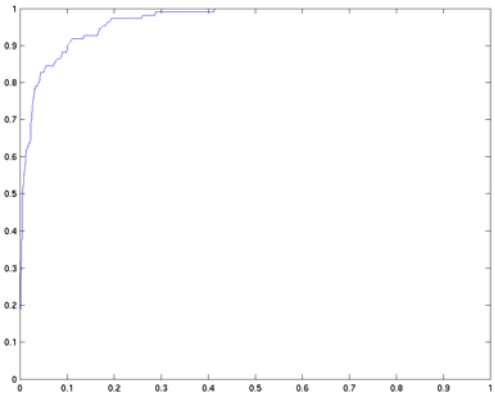
Target C	Target D
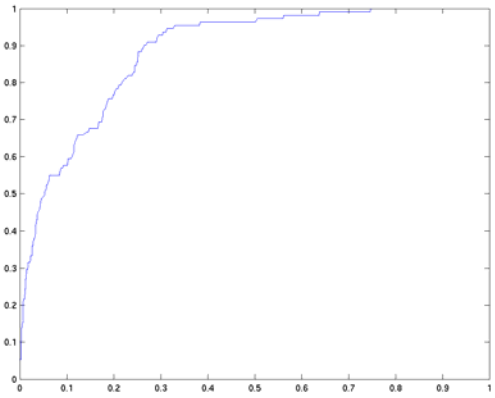	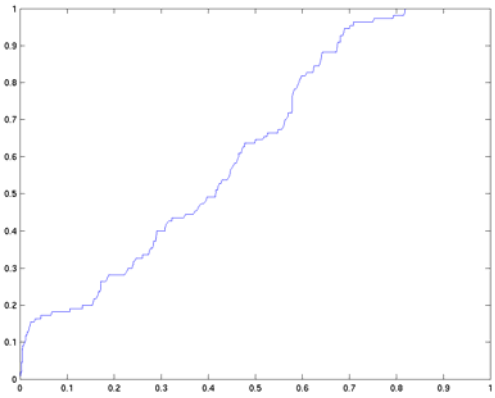
Target E	Target F

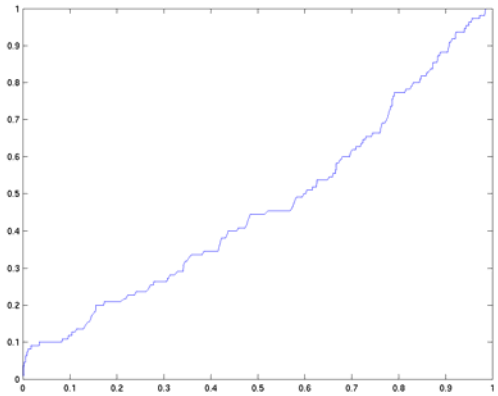

Target H

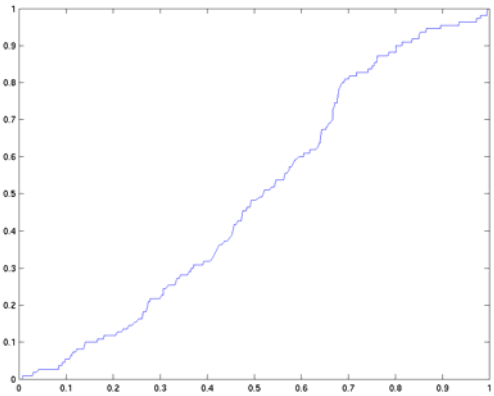

Target I

Figure 4.1: ROC curves showing probability of detection versus false alarm as correlation threshold is varied for Targets A to I excluding Target G.

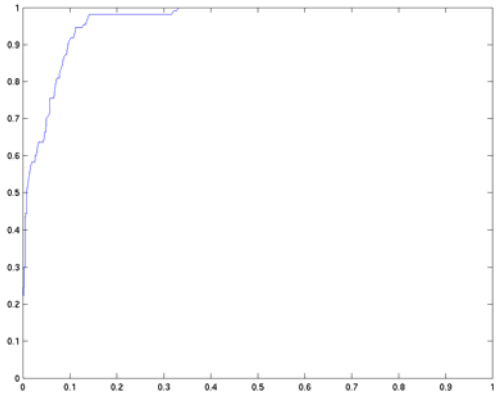

Target G

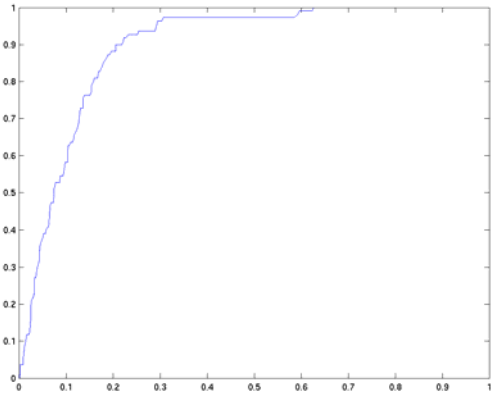

Target G using simulated training images

Figure 4.2: ROC curves showing probability of detection versus false alarm as correlation threshold for Target G using training database from in situ trial data(left) and from simulated signature predictions (right).

The performance against the military vehicles will now be examined more closely. Operationally, a single correlation threshold needs to be set and the results of section 3 suggest that a value of 0.8 is a suitable choice since within-class variations still produce values exceeding this. Using this threshold, the probabilities of detection and false alarm shown in Table 4.5 are obtained.

It can be seen that the probabilities of false alarm are all around 0.1 (although that for Target G is a little higher than the rest) whilst the probabilities of detection vary from 0.8 to 0.98 reflecting the varying degrees to which each target is distinguishable from the others. From an operational perspective, this means that to achieve a detection probability of between 80% to 100% a false declaration will be made 10% of the time. It should be noted that, from the results of section 4.2, it can be concluded that most of the false declarations will arise from other military vehicles since the non-military objects were easily classified as being unrecognised.

An important operational factor for classification algorithms is the question of how the training database of imagery is populated. In these experiments, the test and training images were all obtained form exactly the same experimental trial. However, in practice, the training imagery may have to be obtained using turntable ISAR imaging or through the use of signature predictions using CAD (computer aided design) models of the vehicles of interest [2]. The impact of this disparity between the training data source and the operational data needs to be investigated.

A limited assessment of this issue has been made under the current study. For Target G, a training set consisting of signature predictions was generated at the appropriate resolution and geometry. The single target identification performance was then assessed as before using all the *in situ* trial test images and resulted in the ROC curve shown in the right of Figure 4.2. It is very encouraging that a significant level of classification performance has been achieved in this case. However, it is clear that the performance is also significantly worse than when test and training data are from the same data source as in the ROC curve on the left hand side of Figure 4.2. Using a correlation threshold of 0.8, the probability of false alarm in this case is 0.09 whilst the probability of detection is 0.55. Thus, in comparison to the results above for the same data sources, the false detections have been maintained at around 10% whilst the correct declarations have fallen substantially to 55%.

The performance results presented in this section have demonstrated that single target identification can be achieved using a template-matching approach but that the achievable performances are limited by the practical consideration that the training database will be populated using a different data source than that which will be used operationally. The conclusion is that improved performance needs to be achieved using algorithms which are, in particular, robust to the use of data from different sources, e.g. ISAR turntable imagery or signature predictions.

5. CONCLUSIONS

The results of various performance assessments have been reported using a set of four military vehicles and five non-military objects acting as “confusers”. It has been found that detection rates for a specific military vehicle within this target set ranges from 80% to 98% depending on the vehicle type with a false classification rate of about 10%. These results were obtained using training and test imagery from the same experimental data source. However, in practice the training database will be populated beforehand using, for example, ISAR turntable measurements or signature predictions. A limited experiment using training data for one vehicle generated from a signature prediction model revealed a drop in performance to 55% for a false alarm rate of about 10%.

The performance results which have been obtained have demonstrated that single target identification can be achieved using a template-matching approach but that the achievable performances are limited by the practical consideration that the training database will be populated using a different data source than that which will be used operationally. The conclusion is that improved performance needs to be achieved using algorithms which are, in particular, robust to the use of data from different sources, e.g. ISAR turntable imagery or signature predictions. A possible avenue of future research is thus the use of a classification approach which exploits understanding of the physics of the radar interaction with the target [2].

ACKNOWLEDGEMENTS

This work was supported by the UK MOD under the Applied Research Programme contract number A/CTA/N03504 entitled “All Weather Target Engagement”.

REFERENCES

[1] [1] C J Oliver and S Quegan, “Understanding Synthetic Aperture Radar Images”, Artech Housee, 1999.

[2] [2] D B Andre, “Generation of Simulated radar ground-target database, its validation & ATR performance”, RTO Symposium on Target Identification and Recognition using RF sensors, Oslo, 11-13 October, 2004.

APPENDIX

The data sets used in this study all consisted of fully polarimetric, 30cm resolution X-band imagery. The first data set was obtained at a Regular Army Assistance Trial (RAAT) on Salisbury plain in which spotlight imagery of targets in open ground were obtained every degree over 360° at an incidence angle of 5°. An example image is shown in Figure A.1 with labels showing the targets of interest in this study. The second data set consisted of ISAR turntable images of Target G formed every degree over 360° at an incidence angle of 35°. The images at every 10° are shown in Figure A.2. The third data-set consisted of images generated from signature predictions for Target G at 5° for direct comparison with the RAAT trial imagery. These simulated images at every 10° are shown in Figure A.3.

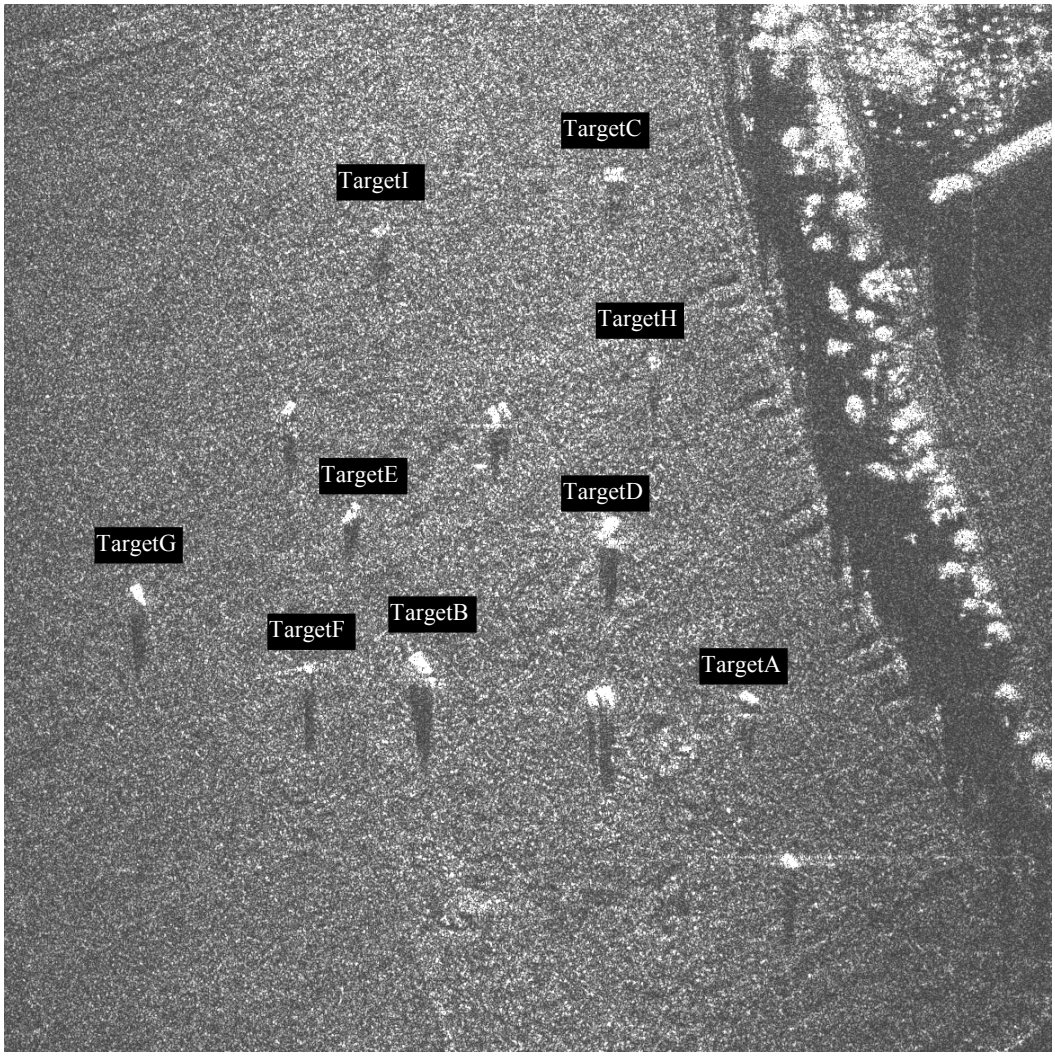

Figure A.1: An example image from the RAAT trial data-set.

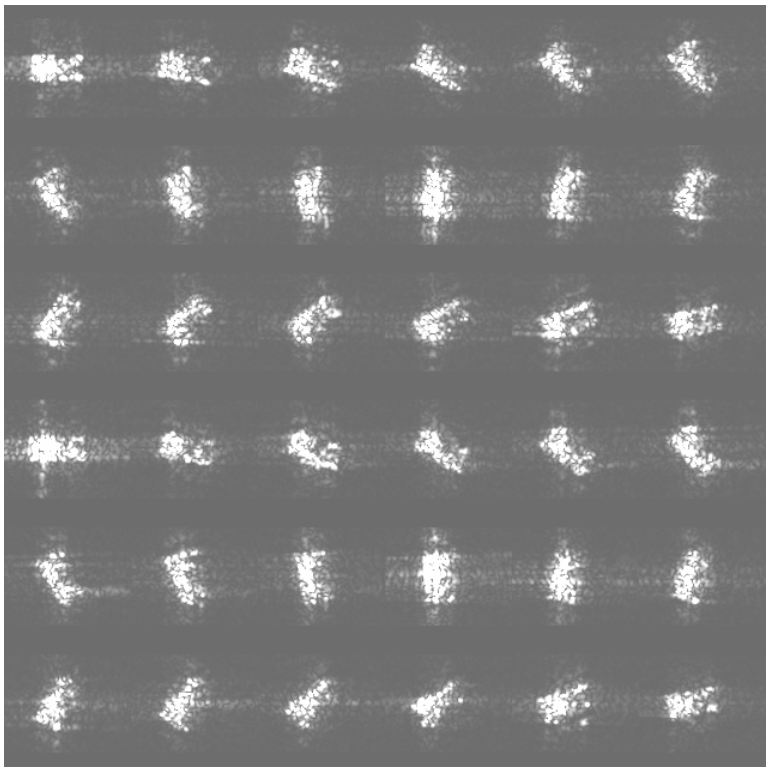

Figure A.2: Images of Target G at 10° intervals from the ISAR turntable data-set

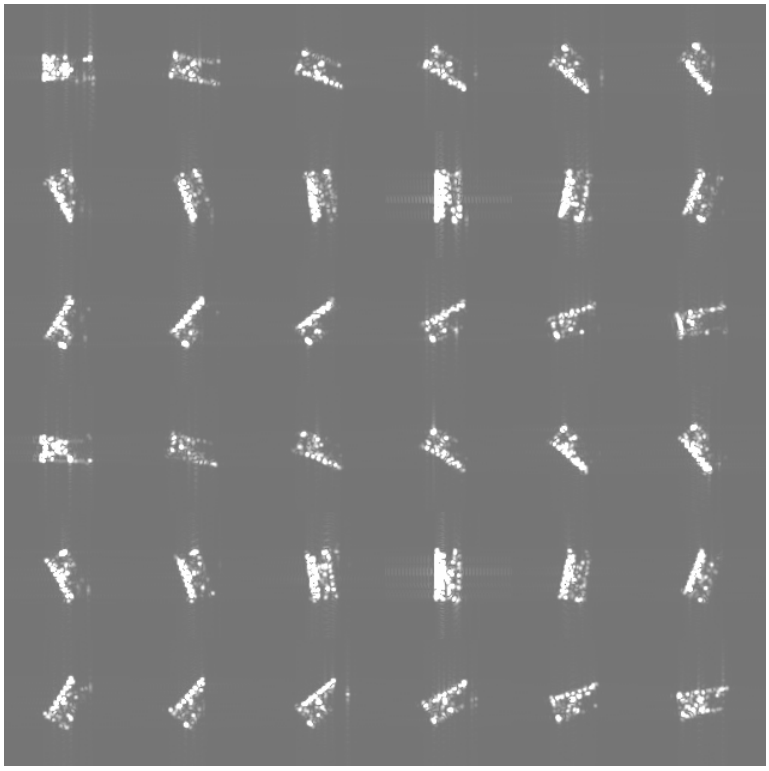

Figure A.3: Images of Target G at 10° intervals from the simulated data-set.

ATR Performance within an Extended X-Band Tower-Turntable Database of Highly Resolved Relocatable Targets

Timo Kempf, Markus Peichl, Stephan Dill, Helmut Süß
DLR (German Aerospace Center)
Microwave and Radar Institute
P.O.-Box 11 16,
82230 Wessling
Germany

ABSTRACT

By means of data from highly resolved tower-turntable ISAR measurements this paper investigates the ATR robustness of small changes in the articulation of targets (e.g. military vehicles) and changes in the incidence angle. The recognition process is based on a template matching method. The two-dimensional templates are generated by extracting the most robust scatterers from the RCS image.

1. INTRODUCTION

Global and reliable reconnaissance using remote sensing techniques requires weather and daytime independent detection, recognition, and identification of interesting objects. Thus a spaceborne high resolution synthetic aperture radar (SAR) system in a spotlight mode can be an appropriate instrument. On this basis we undertook X-band ISAR-measurements on a tower-turntable arrangement to get highly resolved two-dimensional signatures of military and civilian relocatable targets for adequately steep depression angles. Our work is focused on the military vehicles, and we use civilian vehicles as confusers.

Since typical military vehicles consist of several ideally behaving scattering centers which show some robustness to aspect variations, we established a recognition method based on the extraction of these point scatterers. Furthermore, with a demanded declaration time that is sufficiently long, we have the freedom to perform classification via a computationally intensive template matching process. Moreover this method ensures a sufficient inner class robustness, while simultaneously yielding efficient inter class separability.

This paper shall give an overview of the performance of the introduced ATR method using the tower-turntable database, which includes several thousand templates. The classifiers are evaluated by ROC-curves and confusion matrices. To examine the robustness of this recognition method we focus on different articulations of the targets. The articulations were realized by changing the position or pose of movable vehicle parts such as hatches, turrets, and assemblies, or by using camouflage. Additionally, we used small variations of the elevation angle or a modified ground. The results should also provide insight into how many different realizations and poses of one target type have to be stored in a database.

In [1] we already described an attempt to introduce a kind of fingerprint analysis as a situation-optimized tool for reliable target recognition.

The development and investigation of our method is based on ISAR measurements in X band carried out on military vehicles for different steep depression angles realized by a suitable tower-turntable arrangement as shown in fig. 1.

Paper presented at the RTO SET Symposium on "Target Identification and Recognition Using RF Systems", held in Oslo, Norway, 11-13 October 2004, and published in RTO-MP-SET-080.

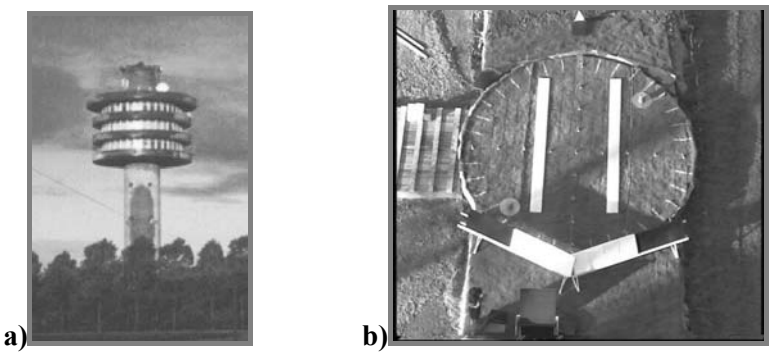

Figure 1: Tower-turntable setup for ISAR measurements, a) four platforms on the tower allow different incidence angles, b) the turntable was covered with soil and grass for a realistic ground, having 9m in diameter and a payload up to 100t.

These data have been used to develop a tomographical processing scheme that delivers a filtered and digitized radar image of those target scatteres, which behave strongly like ideal point scatterers and which are robust to aspect angle variations as illustrated in **fig. 2**.

In a practical use of a military reconnaissance operation such digitized images of an actual scene of interest can be compared successively to similarly processed image templates of a database. In principle, a type specific classifier correlates the current digitized test image with each training image, delivering the highest of the generated correlation values. In the following this value is also used as 'discrimination value'. Our first results indicated that this kind of fingerprint analysis can deliver reliable recognition results with a feasible amount of computational effort.

In order to assess the robustness of this recognition method many ISAR measurement campaigns have been undertaken in the past with focus on small variations of the targets or the scene. The results should also provide an idea how many different realizations of one target type have to be stored in a database, or which poses could be neglected, respectively.

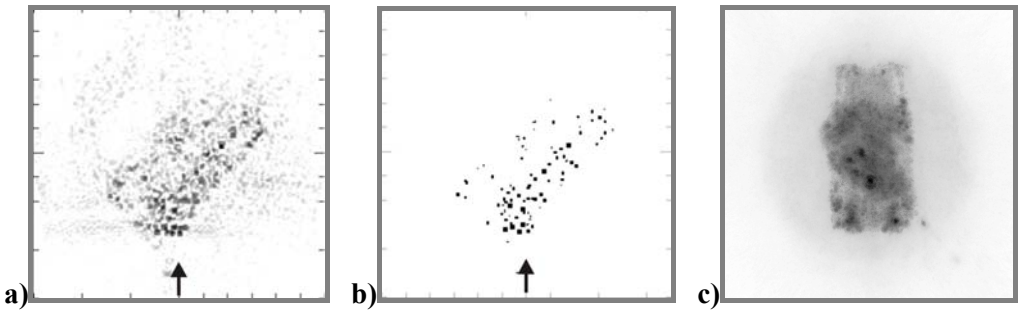

Figure 2: Example of a tomographically processed image, a) RCS after sidelobe suppression, b) a filtered version with the most reliable scatterers for use in ATR, c) an incoherent superposition of single images for a whole 360° rotation of the turntable. The turret and the gun were turned by 40° compared to the vehicles main axis.

The target list of our last campaign included military and civilian vehicles, whereas the intention of the ATR system design is focused on the military targets and the civilian vehicles are mainly used as confusers. Variants have been realized by changing the position or pose of movable vehicle parts like hatches, turrets, and assemblies, for instance, or by partially covering the targets with natural obstacles. Additionally small variations of the elevation angle or a modification of the ground have been used.

For the evaluation of the ATR results, the commonly used receiver operating characteristic (ROC) curves and confusion matrices are computed.

2. CLASSIFICATION RESULTS

The vehicles used are two **battle tanks** of different type (**BTa** and **BTb**), a **lorry** (**LOR**), a military **all-terrain vehicle** (**ATV**), a **VW bus** (**VWB**), a **tractor** (**TRA**), a **weapon-carrier** (**WCA**), and an optical **mockup** of the **weapon-carrier** (**MWC**).

2.1 Test data and training data with different polarization

Measurements were undertaken in HH polarization as well as in VV polarization. In order to demonstrate our approach applied to military targets the data set was divided into VV training data and HH test data. If the target provides enough "ideal" scattering centers like corners, we can expect a satisfying recognition performance. Each data set includes 72 templates corresponding to images in 5° azimuthal steps.

In detail the HH test data includes 12 data sets, 4 sets of battle tank 'a' as shown in **Fig. 3** by no. 1 to no. 4 along the horizontal axis, 4 sets of battle tank 'b' labeled by no. 5 to no. 8, 1 set of the lorry labeled by no. 9, 1 set of the all-terrain vehicle labeled by no. 10, and 2 sets of the VW bus labeled by no. 11 and no. 12. The VV training data includes the same targets with identical articulations and identical measurement geometry. Thus, for each test class a classifier could be established. It should be noted, that the SNR of the HH data was about 15dB less than that of the VV data due to technical reasons.

Fig. 3a) shows the discrimination behaviour of the BTa classifier (fed with the VV data set) for each test template from the 12 HH test data sets. A discrimination value d_{BTa}=1.0 would signify perfect identity of test and training template. **Fig. 3b)** shows the discrimination results of the BTb classifier, **fig. 3c)** that one of the LOR classifier, **fig. 3d)** that one of the ATV classifier, and **fig. 3e)** the discrimination results of the WCA classifier.

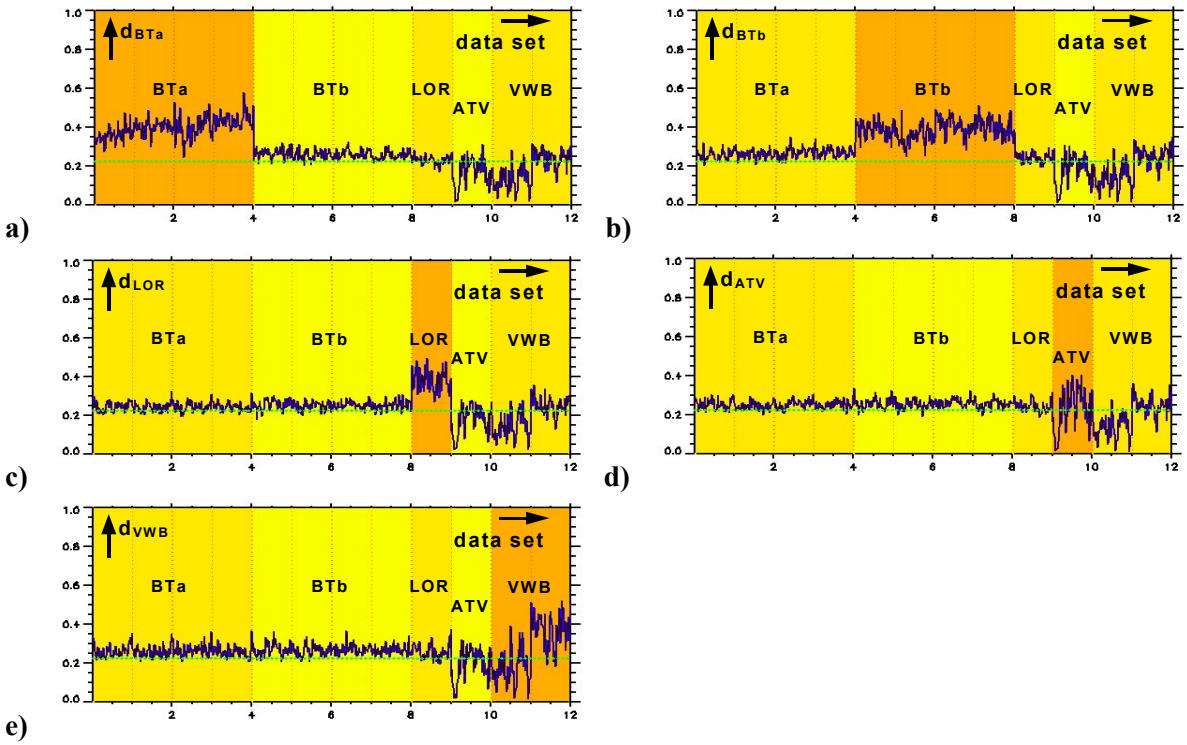

Figure 3: Discrimination results of the classifiers, for a description see text.

The dotted horizontal line represents the decision line for generating the confusion matrix as described below. The discrimination values of the classifiers for the battle tanks are well above this decision line and the discrimination values of the confuser vehicles.

A common tool to represent the property of a classifier is the ROC curve as shown in **fig. 4**. It relates the percentage of correct classification P_{CC} to the percentage of false alarms P_{FA}. This means, for a well adopted classifier the ROC curve will start at the point {1,1} in the graph, then move with a rising threshold close to the ideal point {0,1} corresponding to 100% of correct classification and no false alarm, and finally it drops down to the point {0,0} [2].

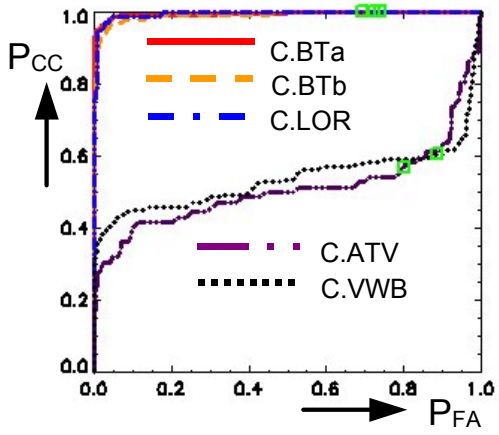

Figure 4 : ROC curves for the classifiers of fig. 3.

The squares mark the threshold points for the confusion matrix. The ROC curves for the battle tank classifiers are close to the ideal point. This confirms our assumption, that a method based on the highly resolved local distribution of robust scatterers applied to these types of vehicles would enable ATR. Additionaly the ROC curve of the lorry classifier shows the same performance, while the ROC curves of the ATV classifier and the VW bus classifier perform worse, since these targets deliver a far less number of robust scatterers.

Table 1a) below shows the corresponding confusion matrix, enabling the comparison of different classifiers on fixed values [3]. The rows represent the test data sets, and the columns denote the training data sets. The column 'OUT' includes the case, where the test target was not part of the training data, respectively. The numbers in the confusion matrix state how many templates of the current test data set yield a discrimination value in the classifier higher than a fixed threshold and higher than the values of the other classifiers. If no other classifier exceeds the threshold, the template is counted to the 'OUT' class.

As a common practice the threshold is chosen to a value that forces the classifiers to declare $P_D = 0.9$. Then the confusion matrix can be reduced to the percentage of correct classification as given by the numbers in the diagonal, and related to the number $P_{CC|D}$ of contributing templates for the fixed P_D. Here it is 98.46%. **Table 1b)** shows these percentages within the rows of the confusion matrix.

The results for the two battle tanks and the lorry show nearly ideal results, and the ATV and the VW bus show a high rejection rate. However, there is a low misclassification rate as indicated by the high $P_{CC|D}$ .In principle this indicates a high performance of this ATR method.

Table 1a). Confusion matrix for the VV trained classifiers on HH test data.

	C.BTa	C.BTb	C.LOR	C.ATV	C.VWB	*OUT*
BTa	**287**	1	0	0	0	***0***
BTb	0	**288**	0	0	0	***0***
LOR	0	0	**71**	0	1	***0***
ATV	2	0	0	**37**	4	***29***
VWB	1	1	1	1	**83**	***57***

Table 1b). Confusion matrix with normalized rows for the VV trained classifiers on HH test data.

	C.BTa	C.BTb	C.LOR	C.ATV	C.VWB	*OUT*
BTa	**99.7**	0.3	0	0	0	***0***
BTb	0.0	**100.0**	0.0	0.0	0.0	***0.0***
LOR	0.0	0.0	**98.6**	0.0	1.4	***0***
ATV	2.8	0.0	0.0	**51.4**	5.6	***40.3***
VWB	0.7	0.7	0.7	0.7	**57.6**	***39.6***

2.2 Test data and training data of different articulations or measurement geometry

The list in table 2a) gives an overview of the training data. The test data consist of the sets listed in table 2b), which almost all are given in VV-polarization*. This list describes first the target type, then the incidence angle, and finally some special articulations.

Table 2a). List of the training data (set number, type, incidence angle, polarization).

1. **BTa 45° HH + VV**
2. **BTb 50° HH + VV**
3. **LOR 50° VV**
4. **ATV 45° HH + VV**
5. **VWB 50° HH + VV**
6. **WCA 45° VV**

Table 2b). List of the test data (set number, type, incidence angle, special articulations).

1.	BTa	45°	no snow crosses
2.	BTa	45°	no snow crosses, hatches open
3.	BTa	45°	turret heading 20°
4.	BTa	45°	turret heading 40°
5.	BTa	42.5°	
6.	BTa	47.5°	
7.	BTa	50°	
8.	BTa	45°	turret heading 90°
9.	BTa	45°	turret heading 180°
10.	BTa	45°	metal plates on ground
11.	BTb	42.5°	
12.	BTb	45°	
13.	BTb	47.5°	
14.	BTb	50°	turret heading -45°
15.	BTb	50°	turret heading -90°
16.	BTb	50°	metal plates on ground
17.	BTb	50°	natural camouflage
18.	LOR	42.5°	
19.	LOR	45°	
20.	LOR	47.5°	
21.	ATV	47.5°	
22.	ATV	50°	
23.	VWB	47.5°	*(HH-polarization)
24.	VWB	47.5°	
25.	TRA	45°	
26.	WCA	42.5°	
27.	WCA	47.5°	
28.	WCA	50°	
29.	WCA	45°	natural camouflage
30.	MWC	45°	

Fig. 5 shows the discrimination results of the classifiers. The discrimination graphs show that the classifiers produce different results for different target articulations. Therefore a closer look on the corresponding ROC curves and confusion matrices shown in **fig. 6** is helpful. **Fig. 6a)** shows a perfect ROC curve for test data set no. 1 and no. 2 where the difference between the test and training data are mounted or dismounted snow crosses or closed or opened hatches. Even though these variations have stronger influences on the radar images as a whole, they offer quite enough redundancy for our ATR approach.

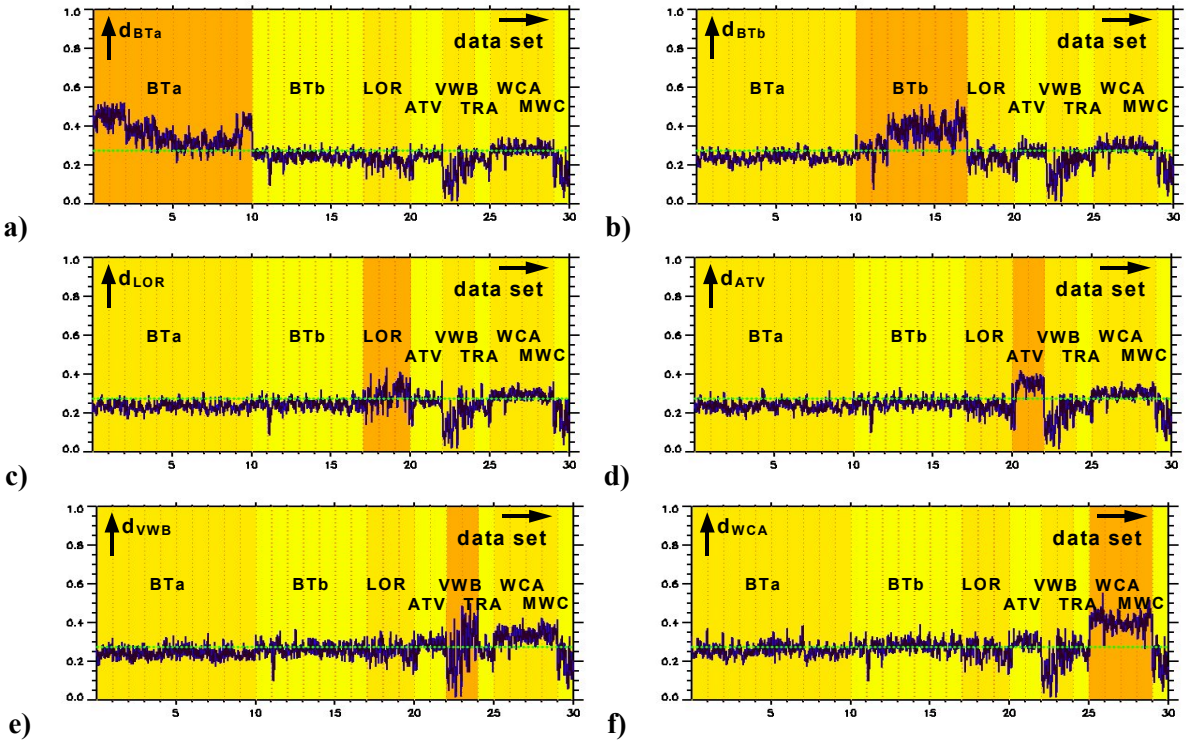

Figure 5: Discrimination results of the classifiers. a) BTa classifier, b) BTb classifier, c) LOR classifier, d) ATV classifier, e) VWB classifier, f) WCA classifier.

A stronger impact on the ATR performance is visible for the case of covering the natural grassy ground with metal plates, as it has been done in the test data sets no. 10 and no. 16 shown in **fig. 6a)** and **fig. 6b)**. The P_{CC} drops down to values below 0.9 and 0.8 for a P_{FA}=0 value.

Similar results can be observed for targets covered with natural camouflage as in the cases of test set no. 17 shown in **fig. 6b)** and no. 29 shown in **fig. 6j)**. Even though the radar images as a whole show serious differences, a satisfying recognition rate can be achieved. Here only the surface of the targets was covered, but much more information is given by the wheels and chassis structures at the sides of these vehicles.

In another test series the turret heading of the battle tanks was varied. **Fig. 6c)** and **6d)** show the corresponding ROC-curves with a very high and thus impressive robustness. This results again from the fact that the most important information is derived from the chassis. The highest degradation of the ATR performance can be observed for test set no. 8. Here the tank has a rather big turret covering a lot of the lower located scatterer centers in this position. The turret structure of the BTb is smaller, and so we don't see such a strong influence on the ROC curve for a similar heading in set no. 15.

Stronger impacts on the ATR performance are visible for differences in the incidence angle between training and test data, even for small variations. **Fig. 6e)** illustrates the results for a difference of 2.5° in incidence angle for the set no. 5 and no. 6, and 5° for set no. 7). **Fig. 6f)** shows the corresponding graphs for an incidence angle difference of 7.5°, 5° and 2.5° corresponding to nos. 11, 12, 13. In this case the 2.5° difference between training and test has less impact on the ROC-curve, but the 5° case gives worse results. In general it can be stated, that there is very much information available from the chassis parts of the tanks, which is relevant for our ATR approach. Due to the steep elevation angles as pretended by space-borne radars, the overlay effect in the SAR imaging can distort the relative location of the scatterers in the templates [4].

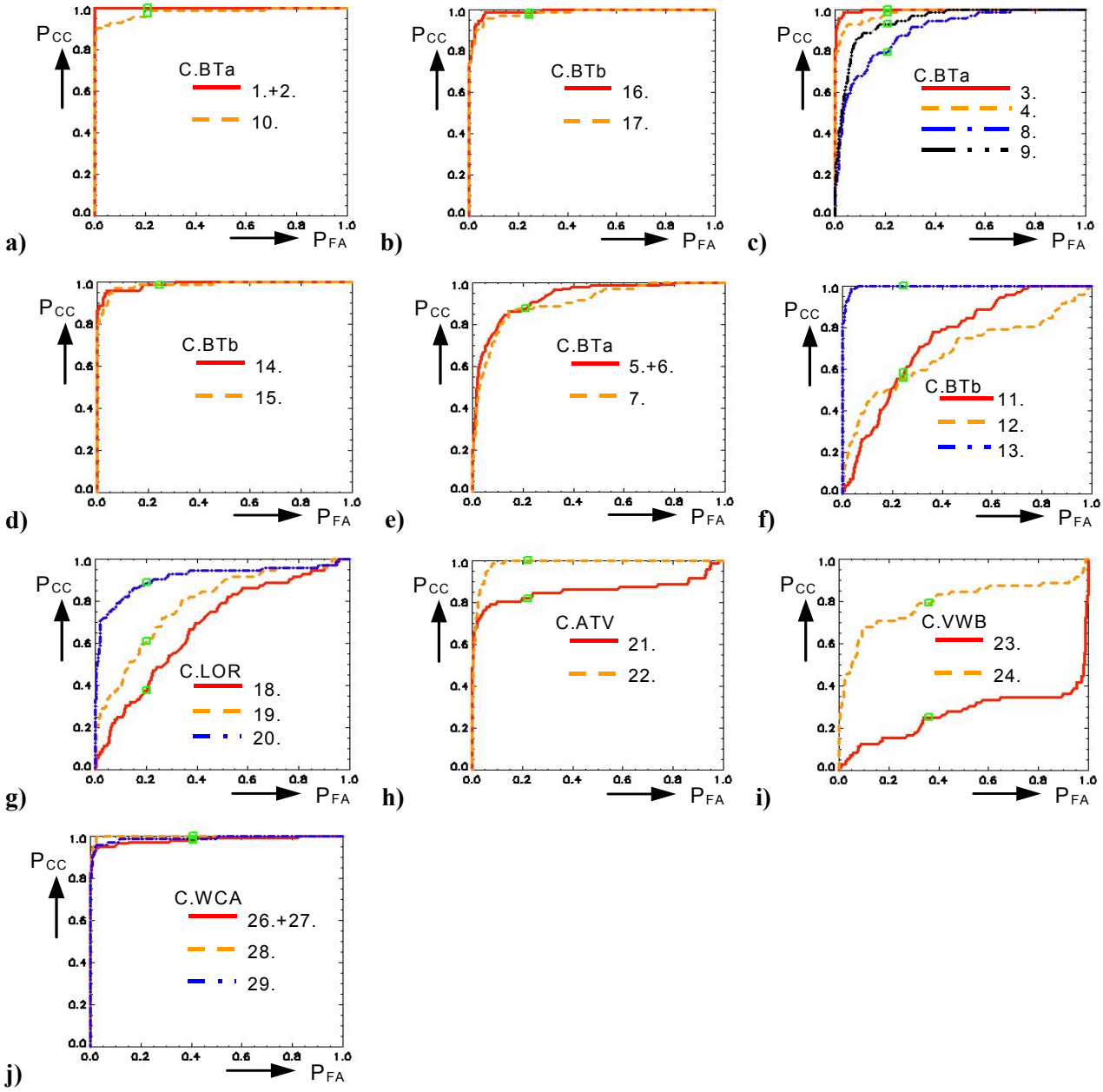

Figure 6: ROC curves for different classifiers and data sets of table 2. See text for further information.

The graph in **fig. 6g)** for the LOR confirms the above observed tendency. The reason that the results of the ATV in **fig. 6h)** don't fit into this behaviour was a SNR problem in the first part of data set no. 21. The worse SNR of the HH data also causes the wide spread of the ROC-curves in **fig. 6i)**, where identical geometrical conditions of the target have been used.

Some additional information about the classifiers may be extrcated from the confusion matrices listed in **table 3**. The P_D is again chosen to 0.9, but here without the confuser data sets of the TRA and the MWC. The corresponding $P_{CC|D}$ is 0.83. The mostly high numbers of the battle tank classifiers confirm the results of **fig. 6**. Note the very low number of misclassifications of the other battle tank, the other non-tank-like targets, and the confusers. However, this performance could easily be optimized by an adaption of the P_D value to the exclusive characteristics of the battle tank classifiers.

Table 3a). Confusion matrix for the data of table 2.

	C.BTa	C.BTb	C.LOR	C.ATV	C.VWB	C.WCA	*OUT*
BTa	**649**	2	1	1	11	23	***33***
1.+2.	**144**	0	0	0	0	0	***0***
3.	**72**	0	0	0	0	0	***0***
4.	**70**	0	0	0	0	1	***1***
5.+6.	**115**	0	0	0	4	16	***9***
7.	**59**	2	0	0	2	3	***6***
8.	**56**	0	1	0	1	3	***11***
9.	**64**	0	0	1	3	0	***4***
10.	**69**	0	0	0	1	0	***2***
BTb	5	**399**	1	0	17	39	***43***
11.	2	**21**	1	0	9	25	***14***
12.	3	**27**	0	0	7	9	***26***
13.	0	**72**	0	0	0	0	***0***
14.	0	**70**	0	0	0	2	***0***
15.	0	**69**	0	0	0	3	***0***
16.	0	**70**	0	0	1	0	***1***
17.	0	**70**	0	0	0	0	***2***
LOR	0	3	**113**	2	22	29	***47***
18.	0	1	**16**	2	14	13	***26***
19.	0	2	**36**	0	5	16	***13***
20.	0	0	**61**	0	3	0	***8***
ATV	0	0	1	**117**	6	11	***9***
21.	0	0	0	**53**	4	6	***9***
22.	0	0	1	**64**	2	5	***0***
VWB	0	0	0	1	**74**	0	***69***
23.	0	0	0	0	**18**	0	***54***
24.	0	0	0	1	**56**	0	***15***
WCA	0	1	0	0	15	**269**	***3***
26.+27.	0	0	0	0	5	**136**	***3***
28.	0	0	0	0	1	**71**	***0***
29.	0	0	0	0	9	**62**	***1***
TRA	0	2	2	2	9	19	***38***
MWC	0	0	1	1	6	9	***55***

Table 3b). Corresponding confusion matrix with normalized rows.

	C.BTa	C.BTb	C.LOR	C.ATV	C.VWB	C.WCA	*OUT*
BTa	**90.1**	0.3	0.1	0.1	1.5	3.2	***4.6***
1.+2.	**100.0**	0.0	0.0	0.0	0.0	0.0	***0.0***
3.	**100.0**	0.0	0.0	0.0	0.0	0.0	***0.0***
4.	**97.2**	0.0	0.0	0.0	0.0	1.4	***1.4***
5.+6.	**79.9**	0.0	0.0	0.0	2.8	11.1	***6.3***
7.	**81.9**	2.8	0.0	0.0	2.8	4.2	***8.3***
8.	**77.8**	0.0	1.4	0.0	1.4	4.2	***15.3***
9.	**88.9**	0.0	0.0	1.4	4.2	0.0	***5.6***
10.	**95.8**	0.0	0.0	0.0	1.4	0.0	***2.8***
BTb	1.0	**79.2**	0.2	0.0	3.4	7.7	***8.5***
11.	2.8	**29.2**	1.4	0.0	12.5	34.7	***19.4***
12.	4.2	**37.5**	0.0	0.0	9.7	12.5	***36.1***
13.	0.0	**100.0**	0.0	0.0	0.0	0.0	***0.0***
14.	0.0	**97.2**	0.0	0.0	0.0	2.8	***0.0***
15.	0.0	**95.8**	0.0	0.0	0.0	4.2	***0.0***
16.	0.0	**97.2**	0.0	0.0	1.4	0.0	***1.4***
17.	0.0	**97.2**	0.0	0.0	0.0	0.0	***2.8***
LOR	0.0	1.4	**52.3**	0.9	10.2	13.4	***21.8***
18.	0.0	1.4	**22.2**	2.8	19.4	18.1	***36.1***
19.	0.0	2.8	**50.0**	0.0	6.9	22.2	***18.1***
20.	0.0	0.0	**84.7**	0.0	4.2	0.0	***11.1***
ATV	0.0	0.0	0.7	**81.3**	4.2	7.6	***6.3***
21.	0.0	0.0	0.0	**73.6**	5.6	8.3	***12.5***
22.	0.0	0.0	1.4	**88.9**	2.8	6.9	***0.0***
VWB	0.0	0.0	0.0	0.7	**51.4**	0.0	***47.9***
23.	0.0	0.0	0.0	0.0	**25.0**	0.0	***75.0***
24.	0.0	0.0	0.0	1.4	**77.8**	0.0	***20.1***
WCA	0.0	0.4	0.0	0.0	5.2	**93.4**	***1.0***
26.+27.	0.0	0.0	0.0	0.0	3.5	**94.4**	***2.1***
28.	0.0	0.0	0.0	0.0	1.4	**98.6**	***0.0***
29.	0.0	0.0	0.0	0.0	12.5	**86.1**	***1.4***
TRA	0.0	2.8	2.8	2.8	12.5	26.4	***52.8***
MWC	0.0	0.0	1.4	1.4	8.3	12.5	***76.4***

In addition, **table 3** shows less performance for the WCA. The column of the WCA classifier shows several cases of misclassifications for other targets. This behaviour could be compensated by a scaling-down procedure for the discrimination values of the WCA classifier. However, we would not get the high performance of the battle tank classifiers as the WCA cannot deliver as much robust information due to its lower size.

Note that the confusion matrix shows a low number of misclassifications for the mock-up MWC by the WCA classifier, which could also be reduced by a corresponding raise of the decision threshold.

3. CONCLUSION

Based on data sets of ISAR tower-turntable measurements, this paper showed the high performance of our specific template matching method for the automatic recognition of battle tanks using a high resolution imaging radar. Special attention was given to the robustness of this method against small changes of the target articulation and pose. Even though the number of data for the special articulations was relatively small and the estimated statistics for the shape of the ROC curves and confusion matrices has therefore only a limited confidence, some concise tendencies could be observed.

In general, it can be recommended that for a training data base, regardless of using measured or synthetic data, more effort should be payed in different realisations of the sensor-target geometry like incidence and aspect angle than in many various articulations of the target. However, the application of our method on other targets than tanks has still to be evaluated.

4. REFERENCES

[1] Kempf, T., and M. Peichl, "A Method for Advanced Automatic Recognition of Relocatable Targets ", Proc. of RTO SET Panel, Prague, Czech Republic, Apr. 2002.

[2] R.A. English, "Classifier Evaluation Methodology using MSTAR Public Data Set", NATO working paper, DRDC Ottawa, Feb. 2003.

[3] Kempf, T., and M. Peichl, "Application of Complex Dual Apodization to high resolution low incidence angle ISAR images", Proc. of German Radar Symposium GRS, Berlin, Germany, Oct. 2000.

5. GLOSSARY

ATR	Automatic Target Recognition
ATV	All-Terrain Vehicle
BTa,BTb	Battle Tank type a/b
C.(BTa)	(Battle Tank type a)-Classifier
HH	Horizontal transmit/receive polarization
ISAR	Inverse SAR
LOR	Lorry
MWC	Mock-up of the Weapon Carrier
P_{CC}	Percentage of Correct Classification
$P_{CC\|D}$	P_{CC} for a fix P_D
P_D	Percentage of Declaration
ROC	Receiver Operating Characteristic
SAR	Synthetic Aperture Radar
SNR	Signal to Noise ratio
TRA	Tractor
VV	Vertical transmit/receive polarisation
VWB	Volkswagen Bus
WCA	Weapon Carrier

Optimizing Single Sweep Range and Doppler Processing for FMCW Radar using Inverse Filtering

A.J. de Jong and Ph. van Dorp
Oude Waalsdorperweg 63
2597 AK, Den Haag
The Netherlands

a.j.dejong@fel.tno.nl

ABSTRACT

We discuss range and Doppler processing for FMCW radar using only a single pulse or frequency sweep. The first step is correlation processing, for which the range and Doppler resolution are limited by the ambiguity function. We show that this resolution can be optimized with an additional inverse filtering step. The method is demonstrated for sinusoidal FMCW radar measurements. Several regularized inverse filters were compared and the non-adaptive pseudo inverse filter gave the best results.

1. INTRODUCTION

In this paper we discuss a technique for simultaneously obtaining range and Doppler information with FMCW radar, using only a single pulse or frequency sweep. The single sweep approach contrasts with the multi sweep approach, where the range info is obtained from the pulse delay and the Doppler info from the phase changes in the range cells from pulse to pulse.

An advantage of single sweep processing is that for a given observation time T the unambiguous range is considerably larger than for the multi sweep approach. The reason is that for multi sweep processing, N sweeps of duration T/N are required to obtain a Doppler axis with N different Doppler cells. A disadvantage of single sweep processing is that the range and Doppler resolutions are generally worse, as we discuss in chapter 2. In this paper we focus on the range and Doppler resolutions for single sweep radar, and in chapter 3 we show how these resolutions can be optimized using inverse filtering. The method is applied to actual measurements of a sinusoidal FMCW radar, as discussed in chapter 4.

2. CORRELATION PROCESSING

2.1 Transmitted and received signals

The transmitted signal is an FM signal around a carrier frequency f_c. The phase of the transmitted signal is given by

$$\varphi(t) = \varphi_0 + 2\pi f_c t + \varphi_m(t),$$

and the instantaneous frequency is found as

$$f(t) \equiv \frac{1}{2\pi}\frac{d\varphi}{dt} = f_c + \frac{1}{2\pi}\frac{d\varphi_m}{dt} \equiv f_c + f_m(t).$$

Paper presented at the RTO SET Symposium on "Target Identification and Recognition Using RF Systems", held in Oslo, Norway, 11-13 October 2004, and published in RTO-MP-SET-080.

The boundaries of $f_m(t)$ determine the bandwidth B of the modulation. Ignoring the initial phase φ_0, the complex transmitted signal reads:

$$\psi_T(t) \equiv \exp[i\varphi(t)] = \exp[i\varphi_m(t)]\exp(i2\pi f_c t) \equiv \mu(t)\exp(i2\pi f_c t).$$

It follows that the transmitted signal can be written as a CW signal times a complex envelope $\mu(t)$. We also need an expression for the received signal of a number of targets k at ranges R_k and with radial velocities u_{rk}. We will use the following approximation, holding for most practical cases [1]:

$$\psi_R(t) = \sum_k V_k \mu(t-\tau_k)\exp[i2\pi(f_c+\nu_k)t],$$

where $\tau_k = 2R_k/c$ is the delay and $\nu_k = 2f_c u_{rk}/c$ is the Doppler frequency. The complex factor V_k contains the attenuation and a possible phase shift.

2.2 The ambiguity function

The objective is to extract the amplitude $|V_k|$, the delay τ_k and the Doppler frequency ν_k for each target k from the received signal $\psi_R(t)$. An ideal approach would be to perform such an operation on $\psi_R(t)$ that we arrive at a function of the following form:

$$Z(\tau,\nu) = \sum_k V_k \delta(\tau-\tau_k, \nu-\nu_k).$$

This would be ideal because this function $Z(\tau,\nu)$ shows sharp peaks at $\tau = \tau_k$ and $\nu = \nu_k$ with amplitude $|V_k|$ for all targets k. An attempt to arrive at this ideal $Z(\tau,\nu)$ is to correlate $\psi_R(t)$ with the following reference signal [1]:

$$\psi_F(t,\nu) = \mu(t)\exp[i2\pi(f_c+\nu)t].$$

This results in

$$Z(\tau,\nu) \equiv \int_t \psi_R(t)\psi_F{}^*(t-\tau,\nu)dt = \sum_k V_k \chi(\tau-\tau_k, \nu-\nu_k),$$

where the function $\chi(\tau,\nu)$ is defined as

$$\chi(\tau,\nu) = \int_t \mu(t)\mu^*(t-\tau)\exp(-i2\pi\nu t)dt.$$

The function $\chi(\tau,\nu)$, which is completely determined by the modulation $\mu(t)$, is known as the ambiguity function [3]. In case $\chi(\tau,\nu) = \delta(\tau,\nu)$, correlation processing would be perfect. Indeed for a (quasi) random modulation, the expectation of the ambiguity function is a delta function [1]. This for instance means that correlation processing is ideal for FM radio signals. More generally, the response $Z(\tau,\nu)$ to a collection of point targets k contains a shifted copy $\chi(\tau-\tau_k,\nu-\nu_k)$ for every target k. The range and Doppler resolutions of the targets is described by the sharpness of the central peak at $\chi(0,0)$.

3. OPTIMIZING CORRELATION PROCESSING

3.1 Inverse filtering

The previous chapter may suggest that the ambiguity function $\chi(\tau,\nu)$ gives the ultimate range and Doppler resolution for a given modulation $\mu(t)$. However, correlation processing as described in chapter 2 is only optimal for (quasi) random signals. In this chapter we show how the resolution and the signal to noise ratio of the correlation result $Z(\tau,\nu)$ can be improved using the well-known technique of inverse filtering [4]. We recall the correlation result:

$$Z(\tau,\nu)=\sum_k V_k\,\chi(\tau-\tau_k,\nu-\nu_k)\,.$$

We now interpret $\chi(\tau,\nu)$ as a point spread or blurring function. Because $\chi(\tau,\nu)$ is exactly known from $\mu(t)$, the blurred shape can be focused to a point with an inverse filter derived from $\chi(\tau,\nu)$. The inverse filter is most conveniently described in the Fourier domain, and therefore we introduce the following Fourier transformations:

$$\zeta(p,q)=F_{pq}\{Z(\tau,\nu)\}\,,$$
$$\xi(p,q)=F_{pq}\{\chi(\tau,\nu)\}\,.$$

In the Fourier domain the correlation is given by

$$\zeta(p,q)=\sum_k V_k\,\exp(-ip\tau_k)\exp(-iq\nu_k)\xi(p,q)\,.$$

Note that in this representation the blurring function $\xi(p,q)$ can be taken out of the summation. This suggests elimination of the blurring with the following filtered version of $\zeta(p,q)$:

$$G(p,q)\equiv H(p,q)\zeta(p,q)\equiv\frac{1}{\xi(p,q)}\zeta(p,q)=\sum_k V_k\,\exp(-ip\tau_k)\exp(-iq\nu_k)\,.$$

Here, $H(p,q)$ is the inverse filter, which is the inverse of the Fourier transform of the ambiguity function. Via an inverse Fourier transform we obtain:

$$g(\tau,\nu)=F_{\tau\nu}^{-1}\{G(p,q)\}=\sum_k V_k\,\delta(\tau-\tau_k,\nu-\nu_k)\,.$$

Thus we eventually arrive at the ideal point target response.

3.2 Pseudo inverse filtering

For the application of inverse filtering in practice, regularization of the inverse filter is necessary. One possibility is the pseudo inverse filter [4]:

$$H_P(p,q)=\frac{1}{\xi(p,q)}\,,\qquad \text{for } |\zeta(p,q)|>K\sigma_N,$$
$$H_P(p,q)=0\,,\qquad \text{for } |\zeta(p,q)|<K\sigma_N.$$

Here σ_N is the noise level and $K > 1$ is a threshold parameter. We see that for (p,q) values where $\zeta(p,q)$ does not sufficiently dominate the noise, $H_P(p,q)$ is cleared. This means that for these (p,q) values, $\zeta(p,q)$ does not contribute to the resulting $G(p,q)$ and $g(\tau,\nu)$.

For noisy signals, noise outliers will be more abundant, and this is particularly devastating at (p,q) values where $|\xi(p,q)|$ is very small. The influence of such outliers can be largely suppressed with a non-adaptive approach, where the filter is cleared where $|\xi(p,q)|$ is small rather than $|\zeta(p,q)|$. This leads to the non-adaptive pseudo inverse filter:

$$H_{PN}(p,q) = \frac{1}{\xi(p,q)}, \quad \text{for } |\xi(p,q)| > K',$$
$$H_{PN}(p,q) = 0, \quad \text{for } |\xi(p,q)| < K'.$$

Here K' is a new threshold parameter. Possibly, one can avoid the discontinuities at the edges of the regions where the filter is cleared with the following modification:

$$H_{PN}(p,q) = \frac{\xi^*(p,q)}{|\xi(p,q)|^2 + K'^2}.$$

This can be regarded as a smoothed version of the non-adaptive pseudo inverse filter.

3.3 The Wiener filter

Similar to the pseudo inverse filter is the Wiener filter [4], which is the optimal filter in the sense of minimizing the expected least square error in the resulting $g(\tau,\nu)$:

$$H_W(p,q) = \frac{\xi^*(p,q)}{|\xi(p,q)|^2 + \sigma_N{}^2 / |\zeta(p,q)|^2}.$$

The Wiener filter is also an adaptive filter requiring the estimation of σ_N. One can introduce an artificial threshold parameter by multiplying σ_N with a factor K, leading to a smoothed version of the pseudo inverse filter $H_P(p,q)$.

4. APPLICATION TO SINUSOIDAL FMCW RADAR MEASUREMENTS

4.1 Sinusoidal FMCW radar

We have applied correlation processing and subsequent inverse filtering on actual measurements of a sinusoidal FMCW radar. For this modulation, we have the following transmitted signal [2]:

$$\psi_T(t) = \exp(i2\pi f_c t + ia\cos 2\pi f_m t) = \exp(ia\cos 2\pi f_m t)\exp(i2\pi f_c t),$$

with the following instantaneous frequency:

$$f(t) = \frac{1}{2\pi}\frac{d\varphi}{dt} = f_c - af_m \sin(2\pi f_m t).$$

We see that the instantaneous frequency variation of the transmitted signal is sinusoidal with bandwidth $B = 2af_m$. The ambiguity function is found as

$$\chi(\tau,\nu) = \int_{<T>} \exp[ia(1-\cos 2\pi f_m \tau)\cos 2\pi f_m t - ia \sin 2\pi f_m \tau \sin 2\pi f_m t]\exp(-i2\pi\nu t)dt\,.$$

Here the integral is only carried out over one modulation period $T = 1/f_m$. Normally the delay τ will be small compared to the modulation period T, so that the latter expression can be simplified by a first order approximation of $\sin(2\pi f_m\tau)$ and $\cos(2\pi f_m\tau)$. This leads to

$$\chi(\tau,\nu) \cong \int_{<T>} \exp(-ia2\pi f_m \tau \sin 2\pi f_m t)\exp(-i2\pi\nu t)dt\,.$$

We now borrow the following expression from the theory of Bessel functions:

$$\exp(iz\sin(\theta)) = \sum_{s=-\infty}^{\infty} J_s(z)\exp(is\theta)\,,$$

where s runs over all integers. Substitution in the previous expression gives

$$\chi(\tau,\nu) = \sum_{s=-\infty}^{\infty} J_s(-a2\pi f_m\tau)\int_{<T>}\exp[i2\pi(sf_m-\nu)t]dt\,.$$

For the computation of $Z(\tau,\nu)$ one can freely choose a set of ν values. Choosing $\nu = nf_m$ with integer n, the integral in the latter expression simplifies to δ_{ns} and we get

$$\chi(\tau, nf_m) = J_n(-\pi B\tau) = (-1)^n J_n(\pi B\tau)\,.$$

This ambiguity function is shown in figure 1. The range, which is proportional to τ runs vertically. In this and all following image plots, darker pixels have higher values. The cross section $\chi(\tau,0)$ is described by $J_0(\pi B\tau)$, with its global maximum at $\tau = 0$ and its oscillations along the τ axis. Cross sections for different $\nu = nf_m$ are described by n^{th} order Bessel functions. The general behaviour of $J_n(x)$ for $n \neq 0$ is that $J_n(0) = 0$, and that $J_n(x)$ slowly increases when x approaches n. Around n, it subsequently arrives at its global maximum and first non-trivial zero and then starts oscillating. This explains the bowtie shape of figure 1.

The Fourier transform $\xi(p,q)$ of the ambiguity function $\chi(\tau,\nu)$ is shown in figure 2. The non-adaptive pseudo inverse filter $H_{PN}(p,q)$ following from it is shown in figure 3. Note the interchange of darker and lighter regions between figures 2 and 3, illustrating that figure 3 is the inverse of figure 2. Also note the white regions with sharp edges where $H_{PN}(p,q)$ is cleared because $|\xi(p,q)| < K'$. Figure 4 shows the inverse filter $h_{PN}(\tau,\nu)$ in the range Doppler domain.

4.2 Inverse filtering for actual measurements

We now discuss the application of inverse filtering on measurements of a ground based sinusoidal FMCW radar observing airborne targets. The range and Doppler resolutions are about 1km and 200Hz respectively. Inverse filtering was carried out with $|Z(\tau,\nu)|$ and $|\chi(\tau,\nu)|$, which gave better results than when we worked with $Z(\tau,\nu)$ and $\chi(\tau,\nu)$. We tried the three different regularized filters discussed in chapter 3 and we found that all of them worked very well for targets dominating the noise. Figure 5 shows

$Z(\tau,\nu)$ for a strong target and figure 6 shows the resulting $g(\tau,\nu)$ after successive inverse filtering. We only show one figure, because the different regularized filters performed equally well for this case.

For noisy targets, we expected the non-adaptive pseudo inverse filter to work best. This is illustrated by figures 7-10. Figure 7 shows $Z(\tau,\nu)$ for a weaker target, and figures 8 to 10 show $g(\tau,\nu)$ for $H_{PN}(p,q)$, $H_P(p,q)$ and $H_W(p,q)$ respectively. For the pseudo inverse filter, the value $K = 2$ was chosen. The noise level σ_N was estimated from (p,q) regions where no target contribution to $\zeta(p,q)$ was expected. Clearly, the resulting $g(\tau,\nu)$ is not extremely good for any of the inverse filters, but $H_{PN}(p,q)$ focuses most of the energy in a relatively small region. In addition, the background is smoother, containing fewer outliers.

Figure 11 shows an interesting measurement with 2 targets. The range runs from about 0 to 100km and the Doppler frequency from about –20kHz to 20kHz. Ground clutter is suppressed with a band filter around 0Hz, which is visible as a slight depression in the centre of the figure. The image shows two clear bowtie shapes with different range and different Doppler frequency. Apparently, one target is an incoming target, while the other is an outgoing target. Note that the target on the right hand side of the plot is accompanied by a bowtie at the same range, but with higher Doppler and with lower intensity. This may well be due to JEM (Jet Engine Modulation) of the main target. Figure 12 shows the compression achieved by inverse filtering using $H_{PN}(p,q)$. Figures 13 and 14 show the same information in surface plots.

5. CONCLUSIONS

In the above chapters we discussed the possibilities of optimizing the range and Doppler resolutions of single sweep FMCW radar processing by an additional inverse filtering step after correlation processing. As discussed, the inverse filter can be derived from the ambiguity function of the chosen modulation, and we have given a number of regularized inverse filters for application in practice.

We have demonstrated the technique for actual measurements of a ground based sinusoidal FMCW radar observing airborne targets. We have compared the results of different regularized inverse filters, and found that all filters performed well for targets dominating the noise. For noisy targets the non-adaptive pseudo inverse filter performed best.

For future research it would be interesting to compare the performance of deterministic modulations to (quasi) random modulations. For random modulations, the expectation of the ambiguity function is already a delta function without inverse filtering, but one may expect more noise outliers.

It might be added that after inverse filtering, the range and Doppler resolutions of single sweep processing can in principle be as good as for multi sweep linear FMCW processing. Then, however, the single sweep radar will need a much high sampling frequency, a much larger data buffer and much faster data processing than the multi sweep FMCW radar. Instead, one will rather use single sweep radar for its potential of a large unambiguous range and Doppler frequency, while the observation time can be short.

6. REFERENCES

[1] R.L. Mitchell, *Radar Signal Simulation* (1976).
[2] M. Skolnik, *Introduction to Radar Systems* (1981).
[3] S.M. Sussman, *Least Square Synthesis of Radar Ambiguity Functions*, Trans. IRE, vol. IT-8, 246-54 (1968).
[4] M. Schwartz. L. Shaw, *Signal Processing* (1975).

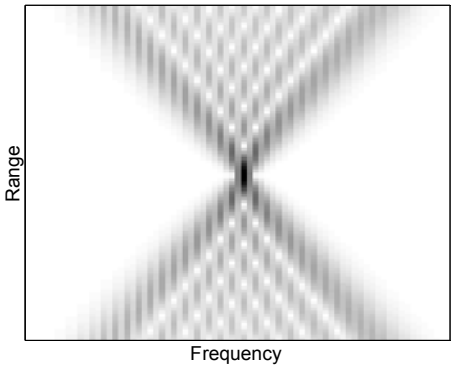

Figure 1: Modulus of the ambiguity function $\chi(\tau,\nu)$. The centre of the plot is $\chi(0,0)$.

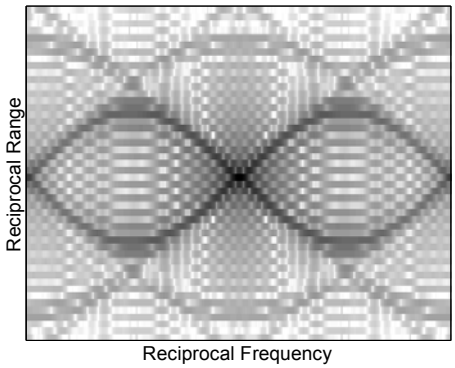

Figure 2: Modulus of $\xi(p,q)$. The centre of the plot is $\xi(0,0)$.

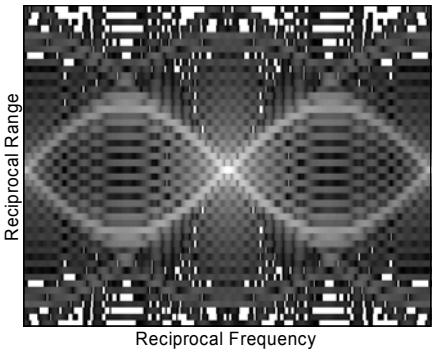

Figure 3: Modulus of $H_{PN}(p,q)$. The centre of the plot is $H_{PN}(0,0)$.

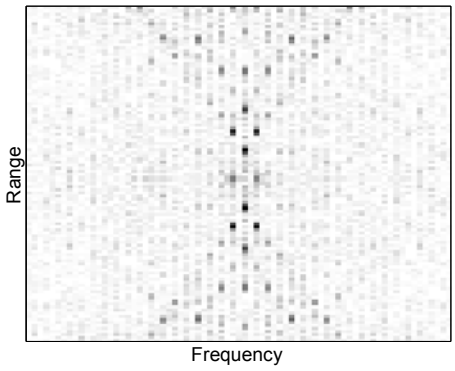

Figure 4: Modulus of $h_{PN}(\tau,\nu)$. The centre of the plot is $h_{PN}(0,0)$.

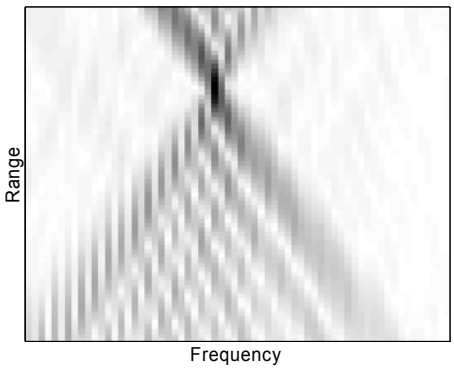

Figure 5: Modulus of $Z(\tau,\nu)$ for a strong target.

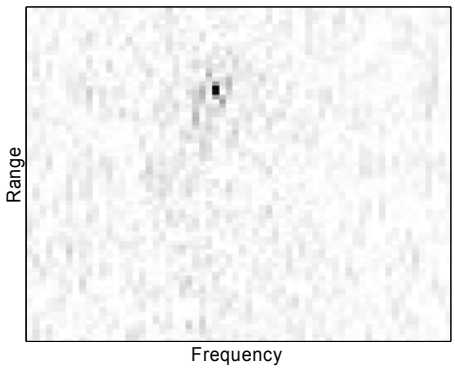

Figure 6: Modulus of $g(\tau,\nu)$ for the target of figure 5.

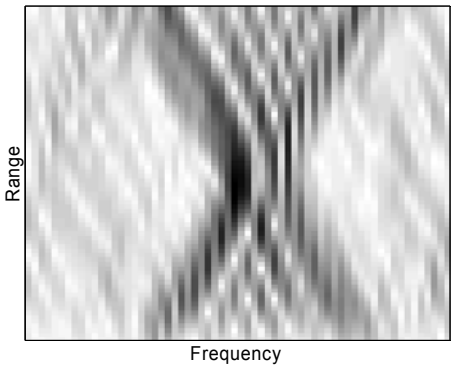

Figure 7: Modulus of $Z(\tau,\nu)$ for a weak target.

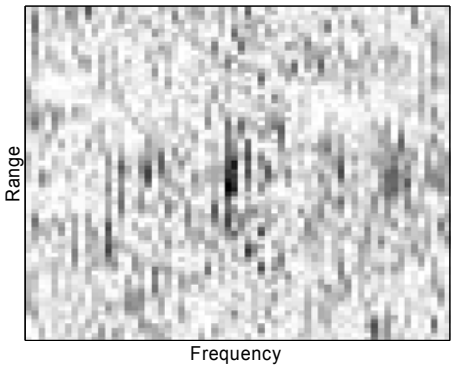

Figure 8: Modulus of $g_{PN}(\tau,\nu)$ for the target of figure 7.

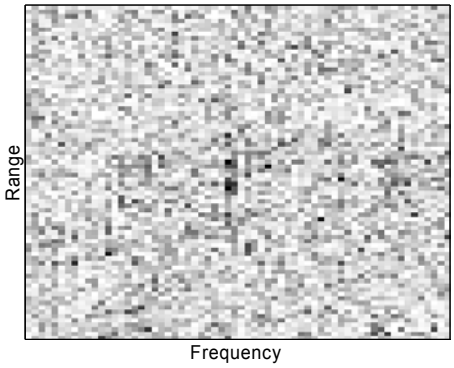

Figure 9: Modulus of $g_{P}(\tau,\nu)$ for the target of figure 7.

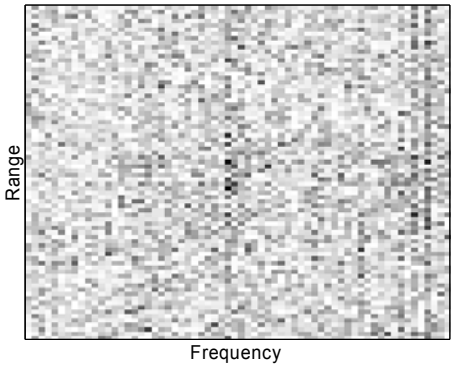

Figure 10: Modulus of $g_{W}(\tau,\nu)$ for the target of figure 7.

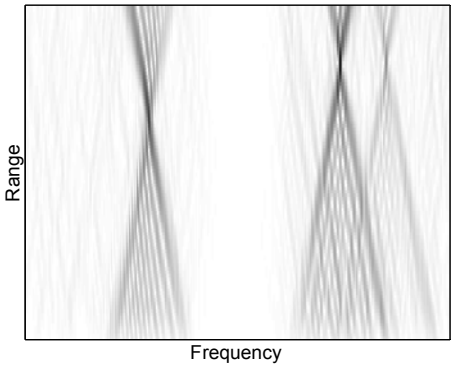

Figure 11: Modulus of $Z(\tau,\nu)$ for a case of multiple targets.

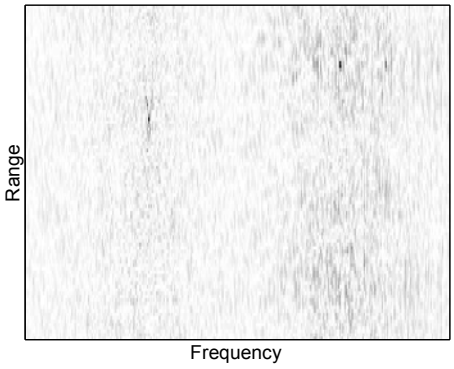

Figure 12: Modulus of $g_{PN}(\tau,\nu)$ corresponding to figure 11.

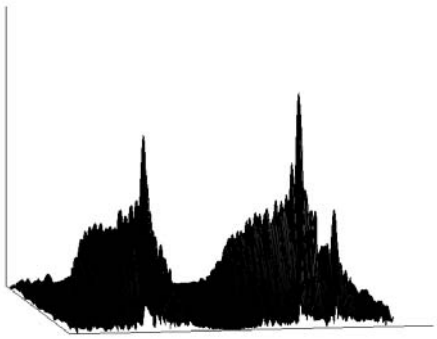

Figure 13: Surface plot corresponding to figure 11. The range axis points towards the reader.

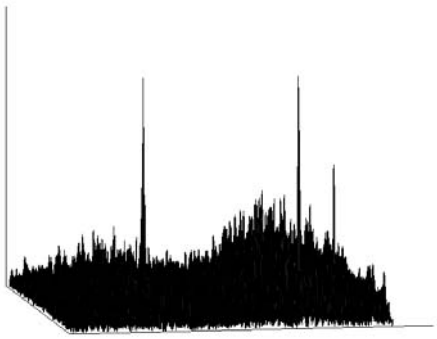

Figure 14: Surface plot corresponding to figure 12. The range axis points towards the reader.

Generation and Validation of a Simulated Radar Ground-Target Database

D. André, D. Blacknell, J. Hare
QinetiQ, St.Andrews Rd, Great Malvern
Worcs. WR14 3PS, UK

DBAndre@QinetiQ.com

ABSTRACT

We generate simulated (I)SAR imagery of a number of ground vehicles with the program Spectre [1] and validate these against turntable (I)SAR imagery from trials. Spectre employs a Physical Optics / Geometrical Optics (PO-GO) or shooting-bouncing-ray high frequency physics model. This approach is employed as standard for high-frequency electromagnetic scattering calculations from large complex bodies, so it is thought that the results have wide relevance. The effects of CAD model complexity and simulation convergence are considered. We evaluate the suitability of the simulated data for use in a database for various kinds of ATR methodologies. There are difficulties in achieving real-time simulations for ATR so we discuss the alternative route of pre-forming a scattering amplitude data-dome for forming monostatic imagery in real-time.

1.0 INTRODUCTION

To form robust Automatic Target Recognition (ATR) algorithms extensive training databases are required. Simulation is seen as a possible route to obtaining a database containing a large variety of imaging scenarios for a wide variety of targets in a wide variety of situations, for a modest cost [2]. The work reported here addresses the generation of a large database of vehicle signature predictions and the comparison of these predictions with real Inverse Synthetic Aperture (ISAR) data for the purposes of validation. The vehicles are modelled ex-situ and are compared with measurements of corresponding vehicles on a Radar Absorbent Material (RAM) covered turntable. The argument in favour of simulation becomes even more favourable if one accepts the point that if the present trend of increasing computer power for a fixed cost continues, it is likely that the possibility of real-time simulation would preclude the need for an imagery database. A database could then consist solely of vehicle Computer Assisted Design (CAD) models which can be articulated by the ATR-simulation software.

The scattering simulation software and the CAD models are discussed in section 2.0. Simulation approximation, convergence and CAD model fidelity dependence have been studied and are described in section 3.0. Detailed feature analysis is described in section 4.0. Validation has been performed through comparison of both simulated and real imagery with the common CAD model to establish that the observed scattering can be jointly associated with structures on the vehicle. Further validation through the use of correlation measures has been undertaken, and is described in section 5.0.

The construction of a database of simulated SAR imagery is greatly facilitated by the pre-calculation of a fully polarimetric K-space representation of the Electromagnetic (EM) scattering. Development of this "datadome" concept to support database generation and image formation research has also been undertaken and is described in section 6.0.

Paper presented at the RTO SET Symposium on "Target Identification and Recognition Using RF Systems", held in Oslo, Norway, 11-13 October 2004, and published in RTO-MP-SET-080.

2.0 FORMATION OF SIMULATED RADAR IMAGERY

2.1 Scattering Software

The EM-simulations were performed for monostatic scattering and a number of runs were carried out at X-band with the QinetiQ prediction code Spectre [1]. The physics models incorporated are the Physical Theory of Diffraction (PTD), the Physical Optics (PO) and Geometrical Optics (GO) approximations [3]. The PO-GO approximation is often called the "shooting-bouncing ray" model. The PTD calculation takes edge effects into account, and PO-GO approximate ray scattering from flat faceted surfaces. In the latter case rays can bounce from a number of surfaces, and if a ray bounces N-times before scattering back to the radar, then this is known as an Nth order scattering effect, or a Multi-Bounce-N event (MB-N). This approach is employed as standard for electromagnetic scattering calculations from large complex bodies at high frequency, so it is thought that our results have wide relevance.

The scattering amplitude as a function of frequency, azimuth and elevation is obtained and is employed to form radar imagery via interpolation, window weighting and the Fourier transform. We have investigated the effects of the various approximations.

2.2 CAD Models

Seven CAD models were obtained for EM-simulation. Here we discuss the T72 main battle tank. These were obtained as part of the CEPA collaboration [4] with three levels of fidelity, to investigate simulation convergence. The low and medium fidelity models in Figure 1 have 9611 and 24808 facets respectively. The high fidelity model in Figure 2 has 37701 facets. Note that both the medium and high fidelity T72 models have high fidelity wheels and tracks but that the low fidelity model does not. At high radar frequency we find this affects the scattering properties a great deal and, in particular, the convergence of scattering amplitude as a function of multi-bounce order.

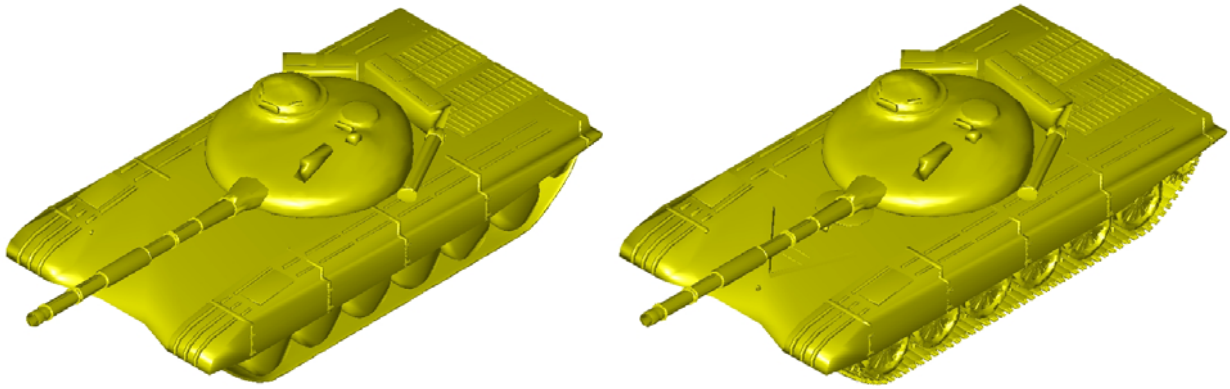

Figure 1: T72 CAD models. Left: low level of fidelity with 5307 vertices and 9611 faces. Right: medium fidelity model with 21561 vertices and 24808 faces. The low fidelity model has highly simplified tracks and wheels.

3.0 APPROXIMATION AND CONVERGENCE

3.1 Reciprocity

Polarimetric radars can transmit and receive two orthogonal polarisations. In the linearly polarised case the polarisations are labelled H for horizontal and V for vertical. In this way four transmit-receive combinations are possible (HH, HV, VH and VV). This additional data allows a more detailed examination of the scattering mechanisms.

The results from Spectre are generally not reciprocal. In the monostatic case this implies that HV simulation results erroneously differ from the VH results. This is not the case in reality. This is due to a failing of high frequency approximation physical models. The PO approximation is not reciprocal [5] and this problem is further exacerbated by having to employ PO-GO. This is where in order-N interactions, the first N-1 are modelled with GO reflections and only the last interaction is modelled with PO scattering. This is a standard high frequency modelling technique. For complex bodies there is very little alternative to applying PO-GO given the exponential increase in required computing power with scattering interaction order, which would occur for full PO scattering prediction.

3.2 Further Numerical Approximations

Beyond the underlying high-frequency ray-tracing approximation upon which the Spectre physics model is based, and the fact that the CAD-model is also approximated, other approximations were employed to reduce the computational run-time. Among these was a frequency sweep approximation. Here the fundamental scattering amplitude of any given facet is assumed to remain independent of frequency so that all variation within the band is solely due to the ray-path length difference in units of wavelength, and due to interference between scatterers as a result of this. This is found to be a very good approximation at HF. Various other approximations were employed, including an azimuth interpolation and a truncation of the scattering when it is away from the specular reflection direction by more than 30º. These are described in [6].

3.3 Convergence

Simulated radar imagery results for the low and medium fidelity T72 models were decomposed into pure edge diffraction contributions and pure N-bounce ray components [1][3][6]. This was done to help understand the origin of features and to estimate whether the imagery has converged as a function of increasing ray-bounce. The imagery has a resolution of 10cm. In Table 1 we see how the simulated imagery for the low fidelity model converges reasonably well by MB-4. The tables show imagery in the two polarization channels HH and HV. The rows 1-3 in Table 1 show increasing MB components from order 4 to order 6. The bottom row consists of all the components added together coherently. We see that very few dim scattering centres are apparent for the MB-4 events image (NB: the colour-scale is reset in each image). The same cannot be said for the medium fidelity T72 for which the corresponding component can be found in Table 2. We see that convergence is not achieved. This is due to the higher complexity of the wheels and tracks on this model (see Figure 1). However the sum-total images are more realistic than in the lower fidelity simulation in that the wheels and tracks are now much more prominent than in the imagery for the low fidelity model (see for example [7]).

Investigation has shown that for the medium and high fidelity models, for some aspect angles back scattering only reduced considerably after 5 or 6 bounces. Because of the complex nature of the high fidelity targets, some features may remain bright for even higher bounces, possibly with no convergence as a function of multibounce. This can certainly be the case for general cavity back-scattering [8][9]. Furthermore, in a complex target, even after we have seemingly obtained convergence with MB-N0, where N0 is any positive integer, we could never be sure that there would not occur a bright response at MB-N, where N>N0. Indeed we could purposefully contrive a simple target consisting of N mirrors, and seemingly obtain what looks like convergence with MB-N0 where N0<N, and yet if we have arranged the mirrors correctly, have a very bright response at MB-N. This could be done for any positive integer N.

For the simulated image database we have settled for the combination of diffraction and multibounce up to and including third order scattering events (MB-3). Higher order events were not calculated due to the computational cost involved in calculating the full azimuthal dataset over the full 360º.

Table 1: Simulation multibounce (MB-N PO) component and sum-total images, showing convergence of scattering response with increasing multibounce, for the low fidelity T72 in the polarization channels HH and HV. The bottom row shows all components added together coherently. Resolution is 10cm (NB: the colour-scale is reset in each image).

	HH	HV
MB-4 PO	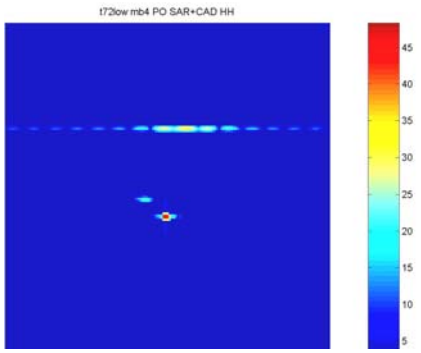	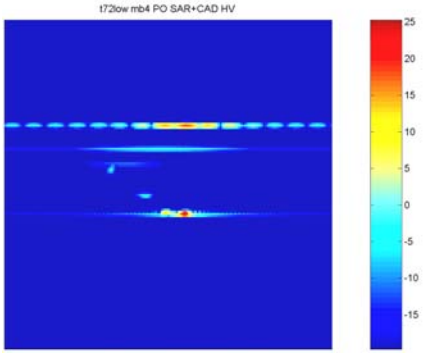
MB-5 PO	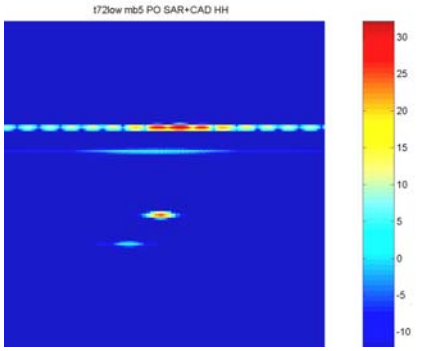	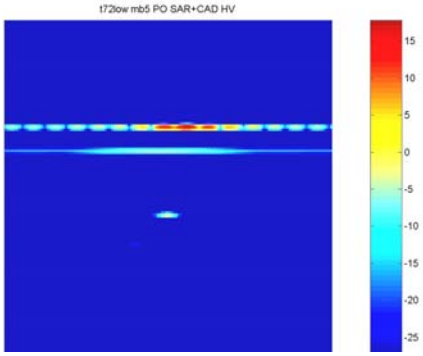
MB-6 PO	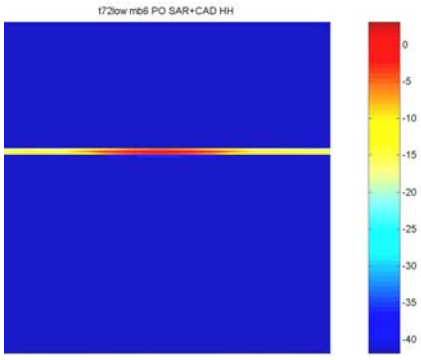	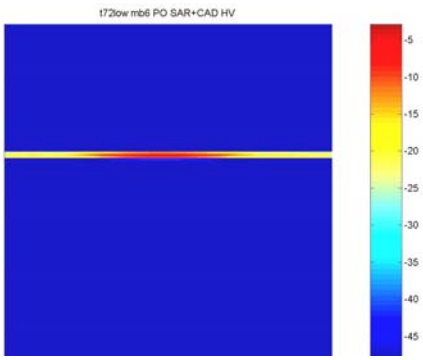
MB-1+2+…+6 PO + PTD	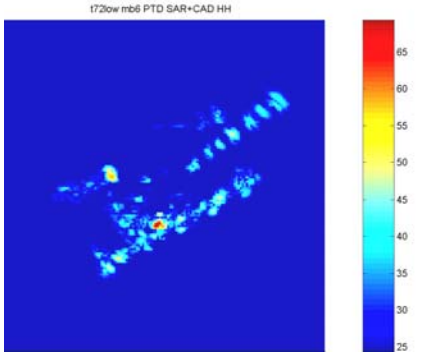	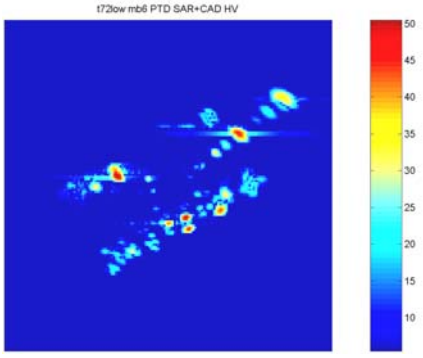

Table 2: Simulation multibounce (MB-N PO) components and sum-total images, showing convergence of scattering response with increasing multibounce, for the medium fidelity T72 in the polarization channels HH and HV. The bottom row shows all components added together coherently. Resolution is 10cm (NB: the colour-scale is reset in each image).

	HH	HV
MB-4 PO	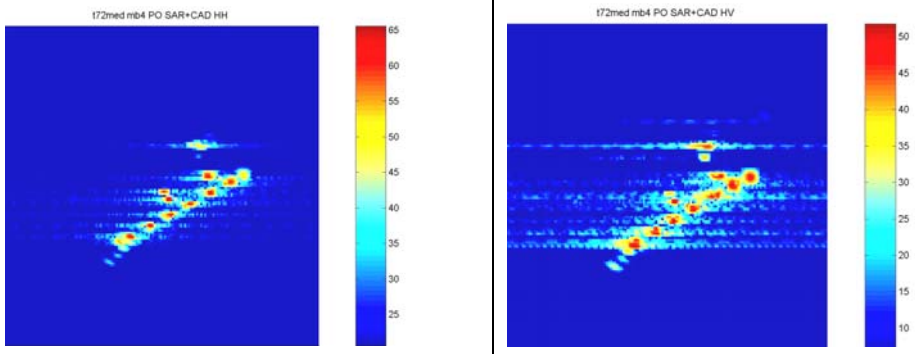	
MB-5 PO	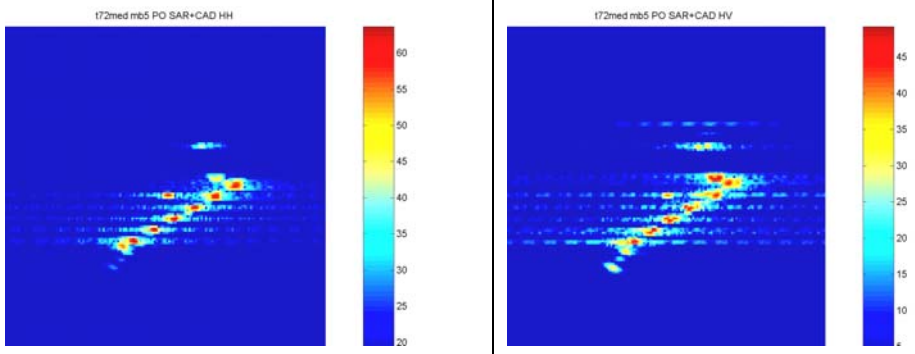	
MB-6 PO	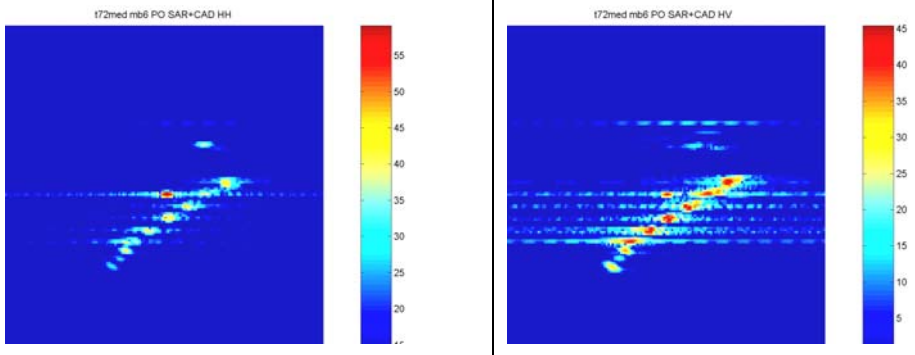	
MB-1+2+…+6 PO + PTD	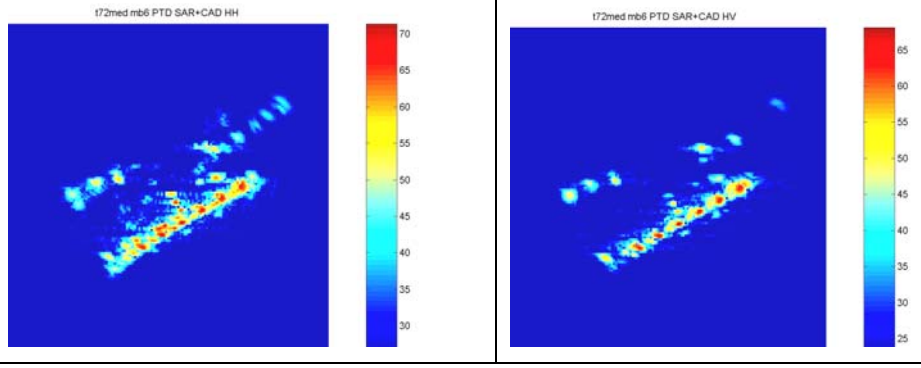	

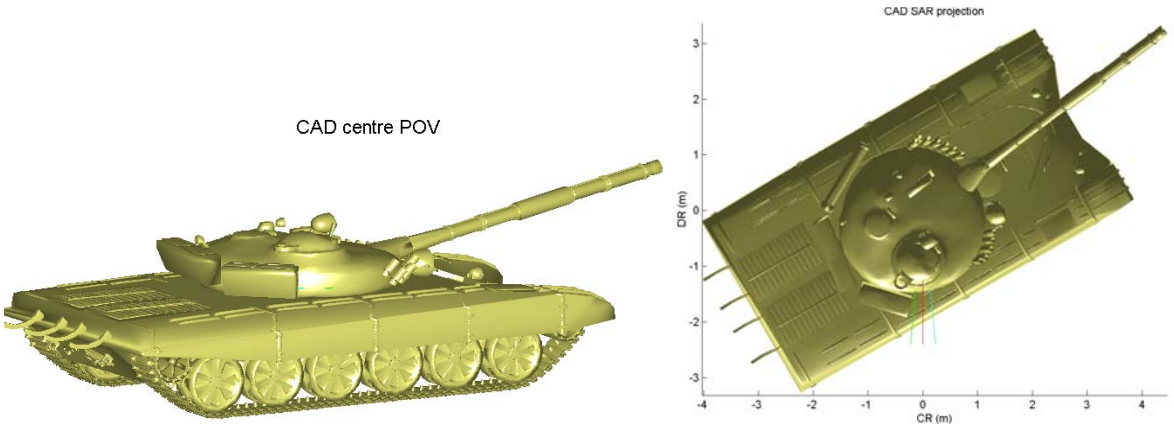

Figure 2, Left: High fidelity T72 Radar Point of View (POV) in the centre of the azimuthal imaging aperture used to form the radar imagery portrayed in Figure 3. Azimuth angle az=120° and elevation el=10°. Right: High fidelity T72 projection corresponding to that in Figure 3. The extent of the azimuthal imaging aperture is portrayed with the green and blue lines, and that the red line corresponds to the central POV. This aperture is required for the formation of 10cm resolution imagery at X-band. The illumination on the model is from the intended radar direction, thus giving an indication of the location of possible scattering hot-spots.

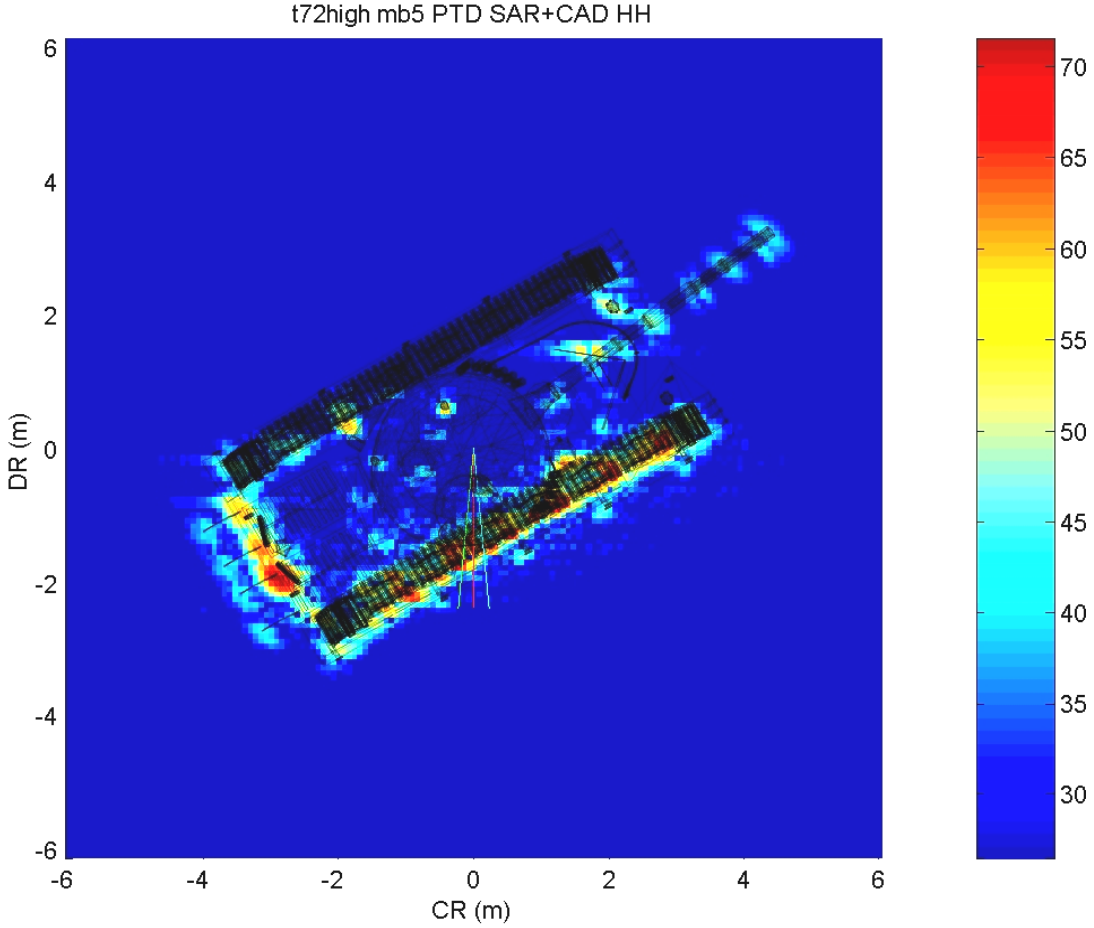

Figure 3: Diffraction plus multibounce up to order 5 (PTD + MB-1 +… MB-5) simulated radar image of high fidelity T72 with CAD wire-frame superimposed. Three lines represent radar POV azimuth aperture extent and centre.

4.0 FEATURE ANALYSIS

A feature analysis was carried out consisting of overlaying a partially transparent CAD wire-frame model onto the corresponding radar image, and comparing with radar Point of View (POV) CAD projections. This has greatly helped us to identify radar scattering hot-spots, their origins and their subsequent scattering centres in the imagery.

In Figure 2 on the left we see the high fidelity T72 central POV CAD projection corresponding to the radar image in Figure 3. In Figure 2 on the right we see the CAD projection corresponding to that in the associated radar image. A partially transparent projection of the wireframe is superposed onto the radar image and we can see how well they correspond. Note that this latter projection is not a top projection, but is at 10º from the vertical in the appropriate direction. This is because the radar elevation is at 10º. This distinction seems small here, but helps to explain the minutiae of overlay effects. The distinction becomes crucial for higher elevation angle imagery interpretation. We note that the track and wheel scattering responses are not in a straight line, but are slightly arced in the radar imagery. This is a layover effect which is readily understood through application of the wireframe overlay.

Note that the extent of the azimuthal imaging aperture is portrayed with the green and blue lines both in the radar image and in the corresponding CAD projection (Figure 2, right). The red lines correspond to the central POV, and the green and blue lines correspond to the azimuth aperture extent limits (necessary for 10cm resolution). Analysis of the variation of POV within a single image has helped us to identify unstable scatterers. For example those which become obscured during part of an aperture. Scattering centres which correspond to unstable scatterers lead to cross-range smearing. An example is provided by the wheel to the rear and left of the T72. Note that the imaging geometry described here was also employed in the formation of the imagery in Table 1 and Table 2.

The feature analysis was carried out both for simulated and trials imagery of various vehicles at 30cm resolution. Generally the corresponding scatterer locations were found to have been predicted correctly, however often the predicted brightness of these scattering centres was incorrect. This type of observation and others like it guide the appropriate choice of feature extraction algorithm to be applied in simulated database ATR. In the following section we do not describe feature extraction procedures, but merely apply normalised image correlations between real and simulated datasets and discuss results.

5.0 CORRELATION OF SIMULATED AND TRIALS ISAR IMAGERY

5.1 Correlation Procedure

Here we describe the results of correlating the simulated and the trials imagery. Before correlating, the polarimetric span was taken

$$Span = \sqrt{|HH|^2 + 2|HV|^2 + |VV|^2} \qquad \text{Equation 1}$$

where *HH*, *HV* and *VV* are the images in these respective polarimetric channels and the sum is carried out on a pixel-by-pixel basis. Taking the span generally gave rise to more consistent correlation results. Next the images were normalized as follows: the mean was subtracted and the result was divided by the standard deviation. For the image F, the normalized image F_n is

$$F_n(i,j) = \frac{F(i,j) - \overline{F}}{\sqrt{\sum_{i'}\sum_{j'}\left[F(i',j') - \overline{F}\right]^2}} \qquad \text{Equation 2}$$

where the over-bar indicates the mean value of the image.

Depending on the goal one wishes to achieve, one may scale the images in different ways. For example to enhance the bright peaks, one could square the images, or to bring out the overall structure one could take the square root of the image, or take the logarithm. Prior to normalizing the images we have chosen to take the logarithm and to take a threshold from below at 45dBm^2 from the image maximum value. This is not appropriate for some types of imagery and this depends upon the noise threshold amongst other things.

The image correlation C is defined as follows

$$C(i,j) = \sum_{i'} \sum_{j'} f(i',j')\, g(i'-i, j'-j) = IFT\left[F\, conj(G)\right] \qquad \text{Equation 3}$$

where f and g are the images to be correlated, F and G are their Fourier transforms, IFT[·] is the inverse Fourier transform and $conj(\cdot)$ is the complex conjugate. Because the images have been normalized, the values of C vary only from 0 to 1. From the correlation image C one can extract the maximum correlation, and its position, which indicates to where one of the images should be shifted for the best template match.

5.2 Correlation Results

Polarimetrically-calibrated X-band turntable trials imagery at 30cm of a military vehicle was obtained. The corresponding CAD model was at very high fidelity, with just under 100000 facets. Even though the model was at high fidelity, it was still noticeable that particular details did not match. We should note however that this is also the case between different real vehicles of the same type. We are forced to take the view that any robust ATR algorithm must compensate for this inherent variation. The database for each consisted of 360 images at 1° intervals in all polarisations. The simulations only took into account edge diffraction and first to third order multibounce interactions. Due to run-time considerations no higher interactions were calculated here.

In Figure 4 on the left we see maximum correlation results between the experimental and numerical imagery of vehicle 1 as a function of aspect angle. The average correlation is about 0.8. On the right of Figure 4 we see the shift distance of image 1 for maximum correlation with image 2. This distance roughly follows a cosine curve which simply reflects the fact that the centre of rotation of the trials vehicle is not exactly collocated with that of the simulated vehicle.

In Figure 5 we see maximum correlation results between the experimental vehicle 1 dataset and a simulated vehicle 2 dataset. The average correlation decreased to about 0.7, which is lower than for the same type vehicle case. Although we indeed find that correlations are now lower, the difference is only around 0.1. We conclude that simple template matching is not sufficient to make optimal use of simulated imagery databases. It is likely that feature extraction based on scatterer position may be a better approach. In Figure 5 on the right, we see the template shift for maximum correlation. We see that a sinusoid of the appropriate period can no longer be fitted, supporting the conclusion that the vehicles being matched are of different types.

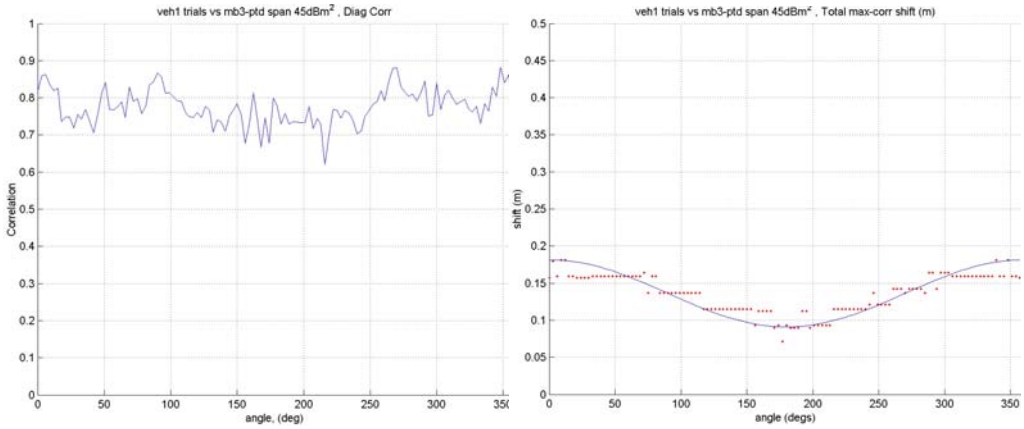

Figure 4, Left: Equal-angles maximum correlations as a function of azimuth (equal aspect image. Right: Template shift distance to maximum correlation for equal aspect image comparisons. The points follow a sinusoid.

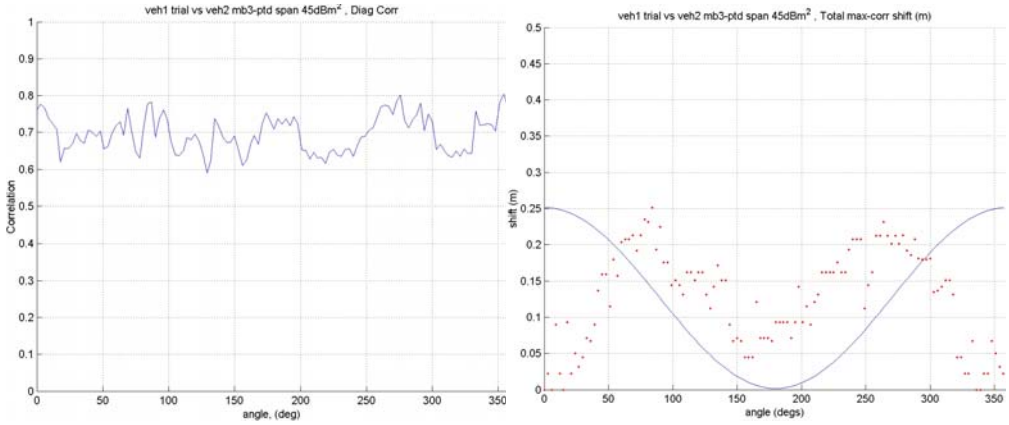

Figure 5, Left: Equal-angles maximum correlations as a function of azimuth (equal aspect image comparisons). Right: Template shift distance to maximum correlation for equal aspect image comparisons. The points do not follow a sinusoid with the expected period.

6.0 SCATTERING AMPLITUDE DATADOME

The practicality of avoiding the need to generate large databases of simulated imagery for many possible imaging geometries and platform trajectories can be addressed by the introduction of the "data-dome" concept.

In constructing an image database for ATR, various factors such as the introduction of radar resolution as a variable, or the "angle of squint" variable in SAR squint mode imaging can have a drastic impact on the size of the image database. Clearly there are many other factors which can have a significant impact on imagery and these include elevation angle, centre frequency of image support, pixel spacing, windowing type for side-lobe suppression to name but a few. For this reason we argue the case for the pre-calculation of a frequency wide-band fully polarimetric scattering amplitude data-dome, which can be employed in forming imagery to the exact required specifications quickly. The other point is that potentially, the imagery can be formed with the data-dome in real-time.

The scattering amplitude datadome is a K-space or Fourier domain spherical shell of scattering amplitude values. Frequency is represented as distance from the origin and both azimuth and elevation in this space represent the radar-pulse direction towards the target azimuth and elevation angles. If one requires say a maximum of 5cm resolution for a ground vehicle, such a data-dome can be voluminous and can occupy storage space of the order of 90Gb. However this quantity easily fits onto a single modern, fast and inexpensive hard-disk.

We have formed such data-domes for simple test objects, consisting of collections of cubes however it was soon realised that forming a high resolution data-dome for a large ground target would be highly non-trivial in terms of computational expense. To continue our preliminary investigation we have obtained an unclassified datadome corresponding to a civilian digger vehicle (JCB or Backhoe), known as the "Backhoe datadome" [10]. This data was created with the simulation tool X-Patch [11]. This software also employs the high-frequency PO-GO approximation. The data has a frequency bandwidth of 6GHz with a centre frequency of 10GHz and an angular sampling in azimuth and elevation of 0.07°. The data-dome allows very high resolution imaging, potentially down to 3cm, for a target of about 15m in length.

Initial investigations have shown that 2-D image formation from such a dome is rapid and provides a feasible way forward to overcoming the present inability to perform scattering predictions in real-time. Clearly, for complex targets this is the case because simulation run-time is simply replaced by data retrieval-time plus data interpolation-time. Specifically, if the data dome is stored upon a fast data access medium and if the target CAD model is of a medium to high level of fidelity, then the ratio of simulation run-time plus image formation time, to data-dome data retrieval plus data-interpolation plus image formation time, may be of the order of 1000. This is certainly the case if high resolutions are required.

Due to the ease in obtaining the Fourier domain image support, the data-dome approach has allowed us to perform timely investigations of non-trivial effects such as varying overlay, lighting, obscuration and multipath effects in 2-D imagery. These should all be thoroughly understood to allow the formation of an effective ATR template matching scheme. Further studies of 3-D radar image formation were also undertaken with relative ease.

7.0 CONCLUSION

Our ISAR image comparisons consisting of feature analysis and correlation have shown that simulated imagery is broadly similar to trials imagery, although there are always specific differences. Scattering centres generally exhibit different relative brightnesses and additionally trials imagery is subject to the appearance of random scatterers. These differences are partly due to differences between the CAD models and the real vehicles, and also due to the high-frequency scattering approximations implemented. One can go on to argue that the differences are partly due to environmental effects and to inherent instabilities in the equipment. Additionally real vehicle surface roughness and coatings affect EM-responses. Although in the trials Radar Absorbent Material (RAM) coatings were employed on the turntable surface, there are still likely to be significant multi-path ground interactions, due to the turntable base disk being neither large enough nor perfect enough.

There is of course always some variation between the vehicles of the same class, which cannot be accounted for in any one CAD model. For example on the day of the trials some of the cam baskets were filled or covered, some of the wing-mirrors were in position, others not. The periscope mirrors were at different orientations, and of course the tracks and wheels could never be deployed in any exact way. One could not for example expect even trials imagery of the same vehicle, taken on different days to be the same [12].

Many approximations are carried out for the EM-simulations. We have described some of these approximations, convergence issues and even the effect of employing different CAD fidelities. It was found that higher detailed wheels and tracks give more realistic imagery, however they are less likely to converge as a function of ray-bounce.

From our detailed feature analysis we have come to the conclusion that we are able to predict the location of prominent scatterers, although they are often of a brightness different to that seen in actual trials imagery. It is our opinion that for successful ATR we will need to extract robust and prominent features automatically and we will need to emphasise the positional information over the brightness information. This work is ongoing and we have not been discouraged by our results. It may well be the case that converged EM-simulation (which are often not possible [7][8][9]) may not be required for ATR.

Data-dome studies have shown that tailored image formation is extremely rapid, sometimes of the order of 1000 times more rapid, depending upon the specific situation, when compared to the time taken for simulation plus image formation. For example, the specific relative speed would depend upon CAD model complexity, the simulation approximations employed and on the required resolution. We can see that this must be the case because simulation run-time is simply replaced by data-retrieval followed by data-interpolation time.

All possible imagery databases for a given target could be replaced by a data-dome with a suitable image formation algorithm. For example, for ATR using a database of pre-formed imagery one must be careful to employ the appropriate image database to the corresponding imagery. For example, in squinted imagery it can be shown that layover always occurs in one direction for images formed with data from any part of a straight radar platform track, whereas for ISAR imagery it always occurs towards the imaging platform instead. For a broadside elevation angle of more than 20° this difference can be clearly seen, when comparing images from equal illumination directions.

In the case of wide-aperture imaging, which is required for high resolution SAR and even more-so at low frequency bands, ISAR and SAR can also be very different at such elevations. This is because, whereas in ISAR imaging the elevation angle remains constant, in the case of SAR, the elevation angle is actually changing along the course of the aperture. Thus in the case of complex target imaging where scattering amplitude can change considerable for small elevation angle changes, the image type itself (SAR, ISAR, Squint mode SAR) can have a large impact on the imagery. The availability of a data-dome allows one to accommodate all these imaging scenarios in real time and can also reduce the overall size of an ATR database.

8.0 ACKNOWLEDGEMENT

This work was sponsored by the Electronic Systems domain of the UK MOD Corporate Research Program.

9.0 REFERENCES

[1] Spectre (formally known as RESPECT). S.D.Turner, *RESPECT: Rapid Electromagnetic Scattering Predictor for Extremely Complex Targets*, Radar and Signal Processing, IEE Proceedings F, Volume: 137, Issue: 4l

[2] Hummel R. *Model-Based ATR Using Synthetic Aperture Radar*, IEE International Radar Conference, 7-12May 2000, pp856-861.

[3] Knott E, *Radar Cross Section,* 2nd edition, Artech House 1993.

[4] CEPA: Supplement No JP 1.18 to the WEAG Memorandum of Understanding for Technology Arrangement for Laboratories for Defence European Science (Thales), concerning Target and Target Background Modelling Validation for High-Resolution Radar. July 2002.

[5] Ulaby F. *Radar Polarimetry for Geoscience Application*, Artech House 1990.

[6] Turner S. *Spectre user guide,* Unpublished QinetiQ Report.

[7] Rihaczek A. *Theory and Practice of Radar Target Identification*, Artech House 2000.

[8] MacKay A. *An Application of Chaos Theory to Ray Tracing in Ducts*, Unpublished DERA report.

[9] Smilansky U. *Chaotic Scattering of Microwaves*, Journal of Radio Science, Sept 2001.

[10] Backhoe Sample Public Release Visual-D Challenge Problem, http://www.sdms.afrl.af.mil/main.htm

[11] X-Patch, http://www.saic.com/products/software/xpatch

[12] Bennett A. *The Stability of Polarimetric Features for Target Classification From SAR Imagery*, IEE RADAR2002 conference publication, No.490, pp395-9.

Ground Target Signal Simulation by Real Signal Data Modification

Witold CZARNECKI
MUT – Military University of Technology
ul.S.Kaliskiego 2, 00-908 Warszawa
Poland

w.czarnecki@tele.pw.edu.pl

SUMMARY

Simulation techniques offer very often the only realistic methods of signal processing quality assessment. Standard approach to signal simulation needs prior definition of signal model before construction of signal simulation algorithm. Sufficient number of signal data are necessary for definition of good signal model. Signal data available are not always satisfactory numerous. An approach is proposed to cope with this problem by simulating signal realizations as modifications of real, registered signal. Methods of modification of real signals in time-space domain as well as in frequency domain are proposed. Results of simulation experiments are presented.

1.0 INTRODUCTION

Simulation of an object or phenomenon consists in generation of their replicas similar in a sense with the original. Simulation of a signal **x** should produce an artificial signal **s** having the same probabilistic characteristics as simulated signal. In the case of a stationary signal the probabilistic criterion of comparison is most frequently defined on the basis of marginal probability distribution (MPD) and autocorrelation function (ACF) or equivalently power spectral density (PSD). Simulation of a signal can though be looked at as a generation of a random process of given MPD and ACF. Such an approach requires prior definition of a signal model before a simulation algorithm design. Reliable modelling needs sufficient number of real signal data collected during open-air experiments. This condition is usually difficult to be satisfied in the case of ground target radar signals for technical as well as economic reasons. The difficulties mentioned above are even more serious in the case of air-borne radar systems. The efficient use of available real signal data is of primary importance.

Simulation of a signal is usually a processing of a sequence of independent random samples of appropriate probability distribution. The processing should be such as to produce the output signal of desired properties i.e. MPD and AFC. Thus any simulation experiment generates a signal realization that should be positively verified by successful estimation of both functions. Such an approach is a classical simulation of a signal. The proposed approach to signal simulation is based on an idea that simulation by independent random samples processing can be replaced by real signal samples processing that is the white noise signal processing is replaced by the processing of real signal. It means that in the latter case the processing should be an appropriate modification of real signal producing a new signal realization on the basis of a real one.

2.0 PROBLEM DEFINITION

The two approaches to simulation are presented schematically on Fig.1. If we assume that a signal x(t,**A**) depends on time t and a random variable **A** then the result of any simulation is its realization x(t,α).

Paper presented at the RTO SET Symposium on "Target Identification and Recognition Using RF Systems", held in Oslo, Norway, 11-13 October 2004, and published in RTO-MP-SET-080.

Looking at a real signal (real is used here in a sense physical, registered in a physical experiment for example) as a realization $x(t,\alpha_1)$ of the signal $x(t,\mathbf{A})$ we want to produce its new hypothetical realization $x(t,\alpha_2)$ by a modification of the real signal (i.e. the realization $x(t,\alpha_1)$). The

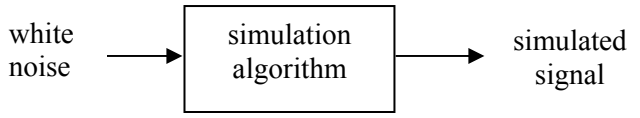

a) standard scheme of simulation

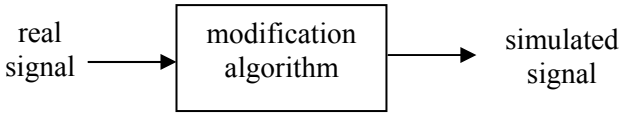

b) proposed scheme of simulation

Fig.1 Two schemes of signal simulation

time t is used for simplicity of simulation idea presentation. In a case of 2-d signals (like SAR signals) t should be replaced by two variables t and u [Sou] representing range and cross-range signal dependence. In discrete case the signal realizations takes on the form $x(m,n,\mathbf{A})$ with m=1,2,…M and n=1,2,…N. It is necessary that the modification algorithm be of nondeterministic character. It will enable to generate many new realizations $x(m,n,\alpha_n)$ on the basis of one real signal and to cope with the problem of limited number of data available. As mentioned earlier the modified version of the signal is a hypothetical realization. To be sure that such a hypothesis can be accepted it should be verified which needs a definition of appropriate criteria.

The basic difference between the two approaches lies in the role played by the simulated signal model. In the first case the signal model ought to be defined on the basis of signal data in order to design the simulation algorithm and in the second one the signal model is hidden in the internal structure of the available signal data and need not to be defined. So the problem of number of signal data necessary for reliable model definition looses its importance and instead the problem of appropriate algorithm of real data modification arises. The modification algorithm should preserve the MPD and ACF. While defining the algorithm of modification one should consider signal structure. The problem will be presented below.

The verification of simulation results should allow to found the similarity of MPD and AFC of the real and simulated (modified) signals. The principal rule adopted for all simulation algorithms was that signal modification should not change its ACF and if so the changes produced should be of minor importance. In effect only the MPD needed to be verified and typical goodness of fit test T were applied.

$$T = \sum_{i=1}^{K} \frac{(s_i - x_i)^2}{x_i}$$

where: K – number of equal subintervals in the range of real signal variation $[x_{min}, x_{max}]$,
$\{s_i;\ i=1,\ldots K\}$ set of numbers describing how many samples of the simulated signal **s** belong to i-th subinterval,
$\{x_i;\ i=1,\ldots K\}$ set of numbers describing how many samples of the real signal **x** belong to i-th subinterval.

The hypothesis that the real and simulated signals MPD functions were identical was rejected if the statistic T known as Pearson's test statistic was greater than the critical value c defined by the equation

$$P\{T \geq c\} = \alpha$$

If the hypothesis on goodness of fit of MPD functions is sustained and the assumption of AFC invariance is made the result of simulation by real signal modification can be accepted at the α significance level.

3.0 SIMULATION ALGORITHMS

The real signal x( ) can be modified either in the time-space domain or in the frequency domain. The modification should guarantee invariance of typical signal properties or insignificant changes of them. In the case of SAR signal its inherent property is a spherical phase modulation [Sou]. The information on signal phase is contained in in-phase and quadrature components of complex SAR signal. The available signal data used in simulation experiments were all in base-band form. Examples of image representation of real and imaginary parts, magnitude and phase as well as amplitude and phase spectra of a base-band SAR signal used for simulation experiments are shown on Fig.2. The rectangles on the magnitude image represent windows for analysis of an object (red) and noise background (blue) properties. This colour convention will be used for verification result presentation. Considering complex nature of SAR signal it is necessary to define the modification algorithm of its complex form or equivalent simultaneous modification of its components. An inspection of the signal data and an analysis of the processes generating the real signal in SAR systems lead to a conclusion that modification algorithm should change the signal in such a way that the relation among arguments of samples whose pixels are situated in one line of image signal representation will not undergo significant variations. This conclusion defines an important constraint on a strategy of phase value manipulation. Taking this into account three types of modification algorithms were proposed for numerical simulation experiments. In all algorithms modifications are introduced to both signal components individually. It is especially convenient in the case of discrete Fourier transformation because the spectra of signal components (both composed of real elements) are symmetric.

3.1 MODIFICATION OF REAL SIGNAL COMPONENT PHASE SPECTRA ON LINE-BY-LINE BASIS – ALGORITHM NO 1

The assumption made for the algorithm was that the phase spectra of analogous lines in both signal components can be slightly changed independently. Generally any change in phase spectrum does not influence the ACF. However, it affects the MPD and the changes produced depend on an intensity of phase modification. As was supposed earlier the modifications should not destroy the phase relations among signal samples in each component as well as between both components. Signal data in $x_{re}(m,n)$ and $x_{im}(m,n)$ define set of complex samples arranged in M lines each having N elements. Each line of both components can be modified according to the scheme presented on Fig.3 provided that the power of additive phase noise is not too great. In the simulation experiments the value of its variance σ^2_{Noise} was chosen such as to assure a positive verification of simulation results. The results of simulation verification are presented on Fig.4. Pearson's test statistic for K=20 intervals is shown as a function of ratio of variances of additive noise component σ^2_{Noise} and phase spectrum variance σ^2_{Ph}. Green line represents critical value c=30,14 equal chi-square percentile $\chi^2_{0.95}(19)$. Particular simulated background and object were obtained for variance ratio equal 0,16.

3.2. MODIFICATION OF REAL SIGNAL COMPONENT VALUES ON LINE-BY-LINE BASIS – ALGORITHM NO 2

The assumption made for the algorithm was that the values of elements of analogous line in both components can be slightly modified provided that the modifications will not change the argument of the complex signal elements. In contrast to the algorithm No 1 the modification of both signal

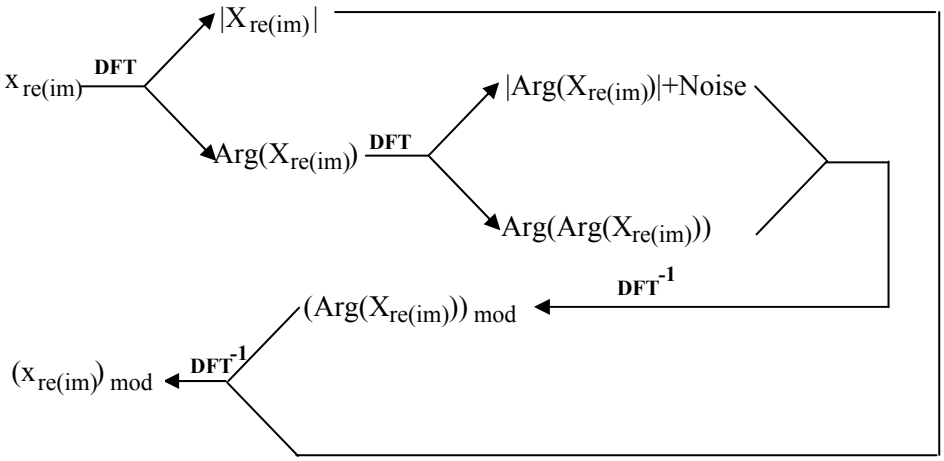

Fig.3 Algorith No 1

components are not independent. The algorithm proposed is presented schematically on Fig. 5. The procedures of simulation and verification were the same as in the case of algorithm No 1. The result of simulation are shown on Fig. 6. Particular simulated background and object were obtained for variance ratio equal 0,30.

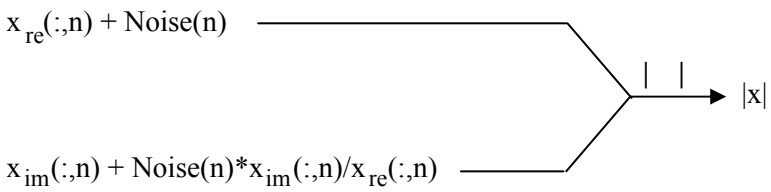

Fig.5 Algorithm No 2

3.3 MODIFICATION OF 2-D PHASE SPECTRUM – ALGORITHM NO 3

Two previously described modification algorithms used 1-d processing that utilize the relations among the signal samples that form lines of the image signal representation. A 2-d processing of the whole signal image seems interesting as a more advanced form of processing. In the case of 2-d spectrum the modification of phase spectrum does not influence the ACF too. The changes of the signal form and changes of the MDP in consequence are fine if the phases of the dominating spectrum components rest untouched. The problem is how to induce phase changes and not to destroy the spherical phase modulation structure. It can be done if chosen at random spectrum elements are modified in such a way that their phases are interchanged with the nearest neighbours of the same spectrum line. The chosen elements

should not be dominant elements of the spectrum which means that a threshold value should be defined. It can easily be done by defining an appropriate region of great spectrum elements that are clustered due to the low pass character of the baseband SAR signal. The proposed algorithm is presented schematically on the Fig.7. The choice of random position consist in making m equal to an integer out of {2,3,…M} and n equal to an integers out of {2,3,…N-1}. The result of simulation are shown on Fig. 8. Particular simulated background and object were obtained for KK=200 modification iterations.

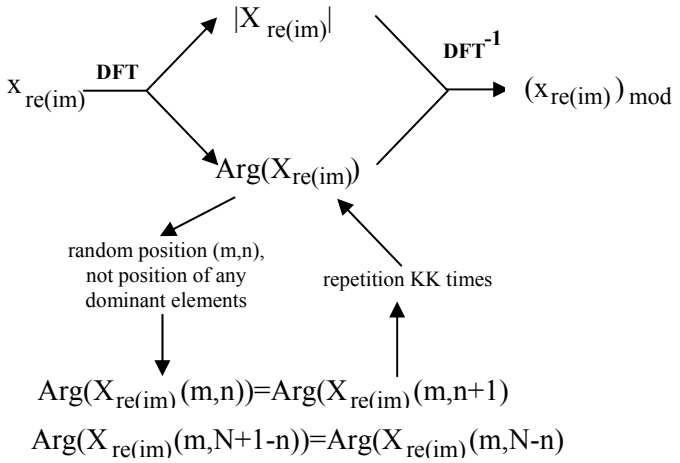

Fig.7 Algorithm No 3

The algorithm No 3 has 2 parameters: the radius rr of circular exclusion region around constant component of real signal spectrum and the number of iterations KK. The first enables to eliminate an eventual choice of a position of a dominant spectrum component, the second determines the number of phase changes done during the simulation experiment. Both parameters make it possible to simulate an object on the noise background with different signal to noise ratio. Pearson's test statistics in function of number of iteration for different radii rr are shown on Fig.9. As is clearly seen the dynamics of Pearson's test statistics becomes greater for smaller radii due to involvement of strong spectrum elements in the process of signal modification. Similar results can be obtained by making greater the number of iteration KK. Signal images with different signal to noise ratios obtained for different numbers of iterations are shown on Fig.10.

4.0 REMARKS AND CONCLUSIONS

A common feature of the simulation algorithm presented in this paper is the role played by the real signal which is treated as a sort of template. But it should be taken into consideration, that the real signal takes on one of many possible forms and can be treated as a realization of the signal we want to simulate. For this reason Pearson's test statistic can be assessed less rigorously. It seems possible to simulate successfully signals of interest in spite of greater than acceptable values of Pearson's test statistic. This remark is valid for all three algorithms. The results of numerical experiments show qualitatively the properties of the algorithms. The numerical values of algorithm parameters should be determined experimentally.

Algorithm No 3 seems to be the most efficient because of relative computational simplicity and lesser time consuming.

REFERENCES

[Bro] Brown CG. Sarabandi K. Gilgenbach M.: Physics-based simulation of high-resolution polarimetric SAR images of forested areas, 2002 IEEE International Geoscience and Remote Sensing Symposium. 24th Canadian Symposium on Remote Sensing. Proceedings (Cat. No.02CH37380). IEEE. Part vol.1, 2002, pp.466-8 vol.1.

[Cim] Cimmino S. Franceschetti G. Iodice A. Riccio D. Ruello G.: Efficient spotlight SAR raw signal simulation of extended scenes, IEEE Transactions on Geoscience & Remote Sensing, vol.41, no.10, Oct. 2003, pp.2329-37.

[Fran] Franceschetti G. Iodice A. Riccio D. Ruello G.: SAR raw signal simulation for urban structures, IEEE Transactions on Geoscience & Remote Sensing, vol.41, no.9, pt.1, Sept. 2003, pp.1986-95.

[Sou] Soumekh M.: Synthetic Aperture Radar Signal Procesing with MATLAB Algorithms, John Wiley & Sons, Inc.1999

[Vit] De Vita F. Mori A.: Raw/SLC signal simulator for spaceborne interferometric SAR systems, IGARSS 2000. IEEE 2000 International Geoscience and Remote Sensing Symposium. Taking the Pulse of the Planet: The Role of Remote Sensing in Managing the Environment. Proceedings (Cat. No.00CH37120). IEEE. Part vol.2, 2000, pp.785-7 vol.2.

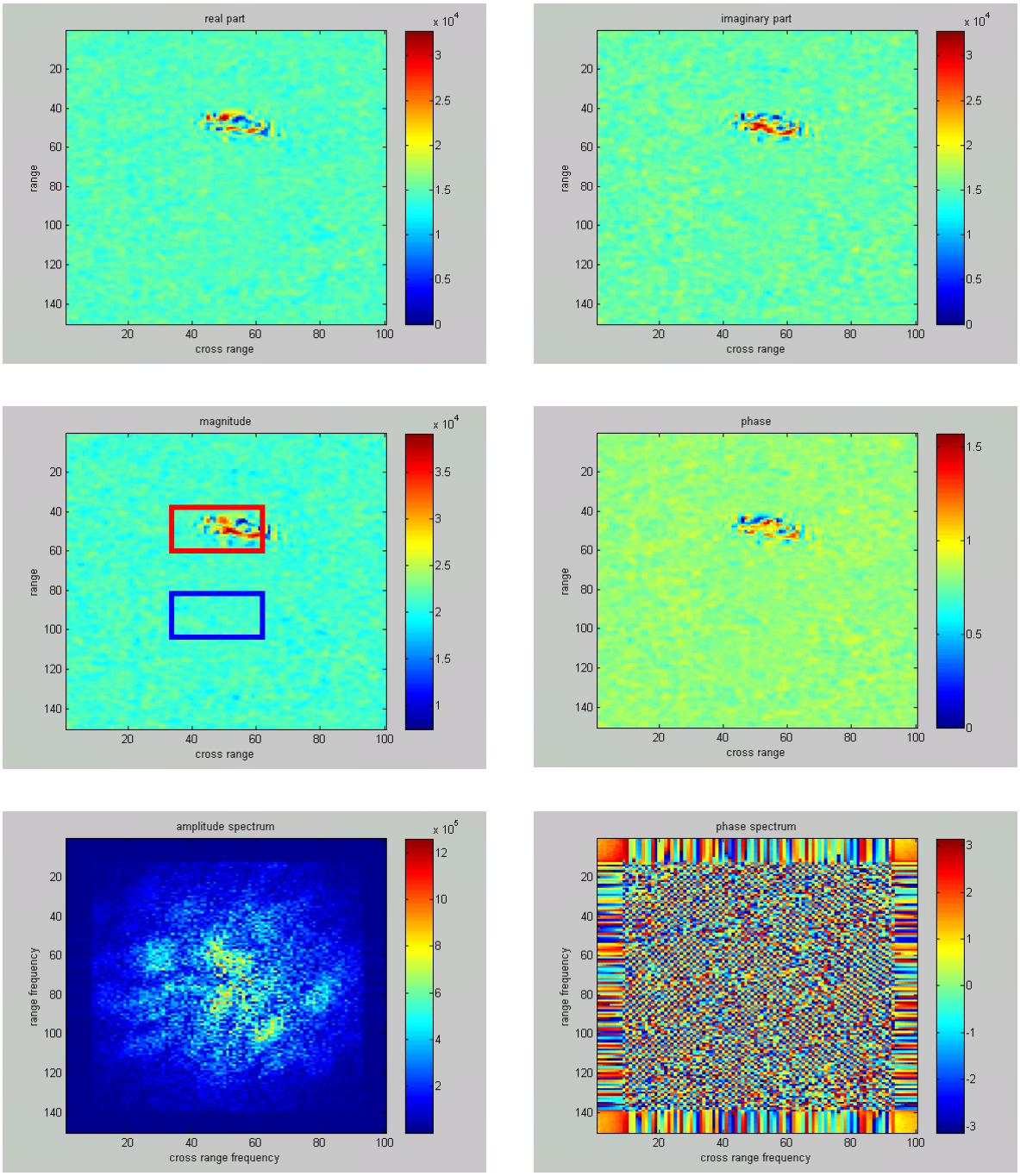

Fig.2 SAR signal

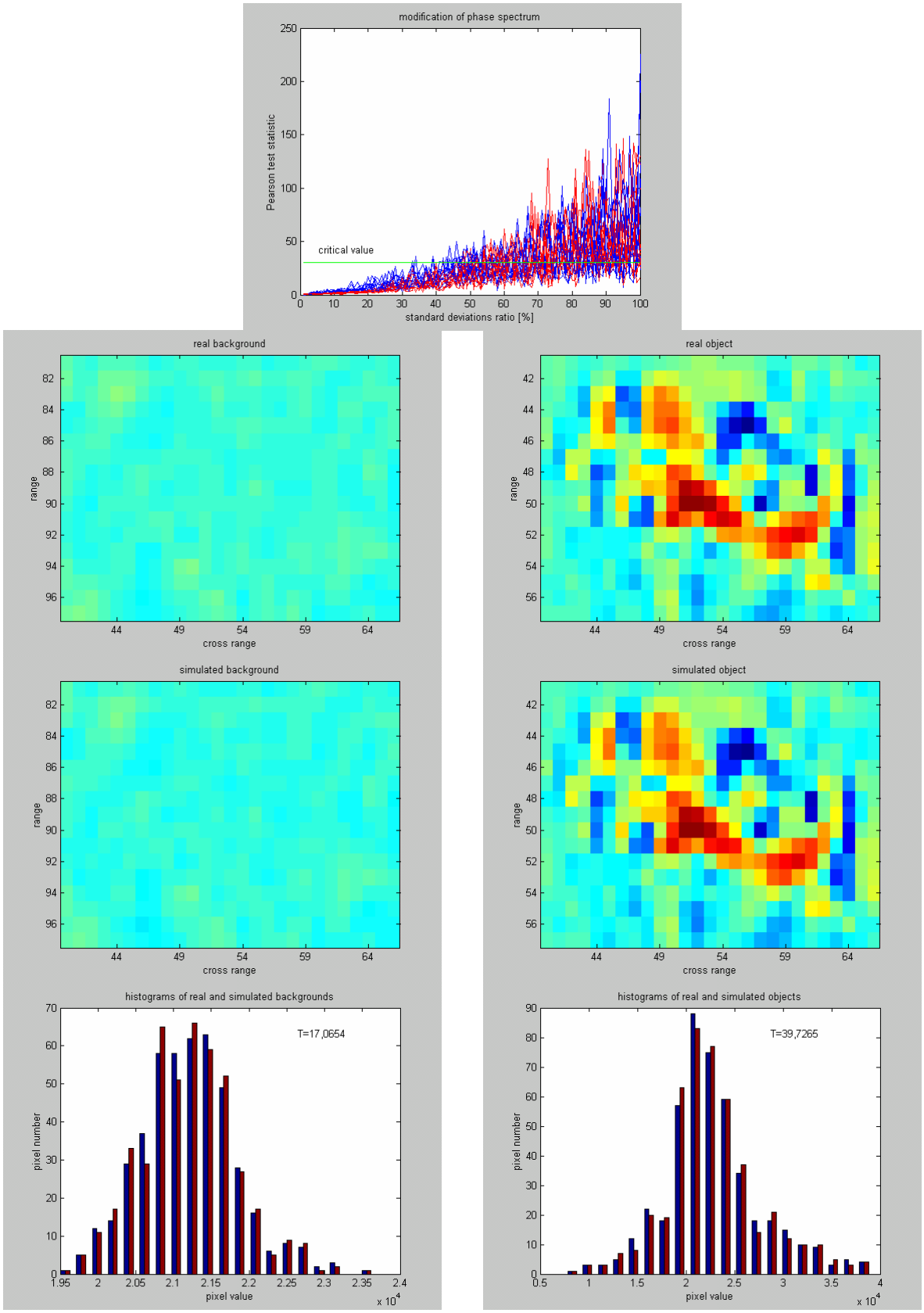

Fig.4 Results of simulation – algorithm No 1.

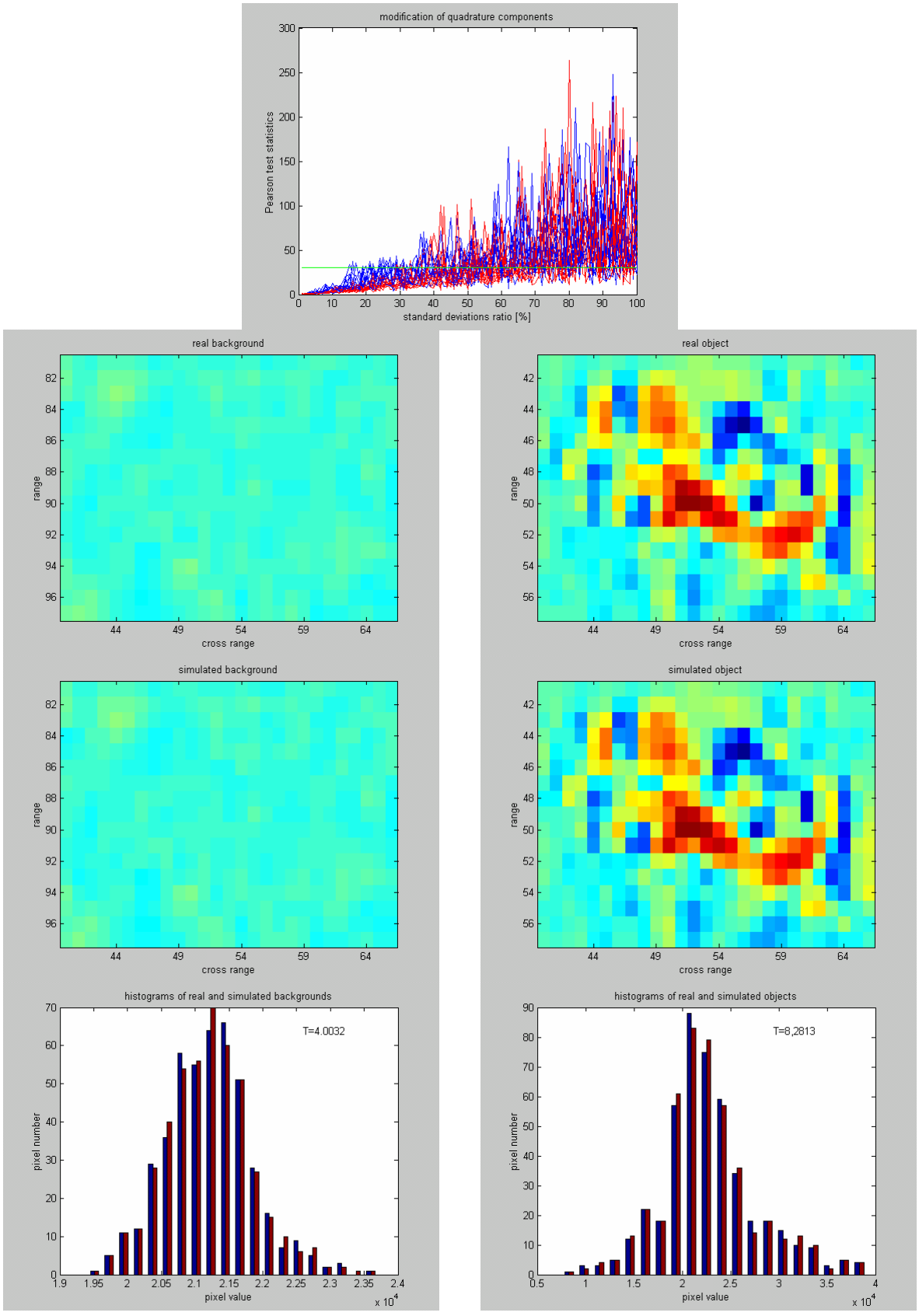

Fig.6 Results of simulation – algorithm No 2.

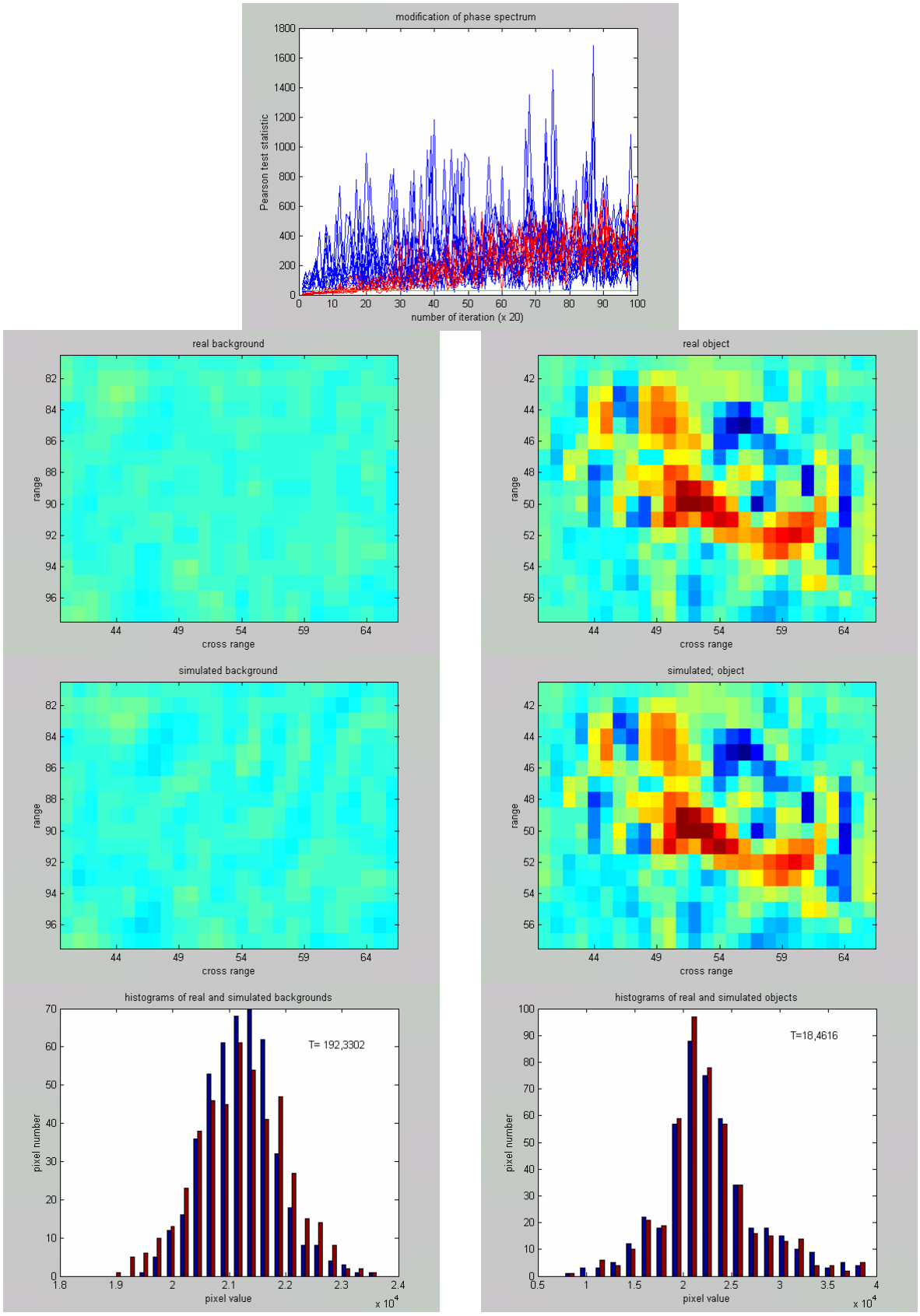

Fig. 8 Results of simulation – algorithm No 3.

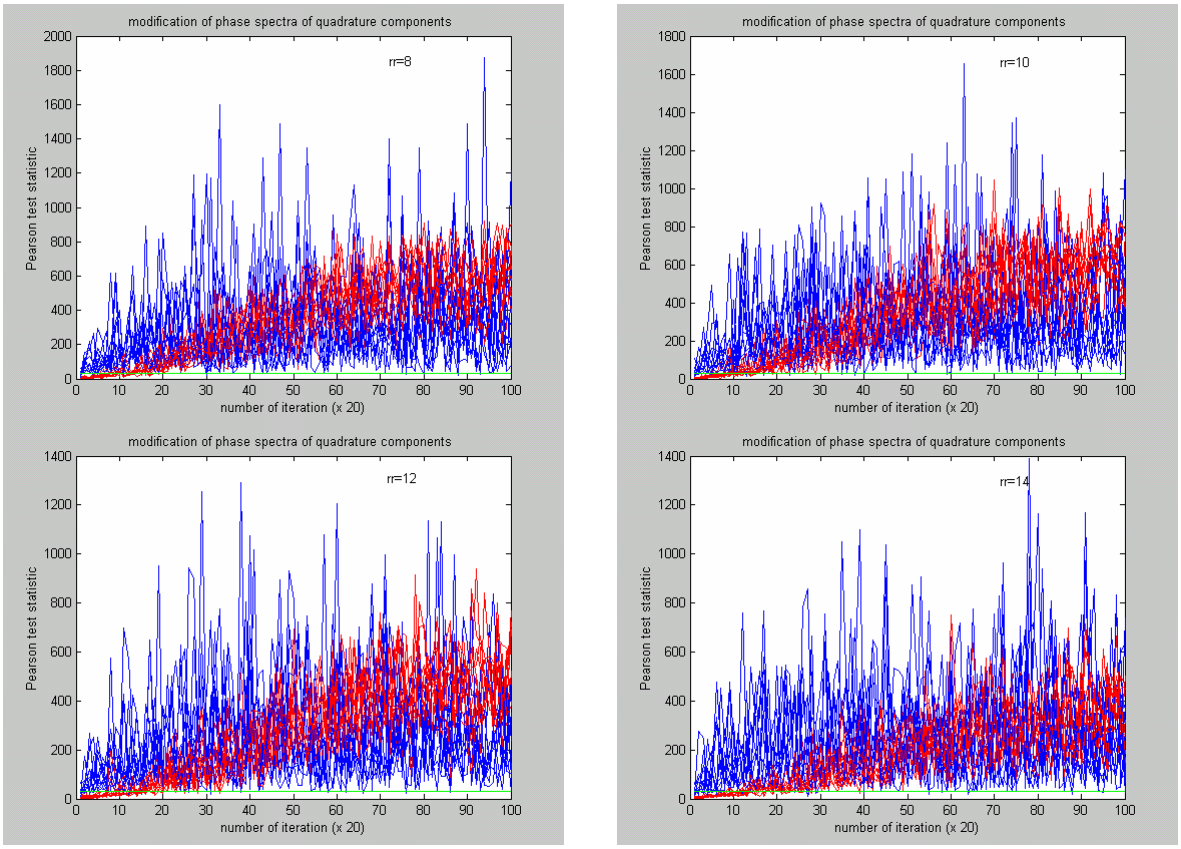

Fig.9 Pearson's test statistic for different radii of circular exclusion region rr

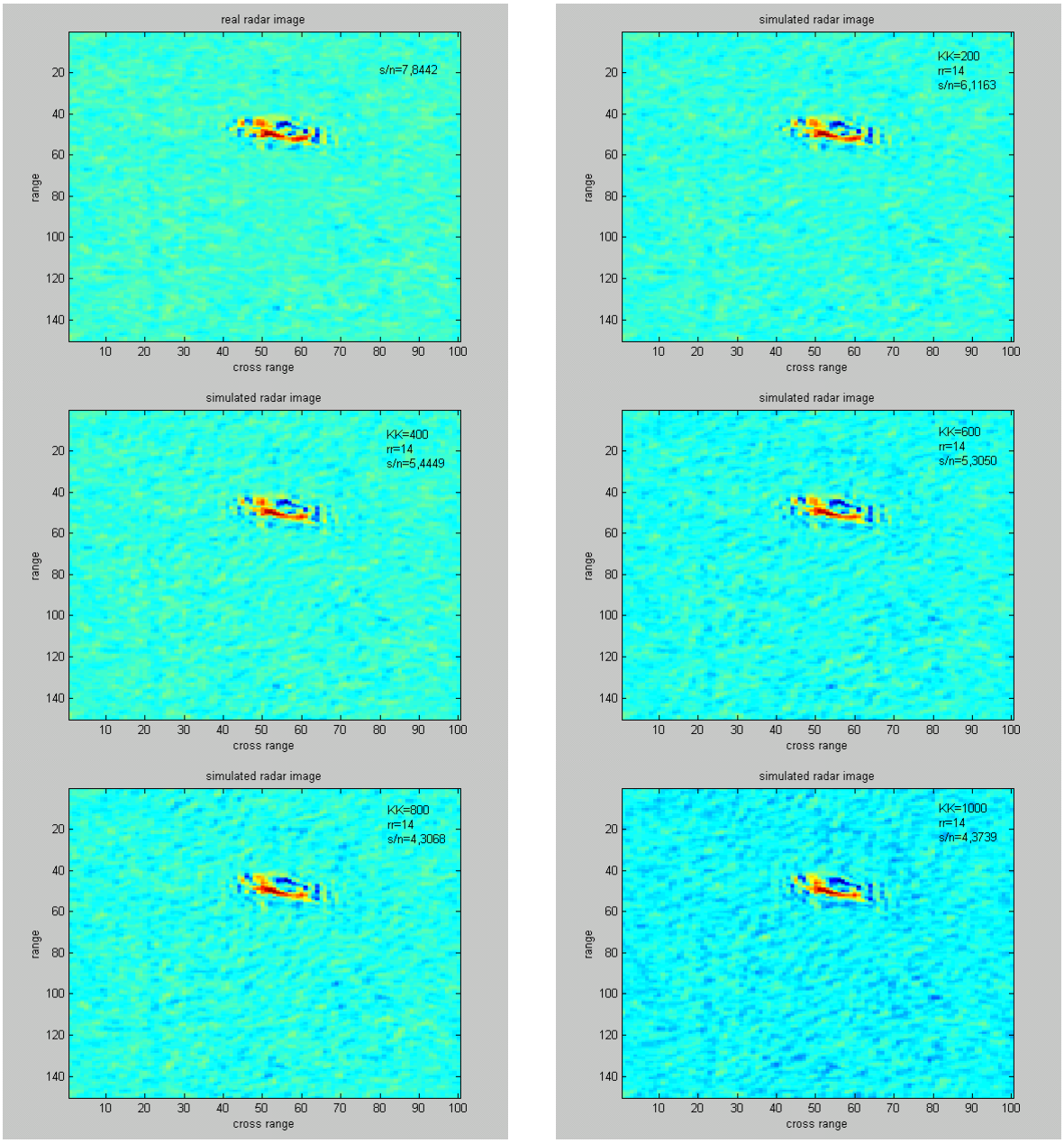

Fig.10 Signal images of different signal to noise ratio s/n obtained for different number of iteration KK and constant radius of circular exclusion region rr=14 – algorithm No 3

Evaluation of Bayes, ICA, PCA and SVM Methods for Classification

V. C. Chen
Radar Division, US Naval Research Laboratory
4555 Overlook Avenue, S.W.
Washington DC 20375
USA

vchen@radar.nrl.navy.mil

ABSTRACT

In this paper, we introduce the basic concepts of some state-of-the-art classification methods, including independent component analysis (ICA), principal component analysis (PCA), Bayes method, and support vector machine (SVM) or kernel machine. We discuss their function in the classification and evaluate their performance for different applications.

1 STATISTICAL CLASSIFICATION

Classification means to resolve the class of an object, e.g., a ground vehicle vs. an aircraft. *Recognition* means to determine whether the ground vehicle is a truck, a school bus, or a tank. *Identification* means to identify the type or model of the target (T72 tank or M60 tank). *Statistical classification* utilizes the statistical *pattern recognition* method for classification, recognition and identification [1]. A *pattern* is a characteristic of an observation, such as a speech signal or a human face image. A structural characteristic extracted from a pattern is called a *feature*. It can be a distinctive measurement, a transformation, or a structural component. The process of converting a pattern to features is called *feature extraction*. Each pattern can be viewed as a point (or a vector) in the *feature space*. The best features are selected using a *feature selection* algorithm. The selected features should best represent the classes or best represent the distinction between classes. The dimensionality of the selected feature space can also be greatly reduced compared to the full feature space.

The statistical classification process based on the probability distributions of the feature vectors can be described as follows:

(1) First, define the classes of patterns:

$$(C_1, C_2, ...C_M)$$

(2) Then, extract and select the best features from a pattern:

$$x = (x_1, x_2, ..x_N)$$

(3) Then, specify or learn the conditional probability function of a feature vector x belonging to class C_i:

$$p(x|\ C_i)$$

(4) Then, chose a decision rule (Bayes rule, maximum likelihood rule, Neyman-Pearson rule, or other rules).

(5) Finally, find the decision boundaries.

Paper presented at the RTO SET Symposium on "Target Identification and Recognition Using RF Systems", held in Oslo, Norway, 11-13 October 2004, and published in RTO-MP-SET-080.

The complete statistical classification process, as shown in Figure 1, includes pre-processing of observed or sensed data (such as segmentation, noise removal, filtering, spatial or temporal localization, and normalization of patterns), feature extraction, feature selection, learning, and classification. Feature extraction is accomplished with the principal component analysis (PCA) or independent component analysis (ICA). Then, in feature selection, the methods used include branch and bound search (B & B), sequential forward selection (SFS), sequential backward selection (SBS), sequential forward floating search (SFFS) and sequential backward floating search (SBFS). Finally, learning and classification are accomplished with Bayes classifier, k-nearest neighbor (k-NN) classifier, linear discrimination classifier (LDC) and support vector machine (SVM) as indicated in Figure 1.

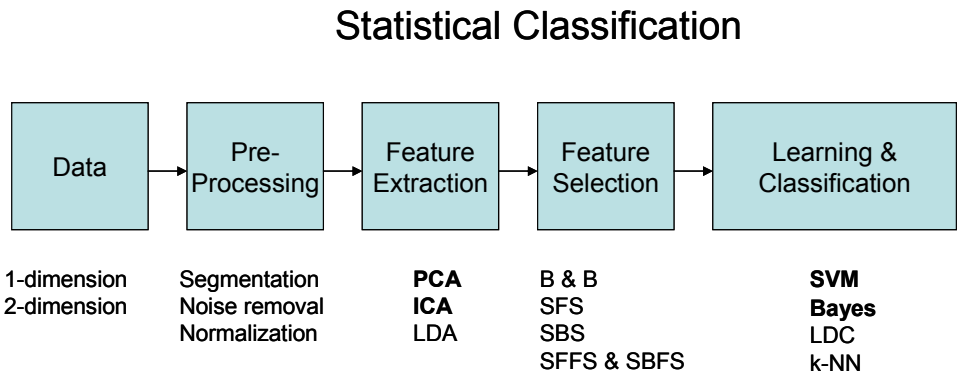

Figure 1. Basic stages of the statistical classification process.

2 FEATURE EXTRACTION

2.1 Feature Extraction and Dimensionality Reduction

Feature extraction converts data patterns to features, which are condensed representations of patterns and contain only salient information (as shown in Figure 2). The converted features should represent patterns with minimal loss of the information required for best classification. Features include non-transformed structural characteristics, transformed structural characteristics, and structures (such as lines, slopes, corners, or peaks). Non-transformed structural characteristics are obtained directly from sensor observations such as amplitudes, phases, time durations, or moments. Transformed structural characteristics are obtained from transformations such as the Fourier transform, wavelet transform, time-frequency transform, singular value decomposition, or Karhunan-Loeve transform.

Linear transforms, such as PCA and linear discrimination analysis (LDA), are widely used for feature extraction and dimensionality reduction. PCA is the best-known unsupervised linear feature extraction algorithm; it is a linear mapping which uses the eigenvectors with the largest eigenvalues. LDA is a supervised linear mapping based on eigenvectors, and it usually performs better than PCA for classification. ICA [2-4] is also a linear mapping but with iterative capability, which is suitable for non-Gaussian distributions. ICA decomposes a set of features into a basis whose components are statistically independent. It searches for a linear transformation W_{ICA} (or weight matrix) to express a set of feature vectors $X = (x_1, x_2, \ldots x_N)$ as a linear combination of statistically independent vectors $Y = (y_1, y_2, \ldots y_N)$, so that the transformed components $Y = W_{ICA}{}^T X$ are independent, that is, knowledge of the value of y_i provides no information on

the value of y_j for $i \neq j$. There is no closed form solution for finding the weight matrix W_{ICA}. Therefore, iterative algorithms have been proposed to search for a weight matrix. PCA only requires that the coefficients y_i and y_j be uncorrelated, i.e.

$$\text{cov}(y_i, y_j) = E\{y_i, y_j\} - E\{y_i\}E\{y_j\} = 0$$

However, independence is a stronger requirement, because independent components are uncorrelated, but uncorrelated components may not be independent. Thus, the ICA accounts for higher order statistics and provides a more powerful data representation than PCA.

Kernel PCA is a nonlinear feature extraction method based on eigenvectors, which maps input patterns into a new feature space through a nonlinear function, and then performs a linear PCA in the mapped space.

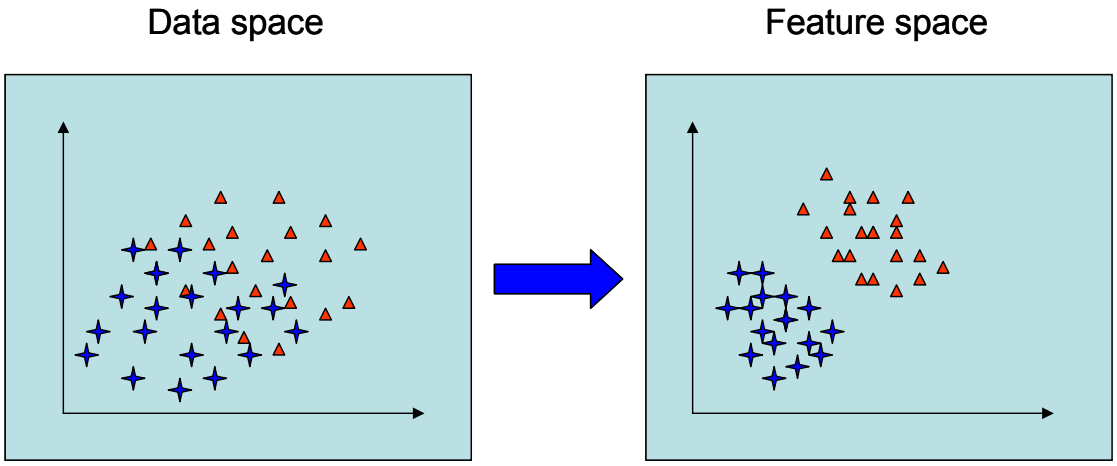

Figure 2. Feature extraction converts data pattern space to feature space.

2.2 PCA vs. ICA

PCA is a classical projection method used in signal analysis. ICA was originally used for separating mixed signals into independent components; this process is called *blind source separation* (BSS). The goal of PCA is to minimize the projection error, but the goal of ICA is to minimize the statistical dependence between basis feature vectors. Recently, ICA has been applied to image analysis. Some results show that ICA outperforms PCA, and others show that there is not much performance difference between ICA and PCA. We should realize that the nature of our classification task affects the evaluation. For some classification tasks, if the global properties such as width and length are more important, then they are more easily extracted by PCA than ICA. If features such as time-frequency signatures are more spatially localized, ICA is better than PCA. For small ship classification, the global features are more important than localized spatial features, as illustrated in Figure 3. Thus, PCA is good enough for feature extraction. However, for micro-Doppler time-frequency signatures, the localized spatial features are more important, and the ICA should be used in feature extraction as illustrated in Figure 4.

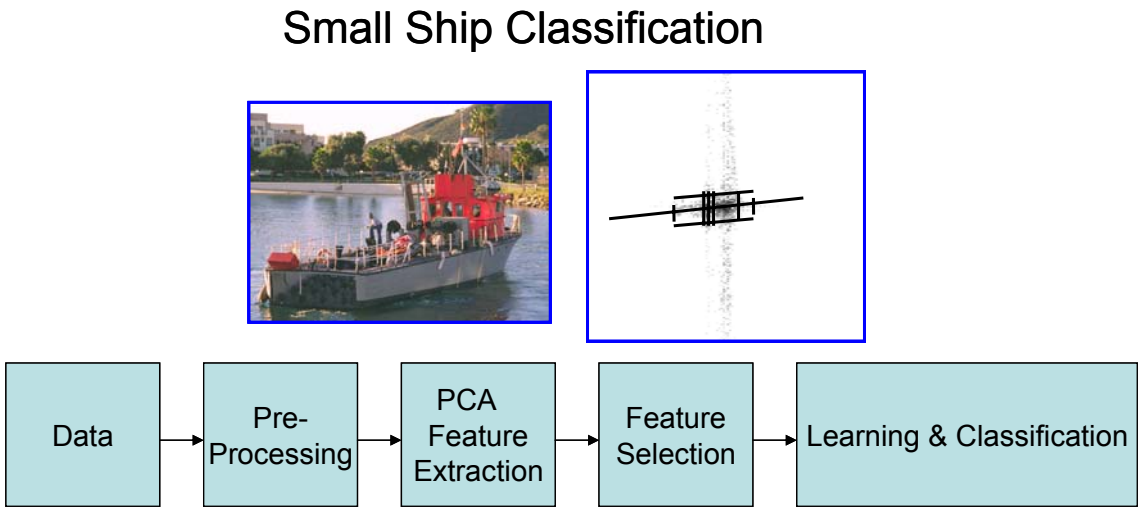

Figure 3. Using PCA for small ship feature extraction.

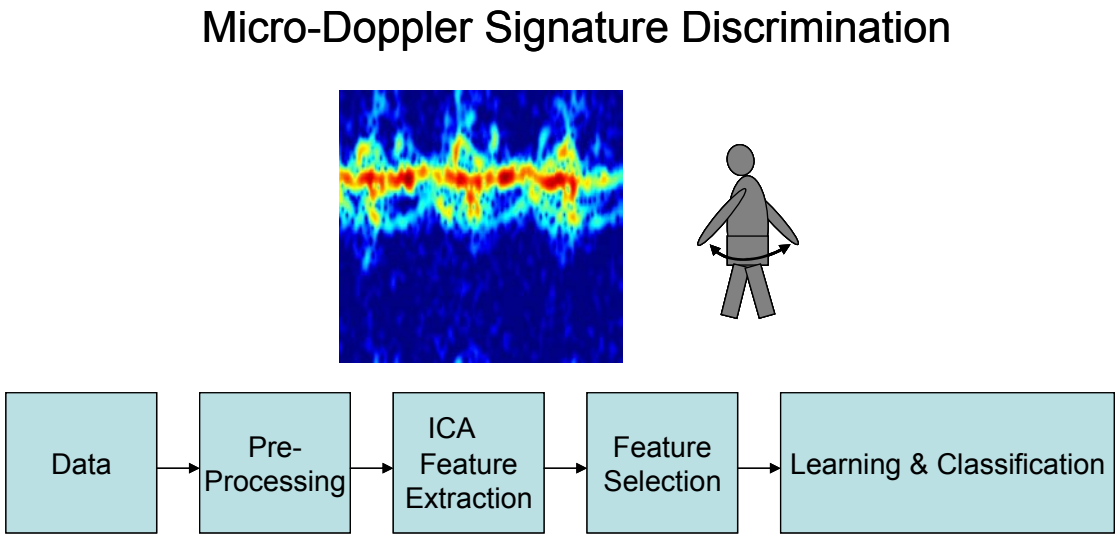

Figure 4. Using ICA for micro-Doppler time-frequency signatures discrimination.

3 FEATURE SELECTION

The purpose of feature selection is to determine a subset within the set of features in order to minimize the classification error based on various criteria [1]. A straightforward method of feature selection is the

exhaustive search that selects the best features and minimizes the classification error. Another efficient feature selection method is the *sequential forward and backward selection* (SFBS). Forward selection means a bottom up process that begins with an empty set and selects the first feature that is the best feature. Then, at each step, it selects the best feature from the remaining set, which, combined with the features already selected, gives the best value under the selection criterion. Backward selection is a top down process which removes features from the feature set. However, it cannot re-select those removed features even if they would be useful for further processing.

Suppose there is a set of N features represented by Y and M features of a subset represented by X. Let $J(X)$ to be a *criterion function* for selecting X from Y. Then, the selection procedure can be summarized as (1) searching to find all possible subsets of size M from N features and (2) selecting the subset X with the largest value of $J(X)$ as the optimal subset. Most selection methods use the classification error of a selected feature subset to evaluate the effectiveness of the selection method.

The searching methods include:

(1) Exhaustive search.
(2) Branch and bound search (B & B): The criterion function is monotonic and the performance of a subset can be improved when adding a feature to it.
(3) Sequential forward selection (SFS): Evaluate a feature set by adding one feature at a time. Once a feature is added, it cannot be discarded.
(4) Sequential backward selection (SBS): Evaluate a feature set by deleting one feature at a time. Once a feature is deleted, it cannot be re-entered into the feature subset.
(5) Sequential forward floating search (SFFS) and sequential backward floating search (SBFS): Backtrack as long as there are improvements of the current feature set compared to the previous feature set. Performance is comparable to the B & B method with a lower computational cost.

4 LEARNING AND CLASSIFIER

The effectiveness of the feature space depends on how well different classes can be separated in the space. The objective of classification is to find decision boundaries between classes in the feature space that can best separate different classes. These decision boundaries are determined by the probability distributions of the patterns associated with each class. The probability distributions can be either specified or learned, i.e., boundaries can be found by either specifying the parametric format of the boundaries (such as linear or quadratic) or by finding them by learning through a training process.

The performance of a classifier depends on the number of available training samples. Learning includes supervised learning and unsupervised learning. Supervised learning requires that the training samples be labelled by their classes. Unsupervised learning does not require labelled training samples and the number of classes must be learned.

Classical classification methods include the Bayes, k-NN, LDC, and others. *Support vector machine* (SVM) is a modern classification method with a nonlinear classification function using an iterative method [5-7]. It can maximize the margin between the classes by selecting a minimum number of support vectors.

4.1 Bayes Classifier

The Bayes classifier assigns a pattern to the class that has the maximum estimated posterior probability. Given a pattern x, the posteriori conditional probability that the pattern belongs to the class C is determined by

$$P(C \mid x) = \frac{P(x \mid C)P(C)}{P(x)},$$

where $P(x)$ is the a priori probability that a pattern is x, $P(C)$ is the a priori probability that a pattern belongs to class C, and $P(x|C)$ is the conditional probability that a pattern is x if the pattern belongs to class C.

According to the Bayes rule, assign a pattern x to class C_i if the risk function, given by

$$risk(C_i \mid x) = \sum_{j=1}^{M} l(C_i, C_j) P(C_j \mid x)$$

is minimum, where $l(C_i,C_j)$ is the loss function when C_i is chosen if the true class is C_j, and $P(C_j \mid x)$ is the posterior probability of C_j. The Bayes classifier has the minimum classification error when the probability density functions are known.

4.2 k-Nearest Neighbor (k-NN) Classifier

The 1-Nearest Neighbor rule assigns a pattern to the class of the nearest training pattern without a training process. The classifier using the k-NN rule assigns a pattern to the majority class among k nearest neighbor.

4.3 Linear Discrimination Classifier (LDC)

Assume x_i is a feature vector with d dimensions, and $X = (x_1, x_2, \ldots x_N)$ is the training set with N classes. Given a transformation matrix W, the original feature vector is transformed to a projection feature vector $Y = (y_1, y_2, \ldots y_N)$ with a reduced dimension of d_1 ($d_1 < d$):

$$Y = W^T X .$$

Define a scatter matrix S:

$$S = \sum_{i=1}^{N} (x_i - \mu)(x_i - \mu)^T .$$

where μ is the mean target feature vector. The LDC uses the transformation matrix W_{LDC} that satisfies

$$W_{LDC} = \arg\max_{W} \frac{W^T S_{between} W}{W^T S_{within} W}$$

where the between-class scatter matrix is defined by

$$S_{between} = \sum_{i=1}^{K} N_i (x_i - \mu_i)(x_i - \mu_i)^T ,$$

and the within-class scatter matrix is defined by

$$S_{within} = \sum_{i=1}^{K} \sum_{x_k \in X_i} (x_k - \mu_i)(x_k - \mu_i)^T ,$$

where N_i is the number of training samples in class i, K is the number of distinct classes, μ_i is the mean vector of samples that belongs to class i, and X_i is the set of samples that belongs to class i. To reduce the dimensionality, the LDC should apply the PCA first.

4.4 Support Vector Machine

SVM is an unsupervised approach based on statistical learning theory. It estimates the optimal boundary in the feature space by combining a maximal margin strategy with a kernel method; this process is

called a *kernel machine*. The machine is trained according to the *structural risk minimization* (SRM) criterion [5,6]. The decision boundaries are directly derived from the training data set by learning.

The SVM maps the inputs into a high-dimensional feature space through a selected kernel function. Then, it constructs an optimal separating hyper-plane in the feature space. The dimensionality of the feature space is determined by the number of support vectors extracted from the training data (see Figure 3). The SVM can locate all the support vectors, which exclusively determine the decision boundaries. To estimate the misclassification rate (risk), the so called *leave-one-out* procedure is used. It removes one of N_i training samples, performs training using the remaining training samples, and tests the removed sample with the newly derived hyperplane. It repeats this process for all of the samples, and the total number of errors becomes the estimation of the risk.

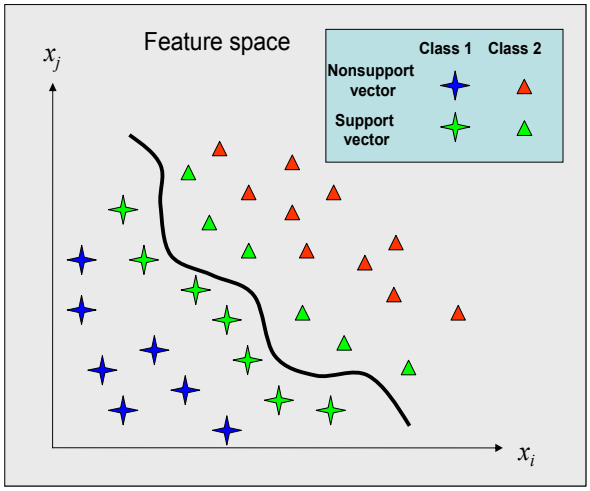

Figure 3. Optimal boundary serached by the SVM.

4.5 Classifier Evaluation

Pattern recognition software packages and toolboxes are widely available [8]. To evaluate different classifiers, we create a 2 dimensional dataset generated with 100 samples for each class. Among the 100 samples, 20 samples are used for training and 80 samples are for testing. Four classifiers (LDA, k-NN, Bayes, and SVM) are compared. Note that here the data is generated by a random generator.

In the first example, two classes of samples are overlapped in the 2-D feature space. Figure 4 shows the decision boundaries found by (a) LDC, (b) Bayes, (c) k-NN and (d) SVM. Figure 5 shows classification error rates or the receiver operation curve (ROC) of the corresponding four classifiers.

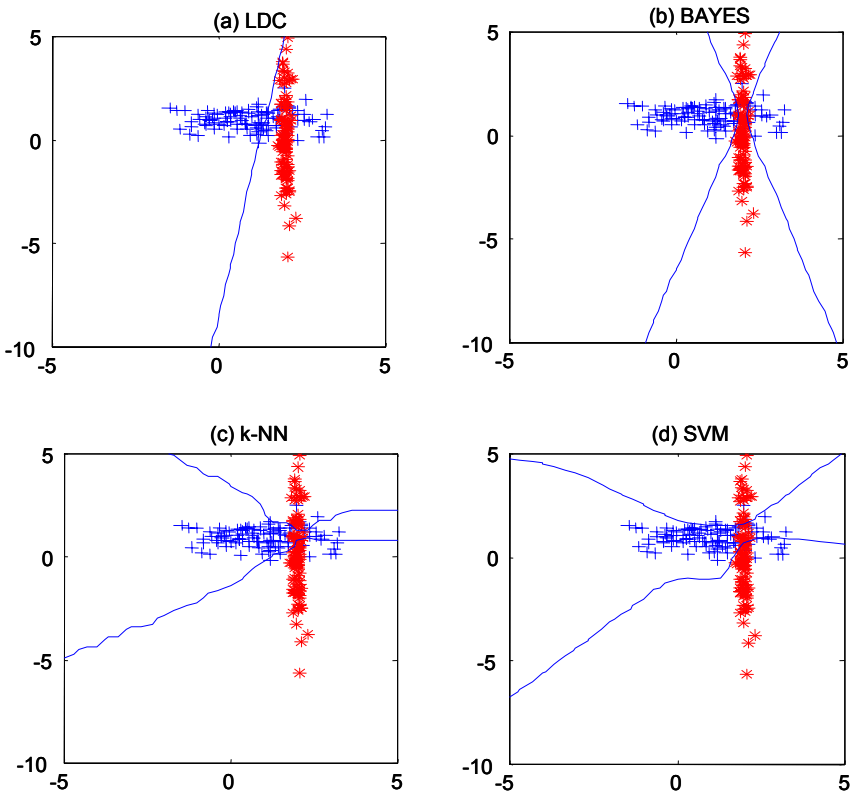

Figure 4. Classifier boundary found by (a) LDC, (b) Bayes, (c) k-NN, and (d) SVM for two overlapped classes in 2-D feature space.

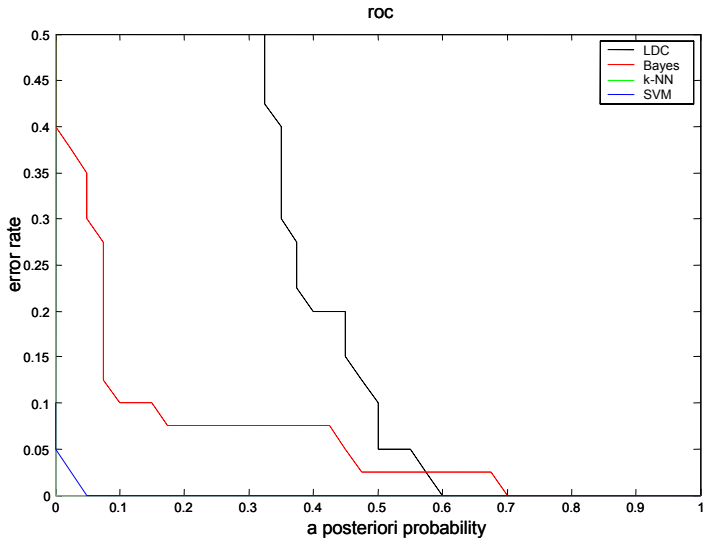

Figure 5. Two classes' classification error rates for the four classifiers.

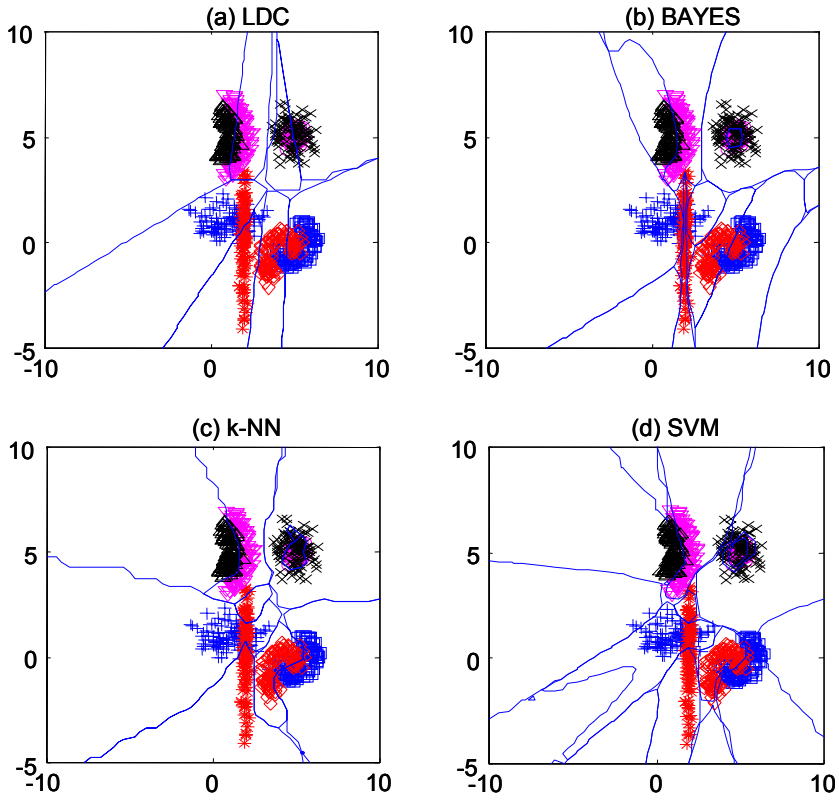

Figure 6. Classifier boundary found by (a) LDC, (b) Bayes, (c) k-NN, and (d) SVM for eight overlapped classes in 2-D feature space.

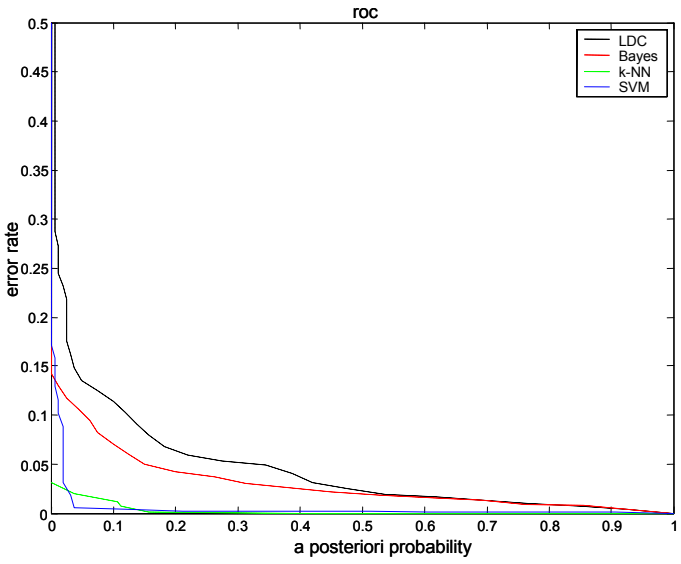

Figure 7. Eight classes' classification error rates for the four classifiers.

The second example is eight mixed classes of samples overlapped in the 2-D feature space. Figure 6 shows the decision boundaries found by (a) LDC, (b) Bayes, (c) k-NN and (d) SVM. Figure 7 shows the classification error rates of the corresponding four classifiers.

From the above two examples, we see that SVM can find more complicated decision boundaries, and the classification errors of k-NN and SVM are considerably lower than others.

5 SUMMARY

We have introduced the basic concept of ICA, PCA, Bayes, and SVM, and we have discussed their functions in classification and evaluated their performances for different applications. If global properties are more important, then these features are more easily extracted by PCA than ICA. If the features are more localized, ICA is better than PCA. For small ship classification, where global features are more important than localized spatial features, PCA is good enough for feature extraction. However, for micro-Doppler time-frequency signatures, the localized spatial features are more important, and ICA should be used in feature extraction. From two simulated examples, we see that SVM can find more complicated decision boundaries, and the classification errors of k-NN and SVM are considerably lower than the others.

6 ACKOWLEDGEMENT

This work was supported by ONR, through the NRL base program.

REFERENCES

1. A.K. Jain, R.P.W. Duin and J. Mao, "Statistical pattern recognition: A review", *IEEE Trans. on PAMI*, vol.22, no.1, pp.4-37, Jan. 2000.
2. A. Hyvarinen and E. Oja, "Independent component analysis: Algorithms and Applications", *Neural Networks*, 13(4-5), pp.411-430, 2000.
3. A. Bell and T. Sejnowski, "An information-maximization approach to blind separation and blind deconvolution", Neural Computation, 7, pp.1129-1159, 1995.
4. P. Comon, "Independent component analysis: A new concept?" Signal Processing, 36(3),pp.287-314, 1994.
5. C.J.C. Burges, "A tutorial on support vector machines for pattern recognition", *Data Mining and Knowledge Discovery*, 2, pp.121-167, 1998.
6. V. Vapnik, *Statistical Learning Theory*, John Wiley and Sons, Inc., New York, 1998.
7. Q. Zhao and J. Principe, "Support vector machines for SAR automatic target recognition", *IEEE Trans. on AES*, vol.37, no.2, pp.643-654, 2001.
8. R.P.W. Duin, *PRTools – A Matlab Toolbox for Pattern Recognition*, http://www.ph.tn.tudelft.nl/prtools.

An Adaptive Unified Algorithm for Both Detection and Recognition

Keith D Copsey and Chris J S Webber
QinetiQ
Malvern Technology Centre
St Andrews Road, Malvern
Worcestershire, WR14 3PS
United Kingdom

K.Copsey@signal.QinetiQ.com and C.Webber@signal.QinetiQ.com

ABSTRACT

An adaptive neural-network approach to target- and clutter-modelling is introduced. A key novelty of this approach is that both targets and clutter can be modelled within the same neural network, so that detection and recognition can take place simultaneously within an integrated framework. The approach can therefore be applied across the spectrum of ATR discrimination levels, e.g.: detection of unknown targets in clutter; detection of specific designated targets in clutter; recognition of target subclass post-detection. The approach is designed to be generically applicable, to data from a variety of sensors, including HRRPs, SAR intensity imagery, complex SAR imagery, visible and EO imagery, and burst-illumination LIDAR. This generic applicability is attributable to the fact that the algorithm adaptively models training-exemplar data of arbitrary type and dimensionality. Unlike many current approaches to target detection, this approach can exploit a wide range of cues for discriminating targets from clutter objects, including detailed grey-level shape information and, for RF sensors, complex/phase information. Furthermore, the approach is quick to use in operation, and has been designed with hardware implementations in mind. Successful results are presented for a target (designated building) detection and identification problem using real SAR imagery. The approach has been designed to have the future potential to offer other very significant new capabilities, e.g. the potential for reducing false-alarm rate in urban clutter and improving robustness to extended operating conditions.

1.0 INTRODUCTION

1.1 Integrated approach to target detection and recognition

This paper concerns an adaptive neural-network approach to target- and clutter-modelling. A key novelty of the approach is that both targets and clutter can be modelled within the same neural network, so that detection and recognition can take place simultaneously within an integrated framework. The approach can therefore be applied across the spectrum of ATR discrimination levels, e.g.:

- Detection of unknown targets in clutter;
- Detection and recognition of specific designated targets in clutter;
- Recognition of target subclass post-detection.

The proposed approach is designed to be generically applicable to data from a variety of sensors, including HRRPs, SAR intensity imagery, complex SAR imagery, visible and EO imagery, and burst-illumination LIDAR. This generic applicability is attributable to the fact that the algorithm adaptively models training-exemplar data of arbitrary type and dimensionality.

Paper presented at the RTO SET Symposium on "Target Identification and Recognition Using RF Systems", held in Oslo, Norway, 11-13 October 2004, and published in RTO-MP-SET-080.

When used for target detection, the approach exploits the kind of knowledge of the *signature* of the target that would conventionally be used only at the post detection identification stage, in order to influence the *detection* decision. This allows potentially crucial signature information (e.g. detailed grey-level shape information and, for RF sensors, complex/phase information) to be used at the earliest stages of target detection. This offers the potential to mitigate the false-alarm rate of the detection process very significantly. The resulting "identify-for-detect" principle is analogous to the "track-before-detect" principle well known in the context of tracking algorithms [8]. The key to this unified approach to automatic target detection and recognition lies in the use of a technique with the ability to:

- Model targets with varying degrees of specificity and generalisation, depending on the scenario;
- Model varied and complicated clutter with a high degree of generalisation.

Many potential approaches for modelling both targets and clutter cannot be used for simultaneous target detection and recognition, because of the computational expense involved in conducting the comparisons at each location. In contrast, the proposed algorithm is quick to use in operation, and has been developed with hardware implementations in mind.

1.2 Background

The developed approach is the result of neural network research into transformation-robust pattern recognition. The motivating aim has been to develop techniques that enable target detection and recognition to be robust to both continuous and discontinuous complex transformations (where complex transformations are defined to be transformations of individual objects within the sensor image, as opposed to simple perspective transformations of the whole image). In the ATR context, continuous complex transformations include 3-D rotation and articulation (e.g. the rotation of a tank's turret with respect to its hull). Examples of discontinuous complex transformations include the replacement of one type of vehicle with another of similar type, partial occlusion, differences in equipment fit, and change in operational configuration.

Complex transformations are intimately associated with ill-defined properties of the objects to be recognised. It is likely that characterisation of these properties will require reference to a complex, nonlinear, hierarchical pattern recognition technique, with the ability to adapt to training data that is characteristic of those ill-defined properties. A neural network is such a technique.

In the neural network literature, the term "invariance" is used to refer to what the military user or systems designer would term "robustness"; neural network papers generally adopt the mathematical terminology of group theory rather than the terminology of the ATR application domain. A neural network (or some part of it) is said to be invariant under a transformation of the data if its recognition output response does not change (or changes only gradually) as the transformation is applied to the data. This property of the recognition response is clearly what is desired if one wishes to build a neural network based ATR system that is robust with respect to variation in the sensor data.

1.3 Outline

The structure of this paper is as follows. Section 2 outlines the concepts behind the adaptive neural network algorithm, by discussing neural network approaches to transformation invariance. Section 3 briefly discusses the approach implemented within algorithms to date. Section 4 presents experimental results for detection and recognition of a particular building within SAR imagery of an urban area. Conclusions and future work are in Section 5.

2.0 ALGORITHMIC CONCEPTS

2.1 Discussion of neural network approaches to transformation invariance

Whether explicitly acknowledged or not, many neural networks capable of transformation invariance are symmetry networks [10]. These are neural networks in which some synaptic weights are equal (or approximately equal) to others. Put in another way, these are networks whose configuration of synaptic weights is symmetric (invariant) under certain groups of permutation transformations. This is illustrated graphically in Figure 1. The recognition outputs of neurons that possess this symmetry property are consequently invariant under corresponding groups of transformations on their input data. This conclusion is related to the group-invariance theorem of Minsky & Papert [5], and is explained more fully by Webber [16].

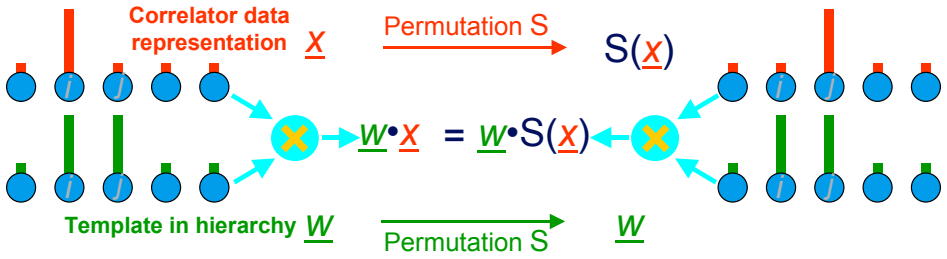

Figure 1: Illustration of a symmetry network. The permutation transformation in the data shown in the top half of the diagram is matched by a permutation in the synaptic weights (the templates in the hierarchy W) shown in the bottom half.

"Weight-sharing" [5][10][11] provides a trivial example of synaptic-weight symmetry in a symmetry network, although this does not begin to exemplify the full potential of synaptic-weight symmetry as a means of achieving transformation robustness. In a weight-sharing architecture, an array of neural network recognition nodes ("neurons") is forced to generate an output recognition response that is invariant with respect to global 2-D translations of the whole image. This is achieved by constructing the architecture of the network so that neighbouring neurons in the array share neighbouring input connection weights (neighbouring "synaptic weights") in common, *i.e.* the architecture is constructed so that neighbouring synaptic weights of neighbouring neurons are equal. The result is that as objects are translated across the sensor image, the recognition responses of the neurons are correspondingly just translated across their array rather than being changed entirely beyond recognition. This trivial example of a symmetry network therefore exhibits the same translation invariance property as the standard template correlator. More sophisticated forms of synaptic weight symmetries than simple globally translation-invariant weight-sharing can be designed into neural network architectures. The rotation-invariant network of Fukumi et al [1] (applied to coin recognition), the handwritten zip-code recogniser of Le Cun et. al. [4] and the Neocognitron [2][3] all use built-in weight equalities implicitly to achieve their transformation robustness.

In all the examples in the previous paragraph, the weight symmetries are designed into the architecture at the outset (*a priori*) and are not derived by learning. Such static or "hard-wired" weight symmetries are rarely sufficient for handling transformations more sophisticated than simple global transformations of the whole sensor image such as 2-D translation, rotation and scale magnification. This is because prior knowledge of the transformation properties of individual objects is generally insufficient or too ill-defined to allow the neural network's designer to understand how to hard-wire appropriately sophisticated and complex weight symmetries into the network's architecture; in other words, *object/model-dependent* weight symmetries will be necessary for true robustness to articulation and changes in operational configuration.

Some improvement on hard-wiring fixed symmetries in this way may be obtained by constraining the network learning algorithm's equations to enforce and maintain particular groups of simple weight symmetries throughout the learning process. An example is provided by Rumelhart et al. [7], in which weight sharing constraints on the learning equations were used to distinguish T and C shapes in simple synthetic images, independently of 2-D translation and 90^{o} rotation. This approach still has the disadvantage that the network designer must understand exactly what groups of symmetry transformations are to be imposed on the learning equations, and how to do so.

In each of the approaches outlined above, the algorithm's designer imposed onto the neural network a particular, known, well-defined group of transformation invariances. In the case of ill-defined, complex, object-dependent transformations such as articulation or changes in operational configuration, the designer generally has insufficient understanding of how to impose the ill-defined invariances onto the network in the form of supervisory knowledge. To address this problem, one needs a data-driven means of acquiring robustness/invariance under these transformations, through unsupervised learning of real data representative of the particular objects that undergo these object-dependent transformations.

2.2 Symmetry-preserving networks

Our solution is based on Webber's discovery that a new class of unsupervised neural networks ("symmetry-preserving" networks) can detect invariances/symmetries in the probability distribution function (PDF) of their training data, and exploit that new functionality to develop robust response with respect to precisely those transformations. In other words, this new class of algorithms can *preserve* the symmetries of the data's PDF, in the form of matching symmetries in the trained configuration of synaptic weights and consequently in the form of matching invariances in the network's recognition output. In principle, such networks can acquire robustness with respect to all manner of ill-defined complex transformations of objects in their training data, both continuous and discontinuous discrete transformations, simply through exposure to training data containing sufficient (but far from exhaustive) numbers of exemplars of the transformed objects. These claims are proved algebraically in Webber [16]. That paper also demonstrates this new functionality using real images having the full statistical complexity of natural scenes and shows that, through exposure to natural scenes, symmetry-preserving networks can derive and explain the translation-invariance properties of the complex cells of the visual cortex. Webber [17] goes on to demonstrate that, through exposure to natural scenes, symmetry-preserving networks can generate fully translation-, rotation- and scale-invariant codes for natural images. Symmetry-preserving network algorithms tend to be algorithmically simple, with the advantage that fast hardware implementations are feasible.

2.3 Componential coding, aka combinatorial, multiple-cause or factorial coding

The unsupervised neural network learning algorithms applied here to integrated target detection and recognition are capable of adaptively deriving *componential codes* to encode/model their training data. Componential coding has been alternatively called constituent coding, multiple-cause coding, combinatorial coding and factorial coding by various papers that have illustrated the concept using simplified synthetic data, e.g. [13][9]. It has since been applied to real data, e.g. for modelling handwriting [14] and for modelling sensor signals for the purpose of machine condition monitoring [15][6]. The idea is that sensor data having enormous variability may nevertheless be modelled effectively, by factorizing the variability down into its constituent building blocks, or components. Thus, one attempts to model the various exemplars of data as variable combinations of the building-block components, in the same way that the many tens of thousands of words in the English language may be represented as various combinations of 26 letters. The adaptive learning property of the algorithm is needed to derive the appropriate building blocks from the data, because these are generally not known a priori.

Componential coding is the approach used here to model the combinatorial complexity of urban clutter. We introduce a classifier that can distinguish designated targets from clutter by comparing the sensor image against a clutter model that *combines* building block components according to a statistical framework. (Figure 4 will show a few examples of the building blocks we derive from an urban clutter training set.) This is a much more sophisticated approach than simply attempting to compare the sensor image directly against a library of target exemplars and a library of clutter exemplars, by measuring which library fits the sensor image best. Indeed, attempting simply to compare the sensor image directly against a library of clutter exemplars could never produce robust performance, because one would need an effectively infinite number of exemplars to catalogue the enormously variable complexity of possible urban clutter scenes. This is the main reason why conventional correlation-filter or template-matching methods have not been effective in discriminating targets from urban clutter. In contrast, an adaptive clutter model that can *interpolate* between training exemplars by attempting to model them as combinations of building-block components has a far better chance of being able to model the enormous variability of urban clutter sufficiently well to be useful as part of an effective classifier.

3.0 USE OF THE APPROACH

3.1 Single-layer implementation

Learning algorithms capable of symmetry preservation have been incorporated into a Bayesian density estimation framework, and can be used to produce a likelihood distribution for the training data. To date only a single-layer implementation of these algorithms has been developed and assessed for radar target detection applications. A multi-layer implementation that will perform hierarchical feature extraction is under development. Such a multi-layer implementation is likely to be necessary for ATR that is robust to extended operating conditions (EOCs).

3.2 Clutter and target likelihoods

For the problem of recognition of target subclass post-detection, these algorithms are trained on exemplars of each target subclass. This would allow any subsequent unseen training data to be compared against each trained subclass model in order to generate a separate likelihood for each target subclass. After specifying prior subclass probabilities, Bayes' theorem can then be used to classify new objects by means of posterior subclass probabilities in the conventional Bayesian manner, e.g. [12].

For the problem of integrated target detection and recognition in clutter (identify-for-detect), a likelihood distribution is learned for the clutter as well as the target. This allows target detection in clutter to be performed, by comparing the relative likelihoods with which the image chip around any given location in a SAR scene matches the target and clutter models. In such cases, training the algorithm produces:

- A set of parameters θ_c that define the likelihood map for the clutter;
- A set of parameters θ_t that define the likelihood map for the target.

For a scene x, these can be used to produce a clutter likelihood map $l_c(x|\theta_c)$, and a target likelihood map $l_t(x|\theta_t)$. Using Bayes' theorem these can be combined to provide a map of the posterior target class probability:

$$p(t|x) = \frac{\pi_t l_t(x|\theta_t)}{\pi_t l_t(x|\theta_t) + \pi_c l_c(x|\theta_c)} = \frac{l_t(x|\theta_t)}{l_t(x|\theta_t) + \frac{\pi_c}{\pi_t} l_c(x|\theta_c)} \qquad (1)$$

where $\pi_t > 0$ and $\pi_c > 0$ are the prior probabilities for target and clutter respectively, subject to $\pi_c + \pi_t = 1$. Target-versus-clutter decisions can then made by comparing the posterior target class probability against a pre-specified threshold, and the value of this threshold may be varied in order to trace out a receiver-operator characteristic (ROC) curve. Note that an identical ROC curve may be produced by fixing the threshold for the posterior probability at some nominal value (say 1/2) and instead varying the ratio π_t / π_c, i.e. the ratio of the prior probability for targets against the prior probability for clutter.

4.0 EXPERIMENTAL RESULTS

4.1 Introduction

The proposed approach has been applied to the problem of recognising a particular building within SAR imagery of an urban area. Detection of specific building types could have many military uses, such as:

- Detection and identification of terrorist training facilities.
- Detection and identification of complexes associated with the development and storage of Weapons of Mass Destruction (WMD).
- Detection and identification of civilian buildings that define exclusion areas for weapon engagement, such as hospitals and schools.

The main purpose of the example is, however, to provide an initial proof of principle for the application of these new techniques to the generic problem of target detection and identification in urban clutter using SAR imagery. These techniques will in future be applied to the more specific problem of detecting military vehicles in urban clutter. In the mean-time, several factors must be taken into account when considering the relevance of the building identification results to the problem of military vehicle detection and identification. Firstly, the selected target building is larger than most military vehicles; thus, more "pixels on target" are available than is usual, which it could be argued may make the task of detecting and identifying a particular building type easier than the task of detecting and identifying a particular military vehicle type. However, a counter-argument is that size information cannot be exploited as a discriminant between the target and the clutter when the target is a building of similar size to the surrounding clutter buildings; this factor makes detecting building types more challenging than detecting vehicle types for methods that (unlike this method) rely only on size discriminants. Another counter-argument is that the target building is likely to have more features in common with the surrounding clutter buildings than a military vehicle would have in common with the surrounding clutter buildings. Thus, some features that could be used to distinguish a vehicle from a building (perhaps related to different radar cross-sections from different types of material) can no longer be exploited as discriminants when distinguishing buildings from other buildings.

4.2 Experiments

The dataset used for this demonstration consists of high-resolution SAR imagery of a built-up area. Specifically, the dataset consists of 18 SAR images of the urban scene, from a range of different aspect angles. All 18 images were 512×512-pixels in size. 10 of these were used for training, with the 10 successive training images separated by 4-degree intervals in aspect angle, and the other 8 were used for testing, with the 8 successive test images separated by 4-degree intervals in aspect angle. Alternate aspect angles were used for training and testing to ensure a proper test of generalisation over aspect angle, i.e. no test image was closer than 2 degrees in aspect angle to any training image.

Examples of the SAR imagery are shown in Figure 2, with the designated (target) building ringed. It is clear that there are many clutter objects that have returns of similar size and intensity to those from the selected target. Figure 3 displays extracted (64×64-pixel) image chips, centred on the target.

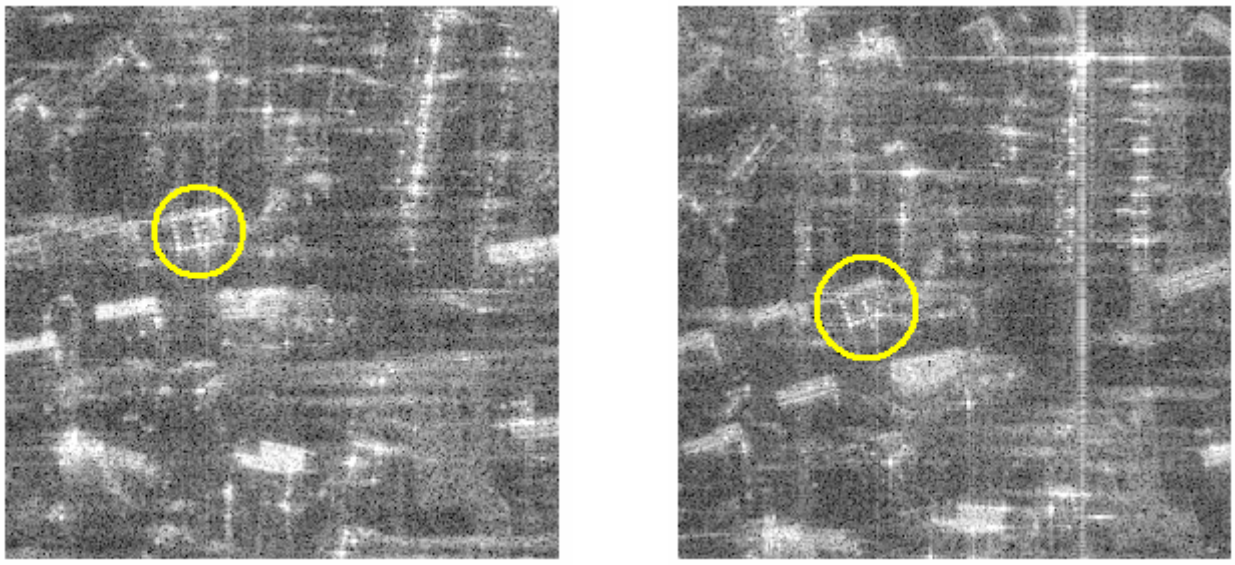

Figure 2: Examples of the SAR imagery of an urban scene, with the designated (target) building ringed in yellow. The left-hand image is view A and the right-hand image is view B.

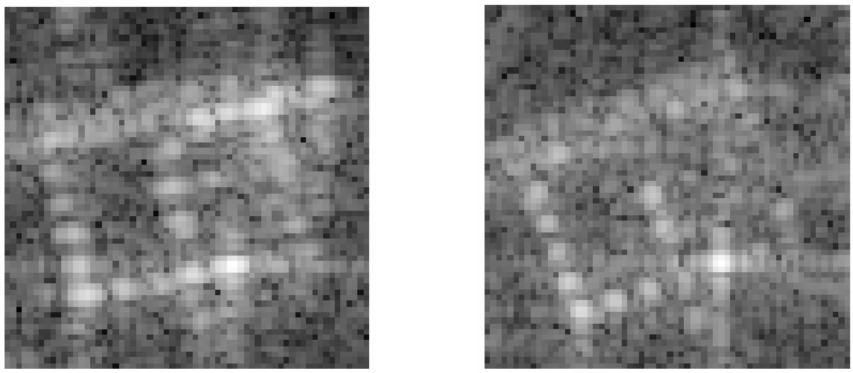

Figure 3: Examples of extracted target chips from the SAR imagery. The left-hand chip is extracted from view A and the right-hand chip is extracted from view B.

Training data for the target model were obtained by manually locating the target in each of the training images and, for each training image, extracting a 64×64-pixel image chip centred on the target. This produced 10 target-model training chips. Training data for the clutter model was obtained by sliding 64×64-pixel input windows over the entire set of training imagery. Some of the building blocks that constitute the trained clutter model are displayed in Figure 4.

Input windows that contained the target were not removed from the training data for the clutter model. The motivation for not removing the targets from the clutter training data is that it allows the clutter model to be trained on large areas of surveillance imagery, without human intervention to edit out targets. This introduces the potential to train the clutter model in situ, at the same time as the sensor platform surveys the area in which targets are to be detected. This mode of operation allows the clutter model to be refined so as to model the target's local environment optimally. The inclusion of targets in the clutter training data has minimal effect on the properties of the trained clutter model, and so does not cause significant degradation in the performance of the target-versus-clutter likelihood comparison. This is because the clutter model is trained in order to derive building blocks that best model the average properties of the

bulk of the clutter training data, so the inclusion of a few targets amongst the clutter training data will bias this average insignificantly. This is in marked contrast with the effect that including targets among the clutter exemplars would have on traditional template-matching classifiers (correlation-filters); for template-matching classifiers, any target chips that pollute the clutter training data would match as would the exemplars of the target. This is another advantage of the componential coding approach over traditional template-matching classifiers, over and above the combinatorial complexity issue discussed earlier.

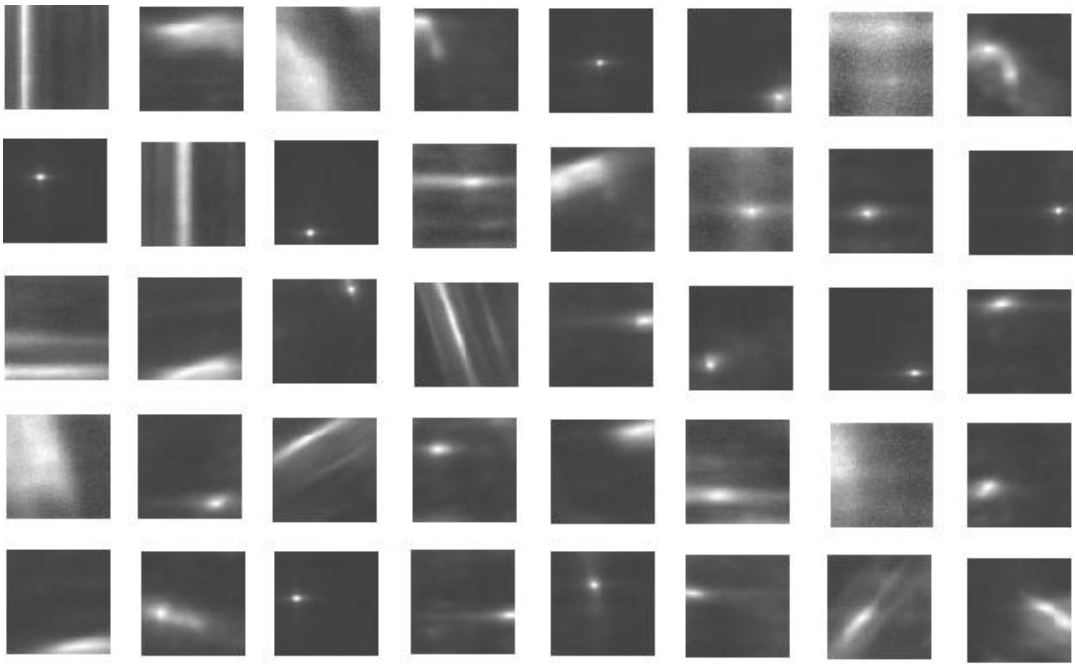

Figure 4: A subset of the building blocks that define the trained clutter model.

4.3 Results

The trained target and clutter models are used to produce target and clutter likelihood maps for each test scene. Once the target and clutter prior probabilities are specified, these likelihood maps can be used to produce a map of the posterior target class probabilities for each scene, using equation (1). Figure 5 displays the posterior class probabilities for views A and B, using a low ratio for the prior probability of a target versus the prior probability of clutter. Grey boxes have been centred on the locations for which the posterior class probabilities are higher than 0.5. For view A, the only detection box is centred on the target. For view B, there are two areas in which the posterior class probability is higher than 0.5. The upper area corresponds to the target, while the lower area is the result of a clutter false alarm.

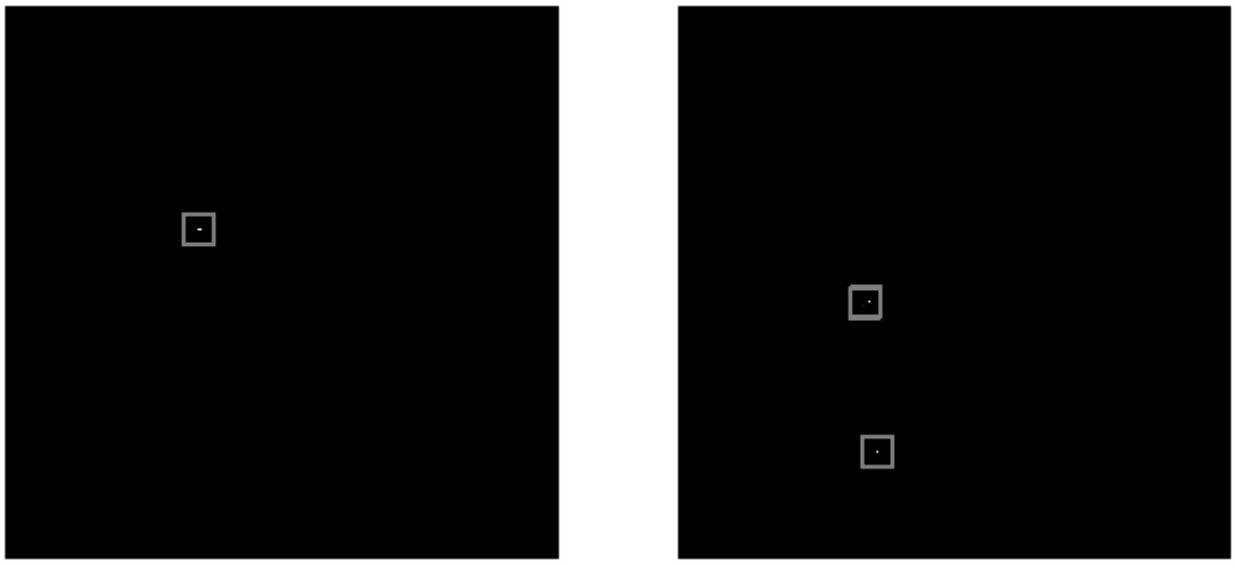

Figure 5: Posterior target class probability maps. The left-hand image is for view A and the right-hand image is for view B. Detections are surrounded by grey boxes.

Increasing the ratio of the prior probability for targets to the prior probability for clutter results in plots for the posterior target class probability that display more false alarms. (Increasing the ratio of the prior probabilities for a fixed value of the detection threshold on the posterior target probability is mathematically equivalent to reducing the detection threshold on the posterior target probability for a fixed value of the ratio of prior probabilities, as has been explained earlier.) Consequently, either varying the ratio of the prior probabilities for a fixed value of the detection threshold on the posterior target probability or varying the detection threshold on the posterior target probability for a fixed value of the ratio of prior probabilities will trace out an identical Receiver Operating Characteristic (ROC) curve for the target detection probability as a function of the false alarm rate. This ROC curve is provided in Section 4.5.

4.4 Baseline results

As an indicator of algorithm performance, two sets of baseline results are presented. Namely:

- Application of a correlation-filter (template matching).
- Application of a correlation-filter to the areas identified as anomalous by a Constant False Alarm Rate (CFAR) filter.

The templates for the correlation-filter were the same training target chips that were used to train the target model of the adaptive neural network algorithm. The same image chips as were used to train the clutter model of the neural network algorithm cannot be used as negative exemplars by the correlation-filter. This is because, for any correlator-filter classifier to function, the target would have to be manually edited out from the clutter training data, and this requirement would remove the operational potential for collecting the training data for the clutter model in-situ. More significantly, it would in general be impractical to use clutter chips as negative exemplars for a correlation-filter classifier, because an effectively infinite library of such negative exemplars would be required in order to provide robust generalisation to unseen clutter configurations. In contrast, the adaptive neural network algorithm presented in this paper avoids this problem, by using an adaptive interpolating clutter model to extract the building-block components of the clutter, and thus to model unseen clutter configurations as variable combinations of these building-block components.

The CFAR-filter assumed a Gaussian background noise distribution for the logarithms of the amplitudes of the complex-valued SAR returns.

Figure 6 displays the correlation-filter maps (i.e. the maximum correlation values over all target templates, as a function of image location) for views A and B. Both images are displayed using the same grey-scale map (i.e. the same relationship between correlator output value and pixel brightness). Comparison with the target locations in Figure 2 reveals that there is a (local) peak corresponding to the target in the correlation map for each of the two views; however, many clutter objects also give large correlation values.

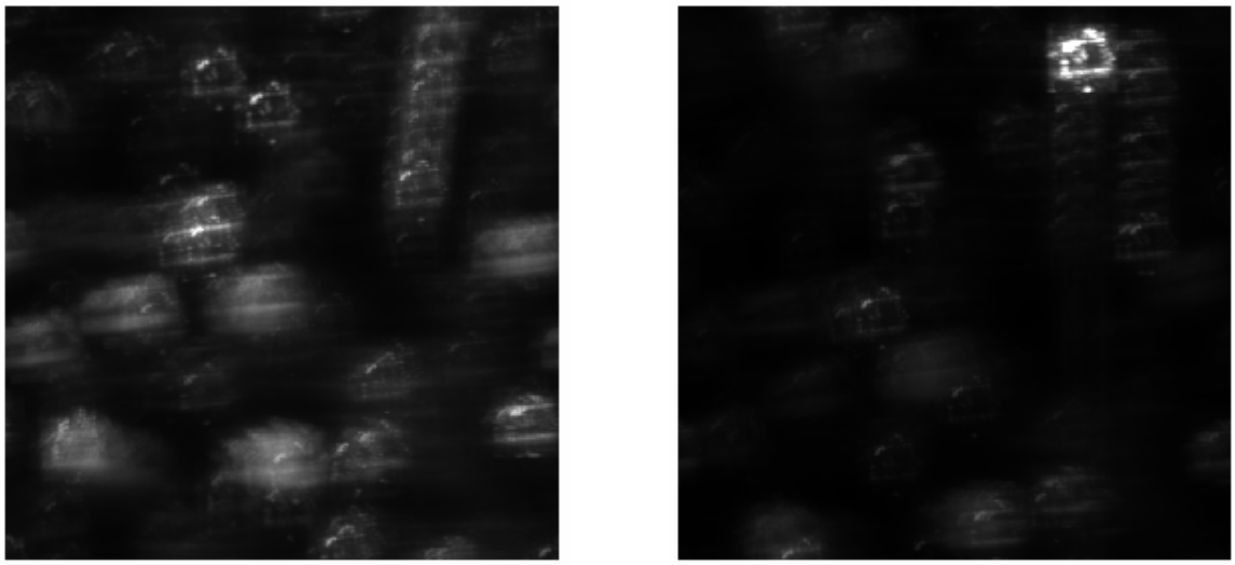

Figure 6: Maps of the outputs from a correlation-filter. The left-hand image is for view A and the right-hand image is for view B.

For the same views A and B, Figure 7 displays the outputs obtained by applying a correlation filter to the areas identified as anomalous by a CFAR filter; thus, the template-matching identification capability of the correlation filter is used to mitigate the initial false-alarm rate of the CFAR filter. Again, both images are displayed using the same grey-scale map. Comparison between the plots in Figure 7 with those in Figure 6 shows that one is able to remove many of the correlation peaks caused by clutter objects by combining the CFAR and correlation filters. Moreover, this does not seem to be at the expense of peaks at the target location. However, there are still considerably more false alarms than from the neural network algorithm (see Figure 5). The relative performances are quantified in ROC curves in Section 4.5.

4.5 ROC curve comparison

Visual comparison of Figure 5, Figure 6 and Figure 7 indicates that the adaptive neural network algorithm provides lower false alarm rates than the CFAR-filter/correlation-filter chain, which predictably provides lower false alarm rates than the correlation-filter alone. A more rigorous assessment of algorithm performance is possible by comparing ROC curves.

Figure 7: Maps of the output from a correlation-filter applied to the areas identified as anomalous by a CFAR filter. The left-hand image is for view A and the right-hand image is for view B.

To calculate these ROC curves, binary decisions between target and clutter are made for the pixels in a processed image, by applying a simple threshold to the image. If a pixel value lies above the threshold, then the pixel is declared to be a target, while if a pixel value lies below the threshold, the pixel is declared to be clutter. Targets are only counted once; exclusion zones around the targets have been applied in order to avoid counting the extremities of targets as clutter. By altering the threshold a ROC curve of target detection probability versus false alarm rate is obtained. For the adaptive neural network algorithm the processed image is the map of the posterior target class probabilities. Selection of the threshold therefore corresponds to a threshold on the posterior class probability. For the two baseline algorithms the processed images are the correlation filter outputs (applied to areas identified as anomalous by the CFAR-filter in the second case). The obtained ROC curves are display in Figure 8.

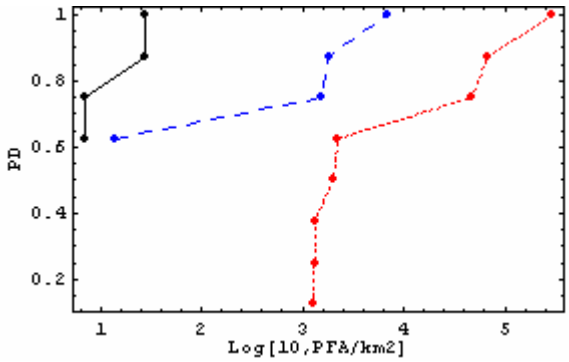

Figure 8: ROC curve comparison. Target detection probability along vertical axis, Log_{10} of false alarm rate per square km along horizontal axis. The black (solid) line is for the adaptive neural network algorithm, the blue (dashed) line is for a correlation-filter applied to the areas identified as anomalous by a CFAR filter, and the red (dotted) line is for a correlation-filter alone.

The curve for the adaptive neural network algorithm is closer to the top-left corner than the curves obtained using the two baseline techniques, indicating that better target detection and identification performance is being obtained. However, two caveats must be borne in mind when interpreting the results from this single experiment:

- Each target is only counted once, so the jumps in target detection probability are very coarse.
- No post-processing has been applied to cluster the detections, so there is some double counting of false alarms (visual inspection indicates that this double counting is likely to have more of an adverse effect for the correlation-filter baseline algorithm than the other algorithms). Clustering detections in urban clutter can be a very difficult exercise because, with so many clutter detections in the close vicinity of the target, it can be far from obvious how to design a clustering algorithm to deduce where the target detections end and the clutter detections begin.

5.0 CONCLUSIONS

This paper has introduced an adaptive neural-network approach to target- and clutter-modelling. The approach is such that both targets and clutter can be modelled within the same neural network, so that detection and recognition can take place simultaneously within an integrated framework. The algorithms can therefore be applied across the spectrum of ATR discrimination levels, e.g.: detection of unknown targets in clutter; detection of specific designated targets in clutter; recognition of target subclass post-detection. The approach builds on the unsupervised neural network principle of symmetry-preservation. Symmetry-preserving networks can detect invariances/symmetries (under complex transformations) in the PDF of their training data and exploit that functionality to develop robust responses with respect to precisely those transformations. We believe that such networks could ultimately offer the potential for target recognition with robustness to EOCs, although this has not been addressed in this paper. The paper provides an initial proof of principle for the application of componential coding to target detection and identification, using real SAR imagery in urban clutter; componential coding offers a new handle on modelling the combinatorial complexity of urban clutter. This demonstration concerned recognition of a particular building within SAR imagery of an urban area. Superior performance (in terms of target detection probability at a given false alarm rate) was obtained, compared to two baseline approaches based on a correlation-filter (template matching), one of which also exploits a CFAR filter as an initial detection stage. Planned future work will more fully assess the componential coding approach for target detection in urban clutter, and investigate the symmetry-preserving functionality with the aim of improving robustness to EOCs.

6.0 REFERENCES

[1] Fukumi M, Omatu S, Takeda F, Kosaka T, Rotation-invariant neural pattern recognition system with application to coin recognition, *IEEE Transactions on Neural Networks* 3, pp 272-279, 1992.

[2] Fukushima K, Miyake S, Neocognitron: A new algorithm for pattern recognition tolerant of deformations and shifts in position, *Pattern Recognition* 15, pp 455-469, 1982.

[3] Himes G S, Inigo R M, Automatic Target Recognition using a Neocognitron, *IEEE Transactions on Knowledge and Data Engineering* 4(2), April 1992.

[4] Le Cun Y, Boser B, Denker J, Henderson D, Howard R, Hubbard W, Jackel L, Backpropagation applied to hand-written zip code recognition, *Neural Computation* 1, pp 541-551, 1989.

[5] Minsky M L, Papert S A, Perceptrons, MIT, 1969.

[6] Payne B, Gu F, Webber C J S & Ball A. Componential coding in the condition monitoring of electrical machines, Part II - Application to a conventional machine and a novel machine, *Proceedings of the Institution of Mechanical Engineers* 217(C8), pp 901-915, 2003.

[7] Rumelhart D E, Hinton G E, Williams R J, Learning internal representations by error propagation, *Parallel Distribution Processing: Explorations in the Microstructures of Cognition, ed. D E Rumelhart, J L McClelland* 1, pp 318-362, 1986.

[8] Salmond D J, Birch H, A particle filter for track-before-detect, *Proc. of American Control Conference, Arlington, VA, June 25-27, 2001*, Vol 5, pp 3755-3760, 2001.

[9] Saund E, A multiple cause mixture model for unsupervised learning, *Neural Computation* 7, pp 57-71, MIT Press, 1995.

[10] Shawe-Taylor J, Building symmetries into feedforward networks, *Proc. of First IEEE Conference on Artificial Neural Networks*, pp 158-162, 1989.

[11] Shawe-Taylor J, Symmetries and discriminability in feedforward network architectures, *IEEE Transactions on Neural Networks* 4, pp 816-826, 1993.

[12] Webb A R, Statistical Pattern Recognition, John Wiley & Sons, Chichester, 2nd edition, 2002.

[13] Webber C J S, Self-organisation of transformation-invariant detectors for constituents of perceptual patterns, *Network: Computation in Neural Systems* 5, pp 471-496, IOP Press, 1994.

[14] Webber C J S, Emergent componential coding of a handwriting-image database by neural self-organisation, *Network: Computation in Neural Systems* 9, pp 433-447, IOP Press, 1998.

[15] Webber C J S, Payne B, Gu F & Ball A. Componential coding in the condition monitoring of electrical machines, Part I - Principles and illustrations using simulated typical faults, *Proceedings of the Institution of Mechanical Engineers* 217(C8), pp 883-899, 2003.

[16] Webber C J S, Self-organisation of symmetry networks: Transformation invariance from the symmetry-breaking mechanism, *Neural Computation* 12(3), pp 565-596, MIT Press, 2000.

[17] Webber C J S, Predictions of the spontaneous symmetry-breaking theory for visual code completeness and spatial scaling in single-cell learning rules, *Neural Computation* 13(5), pp 1023-1043, MIT Press, 2001.

7.0 ACKNOWLEDGMENT

This research was sponsored by the UK MOD Corporate Research Programme.

Full-Polarimetric Analysis of MERIC Air Targets Data

C. Titin-Schnaider, P. Brouard
ONERA
Chemin de la Hunière et des Joncherettes
91120 Palaiseau
France

Cecile.Titin-Schnaider@onera.fr , Philippe.Brouard@onera.fr

ABSTRACT

This paper addresses the detailed analysis of full polarimetric radar images, obtained from real data, by using the Polarimetry theory parameters.

The experimental ground based radar station MERIC has been designed at ONERA to perform full polarimetric measurements on non-cooperative in flight airplanes.

The first promising results of an analysis carried out from a MERIC full-polarimetric ISAR image of a liner are presented.

1.0 INTRODUCTION

The theory of polarization has been studied [1] for several decades. However, its implementation has been delayed while waiting for technological progress. At present, experimental high resolution radar can provide full-polarimetric data with the required magnitude and especially phase accuracy.

Some full polarimetric airborne SAR radars have already been developed. Full-polarimetric SAR images analysis (produced from RAMSES data, for example), has shown promising results regarding the vegetation classification and the analysis of motionless ground targets.

For In-flight target studies, 2D-ISAR radar imaging is a well-established method giving the reflectivity distribution of target scatterers. Full-polarimetric ISAR imaging will be introduced and discussed. It will be shown that Polarimetry provides additional information about scatterers electromagnetic behaviour.

The full-polarimetric ground based radar station MERIC has been designed to measure in-flight targets [4], in order to create full-polarimetric data base. The analysis of a civilian aircraft is presented to illustrate Polarimetry potentiality.

2.0 ISAR FULL-POLARIMETRIC IMAGING

2.1. Radar images

Radar targets can be split into two main classes depending on how elementary mechanisms add in the resolution cell.

- If they add incoherently, scattering mechanisms are represented by random variables and the statistical (or general) theory of polarization is applicable. This is the case for large natural areas like forests, fields, meadows....

Paper presented at the RTO SET Symposium on "Target Identification and Recognition Using RF Systems", held in Oslo, Norway, 11-13 October 2004, and published in RTO-MP-SET-080.

- If they add coherently, electromagnetic scatterings are coherent and the deterministic theory of polarization is applicable. This is mainly the case for man-made or artificial targets like aeroplanes, trucks, railways ... Radar images of these targets are characterized by a small number of bright scattering centres.

2.2. Point Object Model

- A common assumption for radar artificial radar targets is the 'Point Object Model' (POM). According to this model, any target is described by a collection of isotropic point scatterers.
- Polarimetric measurement give access to the target backscattered matrix [S].

In the POM frame, this matrix can be represented by a sum on N elementary scattering matrices [s_i], phase shifted according to the scatterers locations $\vec{x}_i$:

$$[S](\vec{k}) = \sum_{i=1,N} [s_i]\, e^{j2\vec{k}\cdot\vec{x}_i}$$

where $\vec{k} = \frac{2\pi f}{c}\frac{\vec{r}}{r}$ is the wave vector depending on frequency f and incidence angle.

For any radar system, the image $[I](\vec{x})$ is obtained through a Fourier Transform:

$$[I](\vec{x}) = \int [S](\vec{k})\, e^{-j2\vec{k}\cdot\vec{x}}\, d\vec{k}$$

Assuming the elementary matrices [s_i] do not vary with frequency and orientation, the image is given by:

$$[I](\vec{x}) = \sum_{i=1,N} [s_i]\, \delta(\vec{x} - \vec{x}_i)$$

where $\delta(\vec{x})$ is the Dirac distribution.

In practice, measurements are recorded over a limited frequency bandwidth and over a bordered incidence domain. Therefore, the Point Spread Function (PSF) $G(\vec{x} - \vec{x}_i)$ replaces the Dirac distribution:

$$[I](\vec{x}) = \sum_{i=1,N} [s_i]\, G(\vec{x} - \vec{x}_i)$$

This equation shows that the resulting image can be considered as the complex sum of each point scatterer image. Bright scattering centres are no longer point centres. They have a stretch in space characterized by the PSF. The same elementary scattering matrix is associated with all pixels in the vicinity of a point scatterer with a strength given by the PSF. If the scatterers are far enough from each other, their PSF do not interfere and the true elementary matrices $[s_i]$ are obtained at locations $\vec{x}_i$. A target is therefore described by a set of point scatterers whose elementary scattering matrices and locations are known.

In practice, the scattering matrix of a given scatterer is always more or less distorted by the scattering matrix of the other scatterers. The higher is the resolution, the smaller is the PSF and the less distorted are the elementary scattering matrices.

A 2D ISAR image is a projection of the 3D scatterer distribution onto a 2D plane. Some different scatterers can then be confused. This problem increases for the 1D representation: a range profile being the

projection on the line of sight of the 3D distribution of scatterers. So in this case a larger number of scatterers can be mixed together.

2.3 ISAR imaging

To build the ISAR image of a moving target with the required transversal resolution, the radar has to track the target in order to acquire measurements during a sufficiently long duration. Each complex range profile thus acquired must be aligned with the preceding profile using a complex correlation method.

Phase distortion due to the translation motion of the moving target is compensated using the DSA (Dominant Scatterer Algorithm) method. The principle of this method is to select the bright scatterer showing the least amplitude variation as a reference point,

At radar wavelengths, the returned signal is dominated by backscattering from features like corners, edges and surface discontinuities… The objective of radar classification based on classical ISAR imaging is to consider rather the locations and RCS level of scatterers than target shape. Full polarimetric radar data makes it possible to also use electromagnetic mechanisms creating the scatterers.

3.0 POLARIMETRIC PARAMETERS

The nature of deterministic mechanisms can be characterised by several sets of polarimetric parameters. These sets are globally equivalent. However their sensitivity to electromagnetic properties can be different.

3.1. Sets of polarimetric parameters

It is well known that deterministic mechanisms are described by a 2 by 2 complex matrix: the scattering matrix. Under the reciprocity postulate and given its absolute phase is ineffective for describing the physical mechanism, it depends on five independent parameters. Several sets of parameters have been proposed in the literature:

- The Fork parameters set:

According to [1] the back-scattering matrix of any deterministic mechanism can be mathematically represented by several operators:

$$[S] = e^{-i\psi[\sigma_0]} e^{-i\tau[\sigma_2]} [S_d] e^{-i\tau[\sigma_2]} e^{i\psi[\sigma_0]}$$

where: $[S_d] = \mu e^{i2\nu} \begin{bmatrix} 1 & 0 \\ 0 & (tg\gamma)^2 e^{-i4\nu} \end{bmatrix}$ and where the four Pauli matrices are noted $[\sigma_j]$, $j = 0,3$.

It depends on the five Polarization Fork angles: $\psi, \tau, \gamma, \nu, \mu$ The variation ranges of the Polarization Fork parameters are as follows:

$$-\pi/2 < \psi < \pi/2 \quad -\pi/4 < \tau < \pi/4 \quad -\pi/4 < \nu < \pi/4 \qquad 0 < \gamma < \pi/4$$

The orientation angle ψ gives the tilt of the target versus the horizontal polarization, in the plane perpendicular to the radar line of sight. The symmetry angle τ indicates the symmetry rate versus an axis or a plane (if τ is low the scatterer is symmetric and if it is high it is not symmetric). The skip angle ν gives information about the parity of the number of scatterings (if ν is low this number is even, if ν is

high it is odd). The polarizability angle γ provides information about the ability of the scatterer to polarize the waves on a particular polarization (if γ is low the scatterer is polarizing and if γ is high it is not).

- The Huynen parameters set:

This set contains nine real parameters [1]:

the orientation angle ψ and the disoriented (orientation extracted) Muller matrix parameters:

$$2A_0, B_0 + B, B_0 - B, C, D, E, F, G$$

In the deterministic case, these parameters are linked by four relations:

$$2A_0(B_0 + B) = C^2 + D^2 \qquad 2A_0 E = DG \qquad 2A_0(B_0 - B) = G^2 \qquad 2A_0 F = CG$$

All these parameters are homogeneous to a power. The span is an invariant quantity (independent of any polarization base change) representing the total RCS back-scattered by the target:

$$span = |S_{hH}|^2 + |S_{hV}|^2 + |S_{vH}|^2 + |S_{vV}|^2 = 2A_0 + (B_0 - B) + (B_0 + B)$$

A feature vector valid for identification (independent of total power information) is obtained through the unit span normalization: $2A_0 + (B_0 + B) + (B_0 - B) = 1$

The Huynen parameters can be written [1] as a function of the Fork parameters. Then, it is easy to maximise each Huynen parameter. Figure 1 a, b, c, d, e, f, g contains the combs obtained when parameters $2A_0, B_0 + B, B_0 - B, C, D\ E, F, G$ are respectively maximised. One can notice that maximising any generator parameter $2A_0$, $B_0 + B$ and $B_0 - B$ leads to a comb with only one peak (1a, b, c). The maximum of any other parameter corresponds to a comb with three equal peaks (1d, e, f, g, h).

Therefore, the unit span constraint leads to a set of eight characteristic feature combs (figure 1) with either one peak (equal to 1) or three equal peaks (equal to ½). The very good continuity from one feature comb to another is an important advantage for a classification algorithm based on correlation between measured and reference combs.

In practice, most of the analysed scattering centres are symmetrical ($\tau \approx 0$). Therefore, we often have: $E = F = G = 0$.

Only the five first combs of figure 1 are frequently found. The main electromagnetic mechanisms are:

- Specular reflection on a smooth surface locally spherical or on a plate. In this case the dominating parameter is $2A_0$ (figure 1a).

- Scattering on a sharp edge or on a long and thin wire described by a comb looking like figure 1d. A maximum value of parameter C corresponds to three equal peaks for $2A_0$, $B_0 + B$ and C.

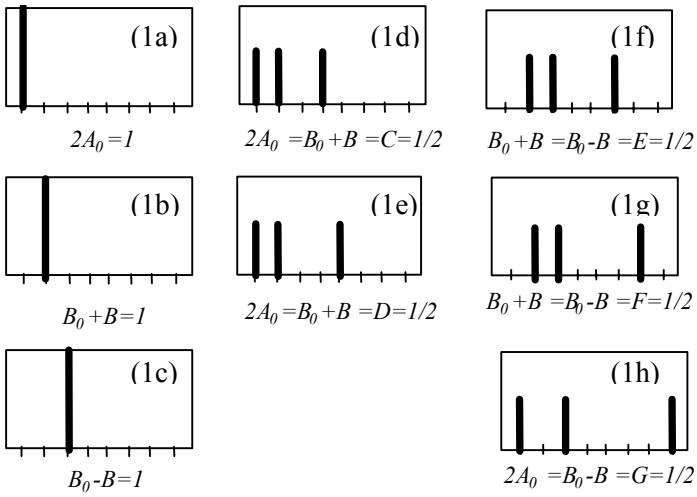

Figure 1 : the eight characteristic combs

- A difference between the two local curvatures is characterized by an increase of parameter D. A maximum value of D corresponds to three equal peaks for $2A_0$, B_0+B and D (figure 1e). It describes the quarter-wave dephasors according the sign of D.
- The maximum of parameter F is described by three equal peaks (figure 1g). It corresponds to helices according the sign of F.

4.0 POLARIMETRIC ANALYSIS OF AN AIRCRAFT

A specific software has been designed at ONERA to assist polarimetric analysis of full-polarimetric radar images. In particular, it can be used to calculate and show the image of any polarimetric parameter for any selected area. Several recognition methods can be used to improve the analysis (based on a comparison between either scattering matrices or combs of Huynen parameters…).

As an example, results obtained from a full-polarimetric analysis of a civilian aircraft measured by MERIC radar, are presented. The chosen aircraft is a Mac Donnel Douglas MD 82 in take-off phase. A photo (figure 2) gives an idea of the aircraft presentation with regards to the radar during the measurements.

The RCS images of the four r(eceive)/T(ransmit) polarizations hH, hV, vH and vV are given in figure 3. About ten main bright spots appear very clearly. The great similarity between the hV and vH images (in accordance with the reciprocity postulate) can be seen. These four images show that co and cross polarized images must be taken into account.

The bright spot areas are defined by selecting all pixels with span greater than a given level. In figures 4 to 7, the eliminated pixels are indicated in light green.

Images of the Huynen parameters 2A0 (Figure 4) and B0+B (Figure 5) show that these parameters are very discriminating. The higher values (in warm colours) of parameter 2A0 indicate the surface mechanisms locations. On the other hand, the higher values (in warm colours) of parameter B0+B show the double-bounce areas. The analysis can be refined by calculating the comb of Huynen parameters for various selected variable size areas. This kind of analysis allows us to identify numerous scatterers.

Automatic recognition algorithms can be applied on each pixel to obtain a classified image: a set of mechanisms are stored in the reference memory. The most likely mechanism of the reference memory

(according to an appropriate rule of comparison) is allocated to each pixel. The algorithm can be based equally well on either a comparison between scattering matrices [2] or on a comparison between Huynen parameters combs. A classified image is presented on the right part of Figure 6 and Figure 7.

The mechanisms are represented by a specific colormap: Surface mechanism ("S") in blue, Double-bounce or dihedral type mechanisms ("Dd") in red. The dipole type mechanisms indicating lengthened targets ("Dp") are referenced in yellow. Positive or negative quarter-wave dephasors devices ("Q$\pm$") in purple and mauve colours. Two intermediate mechanisms are introduced: cylinder ("C") between surface mechanism and dipole; lengthened dihedral corner ("DdL") between dihedral and dipole. Among non-symmetrical targets, the right and left helices ("H$\pm$") are associated with white and black. The light grey ("X") or dark grey ("Y") colours indicate symmetric and non-symmetric unrecognized mechanisms respectively.

Numerous scatterers generating surface (right part of figure 6) and double-bounce mechanisms (right part of figure 7) have been recognized. On the left part of figures 6 and 7, identified mechanisms locations are indicated.

Surface scatterers are identified in blue and green on figure 6. They are located on:

- the end of the tail flat (1),
- the left (2) and right (3) engines,
- the fuselage (4), (6), (8),
- the end of the wing (5),
- the opposite part of the fuselage (7).

Double-bounces are identified on figure 7. They indicate the following interactions:

- rudder - right part of the horizontal tail flat (1),
- rudder - left part of the horizontal tail flat (2),
- back of right engine (3),
- trailing edge flap control systems casing - underside of right wing (4),(5),(6),
- fuselage - back of the right wing (7),
- fuselage - front of the right wing (8),
- fuselage – antennas (9),(10), (11).

5.0 CONCLUSION

Like all man-made targets, aircraft radar images are characterized by a collection of bright scatterers. Conventional 2D-ISAR imagery can determine their location and RCS. Full-polarimetric ISAR imaging provides access to extra information about the electromagnetic mechanisms that creates them.

This study, carried out on real data provided by MERIC full-polarimetric radar, shows that a lot of information can be obtained using Polarimetry. Mechanisms like specular reflection on plate or on curved surface, edge diffraction, double-reflection, surface waves, surface discontinuity…. can be recognized.

Future measurements that will be provided by MERIC station can be used to build a full-polarimetric database of air targets. From this database, suitable methods of automatic target recognition will be

proposed and tested on fully or partially real polarimetric data, in order to assess the usefulness of Polarimetry.

6.0 REFERENCES

[1] Huynen J.R., "Phenomenological theory of radar targets". Phd Thesis, 1970

[2] Cameron W.L., Leung L.K., "Identification of elemental polarimetric scatterer responses in high-resolution ISAR and SAR signature measurements", Second international workshop on radar polarimetry, Nantes, September 1992.

[3] Titin-Schnaider C., Dreuillet P., "Analyses polarimétriques haute résolution de mesures de cibles radar en laboratoire", JIPR, Nantes, mars 95

[4] Titin-Schnaider C., Attia S.," Calibration of the MERIC Full-Polarimetric Radar: theory and implementation ". Aerospace Science and Technology – August 2004

7.0 GLOSSARY

MERIC : Moyen Expérimental pour la Reconnaissance et l'Identification des Cibles

RAMSES : Radar Aéroporté Multi Spectral d'Etude des Signatures

Figure 2 : MD82 picture in taking off phase

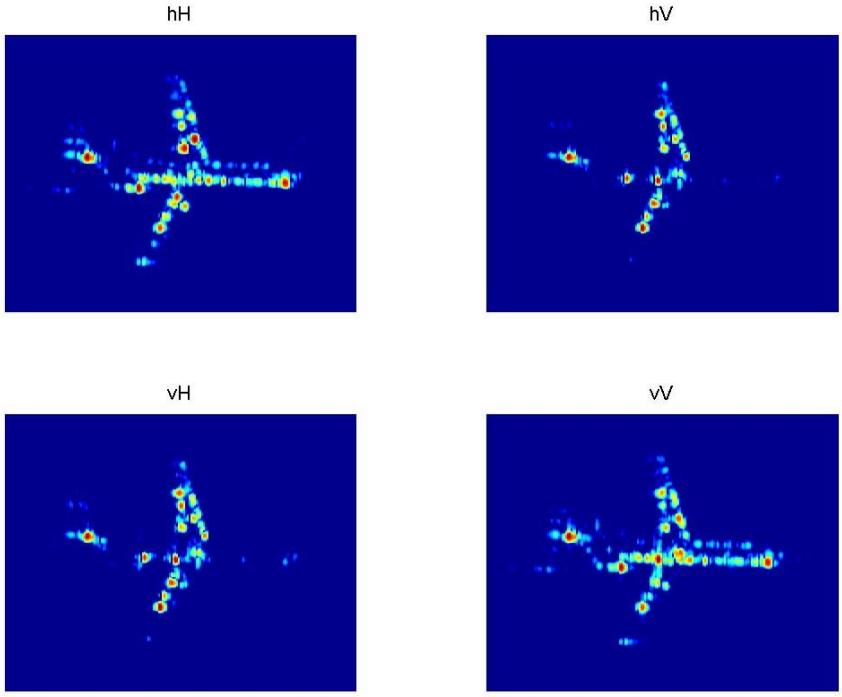

Figure 3 : four-polarimetric RCS ISAR images

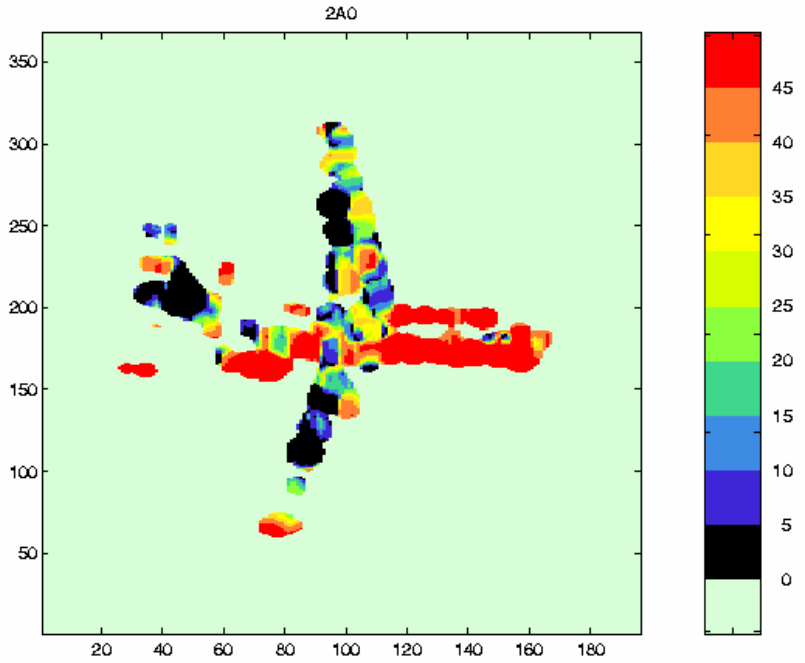

Figure 4 : 2A0 parameter image

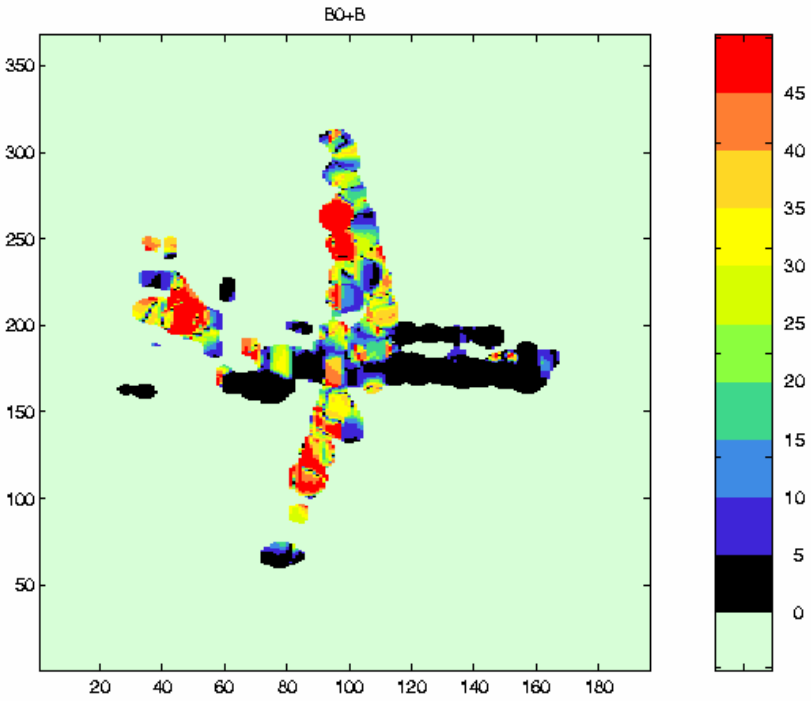

Figure 5 : B0+B parameter image

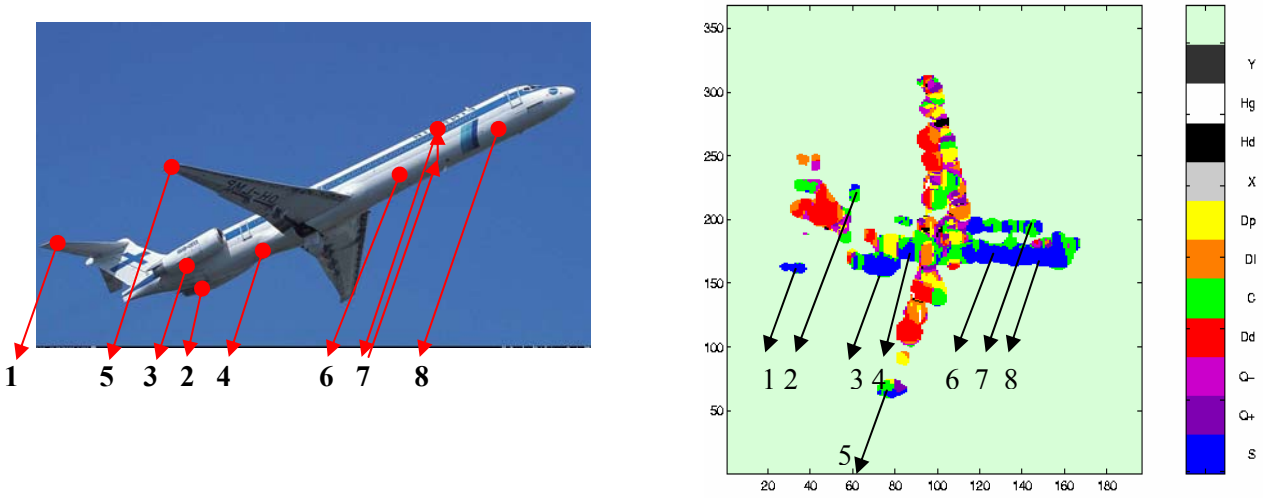

Figure 6 : surface mechanisms analysis

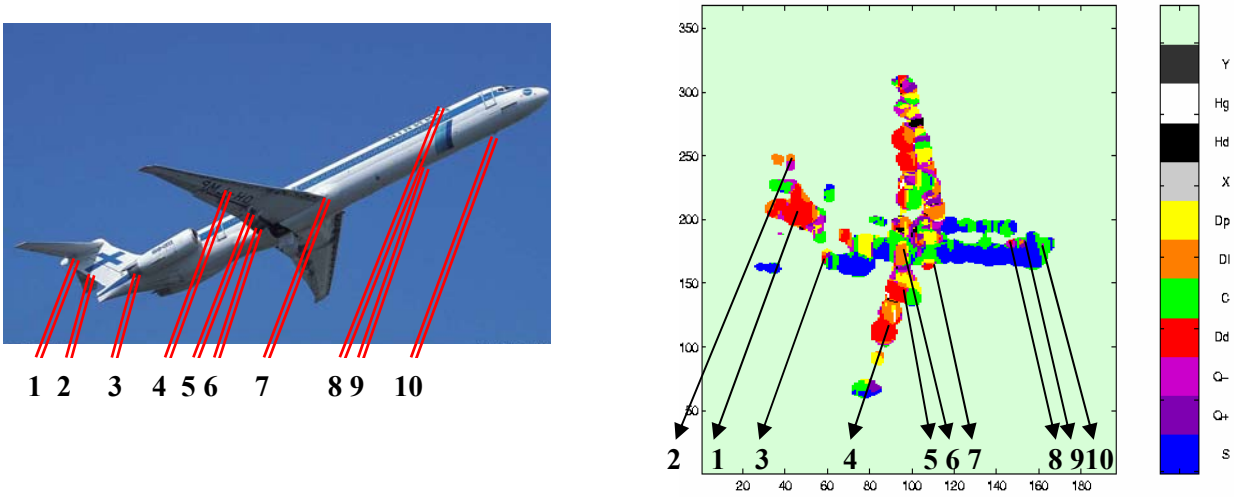

Figure 7 : double-bounce mechanisms analysis

Advances of Techniques for Utilizing Polarimetric Features of Radar Targets

Ernst Krogager
Danish Defence Research Establishment
Ryvangs Allé 1
DK-2100 Copenhagen Ø
Denmark

ABSTRACT

The scattering properties of a radar target can only be fully characterized by measuring a scattering matrix in which the elements represent the combinations of transmit and receive polarization states. The amount of information gathered by a traditional single polarization radar may therefore be even very limited, for example when the single polarization response is near zero while the cross polarized return is at a maximum. By polarimetric processing, different scatterers, i.e., scattering mechanisms, can be completely and coherently separated, even if they are located within the same resolution cell of the radar image. This is particularly important in relation to non-cooperative target identification and recognition. Nevertheless, the practical utilization of polarization for optimizing information content has not gained more widespread interest until very recently. This is mainly due to a lack of proper technology in the past, but also due to negative conclusions drawn from early experiments with polarimetric radar. At the moment, significant efforts are put into the development of techniques for efficiently and conveniently handling polarimetric data. Such techniques differ considerably from techniques known from traditional single polarization target imaging, since one has to deal with a matrix for each resolution cell instead of just a single scalar. In this paper, some of the advances and advantages of polarimetric radar techniques will be reviewed and presented in an application-oriented perspective, emphasizing the potential of utilizing the information contained in the polarization transforming properties of radar targets.

INTRODUCTION

The vectorial nature of the electromagnetic fields, on which any radar system is based, implies that the full amount of potentially available information can only be exploited by employing polarimetric radar systems, i.e., systems capable of measuring all four combinations of two orthogonal polarizations. For simplicity and cost-effectiveness, however, traditional operational radar systems have been single-polarization systems employing one and the same polarization on both transmission and reception. Such systems have obviously served many needs satisfactorily, but for modern high resolution applications, such as target classification, identification and recognition, the properties and capabilities of polarimetric systems cannot be ignored without a severe loss of useful target information. This was realized rather early in civilian remote sensing applications using high-resolution SAR (Synthetic Aperture Radar) systems, and single-polarization systems would simply not be able to produce the classification results that are delivered by modern polarimetric SAR systems.

In the military community, however, the issue of polarimetric radar has been surrounded by skeptics and opposition, largely based on claims that the money could be spent more efficiently on other performance parameters, like range resolution. One reason for this, of course, is the obvious fact that the polarimetric techniques could not readily be implemented as upgrades to existing radars. Nevertheless, with the technological developments that have taken place in recent years, the implementation of full polarimetric

Paper presented at the RTO SET Symposium on "Target Identification and Recognition Using RF Systems", held in Oslo, Norway, 11-13 October 2004, and published in RTO-MP-SET-080.

capability should no longer be considered as an unrealistic sophistication that the military does not need. On the contrary, the additional information provided by such systems could be crucial for satisfactorily solving the complex tasks required in today's battlefields. Therefore, a relevant question is rather: Can the military of the future afford to continue ignoring the additional information that can be accessed by polarimetric radar systems only? In the following, the basic properties and characteristics of polarimetric radar data will be reviewed in an application-oriented perspective.

POLARIMETRIC PROCESSING TECHNIQUES

The first systematic studies of the utilization of the polarization of radar waves were carried out by Kennaugh in the early 1950's. During these studies, the eigenvalue problem associated with the 2x2 scattering matrix was considered, and it was later treated in great detail by Huynen, who rigorously formulated the existence of maximum and minimum (null) polarizations. He pointed out how these can be made to form the so-called Huynen-fork on the Poincaré sphere, and he presented an elegant mathematical formulation of how the scattering matrix can be represented by a set of five independent real parameters, the so-called Huynen-Euler parameters. In these early days of radar polarimetry, the handling and analysis of the multi-channel data posed quite a challenge, and original geometrical representations and interpretations were developed alongside with the underlying mathematical formulations. Undoubtedly, this contributed to scaring away many a radar engineer from considering any practical utilization of such techniques.

With the advent of the digital computer, polarimetric data can be visualized and handled without mastering the complex mathematics and the associated geometrical constructions. Once the algorithms are implemented, the digestion is taken care of by the computer, and the results are presented in easily interpretable graphical outputs. General classification algorithms may take virtually any raw data and convert the information contents to useful end-results. Nevertheless, the compact forms from the early days should not be forgotten, and could in fact contribute to making the processing more efficient. A good example of this is the aforementioned Huynen-Euler parameters, and this is where we shall take the outset for a review of the fundamental properties of polarimetric radar data.

NULL-POLARIZATIONS AND HUYNEN-EULER PARAMETERS

The complex-valued scattering matrix with the four combinations of transmit and receive polarization (horizontal and vertical in the most common, linear polarization basis), containing a total of six independent parameters,

$$[S] = \begin{bmatrix} HH & HV \\ VH & VV \end{bmatrix},$$

can be transformed to a diagonal form (with no cross-polarization terms) and represented by another six real parameters in the following form,

$$[S] = m \begin{bmatrix} e^{j2(\nu+\zeta)} & 0 \\ 0 & \tan^2\gamma\, e^{-j2(\nu-\zeta)} \end{bmatrix},$$

which is the scattering matrix that would be measured by transmitting and receiving the associated optimum polarization (in general elliptical).

The following interpretations are commonly assigned to the individual parameters:

m (m≥0), the maximum polarization, i.e., the maximum attainable response from the target, which would be obtained if the optimum polarization were used by the radar.

. (-180E<.#180E), the absolute phase of the scattering matrix.

< (-45E<<#45E), the skip angle, related to the number of times a return signal has been reflected within the target; if the return signal is predominantly due to scattering mechanisms with an odd number of reflections (or bounces), < will be close to zero; for this reason, < has also been referred to as the degree of double bounce, but it should be noted that targets can have <=45E even when only a minor part of the reflected signal is due to even-bounce scattering.

((0E#(#45E), the characteristic angle, also denoted the polarizability angle (Holm), the latter referring to the fact that targets with (=45E do not repolarize the incident wave while targets with (=0E completely determine the polarization of the returned wave.

The last two of the six parameters characterize the associated optimum polarization:

P (-90E<P#90E), the orientation angle of the target, determining the orientation angle of the optimum polarization for the target.

ϑ_m (-45E#ϑ_m#45E), the helicity angle, which represents the ellipticity of the optimum polarization for the target.

The advantage of these parameters is that they are invariant descriptors and therefore can be determined independently of the polarization basis (e.g., linear or circular) that was used to measure the raw data of the scattering matrix – provided that the data have been properly calibrated.

POLARIMETRIC DECOMPOSITION

To illustrate the significance of such a characterization, let us consider the measured radar response from a dihedral (also referred to as a diplane in the following), which is an important type of scatterer in practical applications. It is characterized by the following scattering matrix,

$$[S]_{dihedral(\theta)} = \begin{bmatrix} HH & HV \\ VH & VV \end{bmatrix} = m \begin{bmatrix} \cos 2\theta & \sin 2\theta \\ \sin 2\theta & -\cos 2\theta \end{bmatrix}$$

The true strength (radar cross section) of such a scatterer is given by *m*, but evidently, the RCS value which is measured by a traditional radar system (e.g., HH-polarized) will depend heavily on the actual orientation angle of the scatterer. In contrast, a polarimetric radar will be able to tell the true strength, and in addition, the orientation angle, θ, can be determined.

From this simple example, it is clear how a polarimetric radar can provide useful target information, which could never be extracted by a non-polarimetric radar, and which could be of decisive importance for correct classification of complex targets.

Another unique advantage of a polarimetric radar system is the ability to distinguish between different *types* of scatterers, notably between even- and odd-bounce scattering contributions. To illustrate this, let us consider the combined scattering from a sphere and a dihedral located within the same resolution cell.

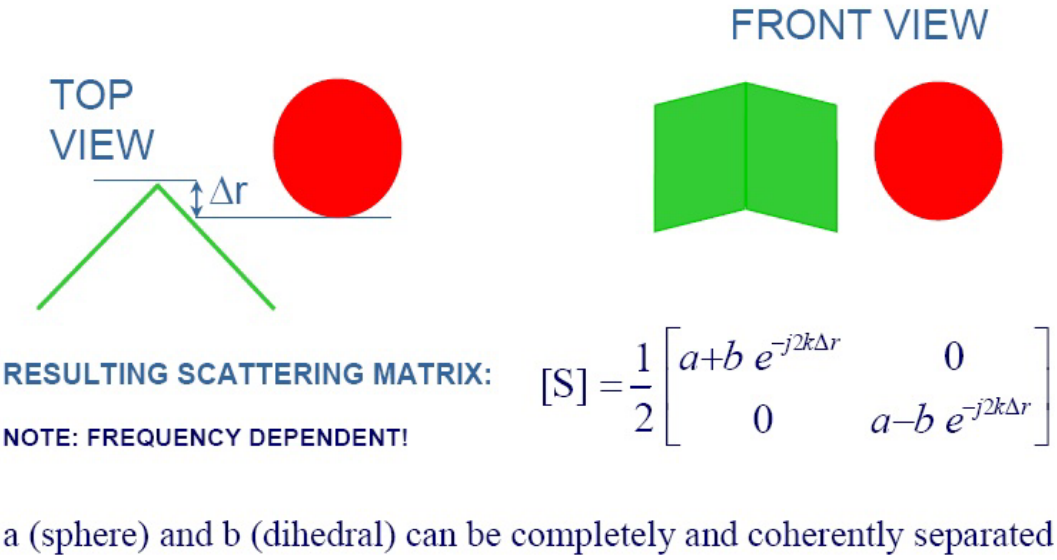

Fig. 1: Combined scattering from odd-bounce reflector and even-bounce reflector. Sum and difference of the diagonal elements of the scattering matrix separate sphere and diplane contributions completely, whereby interference between these two scattering mechanisms is eliminated.

The individual unity scattering matrices are given by,

$$[S]_{sphere} = \begin{bmatrix} 1 & 0 \\ 0 & 1 \end{bmatrix}$$

$$[S]_{diplane(\theta)} = \begin{bmatrix} \cos 2\theta & \sin 2\theta \\ \sin 2\theta & -\cos 2\theta \end{bmatrix}$$

while the combined scattering from a sphere of strength a and a diplane of strength b can be expressed as follows, provided that the phase centers are at the same range ($\Delta r = 0$ in Fig. 1),

$$[S]_{sph+dipl(\theta)} = \begin{bmatrix} HH & HV \\ VH & VV \end{bmatrix} = a\begin{bmatrix} 1 & 0 \\ 0 & 1 \end{bmatrix} + b\begin{bmatrix} \cos 2\theta & \sin 2\theta \\ \sin 2\theta & -\cos 2\theta \end{bmatrix}$$

By the simple operation $HH + VV$, the sphere contribution can be completely and coherently separated from the corner reflector contribution. This means that the interference between the two contributions, which is unavoidable in the single polarization case, can be eliminated, so that the true intensity of the scattering centres can be determined. For high-resolution ISAR imaging, where the required motion compensation is usually based on a single, dominating scattering contribution, this is of great significance, because a more stable phase history can be obtained if interference between scattering constituents can be avoided or reduced.

PAULI SPIN MATRIX DECOMPOSITION

More generally, the above decomposition is expressed by the Pauli decomposition, based on the Pauli spin matrices, as follows,

$$[S] = k_1[S]_{sphere} + k_2[S]_{diplane(0°)} + k_3[S]_{diplane(45°)}$$

where the coefficients are given by,

$$\underline{k} = \begin{bmatrix} k_1 & k_2 & k_3 \end{bmatrix} = \frac{1}{\sqrt{2}} \begin{bmatrix} S_{HH} + S_{VV} & S_{HH} - S_{VV} & 2S_{HV} \end{bmatrix}^T .$$

This is a so-called coherent decomposition, in which the elements are complex values, i.e., they have an absolute phase term associated with them and have to be added as complex (voltage related) quantities, unlike the incoherent formulations which operate on real (power related) quantities. The three involved component matrices (sphere, 0° rotated diplane, and 45° rotated diplane) form an orthogonal set which is often used as the outset for further incoherent, statistical processing in terms of covariance and coherency matrices. However, in this review of the more fundamental properties of polarimetric radar data, we leave these approaches out of consideration.

The coefficients of the Pauli decomposition (k_1, k_2, k_3) can be used as features for automatic classification algorithms as an alternative to the direct use of the *HH, HV, VV* elements. Likewise, the magnitudes of the elements are frequently used to generate RGB images from high-resolution SAR/ISAR data. The Pauli components have a closer relation to the underlying physical scattering mechanisms than the raw elements of the scattering matrix, and hence are more suited for interpretation of the data. However, the components still depend on the measurement basis, i.e., the orientation of the scatterer relative to the radar. Moreover, the fact that two of the components effectively represent double-bounce scattering renders the interpretation somehow ambiguous.

SPHERE, DIPLANE, HELIX DECOMPOSITION

In an attempt to remedy these deficiencies, the sphere, diplane, helix decomposition was developed, based on the observation that any given symmetric scattering matrix can be represented in terms of the elementary scattering matrices for a sphere, a dihedral (diplane), and a helix,

$$[\mathrm{S}] = e^{j\varphi} \{ e^{j\varphi_s} k_s [\mathrm{S}]_{sphere} + k_d [\mathrm{S}]_{diplane(\theta)} + k_h [\mathrm{S}]_{helix(\theta)} \}$$

$$[\mathrm{S}]_{sphere} = \begin{bmatrix} 1 & 0 \\ 0 & 1 \end{bmatrix}$$

$$[\mathrm{S}]_{diplane(\theta)} = \begin{bmatrix} \cos 2\theta & \sin 2\theta \\ \sin 2\theta & -\cos 2\theta \end{bmatrix}$$

$$[\mathrm{S}]_{helix(\theta)} = \frac{1}{2} e^{\mp j 2\theta} \begin{bmatrix} 1 & \pm j \\ \pm j & -1 \end{bmatrix}$$

In terms of the elements of the scattering matrix in a circular polarization basis, the parameters of this decomposition are given as follows,

$$k_s = |S_{RL}|; \quad k_d^+ = |S_{LL}|; \quad k_d^- = |S_{RR}|$$
$$k_h^+ = |S_{RR}| - |S_{LL}|; \quad k_h^- = |S_{LL}| - |S_{RR}|$$
$$\varphi = \tfrac{1}{2}(\varphi_{RR} + \varphi_{LL} - \pi)$$
$$\theta = \tfrac{1}{4}(\varphi_{RR} - \varphi_{LL} + \pi)$$
$$\varphi_s = \varphi_{RL} - \tfrac{1}{2}(\varphi_{RR} + \varphi_{LL})$$

The transformation from the linear polarization basis to the circular polarization basis is simply given by these formulas,

$$S_{RR} = j S_{HV} + \tfrac{1}{2}(S_{HH} - S_{VV})$$
$$S_{LL} = j S_{HV} - \tfrac{1}{2}(S_{HH} - S_{VV})$$
$$S_{RL} = \tfrac{j}{2}(S_{HH} + S_{VV})$$

The advantage of this orientation invariant representation is that a pure even-bounce scatterer always shows up in just one component. On the other hand, if two or more even-bounce scatterers are present within the same resolution cell, this may result in both diplane and helix components in the polarimetric decomposition. Mathematically, this is because the diplane and helix matrices are not orthogonal. In practical applications, the helix component may be considered as a measure of the purity of the diplane component, which may be of importance for determining suited dominant scatterers for motion compensation in high-resolution SAR/ISAR imaging.

APPLICATION EXAMPLES

An illustrative comparison of the Pauli and the SDH representations is shown in Fig. 2 and Fig. 3. These figures show part of a scene with Copenhagen Airport at L-band and a resolution of 1.5 m. Note how double bounce reflections stay green in the SDH representation, while they fall in the red and green channel of the Pauli representation, depending on the incidental orientation angle.

In Table 1, an extract of some classification experiments is shown, based on data from the German E-SAR system operated by the German Aerospace Centre (DLR). The classification performance of three different feature sets has been compared for a scene at the Oberpfaffenhofen test site [8]. The training areas were classified into the following categories: water, houses, roads, trees, grass, field 1 and field 2. The overall accuracy is summarized in Table 1 for two different algorithms: maximum likelihood and minimum distance. A detailed discussion of the results may be found in [8] and [9], and is not within the scope of the present paper. However, some main observations are in order. The SDH set of parameters clearly results in the best classification performance, while the Pauli coefficients, rather surprisingly, do not result in a better performance than using the raw scattering matrix elements. It should be noted, however, that not all the available information in the scattering matrix (5 relevant independent parameters per pixel) has been used in the above sets of parameters. In fact, only the magnitudes of the complex coefficients have been used. The results therefore seem to indicate that the SDH decomposition is an efficient way of confining as much information as possible in only three parameters, which is of importance in relation to efficiency of automatic algorithms. The classification performance if only one of the polarimetric channels, e.g. HH alone, had been used, was not included in these tests.

Despite the fact that the above classification results were obtained for classification of extended ground targets using SAR data, similar results should be expected for classification of air targets using 2D ISAR data as well as 1D HRR data.

CONCLUSIONS

The basic properties and capabilities of polarimetric radar were reviewed in an application oriented perspective. It was demonstrated how target characteristic features, which cannot be determined from traditional single-polarization data, can be easily extracted from fully polarimetric radar data. Such information could be of decisive importance for successful radar target identification and classification, but also other applications, such as weather radar, greatly benefit from the extra information provided by a fully polarimetric capability.

"Any radar should be polarimetric." *– Dr. Richard Huynen*

Fig. 2: Part of Copenhagen Airport. L-band, SDH: red=sphere, green=diplane, blue=helix.

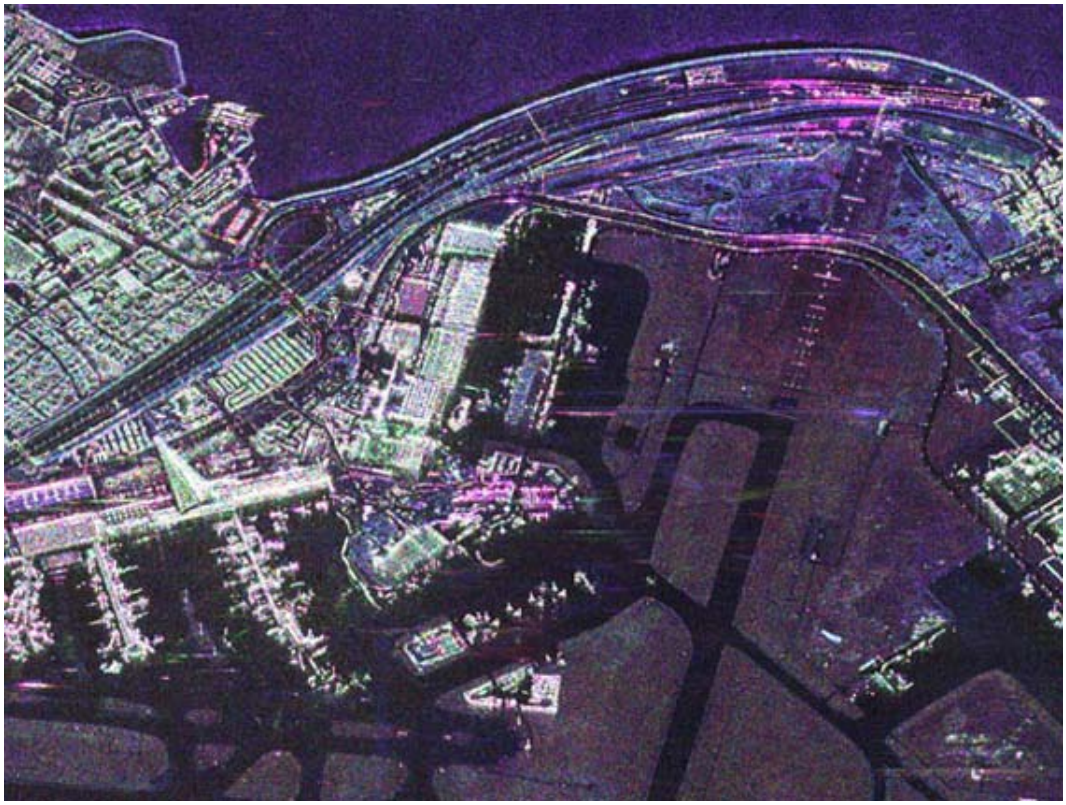

Fig. 3: Part of Copenhagen Airport. L-band, Pauli: red=HH-VV, green=HV+VH, blue=HH+VV.

Table 1: Accuracy estimates of classification tests (15x15-pixel averaging window)

Classification algorithm **Polarization parameters**	Maximum likelihood Ov. Acc. (%)	Minimum distance Ov. Acc. (%)
HH, HV, VV magnitudes	57.03	50.96
Characteristic null-polarisations	66.24	64.41
Pauli coefficients	57.61	52.27
SDH coefficients	87.37	77.04

REFERENCES

[1] Kennaugh, E.M., Effects of Type of Polarization on Echo Characteristics, The Ohio State University, Antenna Laboratory, Columbus, OH, Reports 381-1 to 394-24, 1949-1954.

[2] J.R. Huynen, "The Phenomenological Theory of Radar Targets", Doctoral Thesis, Technical University of Delft, Netherlands, 1970.

[3] E. Krogager, "Aspects of Polarimetric Radar Imaging", Doctoral Thesis, TUD, Lyngby, Denmark, May 1993

[4] E. Krogager and Z. H. Czyż, "Properties of the sphere, diplane, helix decomposition", Proc. 3rd International Workshop on Radar Polarimetry, JIPR 1995, Nantes, France, 21 - 23 March 1995, pp. 106-114.

[5] W.L. Cameron, N. N. Youssef and L. K. Leung, "Simulated polarimetric signatures of primitive geometrical shapes", IEEE Trans. Geosci. Remote Sensing, vol. 34 (3), pp. 793-803, May 1996.

[6] S.R. Cloude and E. Pottier, "A Review of Target Decomposition Theorems in Radar Polarimetry", IEEE Trans. Geosci. Remote Sensing, vol. 34, 2, pp. 498-518, Mar. 1996

[7] S.R. Cloude and E. Pottier, "An entropy based classification scheme for land application of polarimetric SAR", IEEE Trans. Geosci. Remote Sensing, vol. 35 (1), pp. 68-78, January 1997.

[8] S.R. Cloude and K.P. Papathanassiou, "Polarimetric SAR interferometry", IEEE Trans. Geosci. Remote Sensing, vol. 36 (5), pp. 1551-1565, September 1998.

[9] V. Alberga, M. Chandra and L. Pipia, "Supervised classification of coherent and incoherent polarimetric SAR observables: comparison and accuracy assessments", Proceedings of SPIE - SAR Image Analysis, Modeling, and Techniques V, vol. 4883, pp. 181-191, 23 - 24 September 2002, Agia Pelagia, Crete, Greece.

[10] V. Alberga, "Comparison of polarimetric methods in image classification and SAR interferometry applications", Ph.D. thesis, Technical University of Chemnitz, Germany, January 2004.

[11] V. Alberga and M. Chandra, "Volume decorrelation resolution in polarimetric SAR interferometry", Electronics Letters, vol. 39 (3), pp. 314-315, February 2003.

Robust Polarimetric Scatterers Extraction for SAR ATR

Luc VIGNAUD
ONERA
BP 72 29 avenue de la division Leclerc
92322 CHATILLON CEDEX
FRANCE

vignaud@onera.fr

ABSTRACT TITLE

We present a new tool for extracting robust and stable polarimetric scatterers from ground target SAR data with applications to Automatic Target Recognition (ATR). This combination of signal processing algorithms enables us to synthesize the fully polarimetric scatterers information contained in a collection of adjacent SAR images (i.e. looks) and derives the probabilities for individual (or groups of) scatterers to be active and stable over a certain observation angle for the target under test. It is based on an autofocus polarimetric version of the CLEAN-RELAX algorithm, which is followed by a tracking on both the position and polarimetric information of the extracted scatterers over some angular extension (or separate looks). A sub-pixel autofocus and a local relaxation is embedded in the algorithm to achieve a better extraction. Residual translations between focused looks are then estimated through a simple correlation scheme or using the following scatterers tracking. Individual extracted scatterers are tracked from one look to another using a matching criteria based both on the distance and the fully polarimetric magnitudes. We then derive the most probable target signature, which may be used as template for classification purposes. This process may also be very useful when working with target variants, in order to define which part of the target may remain stable and potentially useful for the classification stages. Moreover, this makes a tremendous information compression, which becomes mandatory when working with large data collections. We show an application of the technique on a real dataset that was provided by Qinetiq to Nato SET 053 group for ATR evaluation purposes.

1.0 INTRODUCTION

Synthetic Aperture Radar (SAR) images are highly dependent on target aspect, they contain speckle and not clear edge maps, all of which makes traditional classifiers that compare target signature intensities with references not very efficient. Intensity variations cause significant changes in the image correlation between test and train set. Some studies have worked on the use of local maxima (peaks or elementary scatterers) as classification features, but such features seem quite sensitive to target variations and, furthermore, different targets may have very similar peaks distribution. The four channel polarimetric peaks information can be added to better characterize and separate the target signatures among each other [9]. We propose to increase the robustness of these features by working on “stable” peaks that remain active on a wide angular aspect angle with almost unchanged polarimetric properties. Such peaks bear a stronger probability to be characteristic of the scattering of major parts of the target, which makes them less sensitive to targets variants and, by definition, to aspect angle errors that could be made in the a priori target orientation detection for instance.

We propose to find these stable scatterers by applying several signal processing algorithms to a collection of SAR images (or “looks”) representing the target signature over a wide aspect angle (typically up to 10°), each look being coherently formed over a smaller angular aperture. This may correspond to the situation where a radar does some spotlight imaging over a given target.

Paper presented at the RTO SET Symposium on “Target Identification and Recognition Using RF Systems”, held in Oslo, Norway, 11-13 October 2004, and published in RTO-MP-SET-080.

Most of these algorithms are original or give polarimetric extensions to existing ones. The analysis is made in three major steps. First, we extract the peaks location and their polarimetric information in each look. This first stage separates the target elementary scatterers from the clutter response: a polarimetric extension of the CLEAN/RELAX peak extraction algorithm is derived to extract both the position and polarimetric magnitudes of elementary peaks within the resolution cells. This iterative processing also includes an embedded "autofocus" to compensate for any sub-pixel residual error done while forming the SAR image. We call "hyperlook" the result of this extraction, i.e. the spatial positions $(X_i, Y_i)_{i=1:N}$ and polarimetric magnitudes[1] $A_i = (A_i^{HH}, A_i^{HV}, A_i^{VH}, A_i^{VV})_{i=1:N}$ of the N extracted peaks. Each hyperlook forms a concise description of the polarimetric target signature at a specific aspect angle. In a second step, we apply a feature-matching algorithm on pairs of hyperlooks through a graduated assignment technique that we have adapted to take into account both the spatial and a "polarimetric" distance between peaks. This algorithm finds the possible connection between a peak (X_i, Y_i, A_i) in one hyperlook and a peak (X_j, Y_j, A_j) in another; this matching scheme is optimized on a one to one basis while preserving the possibility for an "unstable" peak not to connect. In this procedure, we also estimate the residual translation between the different looks and compensate for it. Then, the result of this matching procedure enables us to derive the stability of the individual extracted scatterers by looking at the connection map for each peak and build the most stable peaks distribution that can be used as template for classification purposes.

We will show the application of the major steps of the proposed analysis scheme on real SAR data and its evaluation on a simple classification test.

2.0 POLARIMETRIC STABLE SCATTERERS EXTRACTION

2.1 Autofocus Polarimetric CLEAN/RELAX algorithm

In classical radar imaging, the basic assumption lays in the ideal bright points model (or canonical peaks) of elementary scatterers that compose the scene to be imaged: the discrete data model is usually written as a set of N complex sinusoids with "frequencies" $(\mathrm{X_k}, \mathrm{Y_k})_{\mathrm{k=1,\ldots,N}}$ and amplitude $\mathrm{A_k}$ in noise e.

$$\mathrm{H(K_x, K_y)} = \sum_{\mathrm{k=1}}^{\mathrm{N}} \mathrm{A_k}\ \mathrm{e}^{\mathrm{j(K_x X_k + K_y Y_k)}} + \mathrm{e(K_x, K_y)} \tag{1}$$

and the image $\mathrm{I(X,Y)}$ is then the 2D spectra of the formatted radar data $\mathrm{H(K_x, K_y)}$ with $K_x = 4\pi f \sin\theta / c$ and $K_y = 4\pi f \cos\theta / c$, with frequency f in the radar bandwidth Δf and observation angle θ within $\Delta\theta$. In Synthetic Aperture measurements the angle θ is linked to the observation time T through the relative motion of the target and the radar.

Under this assumption, the extraction problem matches the signal processing formulation of super-resolution. An extended analysis of the various spectral estimation methods that can be used is given, from a signal processing view in [1], and applied to SAR imaging in [2]. However, most of the methods require an *a priori* knowledge or estimation of the number of reflectors, which deeply limits their application to SAR imaging and features extraction.

Unlike these, the CLEAN/RELAX algorithm [3][4][5] is an asymptotically statistically efficient estimator that minimizes the following nonlinear least squares criterion:

$$\mathrm{C(X_k, Y_k, A_k, M)_{k=1,\ldots,M}} = |\,\mathrm{H} - \hat{\mathrm{H}}_{\mathrm{M}}\,|^2 \tag{2}$$

with $\hat{\mathrm{H}}_{\mathrm{M}} = \sum_{\mathrm{k=1}}^{\mathrm{M}} \mathrm{A_k}\ \mathrm{e}^{\mathrm{j(K_x X_k + K_y Y_k)}}$.

[1] H stands for horizontal polarisation, V for vertical ; first letter for emission second for reception

One advantage is that the number of elementary peaks is estimated within the algorithm. CLEAN belongs to a family of iterative methods, which, within each iteration, search for the biggest peak in a complex image and subtract its complex contribution in its corresponding Fourier spectrum. RELAX basically extends the CLEAN algorithm with a relaxation step. See [3][4][5] for a more detailed description of both algorithms and their implementation.

2.1.1 CLEAN/RELAX architecture

CLEAN is a deconvolution technique that can be summarized in the following steps :

- Find the brightest point in the image
- Measure the complex amplitude and the location of the brightest point
- Form a new image by subtracting ("cleaning") the complex contribution of this point in the Fourier spectra of the image
- Repeat the procedure on the next brightest peak, and so on.
- Stop the procedure when the power of last extracted scatterer is below a chosen level or the noise (clutter) level is reached.

The RELAX algorithm simply add a secondary CLEAN cycle to each peak close to a newly estimated one: each peak contribution is then estimated taking into account its neighbourhood by forgetting (“un-cleaning”) previous estimations and re-estimating them one by one. This adds some robustness to the extraction at the price of an increased computer load.

Adaptation of the CLEAN algorithm to polarimetric data is rather straightforward. Rather than using CLEAN on each polarimetric channel, which would need to reconnect extracted peak between channels, we propose to work on the polarimetric span image $\mathrm{I}^{\mathrm{span}}$ to first estimate the location of the brightest peak at each step:

$$\mathrm{I}^{\mathrm{span}} = \sqrt{(I^{HH} I^{HH^*} + I^{HV} I^{HV^*} + I^{VH} I^{VH^*} + I^{VV} I^{VV^*})} \tag{3}$$

with I^* being the complex conjugate of I.

Then, the peak magnitude can be measured in each channel separately, and so is done the cleaning process.

2.1.2 Adding autofocus to the peak extraction

Refined image focusing is often neglected although it deeply influences the extraction quality. The image patches we are dealing with are often extracted from larger scene for which an average focusing has been done (presumably up to the radar resolution cell). But small residual motion errors create phase shifts that may slightly distort the peaks response: these errors will eventually be cumulated through the cleaning stage of the CLEAN/RELAX algorithm. In the presence of such errors $\delta R(\theta)$, the data model equation (1) becomes:

$$\mathrm{H}(\mathrm{f},\theta) = \sum_{\mathrm{k}=1}^{\mathrm{N}} \mathrm{A}_{\mathrm{k}}\ \mathrm{e}^{\mathrm{j}4\pi \mathrm{f}(\mathrm{X}_{\mathrm{k}}\sin\theta + Y_{\mathrm{k}}\cos\theta + \delta R(\theta))/c} + \mathrm{e}(\mathrm{f},\theta) \tag{4}$$

For rather small frequency bandwidth, angular aperture, and residual errors, this can be approximated at first order to:

$$H(K_x,K_y)=\sum_{k=1}^{N}A_k\, e^{j(K_xX_k+K_yY_k)}e^{j\varphi(K_x)}+e(K_x,K_y) \tag{5}$$

This shows that residual errors will mainly distort the cross-range components of the image $I(X,Y)=FT\left[H\left(K_x,K_y\right)\right]$.

The least square criterion (2) has then to be changed to:

$$C(X_k,Y_k,A_k,M,\varphi)_{k=1,\ldots,M}=\left|H(K_x,K_y)\,e^{-j\varphi(K_x)}-\hat{H}_M(K_x,K_y)\right|^2 \tag{6}$$

The solution of this problem can be wrapped into the CLEAN/RELAX architecture as shown in [6] and [7]. At each CLEAN extraction step, we obtain an estimation of the phase distortion via:

$$e^{-j\hat{\varphi}(K_x)}=\sum_{K_y}H^*(K_x,K_y)\,\hat{H}(K_x,K_y) \tag{7}$$

which we use to correct the entry data for a completely new CLEAN/RELAX cycle.

When working with polarimetric data, the focusing can be done on each channel separately in case of phase centre mismatch between the different channels.

The autofocus is turned off when the induced changes or the estimated phase variations fall below a certain level.

2.1 Graduated assignment algorithm and softassign

We have applied the polarimetric CLEAN/RELAX extraction on a set of L successive SAR looks. As a result we now have L sets of extracted scatterers described using their position and polarimetric magnitude $\left[X_i^l,Y_i^l,A_i^l\right]_{i=1:N_l;l=1:L}$ which we call "hyperlooks". We know want to link the scatterers information over the various aspect angles. But even at nearby aspects, features may shift, disappear or appear: we wish to find a correspondence between two sets of extracted scatterers where some may be missing, added or displaced, in the presence of a global residual translation between the two sets. We also wish a one to one matching. Note that a coarse estimation of the global translation can be found through the spatial correlation of the two reconstructed images once we have applied the known relative rotation between looks. We will use a matching algorithm proposed by Meth in [11] which use a method developed by Gold & al. in [12] and [13] called graduated assignment, which is based on works made in [14][15] and called "softassign".

The graduated assignment technique is a specialized method of efficiently finding good suboptimal solutions for optimization problem that use a match matrix to explicitly denote an assignment between one set of objects and another. Match matrix is a 0-1 matrix with 1 denoting that a given point in one set is assigned to a given point in the other set. Graduated-nonconvexity is used to turn these discrete variables into continuous ones in order to reduce the chances of getting trapped in local minima. Technique is iterative, where at each step, an estimate of the match matrix is made and then "softassign" is used to ensure that the match matrix remains the continuous analog of a true assignment. Softassign is a method employed to satisfy assignment constraints: one feature in one image can match to at most one feature in the other. In practice, one can show that it can be done by an iterative process of alternatively normalizing the rows and columns.

Let us consider two hyperlooks $\left[X_i^1,Y_i^1,A_i^1\right]_{i=1:N_1}$ and $\left[X_j^2,Y_j^2,A_j^2\right]_{j=1:N_2}$ corresponding up to a translation $\left(t_x,t_y\right)$. A match matrix $M_{i;j}$ is defined such that $M_{i;j}=1$ if point i in first look corresponds to point j in

the second look, and 0 otherwise. Up to this point note that the match matrix is a kind of permutation matrix. An extra row and column are added to the match matrix $M_{i;j}$ to hold the slack variable in order to handle spurious or missing links: $M_{i;N_2+1}=1$ if peak i is an outlier, 0 otherwise and $M_{N_1+1;j}=1$ if point j is an outlier, 0 otherwise. $M_{i;j}$ is then a N_1+1 by N_2+1 matrix.

An objective function is then formulated [11]&[12]:

$$\begin{aligned} E\left(M_{i;j},t_x,t_y\right) \;=\; & \sum_{i=1}^{N_1}\sum_{j=1}^{N_2} M_{i;j}\times D_{i;j}\left(t_x,t_y\right)-\alpha\sum_{i=1}^{N_1}\sum_{j=1}^{N_2} M_{i;j} \\ & +\sum_{i=1}^{N_1}\mu_i\left(\sum_{j=1}^{N_2+1} M_{i;j}-1\right)+\sum_{j=1}^{N_2}\nu_j\left(\sum_{i=1}^{N_1+1} M_{i;j}-1\right)+\frac{1}{\beta}\sum_{i=1}^{N_1+1}\sum_{j=1}^{N_2+1} M_{i;j}\left(\log M_{i;j}-1\right) \end{aligned} \tag{8}$$

With $D_{i;j}=\sqrt{\left(X_i^1-X_j^2-t_x\right)^2+\left(Y_i^1-Y_j^2-t_y\right)^2}$ the square Euclidean distance. We modify this distance to take into account the polarimetric dimension. Let us define the normalized polarimetric scalar product as:

$$PSP\left(A_1,A_2\right)=\frac{\sqrt{\left(A_1^{HH}A_2^{HH^*}+A_1^{HV}A_2^{HV^*}+A_1^{VH}A_2^{VH^*}+A_1^{VV}A_2^{VV^*}\right)}}{A_1^{span}A_2^{span}} \tag{9}$$

PSP is closed to 1 if peaks have similar polarimetric response and 0 if the polarimetric scattering mechanisms are completely uncorrelated. Then we can replace $D_{i;j}$ by $D_{i;j}/PSP\left(A_i^1,A_j^2\right)$ in (8) to get an objective function that takes both the spatial distance and polarimetric distance into account. Then peaks that are spatially close may not connect if their polarimetric response is very different. The first term in the cost function (8) is then a spatio-polarimetric distance measurement of connected peaks once they have been compensated for the residual translation. The second term is added to encourage the match within a tolerance distance controlled by parameter α. The third and fourth terms contain Lagrange multipliers for the raw and column sums: this imposes the two-way constraints for one to one matching. Last term permits the translation of the problem from a binary formulation to a continuous [0,1] interval: it is similar to a barrier function. This smoothing function pushes the minimum of the objective away from discrete local minimal points by making the objective more convex, with the convexity control parameter β (similar to a relaxation temperature) that may be adjusted to slowly move the matrix closer to 0-1 values.

Minimum of the objective function may then be found by choosing a sequence of increasing β and minimizing the objective at each step. Minimization is done with respect to the matrix elements $M_{i;j}$ and Lagrange multipliers μ_i and ν_i by setting the respective partials to zeros. Minimization with respect to Lagrange parameters is called softassign, which turns to be a simple alternate normalization of the rows and columns of the estimated objective function $\hat{M}_{i,j}=\exp\left(-\beta\times D_{i;j}\left(X_i^1,X_j^2,Y_i^1,Y_j^2,\hat{t}_x,\hat{t}_y\right)/PSP\left(A_i^1,A_j^2\right)-\alpha\right)$.

Please refer to [11] and [12] for a more detailed description of the algorithm implementation.

3.0 AUTOMATIC TARGET RECOGNITION APPLICATION

We will go through the steps described in the first section and see how it can be applied to real SAR data that were provided by QINETIQ UK.

For the demonstration matter, we have taken 3 sets of SAR images, composed each of 5 looks corresponding to the observation of two different targets at the same angular aspect (azimuth and depression angle), target 1 being observed twice in two sets artificially named “test set” and “train set” (see figures 1 to 3). Looks are separated by 2° so the overall rotation is about 10°. Note that the two targets have almost the same size and look roughly similar to the eye.

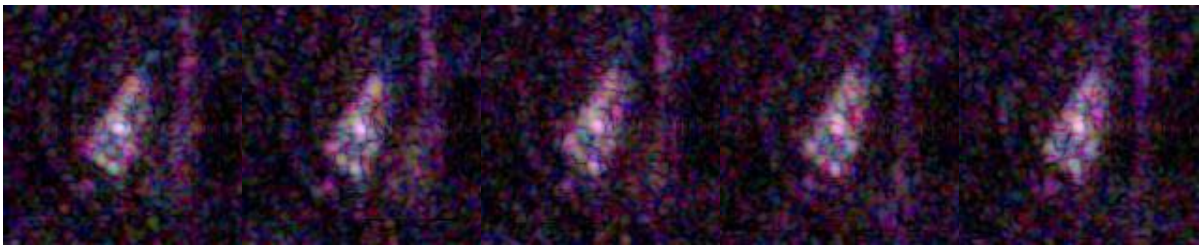

Figure 1: Target 1 test set raw looks (HH: red; HV/VH: green; VV: blue).

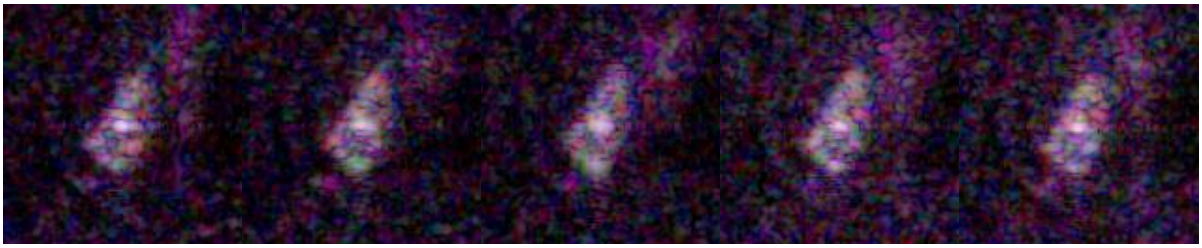

Figure 2: Target 1 train set raw looks.

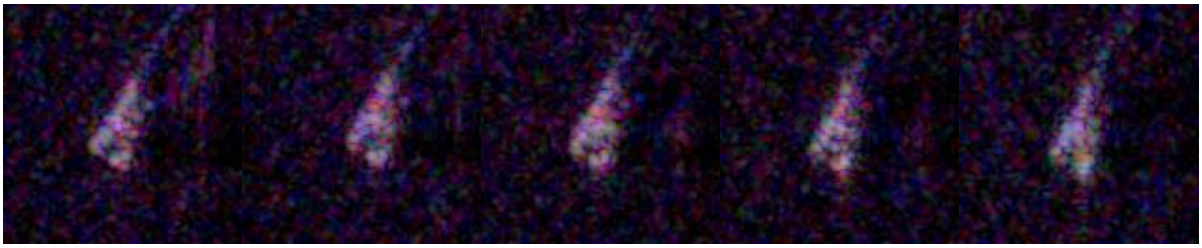

Figure 3: Target 2 train set raw looks.

We then have extracted the elementary scatterers for each look (see figures 4 to 6). Please note that super-resolution by factor 2 was used when reconstructing the images in figures 4 to 6 to allow a better distinction of the individual extracted peaks. Using the graduate assignment we have found the connection maps between peaks of each set. We then have looked for the peaks that were connected in at least three looks over the five, and we have rebuilt their corresponding image (figure 7): we clearly see the similarities of polarimetric stable peaks in the first two sets, while the third one has a quite different distribution. If we finally try to match the stable peaks between the three different sets, we have a 70 to 80% matching (depending on the polarimetric distance level we choose) between the first two, i.e. from same class, and only 15 to 20% matching with the third one (other class).

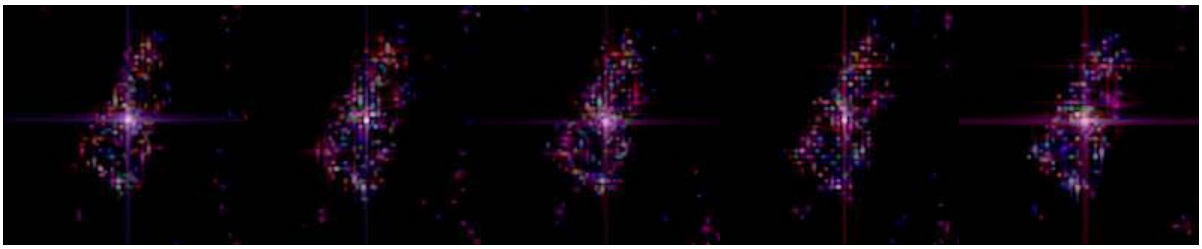

Figure 4: Target 1 test set: hyperlooks (polar. peaks extraction result of figure 1) .

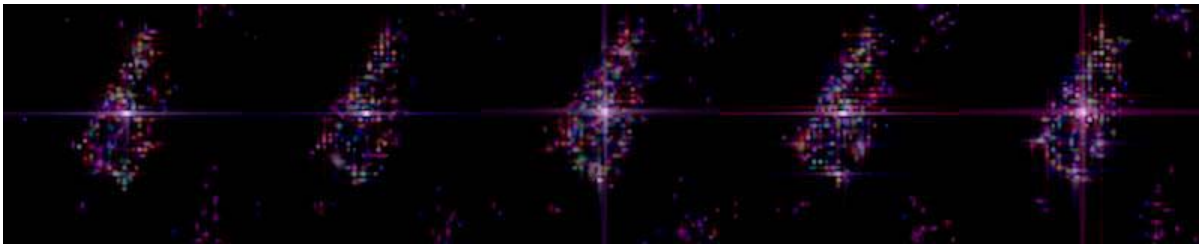

Figure 5: Target 1 train set: hyperlooks of figure 2.

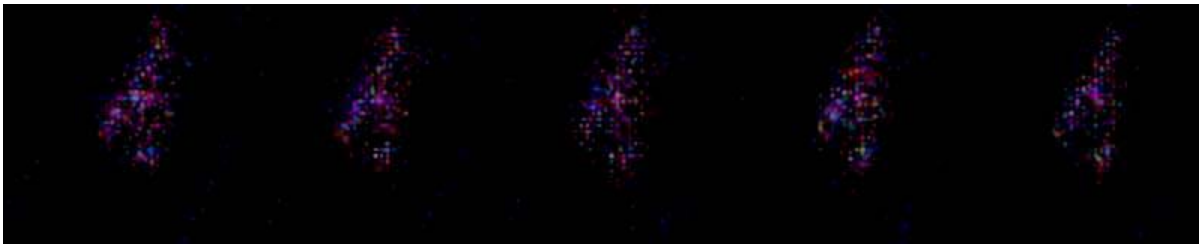

Figure 6: Target 2 train set: hyperlooks of figure 3.

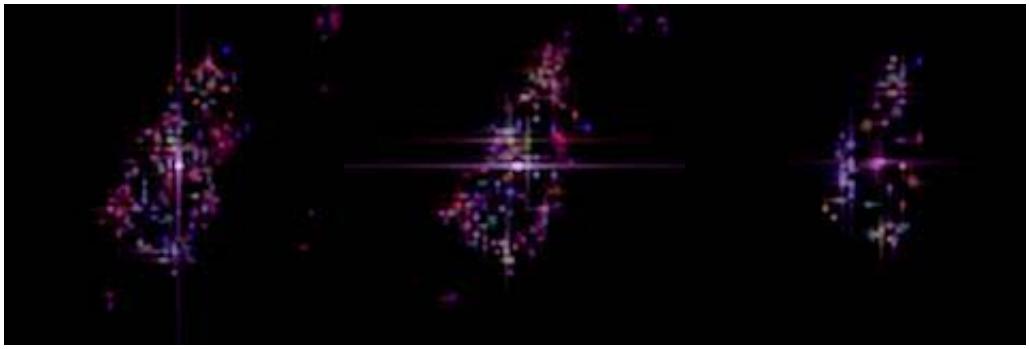

Figure 7: Most stable peaks for target 1 test set (left) target 1 train set (middle) & target 2 train set (right).

We have repeated this experiment using four different targets with about 25 separated "5 looks test sets" (360° round) per target. Each set being tested against all the other targets for the similar observation angles. We are then able to build ROC curves giving the Percentage of Correct Classification against the Percentage of False Alarm obtained using different classification features. We have tested two features: the first one is the maximum of the raw looks image correlation and the second one is the stable

polarimetric scatterers matching percentage obtained using our algorithms. Results are shown figures 8 and 9 and show the advantage of using the stable scatterers rather than the raw image correlation: mean behaviour (dash curve) is almost 20% higher at any PFA level.

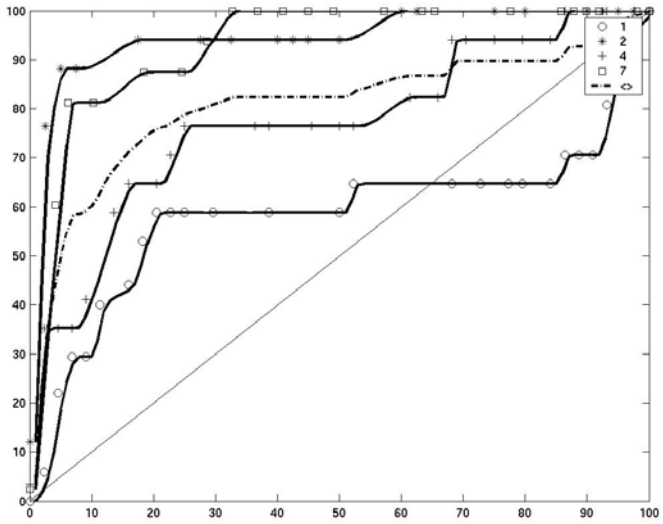

Figure 8: ROC curve for classification using maximum of raw look image correlation (X-coordinate: Percentage of False Alarm; Y-coordinate: Percentage of correct classification).

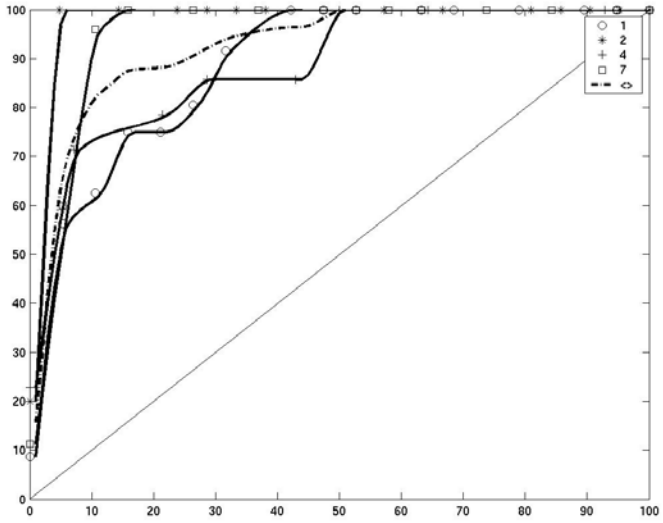

Figure 9: ROC curve for most stable polarimetric scatterers matching (X-coordinate Percentage of False Alarm; Y-coordinate Percentage of correct classification).

4.0 CONCLUSION

We have presented some new signal processing tools that can be applied to polarimetric SAR images of targets. The autofocus polarimetric CLEAN/RELAX algorithm is useful to precisely extract the

elementary scatterers from the clutter background. Then an assignment method is able to achieve a fine peak matching taking polarimetry into account. We have shown their possible application to extract the most stable polarimetric scatterers from a sequence of SAR raw images, which can be used as a characteristic template for classification purposes. We guess they can have many other usages, such as target analysis, SAR image enhancement … A more extensive analysis of the scatterers stability within the possible target variants could be investigated using such algorithms.

The author would like to thank QINETIQ for the excellent polarimetric data provided.

[1] S.L. Marple . *Digital spectral analysis with applications*. Englewood Cliffs, NJ: Prentice, 1987

[2] S. R. De Graaf . "SAR Imaging via modern 2D spectral estimation methods". *IEEE Trans. on Image Processing 7(3),* pp729-761, May 1998.

[3] J. Tsao and B. D. Steinberg, "Reduction of Sidelobe and Speckle Artifacts in Microwave Imaging: the CLEAN Technique", *IEEE Transactions on Antennas and Propagation , 36(4):* pp543-556. 1988

[4] J. Li, et P. Stoica, "Efficient Mixed-Spectrum Estimation with Applications to Target Feature Extraction", *IEEE Transactions on Signal Processing 44(2),* pp.281-295. 1996

[5] J. Li, "Implementation of the RELAX algorithm", Correspondence in IEEE Trans. on Aerospace and Electronic Systems 24(2), pp657-664. 1998

[6] L. Vignaud, "Imagerie radar de satellites : techniques de relaxation haute résolution et cinématique, pour l'extraction, l'autofocalisation et le suivi à grand angle de points brillants", Technical Report 36/5169 DEMR/Y, ONERA, Châtillon, France, Juillet 1999

[7] Zheng, Y., and Bao, Z.: 'Autofocusing of SAR images based on RELAX'. Proc. IEEE Int. Conf. Radar 2000, May 2000

[8] B. Bahnu, G. Jones, J. Ahn, M. Li, and J. Yi. "Recognition of articulated objects in SAR images." Proceedings ARPA Image Understanding Work- shop, pages 1237-1250, February 1996

[9] L. M. Novak, G. J. Owirka, and C. M. Netishen. "Performance of a high-resolution polarimetric SAR automatic target recognition system". Laboratory Journal, 6(1):11-23, 1993.

[10] R. Meth and R. Chellappa. "Target indexing in synthetic aperture radar imagery using topographic features". Proceedings, International Conference on Acoustics, Spee2158, May 96.

[11] R. Meth and R. Chellappa. "Feature matching and target recognition in synthetic aperture radar imagery" Acoustics, Speech, and Signal Processing, 1999. ICASSP '99. Proceedings., 1999 IEEE International Conference on ,Volume: 6 , 15-19 March 1999 Pages:3333 - 3336 vol.6

[12] S. Gold, A Rangarajan, & Als "New Algorithms for 2D and 3D Point matching : Pose estimation and Correspondence", Pattern Recognition, 1998 .

[13] Gold S. & Rangarajan A Graduated assignement algorithm for graph matching, IEEE Transaction on Pattern Analysis and Machine Intelligence, 18(4):pp377-388, 1991

[14] R. Sinkhorn, "A Relationship Between Arbitrary Positive Matrices and Doubly Stochastic Matrices", Ann. Math. Statistics, vol 35, pp. 876-879, 1964

[15] J. S. Bridle "Training Stochastic Model Recognition Algorithms as Networks Can Lead to Maximum Mutual Information Estimation of Parameters", D. S. Touretzky, ed Advances in Neural Information Processing Systems 2. San mateo, Calif. : Morgan Kaufman, 1990, pp. 211-217

The Role of Feature Enhanced Processing for Automatic Target Recognition using High Resolution Polarimetric SAR Data

Albertus van den Broek/ Philippe Steeghs/ Rob Dekker
TNO Physics and Electronics Laboratory
P.O. Box 96864
2509 JG The Hague
The Netherlands

vandenbroek/steeghs/r.j.dekker@fel.tno.nl

ABSTRACT

We have studied the effect of feature enhanced processing on the discrimination of targets in high-resolution polarimetric ISAR and SAR images. This is done by comparing feature-based classification results for original images and images which have been pre-processed to enhance target features. The data comprised four military targets: T72, ZSU23/4, T62, and BMP2. Images at a resolution of 10 cm have been extracted from the ISAR data for a complete aspect range of 360 degrees. The SAR images were taken from the MSTAR database with a resolution of 30 cm.

These images have been processed in order to enhance the geometrical delineation of the targets or to enhance point scattering. We have composed feature vectors out of individual features, which were extracted from the original and the enhanced images. The feature vectors are divided into three categories: radiometric, geometric and polarimetric. A maximum likelihood classifier was used to obtain discrimination results.

Knowledge about the aspect angle allows target discrimination per aspect angle interval, which will improve classification results. We have investigated the effect of feature enhanced processing on pose estimation. Pose estimation was obtained from the Radon transform of the original and enhanced imagery.

We found that the features extracted from enhanced images give slightly better results compared to features extracted from the original images. For the high-resolution enhanced ISAR data reasonable discrimination (about 80%) was obtained compared to the enhanced MSTAR data (about 60%), when radiometric and geometric features are used. Using the polarimetric features the discrimination results could be improved to 85%.

For aspect angle determination using the Radon transformation and for target discrimination per aspect angle interval no significant improvement was obtained using feature enhanced processing. The aspect angle could be determined up to an accuracy of 10-15 degrees, depending on the target. Discrimination per aspect interval using radiometric and geometric features shows results of 90% for the ISAR and 75% for the MSTAR images. Polarimetric information improves the results up to 97% for the ISAR images.

Paper presented at the RTO SET Symposium on "Target Identification and Recognition Using RF Systems", held in Oslo, Norway, 11-13 October 2004, and published in RTO-MP-SET-080.

1. INTRODUCTION

With the increasing use of UAVs for RSTA purposes also the interest in SAR imaging systems is growing, because of their unparalleled all-time and all-weather capability. In this context a study for the Dutch MOD was defined in which the role of SAR for ground surveillance is investigated. This study is carried out within the framework of the NATO/SET/TG14 research group, which focuses on robust acquisition of relocatable targets with advanced millimetre wave techniques. By participating in the group we have access to a database with high resolution SAR and ISAR data for various targets and scenes. This database was created and is maintained by the group to study automatic target recognition techniques in the millimetre wave domain. The US Army Research Laboratory (ARL) has contributed to the database with high-resolution (10cm) polarimetric ISAR data of four military targets at 35 Ghz. These data comprised two main battle tanks (T72, T62) an air defence unit (ZSU-23-4) and an infantry-fighting vehicle (BMP2). In a previous paper Van den Broek et al. [1] have studied the robustness of features against aspect variability for the purpose of target discrimination. They have shown that individual features show a strong variability as a function of aspect angle and cannot be used to discriminate between the targets irrespectively of the aspect angle. The use of feature vectors, which combine radiometric, geometric and if available polarimetric information, gives reasonable results. They also showed that the aspect angle could be determined sufficiently accurate using the Radon transformation, so that target discrimination per aspect interval is possible. Discrimination results per aspect interval are significantly higher up to 20% compared to results irrespective of the aspect angle. We study here the influence of feature enhanced processing using the same data set and method as in Van den Broek et al. [1] by comparing the results from the original images and from the feature-enhanced images. The paper is organised as follows. In section 2 we describe the data. In section 3 we discuss feature enhanced processing. In section 4 we describe the features and the classification method followed by results. In section 5 we focus on pose estimation and in section 6 we give a summary.

2. DESCRIPTION OF THE DATA

2.1 High resolution polarimetric ISAR data

The ARL-ISAR measurements were performed with a fully polarimetric stepped frequency radar. The measured data are in the frequency domain and the spatial domain image is obtained through a 2-D inverse FFT [4]. Hamming weighting was applied to reduce the sidelobes of the impulse response. The following table summarizes the main properties of the data and images.

Table 1. ARL-ISAR data parameters

Band	Ka	Angle sampling interval	0.015º
Centre frequency	34.25 GHz	Nr. of samples (azimuth)	160
Bandwidth	1511.64 MHz	Resolution (azimuth)	10 cm
Frequency step	5.928 MHz	Polarisations	HH, HV, VH, VV
Nr. of samples (range)	256	Depression angle	10º (BMP2, T72, T62) and 12º (ZSU23-4)
Resolution (range)	10 cm	Incidence angle	80º (BMP2, T72, T62) and 78º (ZSU23-4)
Coherence interval	2.4º	Number of looks	Single Look

In this way a set of 397 fully polarimetric 10 cm resolution images was created covering the complete range of 360 degrees of aspect. This implies one image for every 0.9 degree of aspect. In figure 1 we show 10 cm ARL-ISAR images for the T62, T72, BMP and ZSU targets for one aspect angle.

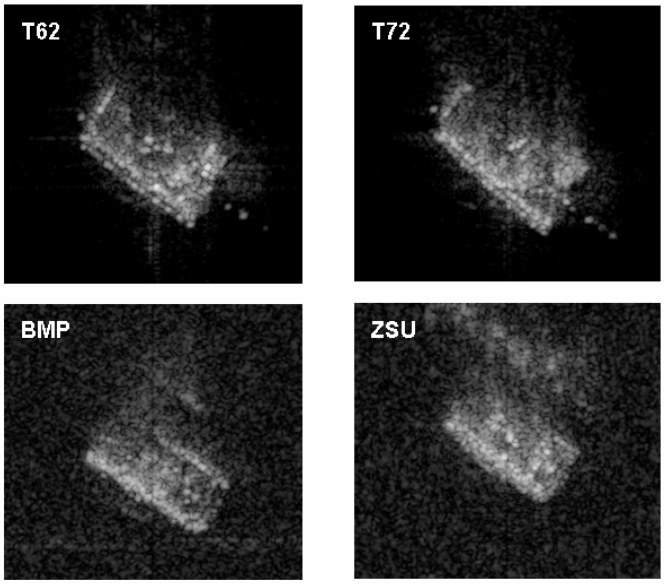

Figure 1. ARL-ISAR 10 cm resolution images for the T62, T72, BMP and ZSU targets.

2.2 MSTAR data

MSTAR data from the public database were used for comparison. These data were taken from data collection 1 (September 1995) and data collection 2 (November 1996). Data were collected at X-band, HH polarisation with about 30 by 30 cm resolution for various aspect angles covering the complete circle of 360 degrees. The depression angle of the selected data was 15 degrees. The MSTAR data comprised 275, 195, 196 and 276 aspect angles for the T62, T72, BMP and ZSU targets respectively. See Table 2 for further details.

Table 2. MSTAR data

Target	MSTAR data collection	Type
T62	data collection #2, scene 1	T62
T72	data collection #1	T72 variant SN_812
BMP	data collection #1	BMP-2 variant SN_9563
ZSU	data collection #2, scene 1	ZSU 23/4

We use the results from the MSTAR data for comparison with the results from the ARL-ISAR data. The comparison is not straightforward since there are differences in elevation angle (15 degrees versus 12/10 degrees) and the frequency band (Ka band versus X-band) used. In Figure 2 we show MSTAR data for the T62, T72, BMP and ZSU targets for one aspect angle.

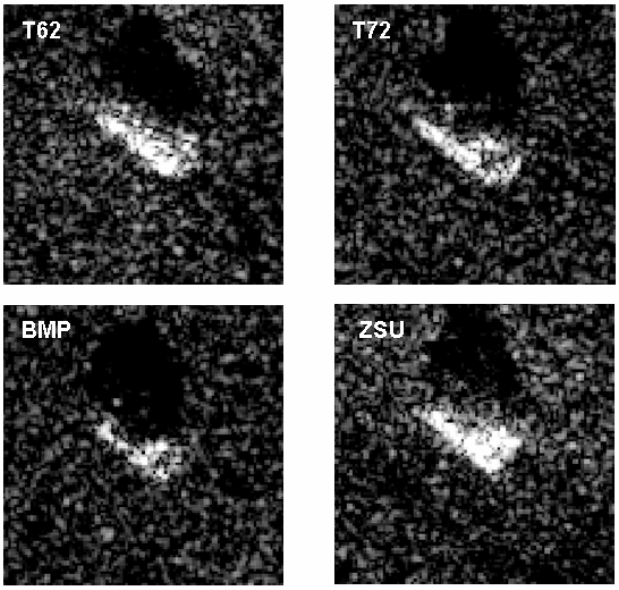

Figure 2. MSTAR 30 cm resolution images for the T62, T72, BMP and ZSU targets.

3. FEATURE ENHANCED PROCESSING

Following Çetin et al. [3] feature-enhanced image formation is achieved through an optimization process. The objective of this optimization is to find an estimate of the SAR reflectivity field $\mathbf{f}$ from the measurement $\mathbf{g}$ by minimizing the objective function:

$$J(\mathbf{f}) = \|\mathbf{g} - \mathbf{T}\mathbf{f}\|_2^2 + \lambda_1 \|\mathbf{f}\|_k^k + \lambda_2 \|\mathbf{D}|\mathbf{f}\|_k^k. \quad (1)$$

Here $\|\cdot\|_k^k$, denotes the l_k norm, $\mathbf{T}$ is a complex-valued SAR observation operator, $\mathbf{D}$ is a 2-D derivative operator, $|\mathbf{f}|$ denotes the vector of magnitudes, and λ_1, λ_2 are scalar parameters. The first term in the objective function is a data fidelity term. The second and third term introduce prior information regarding the field $\mathbf{f}$ into the optimization problem. Each of these terms aims at enhancing a particular feature. The second term can be interpreted as an energy type constraint on the solution. This term enhances dominant point-like features and suppresses artifacts. The derivative term results in a variability constraint on the solution and as a result leads to reduction of the variability in more or less homogeneous regions of the field. The parameters λ_1 and λ_2 can be chosen such that their relative magnitude emphasizes a particular feature. In this case we straightforwardly have chosen λ_1=1, λ_2=0 for *point enhancement* and λ_1=0, λ_2=1 for *region enhancement.* The choice k determines the properties of the prior function (the l_k-norm). For the first case k=1 and for the second case k=1.5 is chosen. The point enhanced processing obviously aims at enhancing the point features in the images and can be used to get a better separation of point scattering versus background scattering and if a finer grid is used to enhance the resolution (superresolution). The region enhanced processing aims at enhancing homogeneous regions in the image

and can be used to better extract the target outline, and to obtain homogenous backscatter within the target box. It also suppresses the background backscatter so that a complete separation of target and backscatter pixels is possible. Figure 3 shows an example of the result before and after feature enhanced processing of the T72 target in the MSTAR database.

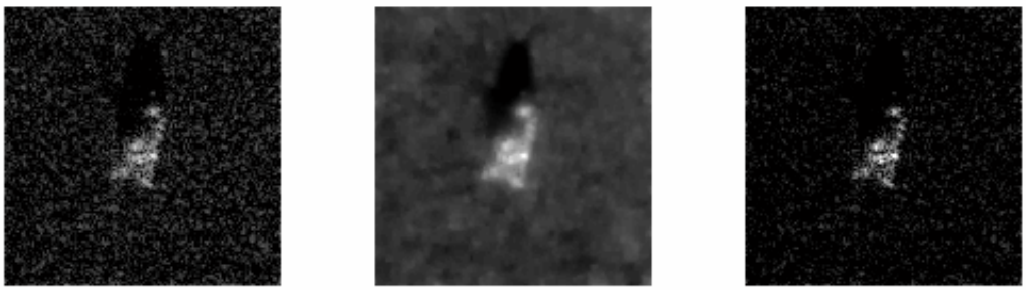

Figure 3. MSTAR data of T72 before (left) and after feature enhanced processing (centre: region enhanced, right: point enhanced).

4.0 TARGET DISCRIMINATION METHOD

4.1 Feature extraction

We selected three classes of features: radiometric, geometric and polarimetric. For each class three features were identified, which are expected to give independent information and are characteristic for the class they belong. Table 3 summarises the features used.

Table 3. **Categories of features used**

Radiometric		Geometric		Polarimetric	
MEAN	mean intensity	*AREA*	area of target	*HHHV*	polarimetric (HH/HV) power ratio
CVAR	coefficient of variation	*NN*	neighbour number	*EVEN*	percent odd
WFR	Weighted rank fill ratio	*LAC* or *FF*	lacunarity index or fill factor	*ODD*	percent even

As a basis to calculate the feature values we first used a CFAR detector [7] to detect target pixels. To obtain so-called CFAR masks we used dB scaled imagery and the CFAR constant was chosen halfway the maximum and the average background of the dB scaled images. Separate results for the CFAR were obtained for the original and feature enhanced processed images. Figure 4 shows examples of the CFAR masks and the corresponding images. For the original imagery obviously only one kind of CFAR mask is available while for the feature enhanced imagery two additional masks are available. In the latter case the

CFAR mask from region enhanced imagery is used, except for the feature *NN*, where the CFAR mask for the original imagery is used and for the feature *WFR,* where the CFAR from the point enhanced imagery is used. In case of enhanced imagery the *LAC* feature is replaced by the *FF* feature (see below).

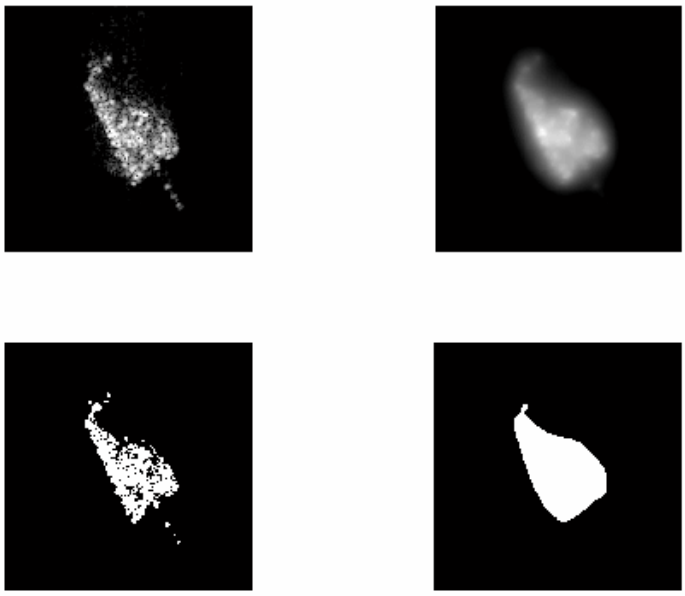

Figure 4. Top: ARL-ISAR T72 image (original: left and region enhanced: right). Bottom: corresponding detected CFAR masks.

Below we give a short description of the features.

MEAN: The mean (μ) of the power of the detected target pixels, which indicates how bright the target appears in the image.

CVAR: The normalized variance of the power of the detected target pixels indicates how smooth or not the scattering is distributed over the target and is defined by

$$cv = \frac{\sigma^2}{\mu^2}. \qquad (2)$$

WFR: This measure is defined as the ratio of the sum of the power of the *N* brightest pixels, and the sum of power of all detected pixels [6]. For the 10 cm resolution images we took N=75 and for the 30 resolution images we took N=10. This feature measures the relative amount of scattering due to 'hot spots'.

AREA: The number of detected target pixels. This feature clearly indicates the geometric extent of the target.

NN: The neighbour number is a measure for the spatial distribution of the CFAR detected target pixels [2].

The number is defined by total number of neighbour pixels of all detected pixels normalized by the total number of detected pixels. This feature is a kind of texture measure indicating how well detected pixels are lumped together.

LAC: The lacunarity index is a textural feature that can discriminate between differently appearing surfaces with the same fractal dimension [8]. It is calculated by counting the number of detected pixels within an $n \times n$ moving window (we use here n=3). For the resulting moving-widow filtered image the coefficient of variation is calculated following Equation 2, only for non-zero values of the detected pixels. This figure gives the lacunarity index and is a measure of the variation in lumpiness of the detected pixels. In other words the feature measures whether the detected pixels form a regular pattern (low value) or an irregular pattern (high value). Obviously, this feature only gives significant information when enough pixels are detected and the resolution is high enough.

FF: The fill factor indicates the fraction of pixels within the CFAR mask from the region enhanced imagery that belong to the CFAR mask of the original images. This feature is used in stead of the lacunarity index in case of feature enhanced imagery.

HHHV: This polarimetric measure is defined as the ratio of total power from the detected pixels in the HV image and the HH image. Note that the pixels are detected on using the HH image. A similar quantity using the HH and VV image is less useful since the HH and VV power are usually strongly correlated.

ODD and EVEN: These polarimetric measures refer to odd and even bounce scatteringand are defined by

$$Odd = \frac{\sigma_{hh} + \sigma_{vv} + 2\,\mathrm{Re}(\rho)}{2}, \tag{3}$$

$$Even = \frac{\sigma_{hh} + \sigma_{vv} - 2\,\mathrm{Re}(\rho)}{2} + 2\sigma_{hv}, \tag{4}$$

where σ is the backscattering coefficient for the various polarisations and ρ is the correlation coefficient of the HH and VV polarisation. The feature percent odd is defined as the percentage of detected pixels for which odd bounce scattering dominates. A pixel is said to be dominated by odd bounce scattering when the odd bounce scattering is at least twice as large as the even bounce scattering. The feature percent even is similar, but now with the even bounce scattering dominating.

Using the method described in the previous section we have produced a database of 9x397 features for the 4 targets in the ARL-ISAR data for both the images without and with feature enhanced processing. For the non-polarimetric MSTAR data only 6 features (radiometric and geometric) could be extracted for the original and the feature enhanced imagery. In Figure 5 we show as example the *AREA* feature as a function of aspect angle for ARL-ISAR images without (left) and with (right) region enhanced processing.

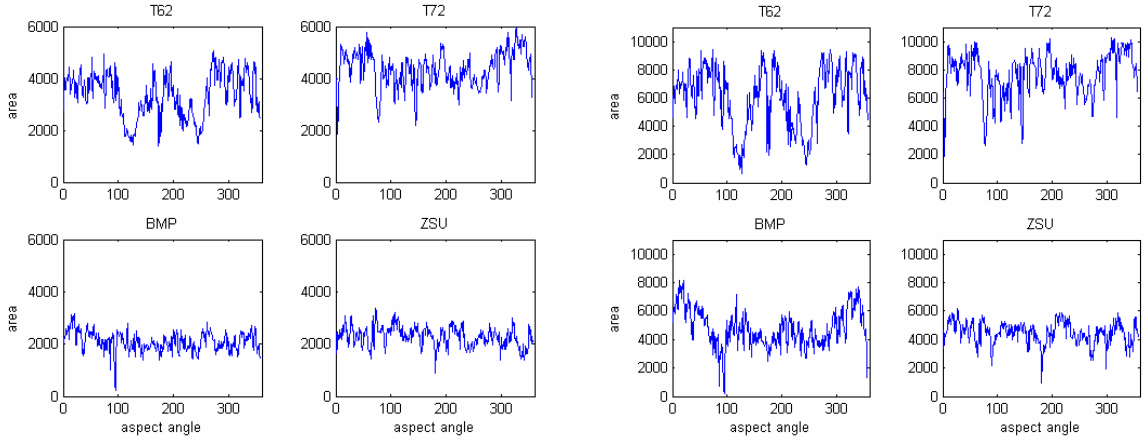

Figure 5. *AREA* feature as function of aspect angle for ARL-ISAR images (left) without and (right) with feature (region) enhanced processing.

4.2 Classification method

It is clear from figure 4 that the individual features can vary significantly especially near aspect angles of 0°, 90°, 180°, and 270°. These aspect angles coincide with observing the targets head-on, sideways or from behind. The capability to discriminate the targets irrespective of the aspect angle is generally low. Either there is large variation, or the more stable features are not very distinctive. This means that one individual feature is never capable of discriminating a target from the other targets irrespective of the aspect angle. In order to study how well we can discriminate the four targets from each other we compose feature vectors with the features extracted in the previous section as the constituting elements. The following 5 categories of feature vectors are used:

$$
\begin{aligned}
\textit{radiometric:} &= [\textit{MEAN, CVAR, WFR}]^T \\
\textit{geometric:} &= [\textit{AREA, NN, LAC}]^T \\
\textit{polarimetric:} &= [\textit{HHHV, EVEN, ODD}]^T \\
\textit{generic:} &= [\textit{MEAN, CVAR, WFR/FF, AREA, NN, LAC}]^T \\
\textit{generic\_pol:} &= [\textit{MEAN, CVAR, WFR/FF, AREA, NN, LAC, HHHV, EVEN, ODD}]^T.
\end{aligned}
$$

The feature vector containing the geometric and radiometric features is called *generic* since it can always extracted from SAR data, regardless whether the data are polarimetric or not. Of course these geometric and radiometric features only contain significant information when enough pixels can be found over the geometric extent of the target, implying that the resolution should be sufficiently high. The *generic_pol* feature vector obviously only applies to fully polarimetric data.

For the four targets we have constructed multi-variate target distributions where the elements of the distribution are the feature vectors at the various aspect angles. The number N corresponds to the number of aspect angles in the data-sets. The dimension of the multi-variate target distribution equals the number of elements in the feature vector used.

For each target distribution we calculated the mean feature vector and also the covariance matrix according to

$$\mu_j = \frac{1}{N}\sum_{i=1}^{N}\vec{x}_i \,, \tag{5}$$

$$\Sigma = \frac{1}{N}\sum_{i=1}^{N}(\vec{x}_i - \vec{\mu}_j)(\vec{x}_i - \vec{\mu}_j)^T \,, \tag{6}$$

where N is the number of aspects used and *j* indicates the T62, T72, BMP or ZSU target. Using these quantities we can now for each target and each aspect image calculate discriminant functions such as

$$d_j(\vec{x}_i) = (\vec{x}_i - \vec{\mu}_j)^T \Sigma_j^{-1}(\vec{x}_i - \vec{\mu}_j) + \log(|\Sigma_j|) \,, \tag{7}$$

where *i* is the aspect angle index and *j* is the target index. The discriminant function is derived from the Bayes' decision rule, which also takes into account the a priori probability. Since this probability is the same for each target, the a priori probability has been omitted here. This is called maximum likelihood discrimination [5]. Note that the discriminant function is only working well under the assumption of normal distributions. Using a feature vector for the 4 targets, we assign the target for which the discriminant function is a minimum. This procedure is repeated for every aspect angle. Next, we compute confusion matrices indicating percentages of correctly and erroneously classifications. Using this method we have produced results for all 5 categories of features vectors.

In table 4 we show the confusion matrices for the *generic* feature vector for the ARL-ISAR and MSTAR data, both for the original and feature enhanced images. In table 5 we give the average percentages of correction classification (PCCs) for all feature vectors and the four cases (ARL-ISAR original, ARL-ISAR enhanced, MSTAR original, MSTAR enhanced). Since the MSTAR data are not polarimetric only three categories of feature vectors has been studied for these data.

Table 4. Confusion matrix for feature vector category *generic*

ARL-ISAR					MSTAR				
Original image					*Original image*				
	T62	T72	BMP	ZSU		T62	T72	BMP	ZSU
T62	80	18	1	1	T62	15	23	27	35
T72	34	66	0	0	T72	7	42	37	13
BMP	0	0	86	14	BMP	1	4	91	4
ZSU	0	0	20	80	ZSU	9	8	5	78
Average Pcc 78					Average Pcc 57				
Feature enhanced					*Feature enhanced*				
	T62	T72	BMP	ZSU		T62	T72	BMP	ZSU
T62	80	18	1	1	T62	25	34	4	36
T72	31	69	0	0	T72	8	66	18	9
BMP	0	0	93	7	BMP	1	12	85	3
ZSU	0	0	12	88	ZSU	14	15	1	70
Average Pcc 82					Average Pcc 61				

Table 5. Average PCCs

	ARL-ISAR		MSTAR	
	Original image	Feature enhanced	Original image	Feature enhanced
Radiometric	54	50	36	32
Geometric	63	69	48	51
Polarimetric	38	41	-	-
Generic	78	82	57	61
Generic_pol	85	86	-	-

If we inspect the confusion matrices for the ARL-ISAR data we find that regardless of the feature enhanced processing most of the confusion is between the T72 and T62 targets, which is not surprising, since both are main battle tanks. For the MSTAR data most confusion is found between T62 and ZSU, and between T72 and BMP. Here, feature enhanced processing helps to reduce the confusion between T72 and BMP. The average PCCs in table 5 indicate that only the geometric feature vector gives a reasonable discrimination between the targets with an average PCC of 69% and 51% for the ARL-ISAR and MSTAR data, respectively. Feature enhanced processing helps to improve the results, especially for the ARL_ISAR data. The *generic* feature vector gives an average PCC of 82% and 61% for the ARL-ISAR and MSTAR data, respectively. Again, feature enhanced processing helps to improve the results, although this improvement is small. Best results (86%) are obtained when polarimetric information is included. In this case no significant improvement is found when feature enhanced processing is applied.

5.0 ASPECT ANGLE DETERMINATION

5.1 Radon transformation

For the goal of aspect determination we consider the Radon transformation of an image (the Radon transform). The Radon transformation of an image *f(x,y)* is defined as

$$g(\rho,\theta) = \int\int f(x,y)\delta(\rho - x\cos\theta - y\sin\theta)dxdy\,, \qquad (8)$$

where δ denotes the Dirac delta function, θ is the rotation angle and ρ is the spatial axis parameter. Ideally a target in an image can be considered as a rectangular shape. The Radon transformation of an image containing such a shape will show a band, with peaks at the angle, for which the rectangle is seen along its long axis. Determination of the maximum in the Radon transformation image therefore gives the aspect angle. This method works well when the backscatter in the target box is homogeneous. However strong point scattering will also give strong peaks in the Radon transform and can hamper an accurate determination of the aspect angle. Also strong sidelobes due to strong scatterers will give erroneous values, typically 0 (180) or 90 (270) degrees. We use therefore images in log (dB) scaling, which suppress variation in backscattering. Figure 6 shows an example of a 10 cm ARL-ISAR image and its Radon transform. Using the method described here we determined the aspect angle for the four targets in original and feature enhanced imagery. For the latter case we used the region enhanced imagery. We also used the CFAR masks obtained from the original and region enhanced imagery to determine the aspect angle. Within the scope of method these masks have the advantage that they are homogeneous but on the other hand are lacking many other target characteristics (see figure 6).

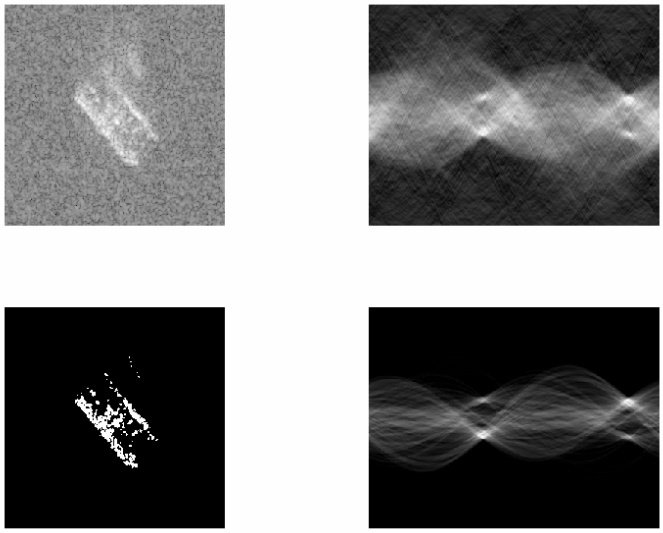

Figure 6. ARL-ISAR image (top left) and its Radon transform (top right), CFAR mask (bottom left) mask and its Radon transform (bottom right).

Note that with this method of aspect angle determination we cannot make distinction between head and rear of the targets. The values therefore are always between 0 and 180 degrees. In figure 7 we have plotted the values found against the actual values for the T72 target in the ARL-ISAR and MSTAR images. This is done for the four cases: original image dB scaled (image Radon), region enhanced image dB scaled (region enh. Radon), CFAR mask from original image (image CFAR Radon), and CFAR mask from region enhanced image (region enh. CFAR Radon). Comparison is done at about every 5 degrees in the complete 360 degrees of angle range.

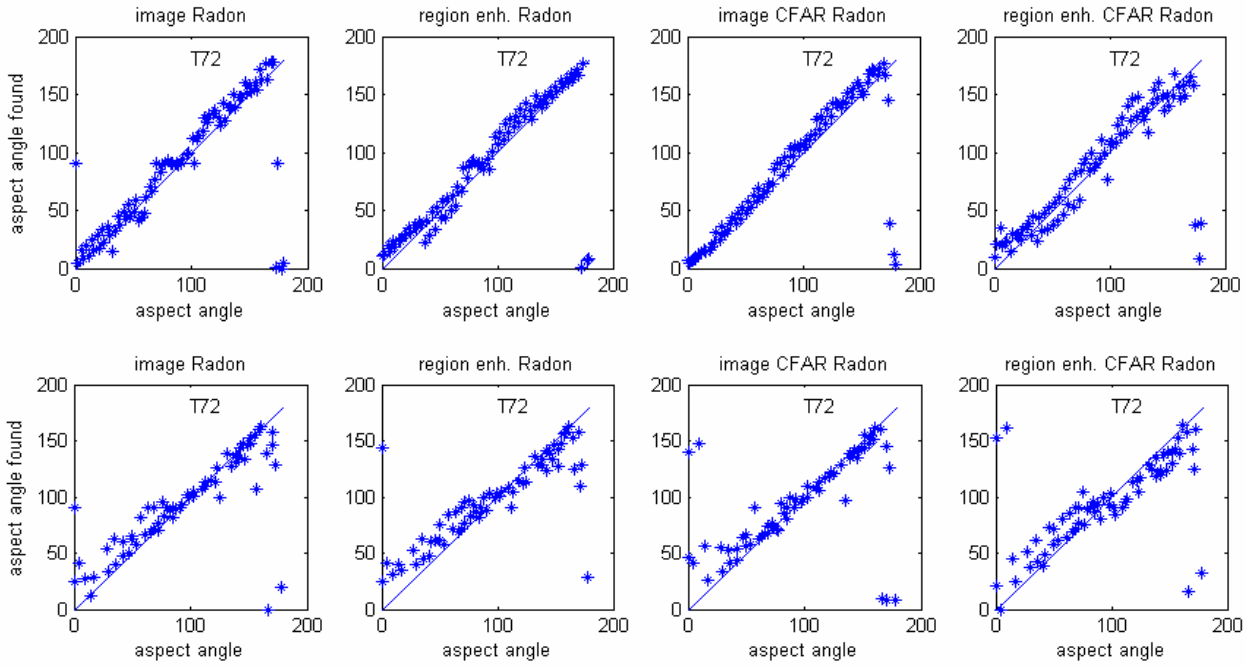

Figure 7. Aspect angles determined with Radon transforms versus the true aspect angle for the T72 target and the four cases. Top: ARL-ISAR and bottom: MSTAR.

To compare the results we calculated the root mean square (RMS) error between the values found and the actual values for the aspect angles. These are summarized in table 6 for the T62, T72, BMP and ZSU targets and the four cases considered.

Table 6. RMS errors in aspect angle determination using Radon transforms

	ARL-ISAR				MSTAR			
	image Radon	region enhanced Radon	image CFAR Radon	region enhanced CFAR Radon	image Radon	region enhanced Radon	image CFAR Radon	region enhanced CFAR Radon
T62	31	9	6	14	37	26	20	14
T72	16	9	10	13	19	19	17	17
BMP	15	9	11	9	24	16	8	12
ZSU	15	17	13	21	36	30	15	22
Average	19	11	10	14	29	23	15	16

Inspection of the average RMS values in table 6 shows that the MSTAR values are larger compared to those for the ARL_ISAR data. This is confirmed by figure 7 where more spread in the data is visible for the MSTAR case. The most accurate aspect angle determination is found when CFAR masks are used. Both CFAR masks based on original and region enhanced imagery are suitable for this purpose with slight better results for the original images. Using CFAR masks the aspect angle can be determined with an accuracy of somewhat larger then 10 degrees for the ARL-ISAR data and about 15 degrees for the MSTAR data. From table 6 it is clear that also target characteristics play a role. For example, aspect angle determination of the ZSU target is less accurate compared to the BMP target, probably due to strong specular reflections which have an effect on the location of the maximum in the Radon transform.

5.2 Target discrimination per aspect interval

In the previous section we have shown that aspect determination is possible with an accuracy of 10-15 degrees. This allows target discrimination per aspect interval, with dimensions in the order 30 degrees or more. In small aspect angle intervals feature values are more stable as a function of aspect angle, so that we overcome the variability of the features against aspect angle and can increase the percentage of correct classification. We divided the full aspect range of 360 degrees into 8 following aspect angle intervals (see figure 8):

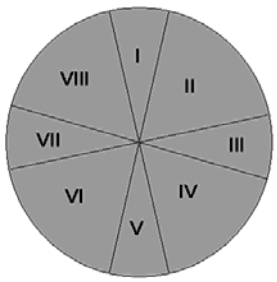

I $345^0 - 15^0$
II $15^0 - 75^0$
III $75^0 - 105^0$
IV $105^0 - 165^0$
V $165^0 - 195^0$
VI $195^0 - 255^0$
VII $255^0 - 285^0$
VIII $285^0 - 345^0$

Figure 8. Overview of aspect angle intervals used.

These aspect intervals are chosen such that we can separate high backscatter (vehicle viewed head-on, sideways or from behind) and lower backscatter (vehicle viewed obliquely). Following section 4.2 we use feature vectors and covariance matrices and compute the discriminant functions following equation 7, but now per aspect interval. We obtain confusion matrices for the four targets per aspect interval and for the four cases considered in section 4.2 cases (ARL-ISAR original, ARL-ISAR enhanced, MSTAR original, MSTAR enhanced). Like in table 5 we give in table 6 the average percentages of correct classification averaged over the 8 intervals for the different feature vectors. Figure 9 shows the behavior of the feature vector *generic* as function of aspect interval.

Table 7. Average PCCs

	ARL-ISAR Original image	ARL-ISAR Feature enhanced	MSTAR Original image	MSTAR Feature enhanced
Radiometric	69	63	50	43
Geometric	79	68	61	61
Polarimetric	51	56	-	-
Generic	90	91	74	75
Generic_pol	96	97	-	-

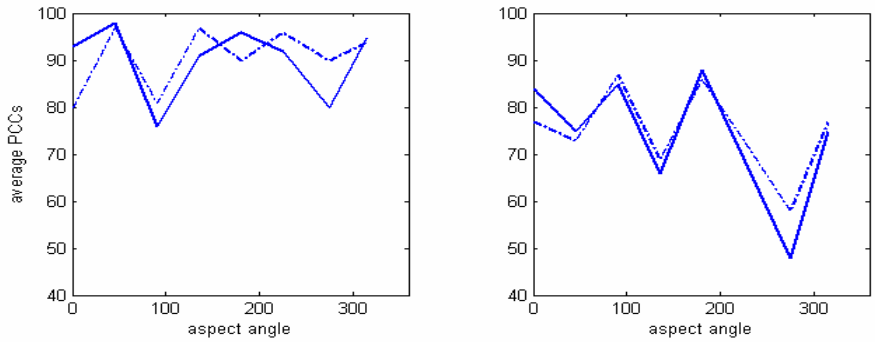

Figure 9. Average PCCs using the *generic* feature vector. To the left the results for the ARL-ISAR data and to right the results for MSTAR data are shown. The solid line is for the original images and the dotted for the feature enhanced images

The results in table 7 show that the average PCCs are significantly higher those in table5, both for the ARL_ISAR data as well as for the MSTAR data. The increase is typically 10%. There is no significant difference when feature enhanced processing is applied. The *generic* feature vector, which can be used for non-polarimetirc data now gives a PCC of 90% for ARL-ISAR data and 75% for the MSTAR data. Especially when the resolution is high enough (10 cm ARL-ISAR data) and when also polarimetric information is used almost complete separation is obtained between the targets (97%). The results for the *generic* feature vector as a function of aspect angle in figure 9 show somewhat lower PCCs when the targets are viewed head-/tail-on or sideways. This is especially true at 270 degrees for the MSTAR data. This may be due to higher double bounce scatter between target and the ground, which is less discriminative. Again the difference between the results from original and feature enhanced imagery is small as a function of aspect angle interval.

6.0 SUMMARY

In this study we have evaluated the role of feature enhanced processing for the discrimination of targets in high-resolution SAR images. The feature enhanced processing aims at enhancing the point features in the images to get a better separation of point scattering versus background scattering (point enhancement), and at enhancing homogeneous regions in the image to better extract the target outline (region enhancement). We used four military targets: T62, T72, BMP and ZSU and images from 2 data-sets: ARL-ISAR (10 cm resolution) and MSTAR (30 cm resolution). We evaluated the discrimination of targets using feature vectors consisting of three categories: radiometric, geometric and polarimetric, extracted from two kinds of images: original and feature enhanced. To obtain results we used a maximum likelihood classifier.

As a first case we studied discrimination of targets irrespective of the aspect angle. Best results are obtained when all feature vector categories are combined, i.e. the radiometric and geometric category, and if available the polarimetric category and when feature enhanced processing is applied. In case of the combined radiometric and geometric feature vector, percentages of correct classification of about 80% could be obtained for the ARL-ISAR data and 60% for the MSTAR data. The use of feature enhancement helps to improve the percentages of correct classification by about 5%.

As a second case we have studied target discrimination per aspect angle interval. In practice this implies that the aspect angle has to be determined. We used the Radon transformation for this purpose. We found that the best way to do this is the use of target CFAR masks as input for the Radon transformation. We found typical accuracies of 10-15 degrees. In this case feature enhanced processing does not substantially improve the results. Discrimination results per aspect interval are significantly better compared to discrimination irrespective of aspect angle. We found percentages of correct classification up to 97% when radiometric, geometric and polarimetric features are used for ARL-ISAR data. When only radiometric and geometric features are used typical average percentages of correct classification of 90% for the ARL-ASAR data and 75% for the MSTAR data are found. Also, in this case feature enhanced processing did not have much effect on the results.

Concluding we can say that feature enhanced processing helps to improve discrimination results when no pose estimation is available. However, in this study feature enhanced processing does not help to obtain more accurate aspect angle information or to obtain better discrimination results per aspect interval. For this study we have chosen one particular way to extract and to process features. Feature enhanced processing opens more possibilities to handle features and this comparative study was not intended to optimize feature extraction and processing using feature enhanced imagery. Also, feature enhanced processing enables the enhancement of point scatterers, target extent, while reducing the background, which is clearly an advantage for visual inspection and interpretation.

7.0 REFERENCES

[1] A.C. Broek, van den, R.J. Dekker, T.P.H. Steeghs, “Robustness of Features for Automatic Target Discriminaton in High Resolution Polarimetric SAR Data”, *Algorithms for Synthetic Aperture Radar Imagery X, Proc. of SPIE, Vol. 5095, 2003*, pp. 242-253.

[2] A.C. van den Broek, R.J. Dekker, W.L. van Rossum, A.J.E. Smith, and L.J. Ewijk, “Feature extraction for automatic target recognition in high resolution and polarimetric SAR imagery”, *TNO report, FEL-00-A2366, 2001*.

[3] M. Çetin, W.C. karl, and D.A. Castañon, “Analysis of the Impact of Feature-Enhanced SAR Image on ATR Performance”, *Proc.of the SPIE Conference on Algorithms for SAR imagery, IX*, *vol.4742, Orlando, FL, April 2002*

[4] C.C. Chen and H.C. Andrews, "Multifrequency Imaging of Radar Turntable Data", *IEEE Trans. on Aerosp. Electron. Syst., Vol. 16, No. 1*, pp. 15-22, 1980.

[5] R.O. Duda and P.E. Hart, *Pattern Classification and Scene Analysis*, John Wiley and Sons, New York, 1973.

[6] D.E. Kreithen, S.D. Halversen, and G.J. Owirka, *"Discriminating Targets from Clutter", Lincoln Laboratory Journal, Vol. 6, No. 1*, pp. 25-52, 1993.

[7] L.M. Novak and S.R. Hesse, "On the performance of order-statistics CFAR detectors", *IEEE Conference Record of the 25th Asilomar Conference on Signals, Systems and Computers, Vol.2*, pp. 835-840, 1991.

[8] Plotnick, R.E., Gardner, R.H., and O'Neill, R.V., 1993, Lacunarity indices as measures of landscape texture, *Landscape Ecology, Vol. 8*, 201-211.

A Numerical Model of ISAR Distortion and an Efficient Procedure for Restoring Distorted ISAR Images

S. Wong, E. Riseborough and G. Duff
Defence R&D Canada – Ottawa
3701 Carling Ave. Ottawa, Ontario, Canada K1A 0Z4

silvester.wong@drdc-rddc.gc.ca

ABSTRACT

Distortion in the ISAR image of a target is known to cause by non-uniform rotational motion of the target during image formation. The conventional explanation describes the image distortion as a quadratic phase distortion effect. This quadratic phase distortion effect is significant only when the target image is integrated over an extended period of time; i.e., over a large angular rotation by the target. In many measured ISAR images such as those from in-flight aircraft, the distortion can be quite severe; but the image integration time is only a few seconds in duration and the target's relative rotational displacement is only a few degrees at the most. Quadratic phase distortion is not adequate in explaining the severe blurring in many of these observations. Furthermore, time-frequency analysis of the distorted images often reveals that the Doppler frequency of the target is fluctuating randomly in nature and displays no quadratic phase behaviour temporally. A numerical model based on a time-varying target rotation rate has been developed to model the observed distortion. It has successfully modelled the severe distortion with all the observed characteristics. The model's simulated results have been validated by experimental data. The severe distortion is attributed to the phase modulation effect where a time-varying Doppler frequency provides the smearing mechanism. It has been shown that the quadratic phase distortion can be considered as a special case of the phase modulation effect. The distortion in ISAR images can be refocused by signal processing techniques. Time-frequency methods, in particular, are quite effective in refocusing distorted (or blurred) ISAR images. In time-frequency processing, an ISAR image of a target is extracted at a particular instant of time; a focused image is thus obtained because the target's motion can be considered as relatively uniform over a short duration. However, there are a large number of time instants to deal with in time-frequency processing. It is impractical to examine all refocused ISAR images to search for the best images. An efficient ISAR refocusing procedure has been developed. An optimum refocused image can be obtained quickly without having to process systematically a large number refocused ISAR images. Examples of refocused ISAR images are given using measured data.

1.0 INTRODUCTION

Inverse Synthetic Aperture Radar (ISAR) imaging provides a 2-dimensional radar image of a target. A 2-dimensional picture can potentially offer crucial distinctive information about the features of the target that can lead to more accurate target identification in Non-Cooperative Target Recognition application. An ISAR image is generated from the target's rotational motion. This motion can sometimes be quite complex, such as the motion of a fast, maneuvering jet aircraft. As a result, severe distortion can occur in the ISAR image of the target [1]. An illustration is shown in Figure 1. Two ISAR images of an in-flight aircraft were taken in a consecutive sequence in time. The image on the left (a) is severely blurred; the image on the right (b) is well

Paper presented at the RTO SET Symposium on "Target Identification and Recognition Using RF Systems", held in Oslo, Norway, 11-13 October 2004, and published in RTO-MP-SET-080.

focused. It has been recognized that a time-varying perturbed motion in the rotation of the target is responsible for the image blurring [2]. Figures 2a and 2b show the azimuth displacements of the same aircraft in Figure 1 as a function of time as recorded independently by a ground-truth instrument mounted on-board of the aircraft. In addition, the temporal phase history of a scattering centre on the aircraft for both the blurred and focused ISAR images also display the same behaviour as the azimuthal motion of the aircraft; this is illustrated in Figures 2c and 2d. It can be seen clearly that there is a direct correspondence between the distortion in the ISAR image and the temporal motion of the target.

Conventional ISAR model attributes the ISAR image distortion to a quadratic phase effect. This quadratic phase is a consequence of a circular motion of target with respect to the radar, resulting in a non-constant Doppler velocity introduced along the radar's line of sight due to acceleration of the target from the circular motion [3]. Quadratic phase distortion does not provide an adequate account of the severe blurring in many of the observations from real targets. Furthermore, time-frequency analysis of the distorted ISAR images often reveals that the motion of the target is fluctuating randomly in nature and displays no quadratic temporal behaviour. In order to obtain a better understanding of the severe distortion in ISAR images, we have developed a numerical model that is based on a time-varying target rotational motion. It will be shown that this model provides a very accurate representation of the distorting mechanism. The model links the distortion phenomenon to a phase modulation effect in the returned radar echo from the target.

In this paper, a description of the ISAR distortion model based on the phase modulation effect will be presented. It will be shown that the quadratic phase distortion can be seen as a special case of phase modulation. An experiment is set up to study the ISAR distortion. Controlled experiments are performed to demonstrate the severe distortion. The experimental data are used to compare and validate the model's simulated results, showing that the phase modulation effect is a reasonable model. An efficient procedure has also been developed, based on the insights gained from the modelling work, to allow a distorted image to be restored quickly. The restoration of distorted ISAR images is relevant and useful in target recognition applications that exploit ISAR imagery.

2.0 ISAR DISTORTION EXPERIMENTS

An ISAR experiment is designed and set up to examine distortion in ISAR images due to time-varying rotational motion. There are a number of reasons why data from a controlled experiment are desirable. In a controlled experiment, the locations of the scattering centres of the target are known precisely and the rotational motion of the target can be programmed to produce the effects that are sought for analysis. Moreover, experiments of a given set of conditions can be repeated to verify the consistency of the results. These are not always possible with real target such as an aircraft.

A delta-wing shaped apparatus, the Target Motion Simulator (TMS), has been built for the ISAR distortion experiments. A picture of the TMS target is shown in Figure 3. The target measures 5 m on each of its three sides. Six trihedral reflectors are mounted on the TMS as scattering centres of the target. A time-varying rotational motion can be introduced by a programmable motor drive. ISAR images of the TMS are collected using a stepped frequency radar waveform at X-band (8.9 GHz to 9.4 GHz). Figure 4 shows a schematic of the experimental set-up. A sequence of ISAR images of the TMS apparatus are shown in Figure 5 as the target makes a transition from a constant rotation to a time-varying rotational motion. The ISAR image is well focused with the 6 reflectors shown clearly when the target is rotating with a constant motion of about 2.0 degrees/s; this is illustrated in Figure 5a. The ISAR images then become distorted when a fluctuating motion is added to the motion of the target as seen in Figures 5b and 5c. This fluctuating motion is shown in Figure 6 and is extracted from the distorted ISAR using time-frequency method [5].

3.0 ISAR DISTORTION MODEL

A numerical model has been developed to simulate the distorting effect of a multi-scatterer target. To simplify the problem, we will consider just one scatterer on the target in describing the model to bring out the basic mechanism more clearly without any loss of generality. The phase of the radar return signal from a scatterer on a moving target is given by,

$$\phi = \frac{4\pi f}{c}\left(R - vt - X(t)\right) \tag{1}$$

where f is the transmitting radar frequency, R is the initial distance of the scatterer on the target from the radar at the on-set of the radar imaging scan, v is the radial velocity of the target and $X(t)$ is the displacement due to the rotation of the target along the radar's line of sight. For simplicity, we consider either a stationary target or perfect translational motion compensation; i.e., v is set to zero. In other words, we focus only on the rotational aspect of the target in forming the ISAR image. Moreover, we assume the rotational axis of the target is perpendicular to the radar line of sight to simplify the geometry.

Consider a scatterer on a 2-dimensional target with a pair of coordinates (x_0 , y_0) with respect to the target's rotational axis. This is shown in Figure 7. A change in the scatterer's coordinates due to rotation at a later time t is given by

$$\begin{pmatrix} x(t) \\ y(t) \end{pmatrix} = \begin{pmatrix} \cos(\omega(t)\,t) & -\sin(\omega(t)\,t) \\ \sin(\omega(t)\,t) & \cos(\omega(t)\,t) \end{pmatrix} \begin{pmatrix} x_0 \\ y_0 \end{pmatrix} \tag{2}$$

Hence, the displacement along the radar's line of sight $X(t) = x(t) - x_0$ due to a rotation of the target is given by

$$X(t) = \left(x_0 \cos(\omega(t)\,t) - y_0 \sin(\omega(t)\,t) \right) - x_0 \tag{3}$$

A fluctuating motion can be described, in general, by a Fourier series; i.e.,

$$\omega(t) = \omega_0 + \sum_{n=1}^{\infty} \left(a_n \sin(2\pi\Omega_n t) + b_n \cos(2\pi\Omega_n t) \right) \tag{4}$$

where ω_0 is the constant rotational rate of the target in the absence of any extraneous fluctuating motion, a_n , b_n and Ω_n can be considered as the random variables for fitting $\omega(t)$ to any fluctuating motion.

An ISAR image is generated using a sequence of HRR profiles. The HRR profile of a scatterer is given by [4],

$$H_n = A_n \exp\left(j \frac{4\pi f_c}{c} (R - X(t)) \right) \tag{5}$$

where A_n is the amplitude of the HRR profile , n is the range-bin index, f_c is the center frequency of the radar bandwidth. R and $X(t)$ are defined in Equation (1). A Fourier transform is performed at each of the range bins over the sequence of HRR profiles to generate an ISAR image; i.e.,

$$I_{n,m} = \sum_{k=0}^{M-1} A_{n,k} \exp\left(j \frac{4\pi f_c}{c} (R - X(t)) \right) \exp\left(j \frac{2\pi}{M} mk \right) \tag{6}$$

where m is the cross-range bin index, $m = 0, \ldots, M\text{-}1$. M is the number of HRR profiles used in the generation of the ISAR image. Effectively, the Fourier transform converts the HRR variable at each range bin from the time domain into the frequency domain. Hence, the cross-range axis of the ISAR image represents the Doppler frequency as observed by the radar. The term that is of interest in the analysis of the ISAR image is the factor containing the temporal rotational motion in Equation (6); i.e.,

$$\begin{aligned} \psi(t) &= \exp\left(-j \frac{4\pi f_c}{c} X(t) \right) \\ &= \exp\left[-j \frac{4\pi f_c}{c} \left(x_0 \cos(\omega(t)t) - y_0 \sin(\omega(t)t) \right) - x_0 \right] \end{aligned} \tag{7}$$

where $X(t) = x(t) - x_0$ is the change in range of the scatterer with respect to the radar along the radar's line of sight. Normally, the ISAR image of a target is captured during a relatively small rotation of the target; for example, the ISAR images generated in Figure 1 correspond to a rotation of about 3 degrees, as indicated in Figure 2. Thus, a small rotation approximation can be assumed (i.e., $\omega(t)t << 1$), to simplify the mathematical description. This helps to bring out the phase modulation effect a bit more clearly. Equation (7) then becomes

$$\psi(t) = \exp\left[-j \frac{4\pi f_c}{c} \left(x_0 \frac{(\omega(t)t)^2}{2} - y_0 \omega(t) t \right) \right] \tag{8}$$

It can be seen from Equation (8) there are two components that affect the phase due to a time-varying rotation, a first order term, $\omega(t)t$ and a second order term $(\omega(t)t)^2$. A further simplifying step is made by considering a time-varying rotational rate,

$$\omega(t) = \omega_0 + \omega_r \sin(2\pi\Omega t) \tag{9}$$

where ω_r is the rotational amplitude of the fluctuating motion and is a function of Ω, the oscillation frequency of the time-varying motion. This is equivalent to taking the first two terms of the Fourier series as given in Equation (4).

Consider a time instant when the scatterer is located $(0, y_0)$, the scatterer's motion is parallel to the radar's line of sight; see Figure (7). Thus this will have the largest Doppler effect as seen by the radar. Substituting Equation (9) into Equation (8),

$$\begin{aligned} \psi(t) &= \exp\left[+j \frac{4\pi f_c}{c} y_0 \left(\omega_0 + \omega_r \sin(2\pi\Omega t)t \right) \right] \\ &= \exp\left[+j \frac{4\pi f_c}{c} y_0 \omega_0(t) t \right] \exp\left[+j \frac{4\pi f_c}{c} y_0 \omega_r \sin(2\pi\Omega t)t \right] \end{aligned} \tag{10}$$

The first factor corresponds to a constant rotation of the target. This factor provides a Doppler shift that allows the placement of the scatterer along the cross-range axis to form an undistorted ISAR image of the target in the absence of any fluctuating motion. The second factor describes the phase modulation effect due to a small fluctuating motion of the scatterer that can introduce distortion. To see how the phase modulation effect comes about more clearly, the second phase factor in Equation (10) can be rewritten as,

$$\mu(t) = \exp\left(\; j \frac{4\pi f_c}{c} y_0 \omega_r \int \sin(2\pi \Omega t) \; dt \right) \tag{11}$$

$$= \exp(-j \; k \; \sin(\eta))$$

$$= \cos(k \sin(\eta)) - j \sin(k \sin(\eta))$$

$$= (J_0(k) + 2J_2(k)\cos(2\eta) + 2J_4(k)\cos(4\eta) + \ldots)$$

$$- j(2J_1(k)\sin(\eta) + 2J_3(k)\sin(3\eta) + 2J_5(k)\sin(5\eta) + \ldots)$$

where

$$k = \frac{4\pi f_c}{c} \; y_0$$

$$\eta = \sin^{-1}\left[\; -\omega_r \int \sin(2\pi \Omega t) \, dt \; \right]$$

and the J_n are the Bessel functions of the first kind of order n. It can be seen from Equation (11) that the phase of a time-dependent rotational motion consists of many higher order sideband components. These higher order sideband components are a consequence of phase modulation arising from the fluctuating motion and they generate a smear in the image as a result.

4.0 NUMERICAL ANALYSIS OF ISAR DISTORTION

Figure 8 shows the distorted ISAR image computed by the numerical model, using the experimental time-varying target motion as shown in Figure 6 as input. The target has rotated about 8 degrees over a 4-s imaging period. It can be seen from Figure 8 that the computed distortion in the ISAR image compares quite well with that in the experimental image in Figure 5c.

A more physical description of how phase modulation leads to distortion can be seen as follows. It is well known that a scatterer will migrate along the cross-range axis in the ISAR image if the scatterer's Doppler frequency f_D is changed during the imaging period [3]. The number of cross-range bins migrated is given by,

$$K = abs\left(\frac{1}{\Delta f_D} (f_{D,t=0} - f_{D,t=T}) \right) \tag{12}$$

for a monotonically changing f_D, where Δf_D is the cross-range resolution. As a result, there will be a "smear" in the ISAR image of the scatterer along the cross-range axis when there is a change in the Doppler frequency during the imaging period. The radar line of sight Doppler frequency of a scatterer on the target will have an

oscillating behaviour due to the time-varying input that drives the target. Figure 9a shows the computed Doppler frequency of scatterer #1 from the distorted ISAR image in Figure 8. The amount of distortion generated at scatterer #1 is the same as the amount of change in the Doppler frequency; this is clearly seen in Figure 9. In this case, the amount of change in the Doppler frequency is ($f_{D,\,max}$ - $f_{D,\,min}$) over the imaging duration. This result is expected since the cross-range dimension of the ISAR image is effectively the Doppler frequency as explained in Section 2.

Note that scatterer #6 in the ISAR image in Figure 8 has hardly any distortion. It corresponds to a scatterer located at (x_0, 0); see Figure 7. The phase of scatterer #6, according to equation (8), is given by,

$$\psi(t) = \exp\left[-j \frac{4\pi f_c}{c} x_0 \frac{(\omega(t)t)^2}{2} \right] \tag{13}$$

That is, the phase is quadratic in $\omega(t)t$. The Doppler frequency of scatterer #6 is illustrated in Figure 10a. Comparing with scatterer #1 (Figure 9a), the change in the Doppler frequency of scatterer #6 is very small; hence there is no noticeable distortion. Thus, the second order term $(\omega(t)t)^2$ has negligible distorting effect compare to the first order term $\omega(t)t$ in Equation (8). To summarize briefly, a scatterer with a changing Doppler frequency due to the target's time-varying motion provides the physical basis for the large distortion in the ISAR image. The model's simulated results are validated by the experimental data, demonstrating that phase modulation provides an accurate picture of the distortion mechanism.

The conventional quadratic phase distortion effect [3] can be considered as a special case of the phase modulation effect. The quadratic phase distortion assumes a target's rotational motion is constant during the imaging period; that is, $\omega(t) = \omega_0$ in Equation (9). Any change in the Doppler frequency by any of the scatterers on the target is due to a non-linear Doppler velocity introduced along the radar's line of sight as a result of acceleration from the rotational motion. This can be seen by substituting $\omega(t) = \omega_0$ into Equation (8). The phase of the rotating scatterer becomes

$$\psi(t) = \exp\left[-j \frac{4\pi f_c}{c} \left(x_0 \frac{(\omega_0 t)^2}{2} - y_0 \omega_0 t \right) \right] \tag{14}$$

Examining a scatterer located at (0, y_0) on a target as shown in Figure 7, Equation (14) becomes,

$$\psi(t) = \exp\left[j \frac{4\pi f_c}{c} y_0 \omega_0 t \right] \tag{15}$$

That is, $\psi(t)$ is a perfect linear phase in time. Therefore, the Doppler frequency is a constant. In other words, for scatterers that have motions nearly parallel to the x-axis, their Doppler frequency will have very little change and thus there will be very little distortion according to Equation (12). For a scatterer located at (x_0, 0), Equation (14) becomes

$$\psi(t) = \exp\left[-j \frac{4\pi f_c}{c} x_0 \frac{(\omega_0 t)^2}{2} \right] \tag{16}$$

Equation (16) displays a phase with a quadratic dependence in time. Hence the Doppler frequency will be changing with time, resulting in a blur in the ISAR image according to Equation (12).

To see how much a distorting effect the quadratic phase would have on the ISAR image, a constant ω_0 value corresponds to the maximum value of the experimental rotational rate, $|\omega_{\max}| = 3.9$ deg./s as given in Figure 6, is used to run the numerical model for the TMS target. The resulting ISAR image is shown in Figure 11. The amount of distortion in the image is much less than that of the case when a time-varying rotational rate $\omega(t)$ is used. This is quite evident by comparing Figure 11 with Figure 8.

Another interesting observation that is worthy to note is that in the quadratic phase distortion case, the largest distortion occurs at scatterer #6 of the target as seen in Figure 11. The large distortion at scatterer #6 can be explained by the fact that the rate of change of the Doppler frequency is maximum for a scatterer that is located near the x-axis in a rotational motion as depicted in Figure 7. At the location (x_0 , 0) and using Equation (2), the movement of scatterer #6 parallel to the x-axis is given by

$$x(t) = x_0 \cos(\omega_0 t) \tag{17}$$

Its velocity parallel to the x-axis is

$$v_x = \frac{dx(t)}{dt} = -x_0 \omega_0 \sin(\omega_0 t) \tag{18}$$

Hence, $v_x = 0$ at the initial position (x_0, 0) and time $t = 0$. The velocity of scatterer #6 is perpendicular to the x-axis. This is intuitively obvious as shown in Figure 7. However, the rate of change of v_x

$$\frac{dv_x}{dt} = -x_0 \omega_0^2 \cos(\omega_0 t) \tag{19}$$

is maximum at (x_0, 0) because $\cos(\omega_0 t) = 1$ at $t = 0$.This implies that the Doppler frequency of scatterer #6 has the largest change along the x-axis; therefore a large distortion occurs as a result.

To illustrate the quadratic phase distortion's dependence on $(\omega_0 t)^2$, the ISAR image in Figure 11 is generated using a generously large ω_0 value; i.e., $\omega_0 = 3.9$ degrees/s. This corresponds to a target rotation of 15.6 degrees over a 4-second imaging time. In the time-varying rotating case (Figure 8), the target rotation is only 8.2 degrees over the 4-second duration. Using a ω_0 value corresponds to a target rotation of 8 degrees, the quadratic phase case is computed again using a lower ω_0 value of 2 degrees/s. The resulting ISAR image of the target is shown in Figure 12. It can be seen that none of the scatterers on the target shows any distortion in the image, even scatterer #6 which should display the most distortion. This result is consistent with the experimental ISAR image shown in Figure 5, where scatterer #6 displays no noticeable distortion. In summary, it is seen from the above analysis that the quadratic phase distortion effect is not adequate for describing the ISAR distortion that is seen in the experimental images. The quadratic phase effect is a second order effect (i.e,. $(\omega_0 t)^2$) and it produces a much smaller distortion than that from the phase modulation effect.

5.0 RESTORATION OF DISTORTED ISAR IMAGES

For target recognition applications, ISAR images of targets must have adequate spatial resolution. According to the principles of ISAR imaging, a long image integration time is required to produce fine image resolution. However, a long image integration time does not always guarantee good cross-range resolution. This is illustrated in the discussion above where it is found that the amount of blurring caused by non-uniform target motion over the imaging period can be quite severe.

Time-frequency techniques have been used to "refocus" blurred ISAR images [5]. As seen from the discussion above, the blurring of ISAR images is a consequence of a time-varying Doppler frequency resulting from non-uniform motion of the target. By extracting an ISAR image of the target at a particular instant of time, a better-focused image can be obtained because the target's motion can be considered as relatively uniform over a short duration. However, there will be a large number of time instants to deal with in most time-frequency processing. Thus, a large number of refocused ISAR images will emerge, corresponding to the number of time instances. For fast, efficient target recognition, it is desirable to make use of only the best refocused image. It is impractical to examine all available refocused ISAR images. Visual inspection manually over a large number of images, or even using an automated image search algorithm only adds complexity to the target recognition process.

A more efficient way to determine the optimum refocused ISAR image is possible, based on the insights obtained from the image distortion analysis conducted above. That is to say, it is found from the experimental and numerical analyses that the blurring is directly related to the amount of change in the Doppler frequency of the target during the imaging duration. This fact is used in the refocusing process. Figure 13 shows another distorted ISAR image of the TMS target. This image is chosen for its varied Doppler frequency over the imaging period. The corresponding temporal Doppler history of the target is shown in Figure 14.

Before discussing how an optimum refocused ISAR image can be determined, it is useful to take a look at samples of the refocused images at various time instants. A refocused ISAR image is reconstructed from the spectrograms of all the down-range bins of the distorted ISAR image at a chosen time instant. The spectrogram is computed using Short Time Fourier Transform (STFT) with a 0.4 s image integration time window. This is illustrated by the duration T in Figure 14. In other words, each time instant represents a 0.4s time segment. Thus it is more accurate to describe a time instant as a short duration of time rather than a precise point in time. Figure 15 shows the refocused ISAR images of the target at 6 time instants as indicated in Figure 14. The ISAR image at time t_a corresponds to the instance when the target has an uniform rotational motion. This image serves as a reference image for comparing with the refocused images at other time instances. Using a 0.4s STFT, the resolution is just barely adequate to resolve the scatterers on the target in the cross-range direction for the uniform rotation case at t_a. A quick inspection of Figure 15 reveals that the best refocused image is at the time instance t_e and the worst images are at t_c, t_d and t_f.

By understanding why the images are the worst at t_c and t_d and why the image is the best at t_e, we can develop an objective methodology on how to reconstruct the optimum refocused ISAR image. The ISAR image at t_c appears compressed. This is due to the small Doppler frequency (i.e., small angular rotational rate) of the target at this time instant. It is even smaller than the uniform rotation case at t_a; this is illustrated in Figure 14. The Doppler motion is too small to separate the scatterers adequately in the cross-range direction. The ISAR images at time t_d and t_f still appear blurry, with some of the scatterers still not properly focused. This is attributed to the fact that the Doppler motion of the target is going through a large temporal rate of change within these time instants, i.e., $\Delta f / \Delta t$ is large.

The ISAR image at t_e has all six scatterers on the target clearly resolved and provides the best-refocused image. There are two reasons why the best image quality is found at time instance t_e. Firstly, the Doppler motion is large, significantly larger than the uniform rotational rate case at the time instant t_a (see Figure 14). Hence the scatterers are much better separated by the large angular rotational rate in the cross-range. Secondly, the temporal rate of change of the Doppler motion in the time interval at t_e is small; i.e., $f/\Delta t$ is small. Therefore, the blurring to the image of the scatterer is kept to a minimum. The STFT window T for time instant t_e is indicated in Figure 14. It can be seen that the Doppler motion varies very little within time instant t_e.

Based on the analysis of the refocused images shown in Figure 15, we have deduced a few simple physical rules that will enable us to extract a relatively well focused image from a blurred ISAR image:

1. From the blurred image, locate a down-range bin where it contains the most severe blurring in the cross-range.

2. Produce a time-frequency spectrogram at the chosen down-range bin, using Short-Time Fourier transform or time-frequency distribution functions [6].

3. From the spectrogram, select a time instance when the variation of the Doppler motion is small (i.e., small $f/\Delta t$) and the value of the Doppler motion is large (i.e., as far away from the zero Doppler frequency as possible).

4. Construct spectrograms at all down-range bins from the blurred ISAR image that contain the target. Recombine the same time instance from all spectrograms to reconstruct a focused ISAR image.

This procedure provides a much faster means of constructing an optimum refocused image. This is because once the appropriate time instance is determined, only one ISAR image needs to be reconstructed. This is obviously much more efficient than extracting ISAR images at all time instances from all spectrograms because the number of time instances is usually very large. Another interesting note is that having a large amount of blurring in the ISAR image may actually be better than having just a small amount of blurring for restoring a focused image. A more severe blurring means that at some time instant, there is a large Doppler motion that can be exploited to get a better-resolved image.

6.0 CONCLUSIONS

From the results of the numerical analysis and the comparison with experimental data, it can be concluded that phase modulation effect can be modelled properly by including the temporal variation of the target's motion in its angular rotational rate. That is to say, the angular rotational velocity must be described as a function of time; i.e.,$\omega(t)$ so that an instantaneous Doppler velocity can be ascribed at any given time. The conventional quadratic phase distortion is shown to be a special case of phase modulation and it is a second order effect. The quadratic phase distortion is much smaller than that from phase modulation where a target displaces only a few degrees in angular rotation during the ISAR imaging period. The distorted image can be refocused using time-frequency analysis methods. An efficient procedure to find the best refocused image from a severely blurred image has been developed and demonstrated.

7.0 REFERENCES

[1] T. Sparr, S-E. Hamran and E. Korsbakken, "estimation and Correction of Complex Target Motion Effects in Inverse Synthetic Aperture Imaging of Aircraft", IEEE Radar 2000 Conference, pp.457-462, USA, May 2000.

[2] V. C. Chen and W. J. Miceli, "Simulation of ISAR imaging of moving target", IEE Proc. – Radar, Sonar and Navigation, Vol. 148, No.3, pp160-166, June 2001.

[3] D. Wehner, "High Resolution Radar", Artech House, Boston, 1987.

[4] S. K. Wong, G. Duff and E. Riseborough, "Distortion in the inverse synthetic aperture radar (ISAR) images of a target with time-varying perturbed motion", IEE Proc. Radar, Sonar and navigation, Vol.150, No.4, pp.221-227, August 2003.

[5] V. C. Chen and H. Ling, "Time-Frequency Transform for Radar Imagery and Signal Analysis", Artech House, Boston, 2002.

[6] Leon Cohen, "Time-Frequency Distributions – A Review"; Proceedings of the IEEE, Vol.77, No.7, pp.941-980, July 1989.

ACKNOWLEDGEMENTS

Financial support by Dr. William Miceli of the US Office of Naval Research–International Field Office under the NICOP program is gratefully acknowledged.

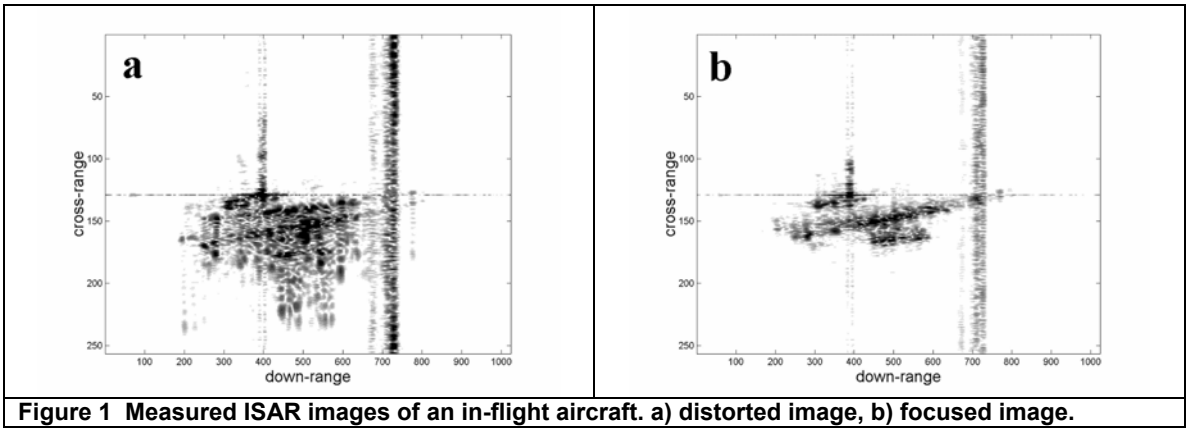

Figure 1 Measured ISAR images of an in-flight aircraft. a) distorted image, b) focused image.

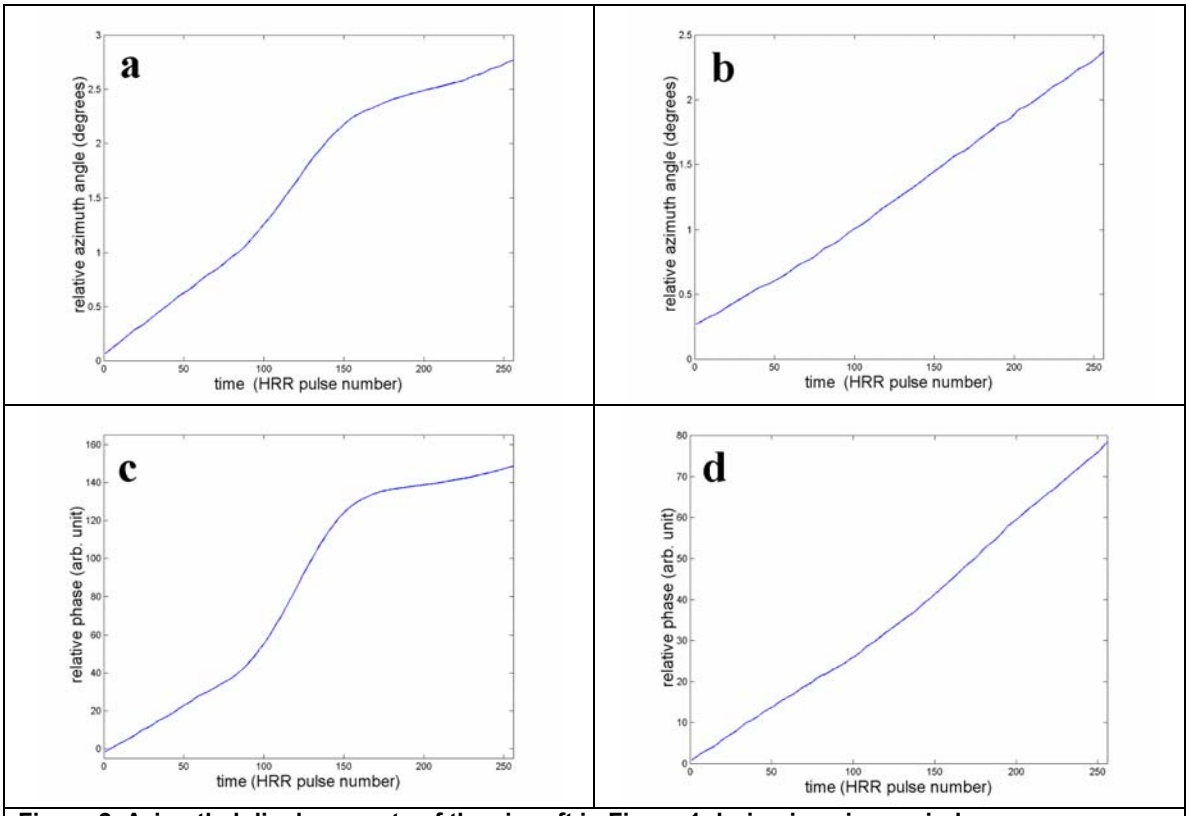

Figure 2 Azimuthal displacements of the aircraft in Figure 1 during imaging period:
a) distorted image, b) focused image.
Temporal phase history of a scattering centre on the aircraft: c) distorted image, d) focused image.

Figure 3 The Target Motion Simulator (TMS) experimental apparatus.

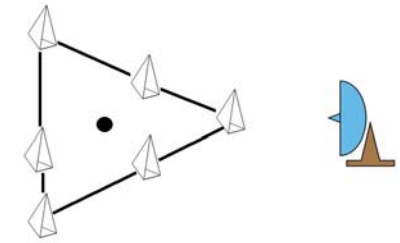

Figure 4 Schematic of the ISAR imaging experimental set-up.

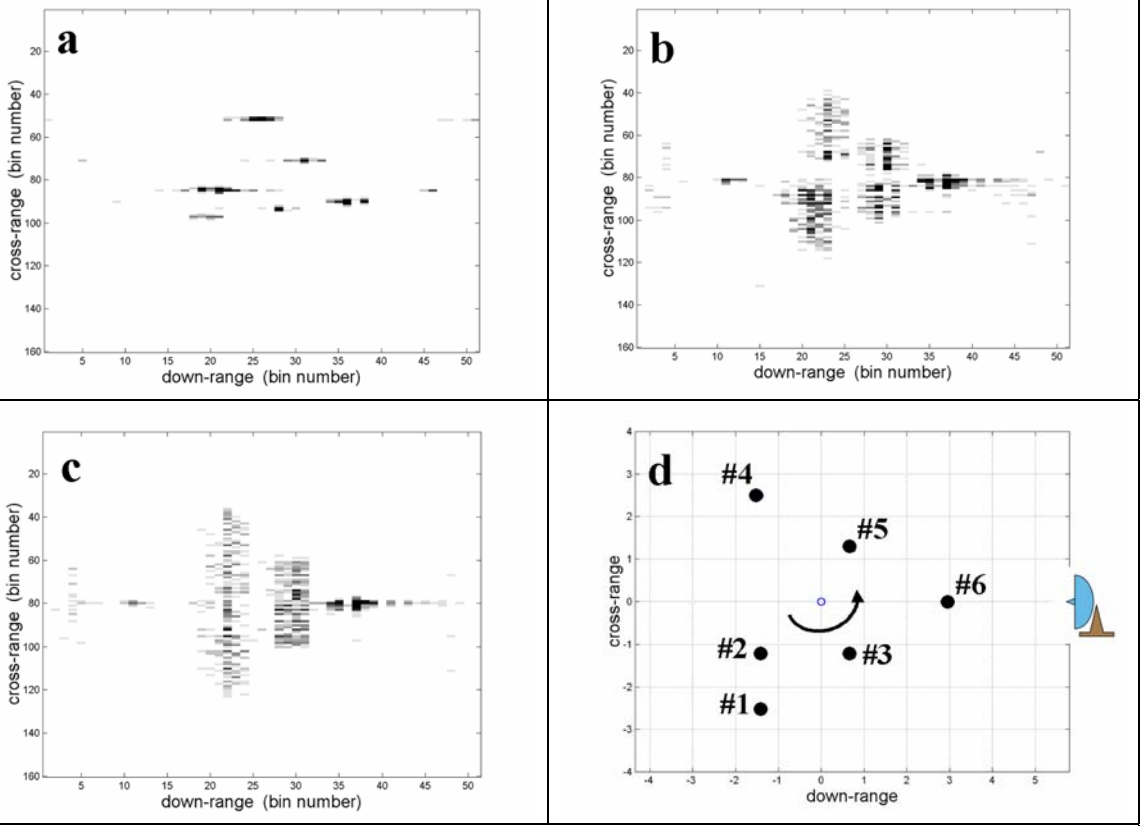

Figure 5 A sequence of measured ISAR images of the TMS target. a) constant rotation at 2 degrees/s, b) oscillating motion introduced to the target's rotating motion, c) target with oscillating motion at a later time, d) the TMS target's orientation with respect to the radar for ISAR image in c). The target is rotated in the counter-clockwise direction.

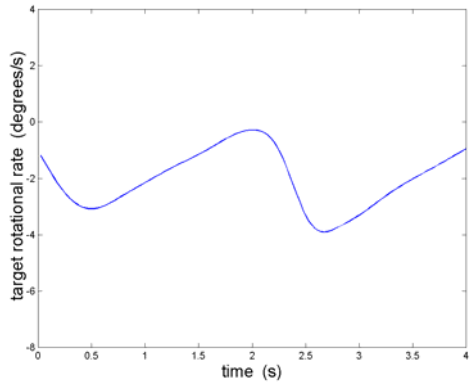

Figure 6 Measured temporal motion of the Target Motion Simulator.

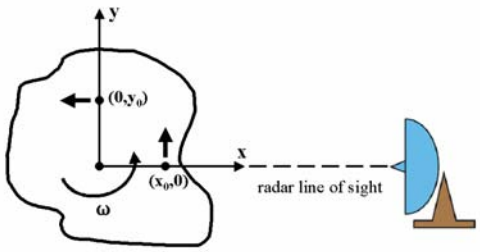

Figure 7 Schematic of a rotating target with examples of two scattering centres illustrated.

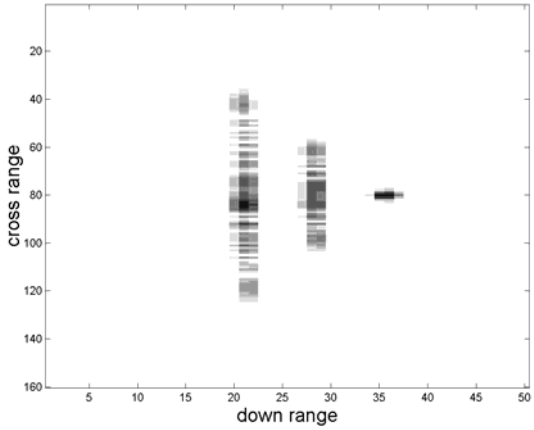

Figure 8 Computed distortion in the ISAR image using the phase modulation model. See and compare with the experimental image in Figure 5c.

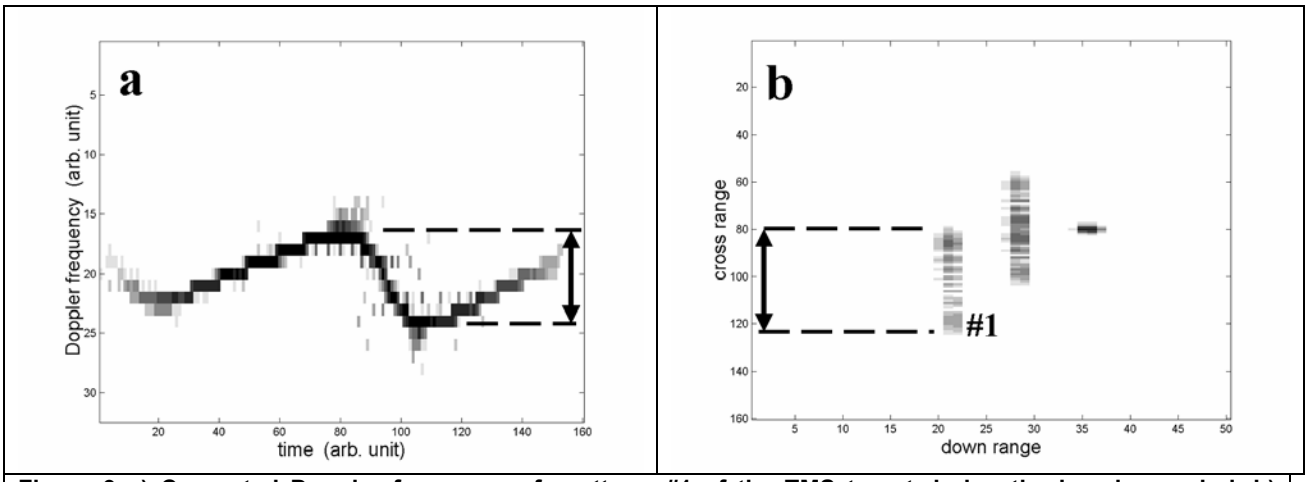

Figure 9 a) Computed Doppler frequency of scatterer #1 of the TMS target during the imaging period, b) Computed ISAR image of the TMS target with scatterers #2 and #4 removed in the computation. The amount of distortion of scatterer #1 corresponds to the amount of change in the Doppler frequency.

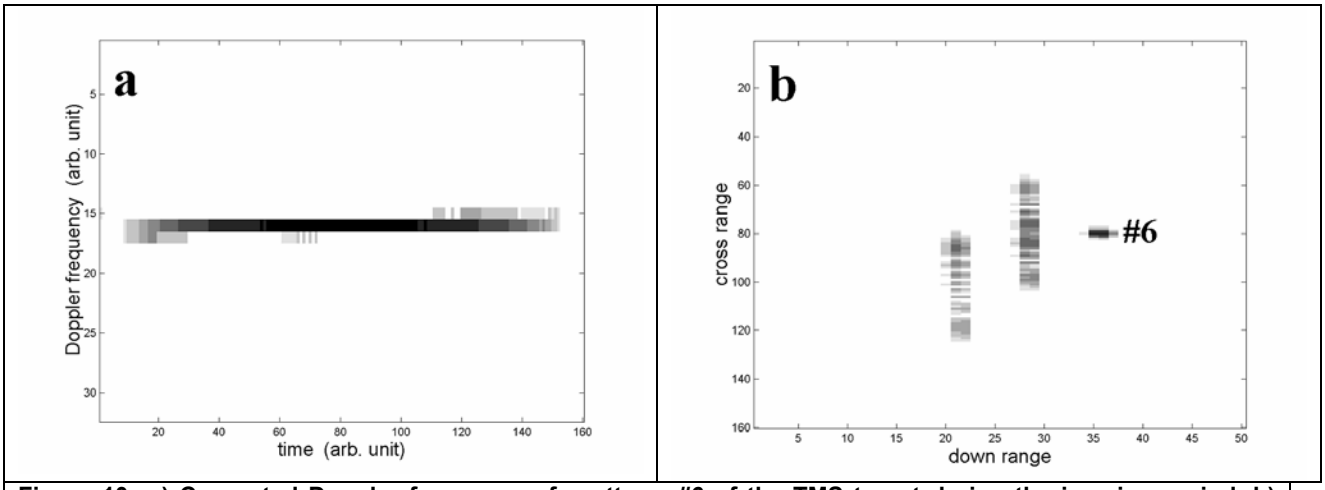

Figure 10 a) Computed Doppler frequency of scatterer #6 of the TMS target during the imaging period, b) Computed ISAR image of the TMS target with scatterers #2 and #4 removed in the computation. The amount of distortion of scatterer #6 corresponds to the amount of change in the Doppler frequency.

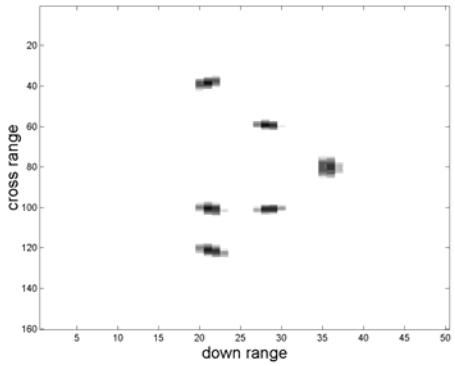

Figure 11 ISAR image of the TMS target using a constant rotational rate of 3.9 degrees/s.

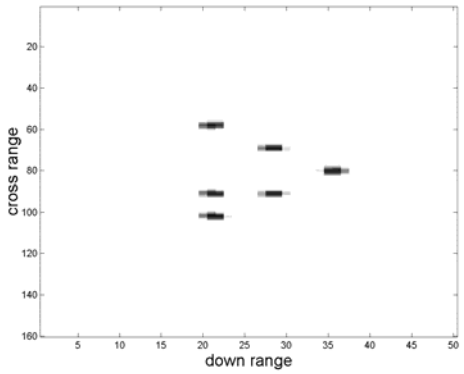

Figure 12 ISAR image of the TMS target using a constant rotational rate of 2 degrees/s.

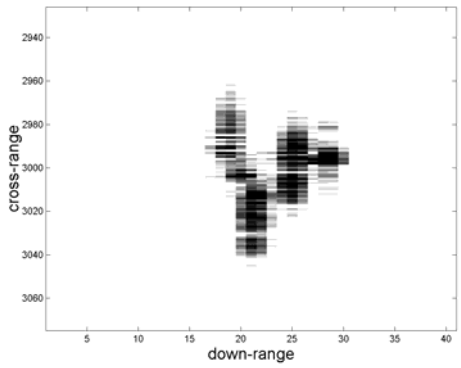

Figure 13 Distorted ISAR image of the TMS target (experimental).

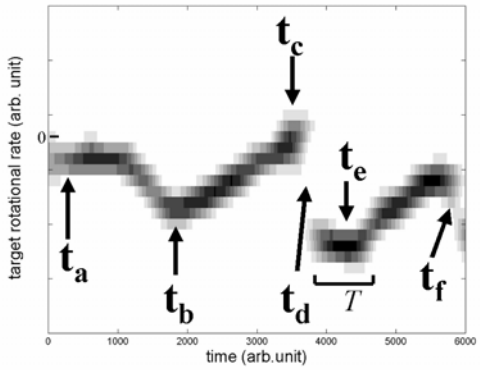

Figure 14 The temporal motion of the target corresponding to the distorted ISAR image in Figure 13. T is the STFT duration.

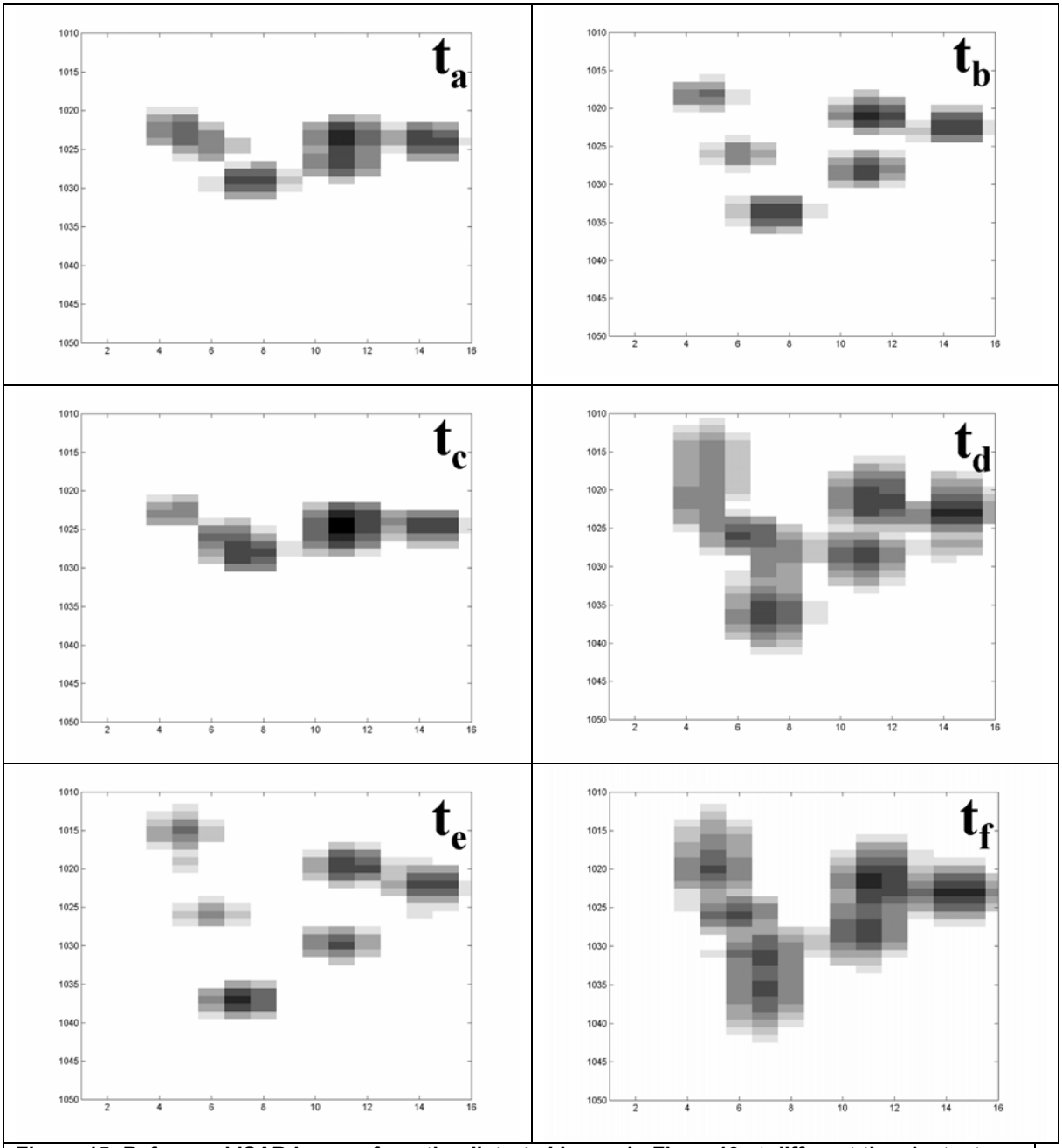

Figure 15 Refocused ISAR images from the distorted image in Figure13 at different time instants as indicated in Figure 14.

Experimental Facility for Measuring Aircraft Inlet/Engine Radar Cross Section

S. Wong, E. Riseborough and G. Duff
Defence R&D Canada – Ottawa
3701 Carling Ave., Ottawa, Ontario
Canada K1A 0Z4

K. K. Chan
Chan Technologies Inc.,
15 Links Lane, Brampton, Ontario
Canada L6Y 5H1

ABSTRACT

A full-size aircraft engine-duct mock-up experimental apparatus has been built to collect cavity radar cross section (RCS) data on aircraft engine inlets. The engine-duct structure is made up of a cylindrical duct with a single fan stage consisting of 30 generic straight fan blades. Experimental results indicate that the azimuthal RCS patterns from the engine-duct are quite complex. Numerical computations using a commercial RCS prediction code are compared with the measured data. The comparisons between measured and computed data have highlighted some of the problems and difficulties currently encountered in cavity RCS modelling. These results indicate that engine-duct RCS modelling is a very challenging problem.

1.0 INTRODUCTION

A recent research effort in Non-Cooperative Target Recognition within the Combat ID community involves the development of a synthetic target signature database for target classifiers. For various technical reasons, a synthetically generated database is regarded as the most practical way of fielding an operational target classifier system [Ref. 1]. Synthetic target signatures are computed using high frequency electro-magnetic radar cross-section (RCS) prediction codes. There has been a great deal of research activities in recent years focusing on cavity RCS modelling of aircraft inlet/engine interface. It has been known that the inlets of aircraft produce a significant RCS contribution to the overall RCS of an aircraft [Ref. 2]. Therefore, cavity RCS computation should be an integral part of the synthetic signature generation process of aircraft.

Although there are many in-depth cavity modelling efforts being conducted in the Combat ID community [Ref. 3], there is still a lack of readily available experimental data to validate the numerical analyses. Moreover, there is virtually no experimental data on full-size engine-duct model available, even in the open literature. In order for the numerical modelling results to be deemed as credible and reliable, they must be validated by experimental data. Sub-scale inlet model data have been found to be unreliable as a predictor of full-scale results [Ref. 4]. Hence for practical aircraft inlet RCS modelling, full-scale experimental data are desirable and pertinent to synthetic target signature generation. Furthermore, we are developing a numerical model for aircraft engine/inlet RCS based on the modal method [Ref. 5, 6, 7]. This modal approach in

Paper presented at the RTO SET Symposium on "Target Identification and Recognition Using RF Systems", held in Oslo, Norway, 11-13 October 2004, and published in RTO-MP-SET-080.

modelling the radar backscattering permits computations on full-size engine-duct structure. To overcome the shortage problem of measured data, we have designed and built a full-size generic aircraft engine-duct mock-up for collecting cavity RCS data.

Computations from a commercial RCS prediction code are compared with the measured data. This permits an assessment of the capability of the current high frequency electro-magnetic RCS computational technology for predicting cavity RCS from targets.

2.0 EXPERIMENTAL SET-UP OF THE ENGINE-DUCT MOCK-UP

All components in the engine-duct mock-up are made of simple geometrical shapes. The inlet duct is a metallic cylinder with a 0.7 m diameter. The length of the duct can be varied up to 2m. The roundness of the cylindrical duct is reinforced by mounting the duct in a wooden circular brace structure. The "engine" is represented by a single fan stage consisting of 30 fan blades. The fan blades are simple, flat metal stripes and have dimensions of 24.6 cm in length, 10.4 cm in width and 0.16 cm in thickness. They are cut using a stencil to ensure all the fan blades are identical. The fan shaft and the nose cone are machined out of solid metal blocks for symmetry and structural rigidity. Great care has been exercised in mounting the fan blades onto the fan shift so that the fan stage is as symmetrical as possible. Each blade is set at a 45-degree angle with respect to the axial axis of the duct. An exposed view of the engine-duct CAD (Computer Aided Design) model is shown in Figure 1. The simple geometry of the engine-duct structure allows measured data to be compared with numerical results in a meaningful and definitive manner. Moreover, the simple geometry of the engine-duct mock-up permits the structure to be built with a greater degree of symmetry. It will be seen later that the symmetry of the experimental apparatus is crucial to collecting meaningful measured data.

The engine-duct mock-up is mounted on a rotating platform. A computer controlled stepping motor is used to drive the rotating platform. The rate of rotation can be varied but is nominally set at 1 degree/s for the RCS measurements. The rotational rate is consistent to within 2 seconds over a 180-second duration over many trial runs. With the stepping motor controlled by the computer, the position of the rotating platform can be reset to the original position almost perfectly. Any positional error in the re-setting of the turntable comes from the backlash of the gearing system. But the backlash error is very small and it takes many runs before a 1 to 2-degree re-setting error is noticed. RCS measurements of the engine-duct mock-up are collected at X-band radar frequencies. The radar frequency can be varied from 8.9 GHz to 9.4 GHz. The radar pulse repetition rate (PRF) is operated at 1kHz (i.e., 1000 measured data points per second) and the received radar signals have a HH polarization.

To ensure that the backscattered radar signal collected is returning from inside the duct only, the exterior of the engine-duct mock-up is covered by radar absorbing material (RAM). A photo of the engine-duct mock-up is shown in Figure 2. The RAM tiles are effective in the 8 to 10 GHz radar frequency region. A background check is conducted to verify that no spurious radar return is detected from the engine-duct. This is done by covering the duct entrance with RAM tiles and a RCS measurement is made by rotating the engine/inlet mock-up from –60 to +60 degrees in the azimuth direction (i.e., horizontally). The background RCS measurement is shown in Figure 3. It can be seen that the radar return is fairly constant over the 120- degree scanned azimuth angle, indicating that there is no spurious reflection from the engine-duct structure.

3.0 RCS MEASUREMENTS AND COMPUTATIONS FROM A SIMPLE DUCT

The duct is initially terminated with a flat plate only; i.e., no fan assembly inside the duct. As a first step, the flat plate termination offers a simpler engine duct geometry that makes it easier for comparing the RCS results

between measured and numerical data. This helps to establish a definitive reference to determine whether the basic scattering processes are being modelled reasonably in the numerical RCS code. An azimuthal RCS measurement of the engine duct is made, scanning from –60 to +60 degrees. The terminating flat plate is located 1m from the duct entrance. The radar frequency is at 8.9 GHz. Figure 4 (solid curve) shows the measured RCS of the engine duct as a function of azimuth angle. The flat plate is then moved back to 1.9m from the duct's entrance and another RCS measurement is made. The azimuthal RCS scan is shown in Figure 5 (solid curve). In both Figures 4 and 5, the RCS peaks on both sides of the zero azimuth-angle can be viewed as side lobes of the circular aperture Airy function of the flat plate, modified by reflections off the wall of the duct. Note that the measured RCS scans are quite symmetrical with respect to the zero azimuth-angle. The signal-to-noise ratio of the measured RCS signal is quite good. The signal is as much as 30dB above the noise floor in comparing with the background noise scan as shown in Figure 3.

A commercial electromagnetic RCS prediction code is used to compute the backscattered RCS from the duct. The RCS code employs the shoot-and-bounce ray tracing technique to compute the backscattered RCS from an object. The dashed curves in Figures 4 and 5 show the computed RCS of the duct with a terminating flat plate as a function of azimuth angle. It can be seen that the computed RCS patterns compare quite well with the measured data up to the first couple of major side lobes on both the positive and negative sides with respect to the zero azimuth-angle. As the azimuth angle is becoming more oblique, the RCS drops abruptly by more than 10dB in both the measured and computed RCS and the RCS patterns in these regions are no longer in agreement between the measured and computed data. However, it does not seem likely that the mismatches at large oblique azimuth angles are due to signal-to-noise issue in the measured data. The measured RCS values at large azimuth angles are still at least 10 dB above the noise floor as evident by comparing the measured RCS scans in Figures 4 and 5 to the noise floor reference as shown in Figure 3. Thus, the comparative results indicate that the computed RCS at large azimuth angle is becoming less accurate.

4.0 RCS MEASUREMENTS AND COMPUTATIONS WITH FAN ASSEMBLY

The fan assembly, i.e., fan blades and nose cone, is inserted in the cylindrical duct and is placed 1.9m inside the duct. The duct is still terminated with a flat plate as the last element inside the duct. RCS measurements are taken at a radar frequency of 8.9 GHz. The results are shown in Figure 6. Figure 6a shows the RCS of the engine-duct mock-up with the fan assembly placed at an arbitrary initial position. The fan assembly is then rotated 10 fan blades over in a clockwise direction. Another RCS measurement is made and the RCS result is shown in Figure 6b. Figures 6c, and 6d correspond to RCS measurements with the fan assembly rotated 20, and 25 blades with respect to the initial position as given in Figure 6a. These experimental results reveal that the azimuthal RCS patterns with the fan stage in the duct are much more complex than a simple duct and the RCS amplitude scintillates very rapidly as the azimuth angle of the engine-duct is changed by only a very minute amount. Furthermore, the results displayed in Figure 6 also indicate that the RCS patterns are somewhat different when taken at different fan positions.

Intuitively, one would expect that these RCS patterns to be identical since the fan assembly is supposed to be symmetrical upon rotation. But the differences in the RCS patterns persist despite diligent efforts trying to make the fan assembly as symmetrical as possible mechanically. However, the RCS pattern is readily reproducible when the fan assembly is returned to any of the four previous specific positions. Thus, it appears that the backscattered RCS pattern from the engine-duct is very sensitive to the symmetry of the fan assembly. In spite of the apparent differences among the four RCS plots in Figure 6, all the RCS peaks occur at the same positions among the four different fan positions. Only the amplitudes of the RCS peaks fluctuate when the fan assembly is rotated. This is shown in the superposition of the four RCS plots in Figure 7 (light solid curves).

The experimental results also reveal that the measured RCS patterns are asymmetric in the azimuth scan. There are more peaks recorded between –60 to 0 degrees than between 0 to +60 degrees. This asymmetry may be attributed to a couple of factors. Firstly, the elevation angle of the engine-duct's azimuthal plane may not be horizontal with respect to the radar transmitter/receiver (i.e., elevation angle is not zero). In other words, the engine-duct may be slightly tilted upward or downward. It is very difficult to align the engine-duct perfectly to the radar. In fact, non-zero elevation angle will be the norm in virtually all real data from in-flight aircraft. Secondly, the fan stage may not be as symmetrical as we would like it to be. The air gaps between the tips of the fan blades and the wall of the duct may not be uniform among the 30 blades. At 9 GHz, the tolerance for any spatial non-uniformity is about 0.002m (i.e., 1/16 λ). This amount of tolerance has not likely been met during the mounting of the fan blades onto the fan shaft. In addition, because the fan blades are made out of long, thin metal strips and they are anchored only at one end (e.g., at the fan shaft), some of the fan blades may be warped slightly due to gravity, by more than the 0.002m tolerances.

Numerical computations of the fan assembly in the duct are performed using the same parameters as the experimental set-up. The computed RCS as a function of azimuth angle is shown by the dashed curve in Figure 7. It can be seen that the computed RCS scan does not agree well at all with the measured data. The computed RCS amplitude tapers off steadily with increasing azimuth angle in both positive and negative directions. The failure in predicting the RCS amplitude correctly, especially at large oblique azimuth angles is a consequence of the shoot-and-bounce ray (SBR) tracing method employed in many of the RCS prediction codes. At large oblique azimuth angles, some of the input rays in the SBR method are lost in the duct and never contribute to the backscattering RCS [Ref. 8]. This is confirmed by monitoring the ray tracing statistics in the numerical computations. It is found that a large percentage of the input rays are lost in the computation as the azimuth angle becomes more oblique.

RCS measurements are also conducted at three different radar frequencies, 8.9 GHz, 9.1 GHz and 9.4 GHz. These are shown in Figure 8. The measured data reveal that the RCS patterns are quite different, indicating that radar backscattering from the engine-duct is very dependent on the radar frequency. The computed RCS at 9.4 GHz is shown in Figure 9. It can be seen that it does not match well with the measured one (i.e., Figure 8c). Furthermore, the RCS scan computed at 9.4 GHz looks very similar to the one that is done at 8.9 GHz as shown in Figure 7 (dashed curve). There is virtually no frequency dependence in the computed outputs. These results indicate that the current RCS prediction technology may still need more developmental efforts.

5.0 CONCLUSIONS

Cavity RCS measurements are conducted using a full-size engine-duct experimental mock-up. These RCS measurements indicate that the backscattering of radar radiation inside a engine-duct cavity structure is very complex. Experimental results reveal that the RCS is very sensitive to even a small change in the azimuth angle and to small mechanical asymmetry of the engine components. The RCS is also dependent on the radar frequency used. These factors pose some interesting challenges to the numerical modelling of engine-duct cavity RCS.

RCS prediction codes based on the shoot and bounce ray tracing method do not appear to be adequate for computing cavity RCS of complex structures such as aircraft engine inlets. Better numerical methods will have to be developed to model the cavity RCS accurately. This could be a critical area in the pursuit of developing realistic synthetic target signatures for target identification/recognition.

REFERENCES

[1] R. van der Heiden, F. C. A. Groen and L. J. van Ewijk, " Aircraft Recognition with Radar Range Profiles using a Synthetic Database", RTO Meeting Proceedings 40, "High resolution Techniques", NATO RTO, Neuilly-sur-Seine, Cedex, France, pp. 57-1 to 57-8, November 1999.

[2] H. T. Anastassiu, "A Review of Electromagnetic Scattering Analysis for Inlets, cavities and Open Ducts", pp.27-40, IEEE Antennas and Propagation Magazine, vol. 45, no. 6, December 2003.

[3] G. H. Goldman, "Characterization of the Effects of Cavities and Canopies on Radar Target Signatures", US Army Research Laboratory, Adelphi, MD, ARL-TN-154, February 2000.

[4] Bill Sweetman, "How LO can you get", Jane's International Defense Review, pp.20-22, January 2002.

[5] K.K. Chan and S. Wong, "Modal Approach to RCS computation of Electrically Large Inlets", IEEE AP-S International Symposium, pp.114-117, San Antonio, US, June 2002.

[6] K.K.Chan and S. Wong, "Accurate RCS Prediction of Electrically Large Jet Inlets and Engines", International Conference on Antennas and Propagation, Session 4b, Exter UK, April 2003.

[7] K.K. Chan, S. Wong and E. Riseborough, "Accurate Radar Cross Section Modelling of Jet Inlets and Engines", NATO Symposium on " Target Identification and Recognition Using RF Systems", Paper P16, Oslo, Norway, October 2004.

[8] A. Mackay, "Application of chaos theory to ray tracing in ducts", IEE Proc.- Radar, Sonar and Navigation, pp.298-304, vol.146, no.6, December 1999.

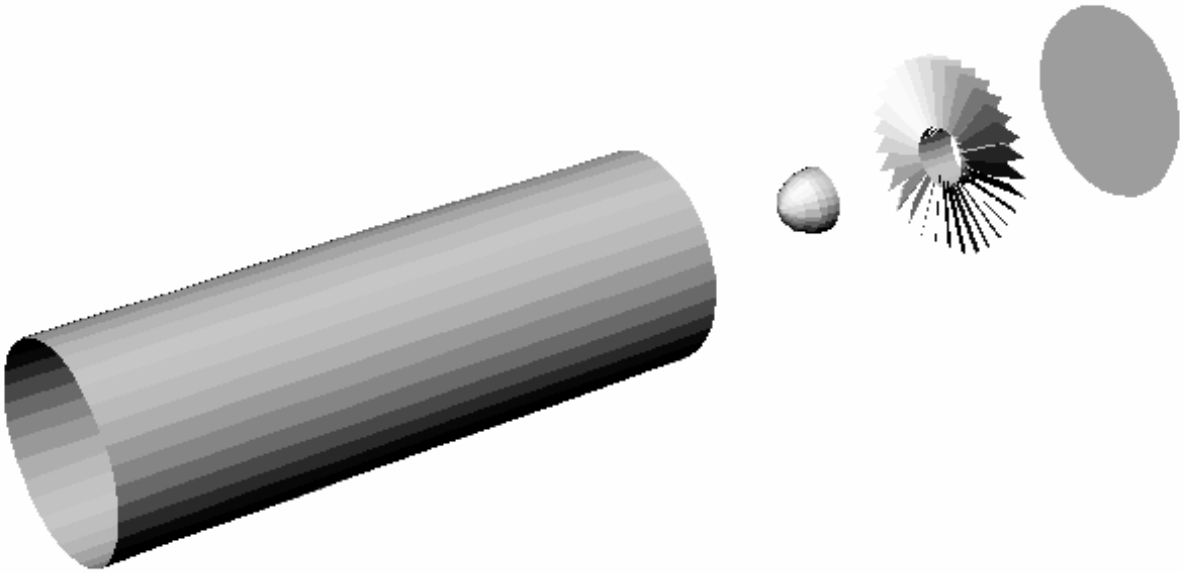

Figure 1 An exposed view of the engine-duct CAD model. From left to right: duct, nose-cone, fan stage and fan shaft, flat plate.

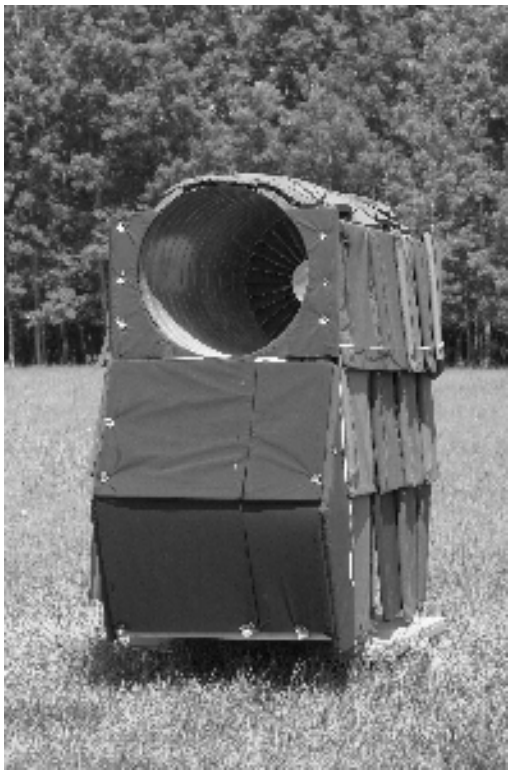

Figure 2 A picture of the full-size engine-duct mock-up with RAM tiles covering the exterior of the experimental set-up.

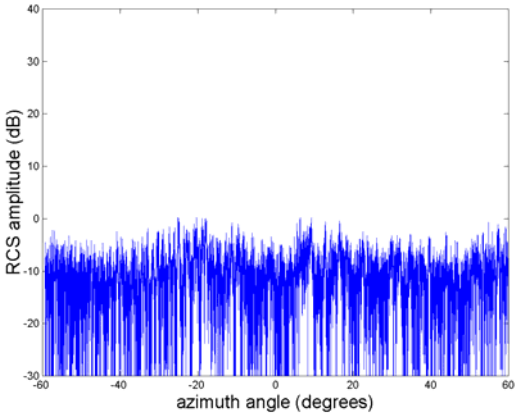

Figure 3 Background RCS measurement of the engine-duct mock-up. Radar frequency = 8.9 GHz.

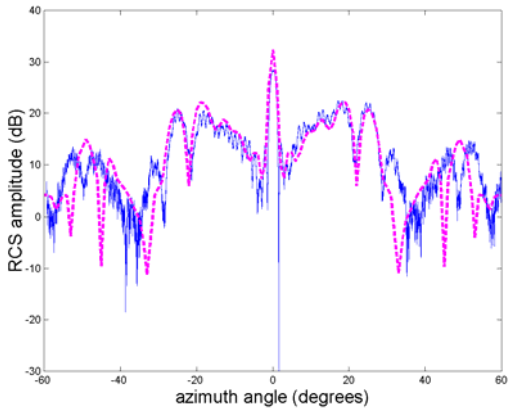

Figure 4 RCS as a function of azimuth angle for a cylinder with a terminating flat plate located 1m inside the duct. Solid curve = measured; dashed curve = computed.

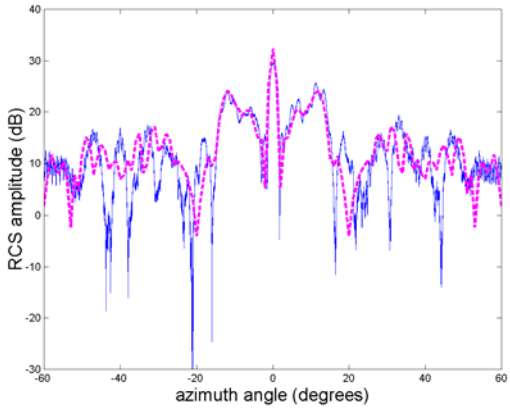

Figure 5 RCS as a function of azimuth angle for a cylinder with a terminating flat plate located 1.9m inside the duct. Solid curve = measured; dashed curve = computed.

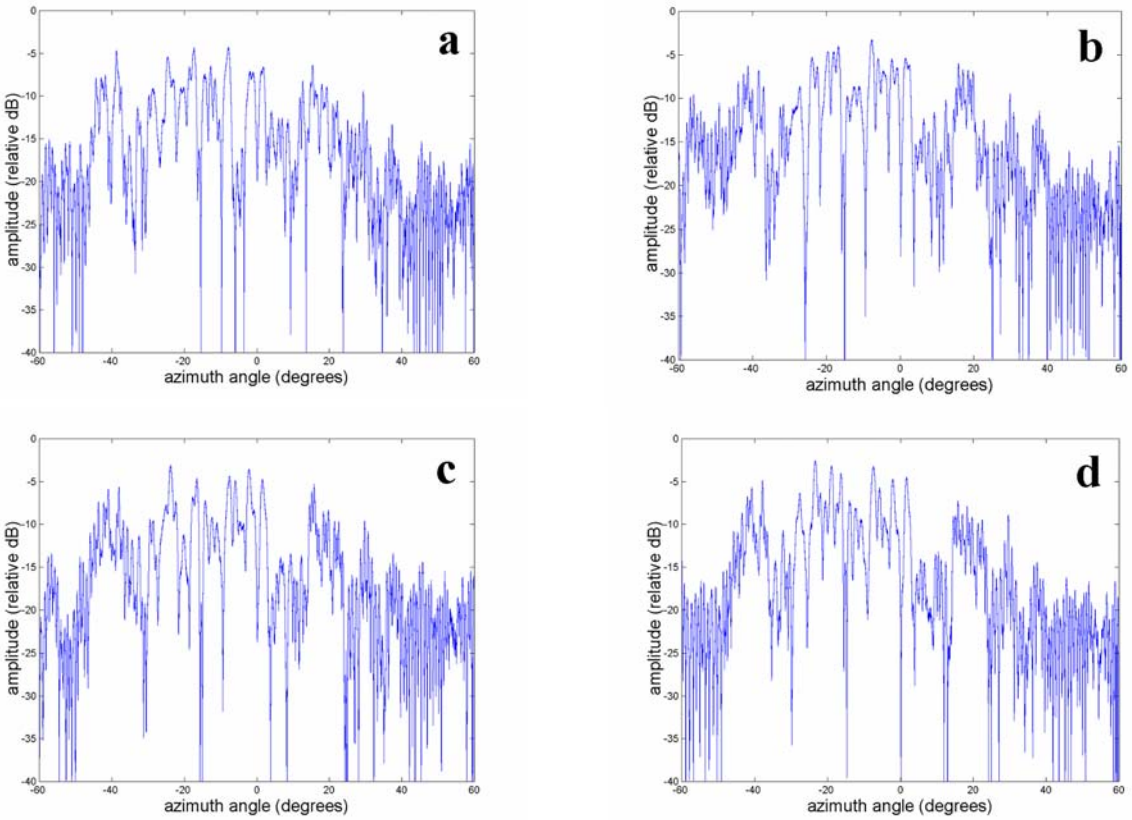

Figure 6 Measured RCS as a function of azimuth angle. Fan assembly is 1.9 m inside duct: a) reference position, rotated b) 10 fan blades, c) 20 fan blades, d) 25 fan blades counter-clockwise from reference position. Radar frequency = 8.9 GHz.

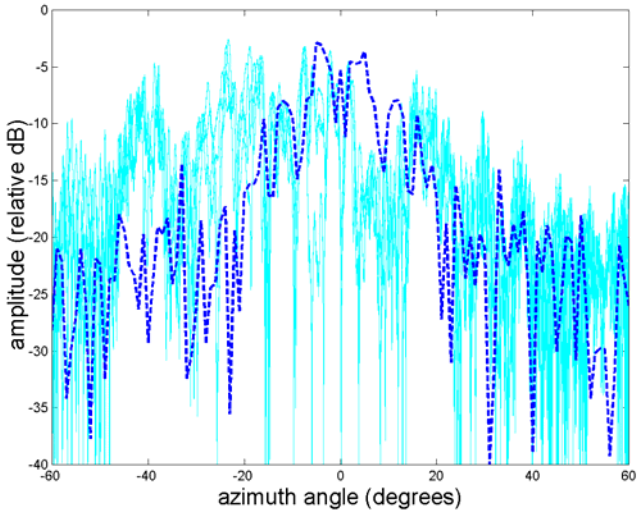

Figure 7 Light solid curve: superposition of the four RCS scans in Figure 6. Dashed curve: computed RCS as a function of azimuth angle. Radar frequency = 8.9 GHz.

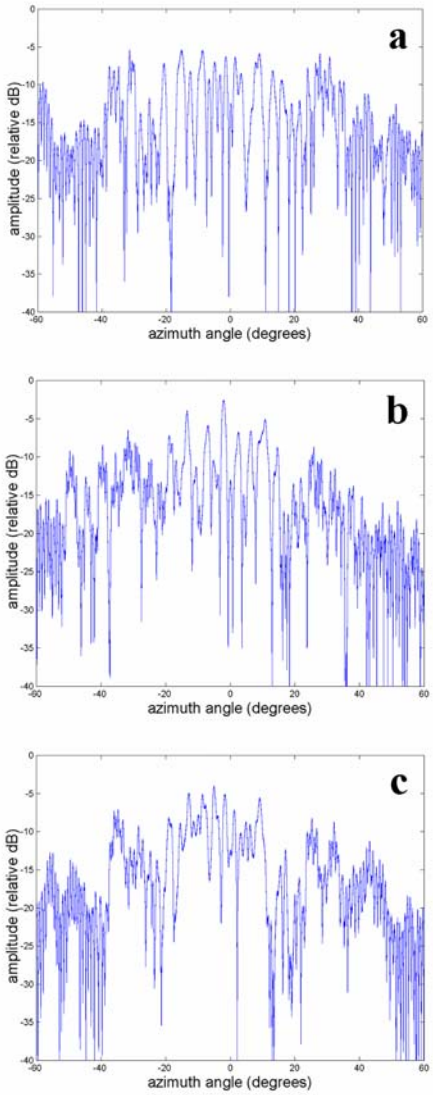

Figure 8 RCS as a function of azimuth angle measured at radar frequency: a) 8.9 GHz, b) 9.1 GHz, c) 9.4 GHz.

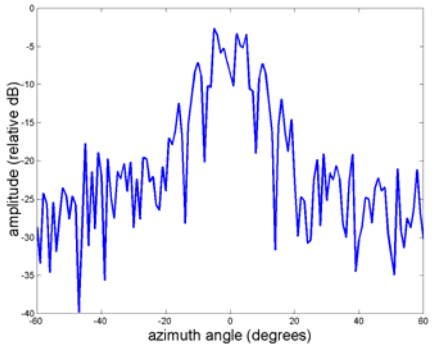

Figure 9 Computed RCS as a function of azimuth angle at 9.4 GHz.

3-D Time/Frequency-Range-Doppler Signatures for SAR Imaging of Ground Moving Targets

V. C. Chen and R. Lipps
Radar Division, US Naval Research Laboratory
4555 Overlook Avenue, S.W.
Washington DC 20375
USA

vchen@radar.nrl.navy.mil

ABSTRACT

In this paper, we introduce the concept of 3-D radar signatures in a slow time-range-Doppler, fast time-range-Doppler and frequency-range-Doppler. Then, we describe how to utilize 3-D time or frequency-range-Doppler signatures to extract information for detecting, relocating and re-focusing moving targets. Finally, we use AN/APY-6 X-band radar data for the demonstration of ground moving target detection.

1 INTRODUCTION

The returned signal from an object to be imaged can be represented as the integration of the contributions from all scatterers in the object [1]:

$$s_R(t) = \int_{-\infty}^{\infty}\int_{-\infty}^{\infty}\int_{-\infty}^{\infty} \rho(x,y,z)\exp\{-j2\pi f_0 \frac{2R_P(t)}{c}\}dxdydz \quad for \;\; 2R_P(t)/c \le t \le T_{PRI} + 2R_P(t)/c \tag{1}$$

where $\rho(x,y,z)$ is the reflectivity function of a point scatterer P at (x,y,z), f_0 is the carrier frequency, c is the speed of electromagnetic wave propagation, $R_P(t)$ is the distance from the radar to the point scatterer P, and T_{PRI} is the pulse repetition interval of the transmitted signal.

After transmitting a sequence of N pulses, the received baseband I/Q signals are organized into N pulses and M range-cells. Thus, a 2-D complex I/Q data array $s_R(r_m, t_n)$ can be obtained, where $m = 0,1,\ldots, M-1$; $n = 0,1,\ldots, N-1$. The M range-cells are represented in the time-domain, also called the fast time. At each range cell, the data across the N pulses constitutes a time history series, also called the slow time.

After range tracking and Doppler tracking, the range aligned profiles become $G(R_m, t_n)$, (m = 0, 1,…, M-1; n = 0, 1,…, N-1). The two-dimensional range profiles are expressed in a range and slow-time domain.

The conventional image formation takes the fast Fourier transform (FFT) for the new time history series and generates an N-point Doppler spectrum called the Doppler profile. By combining the N-point Doppler spectrum at each range cells for all M range profiles, the M-by-N image is formed

$$I(R_m, f_n) = FFT_{t_n}\{G(R_m, t_n)\} \tag{2}$$

where FFT_{tn} denotes the FFT operation with respect to the variable t_n. Therefore the radar image $I(R_m,f_n)$ is a target's 3-D reflectivity mapped onto a two dimensional range-Doppler or range and cross-range plane.

Paper presented at the RTO SET Symposium on "Target Identification and Recognition Using RF Systems", held in Oslo, Norway, 11-13 October 2004, and published in RTO-MP-SET-080.

All information about the object is contained in the two-dimensional complex array $s_R(r_m, t_n)$, called the fast time and slow time domains. To further exploit the information, the generation of a three-dimensional (3-D) feature space is useful.

2 3-D FEATURE SPACE

A 3-D feature space can be generated by using a 2-D time-frequency transform [2] on one of the data dimensions. In the case of SAR imaging, the time-frequency transform can be applied directly to the slow time or the fast time domain, or applied to the Fourier transform of the slow time or fast time domains.

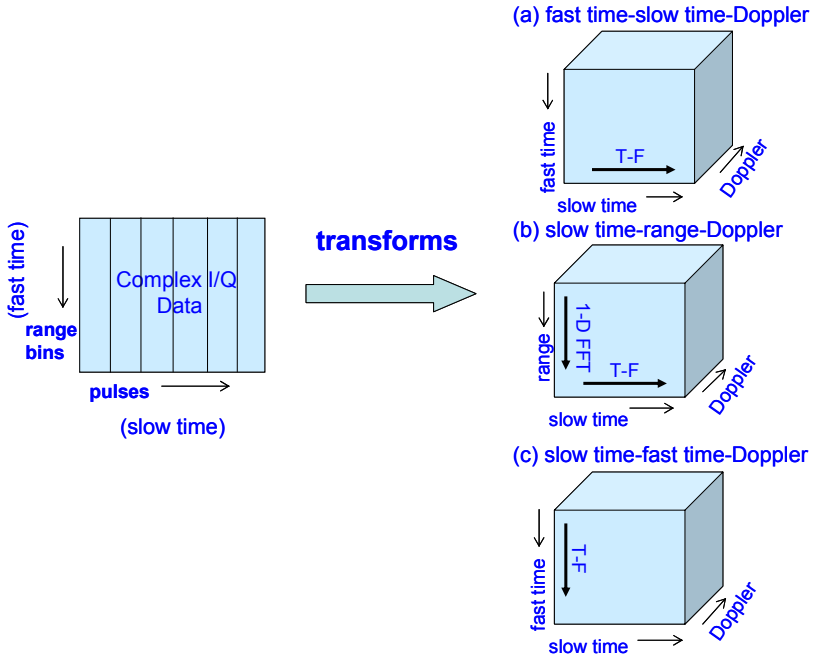

Figure 1. Approaches to generate 3-D feature space.

Figure 1 illustrates some general approaches to generating a 3-D feature space. From a 2-D data space in the fast time and the slow time domains, a 2-D time-frequency transform is necessary to generate a 3-D feature representation. The 3-D feature space can be (a) a fast time-slow time-Doppler space by applying a time-frequency transform to the slow-time domain, (b) a slow time-range-Doppler space by first applying a 1-D FFT to the fast time domain, then applying a time-frequency transform to the slow time domain, and (c) a slow time-fast time-Doppler space by applying a time-frequency transform to the fast time domain, or other combinations.

3 SLOW TIME-RANGE-DOPPLER SPACE

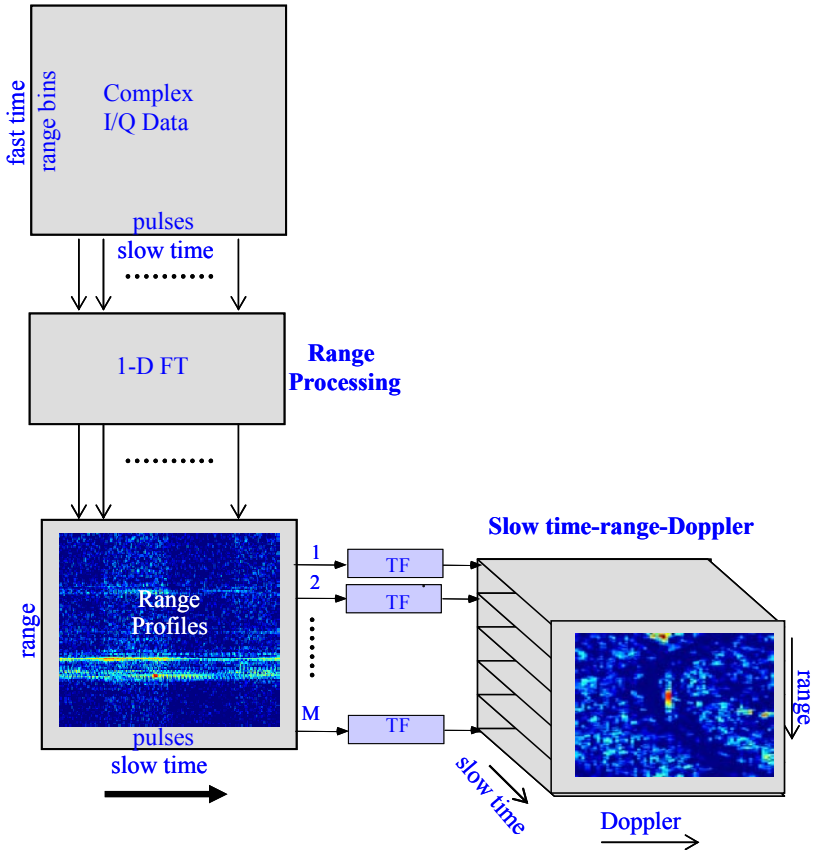

Figure 2. Generate a slow time-range-Doppler feature space.

When the data is formed as a complex 2-D array $G(R_m, t_n)$, (m = 0, 1,…, M-1; n = 0, 1,…, N-1) with M slow time history series, each having the length of N pulses, the 3-D space processing takes a time-frequency transform for each slow time history series and generates an $N\times N$ slow time-Doppler distribution. By combining the $N\times N$ time-Doppler distributions for all M range cells, the $N\times M\times N$ slow time-range-Doppler cube $Q_1(t_n, R_{m,}, f_n)$ can be formed:

$$Q_1(t_n, R_m, f_n) = TF_n\{G(R_m, t_n)\}, \tag{3}$$

where TF_n denotes the time-frequency transform with respect to the variable n. At each sampling time t_i (i=0,1,2..N-1), only one range-Doppler image frame $Q_1(R_m,f_n,t_n=t_i)$ can be extracted from the $N\times M\times N$ slow time-range-Doppler cube. According to the frequency marginal condition, the slow time-range-Doppler feature space and the 2-D range-Doppler image space is related by [1]

$$I(R_m, f_n) = \sum_{t_n=t_0}^{t_{N-1}} Q_1(t_n, R_m, f_n), \tag{4}$$

which means that the 2-D range-Doppler image is just a 2-D slice of the 3-D slow time-range-Doppler space.

Figure 2 shows the typical block diagram of the slow time-range-Doppler processing to generate a 3-D feature space. In short, to retrieve the range information, the FFT is applied to the fast time domain. The complex I/Q 2-D data array becomes a 2-D (slow time and range) array of range profiles. By taking the time-frequency transform in the slow time domain, the slow time-range-Doppler feature space is generated.

4 FREQUENCY-RANGE-DOPPLER SPACE

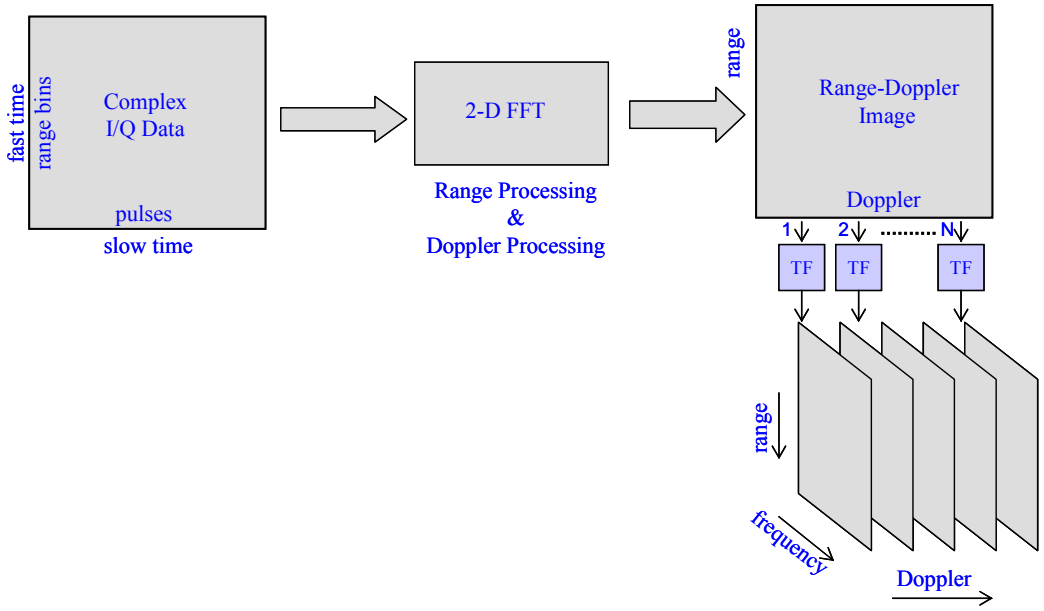

Figure 3. Generate a frequency-range-Doppler feature space.

The 2-D complex I/Q data array $s_R(r_m, t_n)$, (m = 0,1,…, M-1; n = 0,1,…, N-1) in the fast time and slow time domain is used to generate a range-Doppler feature image by applying a 2-D FFT:

$$I(R_m, f_n) = FFT2\{s_R(r_m, t_n)\} \tag{5}$$

Then, a time-frequency transform is applied to each range profile generating an $M \times M$ range-frequency distribution. By combining the $M \times M$ range-frequency distributions at N Doppler cells, the $M \times M \times N$ frequency-range-Doppler cube $Q_2(\omega_m, R_m, f_n)$ can be formed:

$$Q_2(\omega_m, R_m, f_n) = TF_m\{I(R_m, f_n)\}, \tag{6}$$

where TF_m denotes the time-frequency transform with respect to the variable m. At each sampling frequency $\omega_i (i=0,1,2..M-1)$, only one range-Doppler image frame $Q_2(\omega_m=\omega_i, R_m, f_n)$ can be extracted from the $M \times M \times N$ frequency-range-Doppler cube.

Figure 3 shows the typical block diagram of the frequency-range-Doppler processing for generating a 3-D feature space. To retrieve the range-Doppler information, the 2-D FFT is applied to the complex I/Q data array to generate a 2-D range-Doppler image. By taking the time-frequency transform at each Doppler frequency cell along the range domain, the frequency-range-Doppler feature space is generated.

5 DETECTION OF MOVING TARGETS IN SAR SCENE

Traditional SAR processing cannot simultaneously produce clear images of stationary targets and moving targets. Moving targets appear as defocused and spatially displaced objects superimposed on the SAR scene [3,4]. In these cases, an important issue is the ability to detect and focus images of moving targets.

Given a radar velocity v and an initial range from the radar to a moving target R_0, the Doppler rate of the moving target is determined not only by its geometric location (x_0,y_0) but also by its velocity and acceleration. If the Doppler rate cannot be compensated in the data, then the image of the moving target becomes defocused.

When the SAR platform is moving along the azimuth direction at an altitude, and the target is moving with a velocity v_y and an acceleration a_y in the radial direction, and a velocity v_x and an acceleration a_x in the azimuth direction, then the Doppler shift of the returned signal consists of two parts: the part due to the radar motion

$$f_{D_{Radar}} = -\frac{2}{\lambda}\frac{x_0 v}{R_0} + \frac{2}{\lambda}\frac{v^2}{R_0}t \tag{7}$$

and the part due to the target motion

$$\begin{aligned} f_{D_{Target}} &= -\frac{2}{\lambda}\frac{x_0 v_x + y_0 v_y}{R_0} \\ &+ \frac{2}{\lambda}\frac{v_x^2 + v_y^2 + x_0 a_x + y_0 a_y - 2v v_x}{R_0}t \end{aligned} \tag{8}$$

where the first term is the Doppler centroid and the second term is the Doppler rate induced by target motion.

The quadratic phase variation between the target and the radar causes de-focusing of the moving target's image. When stationary objects are well focused, the image of moving targets become de-focused and shifted in the cross-range direction.

In order to detect moving targets, estimate the targets' velocities, and relocate mis-located moving targets, multiple-antenna (such as interferometry, planar apertures, or antenna array) approaches are used. Ground moving target indicator (GMTI) using multiple- antenna is used to reject radar returns from clutter and to detect moving target.

The 3-D slow time-range-Doppler feature space provides moving target features. These features include the target's time-varying Doppler spectrum in the 2-D slow time-Doppler slices and targets' motion trajectories in the 2-D range-Doppler slices. Therefore, for the conventional single channel SAR imaging, moving targets can be detected using these features. In particular a chirp response, indicated by a sloped line in the slow time-Doppler domain, is an indication of a moving target in the scene.

Figure 4 shows a spotlight SAR image with a moving vehicle as indicated. AN/APY-6 radar [5] was used to collect the spotlight SAR data. Because of the target motion, the image of the moving vehicle becomes a smeared strip line in the Doppler (cross-range) domain. There are several other strip lines in the image which may not necessarily be moving targets. To verify that the above indicated strip line is a moving target, let us start with the complex I/Q data and perform the slow time-range-Doppler processing.

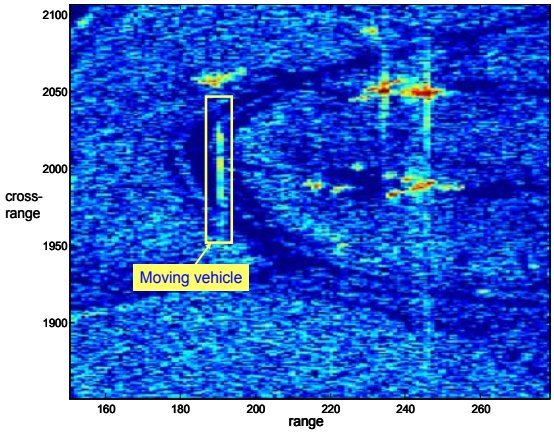

Figure 4. SAR image with a moving vehicle.

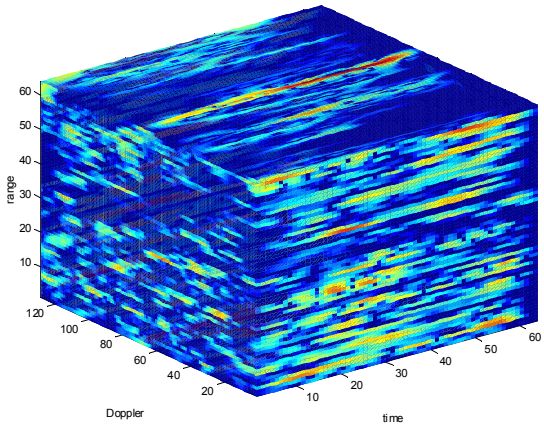

(a) Slow time-range-Doppler cube.

(b) time-Doppler slice.

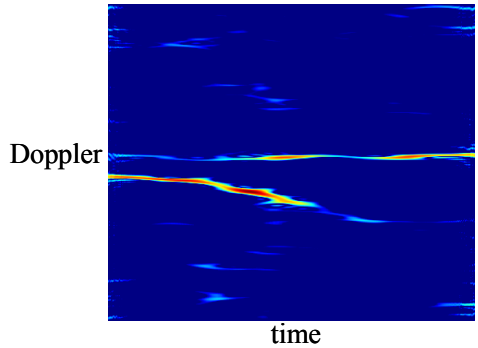

(c) range-Doppler slice.

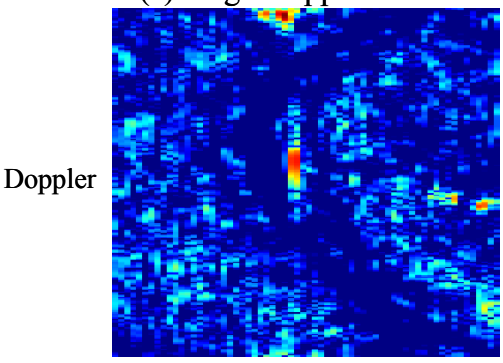

Figure 5. 3-D slow time-range-Doppler processing for moving target detection.

Figure 5 (a) shows the 3-D slow time-range-Doppler cube, (b) shows a 2-D time-Doppler slice which has a sloped time-varying spectrum caused by target motion, and (c) shows a 2-D range-Doppler slice which illustrates the response of the vehicle moving along the cross-range direction. Figure 6 shows the re-focused image of the moving vehicle compared with the unfocused image.

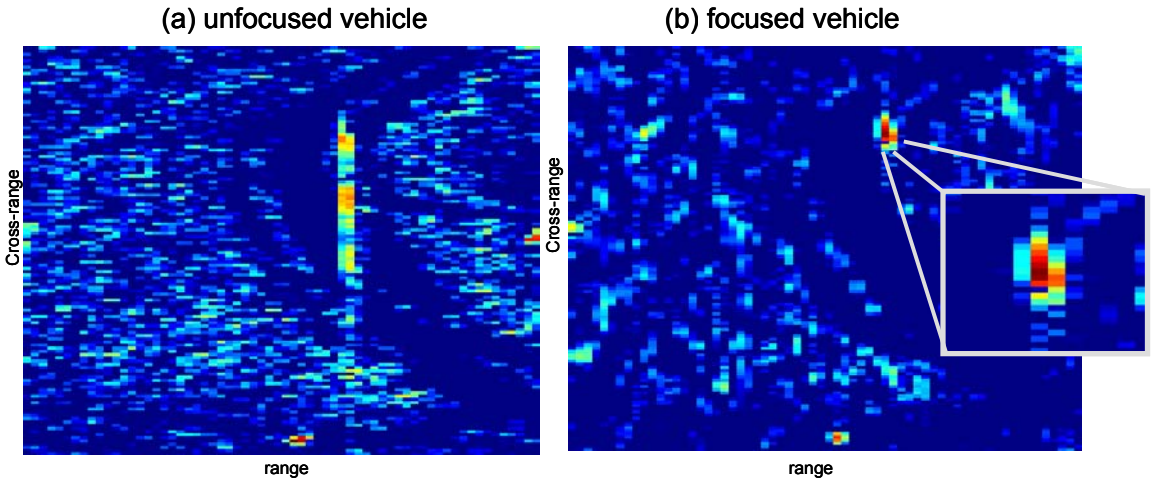

Figure 6. (a) The unfocused image of the moving vehicle; (b) the re-focused image of the moving vehicle by using the slow time-range-Doppler processing.

6 SUMMARY

Using the joint time-frequency transform, a time series can be transformed into a 2-D joint time and frequency space, and a 2-D complex I/Q radar data can be transformed into a 3-D feature space. The 3-D feature spaces can be derived from various combinations of time-frequency transform applied to the fast time and the slow time domains. In this paper, we discussed the 3-D slow time-range-Doppler space and its application to moving target detection and re-focusing. A SAR scene with a moving vehicle generated from AN/APY-6 radar data is used to demonstrate the usefulness of the slow time-range-Doppler feature space for detecting and focusing ground moving targets.

7 ACKOWLEDGEMENT

This work was supported by ONR base at NRL program.

REFERENCES

1. V.C. Chen and Shie Qian, "Joint Time-Frequency Transform for Radar Range-Doppler Imaging," *IEEE Trans.* on AES-34, no.2, pp.486-499, 1998.
2. V.C. Chen, "Time-frequency analysis of SAR image with ground moving targets", *Proceedings of SPIE Conference on Wavelet Applications*, vol.3391, pp.295-302, 1998.
3. V.C. Chen, R. Lipps and M. Bottoms, "Radar imaging of ground moving targets", *Proceedings of the 2001 IEEE Radar Conference*, May 2001, pp.426-431, 2001.
4. V.C. Chen, R. Lipps and M. Bottoms, "Synthetic aperture radar signatures of moving targets", *Proceedings of the 2001 TriService Radar Symposium*, May 2001.
5. W.J. Miceli and L. A. Gross, "Test results from the AN/APY-6 SAR/GMTI surveillance, tracking and targeting radar," *Proceedings of the 2001 IEEE Radar Conference*, pp.13-17, 2001.

Bayesian Approach to Exploiting prior Targeting Information within a Weapon Seeker

Keith Copsey, Richard O. Lane, Sunil Manchanda and Andrew R. Webb
QinetiQ
Malvern Technology Centre
St Andrews Road
Malvern
Worcestershire, WR14 3PS
United Kingdom

K.Copsey@signal.QinetiQ.com, rlane1@qinetiq.com, smanchanda@qinetiq.com,
A.Webb@signal.QinetiQ.com

ABSTRACT

This paper considers an automatic target recognition (ATR) application in which a targeting sensor is used to guide a seeker-equipped weapon to an area containing high-value relocatable targets. The weapon seeker then needs to engage the high value targets, while minimising collateral damage. A Bayesian approach is proposed that enables the weapon seeker to exploit the targeting information before making its final decision. Specifically, the approach matches the scenes in the seeker domain with those from the targeting sensor, while taking into account uncertainty and data latency. The proposed solution utilises a Bayesian technique known as particle filtering. This paper outlines the approach, and presents results for a synthetic example. Future work will conduct a performance assessment using scenarios derived from real long-range and short-range SAR imagery.

1.0 INTRODUCTION

1.1 General

This paper considers the problem of using a targeting sensor to guide a seeker-equipped weapon to an area containing high-value relocatable targets. The aim is for the seeker-equipped autonomous weapon to exploit targeting information before making its final decision. This is illustrated in Figure 1, where targeting data at time t_0 is used to aid classification of the weapon seeker data at time t_1. The generic problem addressed is one where two sensor images, separated in time, are available to classify relocatable targets in a scene. Issues to be addressed include:

- Uncertainty in the targeting identifications.
- Change in the target layout configuration during weapon fly-out (i.e. staleness of the targeting information).
- Differing imaging geometry between the targeting sensor and the seeker.

A particularly adverse effect of the last two items is that a target designated correctly by the targeting sensor may have both a different location and an altered signature by the time that the weapon has reached the targeted area. This will have a significant effect on the ability of the weapon to engage the pre-selected target, especially in typical scenarios where collateral damage must be minimised.

Paper presented at the RTO SET Symposium on "Target Identification and Recognition Using RF Systems", held in Oslo, Norway, 11-13 October 2004, and published in RTO-MP-SET-080.

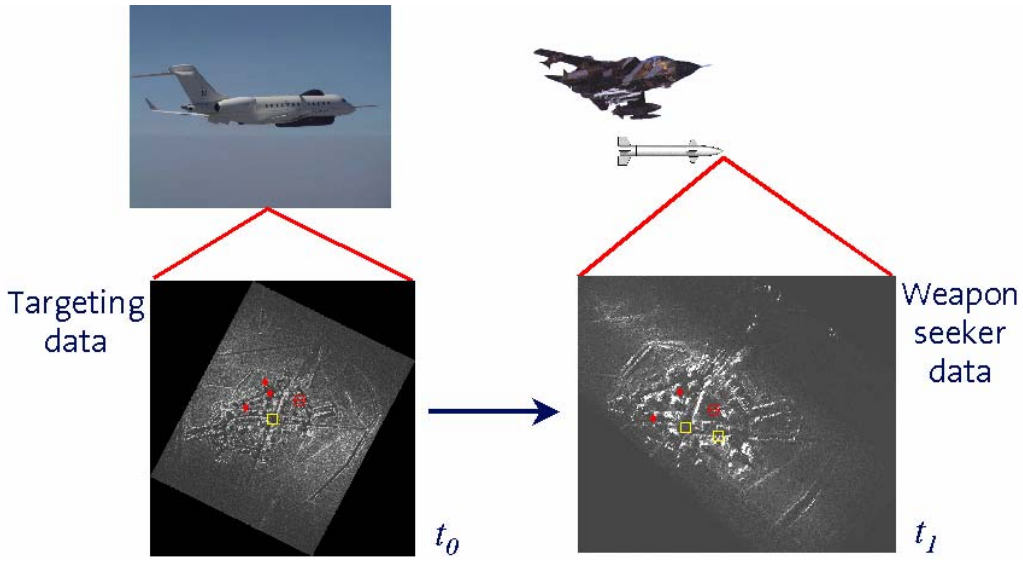

Figure 1: Exploitation of targeting information by a weapon seeker.

1.2 Bayesian approach

A Bayesian approach is proposed which uses a Particle Filter [4] to draw samples from the posterior distribution for the target locations and classes, given the information derived from the targeting sensor and weapon seeker. Since the posterior distribution contains the relevant information on the target locations and classes, the samples can be used as inputs to the final decision making process of the weapon. Successful production of this information will improve the ability of the weapon to engage the targets designated on launch of the weapon, while minimising collateral damage. The proposed approach fits within a larger framework detailed in an accompanying paper [17].

1.3 Bayesian approach

The main motivation behind a Bayesian approach [11] to the problem lies in the unique ability of Bayesian statistics to handle limited and possibly conflicting pieces of information in a fully consistent manner. In particular, Bayesian statistics provides a consistent mechanism for manipulating probabilities assigned to observed data. Further advantages to the use of Bayesian techniques include the ability to cope with additional prior information, perhaps elicited from expert knowledge, and the production of confidence intervals and other statistics for the parameters estimated.

1.4 Outline of the paper

The structure of this paper is as follows. Section 2 specifies the problem being examined. Section 3 proposes a Bayesian solution. Section 4 presents the results for a synthetic example. Conclusions and future work are given in Section 5.

2.0 PROBLEM SPECIFICATION

2.1 Introduction

In the considered scenario, an image from a targeting sensor is obtained at time t_0. Target detection techniques are then applied to obtain a set of targeting detections. An image chip is obtained for each

detected object/target by centring an input window (of sufficient size to cover expected targets) at the location of each detection. ATR algorithms [16] are then applied to estimate the class of the object leading to each detection. If the target classes correspond to high value targets a seeker-equipped weapon is launched to engage the targets.

The weapon seeker reaches and images the highlighted area at a later time, t_1. Similarly to the targeting sensor processing, target detection algorithms are then applied to obtain a set of seeker detections, along with associated image chips (centered on the locations of the detections). The task is to determine the locations and classes of the targets at time t_1, utilising both the seeker information and the targeting information. The solution to this task lies in determining the posterior distribution of the locations and classes at time t_1. For the purposes of this paper it is assumed that we are only interested in the targets detected in the targeting image.

2.2 Related work

Work by Gordon and Salmond [8] tackles the problem of matching target detections from a targeting sensor with a missile seeker, but assumes that no ID information can be inferred from the seeker or targeting measurements. Gaussian models for bulk and individual target motion during weapon fly-out were introduced, and a closed form solution was obtained. Work by the same authors on group and extended object tracking [13] hints at a non-linear approach to the same problem using particle filters [4], but does not take into account object characteristics.

The work described in this paper differs from previous approaches to matching target detections through:

- Estimation of full class probabilities, utilising the targeting and seeker sensor measurements of the objects/targets.
- Potential for modelling complicated target motion during the time-gap between the seeker measurements and the targeting measurements.
- No assumption that a target is correctly designated in the targeting image.

Work by Gordon et al [6] has developed a Bayesian approach to joint tracking and identification, which is relevant to the problem addressed within this paper. The focus within that work was ensuring efficiency for multiple sensor returns.

2.3 Targeting detections

The number of targeting sensor detections at time t_0 is denoted by N_t. The locations of the detections and associated image chips (ID sensor measurements) are denoted by $l_1,\ldots,l_{N_t}$ and $r_1,\ldots,r_{N_t}$ respectively. For notational ease we define $T_i = (l_i, r_i)$ for $i = 1,\ldots,N_t$.

Assuming that there are J possible target classes, the ID sensor measurements are used to obtain J-dimensional class probability vectors ψ_i for each detection, where $\psi_{i,j}$ is the estimated probability that the i-th detection is the j-th class, for $i = 1,\ldots,N_t$ and $j = 1,\ldots,J$. Such class probabilities would be estimated using Bayesian ATR algorithms, or possibly via human intervention.

The measurement errors for the target locations are assigned Gaussian distributions, so that $l \sim N(x, \Sigma_t)$ where x is the actual target location, and Σ_t is the covariance matrix for the measurement errors. The covariance matrix should be determined by considering the sensor performance characteristics along with the imaging conditions.

2.4 Seeker detections

The number of seeker detections at time t_1 is denoted by N_s. Since the targeting sensor indicates that there are N_t targets present, the threshold for detecting objects within the seeker image is assumed to be set so that $N_s \geq N_t$. Adaptation of the proposed approach to cope with $N_s < N_t$ would be trivial. The locations of these seeker detections are denoted $y_1,\ldots,y_{N_s}$, and the associated image chips (ID sensor measurements) are $z_1,\ldots,z_{N_s}$. For notational ease we define $D_i = (y_i, z_i)$ for $i = 1,\ldots,N_s$.

An example of a DBS seeker image is provided in Figure 2. Input windows have been placed on the locations of an example set of seeker detections. The windows are colour-coded so that red indicates an actual target and green indicates the type of background clutter that might pass through the initial target detection stage. These input windows define the image chips that are extracted to provide ID sensor measurements.

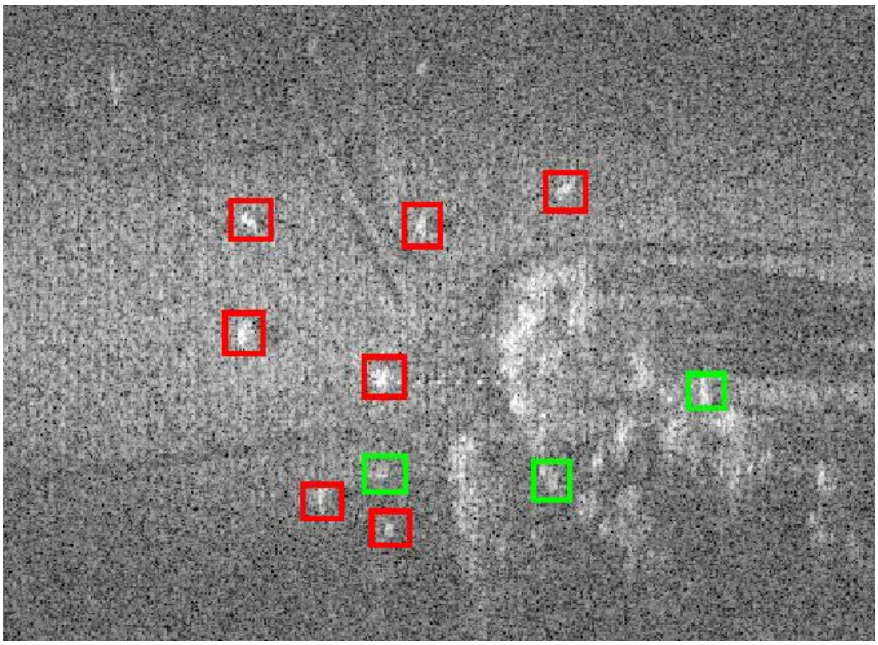

Figure 2: Example of a DBS seeker image (range along the horizontal axis, cross range along the vertical axis). Red boxes highlight targets, green boxes highlight background clutter.

It is assumed that density models (conditional on class) can be estimated for the ID sensor measurements. Estimating these distributions given only limited training data for the weapon seeker is covered in the accompanying paper [17]. These distributions can be represented by $p(z \mid C = j)$, where z is the image chip and j is the index of the class C of the object.

In addition to probability densities for target image chips, it is assumed that a probability density has been estimated for image chips that correspond to the sort of background noise and clutter that will pass through the target detection algorithm. This density is denoted by $p(z \mid C = 0)$.

If the class of a target is unassigned, a mixture distribution is used for the ID sensor measurements:

$$p(z) = \pi_0 p(z \mid C = 0) + (1 - \pi_0) \sum_{j=1}^{J} \pi_j p(z \mid C = j) \qquad (1)$$

where $\pi_1, \ldots, \pi_J$ represent the prior class probabilities excluding background clutter, and π_0 is the prior probability for background clutter. Note that the prior probability for background clutter will be related to the false alarm probability of the detection algorithm, rather than the ratio of background clutter to targets. This reflects the fact that the initial detection stage will already have eliminated most of the background noise.

The measurement errors for the object locations are assigned Gaussian distributions, so that $y \sim N(x, \Sigma_s)$ where x is the actual object location, and Σ_s is the covariance matrix for the measurement errors. As with the targeting sensor, the covariance matrix should be determined by considering the sensor performance characteristics together with the imaging conditions. Locations of any additional targets and background clutter are assumed to be distributed uniformly over the surveyed region.

3.0 BAYESIAN SOLUTION

3.1 Posterior distribution

The actual classes and locations of the targets detected by the targeting sensor at time t_0 are denoted by $(c_1, \ldots, c_{N_t})$ and $(x_{0,1}, \ldots, x_{0,N_t})$ respectively. By time t_1 the new locations are represented by $(x_{1,1}, \ldots, x_{1,N_t})$. This reflects the fact that the targets may have relocated during the weapon fly-out time $t_1 - t_0$. The actual classes are of course unchanged. Using the definitions in Section 2 the posterior distribution of interest at time t_1 is:

$$p(x_{1,1}, \ldots, x_{1,N_t}, c_1, \ldots, c_{N_t} \mid T_1, \ldots, T_{N_t}, D_1, \ldots, D_{N_s}) \qquad (2)$$

3.2 Prior Evolver

A *Prior Evolver* is used to update the information from the targeting sensor to allow for target motion during weapon fly-out. Specifically, this consists of predicting how the detections gleaned from the targeting sensor at time t_0 will have changed by the time t_1 that the weapon seeker views the targeted area. The Prior Evolver can be represented by a distribution:

$$p(x_{1,1}, \ldots, x_{1,N_t} \mid x_{0,1}, \ldots, x_{0,N_t}, c_1, \ldots, c_{N_t}) \qquad (3)$$

In the tracking literature [2] the Prior Evolver corresponds to the system model for the state.

The simplest non-trivial form for the Prior Evolver consists of independent Gaussian perturbations for each detection. Bulk motion of targets (perhaps reflecting the motion of a convoy) can be included easily, using a global Gaussian translation [7]. More complicated motion, incorporating knowledge of the terrain and likely target behaviour, is also possible. For example, targets can be predicted to follow a road network [1][10]. This is done by perturbing the locations using a Gaussian distribution with covariance matrix chosen so that the variance along the road is much higher than the variance orthogonal to the road. This has the effect of making the uncertainty along the road more than the uncertainty orthogonal to the road, which fits with the road motion constraints. Various rules can then be applied for targets near road junctions and for entry/exit conditions from roads. A further possibility is the construction of a potential-

field constraint, to bias predicted target motion in the direction of assumed desired target locations (such as potential hide locations) and away from impenetrable terrain (such as rivers). The tracking literature [12][15] contains examples of such an approach.

3.3 Particle Filter

Analytical calculation of the desired posterior distribution is feasible only for the simplest of measurement distributions and Prior Evolver. Thus, a Particle Filter is used to obtain the samples from the posterior distribution. The particle filter is an extension of importance sampling [5][14] to sequential sampling. For clarity, we now (briefly) describe the underlying idea behind importance sampling.

Suppose that we have a set of n independent samples, $\phi^{(1)},\ldots,\phi^{(n)}$, from a probability distribution with density function proportional to $g(\phi)$, but we are actually interested in making inference on a probability distribution with density function proportional to $f(\phi)$. If a set of unnormalised importance weights:

$$w^{(s)} = f(\phi^{(s)}) / g(\phi^{(s)}), \qquad (4)$$

is defined, the expectation of a function $a(\phi)$ with respect to the distribution defined by $f(\phi)$ can be estimated by:

$$\bar{a}_f = \sum_{s=1}^{n} w^{(s)} a(\phi^{(s)}) \Big/ \sum_{s=1}^{n} w^{(s)} . \qquad (5)$$

Consider now, the special case where the distribution defined by $f(\phi)$ is the posterior distribution for a likelihood function $l(x|\phi)$ and prior distribution $\pi(\phi)$, while the distribution defined by $g(\phi)$ is the prior distribution $\pi(\phi)$. Then, the importance weights defined in (4) become:

$$w^{(s)} = l(x|\phi^{(s)}). \qquad (6)$$

Thus, we have a mechanism for making inference on a posterior distribution by sampling from the prior, and weighting the samples by the likelihood function. This forms the basis for the particle filter solution to our problem. For fuller details of particle filters the reader is referred to the book by Doucet et al [4].

3.4 Application of the Particle Filter

Initialisation of the filter requires a set of N_p equally weighted particles $((x_{0,1}^{(s)}, c_1^{(s)}),\ldots,(x_{0,N_t}^{(s)}, c_{N_t}^{(s)}))$ from the joint posterior distribution for the classes and locations at time t_0. The locations at time t_0 can be sampled according to the distribution for the targeting sensor measurement errors. Using definitions from Section 2.3 we set $x_{0,i} \sim N(l_i, \Sigma_t)$, for $i = 1,\ldots,N_t$. The initial class samples for each detection are drawn probabilistically according to the class probability vectors ψ_i.

The Particle Filter algorithm works by passing samples through the Prior Evolver (defined in Section 3.2). Specifically, for $s = 1,\ldots,N_p$ we:

- Sample $\{x_{1,1}^{(s)},\ldots,x_{1,N_t}^{(s)}\}$ from $p(x_{1,1},\ldots,x_{1,N_t} | x_{0,1}^{(s)},\ldots,x_{0,N_t}^{(s)}, c_1^{(s)},\ldots,c_{N_t}^{(s)})$, the Prior Evolver distribution (defined in Section 3.2).

- Evaluate the importance weights $w^{(s)} = p(D_1,\ldots,D_{N_s} \mid x_{1,1}^{(s)},\ldots,x_{1,N_t}^{(s)},c_1^{(s)},\ldots,c_{N_t}^{(s)})$ using the measurement likelihoods to be defined in Section 3.5.

The weighted samples $((x_{1,1}^{(s)},c_1^{(s)}),\ldots,(x_{1,N_t}^{(s)},c_{N_t}^{(s)}))$ (with weights $w^{(s)}$) can then be used to approximate the required posterior distribution.

If the scenario were to be extended to a full tracking problem in which a time series of seeker images is obtained, this procedure would need to be altered to prevent degenerate weights (i.e. a few particles with very large weights, and the rest with small weights) [6].

3.5 Likelihood

Before the likelihood of the seeker measurements can be calculated, the images from the seeker and targeting sensors need to be registered. Various techniques for image registration could be used [3], such as those that extract and then match lines in the images [18]. In the example presented in this chapter the registration (and the uncertainty in this registration) is incorporated into the Prior Evolver.

Evaluation of the likelihood function is complicated by the need to associate the seeker measurements/detections with the targets. This association requires definition of the set of feasible association hypotheses θ. Each hypothesis associates a subset θ_d of seeker measurements with the detections from the targeting sensor. The cardinality of θ_d is denoted θ_{N_d}, and for each $i \in \theta_d$ we define λ_i to be the target (from the targeting sensor) to which that measurement is assigned. The remaining $\theta_{N_a} = N_s - \theta_{N_d}$ seeker measurements (defined by the indices $i \notin \theta_d$) are taken to correspond to additional targets or clutter measurements. Using the association hypotheses, the likelihood function can be expressed as:

$$p(D_1,\ldots,D_{N_s} \mid x_{1,1},\ldots,x_{1,N_t},c_1,\ldots,c_{N_t}) = \sum_{\theta} \{p(D_1,\ldots,D_{N_s} \mid \theta,x_{1,1},\ldots,x_{1,N_t},c_1,\ldots,c_{N_t}) \times p(\theta \mid x_{1,1},\ldots,x_{1,N_t},c_1,\ldots,c_{N_t})\} \quad (7)$$

Assuming independence between measurements/detections, the likelihood conditioned on the association hypothesis is given by:

$$p(D_1,\ldots,D_{N_s} \mid \theta,x_{1,1},\ldots,x_{1,N_t},c_1,\ldots,c_{N_t}) = \left(\prod_{i\in\theta_d} p(y_i,z_i \mid x_{1,\lambda_i},c_{\lambda_i})\right) \times \left(\prod_{i\notin\theta_d} p(y_i,z_i)\right) \quad (8)$$

where using notation defined in Section 2.4:

$$\begin{aligned} p(y_i,z_i \mid x_{1,\lambda_i},c_{\lambda_i}) &= N(y_i \mid x_{1,\lambda_i},\Sigma_s)\, p(z_i \mid C_i = c_{\lambda_i}) \\ p(y_i,z_i) &= A_s^{-1} p(z_i) \end{aligned} \quad (9)$$

where A_s is the area of the surveyed region.

Following Gordon et al [7], the prior probabilities for the association hypotheses are expressed as:

$$p(\theta \mid x_{1,1},\ldots,x_{1,N_t},c_1,\ldots,c_{N_t}) = \text{Poisson}(\theta_{N_a} \mid \rho\, A_s) \times \text{Bin}(\theta_{N_d} \mid N_t, p_d) \times \left(\frac{N_t!}{(N_t-\theta_{N_d})!\theta_{N_d}!} \times \frac{N_s!}{\theta_{N_a}!} \right)^{-1} \quad (10)$$

The first term of equation (10) models the number of additional target or clutter detections in the processed seeker image by a Poisson distribution with mean ρA_s. Here, additional target refers to a target that was not detected by the targeting sensor, but which is never-the-less a proper target. A clutter detection corresponds to an object that does not belong to any of the J specific target classes. The second term of equation (10) is a Binomial distribution $\text{Bin}(\theta_{N_d}; N_t, p_d)$ for the number of detected targets θ_{N_d}. Specifically, each target from the targeting sensor is assumed to be detected in the seeker image with independent probability p_d (more complicated models would alter p_d according to the class of the target). Given θ_{N_d}, it is assumed that the allowable associations between targets and seeker measurements are equally likely. This produces the third term of equation (10). Allowable associations given θ_{N_d} are obtained by selecting the θ_{N_d} detected targets (the number of such subsets is $N_t!/((N_t-\theta_{N_d})!\theta_{N_d}!)$), and then assigning these targets to the seeker measurements (the number of possible assignments for each subset is $N_s!/\theta_{N_a}!$).

In practical use, many of the association hypotheses will contribute only a negligible amount to the likelihood in (10), and can therefore be removed by a gating procedure based on thresholds for the class probabilities and location measurement errors. The gating procedure works by examining the associations between seeker measurements and Prior Evolver predictions. The procedure is best illustrated with an example. Suppose that it is proposed to associate a Prior Evolver prediction with class $C = j$ and location x with a seeker detection with location y and image chip z. A gating based on the class probabilities is obtained by comparing the posterior class probability based upon the seeker image chip:

$$p(C = j \mid z) = \frac{\pi_j\, p(z \mid C = j)}{\sum_{j'=1}^{J} \pi_{j'}\, p(z \mid C = j')} \quad (11)$$

with a pre-specified threshold. If the probability falls below the threshold then the association is rejected. A gating based upon the location can be obtained by using the seeker location measurement error distribution to set a threshold on the allowable distance between x and y.

3.6 Use of the particles

Numerous quantities of interest can be determined using the particles. These include such quantities as the class probabilities, mean target locations and the most likely association hypotheses for each of the seeker detections. The most likely association hypotheses would be relevant if a specific target is designated in the targeting data as being of interest. The most likely association hypothesis would then indicate which object detected by the seeker is most likely to correspond to the designated target. In this paper we concentrate on the target classes and locations.

The posterior probability that the i-th targeting detection is an object of class j is approximated by:

$$p(C_i = j \mid D_1,\ldots,D_{N_s},T_1,\ldots,T_{N_t}) \propto \sum_{s=1}^{N_p} w^{(s)} I(c_i^{(s)} = j)\ , \quad (12)$$

where I is the indicator function (so $I(x=y)=1$ if $x=y$ and 0 otherwise). The mean locations of the targets at time t_1 can be approximated by:

$$\hat{\mu}_i = E(x_{1,i} \mid D_1,\ldots,D_{N_s},T_1,\ldots,T_{N_t}) = \frac{1}{\sum_{s=1}^{N_p} w^{(s)}} \sum_{s=1}^{N_p} w^{(s)} x_{1,i}^{(s)} \qquad (13)$$

for $i = 1,\ldots,N_t$. Note, however, that estimation of the target locations by the mean of the location posterior distribution might not be appropriate. If the target locations have multi-modal distributions then the mean values might be away from the actual target locations. Ideally, we would examine the full distribution of possible target locations.

4.0 SYNTHETIC EXAMPLE

4.1 Description

The performance of the approach is illustrated with a synthetic example, in which there are three classes of target. Detections in a subset of the x-y plane, along with corresponding image chips were generated randomly to represent the targeting information after application of initial target detection algorithms. The number of targets detected was sampled from a Poisson distribution with restricted range:

$$N_t \sim \text{Poisson}(4) \times I(2 \le N_t \le 5) \qquad (14)$$

The targeting sensor detections were restricted to the region $\{0.0 < x < 1.0, 0.0 < y < 1.0\}$. The covariance matrix of the Gaussian targeting sensor measurement error was given by:

$$\Sigma_t = \begin{pmatrix} 0.025^2 & 0.0 \\ 0.0 & 0.025^2 \end{pmatrix} \qquad (15)$$

Thus the standard deviation of the targeting sensor measurement error was 0.025 along each axis. For the purposes of the documented experiments all targeting detections belonged to the set of three classes (i.e. there were no clutter objects in the targeting detections).

For demonstration purposes, the image chips were replaced by samples from 2-dimensional Gaussian distributions, whose parameters depended on the class of the target. These ID measurements could correspond to length and width, for example. Denoting the mean measurement vectors for class 1, 2 and 3 by μ_1, μ_2 and μ_3 respectively, and the corresponding covariance matrices by Σ_1, Σ_2, Σ_3 we used:

$$\mu_1 = \begin{pmatrix} 1.0 \\ 1.0 \end{pmatrix}, \mu_2 = \begin{pmatrix} 2.0 \\ 0.9 \end{pmatrix}, \mu_3 = \begin{pmatrix} 1.1 \\ 2.0 \end{pmatrix}, \Sigma_1 = \begin{pmatrix} 0.43 & 0.07 \\ 0.07 & 0.43 \end{pmatrix}, \Sigma_2 = \begin{pmatrix} 0.26 & -0.02 \\ -0.02 & 0.30 \end{pmatrix}, \Sigma_3 = \begin{pmatrix} 0.27 & 0.05 \\ 0.05 & 0.41 \end{pmatrix} \qquad (16)$$

The mean vector $\mu_{clutter}$ and covariance matrix $\Sigma_{clutter}$ for the clutter class were:

$$\mu_{clutter} = \begin{pmatrix} 0.5 \\ 0.5 \end{pmatrix}, \quad \Sigma_{clutter} = \begin{pmatrix} 4.0 & 0.0 \\ 0.0 & 4.0 \end{pmatrix} \qquad (17)$$

These measurement distributions were selected to have considerable overlap between the classes. Thus, there will be a non-trivial error rate if classification is attempted using just a single image chip measurement.

Target relocation during weapon fly-out was simulated via a global Gaussian shift of the targets, followed by independent local Gaussian perturbations. Specifically, a global shift of $N(\mu_{global}, \Sigma_{global})$ was applied equally to each target position, followed by an independent perturbation of $N(\mu_{local}, \Sigma_{local})$. The parameters were given by:

$$\mu_{global} = \begin{pmatrix} 0.0 \\ 0.0 \end{pmatrix}, \quad \Sigma_{global} = \begin{pmatrix} 0.2^2 & 0.0 \\ 0.0 & 0.2^2 \end{pmatrix}, \mu_{local} = \begin{pmatrix} 0.0 \\ 0.0 \end{pmatrix}, \quad \Sigma_{local} = \begin{pmatrix} 0.05^2 & 0.0 \\ 0.0 & 0.05^2 \end{pmatrix} \tag{18}$$

To simulate the seeker detections, the relocated targets have been detected with independent probabilities $p_d = 0.8$. Additionally, extra detections in line with a restricted Poisson distribution have been generated. Specifically, extra detections have been generated according to a Poisson distribution with mean $\rho = 2$ but subject to $N_t \le N_s \le 7$. The extra detections were restricted to the region $\{0.0 < x < 1.0, 0.0 < y < 1.0\}$, and were equally likely to be from any of the target classes and the background clutter class. The covariance matrix for the Gaussian seeker measurement error was set to:

$$\Sigma_s = \begin{pmatrix} 0.025^2 & 0.0 \\ 0.0 & 0.025^2 \end{pmatrix} \tag{19}$$

Thus the standard deviation of the seeker measurement error was 0.025 along each axis.

The image chips for the seeker detections were simulated by sampling from 2-dimensional class-conditional Gaussian measurement distributions. The same Gaussian measurement distributions as for the targeting sensor have been used. Although having the same measurement distributions for the targeting sensor and seeker may appear unrealistic, it does not bias the results, because the actual ID measurements are not compared within the Bayesian combination algorithm. Instead, only the likelihood values are combined, via Bayes' theorem.

The Prior Evolver was set to be a global Gaussian perturbation $N(\mu^{PE}_{global}, \Sigma^{PE}_{global})$, followed by independent local perturbations $N(\mu^{PE}_{local}, \Sigma^{PE}_{local})$. If the image chips are ignored, such a specification allows analytical calculations to be made, using Kalman Filters [7]. It is likely that alterations could be made so that the Kalman Filter could be used for the full problem. However to keep the approach generic (*i.e.* applicable to more complicated Prior Evolvers) the full particle filter was used. The parameters used were:

$$\mu^{PE}_{global} = \begin{pmatrix} 0.0 \\ 0.0 \end{pmatrix}, \Sigma^{PE}_{global} = \begin{pmatrix} 0.22^2 & 0.0 \\ 0.0 & 0.22^2 \end{pmatrix}, \mu^{PE}_{local} = \begin{pmatrix} 0.0 \\ 0.0 \end{pmatrix}, \Sigma^{PE}_{local} = \begin{pmatrix} 0.075^2 & 0.0 \\ 0.0 & 0.0.075^2 \end{pmatrix}, \tag{20}$$

Note that the standard deviations of the Gaussian perturbations have been set to be slightly larger than those used to generate the synthetic data, to simulate uncertainty in our knowledge about target relocation. Furthermore, note that the relatively unrestricted target motion is actually making the problem harder, since the lack of constraints means that more particles are needed to ensure that all the possible target behaviour is accounted for.

Within the particle filter algorithm, the parameters of the location and sensor measurement distributions were all set to the same values used to generate the synthetic data. Similarly, the seeker detection probabilities $p_d = 0.8$ and the mean $\rho = 2$ of the Poisson distribution for extra target detections in the seeker image (ignoring the restriction on the number of seeker detections) were all set to the same values used to generate the synthetic data. In real use this would not be possible, and these parameters would need to be estimated, or assigned using expert knowledge.

4.2 Monte Carlo assessment

A Monte Carlo assessment of performance has been conducted. The presented results are based on 200 random simulations, each using 5000 particles. On average there were 3.7 targets detected by the synthetic targeting sensor, and 5.0 objects detected by the seeker.

Two indicators of performance are presented. The first (Table 1) presents the average classification rate for the targets using the Bayesian combination procedure, with the classifications determined according to the maximum class probability calculated using (12). As baseline performance indicators the targeting sensor and seeker sensor classification rates are also presented (for the seeker sensor we treat missed detections as wrong classifications). Both the targeting and seeker sensor results assume that the target relocations are known (i.e. we correctly associate the detections with the actual targets). We can see that the Bayesian approach has been able to maintain the classification rate from the (idealised) targeting sensor, where-as the seeker sensor is penalised for the missed detections. Indeed, the Bayesian approach has actually been able to improve the classification performance over that of the targeting sensor only. This is presumably a result of combining the classification probabilities from the targeting sensor and the seeker.

Targeting sensor only	Seeker only	Bayesian combination
72.5%	59.0%	74.6%

Table 1: Classification rates

The second set of results (Table 2) gives an indication of the performance in determining target locations. In each case the quoted figure is the percentage of detections for which the actual target lay within a circle centred on the detection, with radius equal to three times the average sensor measurement error standard deviation. The detection locations used in the Bayesian combination results were the means of the posterior locations. The performance from the targeting sensor alone is very poor, due to the relocation of targets during weapon fly-out. The idealised seeker is penalised for its missed detections, but overall performs well since the true associations between measurements and targets have been used.

Targeting	Seeker	Bayesian	Bayesian with s.d.
8.2%	80.9%	52.8%	84.5%

Table 2: Performance estimating location

The Bayesian combination algorithm suffers from the fact that only the mean of the posterior distribution has been used, rather than the full posterior distribution. Thus, no account is being made of the estimates of the uncertainty in target location that are inherent within the posterior distribution. To show the effect of this, the percentage of detections for which the actual locations fell within a circle centred on the posterior mean, with radius equal to twice the estimated average posterior standard deviation of the location, is presented to the far right of Table 2. As can be seen by examining the two right-hand columns, taking this uncertainty into account produces much better performance. A factor of two has been used around the average standard deviation, rather than the factor of three used earlier, to penalise the potentially larger (compared to the sensor measurement errors) estimated standard deviations. Specifically, there is a trade-off between correctly estimating the possible variation in the target locations and having such a large spread in the posterior distribution locations that the particles fail to pin-point the targets efficiently (which would negate the military utility of the algorithm).

5.0 SUMMARY AND FUTURE WORK

This paper has successfully developed a Bayesian procedure to enable exploitation of targeting information by a weapon seeker. The aim has been to use a targeting sensor to guide a seeker equipped

weapon to an area containing high-value relocatable targets. The weapon seeker then needs to engage the high value targets, while minimising collateral damage. A Bayesian particle filter based solution has been developed. The procedure has been demonstrated successfully on a synthetic problem. Current work is applying the approach to more realistic scenarios. These scenarios include:

- Complicated target motion during weapon fly-out.
- Use of automated target detection algorithms applied to real data.
- Use of real data chips for the ID sensor measurements of targets.
- Use of more appropriate (and realistic) sensor measurement distributions.

Although, on the face of it, such extensions would be expected to make the problem harder, this is not necessarily the case. For example, real targets might actually be more separable than the overlapping multivariate Gaussian distributions used in the synthetic example. Furthermore, taking into account more sophisticated target motion should improve performance, since it has the effect of constraining the possible target relocations.

6.0 REFERENCES

[1] M.S. Arulampalam, N. Gordon, M. Orton, and B. Ristic. A variable structure multiple model particle filter for GMTI tracking. *Proceedings of 5th International Conference on Information Fusion*, 927–934, 2002.

[2] Y. Bar-Shalom and X.R. Li. *Multitarget-Multisensor Tracking*. YBS Publishing, 1995.

[3] L.G. Brown. A survey of image registration techniques. *ACM Computing Survey*, 24(4):325–376, 1992.

[4] A. Doucet, J.F.G. de Freitas, and N.J. Gordon. *Sequential Monte Carlo Methods in Practice*. New-York:Springer-Verlag, January 2001.

[5] J. Geweke. Bayesian inference in econometric models using Monte Carlo integration. *Econometrica*, 57(6):1317–1339, November 1989.

[6] N. Gordon, S. Maskell, and T. Kirubarajan. Efficient particle filters for joint tracking and classification. *Signal and Data Processing of Small Targets 2002, ed O.E. Drummond*, SPIE Vol 4728, 2002.

[7] N. Gordon, D. Salmond, and D. Fisher. Bayesian target tracking after group pattern distortion. *Signal and Data Processing of Small Targets 1997, ed O.E. Drummond*, SPIE Vol 3163:238–248,1997.

[8] N.J. Gordon and D. Salmond. Bayesian pattern matching technique for target acquisition. *Journal of Guidance, Control, and Dynamics*, 22(1):68–76, January-February 1999.

[9] N.J. Gordon, D.J. Salmond, and A.F.M. Smith. Novel approach to nonlinear/non-Gaussian Bayesian state estimation. *IEE Proceedings-F*, 140(2):107–113, 1993.

[10] T. Kirubarajan, Y. Bar-Shalom, K.R. Pattipati, and I. Kadar. Ground target tracking with variable structure IMM estimator. *IEEE Transactions on Aerospace and Electronic Systems*, 36(1):26–46, January 2000.

[11] P.M. Lee. *Bayesian Statistics, An Introduction*. Arnold, London, 2nd edition, 1997.

[12] P.O. Nougues and D.E. Brown. We know where you are going: tracking objects in terrain. *IMA Journal of Mathematics Applied in Business and Industry*, 8:39–58, 1997.

[13] D. Salmond and N.J. Gordon. Group and extended object tracking. *Proc. of SPIE Conference on Signal and Data Processing of Small Targets 1999, Denver, Colorado*, 3809:284–296, July 1999.

[14] A.F.M. Smith and A.E. Gelfand. Bayesian statistics without tears: A sampling-resampling perspective. *The American Statistician*, 46(2):84–88, May 1992.

[15] C. Sodtke and J. Llinas. Terrain based tracking using position sensors. *Proceedings of 4th International Conference on Information Fusion*, 2, 2001.

[16] A.R. Webb. *Statistical Pattern Recognition*. John Wiley & Sons, Chichester, 2nd edition. 2002.

[17] K.D. Copsey, R.O. Lane, S. Manchanda and A.R. Webb, Bayesian approach to recognising relocatable targets. *NATO RTO SET Symposium SET-080, Target Identification and Recognition using RF Systems*, Oslo, Norway, October, 2004.

[18] M.L. Williams, R.C. Wilson, and E.R. Hancock. Multiple graph matching with Bayesian inference. *Proceedings of the International Conference - Pattern Recognition in Practice V*, 1997.

7.0 ACKNOWLEDGMENT

This research was sponsored by the UK MOD Corporate Research Programme. The authors thank Dr David Salmond, QinetiQ Farnborough, for helpful early discussions.

Bayesian Approach to Recognising Relocatable Targets

Keith Copsey, Richard O. Lane, Sunil Manchanda and Andrew R. Webb
QinetiQ
Malvern Technology Centre
St Andrews Road
Malvern
Worcestershire, WR14 3PS
United Kingdom

K.Copsey@signal.qinetiq.com, rlane1@qinetiq.com, smanchanda@qinetiq.com,
A.Webb@signal.qinetiq.com

ABSTRACT

This paper presents a framework for target acquisition. The targets of interest are relocatable ground vehicles imaged at time $t=t_0$ by a long range targeting sensor and then at a later time $t=t_1$ by a weapon platform. The framework must handle several key issues: changes in scene (vehicle movement between t_0 and t_1); incorporation of domain knowledge (terrain and vehicle type); image registration errors; differences in viewing angle; uncertainty in vehicle type, and location. A modular approach is presented in which the key quantities of interest are probability density functions. There are many technical issues that must be addressed and two in particular are highlighted: the development of generalisation procedures between sensors that enable training data gathered with one sensor to be used to classify data obtained from a different RF sensor (specifically, a procedure to enable ISAR data to be exploited); and the development of techniques that use prior knowledge from a targeting sensor to aid a weapon seeker (the use of targeting information to support acquisition). A Bayesian methodology is adopted and the research is set in the target acquisition context.

1.0 INTRODUCTION

1.1 Target Acquisition

This paper is concerned with the classification of relocatable ground vehicles in weapon seeker data. The overall aim is to develop techniques for target detection and acquisition using data from sensors that differ from the targeting sensors. A Bayesian framework is presented that allows target-specific information acquired by additional (different) sensors, together with domain knowledge of terrain and target properties, to be exploited within the automatic target recognition (ATR) framework for the weapon seeker sensor. There are two sources of additional sensor information that influence the weapon seeker classifier.

1) Targeting data. This is illustrated in Figure 1. A scene of interest is observed at time t_0 by a long range targeting sensor (e.g. SAR). At a later time, t_1, the (evolved) scene is imaged by a weapon seeker. The targeting sensor provides prior knowledge as to the nature and location of target data that may be exploited in the weapon seeker algorithm.

2) Classifier training data. One of the main aims is to enable objects imaged by a weapon's seeker to be classified using ATR systems trained on more readily available ground-based sensor data. The exemplar application used here is to use ATR systems trained on readily available Inverse

Paper presented at the RTO SET Symposium on "Target Identification and Recognition Using RF Systems", held in Oslo, Norway, 11-13 October 2004, and published in RTO-MP-SET-080.

Synthetic Aperture Radar (ISAR) data to classify objects imaged by a Doppler Beam Sharpened (DBS) radar seeker. This is a non-trivial problem since key differences between the measurements from different platforms arise from differences in sensor technology, spatial resolution, polarisation, frequency, imaging geometry and target motion.

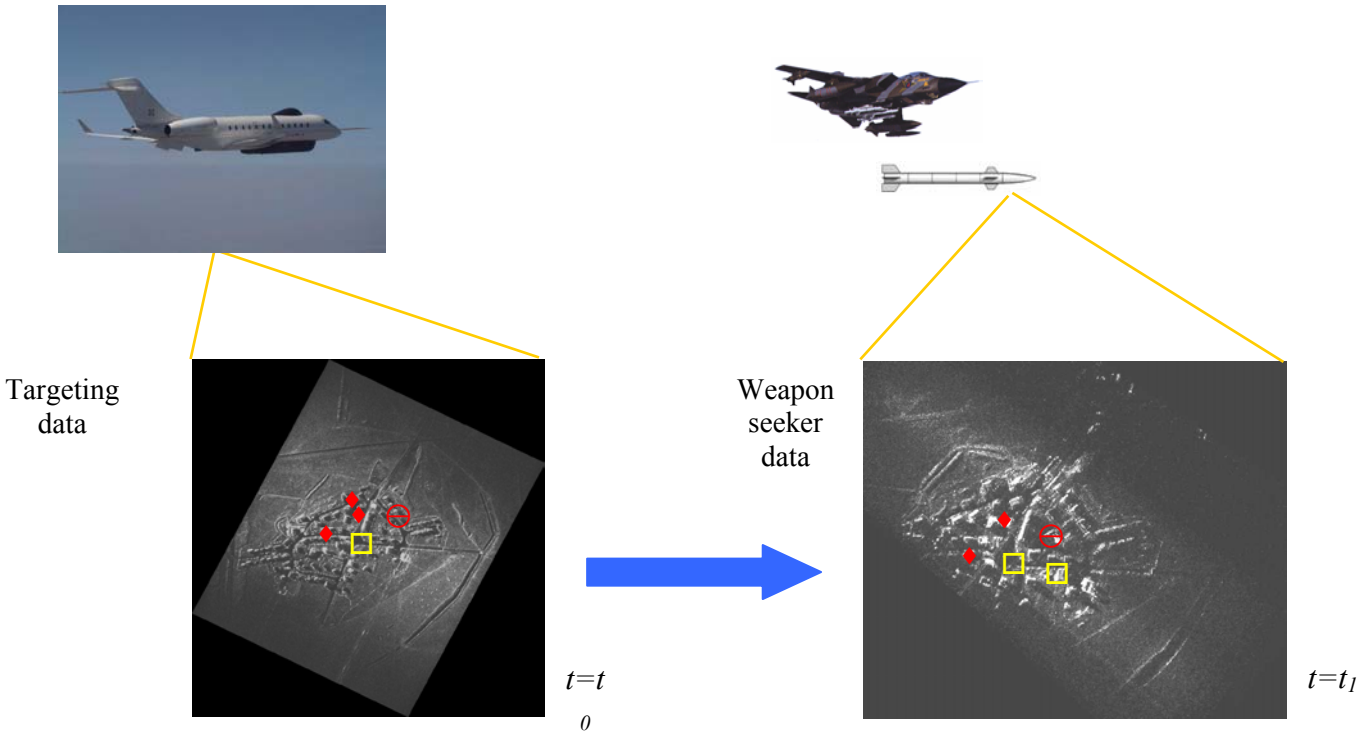

Figure 1: Exploitation of targeting information by a weapon seeker

Among the many issues that must be addressed are:

1) Differing imaging geometry between the targeting sensor and the seeker.

2) Change in the configuration of targets during weapon fly-out (i.e. staleness of the targeting information).

3) Deployment of countermeasures by the targets subsequent to imaging by the targeting sensor.

4) The difficulty (and expense) of obtaining sufficient training data for a weapon seeker ATR system.

5) Uncertainty in target positions and type.

6) Image registration errors.

A particularly adverse effect of items two and three is that a target designated correctly by the targeting sensor may have both a different location and an altered signature by the time that the weapon has reached the targeted area. This will have a significant effect on the ability of the weapon to engage the pre-selected target, especially in typical scenarios where collateral damage must be minimised.

1.2 Aim and Outline of paper

The aim of this paper is to describe a framework for target acquisition that addresses the above issues. Two specific technical issues are highlighted:

1) The development of generalisation procedures between sensors that enable training data gathered with one sensor to be used to classify data obtained from a different RF sensor.

2) The development of techniques that use prior knowledge from a targeting sensor to aid a weapon seeker.

A Bayesian methodology is adopted. The main motivation behind a Bayesian approach is the ability of Bayesian statistics to handle limited and possibly conflicting pieces of information in a fully consistent manner. Further generic arguments in favour of Bayesian techniques include the ability to cope with additional prior information, perhaps elicited from expert knowledge, and the production of confidence intervals and other statistics for the parameters of interest.

Section 2.0 describes the target acquisition framework, with Section 2.1 summarising the technical issues that such a framework must handle and Section 2.2 presenting a framework. Section 3.0 describes the approaches to the two problems above where data from additional sensors is used in the weapon seeker classifier. Finally, we conclude with a summary of the approach.

2.0 A FRAMEWORK FOR TARGET ACQUISITION

2.1 Technical Issues

The following subsections summarise some of the main technical issues that a target acquisition framework must address.

2.1.1 Uncertainty in Vehicle Type

There is uncertainty in vehicle type both within the targeting data and the weapon seeker data. This may be reduced by using contextual information or prior knowledge, but the decision making process must be able to ‘fuse’ both sources of information concerning target type.

2.1.2 Vehicle Movement

The target acquisition procedures must be designed to cope with possible changes in target configuration during weapon fly-out, and possible distortion of signatures due to the deployment of countermeasures. Information that may be exploited includes terrain information, vehicle properties and intelligence information.

2.1.3 Different Sensors

In many applications of pattern classification, including target recognition, the operating conditions for the classifier differ from those used to gather data for training the classifier [6]. Thus, the training conditions are not representative of the expected operating conditions. These differences can be due to a number of factors. The specific aspect that this programme has addressed is the difference of sensors between training and operating conditions. A Bayesian inverse imaging procedure has been developed which allows the seeker data to be classified using ATR systems trained on more readily available (and cheaper) data from a second sensor (in the exemplar application, an ISAR processor). The sensors differ in range and cross-range resolution. By utilising larger amounts of training data covering more varied extended

operating conditions, this procedure is likely to lead to an improved autonomous classification ability for the weapon seeker, that should enable the seeker to identify and react to changes in the configuration of targets during weapon fly-out.

If the ATR system for the sensor providing the training data has some degree of robustness to countermeasures, the proposed seeker ATR system will inherit this robustness, provided that the effects of the countermeasures are similar for the two sensors. However, the caveat has to be added that design of an ATR system that is robust to countermeasures is a current research area in itself.

Proposed approaches to target classifier design currently under investigation include Gaussian mixture models [3], [5], non-linear dimensionality reduction techniques [9], unsupervised ``symmetry-preserving'' neural network techniques [11], [12], and unsupervised encoder networks.

2.1.4 Platform Motion

Uncertainties in platform motion lead to additional differences between training and operating conditions. The inverse imaging procedure above must take account of this through simultaneous auto-focus/super-resolution (see Section 3.2.2).

2.1.5 Different Imaging Geometries

The imaging geometries between the targeting sensor and the weapon seeker will differ. The scene will be observed from different elevations and directions of view. Thus, radar shadow will be different between the two measured scenes leading to a possible source of error in the image registration process.

2.1.6 Registration

In order to fuse the targeting predictions (estimates of target location and type) with the weapon seeker predictions, it is necessary to have a model for the image registration errors. These errors will depend on such factors as the position of the targets in the field of view, the imaging geometries, sensor resolution and target movement.

2.1.7 Vehicle Classes

One of the problems with ATR is the definition of the classes. Vehicles of the same basic type are used for different military purposes and therefore the importance of classifying a vehicle correctly depends on its role. It is not the decision, but the expected utility of the decision that matters classifier design. Therefore, costs of misclassification should be taken into account in the decision making process. The usual criterion of error rate as a means of assessing a classifier is deficient in that it treats all misclassifications equally.

Conversely, vehicles of different type (or the same type with different equipment fits) are used for the same military function leading to radar returns that can vary significantly within the class. Designing classifiers that are robust to intra-class variability can be an important problem to address.

2.1.8 Contextual information

In addition to the information on target type that may be gained from radar measurements of the target, further clues as to target type may result from contextual information and domain knowledge. The type of contextual information that could be incorporated could include the proximity of other potential targets or the type of terrain in which the vehicle is operating. The technical issue to address here is the specification of the domain knowledge and the description of a framework that handles such knowledge, together with target measurements, in a consistent manner.

2.2 Framework

The overall framework proposed by this programme is outlined in Figure 2. A pragmatic Bayesian approach has been proposed in which the various aspects of the problem are treated in a modular fashion, with the outcomes of each module being descriptions of probability distributions that can be combined under a Bayesian probabilistic formalism. An advantage of the modular approach is that existing techniques (such as those developed for registering images from different sensors) can be used where appropriate. In particular, the green boxes in Figure 2 relate to processes where we have relied on current state-of-the-art techniques with minimal customisation. Since many of these processes require further research to provide satisfactory solutions, the formalism is designed in such a manner that new techniques can be incorporated as they reach maturity.

We now consider the main modules in Figure 2 in turn.

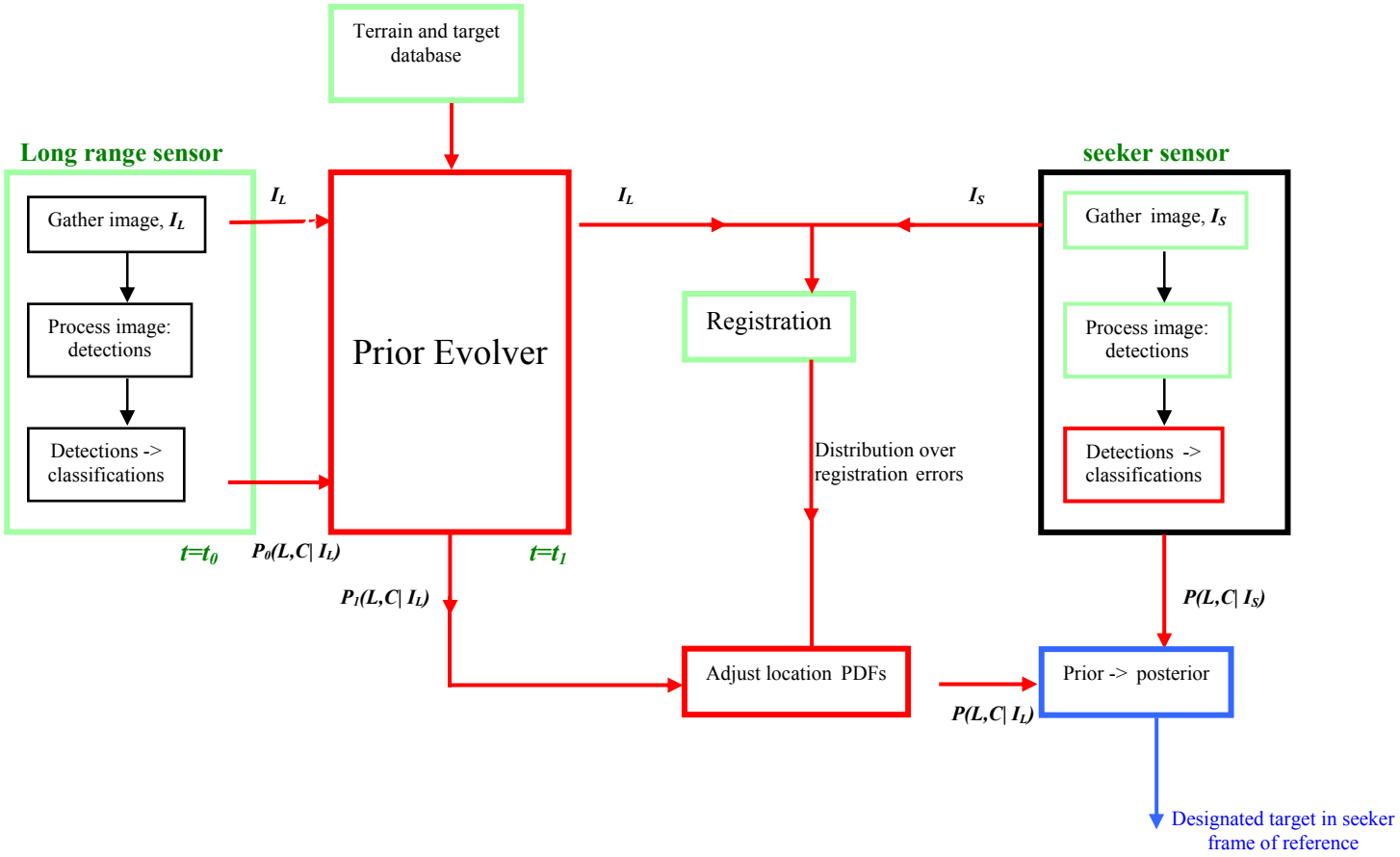

Figure 2: Framework for the exploitation of targeting information by a weapon seeker

2.2.1 Long-range Sensor

The long-range sensor, depicted as the green box on the left-hand side of Figure 2, captures image data, $\boldsymbol{I}_L$, at time $t=t_0$ and processes the data to produce target detections and identifications. This processing may be performed manually, or by some semi-automatic process. The output of this process is an estimate of the

number of targets present, with their locations and types. This is represented by the probability density function, $p_0(L, C \mid \boldsymbol{I}_L)$ where L represents the vector of target locations and C represents the vector of target classes. This captures the uncertainty in the quantities L and C at time $t=t_0$.

2.2.2 Prior Evolver

The prior evolver is used to update the information from the targeting sensor to allow for target motion during weapon fly-out. This consists of predicting how the detections gleaned from the targeting sensor at $t=t_0$ will have changed by the time $t=t_1$ that the weapon seeker views the targeted area. This evolution of the probability density function can be modelled to include bulk motion of targets (perhaps reflecting the motion of a convoy) and more complicated behaviour incorporating knowledge of the terrain and likely target behaviour. The result of this process is the probability density function, $p_1(L, C \mid \boldsymbol{I}_L)$, which is the original distribution evolved to time $t=t_1$. Contextual information and domain-specific knowledge can be incorporated within this density [4].

2.2.3 Seeker Sensor

The seeker sensor box performs a similar operation to the long-range sensor. Image data, $\boldsymbol{I}_S$, is gathered using the seeker sensor, this time at time $t=t_1$, and processed to produce $p(L, C \mid \boldsymbol{I}_S)$, the distribution over locations and classes of target given the seeker data. Note that in this case, the dimensionality of L and C may differ from the long-range sensor case since the seeker detection process may estimate a different number of targets to be present. Also, the locations are measured in the seeker frame of reference.

The on-board classifier that produces the classifications is designed using training data. An approach that uses ISAR data to train a classifier that is applied to DBS images is outlined in Section 3.2.2.

2.2.4 Registration

Registration of the targeting sensor image, $\boldsymbol{I}_L$, to the frame of reference of the seeker produces a translation, with associate errors, expressed as a probability density function.

2.2.5 Adjust Location PDFs

The registration information enables the updated targeting information (expressed in the form of probability density $p_1(L, C \mid \boldsymbol{I}_L)$) to be adjusted to the seeker frame of reference. This is denoted in the figure by the probability density function, $p(L, C \mid \boldsymbol{I}_L)$.

2.2.6 Prior -> Posterior

The incorporation of uncertain targeting information, expressed in terms of the probability density function $p_1(L, C \mid \boldsymbol{I}_L)$, with uncertain seeker detections, described by $p_1(L, C \mid \boldsymbol{I}_S)$, occurs in the (blue) box labelled ``Prior -> posterior'', and is outlined in Section 3.2. The output of this procedure is the updated information (in terms of target class probabilities) for the objects within the seeker frame of reference. This information will improve the ability of the weapon to engage the targets designated on launch of the weapon while minimising collateral damage.

3.0 INCORPORATING ADDITIONAL SENSOR INFORMATION

3.1 Introduction

The previous section described a framework for target acquisition. A modular approach was proposed in which the key quantity of interest was a probability density function. Manipulation of these pdfs by each

module resulted in a description of the designated target of interest in the seeker frame of reference. There are two main areas where information from different sensors has to be combined or fused. One is where the prior targeting information from the long-range sensor is combined with information from the seeker (the 'prior->posterior' box in Figure 2). This is reported in detail in [1]. The second area is where training data from an ISAR sensor is used to train a classifier applied to DBS imagery (the 'Detections-> classifications' box in the seeker sensor). This is reported in [2] and [8]. The approaches are summarised below.

3.2 Exploiting Targeting Information

3.2.1 Targeting detections

The number of targeting sensor detections at time t_0 is denoted by N_t. The estimated locations of the detections and associated image chips (ID sensor measurements) are denoted by $l_1,...,l_{N_t}$ and $r_1,...,r_{N_t}$ respectively. For notational ease, we define $T_i = (l_i, r_i)$ for $i = 1,...,N_t$.

Assuming that there are J possible target classes, the ID sensor measurements are used to obtain J-dimensional class probability vectors ψ_i for each detection, where $\psi_{i,j}$ is the estimated probability that the i-th detection is the j-th class, for $i = 1,...,N_t$ and $j = 1,...,J$. Such class probabilities could be estimated using a standard ATR system or possibly via human intervention.

The measurement errors for the target locations are assigned Gaussian distributions, so that $l \sim N(x, \Sigma_t)$ where x is the actual target location, and Σ_t is the covariance matrix for the measurement errors. The covariance matrix should be determined by considering the sensor performance characteristics along with the imaging conditions.

3.2.2 Seeker detections

The number of seeker detections at time t_1 is denoted by N_s. Since the targeting sensor indicates that there are N_t targets present, the threshold for detecting objects within the seeker image is assumed to be set so that $N_s \geq N_t$. Adaptation of the proposed approach to cope with $N_s < N_t$ would be trivial.

The locations of these seeker detections are denoted $y_1,...,y_{N_s}$, and the associated image chips (ID sensor measurements) are $z_1,...,z_{N_s}$. For notational ease we define $D_i = (y_i, z_i)$ for $i = 1,...,N_s$.

It is assumed that density models (conditional on class) can be estimated for the ID measurements. Estimating these distributions given only limited training data for the weapon seeker is the subject of current research. These distributions can be represented by $p(z \mid C = j)$, where z is the image chip and j is the index of the class C of the object. Ideally, each density estimate should incorporate the uncertainty in the centre of each detected object. Mixture model densities meet many of the requirements for these class-conditional densities.

In addition to probability densities for target image chips, it is assumed that a probability density has been estimated for image chips that correspond to the sort of background noise and clutter that will pass through the target detection algorithm. This density is denoted by $p(z \mid C = 0)$.

If the class of a target is unassigned, a mixture distribution is used for the ID sensor measurements:

$$p(z) = \pi_0 P(z \mid C = 0) + (1 - \pi_0) \sum_{j=1}^{J} \pi_j p(z \mid C = j) \tag{1}$$

where $\pi_1, ..., \pi_J$ represent the prior class probabilities excluding background clutter, and π_0 is the prior probability for background clutter. Note that the prior probability for background clutter will be related to the false alarm probability of the detection algorithm, rather than the ratio of background clutter to targets. This reflects the fact that the initial detection stage will already have eliminated most of the background noise.

The measurement errors for the object locations are assigned Gaussian distributions, so that $y \sim N(x, \Sigma_s)$ where x is the actual object location, and Σ_s is the covariance matrix for the measurement errors. As with the targeting sensor, the covariance matrix should be determined by considering the sensor performance characteristics together with the imaging conditions. Locations of any additional targets and background clutter are assumed to be distributed uniformly over the surveyed region.

3.2.3 Bayesian solution

The actual classes and locations of the targets detected by the targeting sensor at time t_0 are denoted by $(c_1, ..., c_{N_t})$ and $(x_{0,1}, ..., x_{0,N_t})$ respectively. By time t_1 the new locations are represented by $(x_{1,1}, ..., x_{1,N_t})$. This reflects the fact that the targets may have relocated during the weapon fly-out time $t_1 - t_0$. The actual classes are of course unchanged. The posterior distribution of interest at time t_1 is:

$$p(x_{1,1}, ..., x_{1,N_t}, c_1, ..., c_{N_t} \mid T_1, ..., T_{N_t}, D_1, ..., D_{N_s}), \tag{2}$$

the distribution of the locations and types of the targets given seeker and targeting data. In [1], a Bayesian technique based on particle filtering [7] is used to obtain samples from the posterior distribution.

3.3 Generalising Classifiers

We now turn to the problem of designing a classifier for the seeker (DBS) data. We denote measurements in the training (ISAR) conditions by the variable x and measurements in the operating (DBS) conditions by the variable z. We suppose that we have a training set $D = \{x_i, i = 1, \ldots, N\}$ of samples gathered under the training conditions. This training set is used to design a Bayesian classifier (*i.e.* a classifier based on probability distributions for the sensor measurements) [10], which outputs posterior class probabilities for each ISAR measurement of an object to be classified. The posterior class probabilities estimated by the classifier for an ISAR measurement x are denoted by $p(C = j \mid x, D)$, for $j = 1, \ldots, J$ where J is the number of target classes.

In accordance with our operational scenario, during operational use we only have access to a DBS measurement z (rather than the ISAR measurement x) so cannot use the Bayesian classifier directly. To proceed we require a model $p(x \mid z)$ for the relationship between an operational sensor measurement and a training sensor measurement. Then, we can consider the expectation of the posterior class probabilities given the operational sensor measurement:

$$E[p(C = j \mid x, D) \mid z] = \int p(C = j \mid x, D)\, p(x \mid z) dx \tag{3}$$

In this manner, given a model for the conditional density $p(x \mid z)$ we can use the training sensor classifier to classify an operational sensor measurement.

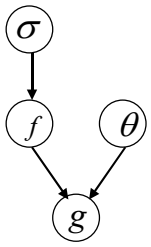

σ	Scattering cross section
f	Scattered field
θ	Defocus parameters
g	Image - either x for ISAR or z for DBS

Figure 3: Imaging framework

We assume a radar sensor measurement process as shown in Figure 3.

For the specified sensor measurement processes, the conditional density $p(x \mid z)$ can be expressed as:

$$p(x \mid z) = \int d\sigma\, p(x, \sigma \mid z) = \int d\sigma\, p(x \mid \sigma) p(\sigma \mid z) \tag{4}$$

The term $p(x \mid \sigma)$ represents the forward sensor measurement process for the training sensor, *i.e.* generation of a training sensor image from an underlying cross section σ (temporarily suppressing the defocus parameters within our notation). The term $p(\sigma \mid z)$ is the restored cross section given the operational sensor measurement. Determination of $p(\sigma \mid z)$ corresponds to a super-resolution problem.

Thus, Equation (4) states that to find the distribution of ISAR measurements that correspond to a DBS image, z, we find the distribution of underlying cross sections, σ, that give rise to z, and then pass these through an ISAR imaging model. The resulting conditional distribution, $p(x \mid z)$, is then substituted into (3) to classify z. Since (3) cannot be evaluated analytically for the majority of sensor models, samples are drawn from the relevant posterior distributions and inference is based on those samples. In [8], a Bayesian approach to simultaneous auto-focus/super-resolution is described. In [2] results of this classification procedure on synthetic data are presented.

4.0 SUMMARY

This paper has described a framework for target acquisition that has the following features

1) It presents a modular approach in which the key quantities of interest passed between modules are probability density functions;

2) It handles uncertainty in target locations and classes;

3) Prior targeting information is combined with seeker data in a consistent manner;

4) A classifier trained on ISAR data may be used to provides estimates of target type for DBS data using a Bayesian auto-focus/super-resolution approach;

5) Knowledge of the properties of vehicle and terrain type may be included in a 'prior evolver';

6) Registration errors are treated probabilistically.

The approaches to two particular aspects of the target detection problem have been outlined, namely

1) the combination of prior targeting data with seeker detections to produce posterior estimates of target locations and classes;

2) the use of a previously trained classifier on data recorded from a different sensor.

5.0 REFERENCES

[1] Copsey, K.D., Lane, R.O., Manchanda, S. and Webb, A.R. (2004). Bayesian Approach to exploiting prior targeting information within a weapon seeker. NATO RTO SET Symposium SET-080. *Target Identification and Recognition Using RF Systems*. Oslo, Norway.

[2] Copsey, K.D., Lane, R.O. and Webb, A.R. (2004). Designing NCTR algorithms when operating sensor conditions differ from training conditions. *Radar 2004*. International Conference on Radar Systems, Toulouse, France.

[3] Copsey, K.D. and Webb, A.R. (2000). Bayesian approach to mixture models for discrimination. *Advances in Pattern Recognition*, F.J. Ferri, J.M. Inesta, A. Amin and P. Pudil (eds). Springer Lecture Notes in Computer Science 1876, 491-500.

[4] Copsey, K.D. and Webb, A.R. (2002). Bayesian networks for incorporation of contextual information in target recognition systems. In T. Caelli, A, Amin, R.P.W. Duin, M. Kamel and D. de Ridder (editors) *Structural, Syntactic and Statistical Pattern Recognition*, Proceedings of the Joint IAPR International Workshops SSPR2002 and SPR2002, Windsor, Canada, August 2002. Lecture Notes in Computer Science 1876, 709-717, Springer.

[5] Copsey, K.D. and Webb, A.R. (2003). Bayesian gamma mixture model approach to radar target recognition *IEEE Transactions on Aerospace and Electronic Systems*. 39(4), 1201- 1217.

[6] Copsey, K.D. and Webb, A.R. (2004). Classifier design for population and sensor drift. *Structural, Syntactic and Statistical Pattern Recognition*, Proceedings of the Joint IAPR International Workshops SSPR2004 and SPR2004, Lisbon, Portugal, August 2004. Lecture Notes in Computer Science, Springer.

[7] Doucet, A., de Freitas, J.F.G. and Gordon, N.J. (2001). *Sequential Monte Carlo Methods in Practice*. New York: Springer-Verlag.

[8] Lane, R.O., Copsey, K.D. and Webb, A.R. (2004). A Bayesian approach to simultaneous autofocus and super-resolution. Proc. SPIE 5427. *Algorithms for Synthetic Aperture Radar Imagery XI*. E.G. Zelnio and F.D. Garber (eds). Orlando, FL, USA.

[9] Maskall, G.T. and Webb, A.R. (2002). Nonlinear feature extraction for MMW image classification: a supervised approach. Proc. SPIE 4726, 353-363. *Automatic Target Recognition XII*. Firooz A. Sadjadi (ed).

[10] Webb, A.R. (2002). *Statistical Pattern Recognition*. Second edition. John Wiley and Sons, Chichester.

[11] Webber, C.J. (2000). Self-organisation of symmetry networks: transformation invariance from the symmetry-breaking mechanism. *Neural Computation*, 12(3), 565-596.

[12] Webber, C.J. (2001). Predictions of the spontaneous symmetry-breaking theory for visual code completeness and spatial scaling in single-cell learning rules. *Neural Computation*, 13(5), 1023-1043.

6.0 ACKNOWLEDGEMENT

This research was sponsored by the UK MOD Corporate Research Programme.

DRFM-Modulator for HRR-Jamming

Øyvind Thingsrud
FFI – Norwegian Defence Research Establishment
Division for Information Management
P.O. Box 25, NO-2027 Kjeller
Norway

oyvind.thingsrud@ffi.no

ABSTRACT

The Digital RF Memory (DRFM) is a key component in modern radar jamming systems. To introduce false targets in a High-Range-Resolution (HRR) radar and other high-resolution imaging radars, a new generation DRFM-system is being developed with far better range resolution and modulation properties. The DRFM also needs better performance in the D/A-converter than in the systems used today, because of the high fidelity jamming signal. This paper is a part of a Master thesis [6] and describes a new type of DRFM-modulator that uses digital signal processing in the frequency-domain for generation of false targets [1]. The modulator is able to produce a radar scene with a number of complex false targets constructed of many single reflectors with individual modulation and with a credible background. Some of the different strategies for the modulator topology will be introduced and discussed. The modulator is being implemented using parallel digital logic in a number of Field Programmable Gate Arrays (FPGA) on a single printed circuit board (PCB) for use in FFIs experimental radar jammer named EKKO II [4].

1.0 BACKGROUND

High-resolution imaging radar is of increasing importance in numerous tasks, both civilian and military. This has resulted in a requirement for research on Electronic Countermeasures (ECM) against this class of radar. Over the last five years one main task in a research program at FFI has been to demonstrate the capability of introducing false information in a controlled, programmable manner in high-resolution radars of various kinds [2]. The work has included theoretical studies, computer modelling, field tests using existing hardware, and development of a whole new system, named EKKO II, designed with the above mentioned task in mind. Figure 1 shows the EKKO II system in X-band configuration.

Figure 1: EKKO II in X-band configuration

Paper presented at the RTO SET Symposium on "Target Identification and Recognition Using RF Systems", held in Oslo, Norway, 11-13 October 2004, and published in RTO-MP-SET-080.

2.0 PROBLEM TO BE ADDRESSED

In the EKKO II experimental radar jammer the synthesis of false targets are realised with *direct modulation* and are implemented in FGPA. Direct modulation is a method where range delay, frequency and amplitude changes for each false point scatterer are generated in dedicated digital branches, as an imitation of the physical reflection process in the nature. This method is easy to understand and synthesises credible targets, but the hardware complexity increases as the number of targets increases.

Thus, new methods for synthesising false targets that are independent of the number of targets are of interest. This paper describes a new type of DRFM-modulator that uses digital signal processing in the frequency-domain. The method is sketched in [1] and presents a possibility to achieve large numbers of false targets without an increasing hardware complexity.

The new DRFM-modulator should produce a radar scene with a number of complex false targets constructed of many single reflectors with individual modulation and with a credible background. The modulator is to be used for synthesis of high-resolution range profiles, as illustrated in Figure 2 and for synthesis of *Synthetic Aperture Radar (SAR)* / *Inverse Synthetic Aperture Radar (ISAR)* images.

Figure 2 contains a SAR image of a cultivated landscape that is overlaid a high-resolution range profile. For synthesising a SAR scene, new high-resolution range profiles with different appearance have to be generated continuously.

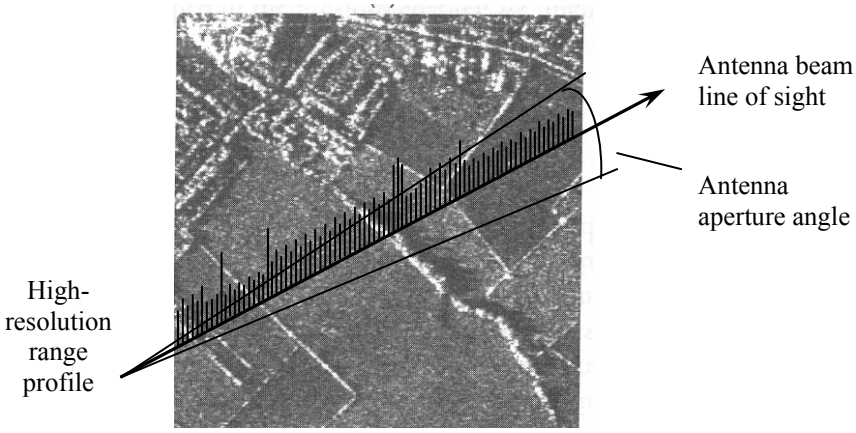

Figure 2: SAR image of cultivated landscape with high-resolution range profile drawn

3.0 INTRODUCTION

A system designed to present false credible information in an arbitrary high-resolution radar system should be designed as a repeater that is able to store the radar signal, for modulation and retransmission. The central component of such a system is the storage device, the *Digital Radio Frequency Memory (DRFM)*, ref Figure 3.

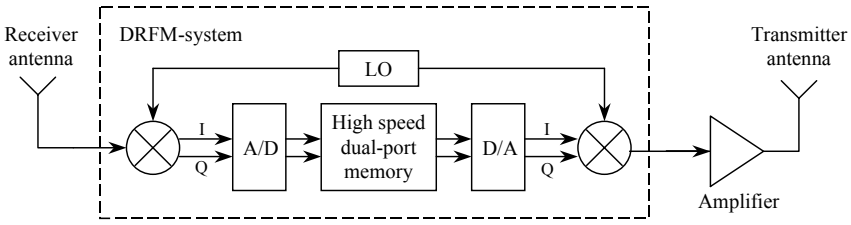

Figure 3: A DRFM radar jamming system

The retransmission of a perfect replica of the radar signal will generate a point target response in the radar. To generate false credible information in a high-resolution radar image though, a target or a scene with spatial extent must be created. Basically this can be done in the time-domain by a digital *Finite Impulse Response (FIR)* filter [3], shown in Figure 4.

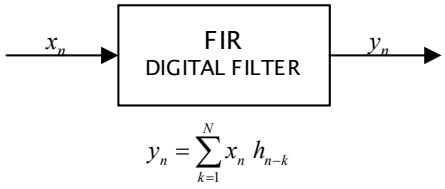

Figure 4: A digital FIR-filter

If the radar signal is the input sequence x_n and the point targets are the filter coefficients in the impulse response h_n, the output sequence y_n is the convolution between sequence x_n and h_n. Sequence y_n is then the desired jamming signal.

The structure in Figure 5 is a parallel realisation of a digital FIR-filter, where the branches with filter coefficients equal to zero are omitted. Here, the output sequence is generated by adding a number of radar signal replicas, each with individual modulation in time, amplitude and phase. This capability is made possible by modern high-speed digital electronics using multiple *Field Programmable Gate Array (FPGA)* circuits. Figure 5 illustrates the parallel time-domain realisation.

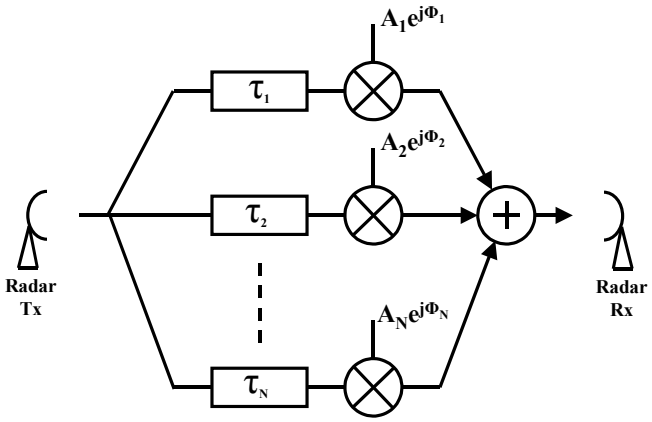

Figure 5: Time-domain realisation of time overlapping radar replicas

Alternatively the convolution between the radar signal and the point targets can be calculated using the *Fast Convolution Process (FCP)* algorithm, which make use of the *Fast Fourier Transform (FFT)* implementation of the *Discrete Fourier Transform (DFT)*. The FCP-convolution is much more efficient with respect to computational requirements than the standard convolution, especially with long sequence lengths, ref [5].

Table 1 shows a computational comparison of number of additions and multiplications for FCP-convolution versus standard convolution. N is the length of the two sequences and L is a legal FFT size ($L=2^m$, where m is an integer) that is greater or equal to N_1+N_2-1, where N_1 and N_2 are the two sequences.

Table 1: Computational comparison for FCP-convolution versus standard convolution

	# Complex additions	# Complex multiplications
Standard convolution	$(N-1)^2$	N^2
FCP-convolution	$3L\log_2 L$	$3L/2\log_2 L+L$

Figure 6 gives a graphical illustration of the equations in Table 1 for some data set sizes of N.

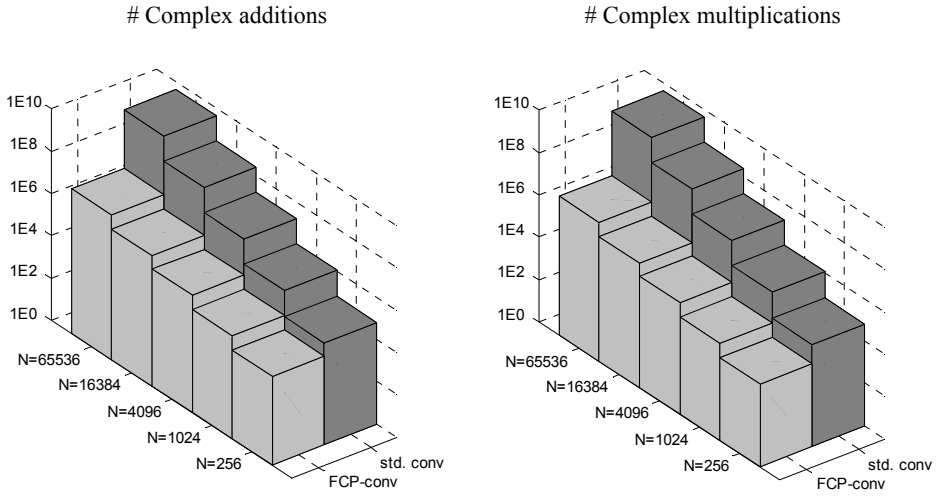

Figure 6: Graphical illustration of the computational loads from Table 1

Using FCP-convolution the total response can be computed fast and directly, rather than implementing the individual delays and modulations in hardware. This can be done by transforming the radar signal and the targets to the frequency-domain, performing calculations, and transforming the combination back to the time-domain. This concept is referred to as *Computed ECM* in [1].

There is a potential for achieving a considerably higher number of radar resolution cells using this approach. Whereas in the direct time-domain implementation the number of targets or resolution cells achieved is limited by the space within the FPGAs, in the Computed ECM case the limiting factors are

system dynamic range, number of sampling bits, calculation speed etc. This is a planned future capability for the EKKO II radar jammer [4]. Figure 7 illustrates the concept of the frequency-domain realisation.

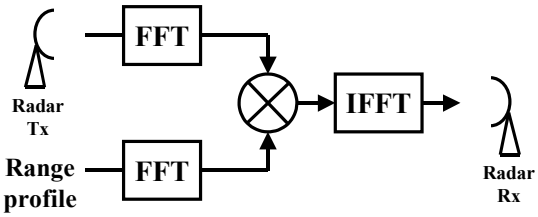

Figure 7: Frequency-domain realisation of time overlapping radar replicas

The advantage of frequency-domain realisation is that the jammers complexity is nearly constant with increasing number of targets in the jamming scene. On the other hand, the complexity does increase with increasing number of samples in the radar signal and with increasing size of the radar scene.

4.0 COMPUTER MODEL

To examine the proposed DRFM-modulator structures, a computer model of the modulator, the target and the high-resolution radar is used. Figure 8 gives a brief description of the simplified computer model.

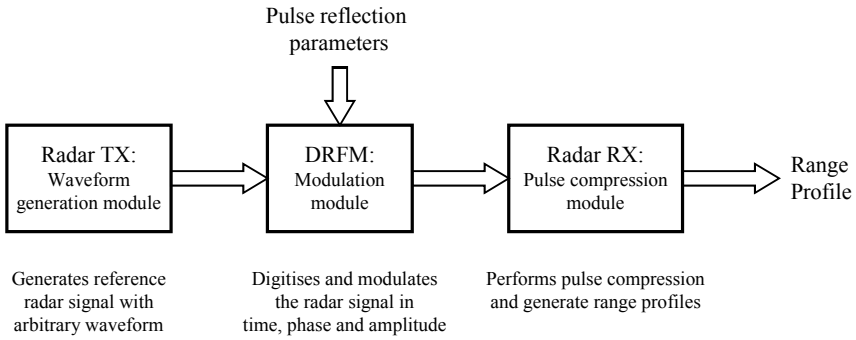

Figure 8: Schematic description of the computer model

Figure 9 gives an example of a HRR profile generated in the computer model. An aircraft with marked reflection points in red is illuminated from a selected angle and with a chosen waveform. In this case the pulse compression leads to range cell size of approximately 4 samples and a total of 125 range cells over the aircraft. Different compression waveforms and factors are supported.

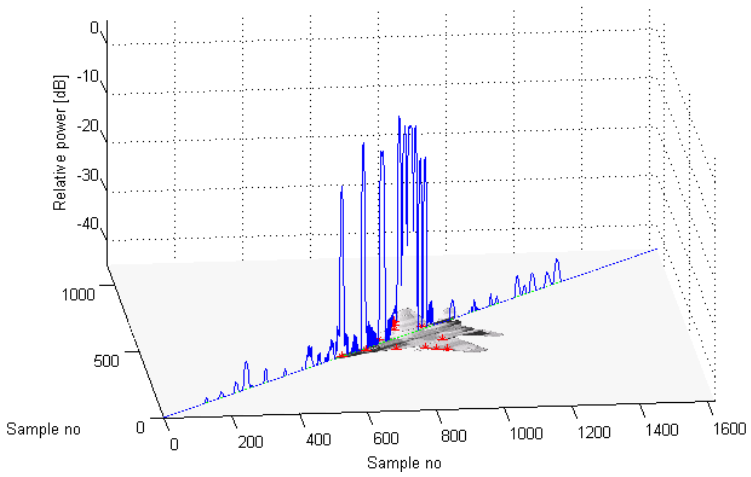

Figure 9: Example of a HRR range profile generated in the computer model

In this paper the computer model is configured with a simplified complex reference target constructed of twelve single point reflectors. Each of the reflectors has different position, amplitude and phase. A chirp radar signal with *Time-Bandwidth product (TBW)* of 127 is then applied to the modulator and the jamming signal is calculated. The last step in the computer model is the pulse compression stage and the generation of the HRR range profiles. Figure 10 shows the simplified complex reference target.

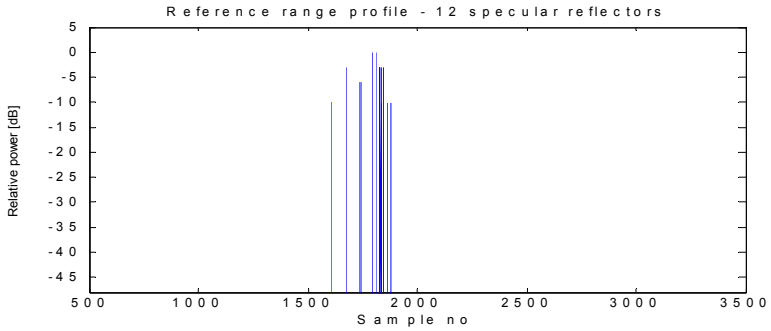

Figure 10: The simplified complex reference target with twelve single point reflectors

For verification of the proposed realisation concepts, the modulator structures and their corresponding range profiles from the computer model are compared and discussed.

5.0 PROPOSED CONCEPTS FOR FREQUENCY-DOMAIN DRFM-MODULATOR REALISATIONS

The following DRFM-modulator realisation concepts are developed for generation of credible targets on HRR-radar, but the conclusions will also be valid for the more advanced SAR and ISAR as well, since a lot of the fundamentals are common to all imaging radars.

The goal for the development is a modulator design with minimum insertion delay and maximum coverage in range. It is desirable to synthesise the complex reflections from each of the targets, and to manage the generation of the background scene. The acceptable values for insertion delay and range

coverage are strongly dependent of the actual radar system. Since the modulator is planned used against different type of radars, the modulator design will make use of the reconfigurable structure of the FPGA.

5.1 FCP-convolution structure

A single FCP-convolution structure is the simplest modulator realisation found using frequency-domain. This structure has however limited throughput and will introduce some delay in the signal flow through the modulator. The throughput is dependent of the implementation of the FFT and the inverse FFT (IFFT), which can be supplied as *Intellectual Property (IP)* cores from for example the FPGA manufacturer. Xilinx CoreGen IP-library supports FFT / IFFT up to 16384 data points at ~170 MHz clock speeds. Specialised manufactures deliver state of the art pipeline IP-cores for high performance transformations for more than 131072 data points at 400 MHz clock rate.

When using FCP-convolution, the length of the FFT transforms i.e. the number of data points in the transform, determine the range extent of the covered scene since the FFT length equals the sum of the number of samples in the radar signal and the covered scene. The available calculation time is usually equal to the radar's *Pulse Repetition Interval (PRI)*, but it varies depending of the actual radar system.

Figure 11 shows a simplified schematic for a modulator using a single FCP-convolution.

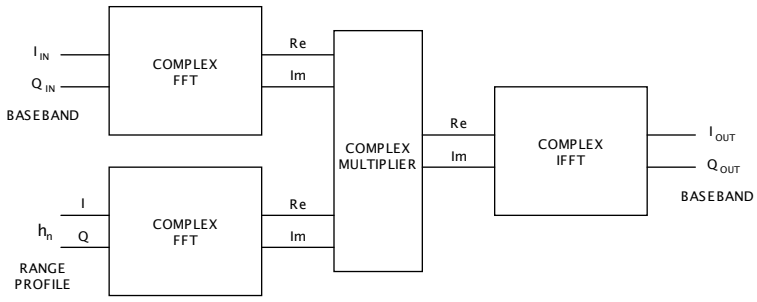

Figure 11: FCP-convolution realisation

The modulator structure is examined using the data model described in chapter 3.0. Figure 12 gives a simulated HRR range profile of the simplified complex target. The range profile in Figure 12 is identical to range profiles generated in the modulator using time-domain realisation.

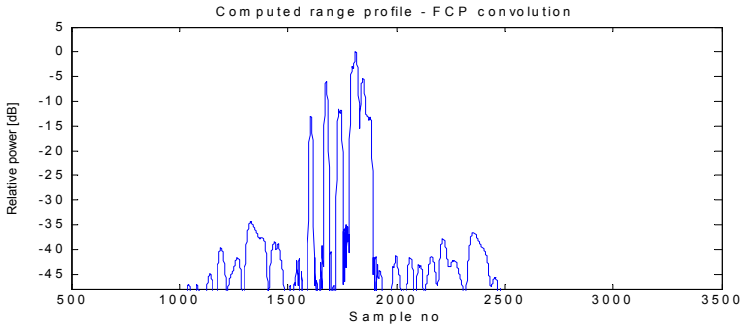

Figure 12: Simulated HRR range profile after pulse compression of example target generated with FCP-convolution

Figure 12 also shows that the pulse compression process generates side lobes at both shorter and longer ranges than the targets reflectors. If the coded radar waveform had better performance on side lobe suppression, the spurious signals in the range profile would have been lower.

5.2 FCP-convolution structure with separate synthesis of object and background

In some instances, a possibility for separate synthesis of object and background is preferable. Figure 13 shows a simplified schematic for a modulator that covers this approach. The complexity grows compared to a modulator without separate synthesis, but the insertion delay is almost the same.

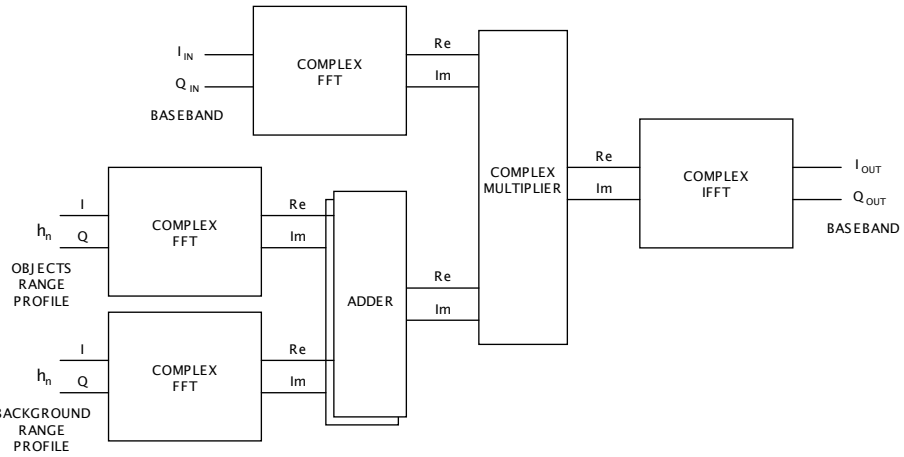

Figure 13: FCP-convolution realisation with separate synthesis of object and background

This modulator realisation is examined in the same manner as last structure by using the data model described in chapter 3.0. Figure 14 shows the simulated high-resolution range profile containing both the simplified complex target and a background profile. The synthesised target is identical to the target in the last structure and the generated background has a uniform and almost constant reflection level throughout the range scene.

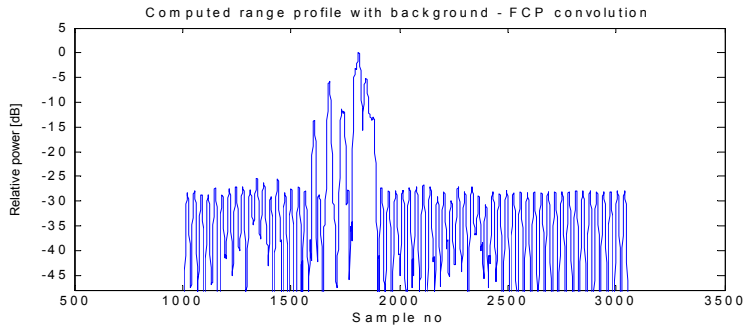

Figure 14: Simulated high-resolution range profile after pulse compression of example target generated with FCP-convolution and separate synthesis of object and background

The background profile in Figure 14 is synthesised with an artificially ideal appearance for demonstration, but with use of other reflection coefficients a credible background can be generated.

5.3 Distributed FCP-convolution structures with parametric generator for background profile

This structure is an example of a versatile, fast and complex modulator realisation. It contains several parallel FCP-convolutions, for higher speed and less insertion delay, connected in a distributed configuration for less complexity. The structure includes a parametric generator for the background profile, which gives a high level description of the appearance over time (mean level, smoothness, distribution, sample rate) throughout the range profile. Usually the background synthesis requires huge amount of reflection coefficients, but with the parametric generator the requirements for configuration data is greatly reduced.

The last feature included in the proposed structure is a set of dual-port memory circuits that separate the high-speed convolution circuits and the modulation coefficient generation process. The circuit separation makes it possible to update the modulation coefficients at a lower sample rate than the convolution-processing rate. In some instances this reduction in update rate gives noticeable improvements. Figure 15 and Figure 16 show a simplified schematic for an extended modulator using multiple FCP-convolutions and a parametric generator for background synthesis.

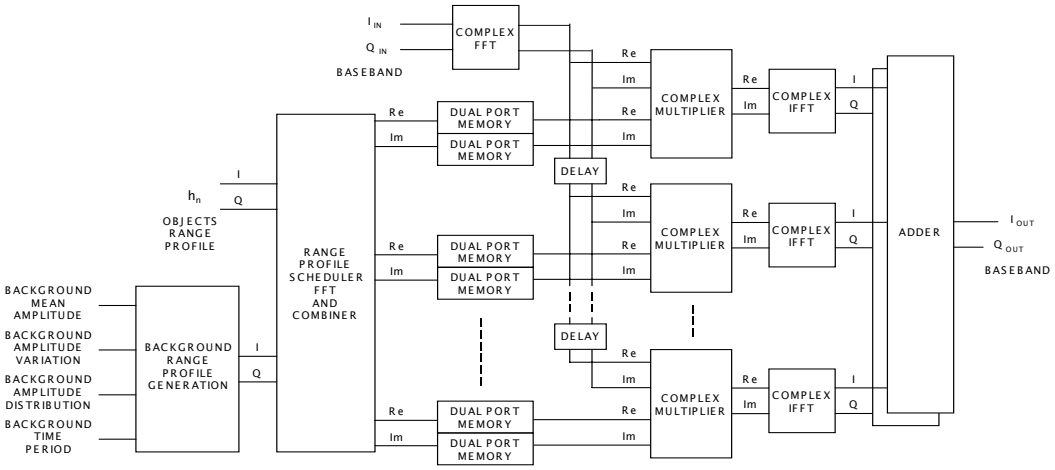

Figure 15: Distributed FCP-convolution realisation with parametric generator for background profile

Because of the separate synthesis of object and background, and the multiple convolution circuits, the complexity increases a lot. Specially the *Range profile scheduler, FFT and Combiner* block grows, as seen in Figure 16.

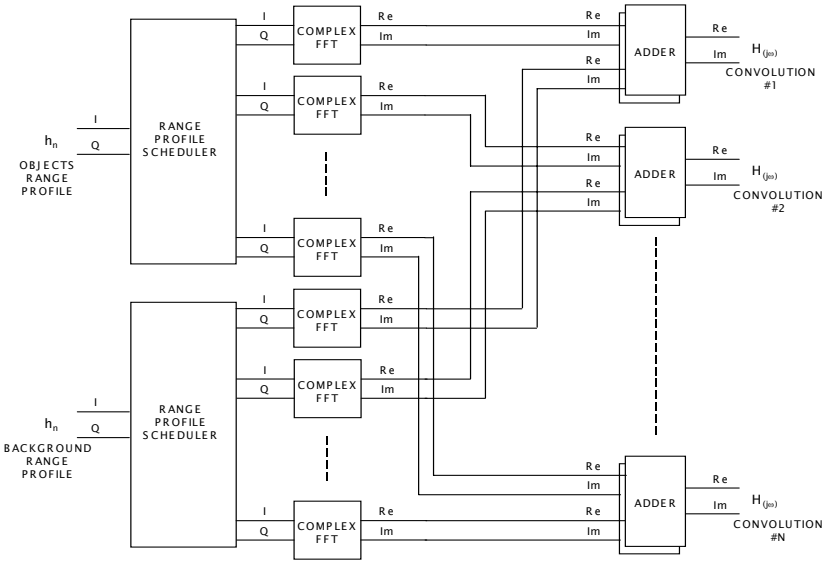

Figure 16: Detail schematic of Range profile scheduler, FFT and Combiner in Figure 15

Figure 17 shows the simulated high-resolution range profile synthesised with the parametric background generator. The generated background has sections with different mean reflective level and smoothness, and some minor areas with highly reflective objects. In the middle of the range profile, a typical shadow can be seen – an area with low reflection. Figure 17 demonstrates of the possibilities and versatility of the parametric generator.

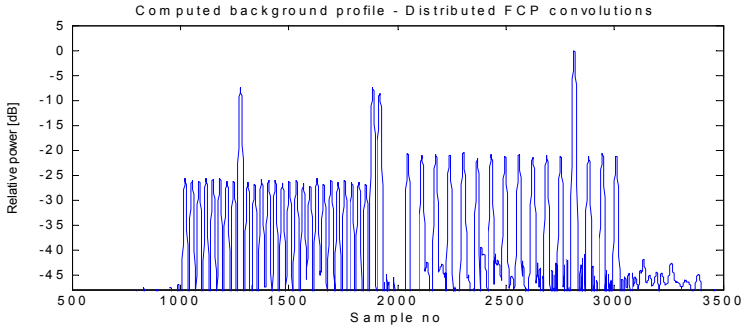

Figure 17: Simulated high-resolution range profile after pulse compression of example background profile generated with parametric generator

To illustrate how the parametric background generator can be used to synthesise credible landscape, a SAR image is used with a high-resolution range profile drawn on top, ref Figure 2. For synthesising a whole SAR scene, the background generator has to be supplied new parameters regularly.

5.4 Future developments

Input parameters for the proposed DRFM-modulator structures have been a radar waveform that has relatively short duration in time and hence short extension in range, and a covered scene with long extension in range. This is not always the case; sometimes the radar waveform has an extension in range as long as the covered scene or even longer. To deal with this situation, the modulator structures have to

be further developed. In the proposed structures only the covered scene is divided in different convolutions, but maybe in the future both the radar waveform and the covered scene have to be divided in individual convolutions.

6.0 DISCUSSION

A single FCP-convolution structure is the simplest modulator realisation and with large FFT/IFFT transformations the covered scene can be large in range as well. On the other hand the processing speed for large FFT/IFFT transformations is quite slow, which result in large insertion delay. Usually, the actual requirements for processing time limits the available range extent of the false radar scene.

An FCP-convolution structure with separate synthesis of object and background is convenient, specially when processing of the two are generated with different processing tools. Separate handling of object and background lead to higher complexity, but not to larger insertion delay. All the other advantages and disadvantages are inherited from the single FCP-convolution structure.

A distributed FCP-convolution structure with parametric generator for background profile is a complex modulator realisation, but it will handle different radar systems and scenes very well. The structure is unique since it generates a credible background profile based on only a parametric description of the background.

7.0 CONCLUSION

All of the proposed structures are suitable for a DRFM modulator realisation, but they are dependent on the actual radar system and the desired range coverage. A distributed FCP-convolution structure with parametric generator for the background profile is the most general construction for different operations, but also the most complex.

8.0 REFERENCES

[1] Saper R. H. and Dyck D.: A computed approach to electronic countermeasures for deception of high resolution radar, RADAR'99, Brest, France, May 1999

[2] Høydal T. O.: Advanced Digital RF Memory (DRFM) Technologies - New Capabilities for Intelligent Radar Electronic Countermeasures, ATEDS/SA Symposium and Exhibition, San Diego, USA, March 2001

[3] Pace P.E., Fouts D.J., Ekestorm S. and Karow C.: Digital false-target image synthesiser for countering ISAR, IEE Proc.-Radar and Sonar Navig., Vol. 149, No 5, Oct 2002

[4] Kristoffersen S. and Thingsrud Ø.: The EKKO II Synthetic Target Generator for Imaging Radar, EUSAR 2004, Ulm, Germany, May 2004

[5] Stearns S. D. and Hush D. R.: Digital Signal Analysis, Prentice Hall, 1990

[6] Thingsrud Ø.: Syntetisk modellering av radarrefleksjoner i FPGA design – En studie av DRFM modulatordesign for høyoppløselig radarjammer, Master thesis (in Norwegian), University of Oslo, July 2004

Time-Frequency Signatures of a Moving Target in SAR Images

Trygve Sparr
Norwegian Defence Research Establishment (FFI)
Land and Air Systems Division
PO Box 25, NO-2027 Kjeller
NORWAY

Trygve.Sparr@ffi.no

SUMMARY

Moving targets within SAR scenes are distorted depending on the particulars of the target motion. For small motions, the uncompensated phase of a point reflector is a sum of a term proportional to the range component of the target motion, and a more complicated term depending on the azimuth motion. The resulting phase may be analysed with time-frequency techniques since the motion effect may alternatively be seen as a time dependent Doppler frequency. An experiment performed with a moving target within a scene collected by the German E-SAR system gave a signature that agrees well with theoretical predictions. Time-frequency analysis, using the smoothed pseudo Wigner-Ville method, gave a linear chirp with superimposed oscillations as predicted from the theory and the target motion.

1.0 INTRODUCTION

Synthetic aperture radar (SAR) is a useful radar technique to generate images of a scene with fairly high resolution from standoff ranges. SAR imaging of stationary scenes is well understood theoretically [1], and the major issue is the speed and accuracy of the SAR processor. For a moving target within the scene, the situation is more complicated. On the one hand, it is easier to detect the target using techniques different form SAR [2]. On the other hand, target motion results in image distortion in the SAR image of the target itself. A well known example is the azimuth displacement of a target with a small constant range rate. More complicated motion leads to other effects. Vibrations and rotations cause micro-Doppler [3], and azimuth smearing may result [4].

We analyse the effect of general target motion on the SAR signal phase. For reasonably small motions, the residual uncompensated phase of a moving point target after the SAR processor consists of two terms, one proportional to the range component of the motion, and one containing the product of the platform motion and the target azimuth motion. This phase can be complicated, and time-frequency methods are useful for the analysis.

An experiment was performed in Lillestrøm, Norway, using the DLR E-SAR from Germany as SAR platform. A moving target with a known motion was present at the time of data collection. The motion was an approximately constant range rate, with an oscillation in the range direction superimposed. Results obtained with time frequency methods agreed well with theoretical predictions.

2.0 MOVING TARGETS IN SAR IMAGES

SAR processors usually assume that the scattering centres within the SAR scene are stationary during the time of data collection. Each point within the scene is then characterized by a unique phase history, and the SAR processor exploits the uniqueness to place the point within the scene.

Paper presented at the RTO SET Symposium on "Target Identification and Recognition Using RF Systems", held in Oslo, Norway, 11-13 October 2004, and published in RTO-MP-SET-080.

2.1 General Motion

We consider a SAR platform moving along a straight line with constant platform velocity v_p. We define the straight line as the x-axis in a cylindrical coordinate system as in [1]. At the time $t = 0$ the radar antenna phase centre is at the origin. At the same time, a target is exactly broadside at the range $d = r_0$. The target has a general motion described by its cylindrical coordinates $s(t)$ as given in fig. 1.

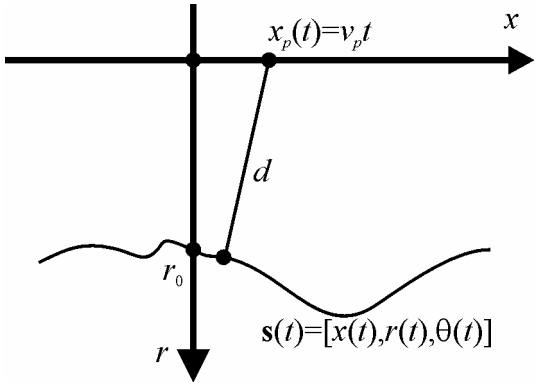

Figure 1: Geometry of a SAR system with a moving target.

Accordingly, the range from the radar to the target at a general time is given by

$$d(t) = \sqrt{\left[v_p t - x(t)\right]^2 + r^2(t)}\,. \tag{1}$$

The usual hyperbolic expression for the point target range history is obtained for $x(t) = 0$ and $r(t) = r_0$. Note that the cylindrical angle θ does not enter the equations as it does not affect the range when the platform trajectory is a straight line. The phase history of the target may then be obtained from

$$\varphi(t) = 2kd(t) = \frac{4\pi}{\lambda} d(t)\,. \tag{2}$$

Ideally, the SAR processor focuses the target using the phase history

$$\varphi_0(t) = \frac{4\pi}{\lambda} d_0(t) = \frac{4\pi}{\lambda} \sqrt{v_p^2 t^2 + r_0^2}\,. \tag{3}$$

Accordingly, the uncompensated phase may be found as

$$\Delta\varphi(t) = \varphi(t) - \varphi_0(t)\,. \tag{4}$$

Depending on the particulars of the motion, the uncompensated phase may result in a wide range of phenomena, from a simple shift in position of the target to a smearing making the target impossible to see.

2.2 Small Motions

Equations (1) to (4) give the general results, but are difficult to analyse directly. If the synthetic aperture is sufficiently short as compared to the distance to the scene, and the target motion is slow as compared to

the platform velocity, the square roots may be approximated by parabolas in the usual way [1]. The results are

$$d(t) \approx r_0 + \frac{v_p^2 t^2}{2r_0} - \frac{x(t)v_p t}{r_0} + \Delta r(t)$$
$$d_0(t) \approx r_0 + \frac{v_p^2 t^2}{2r_0} \tag{5}$$

Here, $\Delta r(t) = r(t) - r_0$, which is much smaller than r_0 under the stated conditions. Accordingly, the phase residual is given by

$$\Delta\varphi(t) \approx \frac{4\pi}{\lambda}\Delta r(t) - \frac{4\pi x(t)v_p t}{\lambda r_0}. \tag{6}$$

Note that for $x(t) = x_0$, a constant, the expression corresponds to the azimuth shift linear phase ramp to move the reflector to the new position when $\Delta(r) = 0$. On the other hand, when neglecting the second term and setting $\Delta r(t) = v_r t$, we get an azimuth phase ramp corresponding to the well known azimuth shift of a target with a moderate constant range rate v_r. A target moving with a constant azimuth rate will however introduce a quadratic phase term, resulting in smearing of the target.

3.0 TIME-FREQUENCY ANALYSIS

The phase residual as calculated in the previous section, given in eq. (6), may alternatively be seen as a Doppler shift. The basis is to define the corresponding Doppler frequency as

$$f_d = \frac{1}{2\pi}\frac{\mathrm{d}\varphi}{\mathrm{d}t}. \tag{7}$$

We see then that a linear phase ramp becomes a constant frequency, while the quadratic phase corresponding to constant azimuth rate becomes a linear chirp. For complicated frequency dependencies, time-frequency methods can be used for analysis.

3.1 Quadratic Time-Frequency Methods

There is a large number of different time-frequency methods that may be applied to a particular problem, and it is not always obvious which one to choose. The Cohen's class of quadratic time-frequency methods [5] offers some attractive alternatives due to the potential for high resolution. This must be balanced against the interference between signal components inherent in such methods. The class is described by

$$C(t, f_d) = \iint W(u, v)\Psi(u - t, v - f_d)\,\mathrm{d}u\mathrm{d}v, \tag{8}$$

with W the baseline Wigner-Ville distribution given by

$$W(t, f_d) = \int_{-\infty}^{\infty} s(t + \tau/2)s^*(t - \tau/2)\exp(-j2\pi f_d \tau)\,\mathrm{d}\tau \tag{8}$$

Various instances of Cohen's class are generated by choices of the kernel function Ψ.

We use two methods, the smoothed pseudo Wigner-Ville (SPWV) [6] and the adaptive optimal kernel (AOK) [7]. Both methods use a kernel that is essentially a low-pass filter, smoothing away high frequency interference, while retaining low frequency signal content. The SPWV is fairly simple and computationally efficient due to the simple separable kernel. The AOK method is more sophisticated as it adapts the kernel to some extent to the underlying signal.

4.0 EXPERIMENTAL RESULTS

A test was performed at Lillestrøm, Norway, 2 Jun 2003, using the German E-SAR system.

4.1 Description of Test

SAR scenes were collected over the test area at X-, L- and C-band. Several experiments were set up at the time. For the present study, a car was used as a moving target. A corner reflector was placed on the roof of the car as shown in fig. 2. The corner reflector was oriented to give maximum reflection in the general direction of the radar.

Figure 2: A standard civilian car with a corner reflector on the roof used as a moving target.

The position of the car was measured using a GPS receiver. The car path was chosen as a small road nearly in the azimuth direction. The road was in the middle of a uniform farming field to minimize clutter problems for the relevant data area. The car path was a fairly slow azimuth motion, about 5 m/s, combined with a side-to-side oscillation covering the width of the road. The aim was a linear motion in azimuth combined with a sinusoidal motion in range.

4.2 SAR Results

Fig. 3 shows a part of an X-band image collected over Lillestrøm. The image is processed by DLR e.V, Germany. Clutter is reduced using multi-look processing and the resolution is approximately 2m. Azimuth is along x-axis and range along y-axis. The bright parts in the left part of the image correspond to buildings at the site of the Norwegian Defence Establishment (NDRE) and some other institutions. The uniform part to the right corresponds to farming fields. The red rectangles show the location of the bright signature resulting from the moving target and a comparable bright signature from a building.

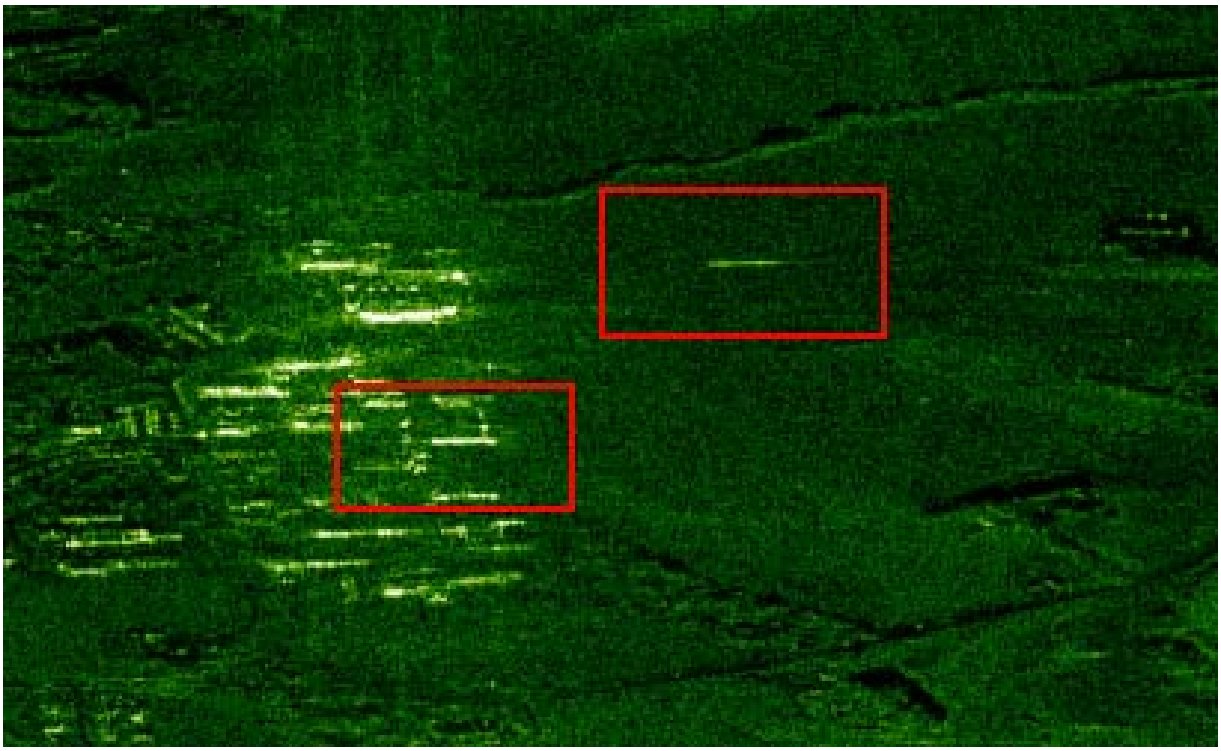

**Figure 3: An X-band SAR image of an area close to Lillestrøm.
The regions within the rectangles are shown in greater detail in Fig. 4.**

Fig. 4 shows close-ups of the rectangles of fig. 3.Both signatures are seen to be smears nearly in the azimuth direction as discussed in section 2.2. Taking an azimuth slice through the single-look complex representation of the signature and inverse Fourier transforming, we obtain a complex time series that may be analysed with time-frequency methods. Time-frequency signatures, calculated with the AOK method are shown in fig. 5.

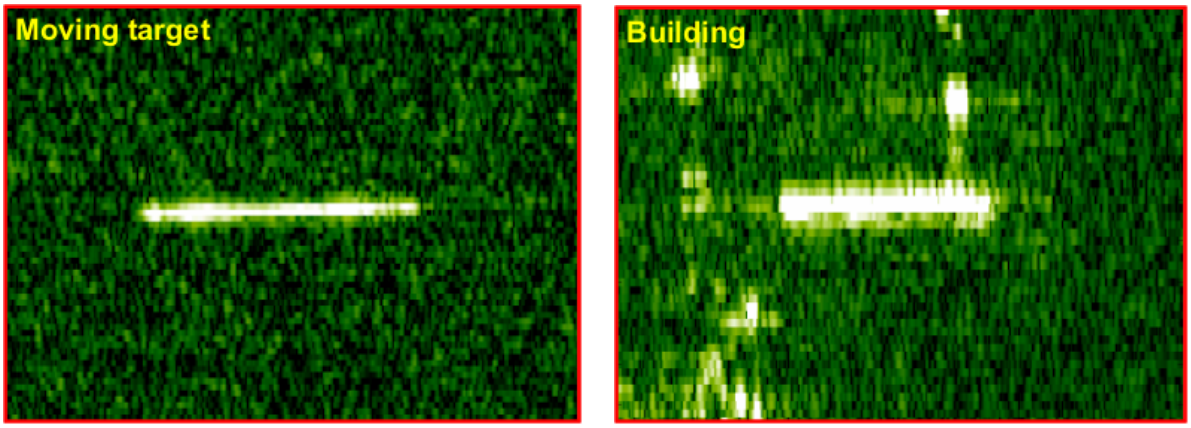

Figure 4: Close ups of the moving target and a building.

Since the ground target motion was approximately linear in azimuth, with a range oscillation superimposed, we expect the signature to be a linear chirp with sinusoidal modulations. The moving target signature in fig. 5 seems to agree well. In comparison, the building signature is different, containing

constant components, as well as wide-band time-limited components. The constant components are probably small reflectors along the edge of the building, while the time-limited wide-band components probably correspond to specular reflections. It is clear that the time-frequency signature can be used to discriminate between the staionary building and the moving target.

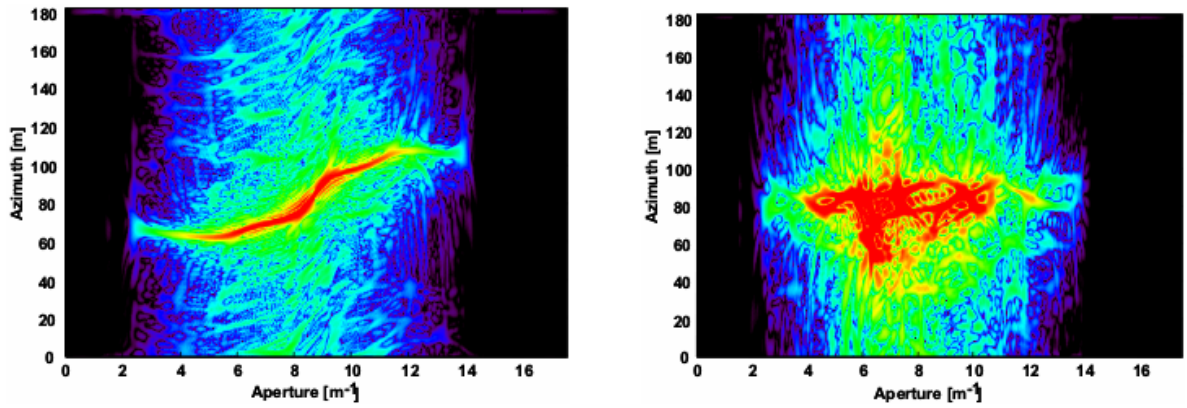

An animation of the time-frequency cube obtained by processing a number of azimuth slices shows the focused moving target moving in azimuth, in agreement with ground truth.

5.0 CONCLUSIONS

Moving targets in SAR images can be analysed and focused using time-frequency techniques. Results from a test show that the time-frequency signatures of a moving target is significantly different from the signature of a stationary building, even when the SAR image of the two are similar. Accordingly, time-frequency techniques are useful in the general problems of moving target detection, focusing and relocation.

6.0 REFERENCES

[1] Transceschetti, G.; Lanari, R.: Synthetic Aperture Radar Processing, Boca Raton, Florida: CRC Press LLC, 1999.

[2] Sullivan, R.J.: Microwave Radar: Imaging and Advanced Concepts, Norwood, Massachusetts: Artech House, Inc., 2000.

[3] Chen, V.C.; Ling, H.: Time-Frequency Transforms for Radar Imaging and Signal Analyisis, Norwood, Massachusetts: Artech House, Inc., 2002.

[4] Sparr, T.; Krane, B.: Micro-Doppler analysis of vibrating targets in SAR, IEE Proceedings on Radar, Sonar and Navigation, Vol 150, No 3, Aug. 2003, pp 277-283.

[5] Cohen, L.: Time-Frequency Analysis, Upper Saddle River, New Jersey: Prentice Hall PTR, 1995.

[6] Auger, F.; Flandrin, P.; Gonçalvès, P.; Lemoine, O.: Time-Frequency Toolbox for Use with MATLAB, 1996.

[7] Jones, D.L.; Baraniuk, R.G.: An adaptive optimal kernel time-frequency representation, IEEE Transcations on Signal Processing, Vol. 43, Oct. 1995, pp. 2361–2371.

[8] Mallat, S.: A Wavelet Tour of Signal Processing, San Diego, California: Academic Press, 1998.

[9] Sparr, T.; Krane, B.: Analysis of phase modulation caused by target motion in SAR images, Proceedings of SPIE, Vol. 5102, 2003, pp 178-188. See following page for “Header/Footer” information.

Super-Resolution Techniques Applied to MSTAR Data

Ing. Silvio D'Ercole
AMS – Engineering and Operation
Radar analysis group
Via Tiburtina Km 12,4
00131 Roma
Italia

sdercole@amsjv.it

ABSTRACT

This paper has been produced in the frame of research group for Automatic Target Recognition (ATR), NATO SET 053 TG 29. One of the biggest challenges for automatic target recognition (ATR) methods is the accurate and efficient extraction of features from synthetic aperture radar (SAR) images. The aim of this work is to evaluate the recognition-oriented properties for 2D modified covariance Super-Resolution technique[1]. Recognition-oriented properties in order to enhance features in the scene that are important for recognition purposes. Performances of the technique are evaluated in this paper by testing robustness of preserving and enhancing features extraction. Results indicate that 2D modified covariance Super-Resolution technique formation method provides images with higher resolution of scatterers, and better separability of different regions as compared to conventional SAR images.

1.0 INTRODUCTION

In order to exploit an automatic recognition based on a SAR imagery system, we need to extract certain features from the reconstructed images. These feature extraction can be difficult when based on SAR images formed by conventional Spectral Analysis methods (Specan), such as the two-dimensional matched filter (2D-MF) for reconstruction of the image of the scene sensed from the SAR. A scheme for such a system is represented in Figure 1 (view of the SAR-SPECAN processing scheme) where the 2D dechirping operation is applied to the hologram to remove the frequency modulation introduced on the echo reflected by the single point scatter by the chirped waveform (along the fast-time axis) and by the changing distance from the moving radar receiver (along the slow-time axis). One challenge is that the resolution of the formed images is limited by the SAR system bandwidth. This complicates point scatterer localization, the images suffer from speckle, and in addition this complicates region segmentation for shape-based recognition. The slant range resolution of a SAR transmitting chirp signals of bandwidth B is $\delta_r = c/(2B)$, where c is the speed of light, whereas the cross-range (i.e. azimuth) resolution is approximately (for small observation angles) $\delta_a = \lambda/(2\Delta\theta)$, where λ is the transmission wavelength and $\Delta\theta$ is the angle under which a generic point is observed during the formation of the synthetic aperture. To improve the resolution beyond these limits (usually denoted as Rayleigh limits) it would be necessary to increase the bandwidth of the transmitted signal and the duration of the observation interval. In both cases, besides the associated cost, there are severe constraints on the instrumentation stability and on the knowledge of the relative motion between the radar and the scene, which has to be compensated for to form the synthetic aperture.

Paper presented at the RTO SET Symposium on "Target Identification and Recognition Using RF Systems", held in Oslo, Norway, 11-13 October 2004, and published in RTO-MP-SET-080.

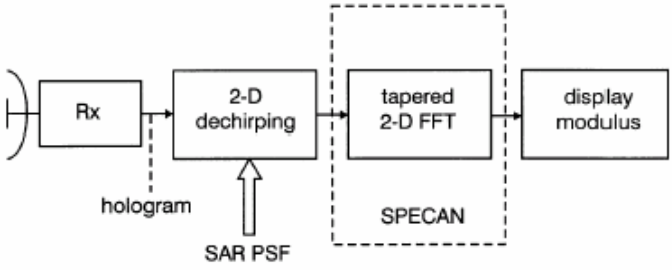

Figure 1. Conventional SAR-SPECAN processing Scheme

Using the 2D-Covariance on SAR images, the resolution can be improved without acting nor on the bandwidth neither on the duration of the observation interval. The improvement of resolution is achieved by finding an adequate parametric model (specifically setting the model orders for the considered 2D AR model) and estimating the parameters of the model.

This method produces images which appear to enhance point-based features (e.g. scatterer locations), and region-based features (e.g. object shapes), such features are important for recognition purposes[2][3][4][5].The AR models are used in this work because they fit well the scattered signal from point reflectors and, to some extent, also the signal from extended scenes. High resolution spectral analysis tools have the advantage, over the conventional FFT, that their spectral resolution improves with increasing SNR. Fourier transform methods obtain a frequency resolution which is constant at about the inverse of the observation time, or, for imaging systems, an angular resolution constant at about the ratio of wavelength to aperture size. The signal backscattered from the scene and captured from SAR has enough signal-to-noise power ratio to exploit for resolution improvement. On the other hand, it is known that the FFT processing is very robust, while super-resolution methods may be sensitive to model errors. A requirement for the application of super-resolution is therefore, that the system accuracy is significantly better than necessary for conventional SAR processing.

In this paper, we use quantitative criteria for evaluating the images produced by this Super-Resolution Spectral Analysis (SR-SPECAN) technique for SAR image formation. Experiments has been done on the Moving and Stationary Target Acquisition and Recognition (MSTAR) public target data set to compare the SAR images formed by the regularized method to conventional images in terms of these quantitative measures. The criteria we use regarding point-based features are target-to-clutter ratio, main-lobe width, peak matching accuracy and average associated peak distance. The metric of peak matching accuracy is particularly useful for testing the super-resolution properties of an image formation technique. The criteria we use for region-based features are segmentation accuracy, and separability of different regions models. The results of this study show that SR-Technique method yields images with higher resolution and better dominant scatterer localization than conventional images, also in considerably reduced amounts of data conditions. In addition when the method is used for region-based extraction, results in enhanced anomaly and speckle suppression in homogeneous regions, and hence, easier-to-segment images.

2.0 SUPER-RESOLUTION OF A SINGLE IMAGE

We now briefly summarize the super-resolution technique developed in [1], [6] and [7]. After having dechirped the SAR hologram, each point scatterer in the SAR scene is encoded into a 2D complex exponential embedded in the white Gaussian noise (WGN), corresponding to the mixture of ground clutter and thermal noise. A conventional spectral analysis (SPECAN), i.e. 2D-FFT, is able to focus at the same time all the point targets in the scene with a resolution equal to the so called Rayleigh limits. Since the dechirped signal backscattered from point targets is made of complex sinusoids with unknown parameters,

super-resolution spectral analysis (SR-SPECAN) techniques can also be applied to extract complex sinusoids embedded in WGN[8]; resolution higher than the conventional SPECAN based on the FFT can be gained. A better discrimination of the point targets in a SAR image is thus obtained by replacing the 2D-FFT with SR-SPECAN techniques. The 2D covariance method[7] estimates the power spectral density of a 2D AR signal via the linear prediction. The AR spectrum depends on the region of support of the processed data. Four regions of supports can be singled out from the grid over which the data are available, namely: the first (upper right hand side), the second (the upper LHS), the third (lower LHS), and the fourth (lower RHS) quarter planes. Thus, four quarter planes (or quadrants) AR spectra are calculated separately; they are combined to form a single unbiased, with circular response (i.e.: with equal resolution along the two orthogonal axes of the data grid), AR spectrum P^{combined} which is derived as follows:

$$\frac{1}{P^{\text{combined}}(f_1,f_2)} = \frac{1}{P^1(f_1,f_2)} + \frac{1}{P^2(f_1,f_2)} + \frac{1}{P^3(f_1,f_2)} + \frac{1}{P^4(f_1,f_2)}$$

where f_1 and f_2 are the spatial frequencies along the two orthogonal axes (in the SAR case, the range and azimuth axes) and P^1, P^2, P^3, and P^4 are the four quarter planes AR spectra. To calculate the single quarter plane AR spectrum the mathematical procedure is the following:

- determine the orders p_1 and p_2, in range and cross-range directions respectively, of the 2D AR model of the data (this step requires a "try and see" procedure and some heuristics; note that the maximum order value is a half of the available data length),
- estimate the 2D AR covariance matrix from the available data,
- write the 2D Yule-Walker equations to find the coefficients of the linear prediction estimator,
- apply the 2D Levinson algorithm to efficiently solve the 2D AR Yule-Walker equations (resort is made to QR decomposition to have a mathematically stable solution).

Because of the computational cost of the technique and of the assumption of a small number of point scatterers against WGN, the above SR-SPECAN technique cannot be applied in one shot to a large SAR image, unlike the 2D-FFT. The practical application of the technique to a SAR image requires the splitting of the image into small sub-images via 2D passband filtering operation, the application of the technique to each sub-image and finally the recombination of the sub-images into the complete super-resolved SAR image.

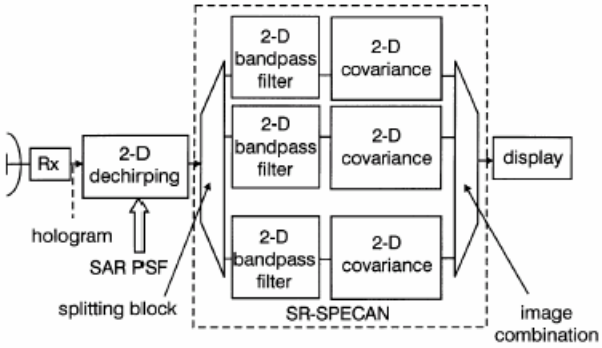

Figure 2. Proposed SR-SPECAN Scheme for SAR images

3.0 FEATURE-BASED CRITERIA FOR EVALUATION OF IMAGE QUALITY

In this section we propose measures for evaluating the quality of images formed by the method outlined in Section 2. Many of these criteria have appeared in the literature before, and they are mostly directed towards images to be used in target recognition tasks.

3.1 Criteria for Point-Enhanced Images

3.1.1 Target-to-clutter ratio

As a measure of accentuation of the target pixels with respect to the background, we will use the target-to-clutter ratio (TCr) in dB, defined as:

$$TCr = 20 \cdot \log_{10}\left(\frac{\max\left(\left|\hat{f}_{i,j}\right|\right)}{\frac{1}{N_c} \cdot \sum_{(i,j)\in\Omega}\left|\hat{f}_{i,j}\right|} \right)$$

Equation 1. Target to Clutter ratio (dB)

where $\hat{f}_{i,j}$ is the reconstructed image, with the pair (i, j) denoting the pixel indices, Ω denotes a clutter patch in the image, and N_c denotes the number of pixels in that patch.

3.1.2 Main-lobe width

As one of the measures of the effective resolution of an image, we will use the 3-dB main-lobe width. To obtain an estimate of the main-lobe width, we concentrate on the target region. In each row and column in the target region of the reconstructed image, we find the first point near the maximum where the reflectivity magnitude is more than 3 dB below the maximum value. We then obtain a better estimate of the 3-dB distance by means of a linear interpolation between pixels. Finally, we average the distances obtained from each row and column in the target region to find an overall estimate of the 3-dB lobe width for a particular image.

3.1.3 Peak matching accuracy

Locations of dominant point scatterers extracted from a target image are important characteristics for recognition. Loss of resolution manifests itself by merging and moving such characteristic points, and this makes the accurate localization of these points in the scene more difficult. Thus, we evaluate the super-resolution properties of our method by measuring how well the dominant scatterers are preserved when we use reduced-resolution data to form the image. For this purpose, we extract the locations of the brightest scatterers from the conventional and the proposed reconstructions using the same reduced-resolution data, and compare these to the "reference" locations of the scatterers. These "reference" positions may be obtained either from the ground truth, in case that is available, or from locations of the scatterers extracted from a higher resolution image otherwise. In order to extract the scatterer locations, we first find the peaks in the reconstructed image. The peaks are taken to be the points where the discrete spatial derivatives of the reflectivity magnitude in both the x and the y directions change sign from positive to negative. Once the peaks are found, we order them based on their magnitude. Once the peaks are extracted, we evaluate how well the coordinates of these peaks match those of the "reference" peaks. This method allows a match declaration between two peaks, if the estimated peak location is within a radius r of the "reference" peak location. Hence it is more powerful than counting only the exact matches, with r used as a variable parameter (r=0 corresponds to counting the exact matches). A one-to-one association of the peaks is made such that the sum of the squared distances between the locations of the "reference" peaks and the corresponding matched peaks from the image is minimized. We can then count the number of matched peaks, to see how well the peaks are preserved.

3.1.4 Average associated peak distance

Another criterion based on peak locations that we will use is the average distance between the two sets of peaks coordinates. To compute this measure, we relax the matching radius r of Sect. 3.1.3, so that each of the peaks from the reconstructed image is matched to a "reference" peak. We then find the average of the distances between these associated peaks.

3.2 Criteria for Region-Enhanced Images

3.2.1 Segmentation accuracy

It is of interest to obtain accurate segmentations of SAR images for effective use of region-based shape features in target recognition. Recently there has been much interest in the development of segmentation algorithms for conventional SAR images. Our region-enhanced images provide easier-to-segment regions as compared to conventional SAR images. We will demonstrate this property by segmenting our reconstructions to target, shadow and background regions by simple adaptive thresholding. To determine the threshold, we find the mean μ and the standard deviation σ of the dB-valued pixel magnitudes in the image. Then, we apply the following decision rule at each pixel:

Equation 2. Segmentation Decision Rule

$$20 \cdot \log_{10}\left(\hat{f}_{i,j}\right) < \mu - c_1 \cdot \sigma \quad \rightarrow \quad \hat{f}_{i,j} \in S$$

$$\mu - c_1 \cdot \sigma \le 20 \cdot \log_{10}\left(\hat{f}_{i,j}\right) < \mu + c_2 \cdot \sigma \quad \rightarrow \quad \hat{f}_{i,j} \in B$$

$$\mu + c_2 \cdot \sigma \le 20 \cdot \log_{10}\left(\hat{f}_{i,j}\right) \quad \rightarrow \quad \hat{f}_{i,j} \in T$$

where T,S,B denote the target, shadow and background regions respectively, and c_1,c_2 are two constants that are fixed beforehand. From a statistical standpoint, it would make more sense to develop a decision metric based on statistics of particular regions. However, our objective here is not to develop the best decision metric, but rather to show that we can obtain reasonable segmentations of the region-enhanced images even by simple suboptimal processing.

4.0 EXPERIMENTAL RESULTS

4.1 Experimental Setup

We use images of T72 (sn 132) tanks, BMP2 (sn c21) tanks, and BTR70 (sn c71) armored personnel carriers from the MSTAR public target data set to evaluate the performance of our reconstructed images in terms of the criteria described in Sect. 3. We use 8 images for each vehicle type, all at 17 depression angle, and evenly spaced in azimuth (approximately 45°) to cover 360°. As we will describe, we also carry out synthetic scene reconstruction experiments to make some evaluations where ground truth is exactly known. In order to apply our algorithm, we need the phase histories (or the range profiles). We obtain the phase histories from the 128 × 128 complex-valued MSTAR images, by undoing the final steps of MSTAR image formation. We first take the 2-D Discrete Fourier Transform (DFT) of the images, then we remove the zero-padding to obtain 100 × 100 phase history samples and next we remove the windowing applied. From the MSTAR file headers, we know that a 35 dB Taylor window has been used. Then we divide the phase history samples by a 2-D Taylor window.

4.2 Super-Resolution Imaging from Full-Resolution Data

We now use the 100 × 100 phase history samples to form Super-Resolved images. We will form interpolated images of a factor 8 over a patch of 64 x 64 centered on target, obtaining a 512 x 512 samples image. Therefore, in order to have conventional SAR SPECAN images of this size for comparison, we first form interpolated 512 × 512 Taylor-windowed Fourier images. Images for both conventional and SR techniques applied for T72, BTR70 and BMP2 are in Figure 3, Figure 4 and Figure 5, the SR images with an AR order determined by a ‘’Try and See’’ procedure, used for both axis, are at the right column. The

dominant scatterer appears to be accentuated as compared to the conventional images at the left column. We do not apply any windowing to the data before processing, since our method is able to suppress sidelobes considerably even with rectangular weighting. However, if desired, the method can be used with windowing. Each image is normalized to their maxima to remove the different scaling factors and finally fused together on a pixel by pixel basis: a non linear fusion law is applied by setting the pixel value of the final image equal to the maximum value of the 25-normalized SR-SPECAN images[9]. This fusion law will yield a final image with the highest number of target scatterers but at the same time will provide the worst background suppression capabilities. See Figure 6 (T72 and BTR70) and Figure 7 (BMP2) for Super-Resolved SPECAN Fused image with maximum technique.

Target Azimuth	T72		BTR70		BMP2	
	Filename	Best Order	Filename	Best Order	Filename	Best Order
0°	HB04025.015	27	HB03973.004	28	HB03893.002	27
45°	HB04034.015	28	HB03982.004	25	HB03901.002	29
90°	HB03852.015	29	HB03988.004	28	HB03909.002	30
135°	HB03802.015	28	HB03995.004	25	HB03917.002	30
180°	HB03809.015	28	HB03938.004	29	HB03926.002	29
225°	HB03935.015	28	HB03947.004	29	HB03875.002	27
270°	HB03824.015	25	HB03956.004	28	HB03876.002	28
315°	HB04016.015	28	HB03964.004	29	HB03884.002	25

Table 1. Best AR order for each 64x64 SR-SPECAN image

Best AR order for each SR-SPECAN image target elaboration are described in Table 1, and taking into account that the maximum order value is a half of the data length (32 in this case for a 64x64 available data), it is clear to see that high AR values (from 25 to 30) are preferred in order to enhance Super-Resolution capabilities.

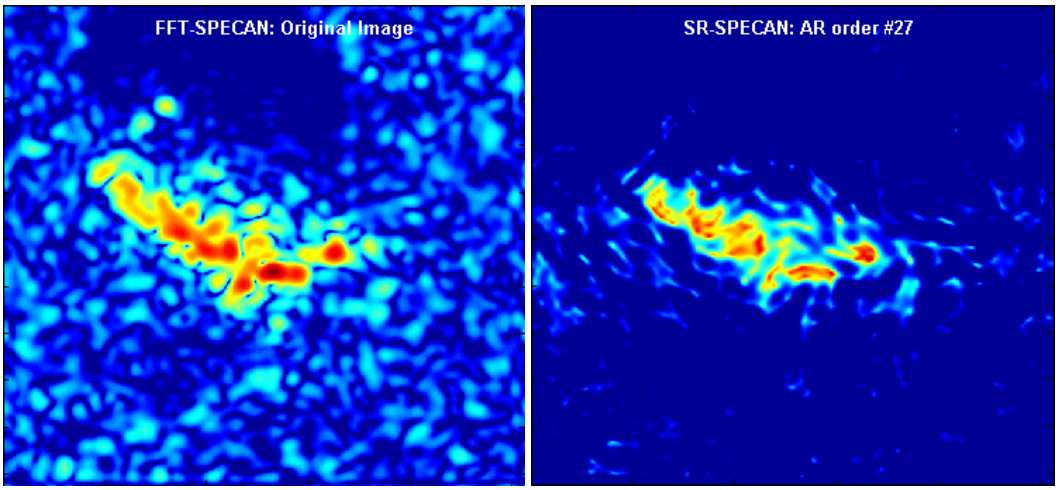

Figure 3. Tank T72 (315° azimuth angle) Left: Specan, Right: SR-Specan with AR order 27 for both axis.

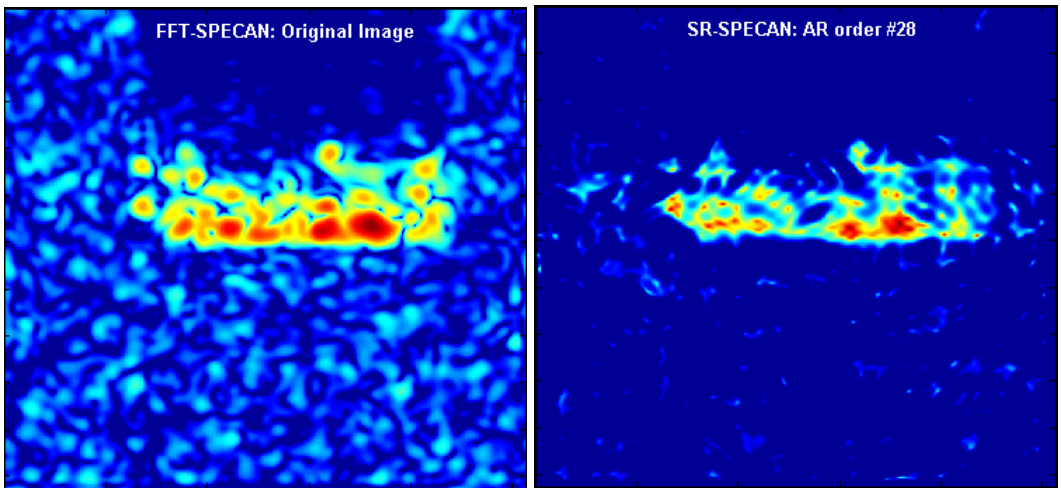

Figure 4. BTR70 (90° azimuth angle) Left: Specan, Right: SR-Specan with AR order 28.

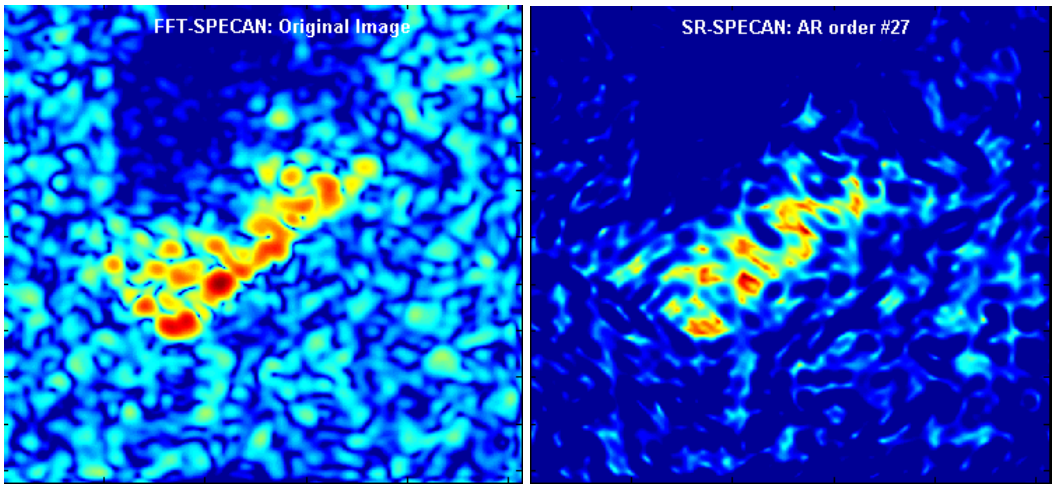

Figure 5. BMP2 (225° azimuth angle) Left: Specan, Right: SR-Specan with AR order 27.

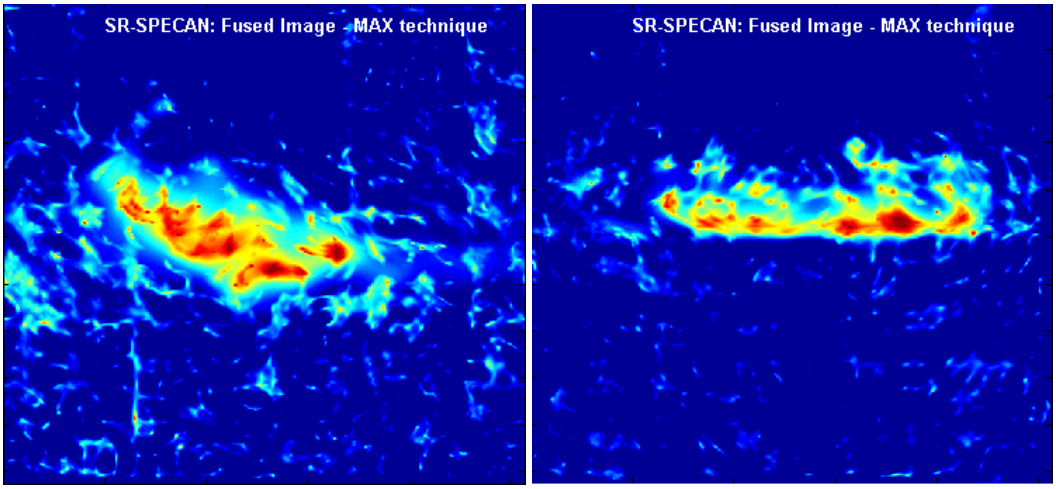

Figure 6. Super-Resolved SPECAN Fused image with MAX technique. Left: Tank T72 (315° azimuth angle) Right: BTR70 (90° azimuth angle)

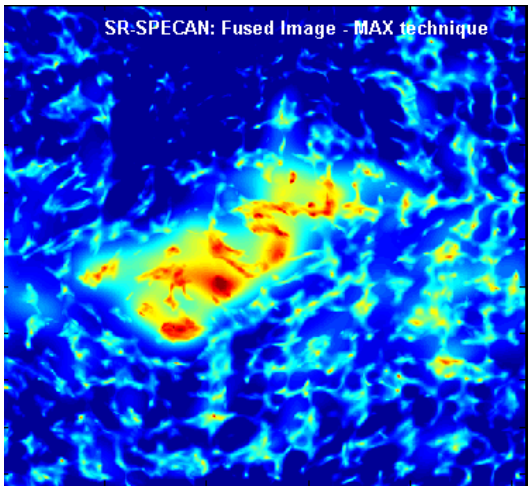

Figure 7. Super-Resolved SPECAN Fused image with MAX technique. BMP2 (225° azimuth angle)

4.2.1 Target-to-clutter ratio

We will quantify the enhancement of the target pixels in the full-resolution data reconstructions by means of their target-to-clutter ratio. We compute the target-to-clutter ratio (TCr(dB)) as defined in Equation 1, by using the bottom 20 rows (2000 pixels) of the reconstructed 100x100 images as the clutter region. Final TCr value is the average over the AR orders SR-SPECAN processing, the AR-values are from 7 to 31. Figure 8, Figure 9 Figure 10 shows the TCr values versus the AR orders for T72, BTR70 and BMP2 respectively, evaluated with an azimuth target angle of 270°. This region is big enough to give a reliable estimate of the mean reflectivity magnitude, and is safe to use, since target and shadow appear to be located outside this region for the entire data set. Table 2 shows the average target-to-clutter ratio achieved by the conventional and the proposed methods over the 8 reconstructed target azimuth variation images for each target type. Last row represent the mean value expressed in dB of the linear TCr evaluated for each azimuth angle. These results indicate a clear improvement of the target-to-clutter ratio by our proposed image formation method.

Target Azimuth	**T72**		**BTR70**		**BMP2**	
	SR	*Conventional*	*SR*	*Conventional*	*SR*	*Conventional*
0°	47.0011	32.1083	54.0255	36.4485	69.3866	42.2303
45°	43.2853	29.2631	34.9206	23.1271	43.912	31.1764
90°	55.2862	35.5263	56.7158	34.2177	64.8596	41.9121
135°	66.1575	41.3393	39.4638	25.3764	42.2591	28.8165
180°	56.4607	36.0822	68.8944	45.3622	55.8789	37.3171
225°	54.6906	36.94	38.7378	27.4282	42.489	30.129
270°	58.4797	36.0718	58.2052	32.8596	61.0104	35.2174
315°	48.633	33.61199	36.9852	22.0673	43.5977	30.581
Average	***56.4244***	***35.7657***	***56.0766***	***34.3262***	***58.8564***	***36.1692***

Table 2. Average target-to-clutter ratios of SR-SPECAN and Conventional processing

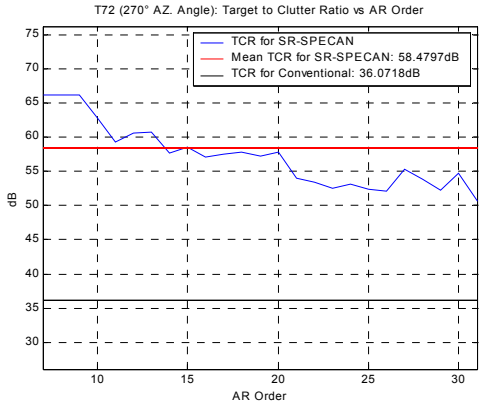

Figure 8. Target to Clutter Ratio vs AR order for T72 (270°)

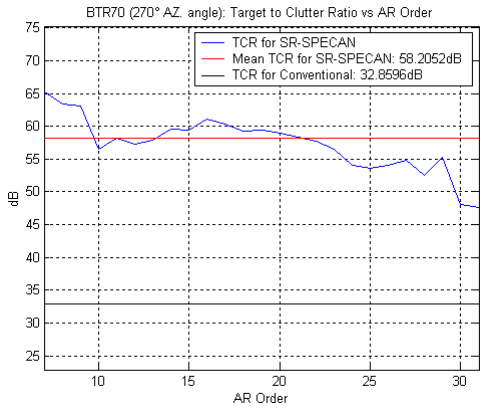

Figure 9. Target to Clutter Ratio vs AR order for BTR70 (270°)

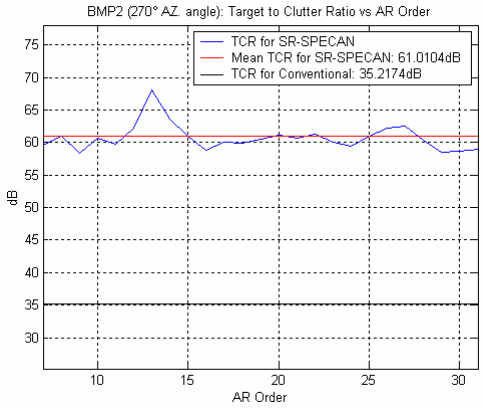

Figure 10. Target to Clutter Ratio vs AR order for BMP2 (270°)

4.3 Point-Enhanced Super-Resolution Imaging from Reduced-Resolution Data

In this section, we carry out experiments on two sets of data: those from the actual MSTAR images, and those from synthetic point scatterer scenes constructed using the MSTAR images. The reason for using synthetic examples is to demonstrate the super-resolution properties of our method in a situation where the ground truth is exactly known. We will present the main-lobe width results for the actual MSTAR reconstructions only. We will present the peak matching accuracy and the average associated peak distance results for both actual and synthetic images. We do not present the target-to-clutter ratio results in this section, since they are very similar to the full-resolution target-to-clutter ratio results. For experiments on actual MSTAR data, we form images from a 50 × 50 subset of the 100 × 100 phase history samples previously used. This results in a two times resolution loss in the range and cross-range directions. All the images we will form in this section are composed of interpolated 512 × 512 from the 50 × 50 subset. The left image in Figure 11 shows Taylor weighted Fourier images from the tank T72 (315° target azimuth) reduced-resolution data. The resolution loss in these images is evident when they are compared to their high-resolution counterparts in left image of Figure 3. We now form Super-Resolved image with an AR order of 20 for each axes, samples of which are shown in the right of Figure 11.

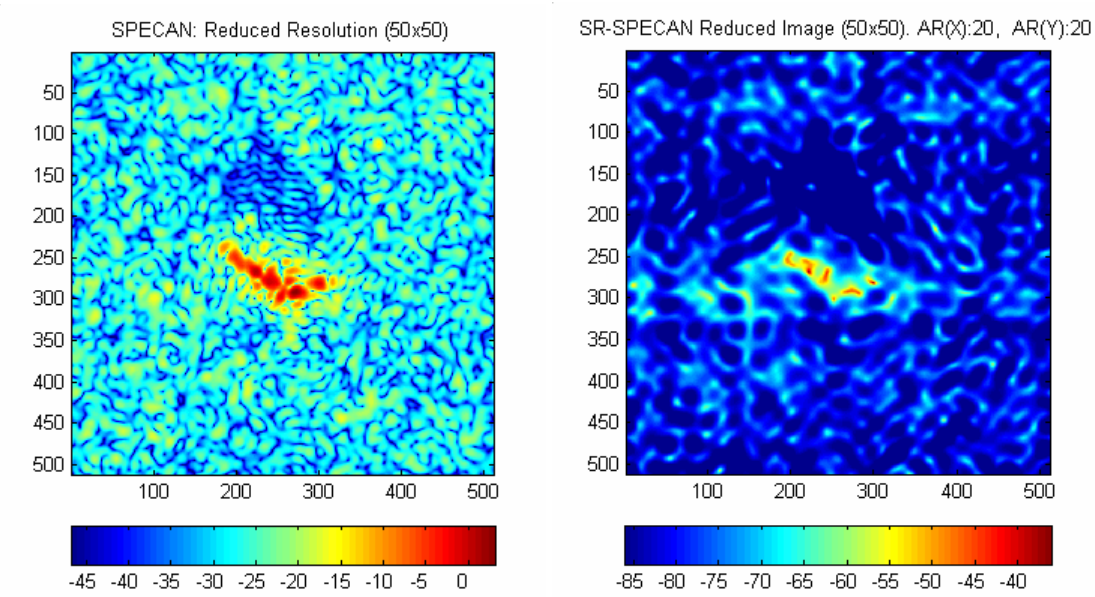

Figure 11. Sample images reconstructed from reduced-resolution (50 × 50) data. Left: conventional SPECAN. Right: proposed SR-SPECAN

The main-lobe-width, as described in Equation 1, of conventional reduced resolution image (50x50) is equal to 0.2650m and 0.0614m for the SR-SPECAN method, a ratio factor of 4.3159 is reached, enhancing the width-lobe-reducing capabilities of our proposed method. We now consider the synthetic examples. To generate synthetic scenes we find the 13 peaks with the largest magnitude in the tank T72 (315° target azimuth) 128×128 Taylor-windowed Fourier images, and form a synthetic scene by placing simulated point-scatterers at the locations of these peaks, with the original complex reflectivity, and zeros in the rest of the scene. An example pixel-plot of the magnitude of such a synthetic scene is shown in Figure 12. We then generate simulated phase histories from this scene. The reconstructed conventional Taylor-windowed image from 64×64 phase history contour plot is shown at the left side, down row, of Figure 13. The average main lobe width is 0.225m, in this case loss of resolution is easy to observe. The corresponding Super-Resolution image produced by our method is shown at the right side, with an average main lobe width of 0.0812m, and we can visually observe that most of the scatterers that were merged by the conventional reconstruction are now resolved.

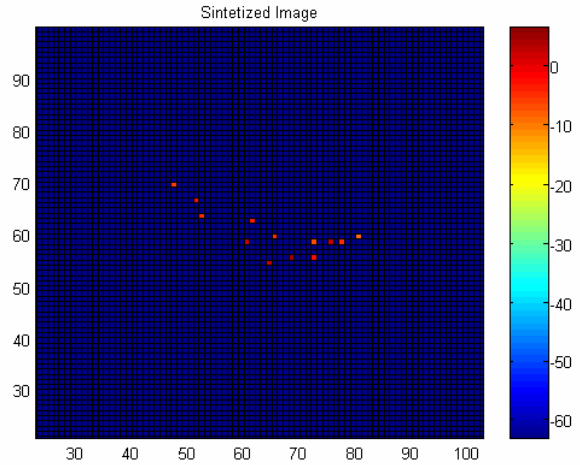

Figure 12. Thirteen points synthetic image from T72 (315° azimuth angle)

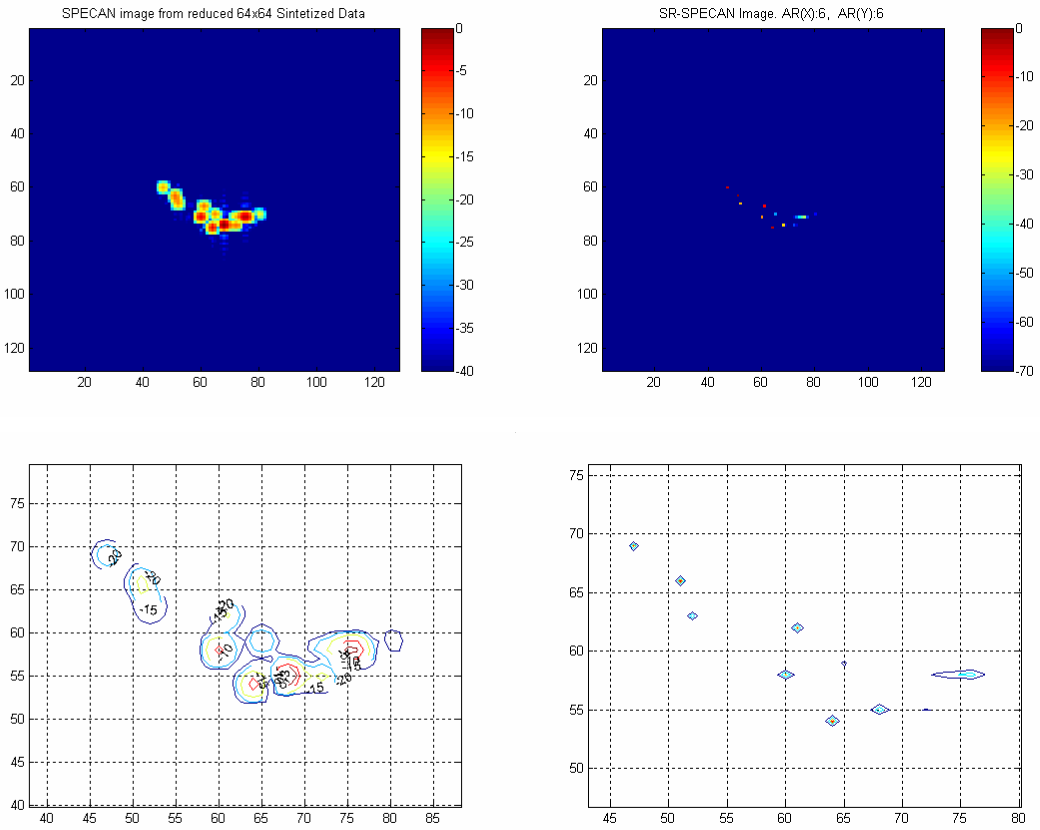

Figure 13. Synthetic T72 image reconstruction from reduced-resolution data. Up: ground truth. Down: results from 64x64 data, left: SPECAN, right SR-SPECAN

4.3.1 Main-lobe width

We compute the average 3-dB main-lobe width (AMLW) as described in Sect. 3.1.2 for all the 8-azimuth-direction reconstructed MSTAR scenes of each target. The AMLW for the proposed method has been calculated as the mean AMLW over the super-resolved images starting from AR order 7, ending to 31 (see Figure 14 for an example on tank T72 with 270° target azimuth angle). The results in Table 3 show that our proposed scheme is able to reduce the lobe width considerably. To put these numbers in perspective, note that the resolution supported by the data is 0.6 m in this experiment. In last row of Table 3 we report the Improvement factor calculated as the ratio of mean AMLW for conventional and proposed method.

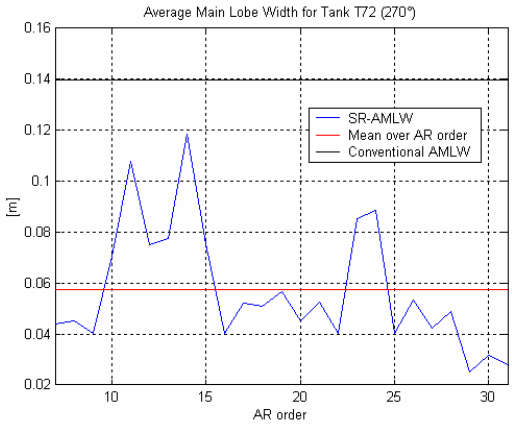

Figure 14. AMLW for T72 image vs AR order

Target Azimuth	**T72**		**BTR70**		**BMP2**	
	SR	*Conventional*	*SR*	*Conventional*	*SR*	*Conventional*
0°	0.1345	0.2144	0.0633	0.1626	0.1368	0.2803
45°	0.0937	0.1889	0.1292	0.1943	0.0817	0.1548
90°	0.0852	0.1803	0.1347	0.2463	0.0835	0.2068
135°	0.0772	0.159	0.1115	0.1745	0.0892	0.2330
180°	0.1412	0.2473	0.1243	0.1962	0.0789	0.1656
225°	0.1337	0.2490	0.0761	0.1582	0.0992	0.1929
270°	0.0574	0.1398	0.0854	0.2780	0.0879	0.3534
315°	0.0892	0.1702	0.0727	0.1874	0.0747	0.1595
Average	***0.1015***	***0.1936***	***0.0997***	***0.1997***	***0.0915***	***0.2183***
I Factor	***1.9***		***2***		***2.38***	

Table 3. Average mail-lobe-widths of images for proposed and conventional methods

4.3.2 Peak matching accuracy and average associated peak distance (AAPD)

We now evaluate how the locations of the dominant peaks are preserved in reduced-resolution data situations by the conventional reconstructions and by our point-enhanced images. For the MSTAR examples, we use the locations of the 13 peaks extracted from tank T72 (315° azimuth angle) Taylor-windowed synthetic image reconstructed from full data (

Figure 12). Figure 15 provides a visual comparison of the peak locating accuracy of the reconstructions from 64×64 data, comparing peaks extracted from our images with those from the conventional ones. The circles indicate the "reference" locations of the 13 dominant scatterers, and the plus signs indicate the peaks extracted from the reconstructed reduced-resolution images. Left side contains results for the conventional images, while right side contains those for the SR images. The clear observation we can make out of these results is that, since conventional image formation causes peaks to merge, some of the peaks in the target area are lost, and peaks outside this area may become dominant. We will now evaluate the peak matching accuracy of our method by using the criterion described in Sect. 3.1.3. In Figure 17, Figure 18, Figure 19, we plot the average number of peak matches for the images formed by the conventional and the proposed methods as a function of the radius r within which a match declaration is allowed, respectively for T72, BTR70, and BMP2. The peak matching accuracy of our images appear to be higher than that of the conventional images. Note that our analysis is based on finding peaks all around the scene. Alternatively, the search for peaks can be done in a pre-determined target region only. The improved accuracy provided by our method is easy to observe in these plots.

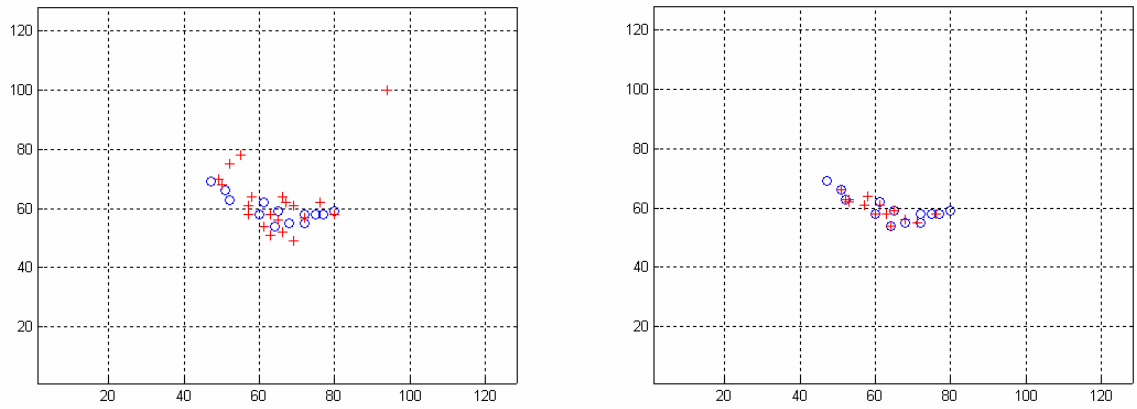

Figure 15. Sample peak extraction results for the synthetic reduced 64x64 T72 scenes. Circles indicate the scatterer locations in the synthetic scene. Plus signs indicate peaks extracted from the reconstructed images. Left: Conventional. Right: Proposed SR method.

The average distance between the true synthesized 13 peaks and the 13 peaks extracted from the reconstructed images as described in Sect. 3.1.4 is 0.46m for conventional method and 0.088m for proposed SR-SPECAN. These results indicate a clear reduction in peak distances by our method. Now we evaluate peak matching accuracy of both conventional and proposed method over reduced resolution method. Reduced images are formed from 64×64 reduced synthetic 256×256 image (loss resolution factor 4). A Taylor-window is applied for conventional method. Table 4, Table 5 and Table 6 show such performance results for each target type. It is clear to see how peak matching probabilities of proposed SR-SPECAN method is higher than that of conventional one with a reduced averaged associated peak distance. The AR order chosen for both axes in SR methods is 3. Figure 16 shows one matching example for BTR70 target, with relative average number of peak matches curves for the synthetic scene as a function of the radius of match declaration.

Target	**T72**			
	SR		*Conventional*	
Azimuth	Matches	AAPD(m)	Matches	AAPD(m)
0°	12/12	0	6/12	0.0167
45°	11/11	0	9/11	0.0111
90°	12/12	0	8/12	0.0530
135°	14/14	0	7/14	0.0429
180°	12/15	0.0167	5/15	0.0766
225°	14/14	0	6/14	0.0471
270°	19/21	0.1972	10/21	0.0883
315°	11/11	0	5/11	0.0483
Average	***96.3%***	***0.0267***	***52%***	***0.048***

Table 4. Peak matching accuracy and average associated peak distance (AAPD) performance for T72 data

Target Azimuth	**BTR70**			
	SR		*Conventional*	
	Matches	AAPD(m)	Matches	AAPD(m)
0°	16/19	0.1207	7/19	0.0866
45°	12/12	0	8/12	0.0405
90°	18/18	0.1128	10/18	0.0200
135°	12/12	0	4/12	0.1377
180°	10/17	0.0200	4/17	0.0854
225°	15/15	0	7/15	0.1178
270°	14/14	0.0706	5/14	0.0400
315°	10/10	0	8/10	0.1361
Average	***92.8%***	***0.0405***	***47.3%***	***0.0830***

Table 5. Peak matching accuracy and average associated peak distance (AAPD) performance for BTR70 data

Target Azimuth	**BMP2**			
	SR		*Conventional*	
	Matches	AAPD(m)	Matches	AAPD(m)
0°	9/9	0	4/9	0.0604
45°	8/8	0	6/8	0
90°	12/23	0.1369	6/23	0.1177
135°	8/8	0	7/8	0
180°	18/18	0.1063	8/18	0.0427
225°	11/11	0	8/11	0.0375
270°	9/19	0.0824	4/19	0.1104
315°	10/10	0	7/10	0.0143
Average	***87.5%***	***0.0407***	***55.1%***	***0.0479***

Table 6. Peak matching accuracy and average associated peak distance (AAPD) performance for BMP2 data

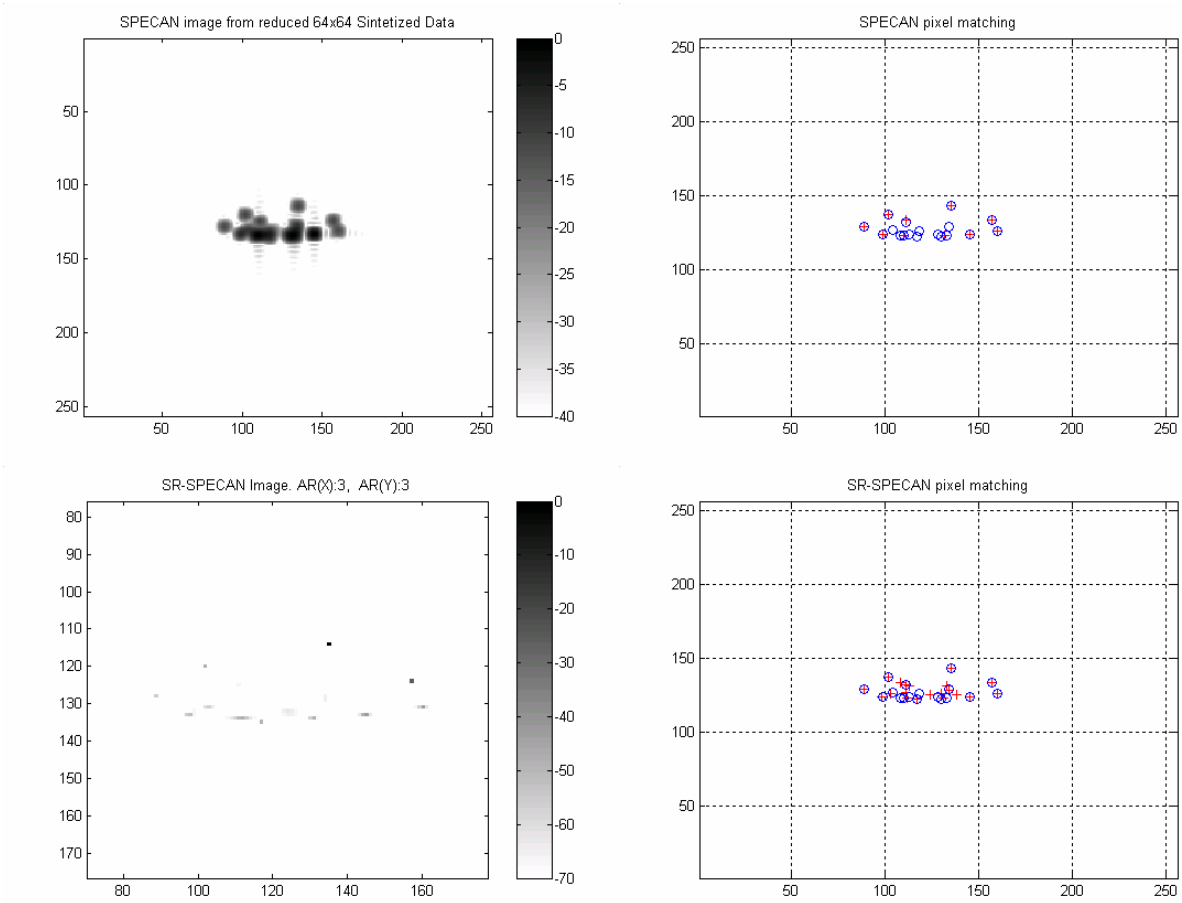

Figure 16. BTR70 (90°) Left column: reconstructed image from reduced 64x64 data. Right: pixel matching image. Top: Conventional. Bottom: Proposed method.

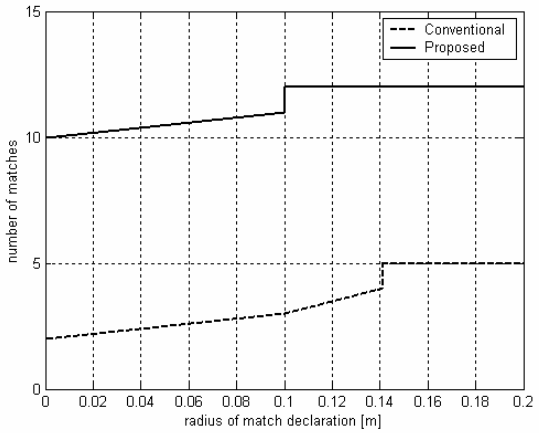

Figure 17. Average number of peak matches for the synthetic T72 (180°) scene as a function of the radius of match declaration r

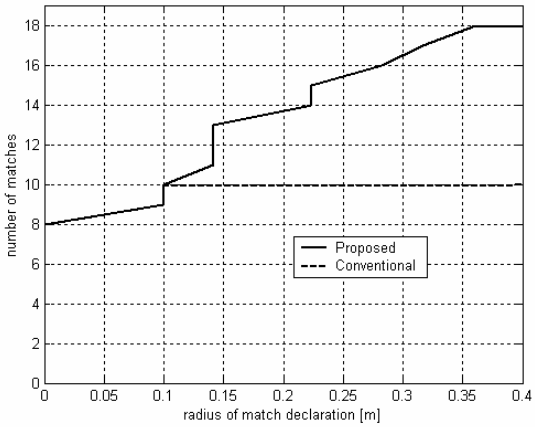

Figure 18. Average number of peak matches for the synthetic BTR70 (90°) scene as a function of the radius of match declaration r

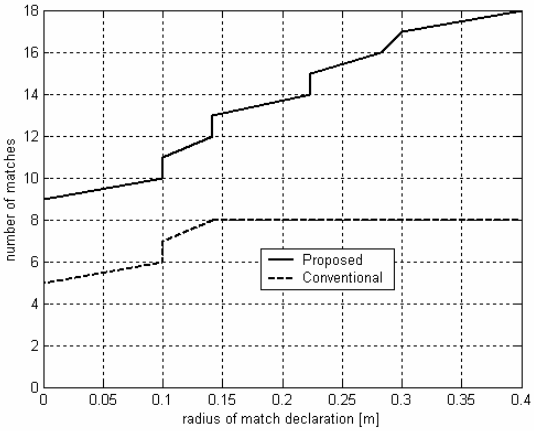

Figure 19. Average number of peak matches for the synthetic BMP2 (180°) scene as a function of the radius of match declaration r

4.4 Region-Enhanced Imaging

We now compare our region-enhanced images with conventional ones in terms of the criteria described in Sect. 3.2.1. Here, we form interpolated images patches (factor 8) from 128 × 128 Taylor-weighted phase history samples. In our proposed SR-method, we use an AR order equal to 20 for each target type and both axis, we will see that low AR values are preferred in order to enhance regions segmentation.

4.4.2 Segmentation accuracy

We segment our region-enhanced images by simple adaptive thresholding as described in Sect. 3.2.1, using c_1=1 and c_2=2 for both proposed and conventional method. Pictures from Figure 20 to Figure 22 shows sample reconstructions using the conventional and proposed method for BTR70 target type. In contrast to the conventional images, the SR reconstructions reduce variability in homogeneous regions, while preserving discontinuities at region boundaries. These results show that segmentation is considerably simplified by our reconstruction method. It is clear to see that such thresholding-based segmentation applied to conventional images, produce results dominated by fluctuations in homogeneous regions. We have also discovered that low AR order values are optimum for best segmentation performance.

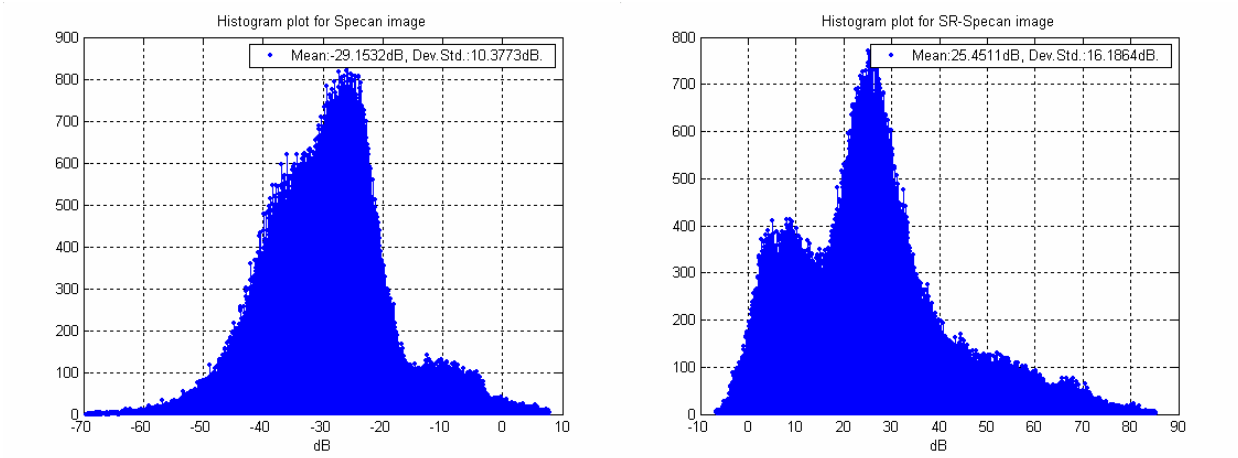

Figure 20. BTR70 (90°). Histogram plot from reconstructed data. Left: Conventional. Rigth: Proposed.

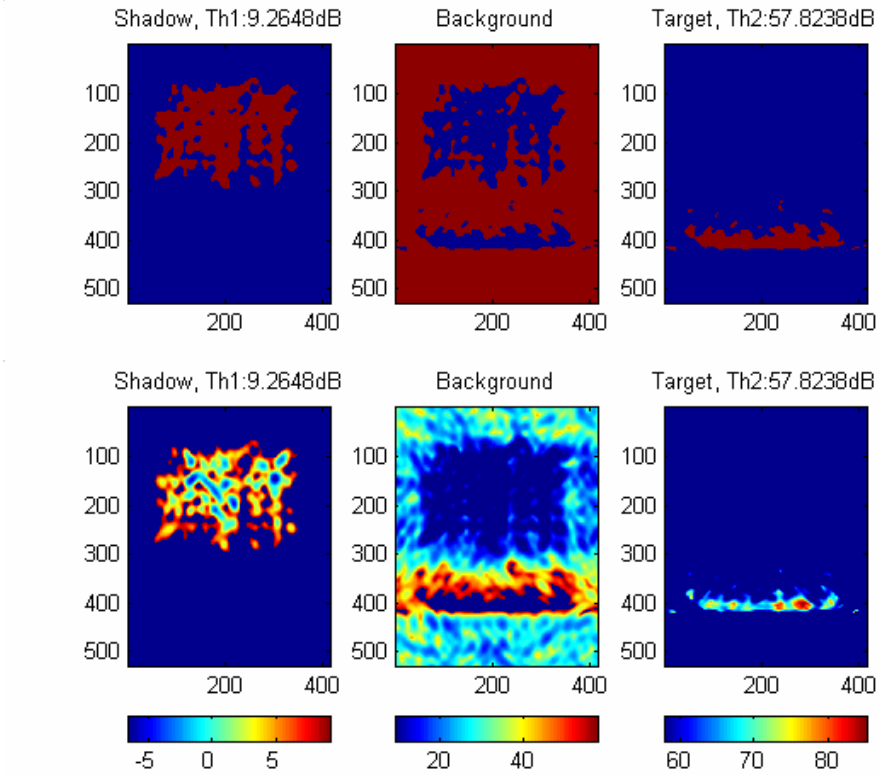

Figure 21. BTR70 (90°). SR-Specan: Results post Image Segmentation. Top row: Binary mask. Bottom row: Results.

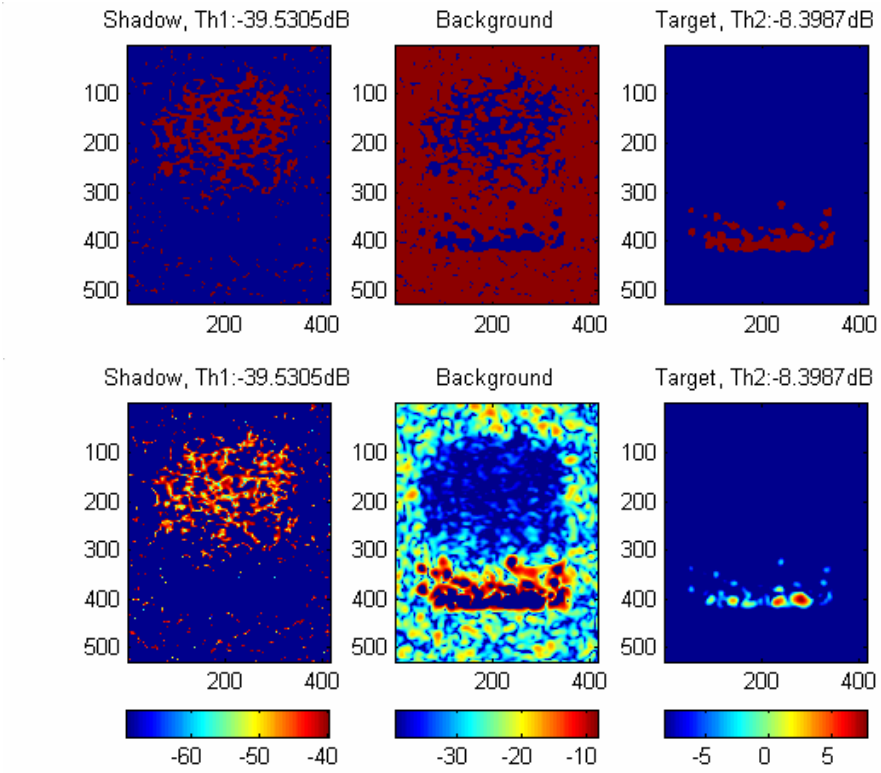

Figure 22. BTR70 (90°). Specan: Results post Image Segmentation. Top row: Binary mask. Bottom row: Results.

5.0 CONCLUSION

We have demonstrated the feature-enhancement properties of Super-Resolution method using 2D modified covariance method through a variety of quantitative criteria. The results indicate that the images produced by this method exhibit super-resolution and improved localization accuracy for dominant scatterers when high AR orders are used, and improved separability for different regions for low AR orders. With these properties, the method seems to have the potential for improving the performance of ATR systems. At the moment polar and multi-frequency data has been used to "combine multi-domain data" with proposed fusion method in order to increase correct classification probabilities. Future work will involve running recognition tests on images produced by this technique, and automatic selection of AR order (Akaike Information Criteria and Minimum description length).

6.0 ACKNOWLEDGMENTS

I personally thank sage colleague Alfonso Farina who let me enter in this NATO research group and helps me in imaging and super-resolution contents too. Debora Pastina (Dept. InfoCom – University of Rome "La Sapienza", via Eudossiana 18, 00184 Rome, Italy) for providing the core of super-resolution algorithm and her patience aid which has been guided me with the use of the software.

7.0 REFERENCES

[1] D.Pastina, A.Farina, J.Gunning, P.Lombardo. "Two-Dimensional super-resolution spectral analysis applied to SAR images". IEE Proc. Radar, Sonar Navigation ,Vol. 145, No. 5, October 1998

[2] B. Bhanu. “Automatic target recognition: state of the art survey”. IEEE Trans. Aerospace and Electronic Systems, AES-22, pp. 364-379, 1986

[3] L.C. Potter, R.L. Moses. “Attributed scattering centers for SAR ATR”. IEEE Trans. Image Processing, 6, pp. 79-91, 1997

[4] G. Jones, B.Bhanu. “Recognition of articulated and occluded objects”. IEEE Trans. Pattern Anaò. Machine Intell., 21, pp.603-613, 1999

[5] J.A. Ratches, C.P. Walters, R.G. Buser. “Aided and automatic target recognition based upon sensory inputs from image forming systems”. IEEE Trans. Patter Anal. Machine Intell., 19, pp. 1004-1019, 1997

[6] S.L.Marple. “A fast algorithm for the two dimensional covariance method of linear prediction”. Proceedings of International conference on Acoustic speech and signal processing, ICASSP 1995, Detroit, MI, pp. 1693-1696.

[7] S.L.Marple: “2D AR algorithm based on the 2D covariance method of linear prediction”, private communication 1994.

[8] S.L.Marple: “Digital Spectral analysis with applications”, Prentice-Hall Inc., 1987.

[9] D.Pastina, A.Farina, P.Daddi, P.Lombardo. “Super-Resolution of polarimetric SAR images of ship targets”. IGARSS 2001

The Polarimetric Dynamical Estimator HRP Improving Success in the Detection Process

Angelo M. Ricci and R. Trinci
Radar Cross Section Dpt. – Istituto per le Telecomunicazioni l'Elettronica "Giancarlo Vallauri"
Italian Navy - Mariteleradar
Viale Italia, 72
57126 Livorno
Italy
tel: +39 0586 238176
fax: +39 0586 238205

mariteleradar@marina.difesa.it - Att. Radar Cross Section Dpt

ABSTRACT

In several circumstances targets at sea are difficult to detect. This difficulty is intrinsically related to the target's physical attributes and its environment (sea and weather conditions).

The possibility of detecting and scaling the ATR levels from detection up to characterization depends on such aforesaid difficulties. In any given situation, are there any physical attributes which might enhance and temporarily stabilize the target radar response and/or the background?

The existence of such attributes could be initially detected by adopting a series of suitable RF radar parameters.

This poster illustrates the results of a technique based on the use of suitable RF parameters, data acquisition and processing methodologies in order to improve the probability of success in the detection process.

An agile full polarimetric multi frequency and PWs radar is used to transmit and receive scattered echoes.

I and Q channels are acquired using four fast, wide BW A/D converters possessing high throughput to memory. This allows the acquisition of a complete set of scattered radar responses from portions of sea surfaces that probably contain a target. Radar responses (echoes) catalogued in a scattering data bank are then used to feed a recursive d & c algorithm employing the polarimetric estimator which indicates the likely presence of targets in the area.

Paper presented at the RTO SET Symposium on "Target Identification and Recognition Using RF Systems", held in Oslo, Norway, 11-13 October 2004, and published in RTO-MP-SET-080.

RADAR MMS 300

Fig. 1

Fig. 2

Fig. 3

(Fig.1 and Fig.2)
MMS300 Radar;
2-18 GHz, polarization and frequency agile, multi PWs.

(Fig. 3)
4-channels A/D converter;
Wide analogic and digital bandwidths with high throughput to memory.

Polarimetric vector

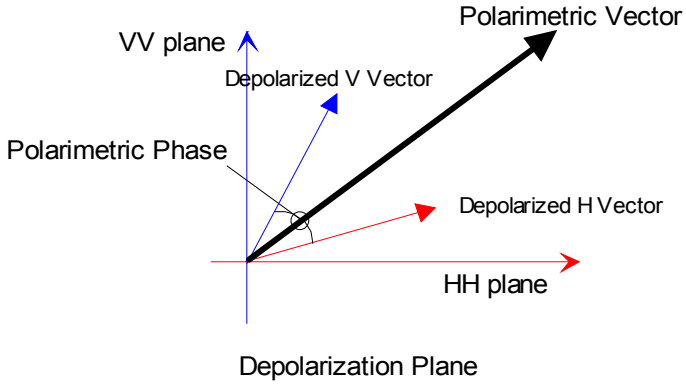

$$\vec{E}_H \bullet \vec{E}_V = \left\|\vec{E}_H\right\| \cdot \left\|\vec{E}_V\right\| \cdot COS\delta$$

The polarimetric vector allows the recovery of the scattered radar energy regardless of the depolarization it may have suffered.

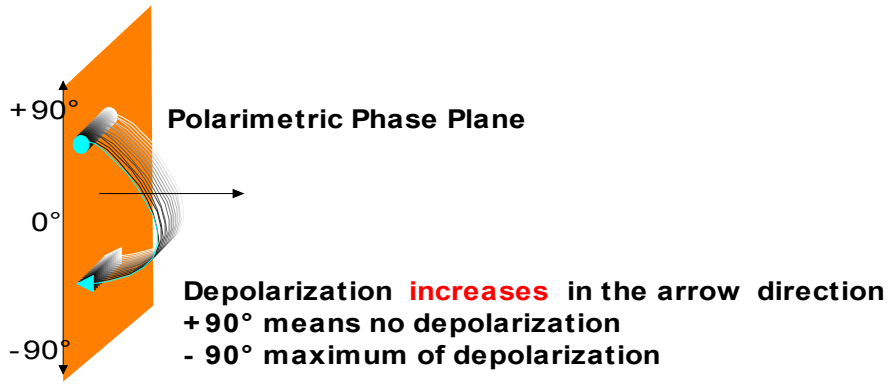

INVARIANCE

With current technology large and small targets may represent the same threat level as well as having the same RCS.
This implies that all targets must be detected however small their RCS.
In a detection process, instead of using RCS, the use of different RF parameters might result in a stable radar response therefore increasing the probability of survival and the possibility of reaching higher ATR levels.
Doing this depends on the existence of certain physical target attributes – referred to as INVARIANT PHYSICAL PROPERTIES - whose radar response is stable.

INVARIANT RADAR QUANTITY
A quantity (tensor, vector or scalar) obtained by the analytic combination of some RF quantities giving a radar response which remains stable even if the interrogating frequency, PWs, and time of observation are altered.

The need

Detection of targets at sea.

The dynamic estimator

A procedure based on the use of the RADAR INVARIANT QUANTITY HRP: a scalar which is stable in time and space and obtained by the right combination of all the elements of the complete scattering matrix.
This scalar is not expected to be dependent on frequency and PWs but is very sensitive to changes in polarization.
Its efficacy is related to both the polarization coherence of the target and the polarization incoherence of the rough sea.

The procedure

A series of bursts are emitted at various frequencies, PWs and polarizations.
Received scattered pulses acquired in different range gates build up the complete scattering matrix.
A recursive algorithm based on a dynamic estimator permits the search for signals compatible with the presence of targets in the marked areas.
Subsequent specialized searches may be conducted in the identified areas by varying transmitted and received RF parameters (frequency, PWs).
Detected targets illuminated with specialized radar RF parameters are then studied in order to scale all levels of the "ATR chain" through the use of the dynamic estimator.
The procedure is not stochastic but deterministic.

Use: Target detection and characterization

Fig.4

Sea and Targets are synthesized

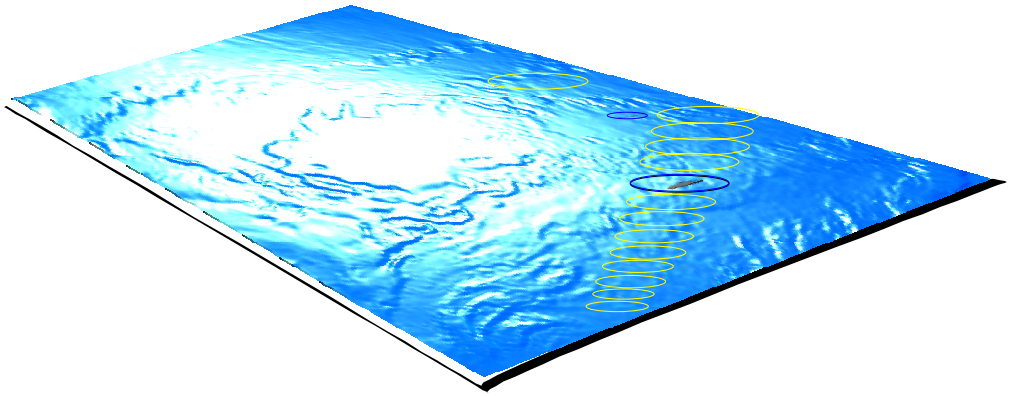

Fig. 5. Polarization area synthesis

A technique capable of calming a rough sea.
Targets are seen as in a calm sea

Fig. 6. Detail of photograph of the Fig.4

A 150-mt ship at anchor with tugboat on starboard side.
Graphs and ISAR radar images presented on right side of poster are referred to this ship.
The anchored ship avoided the necessity of doing range compensation on data.

Uses of dynamic estimator

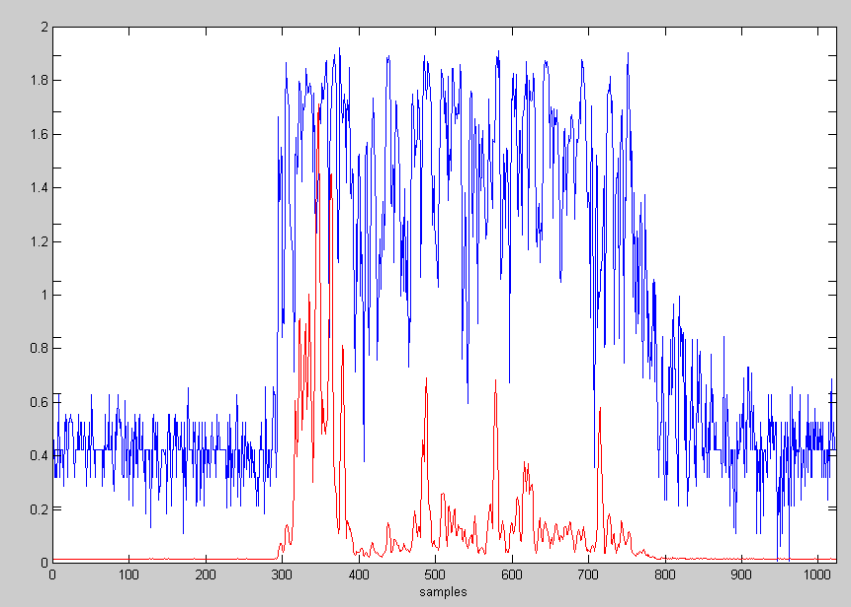

Fig. 7. Blue HRP vs down-range (d.r.) - Red Mag of Polarimetric vector vs d.r.

Trailing and leading edges correspond to interfaces sea-target-sea.

Some detail of the above Fig. 7.

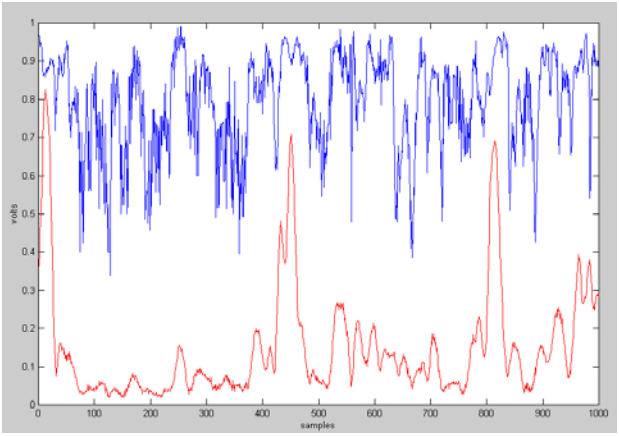

Fig. 8

Blue HRP vs d.r.
Red Mag of Polarimetric vector vs d.r.

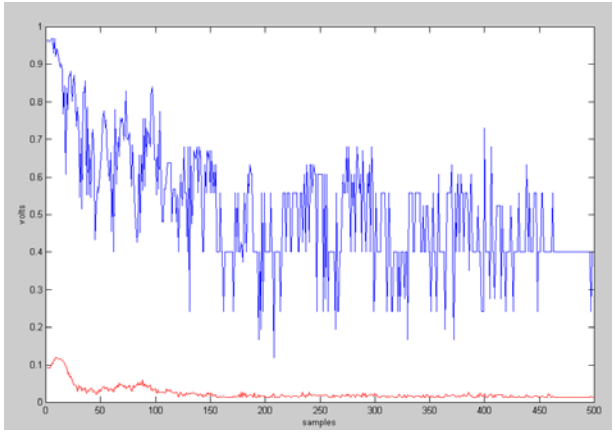

Fig. 9

Blue HRP vs (d.r.)
Red Mag of Polarimetric vector vs d.r.

- Targets are easily and automatically detected;
- The ATR chain can be scaled up to the desired level;
- Potential applications encompass any situation for which an ATR process has to be primed.

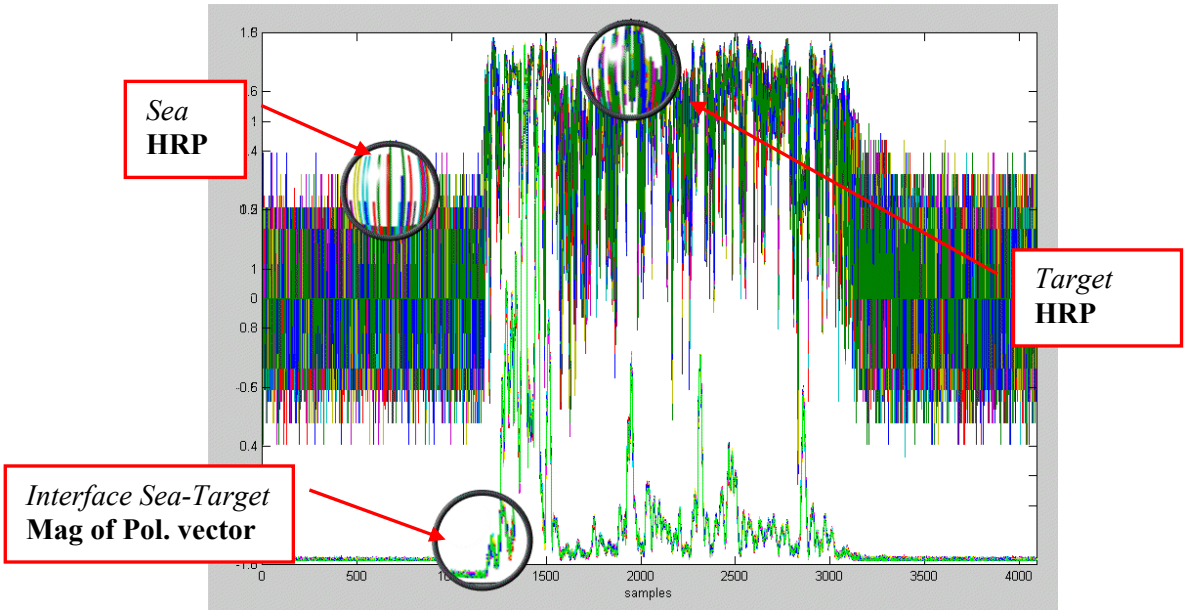

Fig. 10. Upper coloured graphs represent 100 different HRPs vs d.r.
Lower green graphs represent 100 different polarimetric vector MAGs vs d.r.

Each single graph was acquired in single shot. Point-to-point distance on each graph: 7.5 cm.
Graph-to-graph time distance is 1 msec; total observation time: 100 msec.
HRP is also sensitive to small MAG values of the target scatterers.

Below graphs are histograms of different detail part of the HRP signal of the above Fig. 10.

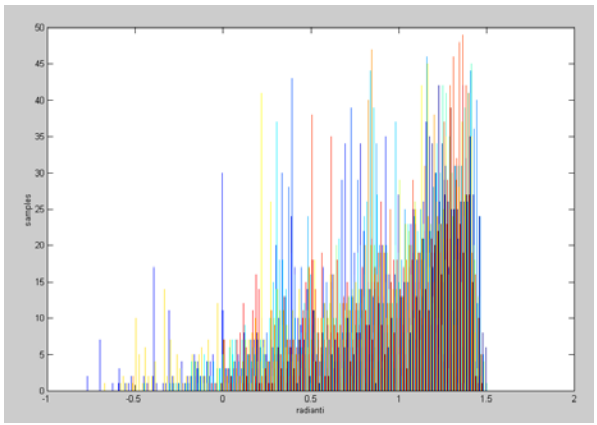

Fig. 11
HRP histogram performed only on entire target echo

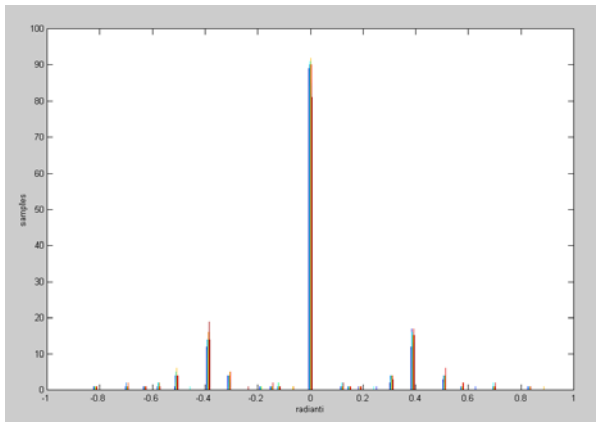

Fig. 12
HRP histogram performed only on sea radar signal

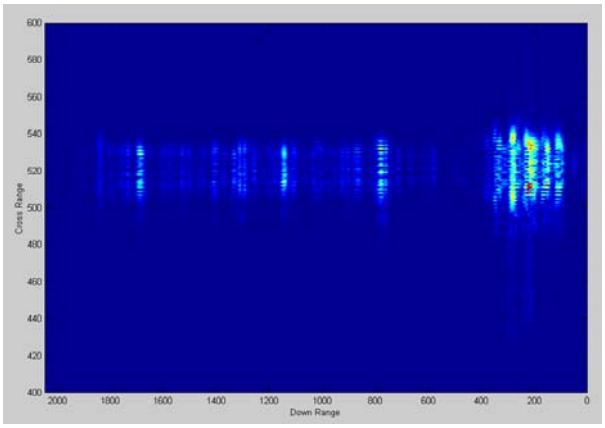

Fig. 13
2D ISAR radar image of circled ship in photograph of Fig.6.
X axis is d.r.; Y axis proportional to elevation angle.
The image is obtained using Magnitude of VV channel.
Down Range spatial resolution (Rayleigh criterium) is about 70 cm.
During observation time the roll angle variation was predominant and permitted a resolution in elevation range of about 4 mt.
Data was not focused nor compensated nor absolutely calibrated

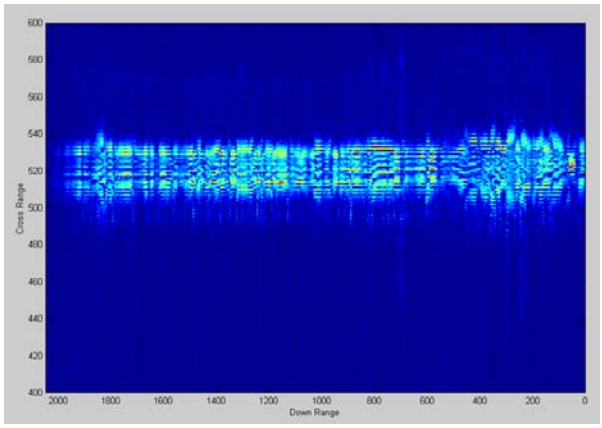

Fig. 14
2D ISAR radar image of the circled ship in the photograph of Fig.6, obtained using HRP.
Target textures, particulars and contours are made evident.

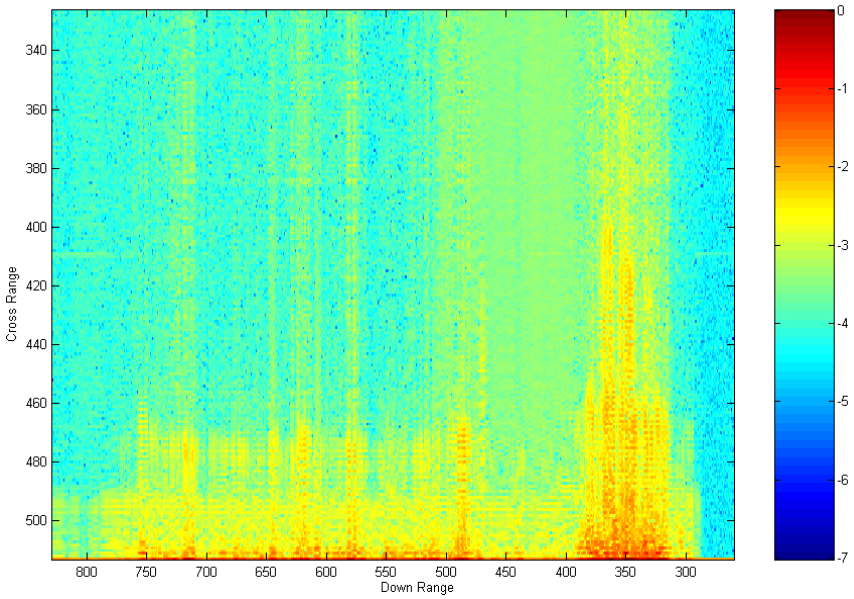

Fig. 15

2D ISAR radar image of circled ship in photograph of Fig.6.
X axis is d.r.; Y axis is proportional (not linearly) to the height of the scatterer in relation to the sea level. The radar image is obtained using the Mag of VV channel. Dedicated processing techniques permitted the extraction of the scatterers having different heights in relation to sea level.

Some verification

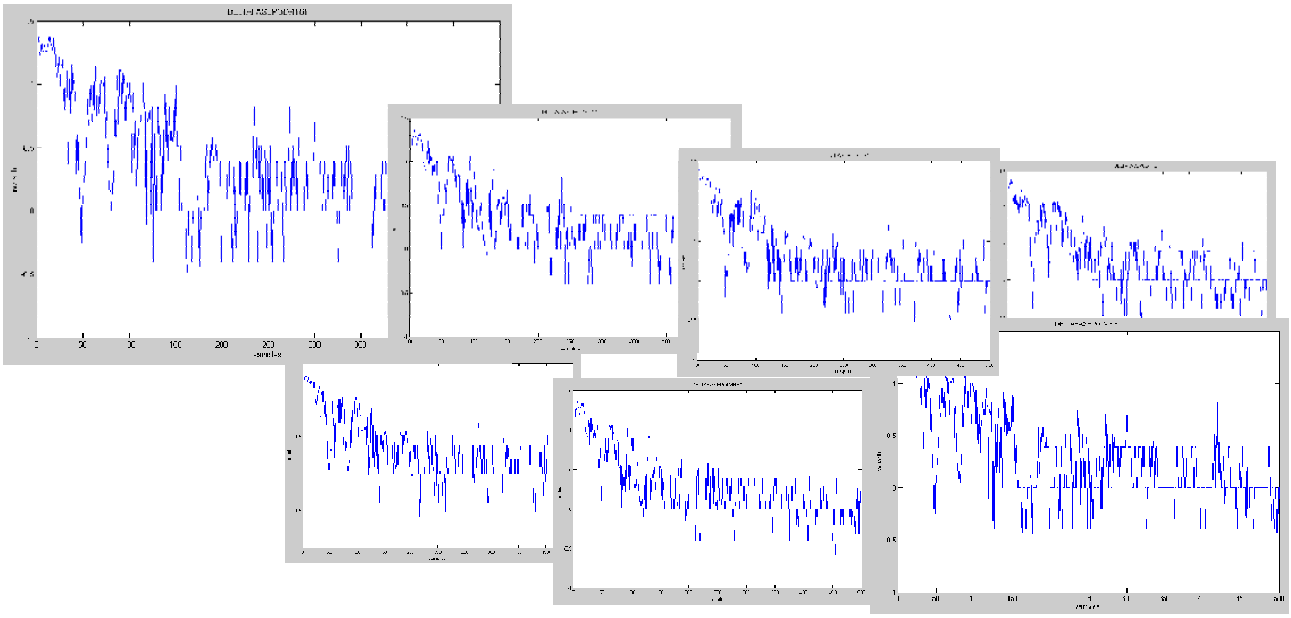

Fig. 16

Each Graph represents HRP vs time (down-range). Raw I & Q data were sampled in single shot. Elapsed time graph-to-graph is 140 msec. X axis is time (sample-to-sample about 500 psec).

Trailing edge of HRP of circled ship in the photograph of Fig.6. HRP is stable in space and with passing time.

ACKNOWLEDGMENTS

Discussion with Dr. Chiti and Dr. Cioni IDS Spa improved this work.

REFERENCES

Polarimetry
Angelo M. RICCI, R. TRINCI
Published for NATO GROUP AC/323 SET-TG15
June 2000

Propagation of short radio waves
Donald E. KERR
McGraw-Hill Book Company
1951

Radar Reflectivity Measurement
Nicholas C. CURRIE
Artech House
1989

Optimum Time-Frequency Distribution for Detecting a Discrete-Time Chirp Signal in White Gaussian Noise

A. Yasotharan
1103-1760 Main Street West
Hamilton, Ontario, L8S 1H2
Canada
yaso-yasotharan@hotmail.com

T. Thayaparan
Defence R & D Canada - Ottawa
Department of National Defence
3701 Carling Avenue
Ottawa, Ontario, K1A 0Z4
Canada
Thayananthan.Thayaparan@drdc-rddc.gc.ca

Abstract

In the continuous-time domain, Maximum-Likelihood (ML) detection of a chirp signal in white Gaussian noise can be done via the line-integral transform of the classical Wigner distribution. The line-integral transform is known variously as the Hough transform and the Radon transform. For discrete-time signals, the Wigner-type distribution defined by Claasen and Mecklenbrauker has become popular as a signal analysis tool. Moreover, it is commonly believed that ML detection of a discrete-time chirp signal in white Gaussian noise can be done via the line-integral transform of the Wigner-Claasen-Mecklenbrauker distribution. This belief is false and results in loss of performance. We derive a Wigner-type distribution for discrete-time signals whose line-integral transform can be used for ML detection of discrete-time chirp signals in white Gaussian noise. We provide simulated Receiver Operating Curves for the Wigner-Claasen-Mecklenbrauker distribution based method and the new ML-equivalent method and demonstrate the suboptimality of the former.

I. Introduction

For a continuous-time signal $r(t)$, the classical Wigner distribution is defined as [1]

$$W_r(t,\omega) = \int r(t+\tau/2)r^*(t-\tau/2)e^{-j\omega\tau}d\tau, \tag{1}$$

where t is time and ω is frequency. In [1], the Wigner distribution was shown to have many properties that make it a useful signal analysis tool.

Suppose we have observed a continuous-time signal $r(t)$ and want to detect the presence or absence in $r(t)$ of a chirp signal

$$s(t) = ae^{j(\omega_0 t+\frac{1}{2}mt^2)}, \tag{2}$$

with unknown parameters a, ω_0 and m, and with the background being additive white Gaussian noise. The classical maximum-likelihood method is equivalent to the hypothesis test

$$\max_{\omega_0,\,m} \left| \int r(t)e^{-j(\omega_0 t+\frac{1}{2}mt^2)}dt \right|^2 \underset{\mathbf{H}_0}{\overset{\mathbf{H}_1}{\gtrless}} \gamma, \tag{3}$$

where

- $\mathbf{H}_0$ is the Noise-Only Hypothesis $r(t) = w(t)$,

Paper presented at the RTO SET Symposium on "Target Identification and Recognition Using RF Systems", held in Oslo, Norway, 11-13 October 2004, and published in RTO-MP-SET-080.

- $\mathbf{H}_1$ is the Signal-plus-Noise Hypothesis $r(t) = s(t) + w(t)$,

$w(t)$ is white Gaussian noise and γ is a threshold whose value is set based on probability of error considerations. More precisely, if the maximum on the left hand side (LHS) of (3) is less than the threshold γ then $\mathbf{H}_0$ is considered true and if the maximum on the LHS of (3) is greater than the threshold γ then $\mathbf{H}_1$ is considered true.

In [2], the hypothesis test (3) was shown to be approximately equivalent to

$$\max_{\omega_0, m} \int W_r(t, \omega_0 + mt) \underset{\mathbf{H}_0}{\overset{\mathbf{H}_1}{\gtrless}} \gamma \tag{4}$$

for chirp signals of large duration. This equivalence was shown in [3] to be exact and valid even for finite-duration signals. More specifically, it was shown in [3] that

$$\left| \int r(t) e^{-j(\omega_0 t + \frac{1}{2} m t^2)} dt \right|^2 = \int W_r(t, \omega_0 + mt) dt, \tag{5}$$

where the quantity on the right hand side is a line-integral transform of the Wigner-distribution variously known as the Hough transform and the Radon transform. Detecting a chirp signal via the hypothesis test (3) is known variously as the correlator method and the dechirp-Doppler method.

A study of the use of time-frequency distributions for detecting signals is found in [4].

For a discrete-time signal $r(n)$, the Wigner distribution defined by Claasen and Mecklenbrauker [5] has become popular as a signal analysis tool. Their definition of Wigner distribution is

$$W_r^{CM}(n, \theta) = 2 \sum_k r(n+k) r^*(n-k) e^{-j2k\theta}, \tag{6}$$

where n is discrete-time and θ is frequency.

Suppose we have observed a discrete-time signal $r(n)$, for $n = 0, \ldots, (N-1)$, and want to detect the presence or absence in $r(n)$ of a chirp signal

$$s(n) = \begin{cases} b_0 e^{j(b_1 n + \frac{1}{2} b_2 n^2)} & \text{if } 0 \le n \le (N-1), \\ 0 & \text{otherwise,} \end{cases} \tag{7}$$

with unknown parameters b_0, b_1 and b_2, with the background being additive white Gaussian noise. Discrete-time chirp signals arise directly in pulse Doppler radars when a target is moving with acceleration [8]. Discrete-time chirp signals also arise in synthetic aperture radars and inverse synthetic aperture radars. A discrete-time chirp signal may also arise as a sampled-version of a continuous-time chirp signal. This is the case, for example, in electronic counter measures to LFM radar and sonar. Many situations where chirp signals occur in nature are described in [9].

For the above discrete-time detection problem, define

$$\Delta_r(c_1, c_2) = \left| \sum_{n=0}^{N-1} r(n) e^{-j(c_1 n + \frac{1}{2} c_2 n^2)} \right|^2. \tag{8}$$

The classical Maximum-Likelihood (ML) method is then equivalent to the hypothesis test

$$\max_{c_1, c_2} \Delta_r(c_1, c_2) \underset{\mathbf{H}_0}{\overset{\mathbf{H}_1}{\gtrless}} \gamma, \tag{9}$$

where

- $\mathbf{H}_0$ is the Noise-Only Hypothesis $r(n) = v(n)$,
- $\mathbf{H}_1$ is the Signal-plus-Noise Hypothesis $r(n) = s(n) + v(n)$,

$v(n)$ is white Gaussian noise and γ is a threshold. We shall henceforth refer to the method of (9) as the *correlator method*. Appendix I gives a brief derivation of the method of (9).

It is commonly and erroneously assumed that the equivalence of (5) for continuous-time signals carries over to discrete-time signals as

$$\left|\sum_n r(n)e^{-j(c_1 n+\frac{1}{2}c_2 n^2)}\right|^2 = \sum_n W_r^{CM}(n, c_1 + c_2 n), \tag{10}$$

where the quantity on the right hand side is the line-integral transform of the Wigner distribution (6). Based on this assumption, it is claimed, erroneously, that ML detection of the discrete-time chirp signal $s(n)$ is equivalent to the hypothesis test

$$\max_{c_1, c_2} \sum_n W_r^{CM}(n, c_1 + c_2 n) \underset{\mathbf{H}_0}{\overset{\mathbf{H}_1}{\gtrless}} \gamma. \tag{11}$$

However, it has been observed in [6] that the W_r^{CM}-based method (11) incurs a 3 dB loss due to non-linearity.[1] In Appendix IV, we provide simulated Receiver Operating Curves for the ML method (9) and the W_r^{CM}-based method (11) and demonstrate the suboptimality of the latter. Moreover, as we will show, the range of unambiguosly measurable values of b_1 for the W_r^{CM}-based method (11) is half of that of the correlator method (9).

In this paper, we derive a time-frequency distribution which is optimum for detecting discrete-time chirp signals in white Gaussian noise, with the optimality being in the sense that ML detection can be carried out via the line-integral transform of the derived time-frequency distribution. The derived time-frequency distribution may be considered a Wigner-type distribution.

It turns out that the Wigner-type time-frequency distribution derived in this paper is the same as that derived by Chan [7] in an effort to solve the problem of aliasing in the Wigner distribution (6). Nevertheless, the optimality property of this distribution for detection of a discrete-time signal was not observed in [7]. Therefore, in the context of signal detection, this discrete-time distribution seems new.

II. Three Wigner-type Time-Frequency Distributions for Discrete-Time Signals

In attempting to write $\Delta_r(c_1, c_2)$ of (8) as the line-integral of a time-frequency distribution of $r(n)$, we arrive at three Wigner-type time-frequency distributions of a discrete-time signal. We first describe these time-frequency distributions and in the next section we describe the actual line-integral transform.

Given a discrete-time signal $r(n)$, we denote $r_\pi(n) = r(n)e^{j\pi n}$. That is $r_\pi(n)$ is the signal obtained by frequency-shifting $r(n)$ by π radians/second.

A. Type-I Wigner Distribution

The type-I Wigner distribution $W_r^I(n, \theta)$ is defined as

$$W_r^I(n, \theta) = \sum_k r(n + k)r^*(n - k)e^{-j2k\theta}, \tag{12}$$

[1]The ratio between the output SNR and the input SNR is (c.f. equation (13) of [6]) $\frac{\text{SNR}_{\text{out}}}{\text{SNR}_{\text{in}}} = \left(\frac{N}{2}\right)\left(\frac{N\text{SNR}_{\text{in}}}{N\text{SNR}_{\text{in}}+1}\right)$, which is less than $N/2$. The ratio approaches $N/2$ as $N\text{SNR}_{\text{in}} \to \infty$.

where n is discrete-time and θ is frequency.

Note that $W_r^I(n,\theta)$ is the same as $W_r^{CM}(n,\theta)$ (c.f. (6)) defined in [5] except for the missing scaling factor 2 at the front.

For a signal $r(n)$ that is zero outside $0 \le n \le (N-1)$, the type-I Wigner distribution $W_r^I(n,\theta)$ is zero outside $0 \le n \le (N-1)$.

The following properties are easy to verify: $W_r^I(n,\theta)$ is real, $W_r^I(n,\theta)$ is a periodic function of θ with period π, $W_{r_\pi}^I(n,\theta) = W_r^I(n,\theta)$. Thus $W_r^I(n,\theta)$ is invariant to frequency-shifting the signal $r(n)$ by π radians/second.

B. Type-II Wigner Distribution

The type-II Wigner distribution $W_r^{II}(n,\theta)$ is defined as

$$W_r^{II}(n,\theta) = \sum_k r(n+k+1)r^*(n-k)e^{-j(2k+1)\theta}, \tag{13}$$

where n is discrete-time and θ is frequency.

For a signal $r(n)$ that is zero outside $0 \le n \le (N-1)$, the type-II Wigner distribution $W_r^{II}(n,\theta)$ is zero outside $0 \le n \le (N-2)$.

The following properties are easy to verify: $W_r^{II}(n,\theta)$ is real, $W_r^{II}(n,\theta)$ is a periodic function of θ with period 2π, $W_r^{II}(n,\theta+\pi) = -W_r^{II}(n,\theta)$, $W_{r_\pi}^{II}(n,\theta) = -W_r^{II}(n,\theta)$. Thus frequency-shifting of the signal $r(n)$ by π radians/second causes a sign change in $W_r^I(n,\theta)$.

C. Type-III Wigner Distribution

The type-III Wigner distribution $W_r^{III}(n,\theta)$ is defined in terms of the type-I and type-II Wigner distributions as follows.

$$W_r^{III}(n,\theta) = \begin{cases} W_r^I(n/2,\theta) & \text{for even } n, \\ W_r^{II}((n-1)/2,\theta) & \text{for odd } n. \end{cases} \tag{14}$$

Note that $W_r^{III}(n,\theta)$ is the same as the "non-aliased discrete-time Wigner distribution" derived by Chan in [7] in an effort to solve the aliasing problem of $W_r^{CM}(n,\theta)$ (c.f. (6)) defined in [5].

For a signal $r(m)$ that is zero outside $0 \le m \le (N-1)$, the type-III Wigner distribution $W_r^{III}(n,\theta)$ is zero outside $0 \le n \le 2(N-1)$. However, if we consider even n to correspond to integer values $n/2$ of time and odd n to correspond to half-integer values $n/2$ of time, then $W_r^{III}(n,\theta)$ is zero outside the time range $0 \le m \le (N-1)$.

The following properties are obvious: $W_r^{III}(n,\theta)$ is real, $W_r^{III}(n,\theta)$ is a periodic function of θ with period 2π. For even n, $W_{r_\pi}^{III}(n,\theta) = W_r^{III}(n,\theta)$. For odd n, $W_{r_\pi}^{III}(n,\theta) = -W_r^{III}(n,\theta)$.

III. A Wigner-Distribution Formulation of the ML Detection Problem for a Discrete-Time Chirp Signal

For a discrete-time signal $r(n)$ that is zero outside $0 \le n \le (N-1)$, we have shown in Appendix II that

$$\Delta_r(c_1,c_2) = \sum_{n=0}^{2N-2} W_r^{III}(n, c_1 + \frac{1}{2}c_2 n). \tag{15}$$

Thus we can calculate $\Delta_r(c_1,c_2)$ by taking the type-III Wigner distribution $W_r^{III}(n,\theta)$ of the discrete-time signal $r(n)$ and integrating it along the line with intercept c_1 (value of θ at $n=0$) and slope $\frac{1}{2}c_2$ (increment in θ per unit increment in n). This property of $W_r^{III}(n,\theta)$ was not observed in [7]. Therefore,

in the context of detection of discrete-time signals, the type-III Wigner distribution $W_r^{III}(n,\theta)$ seems new.

Relationship (15) implies that we can perform ML detection by the test

$$\max_{c_1,c_2} \sum_{n=0}^{2N-2} W_r^{III}(n, c_1 + \frac{1}{2}c_2 n) \underset{\mathbf{H}_0}{\overset{\mathbf{H}_1}{\gtrless}} \gamma, \tag{16}$$

where γ, $\mathbf{H}_0$ and $\mathbf{H}_1$ are as defined for the correlator method (9).

A. Advantages of the Type-III Wigner Distribution Based Method

In Appendix III, we have derived the type-I and type-III Wigner distributions for the discrete-time chirp signal

$$s(n) = \begin{cases} e^{j(b_1 n + \frac{1}{2}b_2 n^2)} & \text{if } 0 \le n \le (N-1) \\ 0 & \text{otherwise.} \end{cases} \tag{17}$$

If the chirp signal has complex amplitude b_0 then the Wigner distributions must be scaled by $|b_0|^2$. Thus, in the absence of any noise or interference, the Wigner distributions $W_r^I(n,\theta)$ and $W_r^{III}(n,\theta)$ are concentrated along a straight line whose intercept of the frequency axis is b_1 and the frequency/time slope is b_2. Therefore, the visual appeal of the W_r^{CM}-based method (11) is retained by the W_r^{III}-based method (16). Moreover, any method of automatically detecting the line where W_r^{CM} is concentrated can be used for automatically detecting the line where W_r^{III} is concentrated.

As the W_r^{III}-based method (16) is mathematically equivalent to the correlator method (9), it has the same Signal-to-Noise (SNR) performance as the ML method.

The properties of the type-I and type-III Wigner distributions stated in Section II show that the range of unambiguously measurable values of b_1 can be doubled by using the W_r^{III}-based method instead of the W_r^{CM}-based method. More specifically,

- for the W_r^{CM}-based method, the interval of unambiguously measurable values of b_1 is $[-\pi/2, \pi/2]$,
- for the W_r^{III}-based method, the interval of unambiguously measurable values of b_1 is $[-\pi, \pi]$, which is the maximum possible.

IV. Conclusion

In this paper, we considered detecting a discrete-time chirp signal, in the presence of additive white Gaussian noise, via the line-integral transform of a time-frequency distribution of the observed signal. We pointed out that the popular method, in which the line-integral transform of the Wigner-Classen-Mecklenbrauker distribution is maximized, is not equivalent to the maximum-likelihood (ML) method. We derived a Wigner-type distribution with the property that maximizing its line-integral transform is equivalent to the ML method. We provided simulated Receiver Operating Curves for the Wigner-Claasen-Mecklenbrauker distribution based method and the new ML-equivalent method and demonstrated the suboptimality of the former. The use of the derived Wigner-type distribution also doubles the range of unambiguously measurable values of the initial frequency parameter b_1 of the chirp signal to the maximum possible $[-\pi, \pi]$.

Acknowledgement

The authors gratefully acknowledge the support provided by Dr. A. M. (Tony) Ponsford, Technical Director of HF radar development at Raytheon Systems Canada Ltd.

APPENDIX I

The Maximum Likelihood Method

Suppose we have observed a discrete-time signal $r(n)$, for $n = 0, \ldots, (N-1)$, and want to detect the presence or absence in $r(n)$ of a chirp signal

$$s(n) = \begin{cases} b_0 e^{j(b_1 n + \frac{1}{2} b_2 n^2)} & \text{if } 0 \leq n \leq (N-1), \\ 0 & \text{otherwise,} \end{cases} \tag{18}$$

with unknown parameters b_0, b_1 and b_2, with the background being additive white Gaussian noise. The classical Maximum-Likelihood (ML) method is then equivalent to the hypothesis test

$$\max_{c_0, c_1, c_2} \Lambda(c_0, c_1, c_2) \underset{\mathbf{H}_0}{\overset{\mathbf{H}_1}{\gtrless}} \eta, \tag{19}$$

where

$$\Lambda(c_0, c_1, c_2) = \sum_{n=0}^{N-1} |r(n)|^2 - \sum_{n=0}^{N-1} \left| r(n) - c_0 e^{j(c_1 n + \frac{1}{2} c_2 n^2)} \right|^2 \tag{20}$$

is the log-likelihood ratio,

- $\mathbf{H}_0$ is the Noise-Only Hypothesis $r(n) = v(n)$,
- $\mathbf{H}_1$ is the Signal-plus-Noise Hypothesis $r(n) = s(n) + v(n)$,

$v(n)$ is white Gaussian noise and η is a threshold whose value is set based on probability of error considerations. When $\mathbf{H}_1$ is considered true, the values of c_0, c_1, and c_2 that maximize $\Lambda(c_0, c_1, c_2)$ are the maximum likelihood estimates of b_0, b_1 and b_2, respectively.

By writing

$$\Lambda(c_0, c_1, c_2) = 2\Re\left(c_0^* \sum_{n=0}^{N-1} r(n) e^{-j(c_1 n + \frac{1}{2} c_2 n^2)} \right) - |c_0|^2 N, \tag{21}$$

$$= N \left(\frac{1}{N^2} \left| \sum_{n=0}^{N-1} r(n) e^{-j(c_1 n + \frac{1}{2} c_2 n^2)} \right|^2 - \left| \frac{1}{N} \sum_{n=0}^{N-1} r(n) e^{-j(c_1 n + \frac{1}{2} c_2 n^2)} - c_0 \right|^2 \right), \tag{22}$$

we conclude that for any fixed (c_1, c_2) pair, $\Lambda(c_0, c_1, c_2)$ is maximized by

$$c_0 = \frac{1}{N} \sum_{n=0}^{N-1} r(n) e^{-j(c_1 n + \frac{1}{2} c_2 n^2)}, \tag{23}$$

and for this choice of c_0, $\Lambda(c_0, c_1, c_2) = \frac{1}{N} \Delta(c_1, c_2)$, where

$$\Delta(c_1, c_2) = \left| \sum_{n=0}^{N-1} r(n) e^{-j(c_1 n + \frac{1}{2} c_2 n^2)} \right|^2. \tag{24}$$

Therefore, the ML method is equivalent to the hypothesis test

$$\max_{c_1, c_2} \Delta(c_1, c_2) \underset{\mathbf{H}_0}{\overset{\mathbf{H}_1}{\gtrless}} \gamma, \tag{25}$$

where γ is a threshold (which can be related to η). When $\mathbf{H}_1$ is considered true, the values of c_1 and c_2 that maximize $\Delta(c_1, c_2)$ are the maximum likelihood estimates of b_1 and b_2 respectively.

Thus the ML method can be implemented as a correlator in the (c_1, c_2) plane. This method is also known as the dechirp-Doppler method, i.e., first multiplying by $e^{-j\frac{1}{2}c_2 n^2}$ to obtain a pure complex exponential, or nearly so, so that there will be little or no loss due to Doppler spreading when estimating the frequency of the pure complex exponential by the conventional Doppler processing method.

APPENDIX II
Computing $\Delta_r(c_1, c_2)$ via the Wigner Distributions

For a discrete-time signal $r(n)$ that is zero outside $0 \leq n \leq (N-1)$, we show how to write $\Delta_r(c_1, c_2)$ (c.f. (8)) as the line-integral of a time-frequency distribution of $r(n)$.

We begin by writing $\Delta_r(c_1, c_2)$ as the double summation

$$\Delta_r(c_1, c_2) = \sum_{n_1=0}^{N-1} \sum_{n_2=0}^{N-1} r(n_1) r^*(n_2) e^{-j(c_1(n_1-n_2)+\frac{1}{2}c_2(n_1^2-n_2^2))}, \tag{26}$$

$$= \sum_{n_1=0}^{N-1} \sum_{n_2=0}^{N-1} r(n_1) r^*(n_2) e^{-j(n_1-n_2)(c_1+\frac{1}{2}c_2(n_1+n_2))}. \tag{27}$$

Then we break the double summation into two double summations - one double summation being over n_1 and n_2 where $(n_1 - n_2)$ is even and the other double summation being over n_1 and n_2 where $(n_1 - n_2)$ is odd. Thus we define

$$\Delta_r^I(c_1, c_2) = \sum_{\substack{n_1=0 \\ (n_1-n_2) \text{ is even}}}^{N-1} \sum_{n_2=0}^{N-1} r(n_1) r^*(n_2) e^{-j(n_1-n_2)(c_1+\frac{1}{2}c_2(n_1+n_2))}, \tag{28}$$

and

$$\Delta_r^{II}(c_1, c_2) = \sum_{\substack{n_1=0 \\ (n_1-n_2) \text{ is odd}}}^{N-1} \sum_{n_2=0}^{N-1} r(n_1) r^*(n_2) e^{-j(n_1-n_2)(c_1+\frac{1}{2}c_2(n_1+n_2))}. \tag{29}$$

To compute $\Delta_r^I(c_1, c_2)$, we use the change of variables[2]

$$n_1 + n_2 = 2m, \tag{30}$$

$$n_1 - n_2 = 2k, \tag{31}$$

define $l = \min(m, N-1-m)$ and obtain

$$\Delta_r^I(c_1, c_2) = \sum_{m=0}^{N-1} \sum_{k=-l}^{l} r(m+k) r^*(m-k) e^{-j2k(c_1+c_2 m)}, \tag{32}$$

$$= \sum_{m=0}^{N-1} W_r^I(m, c_1 + c_2 m). \tag{33}$$

Similarly, to compute $\Delta_r^{II}(c_1, c_2)$, we use the variable change

$$n_1 + n_2 = 2m + 1, \tag{34}$$

$$n_1 - n_2 = 2k + 1, \tag{35}$$

[2]Note that $n_1 + n_2$ is even if and only if $n_1 - n_2$ is even.

define $l = \min(m, N-2-m)$ and obtain

$$\Delta_r^{II}(c_1, c_2) = \sum_{m=0}^{N-2} \sum_{k=-(l+1)}^{l} r(m+k+1) r^*(m-k) e^{-j(2k+1)(c_1 + \frac{1}{2}c_2 + c_2 m)}, \tag{36}$$

$$= \sum_{m=0}^{N-2} W_r^{II}(m, c_1 + \frac{1}{2}c_2 + c_2 m). \tag{37}$$

By combining (33) and (37), we obtain

$$\Delta_r(c_1, c_2) = \Delta_r^{I}(c_1, c_2) + \Delta_r^{II}(c_1, c_2), \tag{38}$$

$$= \sum_{m=0}^{N-1} W_r^{I}(m, c_1 + c_2 m) + \sum_{m=0}^{N-2} W_r^{II}(m, c_1 + \frac{1}{2}c_2 + c_2 m), \tag{39}$$

$$= \sum_{m=0}^{N-1} W_r^{III}(2m, c_1 + \frac{1}{2}c_2 2m) + \sum_{m=0}^{N-2} W_r^{III}(2m+1, c_1 + \frac{1}{2}c_2(2m+1)), \tag{40}$$

$$= \sum_{\substack{m=0 \\ \text{(m is even)}}}^{2N-2} W_r^{III}(m, c_1 + \frac{1}{2}c_2 m) + \sum_{\substack{m=0 \\ \text{(m is odd)}}}^{2N-2} W_r^{III}(m, c_1 + \frac{1}{2}c_2 m), \tag{41}$$

$$= \sum_{m=0}^{2N-2} W_r^{III}(m, c_1 + \frac{1}{2}c_2 m). \tag{42}$$

Thus we have proved (15) of Section III.

APPENDIX III
Wigner Distributions of a Discrete-Time Chirp Signal

Here we derive the type-I, type-II, and type-III Wigner distributions for the discrete-time chirp signal

$$s(n) = \begin{cases} e^{j(b_1 n + \frac{1}{2}b_2 n^2)} & \text{if } 0 \le n \le (N-1) \\ 0 & \text{otherwise.} \end{cases} \tag{43}$$

These Wigner distributions are defined in Section II.

A. Type-I Wigner Distribution

The type-I Wigner distribution $W_s^I(n, \theta)$ is defined as

$$W_s^I(n, \theta) = \sum_k s(n+k) s^*(n-k) e^{-j2k\theta}. \tag{44}$$

The signal product term $s(n+k)s^*(n-k)$ is zero outside the ranges $0 \le n \le (N-1)$ and $-\min(n, N-1-n) \le k \le \min(n, N-1-n)$. Thus $W_s^I(n, \theta) = 0$ outside $0 \le n \le (N-1)$.

Define $l = \min(n, N-1-n)$. In terms of this, for $0 \le n \le (N-1)$,

$$W_s^I(n,\theta) = \sum_{k=-l}^{l} e^{j(b_1(n+k)+\frac{1}{2}b_2(n+k)^2)} e^{-j(b_1(n-k)+\frac{1}{2}b_2(n-k)^2)} e^{-j2k\theta}, \tag{45}$$

$$= \sum_{k=-l}^{l} e^{j(b_1 2k+\frac{1}{2}b_2 4nk)} e^{-j2k\theta}, \tag{46}$$

$$= \sum_{k=-l}^{l} e^{-j(\theta-(b_1+b_2 n))2k}, \tag{47}$$

which is a sum of a geometric series that can be easily evaluated. To do this, we substitute $\alpha = \theta - (b_1 + b_2 n)$ into the summation

$$\sum_{k=-l}^{l} e^{-j2\alpha k} = \begin{cases} 2l+1 & \text{if } \alpha = 0 \bmod \pi, \\ \frac{\sin[\alpha(2l+1)]}{\sin\alpha} & \text{otherwise.} \end{cases} \tag{48}$$

Thus, for $0 \le n \le (N-1)$,

$$W_s^I(n,\theta) = \begin{cases} 2l(n)+1 & \text{if } \alpha(n) = 0 \bmod \pi, \\ \frac{\sin[\alpha(n)(2l(n)+1)]}{\sin\alpha(n)} & \text{otherwise.} \end{cases}, \tag{49}$$

where $l(n) = \min(n, N-1-n)$ and $\alpha(n) = \theta - (b_1 + b_2 n)$. In a 3-dimensional plot, $W_s^I(n,\theta)$ has ridges along the lines given by $\alpha(n) = 0 \bmod \pi$ and the common height of these ridges is $2l(n)+1$.

B. Type-II Wigner Distribution

The type-II Wigner distribution $W_s^{II}(n,\theta)$ is defined as

$$W_s^{II}(n,\theta) = \sum_k s(n+k+1)s^*(n-k)e^{-j(2k+1)\theta}. \tag{50}$$

The signal product term $s(n+k+1)s^*(n-k)$ is zero outside the ranges $0 \le n \le (N-2)$ and $-\min(n+1, N-1-n) \le k \le \min(n, N-2-n)$. Thus $W_s^{II}(n,\theta) = 0$ outside $0 \le n \le (N-2)$.

Define $l = \min(n, N-2-n)$. In terms of this, for $0 \le n \le (N-2)$,

$$W_s^{II}(n,\theta) = \sum_{k=-(l+1)}^{l} e^{j(b_1(n+k+1)+\frac{1}{2}b_2(n+k+1)^2)} e^{-j(b_1(n-k)+\frac{1}{2}b_2(n-k)^2)} e^{-j(2k+1)\theta}, \tag{51}$$

$$= \sum_{k=-(l+1)}^{l} e^{j(b_1(2k+1)+\frac{1}{2}b_2(4nk+2n+2k+1))} e^{-j(2k+1)\theta}, \tag{52}$$

$$= \sum_{k=-(l+1)}^{l} e^{-j(\theta-(b_1+\frac{1}{2}b_2+b_2 n))(2k+1)}, \tag{53}$$

$$= e^{-j(\theta-(b_1+\frac{1}{2}b_2+b_2 n))} \sum_{k=-(l+1)}^{l} e^{-j(\theta-(b_1+\frac{1}{2}b_2+b_2 n))2k}, \tag{54}$$

which is a scaled version of a sum of a geometric series that can be easily evaluated. To do this, we substitute $\alpha = \theta - (b_1 + \frac{1}{2}b_2 + b_2 n)$ into the summation

$$\sum_{k=-(l+1)}^{l} e^{-j2\alpha k} = \begin{cases} 2l+2 & \text{if } \alpha = 0 \bmod \pi, \\ e^{j\alpha}\left(\frac{\sin[2\alpha(l+1)]}{\sin\alpha}\right), \end{cases} \tag{55}$$

or directly into the scaled version

$$e^{-j\alpha}\sum_{k=-(l+1)}^{l} e^{-j2\alpha k} = \begin{cases} e^{-j\alpha}(2l+2) & \text{if } \alpha = 0 \bmod \pi, \\ \frac{\sin[2\alpha(l+1)]}{\sin\alpha}, \end{cases} \tag{56}$$

$$= \begin{cases} (2l+2) & \text{if } \alpha = 0 \bmod 2\pi, \\ -(2l+2) & \text{if } \alpha = \pi \bmod 2\pi, \\ \frac{\sin[2\alpha(l+1)]}{\sin\alpha}. \end{cases} \tag{57}$$

Thus, for $0 \le n \le (N-2)$,

$$W_s^{II}(n,\theta) = \begin{cases} 2l(n)+2 & \text{if } \alpha(n) = 0 \bmod 2\pi, \\ -(2l(n)+2) & \text{if } \alpha(n) = \pi \bmod 2\pi, \\ \frac{\sin[2\alpha(n)(l(n)+1)]}{\sin\alpha(n)} & \text{otherwise.} \end{cases}, \tag{58}$$

where $l(n) = \min(n, N-2-n)$ and $\alpha(n) = \theta - (b_1 + \frac{1}{2}b_2 + b_2 n)$. In a 3-dimensional plot, $W_s^{II}(n,\theta)$ has ridges along the lines given by $\alpha(n) = 0 \bmod 2\pi$ and the common height of these ridges is $2l(n)+2$. In a 3-dimensional plot, $W_s^{II}(n,\theta)$ also has valleys along the lines given by $\alpha(n) = \pi \bmod 2\pi$ and the common depth of these ridges is $2l(n)+2$.

C. Type-III Wigner Distribution

The type-III Wigner distribution $W_s^{III}(n,\theta)$ is defined in terms of the type-I and type-II Wigner distributions as

$$W_s^{III}(n,\theta) = \begin{cases} W_s^{I}(n/2,\theta) & \text{for even } n, \\ W_s^{II}((n-1)/2,\theta) & \text{for odd } n. \end{cases} \tag{59}$$

Define $l(n) = \min(\frac{n}{2}, N-1-\frac{n}{2})$ and $\alpha(n) = \theta - (b_1 + \frac{1}{2}b_2 n)$.
For n even and $0 \le n \le 2(N-1)$,

$$W_s^{III}(n,\theta) = \begin{cases} 2l(n)+1 & \text{if } \alpha(n) = 0 \bmod \pi, \\ \frac{\sin[\alpha(n)(2l(n)+1)]}{\sin\alpha(n)} & \text{otherwise.} \end{cases} \tag{60}$$

For n odd and $0 \le n \le 2(N-1)$,

$$W_s^{III}(n,\theta) = \begin{cases} 2l(n)+1 & \text{if } \alpha(n) = 0 \bmod 2\pi, \\ -[2l(n)+1] & \text{if } \alpha(n) = \pi \bmod 2\pi, \\ \frac{\sin[\alpha(n)(2l(n)+1)]}{\sin\alpha(n)} & \text{otherwise.} \end{cases} \tag{61}$$

Combining the above, for all $0 \le n \le 2(N-1)$,

$$W_s^{III}(n,\theta) = \begin{cases} 2l(n)+1 & \text{if } \alpha(n) = 0 \bmod 2\pi, \\ (-1)^n[2l(n)+1] & \text{if } \alpha(n) = \pi \bmod 2\pi, \\ \frac{\sin[\alpha(n)(2l(n)+1)]}{\sin\alpha(n)} & \text{otherwise.} \end{cases} \tag{62}$$

In a 3-dimensional plot, $W_s^{III}(n,\theta)$ has ridges along the lines given by $\alpha(n) = 0 \bmod 2\pi$ and the common height of these ridges is $2l(n)+1$. In a 3-dimensional plot, $W_s^{III}(n,\theta)$ also has oscillations along the lines given by $\alpha(n) = \pi \bmod 2\pi$; the common period of these oscillations is one and the common (instantaneous) amplitude is $2l(n)+1$.

APPENDIX IV

Receiver Operating Curve Comparison

Here we present the Receiver Operating Curves (ROCs) obtained by simulation of the Type-I and Type-III Wigner distribution based methods for the case $N = 128$ and Output SNR $= 7$ dB, where Output SNR is defined as $N\left(\frac{a}{\sigma}\right)^2$. For simplicity, the parameters of the chirp signal were assumed to be known. The suboptimality of the Type-I Wigner distribution based method can be clearly seen.

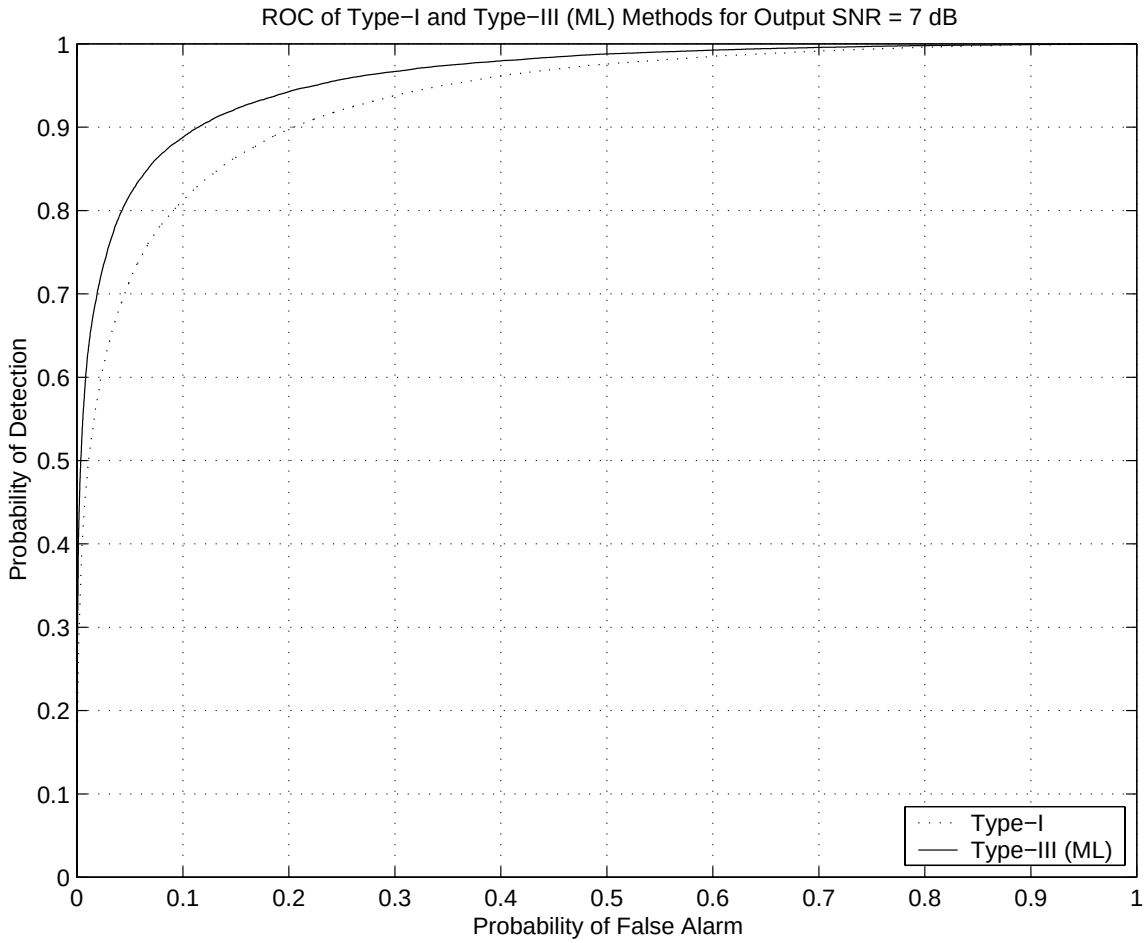

Figure 1: ROCs for probability of false alarm ranging from 0 to 1

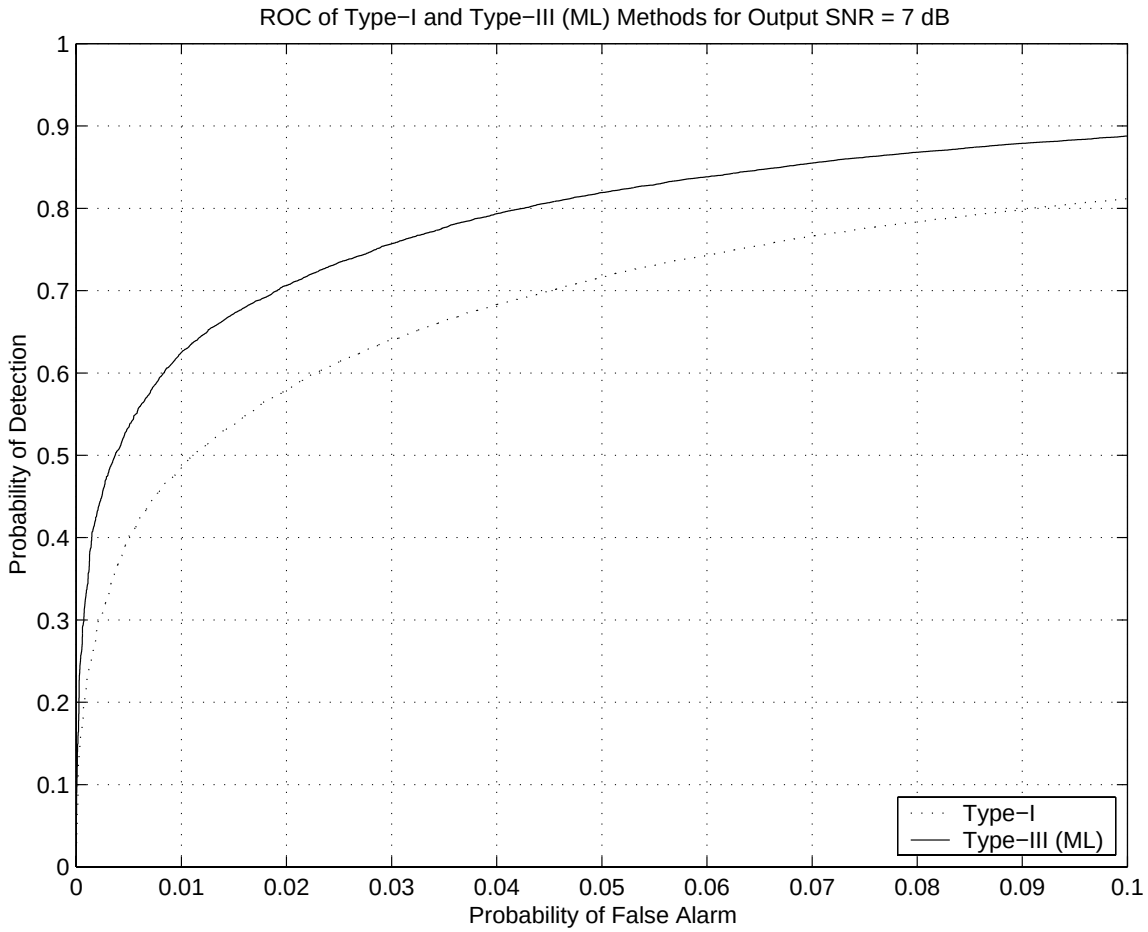

Figure 2: ROCs for probability of false alarm ranging from 0 to 0.1

REFERENCES

[1] T. A. C. M. Claasen and W. F. G. Mecklenbrauker, “The Wigner Distribution - A Tool for Time-Frequency Signal Analysis, Part-I: Continuous-Time Signals”, Philips Journal of Research, Vol. 35, No. 3, 1980, pp. 217-250.

[2] S. Kay and G. F. Boudreaux-Bartels, “On the Optimality of the Wigner Distribution for Detection”, Proc. ICASSP ‘85, pp. 27.2.1-4.

[3] W. Li, “Wigner Distribution Method Equivalent to Dechirp Method for Detecting a Chirp Signal”, IEEE Trans. Acoustics, Speech, and Signal Processing, Vol. ASSP-35, No. 8, August 1987, pp. 1210-1211.

[4] P. Flandrin, “A Time-Frequency Formulation of Optimum Detection”, IEEE Trans. Acoustics, Speech, and Signal Processing, Vol. 36, No. 9, September 1988, pp. 1377-1384.

[5] T. A. C. M. Claasen and W. F. G. Mecklenbrauker, “The Wigner Distribution - A Tool for Time-Frequency Signal Analysis, Part-II: Discrete-Time Signals”, Philips Journal of Research, Vol. 35, Nos. 4/5, 1980, pp. 276-300.

[6] S. Barbarossa, “Analysis of Multicomponent LFM Signals by a Combined Wigner-Hough Transform”, IEEE Trans. Signal Processing, Vol. 43, No. 6, June 1995, pp. 1511-1515.

[7] D. S. K. Chan, “A Non-Aliased Discrete-Time Wigner Distribution for Time-Frequency Signal Analysis”, Proc. ICASSP ‘82, pp. 1333-1336.

[8] A.Yasotharan, T. Thayaparan, Strengths and limitations of the Fourier method for detecting accelerating targets by pulse Doppler radar, IEE Proceedings - Radar, Sonar, Navigation, Vol. 149, No. 2, April 2002, pp. 83 - 88.

[9] P. Flandrin, “Chirps everywhere,” Invited talk given at the CEMRACS “Mthodes Mathmatiques en Traitement d’Images”, Marseille, August 2002. Available in http://perso.ens-lyon.fr/patrick.flandrin/publirecentes.html.

Application of Linear Discriminant Analysis to Doppler Classification

M. Jahangir
QinetiQ
St Andrews Road, Malvern
WORCS, UK, WR14 3PS
United Kingdom

mjahangir@qinetiq.com

ABSTRACT

In this work the author demonstrated a robust and efficient method for implementing Doppler classification through the use of Linear Discriminant Analysis (LDA). LDAs were used to reduce dramatically the data dimensionality and thereby eliminate redundancy and improve the efficiency of the classifier. The performance was assessed on a three-class problem of personnel, tracked and wheeled vehicles. Real radar data from a ground based system were used in the design and testing of the classifier. The classifier algorithm was optimised by choosing the best set of features that maximised the performance and the bootstrap method was used to measure the confidence interval. It was shown that only the first few LDA features were relevant. At the very least these were shown to contain information regarding the frequency extent of target Doppler sidebands. The classifier was shown to be robust to changes in target viewing geometry and speed. Overall, good classification was achieved for personnel with some misclassification between tracked and wheeled vehicles.

1.0 INTRODUCTION

MTI (Moving Target Indication) radars can provide an all-weather, day/night, surveillance capability. Such radar systems provide very efficient location information on moving targets but traditionally have limited recognition capability. Automatic recognition algorithms developed for imaging radars, which exploit target spatial information, are not applicable for MTI systems because they operate in a low resolution mode. However, there is potential for classification based on target Doppler signatures. The Doppler signatures are shifted in frequency in proportion to the target radial velocity. Movement or rotation of structures on a target may induce additional frequency modulations on the returned radar signal and generate sidebands about the Doppler frequency shift of the target's body. The signature characteristics of these Doppler sidebands provide a mechanism for classifying the target of interest.

The Doppler classifier models each target class as a multivariate Gaussian mixture distribution (GMD). The parameters of the GMD model are estimated using labelled training data. The input feature vectors are generated from the radar Doppler spectra. It is assumed that each Doppler spectrum provides an independent feature vector. Training uses multiple Doppler spectra per target class. Recognition is performed using a single Doppler spectrum (feature vector).

The size (and therefore the dimensionality) of the input feature vector depends upon the number of separate frequency bins in the Doppler spectra. Herein lies the limitation of a classification technique that uses the Doppler spectra directly for input feature vectors. Doppler spectra can comprise a large number of frequency bins (several tens, possibly hundreds) to cover sufficiently the full range of Doppler frequencies

Paper presented at the RTO SET Symposium on "Target Identification and Recognition Using RF Systems", held in Oslo, Norway, 11-13 October 2004, and published in RTO-MP-SET-080.

at enough resolution to be able to provide meaningful classification performance. High dimensionality leads to increased classifier complexity. There are more parameters to estimate per target model which results in an increased processing load. Reducing dimensionality makes the classification calculations quicker and saves on data storage space. Furthermore, the original set of variables may contain redundant and irrelevant information. Redundancy would result in the classifier having extra parameters over and above the minimum required to capture the structure within the data. For a finite training set this would lead to poorer estimation of the classifier parameters. Therefore, reducing the dimensionality could also improve classifier robustness.

Linear Discriminant Analysis (LDA) is a well established technique for obtaining a reduced-dimension representation of the data. LDA defines (a few) new variables as linear combinations of the original ones. Evidence from speech recognition has shown that the classification performance improves if features are extracted using LDA [1]. There is a key similarity between speech processing and Doppler processing *i.e.*, both use the spectrogram as the input measurement. LDA could potentially offer a good approach for reducing the number of variables in the Doppler spectra. The technique consists of transforming the Doppler spectra variables using linear combination into a set of features (the feature vector) that are mutually orthogonal. The individual features are assumed to be independent. The transformation is designed to maximise the between-class covariance and minimise the average within-class covariance. The transformed features are ranked in order of the class separability. In theory, the classification performance should increase monotonically as the number of features increases. This allows simple trade-offs to be made between complexity (number of features) and viability (classification performance).

The classification algorithm is developed for a three class problem based on personnel, wheeled vehicles and tracked vehicles. Section 2 gives an outline of the algorithm. It describes the pre-processing, the LDA feature extraction and the Doppler classification stages of the algorithm. The data sets used in this study are described in Section 3. Results are presented in Section 4. Section 5 summarises the conclusions.

2.0 CLASSIFICATION ALGORITHM

2.1 Pre-processing

The objective of Doppler classification is to classify an unknown target as belonging to one of a predefined set of classes based on the measured Doppler spectra. The Doppler spectra are obtained by Fourier transforming a sequence of samples obtained from a single range cell during the radar dwell. Figure 1 compares typical spectra of a wheeled vehicle, a tracked vehicle and a man jogging. The peak in the spectra corresponds to the Doppler shift due to the body of the target. The Doppler sidebands, if present, are due to any parts of the target which are moving independently of the main body at that moment. For the wheeled vehicle there are no Doppler sidebands visible. This can be contrasted with the much more complex, but asymmetrical, spectrum of the tracked vehicle, and this can again be distinguished from the more symmetrical spectrum of the walking man.

The information in the Doppler spectra, however, cannot be used directly for classification. This is because the Doppler radar signature is affected by certain factors such as the radar gain, noise level, *etc*., that are unrelated to the target class but can confuse the classification process. The data can be transformed so that the Doppler signatures are invariant to these factors. This process that is performed prior to classification is termed ‘pre-processing’.

The pre-processing aims to obtain a 2D spectrogram from a long sequence of temporal samples and process each individual spectrum to extract a target Doppler-profile that is independent of radar-calibration and target-velocity. The spectrogram is generated using a short-time Fourier transform. Clutter frequency bins are masked and those that contain noise only are clipped to a minimum value. The peak in

each Doppler-profile is centred which makes the spectrum invariant to target velocity. Finally, the data are normalised with respect to received power and transformed using natural logarithms.

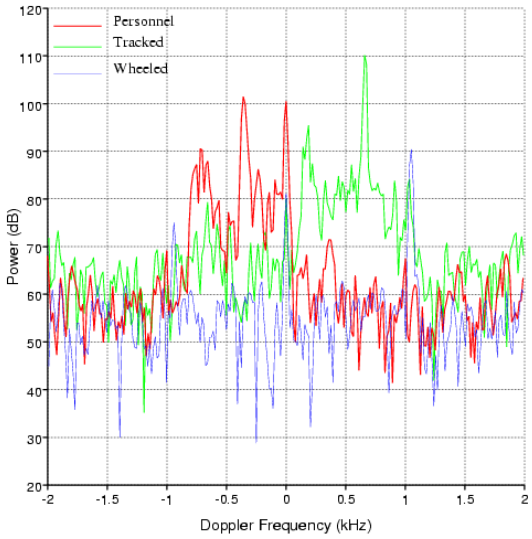

Figure 1: Doppler spectra from land targets

Figure 2 plots the Doppler signatures shown in Figure 1 following pre-processing. All the spectra have equal peak values and are centred on the same Doppler frequency. The pre-processed Doppler signatures are now invariant to changes in radar gain and target bulk velocity.

The pre-processing also partitions the data into five separate velocity bands based on the estimate of the target body velocity obtained using the peak in the Doppler spectrum. This is designed to enable the algorithm to model some aspects of the velocity dependent data attributes. A separate classifier is trained and tested for data from each velocity band.

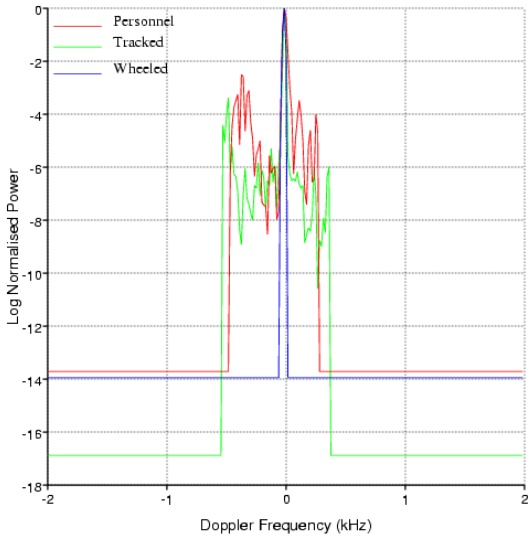

Figure 2: Doppler spectra from land targets following pre-processing

2.2 LDA feature extraction

The pre-processed Doppler spectra are put through the LDA data reduction process using the transformation

$$\mathbf{y} = \mathbf{A}^T \mathbf{x} \tag{1}$$

where $\mathbf{x}$ is the log-normalised Doppler spectrum with p variables, $\mathbf{y}$ is the LDA transformed feature vector with d variables and $\mathbf{A}$ is the $p \times d$ linear transformation matrix. The latter is the feature transformation matrix $\mathbf{A} = \left[\mathbf{a}_1 | \ldots | \mathbf{a}_d\right]$, where $\mathbf{a}_j$ are the eigenvectors of the generalised symmetric eigenvector equation [2]

$$\mathbf{S}_B \mathbf{a} = \lambda \mathbf{S}_W \mathbf{a} \tag{2}$$

The LDA process obtains the transformation that maximises the ratio of between class covariance to average within-class covariance. $\mathbf{S}_W$ is the average within-class covariance matrix given by:

$$\mathbf{S}_W = \sum_{i=1}^{C} \frac{n_i}{n} \hat{\mathbf{\Sigma}}_i \tag{3}$$

where n_i is the number of measurements in the i-th class, n the total number of measurements in the data set, C the number of classes and $\hat{\mathbf{\Sigma}}_i$ is the sample covariance of class i given by:

$$\hat{\mathbf{\Sigma}}_i = (1/n_i) \sum_{q=1}^{n_i} (\mathbf{x}_q - \mathbf{m}_i)(\mathbf{x}_q - \mathbf{m}_i)^T \tag{4}$$

where $\mathbf{x}_q$ and $\mathbf{m}_i$ are the measurement vector and the sample mean for the i-th class respectively. Each of these is a p-dimension vector. The latter is given by:

$$\mathbf{m}_i = (1/n_i) \sum_{q=1}^{n_i} \mathbf{x}_q \tag{5}$$

$\mathbf{S}_B$ is the between-class covariance matrix given by:

$$\mathbf{S}_B = \sum_{i=1}^{C} \frac{n_i}{n} (\mathbf{m}_i - \mathbf{m})(\mathbf{m}_i - \mathbf{m})^T \tag{6}$$

where $\mathbf{m}$ is the sample mean of the entire data.

The number of columns (eigenvectors) in the matrix $\mathbf{A}$ defines the size of the LDA feature vector $\mathbf{y}$. The upper limit for d is the maximum number of non-zero eigenvalues for (2) given by:

$$d_{\max} = \min(p, C-1) \tag{7}$$

Since the eigenvalues for (2) are ordered in terms of class separability, in theory the classification performance should increase monotonically as the size of the LDA feature vector $\mathbf{y}$ is increased. The transformation matrix $\mathbf{A}$ is estimated using the same training data that is used for estimating the classifier parameters. As pre-processing partitions the data in to V_b (=5) different velocity-bands a separate transformation matrix $\mathbf{A}_k$, where $k = 1, \ldots, V_b$ is estimated for each velocity-band. Furthermore, the estimation process requires that the data are class-labelled. One option would have been to use the three

broad-class labels, personnel, tracked vehicles and wheeled vehicles. However, this would have limited $d_{\max}$ to just a maximum of two features. It was felt that this would not have been sufficient to fully exploit the structure in the data. For this reason a fine-class labelling mechanism was adopted to increase C and thereby allow for a higher value for $d_{\max}$ for the transformed feature vector $\mathbf{y}$. The fine-class labelling was based on the target type, its aspect angle and its nominal speed. It may be possible, although this was not proven, that the fine-class categories have some physical justification.

2.3 Doppler classifier

The LDA feature vectors are used as inputs to the classifier. A separate classifier is defined for each of the velocity-bands V. For C broad classes the class membership is denoted by ω_{ik}, $i \in \{1,\ldots,C\}, k \in \{1,\ldots,V\}$. For an unknown feature vector $\mathbf{y}_k$ the class membership will be one that maximises the posterior probability $P(\omega_{ik} \mid \mathbf{y}_k)$. According to Bayes' rule this is equivalent to:

$$P(\omega_{ik} \mid \mathbf{y}_k) = \frac{P(\omega_{ik})P(\mathbf{y}_k \mid \omega_{ik})}{\sum_i P(\omega_{ik})P(\mathbf{y}_k \mid \omega_{ik})} = \frac{P(\mathbf{y}_k \mid \omega_{ik})}{\sum_i P(\mathbf{y}_k \mid \omega_{ik})} \quad (8)$$

where $P(\mathbf{y}_k \mid \omega_{ik})$ is the probability of the feature-vector $\mathbf{y}_k$ from velocity-band k arising from class ω_{ik}, and $P(\omega_{ik})$ is the prior probability of class ω_{ik} being present. All the training classes were assumed to be equally likely. Thus class membership is based on the probability value $P(\mathbf{y}_k \mid \omega_{ik})$ calculated for each broad-class.

Each broad class probability was modelled as a multivariate Gaussian mixture model with a diagonal covariance matrix. The mixture distribution has the same dimensionality as the LDA feature vector. Four mixture components were used. The parameters of the model (mean, variance and weights) were estimated using training data. Performance was evaluated using independent test data.

2.0 DATA SET

Radar data from moving targets were collected using a J-band, horizontal polarisation, short range, ground based system using a 4 kHz pulse repetition frequency. The radar measurements were taken with the antenna pointing in a fixed direction and a control target moving through the radar swath at a specified aspect angle and speed. This constituted a single imaging run and the process was repeated for a number of different target types belonging to the three broad classes. The personnel data were obtained from a trial where two subjects were imaged walking and jogging either towards the radar or moving directly away from it. The vehicle data were obtained from a separate trial where three tracked and two wheeled vehicle types were imaged along 9 different aspect angles travelling at a nominal constant speed. This provided 53 different imaging runs from which data were extracted.

For each imaging run, a number of independent target signature files of four seconds dwell were generated by processing data from different locations along the range swath. The processed range resolution was chosen such that it was wider than the dimensions of the largest target in the data set. All the data files were pre-processed and partitioned into velocity bands. There was an uneven distribution of classes over the velocity bands. The lowest two velocity bands contained mainly personnel targets. All three target classes were represented in the next two highest velocity bands. Velocity band V (targets with velocity 12mph and above) on the other hand had only vehicle targets. The data files were given two different types of labels. Fine labels were used in the estimation of the LDA transformation matrix. A total of 53

fine-class labels were defined as summarised by Table 1. Only broad class labels were used in the training and testing of the classifier.

Broad Class	Target Type	Aspect Angle	Speed	Total per broad class
Personnel	2	2	2	8
Tracked Vehicles	3	9	1	27
Wheeled Vehicles	2	9	1	18
			Total	53

Table 1: Breakdown of fine-class categories for the entire database

3.0 RESULTS

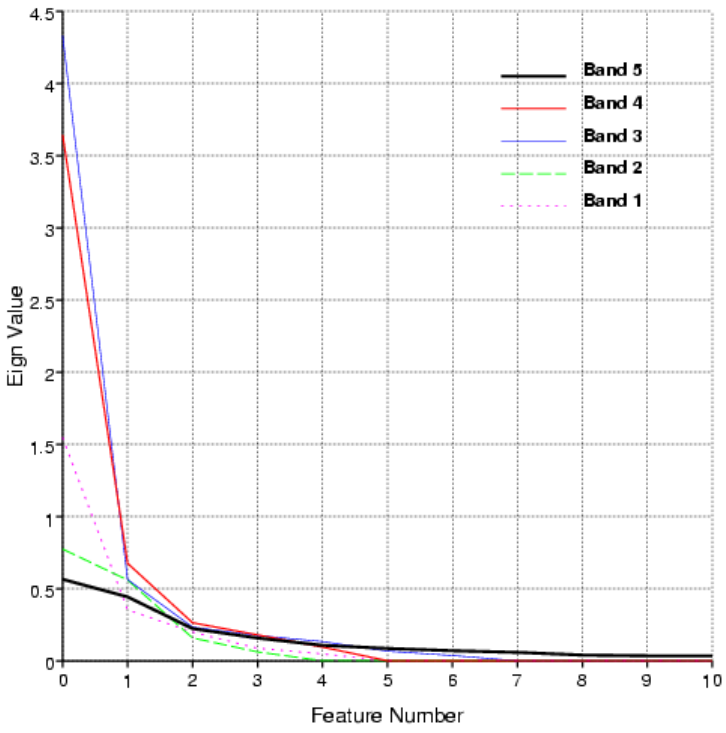

Figure 3: LDA transformation matrix eigenvalues plotted for each velocity-band

Figure 3 shows the comparison of the eigenvalues for the different velocity-band data. The eigenvalues provided some indication of the class separability. As the LDA theory stated, the eigenvalues were monotonically decreasing. Eigenvalues with values close to zero can be assumed to be irrelevant. Velocity-band I and II had data primarily just from the personnel class and therefore there was just one single dominant eigenvalue. Velocity-band III and IV also had a relatively high first eigenvalue. This

suggested that the first eigenvector should provide good class separability. For velocity-band V there were no dominant eigenvalues, however, the first few eigenvalues were non-zero. This suggested that just a few features would probably be sufficient for optimum classification.

Further useful insight into the class separability can be obtained using 2-dimensional scatter plots of the feature vectors. Figure 4 compares the results obtained for plotting the first two LDA features for two different velocity-bands. The left-hand result is for velocity-band III which had data for all three target classes and the right hand result is velocity-band V that had only vehicle data. The feature values are labelled d0 and d1 respectively. Each point in the scatter plot is data from one feature vector.

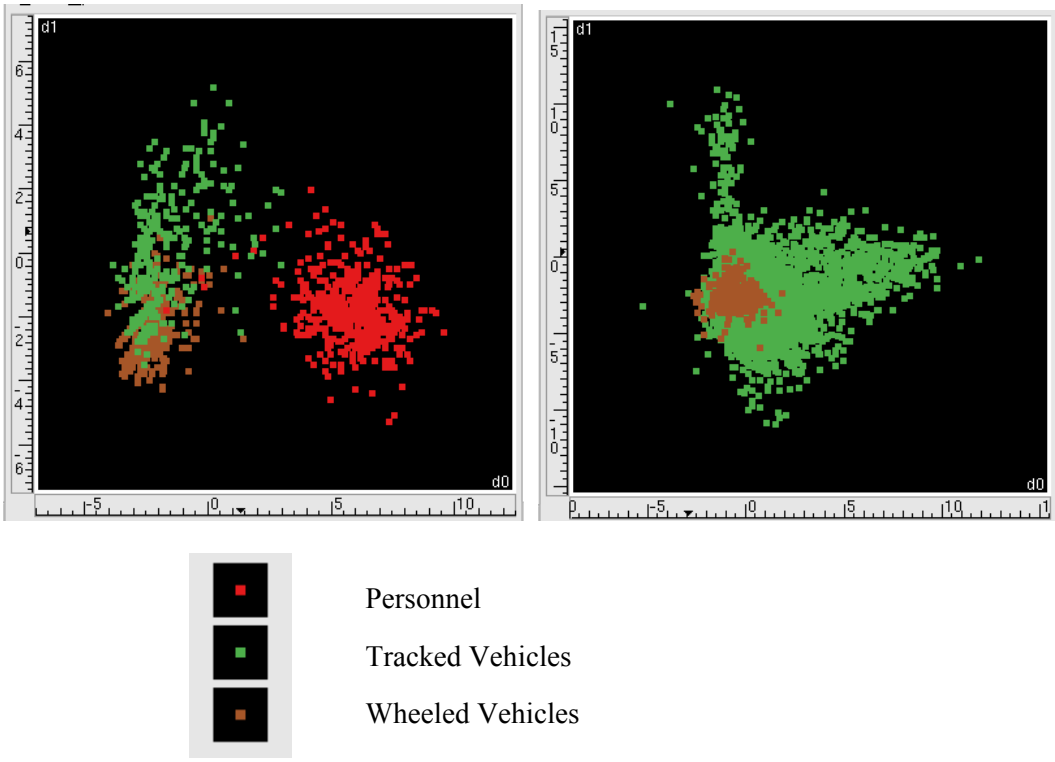

Figure 4: Scatter plot for the first two LDA features. (left image) Velocity-band III (right image) Velocity-band V

From Figure 4 it can be seen that for velocity-band III the personnel class separated completely from the vehicle classes. The vehicle classes also showed some degree of separation but there was some overlap between the tracked and wheeled vehicles. The same result for velocity-band V showed that there was a relatively small region of the feature space occupied by both tracked and wheeled classes. However, this was contrasted by a significantly larger region of the feature space that was occupied exclusively by the tracked class.

It is not trivial to interpret the eigenvectors in a physical manner. One possible method for determining what information is captured by an eigenvector (and therefore the LDA feature) is to look for evidence for any correlation between the LDA feature and ad hoc features that have a physical interpretation. The target Doppler sideband extent can be measured as an ad hoc feature. Empirical analysis showed that tracked vehicles tended to have broad extent whereas wheeled vehicles generally had a narrow Doppler extent. Figure 5 replots the scatter plot of the first two LDA features for velocity-band V highlighting data that has broad Doppler extent. It showed that a majority of the region, that separated the tracked from the wheeled class, was explained in terms of the Doppler extent. Thus the first two LDA features were

capturing information regarding the Doppler sideband extent in some way. The LDA features, however, cannot exactly represent this ad hoc feature since the latter is a non-linear feature.

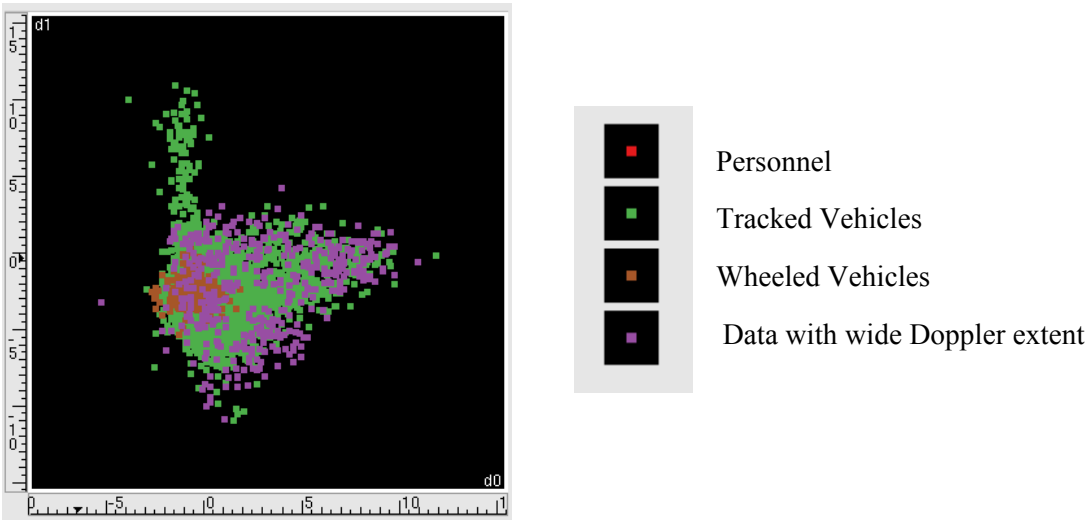

Figure 5: Scatter plot for the first two LDA features for velocity-band V. Data points that corresponded to a wide Doppler extent are highlighted in purple

A separate classifier was implemented for each velocity band. The first two velocity bands had only data from the personnel class and therefore were excluded from the calculations. The data in each of the other three velocity bands were split into training and test sets using a 3-to-1 ratio. Performance results were averaged over all three velocity bands.

Figure 6 plots the percentage correct classification averaged over all three broad classes (personnel, tracked and wheeled vehicles) as the number of features was increased. Results are shown for two cases, (a) feature vectors based upon only LDA features (black curve), and (b) feature vectors that included Doppler sideband extent as an additional ad hoc feature (purple curve).

From the first result it can be seen that with just two LDA features near maximum performance was achieved. For six or higher number of LDA features the performance flattened out. This implies that the useful information is contained in just the first few features. A classifier with just six LDA features would give optimum performance. This equated to a considerable reduction in the data dimensionality and therefore the classifier complexity. Such improvements greatly enhance the viability of the classifier for real-time implementation.

With the addition of the Doppler extent feature, just the first two features alone provided the optimum performance. This pointed toward Doppler sideband extent being an important discriminating feature. It ties in with the observation from the feature analysis which showed a trend for tracked vehicles to have broad extent and wheeled vehicles to have narrow extent. It suggested that the LDA features are capturing the same information as in the Doppler extent of the sidebands albeit using more features. Unlike ad hoc features which are data specific and would often require lengthy and expansive data analysis, the LDA feature extraction process on the other hand would generalise for data with arbitrary attributes.

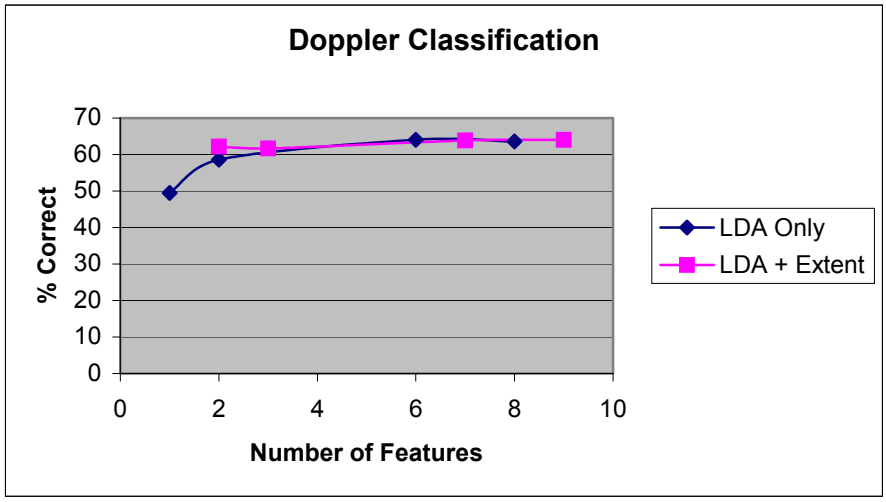

Figure 6: Doppler classification as a function of number of features

OVERALL 62.7% [58.3,67.1]		Classification Decision (%)		
		Personnel	Tracked	Wheeled
Actual Class	Personnel	96.4 [99.8,93.0]	2.7 [0.1,5.3]	0.9 [0,2.9]
	Tracked	0.8 [0.1,1.5]	51.4 [41.7,61.1]]	47.8 [38.2,57.4]
	Wheeled	0.2 [0,0.6]	21.4 [12.6,30.2]	78.4 [69.7,87.1]

Table 2: Confusion Matrix of a Doppler classifier using 6 LDA features. Results averaged over 50 bootstrap replicates

Table 2 provides the confusion matrix for the classifier with six LDA features. The results were generated using 50 bootstrap replicates. Bootstrap is a statistical inference technique, first proposed by Efron [3], which allows a confidence interval to be assigned to the estimated quantity. Table 2 lists the mean of the bootstrap replicates along with the 90% confidence interval shown in square brackets. The results for the confidence interval were only approximate since far more bootstrap replicates (>1000) would be required for a more accurate measure. Nevertheless, the results were useful in determining general performance trends. Earlier the selection of the six LDA feature classifier was based on results that were essentially a single bootstrap replicate. This choice is lent support by the estimate of the 90% confidence interval for this classifier. Since the performance of the other classifiers with fewer LDA features was outside this range it can be concluded that the choice of the optimum is statistically significant.

A per class comparison of the confusion matrix shows that just under half the tracked vehicles are misclassified as wheeled. This is not very surprising given the fact that a substantial proportion of the tracked vehicle data in the data set did not have the distinctive broad Doppler extent that differentiated it from wheeled vehicles. At this stage it can only be hypothesised that the confusion between the two vehicle classes is due to the absence of the track returns. The data were collected from vehicles that had

skirts covering the tracks. This would make the moving parts of the tracks more likely to be visible when viewed front-to-back, and vice versa, but less so at oblique angles. The data supported this inference, with far fewer of the measurements taken for vehicles travelling at oblique angles to the radar reporting the presence of the broad Doppler extent. This was in contrast to tracked vehicles travelling either directly toward or away from the radar, for which the majority of the data had the broad Doppler extent present.

Unlike the two vehicle classes the personnel class separated very well. Some misclassification between personnel and tracked class may be expected since both possess broadening of the Doppler spectra. However, the manner in which the vehicle data were collected (constant velocity with aspect changing between measurements) meant that the personnel class was only being classified against vehicles that were travelling at very oblique angles. From the data it was observed that track returns were often absent when the vehicles were imaged at oblique angles. This may therefore explain the very good separation between the personnel and vehicle classes. More representative data that contains data from slowly moving vehicles with visible tracks would enable a better measure of the true performance.

4.0 CONCLUSION

For the three-class problem the classifier had no difficulty in recognising the personnel class but produced some degree of confusion between the wheeled and tracked classes. The classifier algorithm was optimised by choosing the best set of features that maximised the performance and the bootstrap method was used to measure the confidence interval. It was shown that only the first few LDA features were relevant for Doppler classification. At the very least these were shown to contain information regarding the frequency extent of target's Doppler sidebands.

The classifier was shown to be invariant to target aspect angle and speed and was able to model multiple target types. Models for additional classes that have distinct Doppler characteristics, like helicopters, can be easily incorporated into the algorithm. The LDA feature extraction represents a considerable reduction in data dimensionality and therefore is able to provide for very efficient implementation of the classification algorithm. The LDA based classifier, therefore, offers a very powerful tool for the automatic classification of moving targets from their Doppler signatures.

ACKNOWLEDGEMENTS

The author would like to acknowledge the support of UK MOD for funding this research. He would also like to thank Dr Keith Ponting of 20 20 Speech Ltd in providing support with the development of the LDA classifier. Thanks also go to Ian Finley for the numerous helpful discussions with the author during the course of this work.

REFERENCES

[1] Kumar N., 'Investigation of silicon-auditory models and generalization of linear discriminant analysis for improved speech recognition', Ph.D. dissertation, John Hopkins Univ., Baltimore, MD, 1997.

[2] Devijver P. A. and Kittler J., 'Pattern Recognition, A Statistical Approach', Prentice-Hall, Inc., London, 1982.

[3] Efron B., 'Boostrap Methods. Another Look at the Jackknife', *The Annals of Statistics*, Vol:7, 1979, pp1-26.

Through Wall Detection and Recognition of Human Beings using Noise Radar Sensors

Konstantin Lukin and Vladimyr Konovalov
INSTITUTE for RADIOPHYSICS and ELECTRONICS
National Academy of Sciences of Ukraine
12 Akademika Proskura St., Kharkov, 61085
Ukraine

lukin@ire.kharkov.ua - LNDES@kharkov.com - konovalov@ire.kharkov.ua

SUMMARY

Elaboration of a new approach to solving of a contradictory and challenging problem of through wall detection radar design is the main goal of the paper. Two types of radars have been investigated: (1) CW radar that uses pseudo-random sequence (PRS) of the maximal length (m-sequence), hereinafter referred to as ***PRS-radar*** *and (2) CW radar with use of the noise waveform at corresponding carrier frequency referred to as* ***Noise Radar****. Besides, notional design of* ***Software Noise Radar*** *for these applications is briefly considered.*

1. INTRODUCTION

In spite of numerous R&D focused on surface penetrating radar design, e.g. [1-13], nevertheless there is no radar which enables reliable detecting of live human beings when performing search and rescue operations under conditions of extraordinary situations caused by man-made or natural catastrophes. Detection and identification of terrorists, criminals, etc. is an important problem as well. In particular, the problem gets more complicated in case of non-authorized penetrating into premises and intentional creating conditions which complicate their detection by available means, such as specially trained dogs or very sensitive sound receivers. The presence of extraneous smells is the limiting factor for the first case, while in the second case it is rather difficult to provide silence for rather long period during salvage operations.

The efforts have been spent [9-13] for design of Doppler radar systems intended for detection of various moving objects, including live human beings. The systems created have confirmed applicability of Doppler Effect based methods for detection of live human beings, however, they are not able working effectively under realistic conditions, for example, when attenuation of sounding signals is so large that the signal reflected from the wall exceeds significantly (by factor of many orders) the signal scattered by a target behind the wall. Besides, the need of weak signal detection under presence of strong signal reflected by the wall and other objects brings also considerable difficulties. For the above and some other reasons the known systems are useless for solving the problem of Through Wall Detection and Recognition.

2. PROBLEM POSING

In the radar suggested we also use the Doppler phenomenon, but for so small displacements of the object to be detected that it causes just an amplitude modulation of the optimal receiver output which is essentially a convolution of a broadband sounding signal (the reference) with radar returns, the phase of which is slightly modulated by a target performing slow and small enough periodic or non-periodic

Paper presented at the RTO SET Symposium on "Target Identification and Recognition Using RF Systems", held in Oslo, Norway, 11-13 October 2004, and published in RTO-MP-SET-080.

motions. Such motions can be associated with either human being body displacements or his breathing or even his heart beats. Though the body motion is the main factor in the through wall detection of persons, however the suggested radar potential will be sufficient for detection of even a nonmoving person because of his breathing or even his heart beats. When breathing, the periodic motion of the person's thorax takes place with magnitude of 2-7 mm, while his heart beats may cause periodic motion of the body parts with the magnitude not exceeding 0.2-1mm. Usual clothes of a person (if it is dry) is transparent for electromagnetic waves in the chosen frequency range, while the human body surface (largely consisting of water) is a rather good reflector. Actually separation between Doppler frequencies of breathing and heart beats is required for evaluation of his psychophysical status, while the Doppler signal caused by breathing is sufficient for detection of non-moving person because it significantly exceeds the Doppler signal produced by heart beats. Possible application of the Doppler radar suggested is schematically shown in Fig.1.

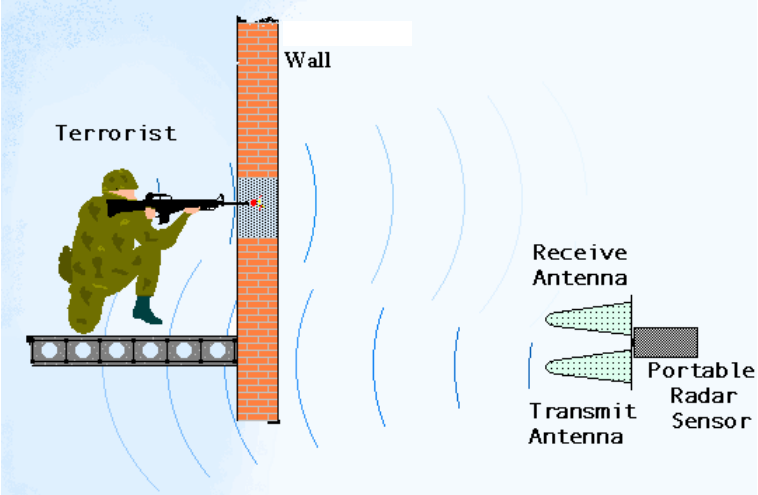

Fig.1. Possible application of the Doppler radar suggested (schematically).

It is known that the range sensitivity of the method attains 10^{-9} m in microwave [14]. Capability of a heart beats detection of a person located behind a break wall having thickness of 10 cm has been experimentally proven in [9]. Despite of an apparent simplicity of the radar, its design is a rather difficult technological problem since the hardware of the radar should meet the whole set of tuff requirements stipulated by the complicated radar conditions:

- Strong reflections of sounding signal by walls which can overload/saturate the radar receiver;
- Strong absorption of electromagnetic energy by walls which cause low levels of radar return;
- Strong interference signals due to multiple reflections of sounding signal from the operator, other rescuers, and other objects;
- Strong interfering signals due to radiation of the radar transmitter.

Operational frequency of the radar is dictated by two contradictory conditions. On the one hand, the shorter the wavelength, the higher sensitivity of the method to the phase modulation and the smaller dimensions of receive and transmit antennas. On the other hand, an increase in a central wavelength of the probing signal is desirable for enhancing the penetrating capability of electromagnetic waves through walls. However, desirable increase of the wavelength is limited, in turn, by two factors: the first one is tied with shielding sounding signals by metallic meshes in concrete walls, while the second one decreases the

RCS of the target when the wavelength exceeds the sizes of the target. The estimation carried out have shown that for conducting of rescue activities in ruins, typical concrete buildings and facilities the most optimal is the frequency range 800 – 2000 MHz.

However, the optimal frequency range chosen according to the above criteria does not allow creating of small-sized portable antennas with high enough directivity. In this range it is possible to count for a width of the antenna pattern of 20° – 30° having side-lobe level about -20dB in both elevation and azimuth planes. It is clear that it is not possible to localize a target using only directivity properties of the antennas. It is necessary also to provide a sufficient range resolution. High range resolution capability of the radar becomes especially important in case when ground around the area of rescue activities is covered with tall grass or bushes, etc. In this case, the radar returns may contain fluctuating components because of their motion due to wind. The Doppler spectrum of these fluctuations contains low frequencies and may have the same frequency range as the Doppler spectrum of the target. This will essentially increase the false alarm probability. Besides, the Doppler spectrum of the signal reflected by the operator, etc. also can fall into the same frequency range with a Doppler spectrum of the required target and exceeds significantly (by many orders) the signal scattered by the target. It is very important to provide a high range resolution for filtering out these signals. This is very important because the signals scattered by persons located in the neighborhood of the radar are by factor of many orders higher, as a rule, of the signals scattered by the target.

As it seen from the above, the impulse volume of the radar should be close to the geometrical volume of a target to be detected, while the side lobes of both the antenna patterns (AP) and ambiguity function (AF) of the sounding signal should be close to zero. In reality, it will not be possible to provide a very low level of AP sidelobes in portable transmit/receive antennas having acceptable sizes, while obtaining extremely small AF sidelobes that will provide the value of a received signal at the level of the receiver inherent noise is a solvable problem. This means that rescue activities are also may be arranged in the way that interferences may be outside the resolution cell of the radar and will not degrade its performance.

The radar should not just detect the presence or lack of a target, but also to point its coordinates as much precisely as possible, and also define the type of the target using its Doppler portrait. High angular resolution required for target position finding is ensured with application of triangulation method provided a high range resolution and a possibility of having two or more measurements. For the radar under consideration the required range resolution should be about of 0.5 – 1.5 m (the sizes of the target). The maximal working range of the radars under consideration, as a rule, is limited to several tens of meters. For applications of the radar inside small premises the minimal working distance should be no more than 1 – 2 m.

The listed above requirements to the radar determine in main the type and structure of the probing signal to be used. Unfortunately, application of pulsed waveform that provides perfectly zero AF range sidelobes is technically impossible in our case because of impossibility to provide simultaneously a very short radar blind zone and a sufficient energy potential. Therefore it is necessary to use a CW wideband probing signal with a large enough base. Among wide class of such signals, the greatest attention deserves random noise and pseudo-noise waveforms in view of sufficient simplicity of their generation and processing. Besides in a number of applications the covert operation of the radar under consideration is required that also is provided by noise waveform application [14-15].

In the paper, we shall consider two types of radars: (1) CW radar that uses pseudo-random sequence (PRS) of the maximal length (m-sequence), hereinafter referred to as **PRS-radar** and (2) CW radar with use of the noise waveform at corresponding carrier frequency referred to as Noise Radar. Besides, notional design of Software Noise Radar for these applications is briefly considered. In all cases correlation processing of the radar returns is used.

3. THE PRS-RADAR

The block diagram of the PRS-radar is presented in Fig.2. It operates as follows. A single frequency signal generated in the oscillator 6 with high frequency stability is fed into the phase manipulator ($\pm\pi$) 2. The phase manipulator 2 executes phase modulation of the signal according to pseudo-random *m*-sequence generated by the oscillator 1. As a result we get a phase-shift keying signal. After its amplification in the amplifier 3, the phase-shift keying signal is radiated by the transmit antenna 4. Unfortunately, because of not perfect rejection of the baseband signals there are three different signals at the phase modulator output, two of which cannot be filtered out from each other: (1) useful sounding signal; (2) spurious baseband PRS signals and (3) spurious monochromatic carrier signal. From the listed above signals the second one is considerably attenuated by a balanced modulator and its power spectrum density (PSD) is much below of probing signal PSD. It is practically completely suppressed in the circuit formed by filter of the modulator, the bandpass power amplifier 3 and frequency characteristic of the transmit antenna. In spite of the signal (3) is suppressed in the balance modulator by 20 – 30 dB (which is a typical suppression factor for realistic broadband modulators), nevertheless it makes the most negative influence onto the radar work and performance. The point is that the signal frequency falls into the frequency bandwidth of the sounding signal (1) and, therefore, also gets amplified in the power amplifier 3 and is radiated by the transmit antenna 4. This mans the sounding signal comprised of two signals: the phase-shift keying signal and single (the carrier) frequency one. The latter has no properties of range selection and, consequently, does not allow obtaining of AF side-lobes level less than – 20 – 30 dB after signal compression. The signal reflected by a target (a person) located behind a concrete wall of width ~ 30 cm apart of 10 m from the radar can be 90 dB lower of a signal reflected by the operator. Therefore, for recovery of usefull signal at the presence of signals from the operator, the range AF side-lobe level should be no more -110 dB. To suppress influence of monochromatic component of the sounding signal in the reference channel of the quadrature receiver the additional modulation has been used using signal generated by 8 which has meander form with phase $2n\tau_p$ where τ_p – duration of elementary pulse PRS, n – integer ≥ 1. The reference signal in the quadrature correlation receiver is formed as follows. The signal from the high-stable quartz resonator 6 is fed into the clock frequency generator 5, which starts the generator of delayed PRS 11. The delay equals round-trip propagation time of the sounding signal to the target (it is prescribed by the operator using PC). Delayed reference PRS is cross-multiplied with the signal of the oscillator 8 in the multiplier, representing the "&" circuit. This multiplied signal is fed into the phase manipulators 10 and 12, while their second inputs are fed by is fed by quadrature components of the carrier oscillator 6. Signals from phase manipulators 10 and 12 are fed into the mixers 15 and 16 in the quadrature correlation receivers.

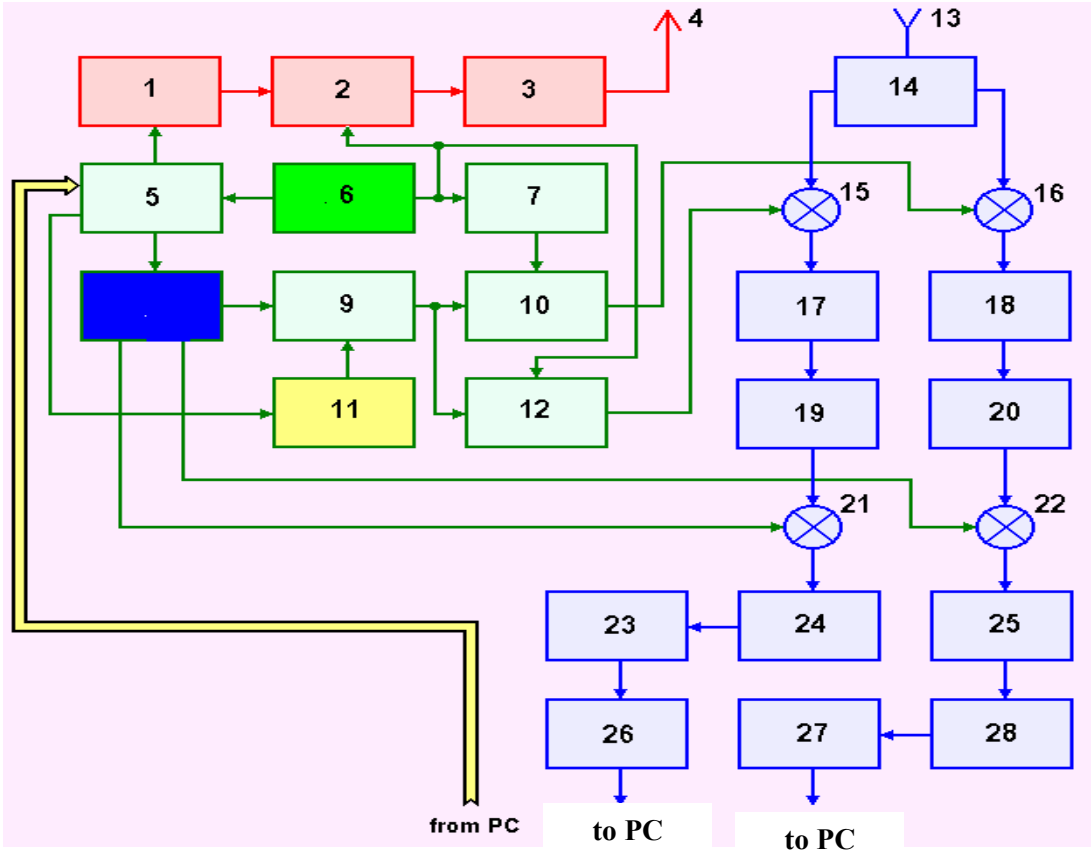

Fig.2. Block-diagram of the PRS-radar
1 – PRS-oscillator, 2, 10, 12 – phase manipulator, 3 – power amplifier, 4 – transmit antenna, 5 – clock frequency oscillator, 6 – quartz stabilized oscillator of carrier frequency, 7 – single frequency phase shifter (π/2), 8 – quadrature oscillator of additional modulation, 9 – digital multiplier, 11 – oscillator of reference PRS, 13 – receive antenna, 14 – LNA, 15 and 21- in-phase mixers, 16 and 22 quadrature mixers, 17 and 18 – IF filters, 19 and 20 – IF amplifier, 23 and 28 – Doppler amplifiers, 24 and 25 – Doppler filter, 26 and 27 – analog-to-digital converters (ADC).

The input signal from the receive antenna 13 and low-noise amplifier of power 14, represents itself an additive mixture of the following signals: 1 – a leakage signal from the transmitting antenna; 2 – a signal from the operator, the maintaining radar; 3 – a clutter signal and signal reflected by the wall; 4 – a signal reflected by a target, which the most weak one. The overall number of signals coming to the receiver input is at least 8. It is easy to see, that due to correlation processing all signals reflected by objects placed outside the correlation volume will be suppressed by factor of $\Delta f_s / \Delta F_{if}$, where Δf_s is effective bandwidth of the sounding signal, ΔF_{if} is effective bandwidth of the filters 17, 18. Therefore the letter should be as smaller as possible.

The dynamical range of the signals at the receiver input is to be very large(~100 dB).

To enlarge dynamical range of conventional receiver the second signal converter has been implemented using mixers 21 and 22, while the amplification rate of amplifiers 14, 19, 20 is made rather small, just to compensate the first down converting losses, and preserving SNR at the IF amplifier output within the whole dynamic range of the received signals. The quadrature signals from IF amplifiers are fed into the mixers 21 and 22, while the signals of additional modulation generator 8 is fed as the reference signals. This allows to suppress all parasitic signals providing high dynamical range of the radar. The signals with

no Doppler shift (an echo from wall, parasitic leakage and coupling of antennas), will be outside the Doppler filters bandwidths 24 and 25. We have two signals having Doppler shifts: signal reflected by target and that scattered by the radar operator. It is important that the signal from the target will pass all circuits without losses, while the signal from the operator will be suppressed by $\Delta f_s / \Delta F_{if}$ time after compression. The dynamical range of the output signals of Doppler filters is essentially decreased, because of suppression of spurious components. After that the main amplification of the received signals is performed in the receiver. Narrowband Doppler signals are sampled and sent into PC for further computer processing: filtering, target detection and identification.

For PRS, the AF range side-lobe equals $1/N$, where $N = 2^k - 1$ is quantity of elementary impulses in PRS, k is an integer number. However, this is valid only for zero Doppler frequency $\Omega = 0$, while for $\Omega > 0$ he AF range side-lobe will increase essentially. For instance, in Fig. 3a the range sidelobe level γ for PRS as function of the Doppler frequency period to PRS period ratio is shown for k = 11. In the same figure the striped line shows range sidelobe level at the absence of Doppler shift. The more N, the higher influence of Doppler frequency shift on to the range sidelobe level. Fig.3b shows Doppler frequency period to PRS period ratio as function of PRS length (parameter k) for which the sidelobe level doubling is achieved.

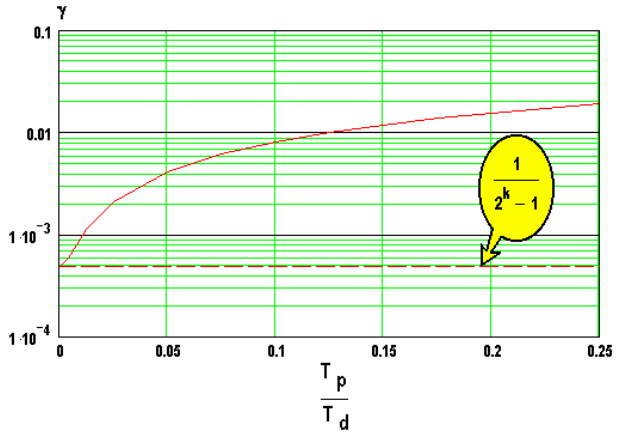

Fig. 3a. Sidelobe level γ for PRS as function of the Doppler frequency period to PRS period ratio :

Td / Tp ***k** = 11; Number of bits in PRS: *N*=2*k*-1**

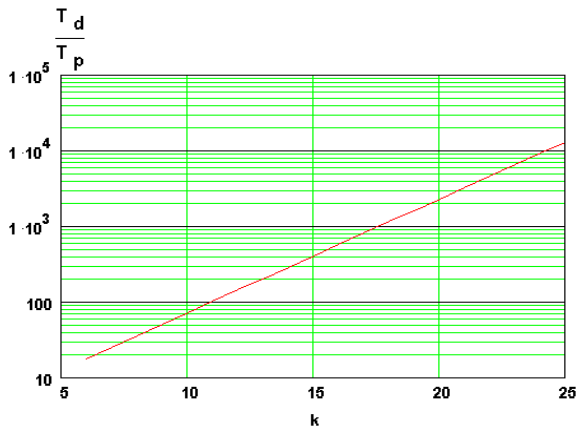

Fig. 3b. Doppler frequency period to PRS period ratio as function of PRS length (parameter *k*) for which the sidelobe level doubling is achieved

It is seen from the above figure, that for the selected duration of the elementary impulse required for providing of the range resolution, we cannot take PRS with an arbitrary number N of elementary impulses aiming decrease in range side-lobes just because of increase in its sensitivity to Doppler frequency shift which results in the growth of range side-lobes.

After final processing of the received signals it is possible to achieve rather good ratio of signals from the target and from the operator. For instance, for the radar having 1W transmit power, 150MHz frequency bandwidth (1m range resolution) of sounding signal, and $N = 65535$ of PRS length, RF losses in wall 50dB and a AP side-lobe level –13dB, the signal from the target located behind the wall at the 10 m

distance from the radar exceeds the signal from the operator by 26dB, that it is quite enough for reliable detection of the target.

5. SOFTWARE NOISE RADAR

Fig.4 shows block-diagram of Software Noise Radar which uses truly noise signal as a sounding one. The latter is generated by noise generator 1 which has its central frequency as a carrier one. The frequency bandwidth of noise signal has the same value as in case of PRS-Radar.

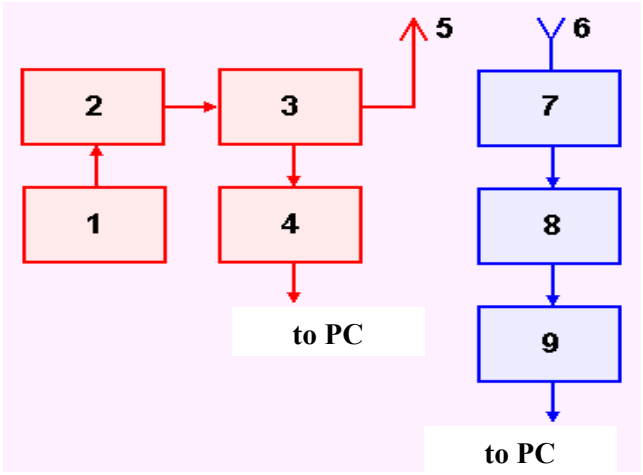

Fig.4. Block diagram noise radar 1 – noise waveform generator; 2 – power amplifier; 3 – directional coupler; 4, 9 – analog-to-digital converters; 5 – transmit antenna; 6 – receive antenna; 7 – RF filter; 8 – low-noise amplifier

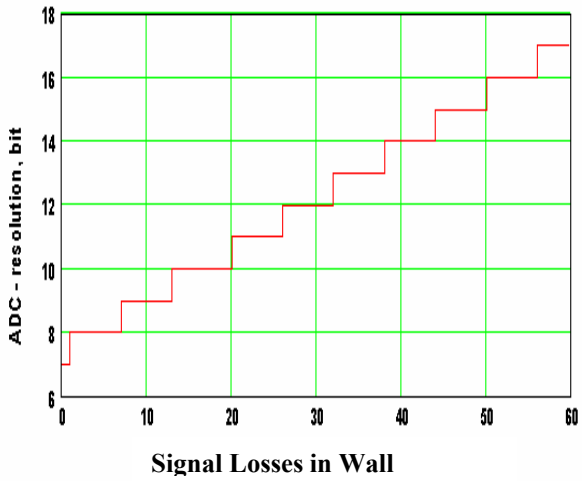

Fig. 5. Number of ADC bits required as a function of signal losses in wall.

The important feature of this radar is that the generator 1 produces sounding waveform with a required bandwidth which supposes no need in such unit as modulator, and therefore, all the problems related to its characteristics influence on to the radar performance are solved in this way. The noise signal gets amplified in the power amplifier 2 up to the required level and is fed into the transmit antenna 5.

As it is known, the delayed copy of sounding signal is necessary when performing correlation reception of noise radar returns. Because in our case the frequency spectrum of sounding signal can be centered in vicinity of 800±(50÷75) MHz, the usage of a fast analog-to-digital converter became feasible. Now days 8-bit ADC with clock frequency up to 2GHz are commercially available at this frequency range. The signal from ADC 4 is fed directly into PC where digital processing enables required delaying of sounding signal to generate the reference.

Block-diagram of the Software noise radar is very simple. In particular, there is no need in quadrature channel since quadrature processing is performed in PC. However, one faced some limitations when

designing such radar. For instance, the signal from receive antenna 6, should go directly to the ADC input 9 just after RF-filter 7 and LNA 8 in the whole dynamical range and frequency bandwidth of the sounding signal. For this purpose the LNA 8 should amplify this signal up to the level r (typically: ±5 V) required for normal operation of the ADC . Besides The number of ADC bits should be high enough to sample the received signal without distortions in the whole dynamical range. For 10mW transmitted power the amplifier gain should be about 55dB that is affordable today, while required number of ADC bits is a challenge for available hardware. In our case the dynamical range of radar returns is mainly dependent on signal absorption in the wall. Fig.5 shows number of ADC bits required as a function of signal losses in the wall in case of 10m distance between radar and the wall. As it is seen from Fig.5 in order to detect a target using Software Noise Radar one has to apply 16-bit ADC with clock rate ~ 500MHz, which should be available in the future. Nevertheless, fast 8-bit ADCs available today (for example, Analog Input Card for PCI Bus "CompuScope 82G" from GaGe corporations) enable design of Software Radar capable of detecting live persons behind brick walls having thickness of 1/4 brick from distance ~ 10m. A low averaged power of RF radiation with very low power spectral density ($7 \cdot 10^{-11}$ W/Hz) of the sounding signal allow to use this radar with no ill effect on people and no electromagnetic interferences for other RF devices that may be used at the same time in the same area.

Fig. 6-8 shows the output signals obtained via computer simulation of the radar under consideration. Fig.6a shows the signal of heart beat of a non-moving person who is delaying his breathing, while Fig.6b shows its frequency spectrum of this signal. The average signal-to-noise ratio is about 10 dB. As it is seen from the figures, detection of a live person is possible even due to detection of his heart beat. Fig. 7 shows the signal from both breathing and heart beats of non-moving person, while Fig.7b shows Doppler spectra of these signals. It is seen, that the related spectra are easily distinguishable. With other things being equal – the signal due to breathing exceeds considerably signal due to hear beats. Received signal from a randomly moving person with maximal amplitude of the motion ~ 1/6 wavelength of center frequency and its Doppler spectrum are presented in Fig.8a and Fig.8b respectively. This signal is dominant above remaining, and on his background signals from breathing and palpitation practically are completely masked.

Obviously, that on the basis of the character of signals and their spectrums one may forecast emotional and physical status of the person located behind an obstruction. For example, when person does not move, but is strongly agitated he will speed up his breathing and heart beats. Motion of the person with big amplitude – will tell us that he has enough room to do that. His lasting motions can tell about his quite good physical status and a that he is doing some operations, etc

Signals of the radar after processing	Spectrums from these signals
PRS-radar	PRS-radar

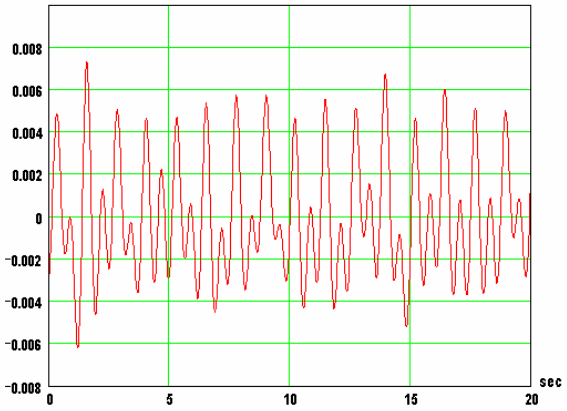

Fig. 6a. Signal scattered by non-moving and non-breathing person. SNR = 10 dB

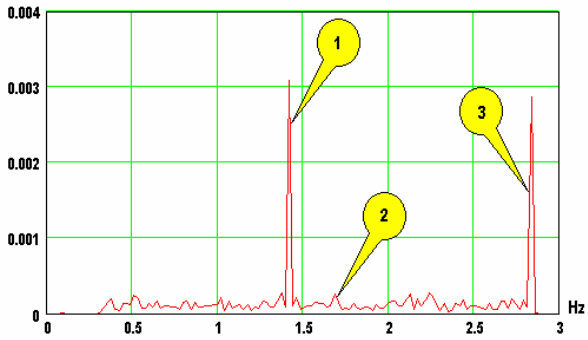

Fig. 6b. Doppler Frequency Spectrum of signal scattered by non-moving and non-breathing person: (1)- first harmonic of the signal; (2)- second harmonic of a signal; (3) -receiver noise floor

PRS-Radar

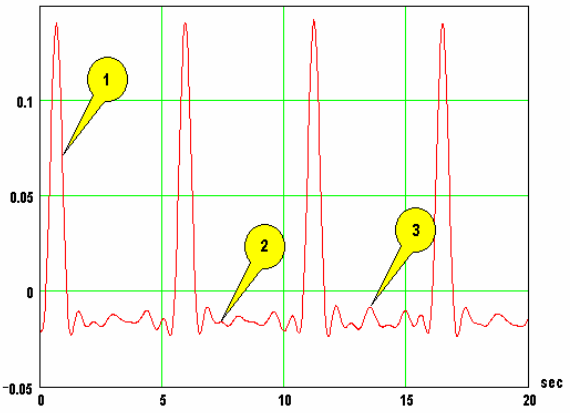

Fig. 7a. Signal scattered by: (1) - non-moving, but breathing person; (2) - heart beat of a person; (3) - receiver noise

PRS-Radar

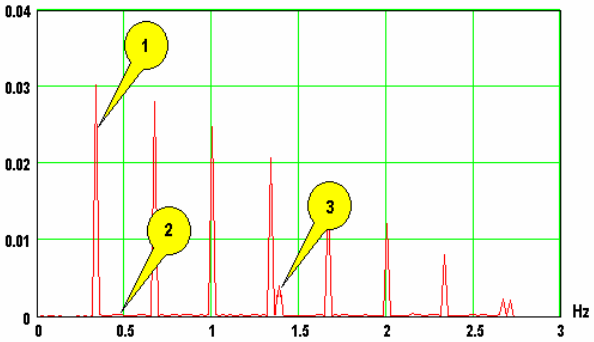

Fig. 7b. Doppler Frequency Spectrum of signal scattered by: (1) - non-moving, but breathing person; (2) - heart beat of a person. (3) - receiver noise

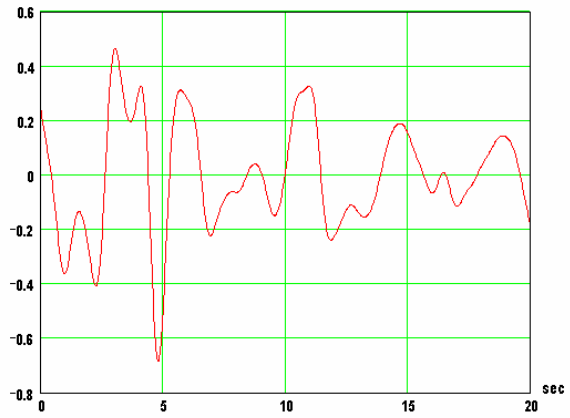

Fig. 8a. Signal scattered by random motion of the person with amplitude about 1/6 of the wavelengths s

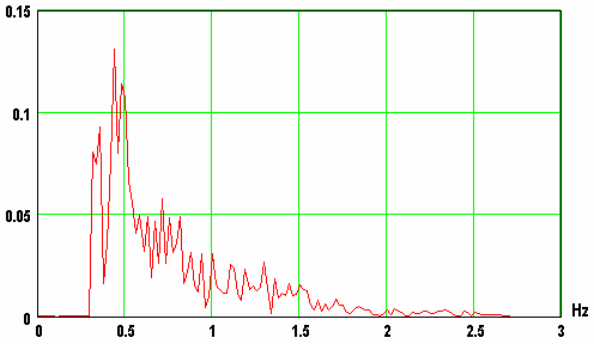

Fig. 8a. Signal scattered by random motion of the person with amplitude about 1/6 of the wavelength

CONCLUSIONS

Radar for Through Wall Detection and Recognition of Human Beings is to be designed on the basis of broadband RF signals with large base. Random Noise and Pseudo Noise waveforms are the most appropriate signals for that radar. Random Noise waveform is more appropriate one when covert operations or/and electromagnetic compatibility with other radar sensors are required. The first waveform is the most applicable one when the highest radar potential is needed, while the second waveform is the best one for those applications where rather low averaged power of RF radiation (having very low power spectral density) is required. For instance, when one has to provide no ill effect on people and no electromagnetic interferences for other RF devices that may be in use at the same time in the same area.. Possibility of detection of a live person behind a thick enough wall is shown when probing signal attenuation rate does not exceed ~ (50-60)dB that corresponds to (25-30)cm of a concrete wall or (40-50)cm of a brick wall. Using temporal and spectral characteristics of the detected signals one can estimate psychophysical status of the person and his activity.

REFERENCES

[1] Tursunhodzhaev H.A., Suharevskij O.I., Zalevskij T.S., etc. The Super-near range location for subsurface objects. Applied Radio Electronics, V.1, No.1, 2002, pp. 5 – 14.

[2] Kopejkin V.V., etc. Holographic subsurface radar: the hardware. Electromagnetic Waves and Electronic systems. 2003, V.8, No.10, pp. 66 – 70.

[3] Daniels, D.J. Surface-Penetrating Radar. – Published by IEE, London, UK, 1996.

[4] Ivashov, S.I., Sablin, V.N., Vasilyev, I.A. Wide-Span Systems of Mine Detection. – IEEE Aerospace & Electronic Systems Magazine, 1999, vol. 14, No. 5.

[5] Ivashov, S.I., Makarenkov, V.I., Razevig, V.V. et al. Remote Control Mine Detection System with GPR and Metal Detector. – Proceedings of the Eight International Conference on Ground Penetrating Radar, GPR'2000. – University of Queensland, Gold Coast, Queensland, Australia. May 23-26, 2000.

[6] Vasilyev, I.A., Ivashov. S.I., Makarenkov, V.I., etc. High resolution sounding of building structure using RF signal. - Radio engineering, 2001, No.8.

[7] Russians Launch Anti-Bugging Radar. – Microwave Journal, February 1998, vol. 41, No. 2, pp. 47, 48.

[8] Barnes, M.A., Nag, S., Payment, T. Covert situational awareness with handheld ultra-wideband short pulse radar. – SPIE Conference on "Radar Sensor Technology VI", Orlando, Fla. 19 Apr., 2001, Proc. SPIE. 2001. 4374.

[9] Bugaev A.S., Vasilyev, I.A., Ivashov. S.I., Razevig, V.V., Shejko A.P. Detection and remote diagnosis of people state beyond the obstacle using radar. Radio Engineering, No.7, 2003, pp. 42 – 47.

[10] Ivashov. S.I., Isaenko, V.N., Konstantinov, V.F. et al. GPR for Detection and Measurement of Filled up Excavations for Forensic Applications. – Proc. of the Seventh Int. Conference on Ground-Penetrating Radar, GPR'98. – University of Kansas, Lawrence, Kansas, USA, vol. 1, May 27-30, 1998.

[11] Greneker E.F. Radar Sensing of Heartbeat and Respiration at a Distance with Security Applications. – Proceedings of SPIE, Radar Sensor Technology II. Vol. 3066. – Orlando, Florida, April 1997.

[12] Immoreev, I.J., Samkov, S.V. Ultra Wideband (UWB) Radar for the Remote Measuring of Main Parameters of Patient's Vital Activity. – Radio Physics and Radio Astronomy (Ukraine), 2002, vol. 7, No. 4.

[13] Staderini E.M. UWB Radars in Medicine. – IEEE Aerospace and Electronic Systems Magazine. 2002, January.

[14] Lukin K. A., "Noise radar technology", Telecommunications and Radio Engineering, vol.55, No.12, pp.8-16, 2001.

[15] Lukin K. A., “The Principles of the Noise Radar Technology**”,** Proc. of the First International Workshop on the Noise Radar Technology, NRTW-2002, September 18-20, 2002,Yalta Hotel, Yalta, Crimea, Ukraine, pp.13-22 ,2003.

Accurate Radar Cross Section Modelling of Jet Inlets & Engines

Kwok Kee Chan
Chan Technologies Inc.
15 Links Lane
Brampton, Ontario L6Y 5H1
Canada

Silvester Wong and Edwin Riseborough
DRDC-Ottawa
3701 Carling Avenue
Ottawa, Ontario K1A 0Z4
Canada

kwok-kee.chan@rogers.com / Silvester.Wong@drdc-rddc.gc.ca / Ed.Riseborough@drdc-rddc.gc.ca

SUMMARY

Most of the industrial software codes used for the prediction of the radar cross-section (RCS) of aircrafts are based on ray tracing. While ray based methods give useful scattered fields from the skin of the aircraft illuminated by an incident plane wave, they largely fail to predict the returns from cavities onboard. As a possible enhancement to these ray-tracing programs, an auxiliary program based on the modal method was developed to predict the scattering of electrically large and complex jet inlets and engines. It is assumed here that these structures can be approximated by a series of rectangular, circular, coaxial and sectoral waveguide sections. Field matching technique is used to give the generalized scattering matrices of the junctions between these waveguide sections. By combining the scattering matrices of the waveguide sections representing the inlet and engine, an overall S-matrix is obtained. Knowing the modes induced at the inlet aperture by the incident wave, the scattered fields from the inlet and engine can be readily predicted in all directions. Such software has been developed. Monostatic RCS measurements of a 0.706m diameter test cylinder containing 30 skewed blades mounted on a centre shaft with a conical hub have been performed at X-band. The dimensions of the structure, the number and orientation of the blades are consistent with existing jet engines. Good agreement between predictions and measurements verify the developed software and analytical method used. This software could generate the database of RCS returns for a given engine over a wide range of aspect angles.

1.0 INTRODUCTION

High range resolution and inverse synthetic aperture radar are promising imaging methods that may be used for non-cooperative recognition of air targets. Both of these methods rely on comparing an observed target return with that from a signature database. It is not practical to generate such a database just from measurements simply because of the large number target types and configurations that have to be tested at a wide range of aspect angles. Further, hostile targets will not willingly submit to such measurements. Hence there is a need for a signature database that is computer generated. Current computer codes are able to predict the electromagnetic scattering from models of aircrafts with varying degree of accuracy that depended very

Paper presented at the RTO SET Symposium on "Target Identification and Recognition Using RF Systems", held in Oslo, Norway, 11-13 October 2004, and published in RTO-MP-SET-080.

much on the precision of the input CAD models. However, none is capable of simulating the significant RCS produced by jet inlets and engines that show up prominently in both HRR and ISAR signatures from in-flight measurements. To rectify this problem, auxiliary software capable of predicting the scattering from jet inlets and engines has been developed. The analysis method used is based on mode or field matching and generalized scattering matrices. Such an approach has been successfully used to treat simple inlet and engine models [2, 4, 5]. The computed scattered fields from the engines can be combined with those from the rest of the aircraft that are calculated using current computer codes to improve on the overall target response. A short description of the method employed is given in section 2. Comparisons of predictions and measurements are carried out in section 3 for a number of configurations. Good agreement is found in most of test cases and conclusion is drawn in section 4.

2.0 MODELLING OF JET INLETS AND ENGINES

A typical scattering problem is shown in Fig. 1 where the inlet is illuminated by an incident plane wave. The waveguide modes induced at the aperture S_g of the inlet are found by field matching [1]. The coefficient, $b_{li}^{(g)}$, of the *i th* guide mode induced by the *l th* space mode is given by

$$b_{li}^{(g)} = -\frac{\sqrt{\eta_i^{(g)}}}{\sqrt{\eta_l^{(s)}}} \iint_{S_g} \bar{e}_i^{(g)*} \bullet \bar{e}_l^{(s)} \, dS$$

This integral can be evaluated analytically for the four combinations between the TE and TM guide mode functions, $e_i^{(g)}$, and the TE and TM space mode functions, $e_l^{(s)}$. The mode impedance is given by η.

Once the induced modes are found, they are propagated into the inlet, which is approximated by a series of uniform waveguide sections. The stepped junctions and waveguide sections are characterized by their generalized scattering matrices, which are cascaded together to give a complete scattering description of the inlet. For a slanted or offset inlet, it is approximated by a series of partially overlapped waveguide sections as shown in Fig. 1. An efficient way of treating the partially overlap stepped junction, which consists of an input waveguide 1, an output waveguide 2 and the in-between common aperture represented as waveguide 0, is to consider all three waveguides together to give a S-matrix characterization of the junction.

$$[S_{11}] = 2\left[P^{(0,1)}\right][W]^{-1}\left[P^{(0,1)}\right]^T - [I] \qquad [S_{12}] = 2\left[P^{(0,1)}\right][W]^{-1}\left[P^{(0,2)}\right]^T$$

$$[S_{21}] = 2\left[P^{(0,2)}\right][W]^{-1}\left[P^{(0,1)}\right]^T = [S_{12}]^T \qquad [S_{22}] = 2\left[P^{(0,2)}\right][W]^{-1}\left[P^{(0,2)}\right]^T - [U]$$

$$[W] = \left[P^{(0,1)}\right]^T\left[P^{(0,1)}\right] + \left[P^{(0,2)}\right]^T\left[P^{(0,2)}\right]$$

$[P^{(0,1)}]$ and $[P^{(0,2)}]$ are the mode coupling matrices between wg. 0 & 1, and wg. 0 & 2 respectively. The coefficients of these matrices are given by the inner products of their mode vectors $\bar{e}_k$, $\bar{h}_k$ as

$$P_{mk}^{(0,1)} = \iint_{S_0} \left[\bar{e}_k^{(0)} \times \bar{h}_m^{(1)}\right] \bullet \hat{z} \, ds \qquad m = 1,.....,M \qquad k = 1,.....,K$$

$$P_{nk}^{(0,2)} = \iint_{S_0} \left[\bar{e}_k^{(0)} \times \bar{h}_n^{(2)}\right] \bullet \hat{z} \, ds \qquad n = 1,.....,N \qquad k = 1,.....,K$$

where there are K modes in waveguide 0, M modes in waveguide 1, and N modes in waveguide 2. These integrals may be evaluated analytically. *[U]* and *[I]* are unit matrices. The number of modes used in each waveguide section is set by the maximum cutoff wave number specified.

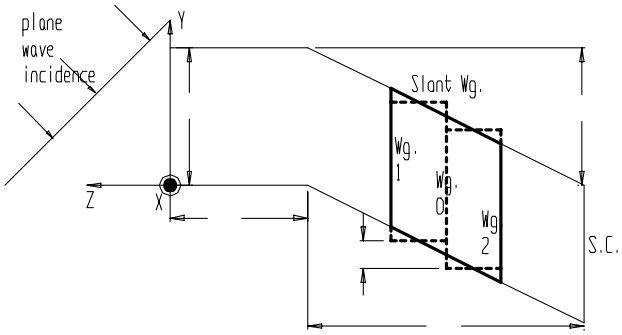

Fig. 1 Plane wave illumination of jet inlet

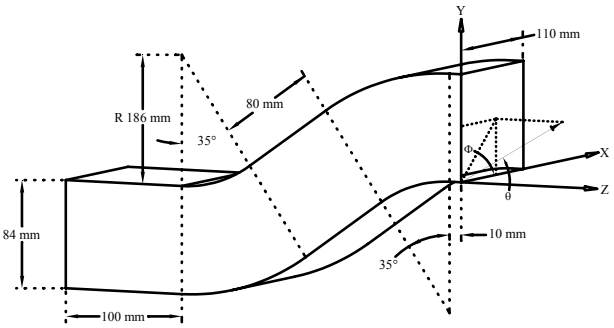

Fig. 2 S-shape Inlet

The general waveguide software was used to analyze the S-shape inlet of Fig. 2. Very good correlation is found between theory and measurement as demonstrated in [2]. Displacement steps between waveguide sections no larger than 0.1λ are sufficient to model a smooth curve inlet. At the end of the rectangular inlet, it transitions into a circular conical cylinder where the engine is located. Modal characterization of the rectangular to circular transition has also been developed. For the present paper, we will concentrate on the modelling of the engine with skewed blades.

The circular cylinder of the engine with the centre shaft is treated as a coaxial waveguide. Both the centre and outer conductors may be varying to represent a conical engine compartment. The centre hub is modelled by a series of stepped centre conductors. The blades mounted on the centre shaft, as shown in Fig. 3, are inclined at an angle with the axis of the engine.

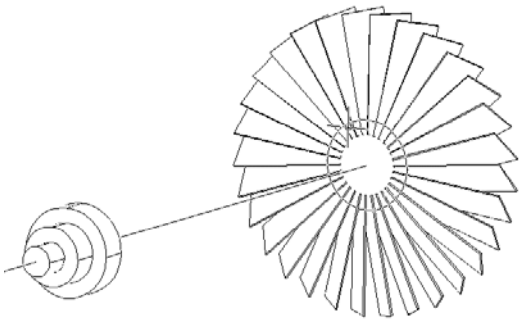

Fig. 3 Skewed blades and centre hub

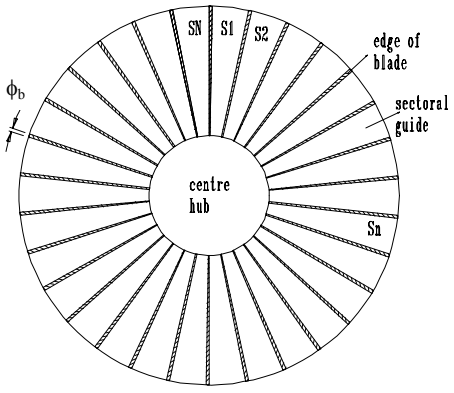

Fig. 4 Coaxial guide – blade junction

The generalized S-matrix characterization of the junction between coaxial waveguide and sectoral waveguides is found by field matching. This formulation is given by Chan [3]. The channel between a pair of skewed

blades is approximated by a slanted or curved sectoral waveguide, which is divided into a number of axially, translated and azimuthally rotated short straight waveguide sections. The S-matrix between two displaced sectoral waveguide sections are defined by the same matrix equations given above for partially overlapped rectangular waveguides. The difference here is the coupling integral can be evaluated in close form only for the azimuthal Φ variable. The integration along the radial direction must be done numerically. Recursive combination of this junction S-matrix and that of the adjacent straight section yields the resultant S-matrix of the slant blade channel. Thus a single stage of blades can now be characterized by the back-to-back combination of a coaxial waveguide to multiple sectoral waveguide junction interconnected by sections of slanted sectoral waveguides.

The S-matrix of the blades need only be computed once. If the blades are rotated, the resultant S-matrix is obtained through a transformation of the non-rotated matrix. A local coordinate system is attached to the blades and it rotates with them. For a complete representation of the fields both the V- and H- sets of modes in the local coordinate system are required. The analysis of the blades is carried out with these local sets of modes. A global coordinate system is placed at the aperture of the engine. The modes resulting from the plane wave illumination are expressed in the global coordinate system. The local system is rotated with respect to the global system by an angle ϕ_0. Because of mode orthogonality, the global TE (TM) V- or H- mode is resolved only into the local V'- and H'- types of TE (TM) mode. The transformation between the global incident modes (a^V, a^H) and the local incident modes ($a^{V'}$, $a^{H'}$) is simply given by

$$\begin{bmatrix} a^{V'} \\ a^{H'} \end{bmatrix} = \begin{bmatrix} C_{11} & C_{12} \\ C_{21} & C_{22} \end{bmatrix} \begin{bmatrix} a^{V} \\ a^{H} \end{bmatrix}$$

Here C_{11} and C_{22} are diagonal matrices with diagonal elements given by $\cos(m\phi_0)$, where m is the mode first index. C_{12} and C_{21} are rectangular matrices because certain modes are present in the V- set and not in the H- set. For instance, the TE_{0n} modes belong to the H-set only while the TM_{0n} modes are in the V-set only. The non-zero entries of C_{12} are given by $\sin(m\phi_0)$ for TM modes and $-\sin(m\phi_0)$ for TE modes. The non-zero elements of C_{21} are given by $-\sin(m\phi_0)$ for TM modes and $\sin(m\phi_0)$ for TE modes. If the reflection matrix of the blades in the local coordinate system is denoted by S_{11}, then the corresponding matrix in the global system is obtained from the transformation $C^T S_{11} C$, where T indicates transposition.

The S-matrices of various stages of blades and the inlet are combined to give the overall scattering parameters characterizing the jet engine. It should be mentioned that both propagating and evanescent modes are used in the field matching to model accurately each junction or structural change. However, only those accessible evanescent modes above a specified threshold are used for the S-matrix combination of the various junctions. This reduces significantly the order of the matrices involved in the computations. Knowing the S-matrix of the engine and the incident modes, the reflected modes at the inlet aperture are readily obtained. Using Kirchoff's diffraction integral, the scattered fields of the aperture modes in all directions are determined analytically.

3.0 VALIDATION OF MODEL

A test cylinder of 0.706 m diameter was fabricated out of metal ventilation duct. A centre shaft of diameter 0.224 m carrying 30 equally spaced blades that are inclined at 45° (stagger angle) to the longitudinal axis is placed inside the cylinder. The axial length of the blade region is 7.62 cm. At the back, the shaft extends 7.30 cm beyond the blade region and terminates into a circular shorting plate, which also forms the supporting structure. At the front of the shaft, a smooth conical hub of 0.164 m axial length is attached. There is an air

gap of 0.5 cm between the end of the blade and the cylinder wall. This facilitates the rotation, axial translation and placement of the blade assembly in an off circular enclosure. The blades are made out of 0.159 cm thick aluminum plates. The blades in the actual fabricated assembly are not identical and they are not normal to the shaft surface. A picture of the cylinder and blade assembly mounted for measurement is shown in Fig. 5. Absorbers were placed around the supporting structure to reduce external reflections.

Fig. 5 Test cylinder with skewed blade assembly

In our idealised approximation of this blade assembly, the blades extend all the way to the wall i.e. there is no air gap, and the blades are always normal to the shaft surface and cylinder wall. The constant thickness of the blade is replaced by a sectoral wall of included angle 0.373°. A sectoral guide of angle 11.627° then represents the blade channel. The twist angle of the blade, defined as the difference in the projected azimuthal ϕ-angles of the front and back edges of the blade, is 39.01°.

All the measurements reported here were taken at the DRDC outdoor test facility [7] using a pulsed radar with 200ns pulse width and 1KHz PRF. The cylinder was placed 125m away. The illuminating beamwidth was 2° AZ x 6° EL. The transmitting and receiving beams were horizontally polarized and only azimuth cuts were made. Hence all the measured monostatic scattered responses are for TM incidence. First, a conducting flat plate was placed at 1 m and 1.91 m inside the cylinder. The measured H-H RCS of the cylinder terminated with a flat plate is plotted in Figs. 6 and 7 for the two plate locations together with the predictions at 8.9 GHz. The data, normalized to the peak at boresight, are shown from -60° to +60° in the azimuth plane. As can be seen, the agreement between measurement and prediction is very good in both cases. There is extraneous reflection from the side or mounting support at the near-in angles and the test article is not symmetrical.

Next, the cylinder with the blade assembly is modelled and tested. In modal analysis, sufficient number of modes must be used to obtain result convergence. To treat the slanted blade channel, 2664 sectoral waveguide modes are used, with the highest approximating mode cutoff wavenumber $k_c = 6.5k_0$ where k_0 is the operating wavenumber. To represent the fields in the circular waveguide and coaxial waveguide regions, it is found that only modes with mode cutoff wavenumber less than $1.3k_0$ need be used. This is demonstrated in Fig. 8, where the RCS of the cylinder with the blade assembly is shown for the cases with $1.3k_0$ and $1.7k_0$ highest mode

cutoff wavenumber. Only small differences are observed between them. Plotted in Fig. 9 is the RCS at 8.9 GHz of the cylinder and blades with two different types of nose cones, 4-step and 6-step hubs of axial lengths 0.21m and 0.164m. These responses are for TE incidence and are more or less the same with minor changes.

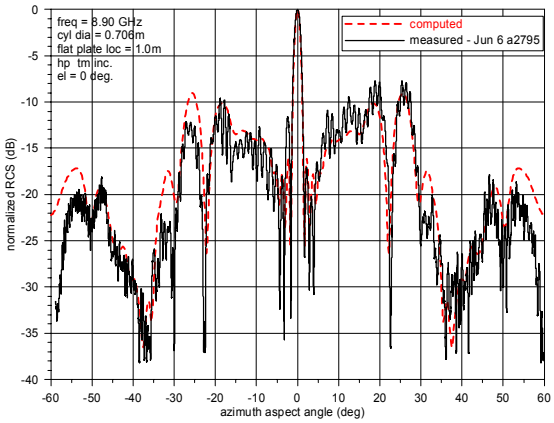

Fig. 6 RCS of cylinder with flat plate at 1m

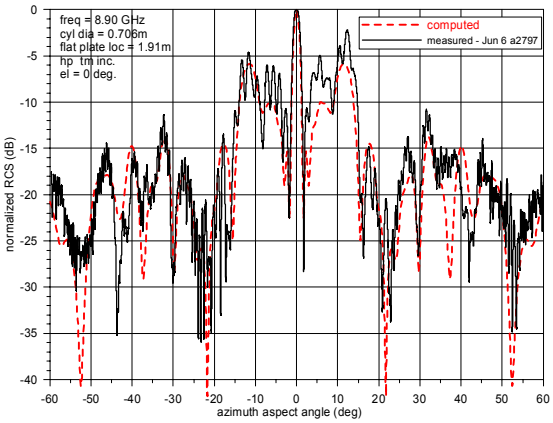

Fig. 7 RCS of cylinder with flat plate at 1.91m

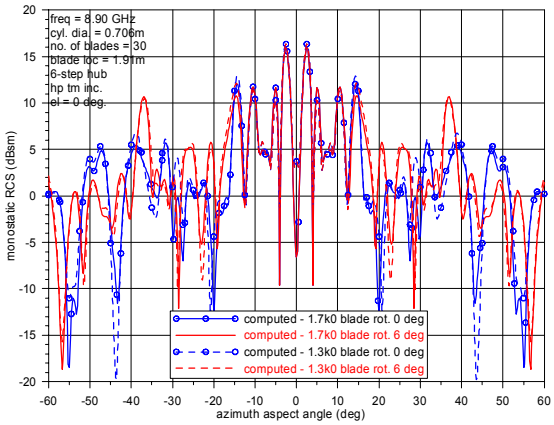

Fig. 8 RCS convergence of cylinder with different number of modes

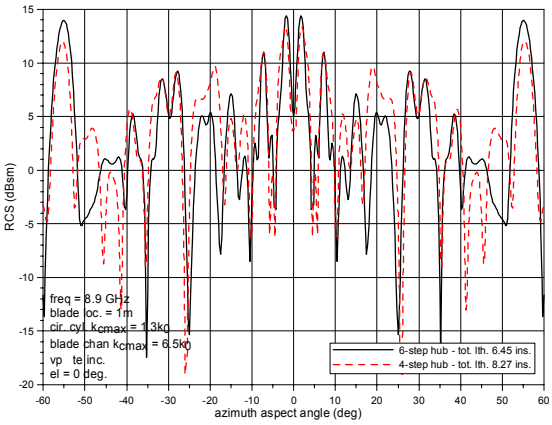

Fig. 9 RCS of blades with different centre hubs

Very often in the RCS modelling of the aircraft, the complexity of the blades in the engine is replaced by a flat plate at the same location. The consequences of this simplification can be seen in Figs. 10 and 11. Here the RCS of the cylinder with flat plate, flat plate with nose cone and skewed plates located 1m and 1.91m from the aperture are plotted for comparison at 8.9 GHz. At boresight, where there is a peak value for the flat plate with and without the nose cone, a null is observed for this particular inclined blades configuration. This is caused by the conversion of the lowest order TE_{11} mode, which carries the most power, into the propagating higher order modes by the single stage of blades. These higher order modes have maximum radiation in different off boresight directions. As a result, the peak backscatter field off axis for the blade assembly is approximately 14 dB below the on-axis maximum of the flat plate, which has been confirmed through measurement. The RCS of the skewed blades is also lowered by approximately the same amount at the other off normal aspect angles. Thus there is substantial error in the simplified model of this engine. Addition of a centre hub to the flat plate causes change only at the near-in aspect angles.

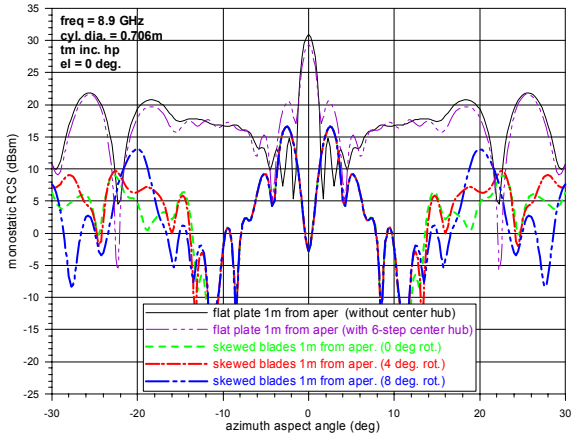

Fig. 10 RCS of cylinder with obstacle at 1m

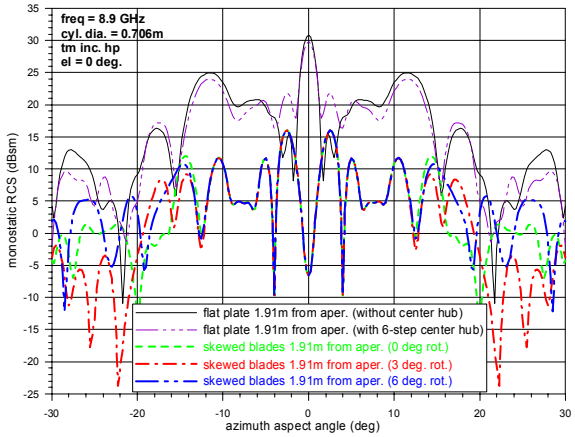

Fig. 11 RCS of cylinder with obstacle at 1.91m

The RCS of the cylinder containing the blade assembly with a smooth conical center hub was measured at 8.9, 9.1 and 9.2 GHz for TM incidence. The blades were placed at two locations, 1m and 1.91m from the aperture. The test data are normalized to the peak response and are plotted in Figs. 12 to 17 for azimuth aspect angles ranging from -60° to +60°. Shown on plots are the predicted RCS for comparison. The center conical hub of 0.163m axial length is approximated by a 6-section center conductor. The diameter of each section is 0.045m, 0.113m, 0.155m, 0.184m, 0.206m and 0.224m. For the circular guide and coaxial guide discontinuities, the highest cutoff wavenumber of the field approximating modes is $1.7k_0$. To represent the fields, the number of circular waveguide modes used is 6268. The number of coaxial guide modes in the respective hub section is 6252, 6108, 5964, 5852, 5744 and 5648. The blade channel field distribution is approximated by 2664 sectoral guide modes. The total memory requirement by the program is 3.6 GB. Each frequency run for any number of aspect angles and polarization states takes about 23 hours on a Sunblade 2000 running at 900MHz. It is possible to reduce the run time by decreasing the number of modes in the various regions with some impact on the computed scattered fields. It should be mentioned that this execution time is at least one to three orders of magnitude faster than existing ray-based or finite element based cavity analysis programs [6] that produce results with questionable accuracy for complex blade arrangement.

When comparing the measurements with the predictions, one should bear in mind that the measured data is a lot noisier due to a drop of 14 dB in the scattered power from the cylinder with the blades. At the test facility, the cylinder is mounted on an azimuth turntable. It is not possible to align the cylinder in elevation with the transmit/receive antenna. This misalignment will cause the two lobes on either side of the boresight direction to become asymmetrical, which is clearly evident here. Further, the computer model is an approximate representation of the test article, in that the air gap at the tips of the blades is ignored and all the blades are not the same. The computed results deal solely with the internal scattering of the cylinder and do not include the reflected fields from the outside of the cylinder or support structure, which is covered by flat absorbing sheets. Such external reflections cannot be eliminated from the measurements. Still, with the coincidence of the major lobes in both amplitude and direction, it can be said that there is fairly good agreement between the test and computed data.

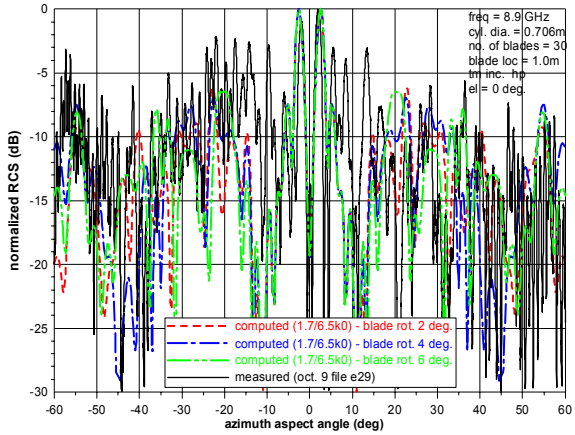

Fig. 12 RCS of cylinder with blades at 1m - 8.9 GHz

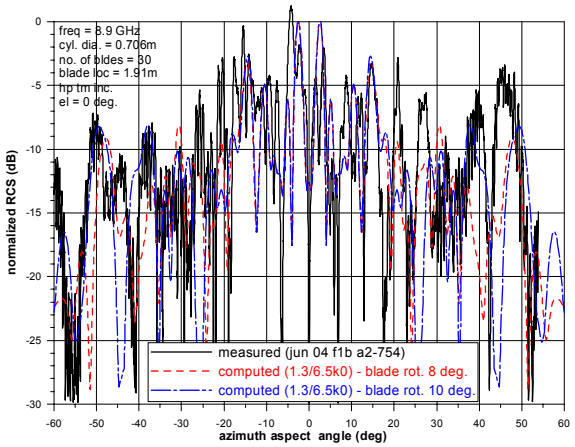

Fig. 13 RCS of cylinder with blades at 1.91m - 8.9 GHz

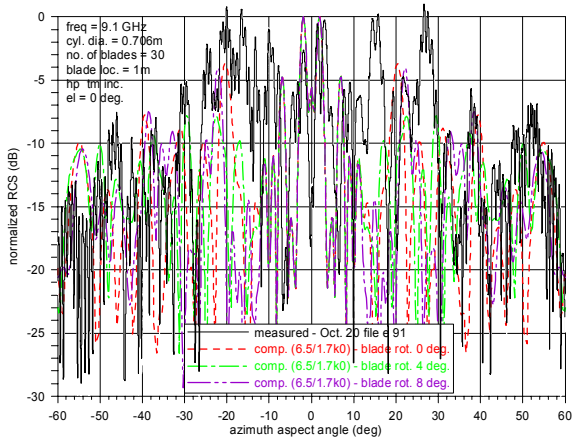

Fig. 14 RCS of cylinder with blades at 1m - 9.1 GHz

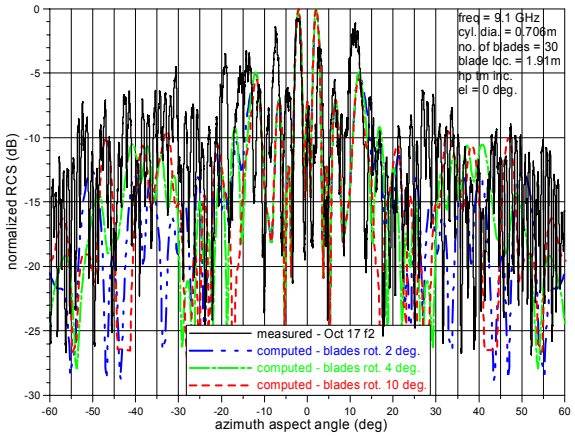

Fig. 15 RCS of cylinder with blades at 1.91m - 9.1 GHz

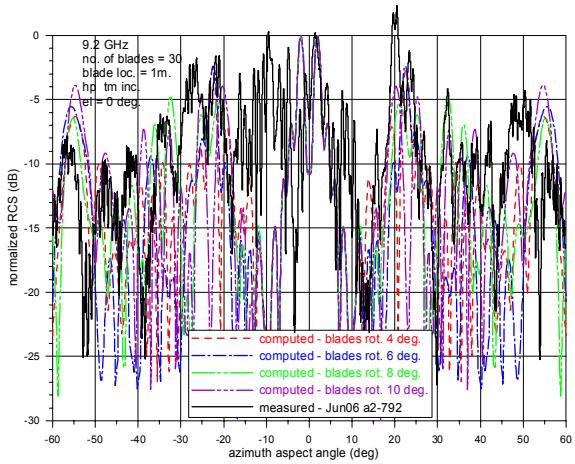

Fig. 16 RCS of cylinder with blades at 1m - 9.2 GHz

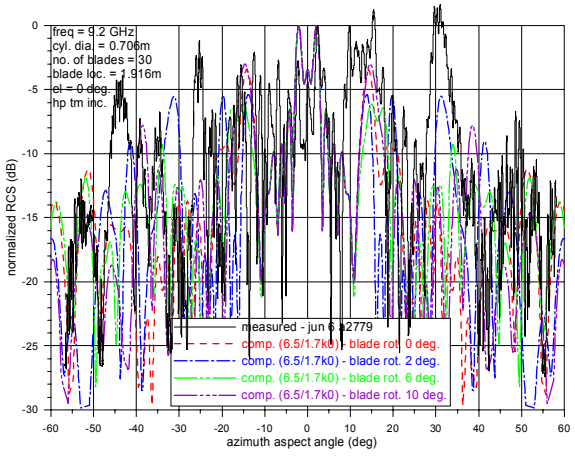

Fig. 17 RCS of cylinder with blades at 1.91m - 9.2 GHz

4.0 CONCLUSION

A procedure based on modal analysis has been presented for the analysis of jet inlets and engines. The complex geometry of a center hub and shaft with inclined blades is successfully treated. A test cylinder with a skewed blade assembly has been built and tested at X-band. Dimensions of the cylinder and blades are similar to those of the present day jet engines. The measured amplitudes of the backscatter fields agree well with the computer simulations. Even though a large number of modes are required for field representation in the cylinder and blade assembly, present day desktop computers can readily handle the computation workload and memory requirement. In this development, canonical waveguide sections are utilized to model the engine so that internal fields can be approximated by analytical modes. Similar modal approach may also be applied to non-standard engine and inlet cross-sections, where numerical modes that meet the boundary conditions are employed instead to provide efficient calculation of their RCS.

5.0 REFERENCES

[1] K.K. Chan and F. Tremblay: "Scattering from rotating blades in a cylinder", International Conference on Radar, Paris, France, May 1994, pp. 83-88.

[2] K.K. Chan and Silvester Wong: "Modal Approach to RCS Computation of Electrically Large Inlets", IEEE AP-S International Symposium, San Antonio, June 2002, Vol. 3, pp.114-117.

[3] K.K. Chan and F. Tremblay: "Mode matching analysis of metallic blades in a cylinder", IEEE AP-S International Symposium, Newport Beach, June 1995, Vol. 1, pp. 38-41.

[4] Anastassiu H.T. et. al., "Electromagnetic Scattering from Simple Jet Engine Models", IEEE Trans. on Ant. & Prop., 1996, Vol. 44, No.3, pp. 420-421

[5] Anastassiu H.T. and Volakis J.L.; "The Modal Matching Technique for Electromagnetic Scattering by Cylindrical Waveguide with Canonical Terminations", IEEE AP-S International Symposium, 1995, Vol. 3, pp. 26-29

[6] K.K. Chan and Silvester Wong: "Accurate RCS Prediction of Electrically Large Jet Inlets and Engines", Twelfth Intern. Conf. on Ant. & Prop., ICAP 2003, U.K., April 2003, Vol. 1, pp.253 - 256.

[7] S. Wong, E. Riseborough and G. Duff: "Experimental facility for measuring aircraft inlet/engine radar cross section", RTO-SET 080 Fall 2004 Symposium, Oslo, Norway, October 2004.

REPORT DOCUMENTATION PAGE

1. Recipient's Reference	2. Originator's References	3. Further Reference	4. Security Classification of Document
	RTO-MP-SET-080 AC/323(SET-080)TP/50	ISBN 92-837-1145-9	UNCLASSIFIED/ UNLIMITED

5. Originator

Research and Technology Organisation
North Atlantic Treaty Organisation
BP 25, F-92201 Neuilly-sur-Seine Cedex, France

6. Title

Target Identification and Recognition using RF Systems

7. Presented at/Sponsored by

The RTO Sensors and Electronics Technology Panel (SET) Symposium held in the Banner Hall at the Defence Museum, Akershus Fortress in Oslo, Norway on 11-13 October 2004.

8. Author(s)/Editor(s)	9. Date
Multiple	October 2004
10. Author's/Editor's Address	**11. Pages**
Multiple	450 (text) 37 (slides)

12. Distribution Statement

There are no restrictions on the distribution of this document. Information about the availability of this and other RTO unclassified publications is given on the back cover.

13. Keywords/Descriptors

Active detection
Aerial targets
CID (Combat Identification)
Cooperative techniques
Electronic countermeasures
Identification systems
Integrated systems
NCTI (Non-Cooperative Target Identification)
Non-Cooperative Target Recognition
Passive detection
Radar detection
Signal processing
Surface targets
Target acquisition
Target classification
Target recognition
Target signatures

14. Abstract

The purpose of this symposium was to review Non-Cooperative Target Identification/Recognition (NCTI/NCTR) R&D efforts available to NATO nations, suggest how and when this technology may contribute to an operational Combat Identification (CID) capability, and address coalition interoperability issues.

The symposium was organized along the following themes: NCTI/NCTR of air targets, surface targets, passive RF systems & technology, and countermeasures against NCTI/NCTR. There were twenty-three oral presentations in the classified sessions, eighteen unclassified oral presentations and sixteen unclassified posters open to Partnership-for-Peace (PfP) nations presentations.

NORTH ATLANTIC TREATY ORGANISATION

RESEARCH AND TECHNOLOGY ORGANISATION

BP 25
F-92201 NEUILLY-SUR-SEINE CEDEX • FRANCE
Télécopie 0(1)55.61.22.99 • E-mail mailbox@rta.nato.int

DIFFUSION DES PUBLICATIONS

RTO NON CLASSIFIEES

Les publications de l'AGARD et de la RTO peuvent parfois être obtenues auprès des centres nationaux de distribution indiqués ci-dessous. Si vous souhaitez recevoir toutes les publications de la RTO, ou simplement celles qui concernent certains Panels, vous pouvez demander d'être inclus soit à titre personnel, soit au nom de votre organisation, sur la liste d'envoi.

Les publications de la RTO et de l'AGARD sont également en vente auprès des agences de vente indiquées ci-dessous.

Les demandes de documents RTO ou AGARD doivent comporter la dénomination « RTO » ou « AGARD » selon le cas, suivi du numéro de série. Des informations analogues, telles que le titre est la date de publication sont souhaitables.

Si vous souhaitez recevoir une notification électronique de la disponibilité des rapports de la RTO au fur et à mesure de leur publication, vous pouvez consulter notre site Web (www.rta.nato.int) et vous abonner à ce service.

CENTRES DE DIFFUSION NATIONAUX

ALLEMAGNE
Streitkräfteamt / Abteilung III
Fachinformationszentrum der
Bundeswehr (FIZBw)
Friedrich-Ebert-Allee 34, D-53113 Bonn

BELGIQUE
Etat-Major de la Défense
Département d'Etat-Major Stratégie
ACOS-STRAT – Coord. RTO
Quartier Reine Elisabeth
Rue d'Evère, B-1140 Bruxelles

CANADA
DSIGRD2
Bibliothécaire des ressources du savoir
R et D pour la défense Canada
Ministère de la Défense nationale
305, rue Rideau, 9e étage
Ottawa, Ontario K1A 0K2

DANEMARK
Danish Defence Research Establishment
Ryvangs Allé 1, P.O. Box 2715
DK-2100 Copenhagen Ø

ESPAGNE
SDG TECEN / DGAM
C/ Arturo Soria 289
Madrid 28033

ETATS-UNIS
NASA Center for AeroSpace
Information (CASI)
Parkway Center, 7121 Standard Drive
Hanover, MD 21076-1320

FRANCE
O.N.E.R.A. (ISP)
29, Avenue de la Division Leclerc
BP 72, 92322 Châtillon Cedex

GRECE (Correspondant)
Defence Industry & Research
General Directorate, Research Directorate
Fakinos Base Camp, S.T.G. 1020
Holargos, Athens

HONGRIE
Department for Scientific Analysis
Institute of Military Technology
Ministry of Defence
H-1525 Budapest P O Box 26

ISLANDE
Director of Aviation
c/o Flugrad
Reykjavik

ITALIE
Centro di Documentazione
Tecnico-Scientifica della Difesa
Via XX Settembre 123
00187 Roma

LUXEMBOURG
Voir Belgique

NORVEGE
Norwegian Defence Research Establishment
Attn: Biblioteket
P.O. Box 25, NO-2007 Kjeller

PAYS-BAS
Royal Netherlands Military
Academy Library
P.O. Box 90.002
4800 PA Breda

POLOGNE
Armament Policy Department
218 Niepodleglosci Av.
00-911 Warsaw

PORTUGAL
Estado Maior da Força Aérea
SDFA – Centro de Documentação
Alfragide
P-2720 Amadora

REPUBLIQUE TCHEQUE
LOM PRAHA s. p.
o. z. VTÚLaPVO
Mladoboleslavská 944
PO Box 18
197 21 Praha 9

ROYAUME-UNI
Dstl Knowledge Services
Information Centre, Building 247
Dstl Porton Down
Salisbury
Wiltshire SP4 0JQ

TURQUIE
Milli Savunma Bakanlığı (MSB)
ARGE ve Teknoloji Dairesi Başkanlığı
06650 Bakanliklar – Ankara

AGENCES DE VENTE

NASA Center for AeroSpace Information (CASI)
Parkway Center, 7121 Standard Drive
Hanover, MD 21076-1320
ETATS-UNIS

The British Library Document Supply Centre
Boston Spa, Wetherby
West Yorkshire LS23 7BQ
ROYAUME-UNI

Canada Institute for Scientific and Technical Information (CISTI)
National Research Council
Acquisitions, Montreal Road, Building M-55
Ottawa K1A 0S2, CANADA

Les demandes de documents RTO ou AGARD doivent comporter la dénomination « RTO » ou « AGARD » selon le cas, suivie du numéro de série (par exemple AGARD-AG-315). Des informations analogues, telles que le titre et la date de publication sont souhaitables. Des références bibliographiques complètes ainsi que des résumés des publications RTO et AGARD figurent dans les journaux suivants :

Scientific and Technical Aerospace Reports (STAR)
STAR peut être consulté en ligne au localisateur de ressources uniformes (URL) suivant:
http://www.sti.nasa.gov/Pubs/star/Star.html
STAR est édité par CASI dans le cadre du programme NASA d'information scientifique et technique (STI)
STI Program Office, MS 157A
NASA Langley Research Center
Hampton, Virginia 23681-0001
ETATS-UNIS

Government Reports Announcements & Index (GRA&I)
publié par le National Technical Information Service
Springfield
Virginia 2216
ETATS-UNIS
(accessible également en mode interactif dans la base de données bibliographiques en ligne du NTIS, et sur CD-ROM)

NORTH ATLANTIC TREATY ORGANISATION

RESEARCH AND TECHNOLOGY ORGANISATION

BP 25
F-92201 NEUILLY-SUR-SEINE CEDEX • FRANCE
Télécopie 0(1)55.61.22.99 • E-mail mailbox@rta.nato.int

DISTRIBUTION OF UNCLASSIFIED RTO PUBLICATIONS

AGARD & RTO publications are sometimes available from the National Distribution Centres listed below. If you wish to receive all RTO reports, or just those relating to one or more specific RTO Panels, they may be willing to include you (or your Organisation) in their distribution.

RTO and AGARD reports may also be purchased from the Sales Agencies listed below.

Requests for RTO or AGARD documents should include the word 'RTO' or 'AGARD', as appropriate, followed by the serial number. Collateral information such as title and publication date is desirable.

If you wish to receive electronic notification of RTO reports as they are published, please visit our website (www.rta.nato.int) from where you can register for this service.

NATIONAL DISTRIBUTION CENTRES

BELGIUM
Etat-Major de la Défense
Département d'Etat-Major Stratégie
ACOS-STRAT – Coord. RTO
Quartier Reine Elisabeth
Rue d'Evère
B-1140 Bruxelles

CANADA
DRDKIM2
Knowledge Resources Librarian
Defence R&D Canada
Department of National Defence
305 Rideau Street
9th Floor
Ottawa, Ontario K1A 0K2

CZECH REPUBLIC
LOM PRAHA s. p.
o. z. VTÚLaPVO
Mladoboleslavská 944
PO Box 18
197 21 Praha 9

DENMARK
Danish Defence Research Establishment
Ryvangs Allé 1
P.O. Box 2715
DK-2100 Copenhagen Ø

FRANCE
O.N.E.R.A. (ISP)
29, Avenue de la Division Leclerc
BP 72
92322 Châtillon Cedex

GERMANY
Streitkräfteamt / Abteilung III
Fachinformationszentrum der Bundeswehr (FIZBw)
Friedrich-Ebert-Allee 34
D-53113 Bonn

GREECE (Point of Contact)
Defence Industry & Research General Directorate, Research Directorate
Fakinos Base Camp, S.T.G. 1020
Holargos, Athens

HUNGARY
Department for Scientific Analysis
Institute of Military Technology
Ministry of Defence
H-1525 Budapest P O Box 26

ICELAND
Director of Aviation
c/o Flugrad, Reykjavik

ITALY
Centro di Documentazione Tecnico-Scientifica della Difesa
Via XX Settembre 123
00187 Roma

LUXEMBOURG
See Belgium

NETHERLANDS
Royal Netherlands Military Academy Library
P.O. Box 90.002
4800 PA Breda

NORWAY
Norwegian Defence Research Establishment
Attn: Biblioteket
P.O. Box 25, NO-2007 Kjeller

POLAND
Armament Policy Department
218 Niepodleglosci Av.
00-911 Warsaw

PORTUGAL
Estado Maior da Força Aérea
SDFA – Centro de Documentação
Alfragide, P-2720 Amadora

SPAIN
SDG TECEN / DGAM
C/ Arturo Soria 289
Madrid 28033

TURKEY
Milli Savunma Bakanlığı (MSB)
ARGE ve Teknoloji Dairesi Başkanlığı
06650 Bakanliklar – Ankara

UNITED KINGDOM
Dstl Knowledge Services
Information Centre, Building 247
Dstl Porton Down
Salisbury, Wiltshire SP4 0JQ

UNITED STATES
NASA Center for AeroSpace Information (CASI)
Parkway Center, 7121 Standard Drive
Hanover, MD 21076-1320

SALES AGENCIES

NASA Center for AeroSpace Information (CASI)
Parkway Center
7121 Standard Drive
Hanover, MD 21076-1320
UNITED STATES

The British Library Document Supply Centre
Boston Spa, Wetherby
West Yorkshire LS23 7BQ
UNITED KINGDOM

Canada Institute for Scientific and Technical Information (CISTI)
National Research Council
Acquisitions
Montreal Road, Building M-55
Ottawa K1A 0S2, CANADA

Requests for RTO or AGARD documents should include the word 'RTO' or 'AGARD', as appropriate, followed by the serial number (for example AGARD-AG-315). Collateral information such as title and publication date is desirable. Full bibliographical references and abstracts of RTO and AGARD publications are given in the following journals:

Scientific and Technical Aerospace Reports (STAR)
STAR is available on-line at the following uniform resource locator:
http://www.sti.nasa.gov/Pubs/star/Star.html
STAR is published by CASI for the NASA Scientific and Technical Information (STI) Program
STI Program Office, MS 157A
NASA Langley Research Center
Hampton, Virginia 23681-0001
UNITED STATES

Government Reports Announcements & Index (GRA&I)
published by the National Technical Information Service
Springfield
Virginia 2216
UNITED STATES
(also available online in the NTIS Bibliographic Database or on CD-ROM)

ISBN 92-837-1145-9